NATO Security through Science Series - C:
Environmental Security

Remote Sensing of the Atmosphere for Environmental Security

Edited by
Agnès Perrin
Najate Ben Sari-Zizi
Jean Demaison

Springer

NATO OTAN

This publication is supported by: The NATO Programme for Security through Science

Remote Sensing of the Atmosphere for Environmental Security

NATO Security through Science Series

This Series presents the results of scientific meetings supported under the NATO Programme for Security through Science (STS).

Meetings supported by the NATO STS Programme are in security-related priority areas of Defence Against Terrorism or Countering Other Threats to Security. The types of meeting supported are generally "Advanced Study Institutes" and "Advanced Research Workshops". The NATO STS Series collects together the results of these meetings. The meetings are co-organized by scientists from NATO countries and scientists from NATO's "Partner" or "Mediterranean Dialogue" countries. The observations and recommendations made at the meetings, as well as the contents of the volumes in the Series, reflect those of participants and contributors only; they should not necessarily be regarded as reflecting NATO views or policy.

Advanced Study Institutes (ASI) are high-level tutorial courses to convey the latest developments in a subject to an advanced-level audience

Advanced Research Workshops (ARW) are expert meetings where an intense but informal exchange of views at the frontiers of a subject aims at identifying directions for future action

Following a transformation of the programme in 2004 the Series has been re-named and re-organised. Recent volumes on topics not related to security, which result from meetings supported under the programme earlier, may be found in the NATO Science Series.

The Series is published by IOS Press, Amsterdam, and Springer, Dordrecht, in conjunction with the NATO Public Diplomacy Division.

Sub-Series

A. Chemistry and Biology	Springer
B. Physics and Biophysics	Springer
C. Environmental Security	Springer
D. Information and Communication Security	IOS Press
E. Human and Societal Dynamics	IOS Press

http://www.nato.int/science
http://www.springer.com
http://www.iospress.nl

Series C: Environmental Security

Remote Sensing of the Atmosphere for Environmental Security

edited by

Agnès Perrin
Laboratoire Interuniversitaire des Systèmes Atmosphériques,
CNRS, Universités Paris VII et XII, Créteil, France

Najate Ben Sari-Zizi
Laboratoire de Spectronomie, Département de Physique,
Faculté des Sciences de Rabat, Université Mohammed V-Agdal,
Rabat, Morocco

and

Jean Demaison
Laboratoire de Physique des Lasers, Atomes et Molécules, UMR CNRS,
Université des Sciences et Technologies de Lille, Villeneuve d'Ascq, France

Springer

Published in cooperation with NATO Public Diplomacy Division

Proceedings of the NATO Advanced Research Workshop on
Remote Sensing of the Atmosphere for Environmental Security
Rabat, Morocco
16–19 November 2005

A C.I.P. Catalogue record for this book is available from the Library of Congress.

ISBN-10 1-4020-5089-5 (PB)
ISBN-13 978-1-4020-5089-3 (PB)
ISBN-10 1-4020-5088-7 (HB)
ISBN-13 978-1-4020-5088-6 (HB)
ISBN-10 1-4020-5090-9 (e-book)
ISBN-13 978-1-4020-5090-9 (e-book)

Published by Springer,
P.O. Box 17, 3300 AA Dordrecht, The Netherlands.

www.springer.com

Printed on acid-free paper

Printed in the Netherlands.

Table of contents

PREFACE

AGNES PERRIN[1]
Laboratoire Interuniversitaire des Systèmes Atmosphériques (LISA), UMR CNRS 7583, Universités Paris 12&7 and CNRS, 61 av. du Général de Gaulle, 94010 Créteil Cédex, France

NAJATE BEN SARI-ZIZI
Laboratoire de Spectronomie, Département de Physique, Faculté des Sciences de Rabat, Université Mohammed V- Agdal,
Avenue Ibn Battouta B.P, 1014, Rabat-Maroc, Morocco

JEAN DEMAISON
Laboratoire de Physique des Lasers, Atomes et Molécules, UMR CNRS 8523, Université des Sciences et Technologies de Lille, F-59655 Villeneuve d'Ascq, France

Recent ecological disasters like, in 2005, the forest fires in Portugal, hurricane Katrina in the USA, and recurrent drought events in many countries of the African continent, make human beings aware of changes in the Earth's climate. At the present time anthropogenic activities lead to the emission of greenhouse gases, pollutants, aerosols and ozone depleting substances and the scientific community in general feels responsible for understanding how changes in atmospheric chemistry can affect the Earth's climate. An Advanced Research Workshop (ARW) with a relatively limited number of participants is highly favorable for close personal contacts and can generate collaborations between advanced and young researchers from NATO, "eligible partner" and "Mediterranean dialogue" countries or, at the very least, to improve the links between them. The idea to organize in 2005 at Rabat (Morocco) an ARW on "Remote Sensing of the Atmosphere for Environmental Security" emerged as soon as NATO opened in 2003 the opportunity to localize such a scientific workshop in the countries of the "Mediterranean dialogue" in the framework of the "Security through Science" programme. The major reason was that a long tradition of research collaboration in molecular physics already exists between the Moroccan laboratory of "Spectronomie de la Faculté des Sciences de Rabat" and various European laboratories (France, Germany,

[1] To whom correspondence should be addressed: Agnès Perrin, LISA, Universités Paris 12 et 7 &t CNRS, bat P1, 61 Avenue du Général de Gaulle, 94010 Créteil (France) ; Email : perrin@lisa.univ-paris12.fr

Czech Republic), among them the French LISA laboratory (Laboratoire Inter-universitaire de Systèmes Atmosphériques). Two women, Dr. Agnès Perrin (CNRS, Universities Paris 12 & 7, Créteil, France) and Prof. Najate Ben Sari-Zizi (Faculty of Sciences, University Mohammed V-Agdal, Rabat, Morocco) acted as co-directors of this ARW, and this also was an opportunity to give value to the new issue of the status of Moroccan women (Moudawana) which was promulgated in 2003. The present ARW effectively gathered, during three working days, 50 participants from 18 nationalities: 12 NATO countries, 2 eligible partner countries and 4 Mediterranean countries. During this ARW, 18 invited and contributed talks were given, together with the presentation of 24 poster papers, and in this way much new material was presented and a very efficient flow of information was achieved.

These proceedings contain the texts of all invited and contributed oral presentations together with the contents of some posters. The chapters in this volume are divided among various different areas.

The first part of this document describes the current capabilities of various satellite experiments which are performing measurements of the Earth's atmosphere. For example, some of the results obtained recently by three experiments onboard the ENVISAT Environment Satellite, namely, the Global Ozone Monitoring Experiment (GOME), the SCanning Imaging Absorption spectroMeter for Atmospheric CHartographY (SCIAMACHY) and the Michelson Interferometer for Passive Atmospheric Sounding (MIPAS) are presented.

For the analysis of spectra recorded by these instruments it is necessary to make good use of efficient radiative transfer codes. These computer codes need as input, a dataset of high quality spectroscopic parameters which can be generated only through a careful analysis of high quality laboratory measurements.

In addition some of the future satellite missions which are under preparation at the European Space Agency (ESA) are briefly described.

The characterisation of pollution in urban areas is of universal concern. The extreme variability of properties of the aerosols in arid and semi arid areas is presented in the context of an experiment performed at Cairo (in Egypt). Also, the growing lack of water in many countries of the Mediterranean area is a large subject of great concern, and recent studies have shown that it is possible to quantify the integrated water vapour in the line of sight of the GPS (Global Position System) satellites.

Finally, the understanding of climate chemistry couplings requires ground based and satellite information to be validated and confronted with the results of chemical transport and atmospheric models. These intercomparisons and validations can be performed when the results are collected in dedicated websites and/or are discussed in the frame of

international agencies and associations. Examples of such comparisons are presented in this book.

We would like to express our deep gratitude to NATO for the generous grant that made it possible to organize the workshop on an international basis. Also significant help, kind invitations, and guest accommodations from Moroccan Institutions as the "Faculté des Sciences de Rabat", the "Université Mohammed V-Agdal" and the "Centre National pour la Recherche Scientifique et Technique" are gratefully acknowledged. Finally we thank the "Ether" French atmospheric chemistry program for additional financial support.

SPECTROSCOPIC MEASUREMENTS OF TROPOSPHERIC COMPOSITION FROM SATELLITE MEASUREMENTS IN THE ULTRAVIOLET AND VISIBLE: STEPS TOWARD CONTINUOUS POLLUTION MONITORING FROM SPACE

KELLY CHANCE
Harvard-Smithsonian Center for Astrophysics, Atomic and Molecular Physics Division, 60 Garden Street, Cambridge, MA, 02138, USA

Abstract. This chapter reviews the current capabilities for ultraviolet and visible spectroscopic measurements of the Earth's troposphere, and discusses what remains to be achieved in the short term to enable global, continuous measurements of atmospheric pollution from space to be undertaken. Challenges in instrumentation, spectroscopy, radiative transfer modeling, and retrievals are discussed. Current and planned satellite instruments with the capability to make tropospheric measurements in the ultraviolet and visible, with their measurement properties, spectral coverage, and target molecules, are presented. Measurement examples are taken from recent work done at the Harvard-Smithsonian Center for Astrophysics, together with our colleagues at a number of institutions. The examples include global tropospheric ozone (O_3) measurements from the nadir geometry; global tropospheric nitrogen dioxide (NO_2); bromine oxide (BrO) in the polar spring, and from salt lakes and volcanoes; global tropospheric formaldehyde (HCHO); and preliminary measurements of glyoxal (CHOCHO). Except for a few remaining developments, the field is shown to be sufficiently mature that global measurements of atmospheric pollution from space may be undertaken.

Keywords: ultraviolet spectroscopy; visible spectroscopy; atmospheric remote sensing; tropospheric composition; radiative transfer modeling; chemistry and transport modeling

A. Perrin et al. (eds.), Remote Sensing of the Atmosphere for Environmental Security, 1–25.

1. Introduction

Since the Scanning Imaging Absorption Spectrometer for Atmospheric Chartography (SCIAMACHY) instrument was proposed[1,2] the capability to measure tropospheric pollutants other than ozone (*cf.* Refs. 3,4) and volcanic sulfur dioxide (SO_2; *cf.* ref. 5) from space using ultraviolet and visible spectroscopy has gradually become established.

It is now possible to make tropospheric measurements of a number of chemical constituents, and to study their sources, sinks, transport, and transformation. This provides critical information on tropospheric oxidation chemistry and pollution of the lower atmosphere, and contributes to process studies, including intercontinental transport of pollution. In addition to O_3 and volcanic SO_2, there are limited measurements of anthropogenic SO_2,[6] as well as the examples cited in the abstract, which are discussed in more detail below. Aerosol and cloud measurements in the ultraviolet and visible are not included here although they are, of course, also of primary importance. In particular, cloud measurements may now be made using spectroscopic methods.[7]

This chapter provides an overview of current results and capabilities which show how ultraviolet and visible spectroscopy is used to elucidate important properties about the Earth's troposphere. This is now a sizable field of research, with some dozen Earth satellites now performing measurements or being planned or prepared for launch. This review uses examples from research done at the Harvard-Smithsonian Center for Astrophysics (CfA), http://cfa-www.harvard.edu/atmosphere/, along with our collaborators. It is not fully inclusive of techniques, groups, and results, due to space limitations. It is intended to summarize many of the technical issues involved in data analysis, show by example the power of this type of measurement, and provide a convenient starting place for further inquiries. There are a number of other active groups performing similar and related work whose websites should be consulted for a broader view.[8]

An overview of the UV/visible atmosphere and the basic measurement techniques is presented, followed by a discussion of issues in algorithm physics, a survey of current and planned instruments, and illustrative examples of the application of UV/visible measurements to tropospheric process studies. The paper will conclude with a brief synopsis of the current state of measurements with respect to requirements for global pollution monitoring from satellites in geostationary orbits.

A distinction is made here between a spectrometer, which makes spectroscopic measurements over a substantial wavelength range at moderate to high spectral resolution, normally of multiple species when being used as an atmospheric instrument, and an instrument measuring at

several wavelength bands to measure (normally) one species. Instruments at both extremes have contributed historically and continue to do so, although there is a marked tendency in the UV/visible to now employ spectrometers with array-type detectors to cover large portions of the spectrum at 0.2-1.0 nm spectral resolution. These measurements are emphasized here.

2. The UV/Visible atmosphere

The solar spectrum can be roughly approximated as a blackbody at 5900 K. The reality, for detailed spectroscopic measurements, is much more complicated. Figure 1 (top) shows a low resolution extraterrestrial solar spectrum (the Fraunhofer spectrum) over much of the UV/visible region;[9-11] Figure 1 (bottom) shows a detailed section of the solar spectrum in a region where NO_2 is commonly measured from space.[9]

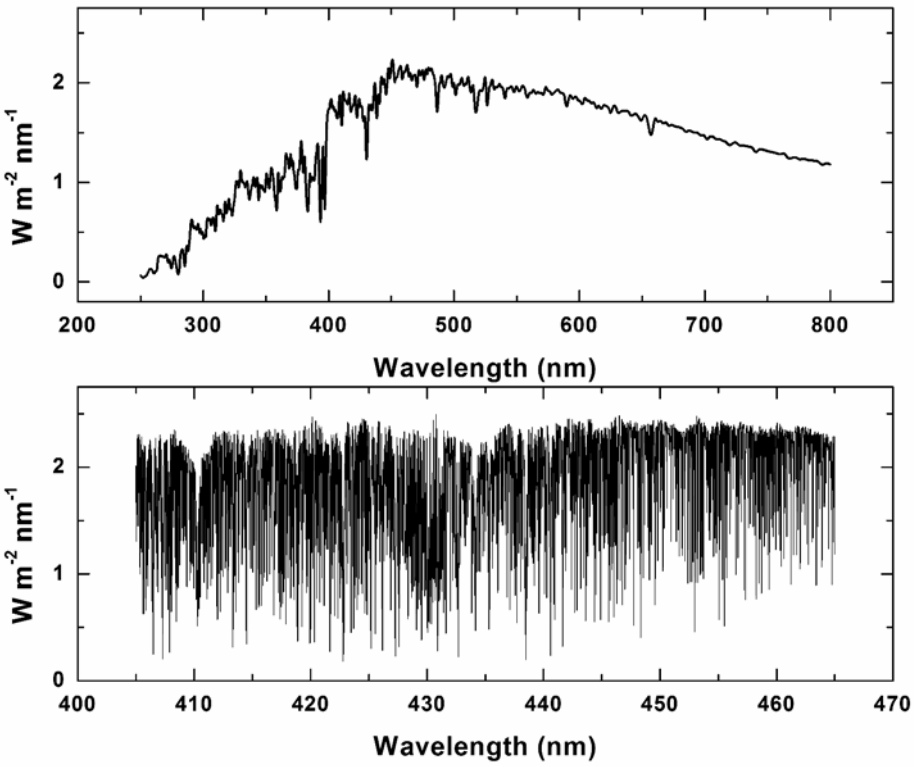

Figure 1. The low resolution extraterrestrial solar spectrum over much of the UV/visible region (top); a detailed section of the solar spectrum in a region where NO_2 is commonly measured from space (bottom).

The source spectrum is seen to be quite complex. To the extent that measurements correspond to simple Bouguet (or Lambert-Beer) absorption this would not present a particular difficulty. In practice, because of the Ring effect (discussed below in **Algorithm Physics**), a detailed knowledge of the solar spectrum is required, particularly for some of the molecules with small absorption: These molecules (including NO_2, BrO, HCHO, CHOCHO, SO_2, and, in parts of the spectrum, O_3) are the most important tropospheric species to be measured from space in this spectral region. Figure 2 shows an overview of the absorptions due to molecules that are now commonly measured from space in the nadir geometry.

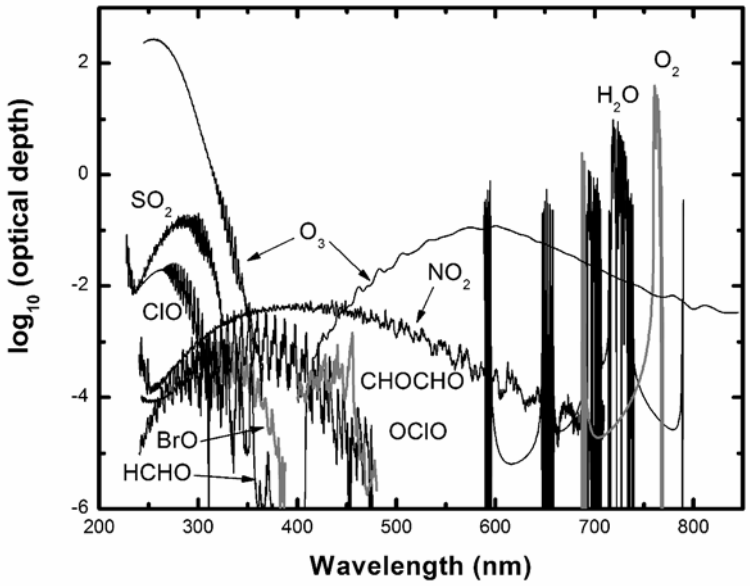

Figure 2. Typical absorptions due to molecules that are now commonly measured from space in the nadir geometry.

Absorptions are for typical measurement geometry and atmospheric concentrations and, for tropospheric gases, under conditions of moderate enhancement, except that SO_2 is increased to an amount typical for a volcanic source and ClO and OClO (stratospheric species) are increased to amounts typically seen in the Antarctic polar vortex. The effects of clouds and of Rayleigh scattering can be gauged from Figure 3, which shows back scattered albedo spectra ($\equiv \pi R/\mu_0 I_0$, where R is the radiance, μ_0 the cosine of the solar zenith angle, and I_0 the irradiance) from Global Ozone Monitoring Experiment (GOME) measurements[12] for two extreme examples. The highest albedo scene, corresponding to full coverage by high clouds, is

white and quite bright, due to the cloud reflectance; the lowest albedo case is a cloud-free scene over the ocean illustrating the low reflectance by water (less than 2% at the infrared end) and the increasing contribution from Rayleigh scattering at shorter wavelengths, as the radiation penetrates to lower altitudes for this cloud-free scene. The inverted Fraunhofer structure in these spectra, most visible below 400 nm, is due to the incomplete cancellation of the structure cause by the Ring effect, discussed below.

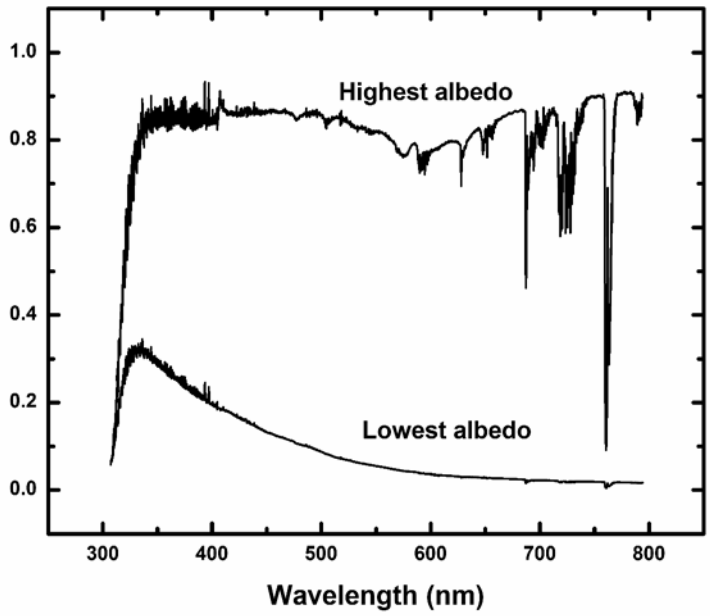

Figure 3. Back scattered albedo spectra from GOME measurements for two extreme examples. The highest albedo scene, corresponding to full coverage by high clouds, is white and quite bright, due to the cloud reflectance; the lowest albedo case is a cloud-free scene over the ocean.

3. Measurement techniques

UV/visible measurements of the atmosphere are made in one of three basic measurement geometries: 1. Nadir - the back scattered light is measured in a geometry where the line of sight intersects the Earth's surface. The light source is solar radiation back scattered from a combination of surface reflectance and cloud, aerosol and Rayleigh scattering. 2. Occultation - The light source is direct illumination by the Sun (or, less frequently, the Moon or stars). 3. Limb scattering - The light source is Rayleigh scattering of solar light in the limb geometry. Information from occultation and limb

scattering measurements is generally limited to the stratosphere and upper troposphere. Most of the information on tropospheric composition, particularly for lower tropospheric pollution studies, comes from nadir measurements although, for O_3 and NO_2, the use of limb-nadir subtraction has been investigated for use in improving tropospheric retrievals.[13]

Analysis of nadir measurements is most commonly made using either fitting to determine a total slant column (SC) abundance, followed by adjustment to determine the vertical column (VC) abundance, or by directly fitting to details in the spectrum to determine a vertical column amount or profile. For slant column measurements, spectra may be fitted by a variety of methods, ranging from directly fitting to the radiance[14] to fitting of a low-pass filtered version of $ln(R/I_0)$ (*i.e.*, DOAS[15]).

Vertical column abundances are then determined by division of the SC by an Air Mass Factor (AMF), which is simply the ratio of the slant to vertical column, determined from knowledge of the vertical distribution, either from climatology or from assimilation of data into chemistry and transport modeling,[16,17] and radiative transfer calculation to take into account Rayleigh and other scattering as well as the spherical atmospheric geometry (*cf*. Refs. 15,16). There may be further correction to account for the (sometimes strong) variation of the AMF over the spectral fitting window. It is also possible to obtain vertical column abundances directly, by including the radiative transfer modeling inside of the fitting procedure.[18]

It was discovered by Singer and Wentworth[19] that Rayleigh scattering, which often complicates retrieval due to its strong ($\approx 1/\lambda^4$) dependence on wavelength, could also serve as a source of information. In the strong Hartley band of ozone at wavelengths <300 nm, back scattered radiation from nadir measurements has not penetrated to the Earth's surface. The source of illumination is Rayleigh scattering. Light of different wavelengths penetrates to different atmospheric depths, depending on the measurement geometry, the strength of the scattering, and the wavelength dependence of the O_3 absorption: The spectrum can be inverted to give a stratospheric ozone profile. This is the basis for BUV/SBUV measurements of ozone profiles.[20] The greater wavelength coverage and higher spectral resolution of more modern spectrometers can improve the situation further. During the sensitivity analyses performed when the SCIAMACHY instrument was being proposed, it was discovered that adding detailed measurements of the strongly temperature-dependent Huggins bands of ozone to the BUV information makes it possible to determine the full atmospheric profile, which includes the tropospheric ozone abundance, directly.[2,21] This has been the basis of retrievals now successfully made using spectra from the GOME and SCIAMACHY satellite instruments, discussed below in **Examples**.

4. Algorithm physics

A number of the technical challenges have had to be addressed in order to successfully analyze UV/visible atmospheric spectra from satellites to the fine level of agreement (as low as several times 10^{-4} of measured radiances in favorable cases[14]) needed for use in atmospheric process studies, and to permit retrievals of ozone profiles and tropospheric ozone to the maximum altitude resolution that the physics in the spectroscopy and radiative transfer permits.

4.1. SOLAR REFERENCE SPECTRA

An extraterrestrial high resolution solar spectrum would be invaluable for the spaceborne measurements. Such a spectrum is needed for wavelength calibration,[22] Ring effect determination,[23-25] determination of the instrument transfer function from flight data, and correction for spectral undersampling.[14,26] Since an appropriate extraterrestrial spectrum does not exist (the extensive SOLSTICE/SUSIM measurements of Ref. 10 are very good in absolute intensity calibration, but have much too low spectral resolution to be used for these purposes), ground-based FTS spectra, in particular a solar spectrum from Kurucz *et al*. at the National Solar Observatory (NSO)[9] has been used extensively, supplemented at wavelengths <305 nm by balloon-based spectra from Hall and Anderson.[27]

4.2. RAYLEIGH SCATTERING AND THE RING EFFECT

Rayleigh scattering is a major contributor, sometimes the predominant contributor, to back scattered light measured in the nadir, depending on wavelength and detailed measurement geometry. For limb measurements, it is the source of the measured light, except for aerosol contributions at lower altitudes. Highly accurate formulations of the wavelength dependences of the cross sections and scattering phase function for Rayleigh scattering by air are available.[24,28,29]

The Ring effect was first noted by Grainger and Ring[30] as a broadening and reduction in depth of solar Fraunhofer lines when viewed from the ground in scattered sunlight. It has now been firmly demonstrated to be the effect of the fraction of Rayleigh scattering by air that is inelastic, *i.e.*, Raman scattering. The Raman scattering is predominantly rotational Raman; it constitutes 4% of the Rayleigh scattering in the UV/visible. Ring effect corrections may now be performed using the molecular physics of the Raman scattering coupled with a suitable solar reference spectrum,[24] in some cases coupled with radiative transfer calculations,[23,25] to the level that negligible uncertainties remain in the spectral fitting from this source of spectral structure.

Vibrational Raman scattering in ocean water can be readily sensed in the UV/visible (it must be corrected for in the spectral analysis for some gases) and it has been suggested that it may be used to "estimate chlorophyll and dissolved organic matter contents" of ocean water.[31]

4.3. WAVELENGTH ISSUES

Ground-based wavelength calibration is insufficient for detailed spectrum fitting of satellite data for several reasons. First, calibration can shift substantially due to launch stresses; second, calibration in flight can vary by substantial amounts, compared to the spectral fitting needs, due to thermal and other in-flight perturbations and instrumental effects (*e.g.*, partial filling of the field-of-view); third, solar irradiances and radiances are often obtained (especially for nadir observations) at substantially different Doppler shifts (up to 0.01 nm at 400 nm). For these reasons, methods were developed first for GOME in-flight spectral calibration, using nonlinear least-squares (NLLS) minimization or spectral cross correlation, where the comparison spectrum in both cases is derived from the NSO spectrum described above.[22] The NLLS method is now used extensively in scientific analyses, and has been implemented in operational algorithms for GOME, SCIAMACHY, the Ozone Monitoring Instrument (OMI), and the Ozone Mapping and Profiler Suite (OMPS).

4.4. REFERENCE SPECTRA

Reference spectra for UV/visible measurements are now included in the HITRAN database,[32,33] and regularly updated. Reference spectra are published sometimes with vacuum wavelengths and sometimes with air wavelengths (often with insufficient detail of laboratory conditions to allow accurate conversion to vacuum). It is highly recommended that vacuum wavelengths be the standard, and that accurate conversion be made when necessary. Highly accurate conversion formulae are available.[29] As UV/visible reference spectra are increasingly determined using Fourier transform spectrometers, this becomes less of an issue, since they measure frequencies, usually in wavenumbers (cm^{-1}), and these are intrinsically in vacuum.

4.5. INSTRUMENT FUNCTION AND SAMPLING ISSUES

Slit functions (instrument transfer functions, ITFs) in flight may differ from those determined in ground calibration. It is often useful to re-determine them in flight. The normal procedure is to combine this fitting with the wavelength calibration using NLLS, where the reference spectrum is a

high-resolution solar spectrum.[14] Spectral undersampling occurs in array-based instruments (or indeed any spectrometer) when spectral measurements are not made at fine enough spacing to Nyquist sample the ITF,[34] and thus provide full knowledge of the spectrum up to the band limit (Nyquist sampling requires sampling to at least twice the highest spatial (*i.e.*, wavelength) frequency admitted by the resolution limit of the instrument). It can be a major source of fitting error in the current generation of satellite-borne spectrometers, particularly as solar irradiance spectra must be resampled in order to be compared to radiances in the spectral fitting process.[14] Where the trace gas absorptions are optically thin, it is possible to effectively correct for most of the undersampling error.[14,35] It is now possible to quantitatively determine the amount a spectrum will be undersampled (or, how close it is to being fully-sampled) for a given instrument configuration during the design phase.[26]

4.6. RADIATIVE TRANSFER MODELING AND CHEMISTRY AND TRANSPORT MODELING

Radiative transfer calculations, usually requiring multiple scattering treatment, and often needing spherical correction or inclusion of polarization, are fundamental to the analysis of UV/visible measurements in nadir and limb geometries. Radiative transfer models are now available for most UV/visible measurement situations.[36-43]

Primarily because of the interference by Rayleigh scattering with geometrical scattering paths in nadir measurements, particularly for tropospheric measurements, it is often necessary to couple radiative transfer calculations with chemistry and transport modeling in order to determine AMFs: The contribution of molecular absorption to backscattered radiance depends significantly on the absorber altitude. Generally, absorbers at lower altitudes contribute less to the observed signal (*cf.* Ref. 16). The GEOS-CHEM and MOZART 3-D tropospheric chemistry and transport models[44-46] are in common use for this purpose.

5. Current and planned instruments

A series of satellite instruments which measured in discrete (sometimes scannable) spectral bands formed the foundation for the present generation of satellite spectrometers which are capable of making extensive tropospheric measurements. The BUV/SBUV instruments, 1970-present (*cf.* Ref. 47) and the TOMS instruments, 1978-present (*cf.* Ref. 48) are predecessors of current spectroscopic UV/visible nadir instruments. Current and planned instruments are summarized in Table1.

Table 1. Current and planned UV/visible satellite spectrometers for tropospheric measurements.

Instrument	Nadir Wavelength Range (nm)	Tropospheric Gases	Launch year
GOME/ERS-2; GOME-2 (×3)/MetOp	240-790	O_3, NO_2, BrO, SO_2, HCHO, CHOCHO, H_2O,	1995; 2006+
SCIAMACHY/Envisat	240-2340	O_3, NO_2, BrO, SO_2, HCHO, CHOCHO, H_2O (plus infrared gases)	2002
OMI/EOS-Aura	270-500	O_3, NO_2, BrO, SO_2, HCHO, CHOCHO	2004
OPUS/GCOM	306-420	O_3, NO_2, BrO, OClO, SO_2, HCHO	2007
OMPS/NPP-NPOESS (×4)	250-380	O_3, NO_2, BrO, OClO, SO_2, HCHO, H_2O	2008+

6. Application of UV/Visible measurements to tropospheric process studies

6.1. GLOBAL TROPOSPHERIC OZONE MEASUREMENTS FROM THE NADIR GEOMETRY

Initial sensitivity studies for GOME and SCIAMACHY indicated that tropospheric ozone could be measurable globally.[2,21] This was first demonstrated with GOME flight data by the Rutherford Appleton Laboratory,[49] and has since been implemented by several other groups, including our work at the CfA[50,51], the University of Bremen, the Space Research of the Netherlands, and the Royal Dutch Meteorological Institute.[8]

Research at the CfA includes full profiles of ozone from nadir measurements by GOME and SCIAMACHY, as well as integrated tropospheric column ozone, and the capability to sample the ozone profiles at selected pressures or altitudes. The application of ozone profiling and tropospheric ozone algorithms to measurements from the OMI instrument is expected to begin in the near future. Figure 4 shows ozone profiles for a full orbit of GOME data on October 22, 1997 (an ozone hole orbit). The stratospheric ozone hole is clearly visible below ~70°S. Significant tropospheric ozone enhancements are visible over the Southern Indian Ocean and Indonesia, due in both cases to biomass burning.[50]

Figure 5 shows monthly mean global tropospheric column ozone from the GOME instrument for October, 1997, where the columns are integrated to the NCEP tropopause height. The ozone distribution shows the well-known wave-1 pattern in the tropics, enhanced in the southern tropics particularly by biomass burning, and a strong band of ozone near 30°S, associated with the Hadley circulation. For a more detailed discussion see Ref. 51. (Figures 4 and 5 courtesy of X. Liu).

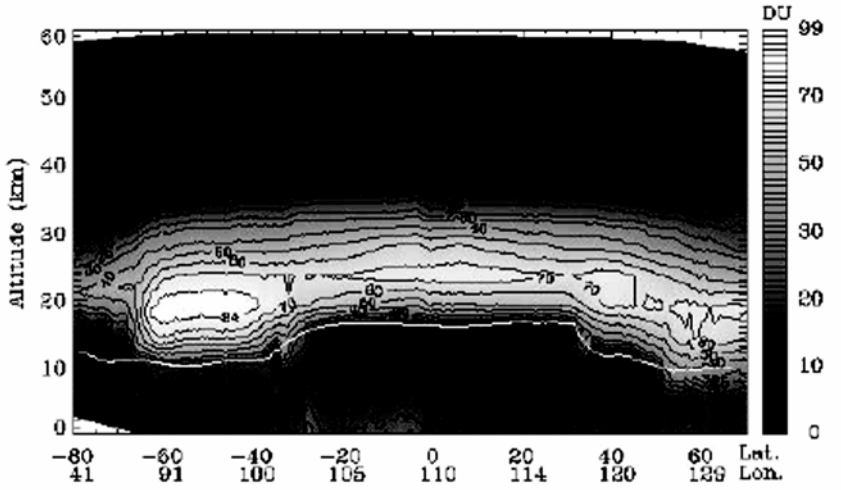

Figure 4. Ozone profiles for an orbit of GOME measurements on October 22, 1997 showing the Antarctic ozone hole and significant tropospheric enhancements over the Southern Indian Ocean and Indonesia.

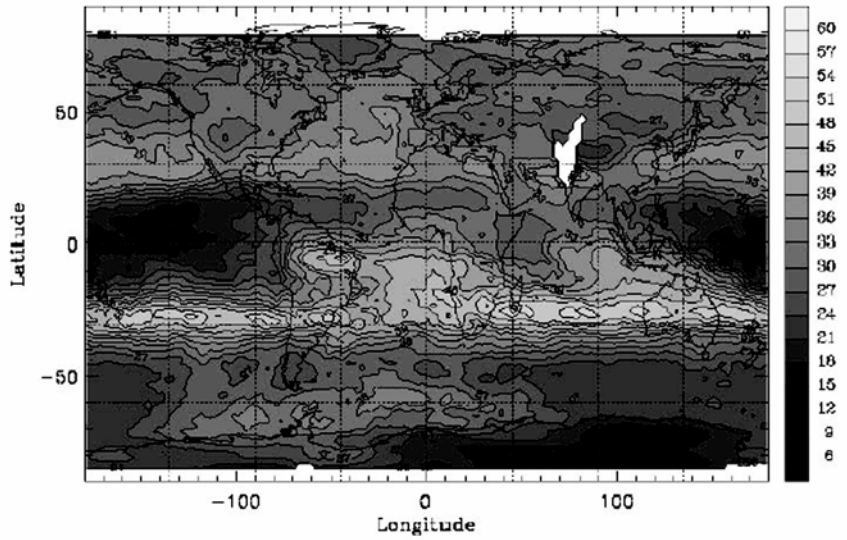

Figure 5. Monthly mean global tropospheric column ozone from the GOME instrument for October, 1997, where the columns are integrated to the NCEP tropopause height.

6.2. GLOBAL TROPOSPHERIC NO_2

Nitrogen dioxide is the primary measurable proxy for NO_x, the reactive nitrogen pollutants.[8,17,52,53] Satellite measurements are used to track pollution and to improve global NO_x emission inventories,[54-56] and for other detailed process studies, such as the release of NO_x from soils,[57] and to

investigate evidence of lightning NO_x and convective transport of pollutants.[58]

Figure 6 shows global and North American tropospheric NO2 derived from SCIAMACHY measurements for May-October 2004, during the 2004 International Consortium for Atmospheric Research on Transport and Transformation (ICARTT) campaign. Intense sources reflect human activity: Urban areas to quite modest size are readily measurable. (Figure courtesy of R.V. Martin and C.E. Sioris.)

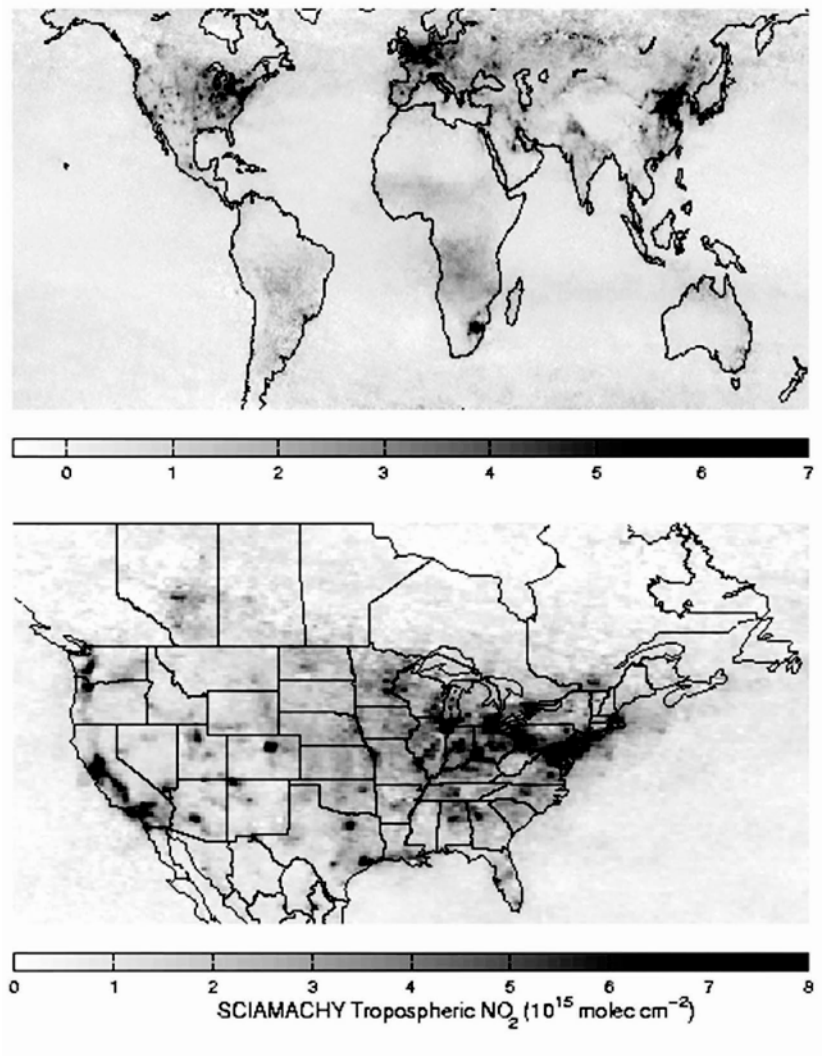

Figure 6. Global and North American tropospheric NO_2 from SCIAMACHY during the 2004 ICARTT campaign.

6.3. BRO IN THE POLAR SPRING, AND FROM SALT LAKES AND VOLCANOES

Initial sensitivity studies for GOME and SCIAMACHY indicated that stratospheric BrO could be measurable globally.[2] It was later discovered from ground-based measurements,[59] and then confirmed by GOME measurements,[8,14] that BrO is released copiously from the ice pack in polar spring, in both hemispheres, with implications for ozone depletion in the polar boundary layer (*cf.* Ref. 60). More recently, BrO has been measured using ground-based spectroscopy from halogen emission over the Dead Sea and the Great Salt Lake,[61,62] and from a volcanic plume.[63] Figure 7 shows BrO derived from OMI spectra over the shelf ice in Antarctica in the Southern Hemisphere spring (left) and for a partial orbit over Hudson Bay, Canada during the Northern Hemisphere Spring (right). Figure 8 shows BrO from OMI over the Dead Sea (left) and the Great Salt Lake (right). Figure 9 shows BrO from OMI from February 2005 during the eruption of the Ambrym Volcano, Vanuatu (16.25°S, 168.12°E). The striping in the images, most obvious in the Figure 7 (right) is an artifact due to incomplete calibration in the Level 1 (*i.e.*, spectral) data products. It should be absent in future versions of the data products. (Figures 7-9 courtesy of T.P. Kurosu.)

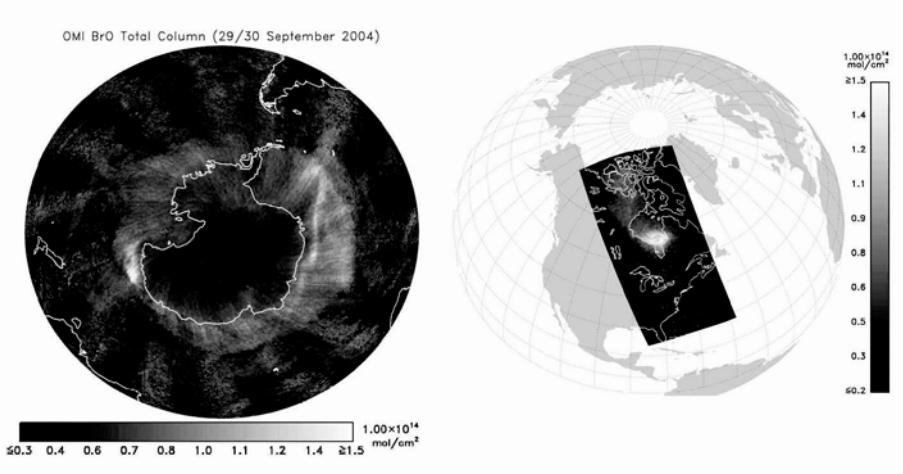

Figure 7. BrO from OMI over the shelf ice in Antarctica in the Southern Hemisphere spring (left) and for a partial orbit over Hudson Bay, Canada during the Northern Hemisphere Spring (right).

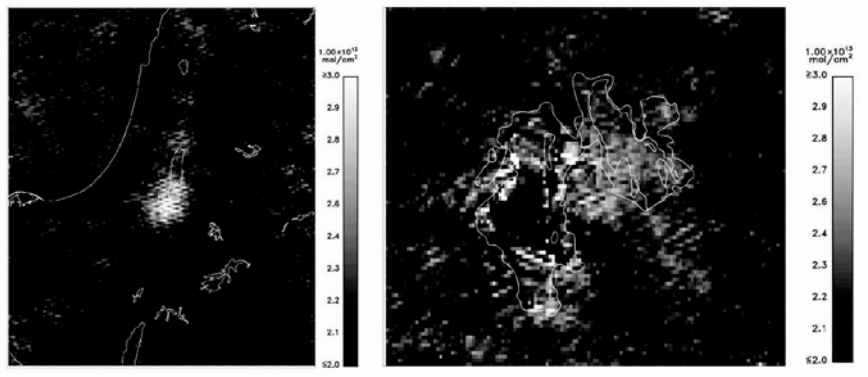

Figure 8. BrO from OMI over the Dead Sea (left) and the Great Salt Lake (right).

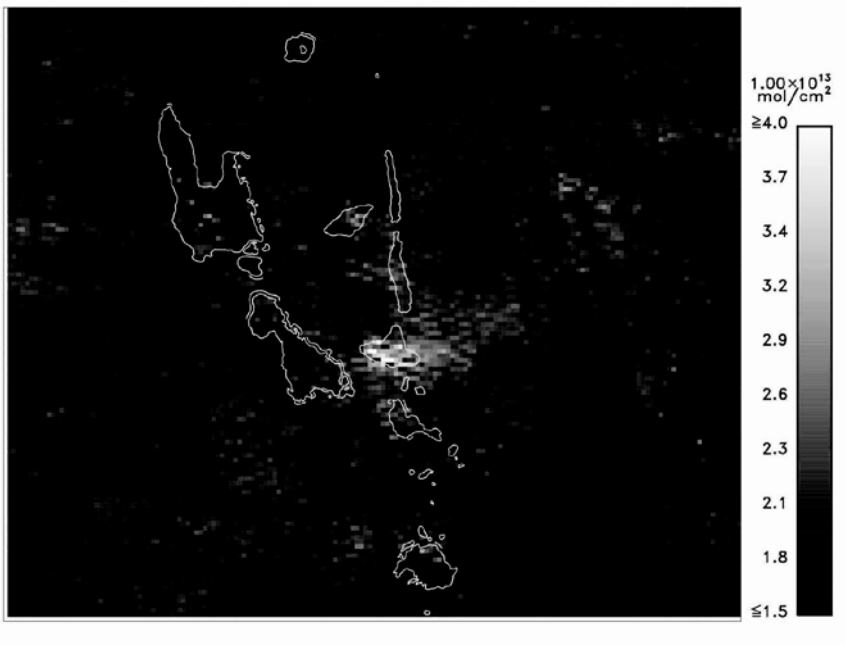

Figure 9. BrO from OMI from February 2005 during the eruption of the Ambrym Volcano, Vanuatu.

6.4. GLOBAL TROPOSPHERIC HCHO

Formaldehyde is currently the primary measurable proxy for volatile organic compounds, VOCs. Tropospheric HCHO measurements derived from GOME have been used to improve VOC emission inventories.[16,52,55,64-67] OMI measurements, which have much higher spatial resolution, show promise for substantially improving the knowledge of VOC emission sources. Figure 10 (left) shows tropospheric HCHO measurements from OMI for summertime (July 2005) over the U.S., where isoprene from trees is the major source, and (right) for Southeast Asia in October 2005, where sources include vegetation, biomass burning, and human activity (agriculture, fossil-fuel use). As with BrO, the Southeast Asia image still contains some residual striping. (Figure courtesy of T.P. Kurosu.)

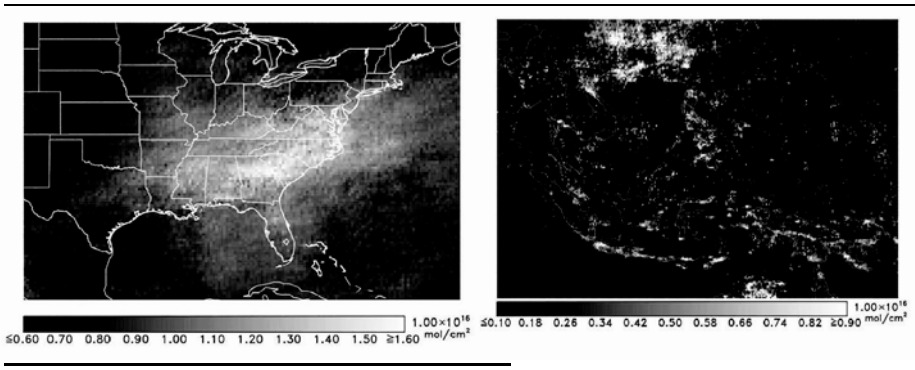

Figure 10. Tropospheric HCHO measurements from OMI for summertime (July 2005) over the U.S., where isoprene from trees is the major source (left), and for Southeast Asia in October 2005, where sources include vegetation, biomass burning, and human activity (right).

6.5. PRELIMINARY MEASUREMENTS OF CHOCHO

CHOCHO is another high-yield product of VOC oxidation, although it has significantly difference source chemistry and a significantly shorter atmospheric lifetime than HCHO. As such, it can provide a probe for VOC emissions with different characteristics than HCHO. CHOCHO has recently been measured in Mexico City using ground-based spectroscopy.[68] Research at the CfA has now shown that CHOCHO can be successfully measured from space, although measurements are preliminary as the algorithm is still undergoing optimization. Figure 11 shows elevated CHOCHO over the Guangzhou, China area in July, 2005. As with BrO and HCHO, some residual striping is evident. (Figure courtesy of T. Kurosu).

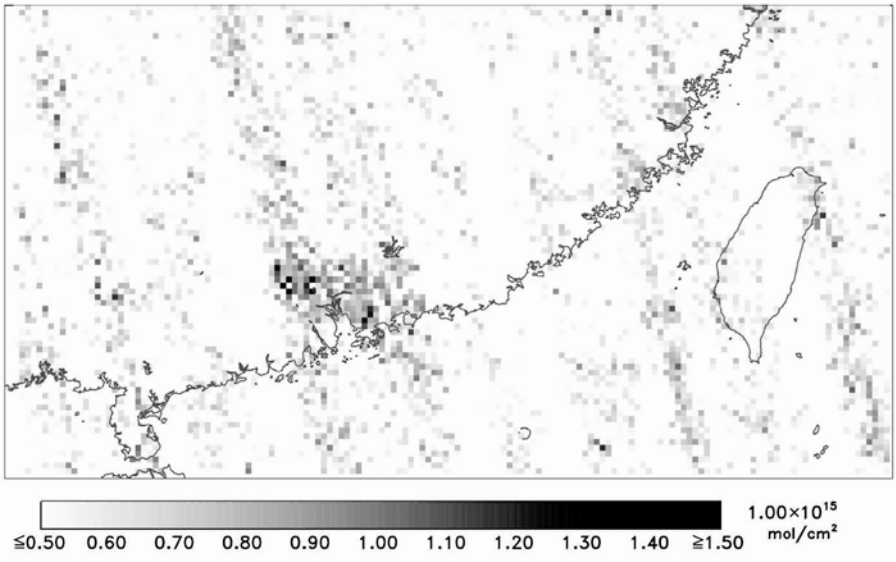

Figure 11. Elevated CHOCHO over the Guangzhou, China area in July, 2005.

7. Requirements for global pollution monitoring

The currently-orbiting satellite instruments which measure the troposphere in the UV/visible from nadir geometry, GOME, SCIAMACHY, and OMI (and design of the OMPS series of instruments), have done much to prepare the way for eventual global and continuous pollution monitoring from space. Robust algorithms for measurement of ozone profiles and tropospheric ozone, NO_2, HCHO, and volcanic SO_2 have been developed, with anthropogenic SO_2 measurement capability under development. Initial measurements of CHOCHO have been made; they should become robust measurement products in the near future. BrO, which has been of primarily stratospheric, and more recently upper tropospheric, interest nonetheless has shown scientifically interesting and readily measurable lower tropospheric features, including BrO from the ice pack and from volcanoes and salt lakes. Global pollution monitoring would almost certainly include infrared measurements as well, particularly of carbon monoxide (CO) and, perhaps, additional ozone measurements.

The following discussion assumes that measurements would be made from geostationary orbit (35,800 km) or, possibly, from inclined 24-hour

orbits, which could make measurements to higher latitudes feasible. At least three instruments would be required for global coverage (six if inclined orbits are used). Spatial resolution requirements will depend upon detailed scientific requirement studies, but they will likely be 10×10 km^2 or smaller. The major tradeoffs are in orbit selection, detector format (linear versus 2-D) and type (CMOS-Si versus CCD), and in scanning mode: even instruments using 2-D detectors would need to raster in order to obtain the required spatial coverage.

The spatial resolution requirement assumed here is: at least 1000 resolution elements in the East-West and North-South directions (i.e., a grid of 1000×1000 elements) for a satellite covering 1/3 of the Earth to latitude limits of $\sim\pm60^{o}$. Any final selection will likely approximate this.

7.1. INSTRUMENT DESIGN

7.1.1. *Scanner*

It is generally desirable to limit the number of mechanisms on a space-based instrument. It is partially for this reason that the OMPS and OMI designs selected the pushbroom technique, employing 2-D detectors (CCDs in both cases), where one CCD dimension is spectral and the other spatial (across-track). The satellite movement then gives the along track variation.[69,70] GOME and SCIAMACHY both employ across-track scanners to achieve spatial coverage. Both scanners are currently working as of this writing: the GOME single-axis scanner for almost 11 years and the SCIAMACHY two-axis scanner for almost 4 years. Thus, the use of a scanning mechanism has been demonstrated to be suitable for use in this application. OMPS will simultaneously measure spectra for 35 across-track ground pixels; OMI measures 60 across-track ground pixels. Neither value is close to what will reasonably be required for geostationary measurement (if they were, a single-axis scanner would still be required). Two-axis scanning will thus be required for successful measurements from geostationary orbit.

7.1.2. *Detectors*

The current generation of satellite spectrometers (summarized above in Table 1) utilizes either 1-dimensional silicon diode array detectors (1024-element Reticon® detectors for GOME and SCIAMACHY) or 2-dimensional CCD devices (OMI and OMPS). Of the two choices, the diode array detectors offer the best performance on a per-pixel basis, having large charge capacities and generally lower dark current. In the most favorable cases, it has been possible to fit GOME spectra, for example, to an RMS of

$<3\times10^{-4}$ of the full scale radiance.[14] CCD detectors at present achieve lower performance on a per-pixel basis but enable multiple spectra to be obtained simultaneously, *i.e.*, spectrum in one dimension and across-track ground pixel position in the other. For low-Earth-orbit measurements they have disadvantages in that the pixel size increases substantial with off-track (*i.e.*, away from nadir) position, and the instrument line shape varies substantially in both the spectral and spatial dimensions. This will be less of a problem for geostationary measurements, assuming that the "across-track" (*i.e*., spatial, or swath) dimension will cover a relatively small fraction of the Earth disk instantaneously, and thus the angular field-of-view of the instrument will be smaller. CCDs are sensitive to degradation from radiation damage. Future instruments employing 2-D detectors may well benefit from the use of 2-D silicon diode array technology which has recently become available in sufficiently large formats, and combines the advantages of both previous types: large 2-D format, high charge capacity (for potentially higher achievable signal-to-noise ratios), and good radiation tolerance. The primary current example is the Rockwell HyViSI® series of CMOS-Si detectors (CMOS-HgCdTe versions are also available for infrared applications). For a recent comparison of CCDs and CMOS detectors see Ref. 71. Linear silicon detectors are now available in larger formats (up to 2048 pixels) with improved performance (*e.g*., Hamamatsu S3904-2048Q). The larger number of pixels allows for extensive wavelength coverage while avoiding spectral undersampling.[26]

7.1.3. *Spectrometer*

The major aspect of spectrometer design that requires improvement applies in the case where 2-D detectors are used. In this case, improved optical design is required to reduce "smile" on the detector arrays, where the spatial and spectral dimensions are not fully orthogonal (and may alias onto one another if the sampling is insufficient), and to reduce the variation of instrument line shape across the spatial dimension.

It would also be useful to consider alternate configurations, for example, where multiple 1-D detectors are used to obtain spectra of different scenes simultaneously. This would improve the characteristics of individual spectra while maintaining at least part of the multiplex advantage of 2-D detectors.

7.2. ORBIT CONSIDERATIONS

A constellation of three satellites in geostationary orbits is commonly considered to be a standard configuration to achieve global coverage up to latitudes limited by viewing angles and physics. Measurements to high

latitudes become difficult due to the high viewing zenith angle: The viewing zenith angle for 60^o looking directly North or South is already quite high (68^o). It increases to more than 84^o for views 60^o East or West. This makes tropospheric measurements, especially in the UV, quite challenging even under high Sun conditions due to the large contribution of Rayleigh scattering to the measured radiances.

The use of inclined 24-hour orbits could improve this situation, at the cost of more instruments or reduced temporal coverage. For example, a satellite in geostationary orbit at 100^oW would effectively cover the U.S. (except for most of Alaska), southern Canada, and South America. Northern Canada would be problematic (as would much of northern Europe for a European member of the constellation). Inclining the orbits to 50^o, with maximum latitude at solar noon, would permit the Northern Hemisphere to be well-covered during most of the day lit parts of the orbits, but would sacrifice coverage of much of the Southern Hemisphere. A second set of satellites with opposite phase would recover this.

8. Conclusions

Issues of instrument requirements (signal-to-noise ratio and spectral resolution) and algorithm physics have largely been addressed in the development of data products for GOME, SCIAMACHY, and OMI. The exact choices for geostationary instruments would need to be made considering the tradeoffs among technical capability, scientific requirements, and cost.

Several algorithm issues remain. These include development of the capability to measure anthropogenic SO_2 and improvements for CHOCHO. The advent (and cost!) of geostationary measurements would also provide an appropriate occasion to revisit some details of fitting algorithms. For example, there remains a degree of arbitrariness among choices of fitting functions for slant column measurements employed for both scientific and operational data products. Choices include directly fitting the radiance R, fitting R/I_0, fitting $ln(R/I_0)$, or fitting a high-pass filtered version of $ln(R/I_0)$ ("DOAS"). All choices are in current use and few data products have benefited from a systematic comparison of choices. A comprehensive review of algorithm physics and reference spectra would also be appropriate to a new program for global measurements.

The major needs for development have been presented in Section 7. The most critical point is that choice of detector type and geometry should proceed together with spectrometer design studies so that the choice is not made prematurely. An alternate orbit choice (inclined 24-hour orbits) has

been presented although it may be that it is not seriously considered due to cost.

Acknowledgements

The author is grateful to his colleagues for sharing figures to include here: Xiong Liu, Randall V. Martin, Christopher E. Sioris, and Thomas P. Kurosu. He also appreciates ongoing collaborations with colleagues Daniel Jacob, Paul Palmer, Yuhang Wang, Lyatt Jaeglé, Robert Spurr, Michael Newchurch, and many others. Research at the CfA is supported by NASA and the Smithsonian Institution. The cooperation of the European Space Agency and the German Aerospace Center on the GOME and SCIAMACHY programs has been generous, and fundamental to this research. This chapter contains non-copyright material from the author's recent publication "Ultraviolet and visible spectroscopy and spaceborne remote sensing of the Earth's atmosphere," *Comp. Rend. Phys. Special issue on Molecular Spectroscopy and Planetary Atmospheres* 6, 836-847 (2005).

References

1. J.P. Burrows and K.V. Chance, SCanning Imaging Absorption spectroMeter for Atmospheric CHartographY, *Proc. SPIE, Future European and Japanese Remote Sensing Sensors and Programs* 1490, 146–154 (1991).
2. K.V. Chance, J.P. Burrows, and W. Schneider, Retrieval and molecule sensitivity studies for the Global Ozone Monitoring Experiment and the SCanning Imaging Absorption spectroMeter for Atmospheric CHartographY, *Proc. SPIE Remote Sensing of Atmospheric Chemistry* 1491, 151–165 (1991).
3. J. Fishman, A.E. Wozniak, and J.K. Creilson, Global distribution of tropospheric ozone from satellite measurements using the empirically corrected tropospheric ozone residual technique: Identification of the regional aspects of air pollution, *Atmos. Chem. Phys*. 3, 893–907, (2003).
4. J. Fishman, J. K. Creilson, A. E. Wozniak, and P. J. Crutzen, Interannual variability of stratospheric and tropospheric ozone determined from satellite measurements, *J. Geophys. Res*. 110, D20306, doi:10.1029/2005JD005868 (2005).
5. A.J. Krueger, S.J. Schaefer, N. Krotkov, G. Bluth, and S. Barker, Ultraviolet Remote Sensing of Volcanic Emissions, in: *Remote Sensing of Active Volcanism*, edited by P. Mouginis Mark, J.A. Crisp, and J. H. Fink, Geophysical Monograph 116, American Geophysical Union, Washington, DC (2000).
6. M. Eisinger and J.P. Burrows, Tropospheric sulfur dioxide observed by the ERS-2 GOME instrument, *Geophys. Res. Lett*. 25, 4177–4180 (1998).
7. J. Joiner, and P.K. Bhartia, The determination of cloud pressures from rotational Raman scattering in SBUV measurements, *J. Geophys. Res*. 100, 23,019–23,026 (1995).

8. http://www-iup.physik.uni-bremen.de/deu/; http://satellite.iup.uni-heidelberg.de/; http://www.ssd.rl.ac.uk/RSG/; http://www.aeronomie.be/; http://www.knmi.nl/omi/; http://neonet.knmi.nl/neoaf/; http://www.sron.nl/; http://hyperion.gsfc.nasa.gov/; http://www.jcet. umbc.edu/; http://www.caf.dlr.de/caf/institut/dfd/; http://www.esa.int/-esaEO/; http://www.space.gc.ca/asc/eng/satellites/
9. R.L. Kurucz, I. Furenlid, J. Brault, and L. Testerman, Solar Flux Atlas from 296 to 1300 nm, National Solar Observatory, Sunspot, New Mexico, 240 pp. (1984).
10. T.N. Woods, D.K. Prinz, G.J. Rottman, J. London, P.C. Crane, R.P. Cebula, E. Hilsenrath, G.E. Brueckner, M.D. Andrews, O.R. White, M.E. VanHoosier, L.E. Floyd, L.C. Herring, B.G. Knapp, C.K. Pankratz, and P.A. Reiser, Validation of the UARS solar ultraviolet irradiances: Comparison with the ATLAS 1 and 2 measurements, *J. Geophys. Res*. 101, 9541–9570 (1996).
11. A. Berk, G.P. Anderson, L.S.Bernstein, P.K. Acharya, H. Dothe, M.W. Matthew, S.M. Adler-Golden, J.H. Chetwynd, Jr., S.C. Richtsmeier, B. Pukall, C.L. Allred, L.S. Jeong, and M.L. Hoke, MODTRAN4 radiative transfer modeling for atmospheric correction, *Proc. SPIE, Optical Spectroscopic Techniques and Instrumentation for Atmospheric and Space Research III* 3756, 348–353 (1999).
12. GOME Users Handbook Manual, ESA Special Publication SP-1182, ESTEC, Noordwijk, The Netherlands (1995).
13. S. Noël, J.P. Burrows, H. Bovensmann, J. Frerick, K.V. Chance, A.P.H. Goede, and C. Muller, Atmospheric trace gas sounding with SCIAMACHY, *Adv. Space Res*. 26, 1949–1954 (2000).
14. K. Chance, Analysis of BrO measurements from the Global Ozone Monitoring Experiment, *Geophys. Res. Lett*. 25, 3335–3338 (1998).
15. U. Platt, Differential Optical Absorption Spectroscopy (DOAS), in: *Air Monitoring by Spectroscopic Techniques*, edited by M.W. Sigrist, Chem. Anal. Ser. 127 (John Wiley, New York, 1994), pp. 27–84.
16. P.I. Palmer, D.J. Jacob, K. Chance, R.V. Martin, R.J.D. Spurr, T.P. Kurosu, I. Bey, R. Yantosca, A. Fiore, and Q. Li, Air mass factor formulation for spectroscopic measurements from satellites: Application to formaldehyde retrievals from the Global Ozone Monitoring Experiment, *J. Geophys. Res*. 106, 14,539–14,550 (2001).
17. R.V. Martin, K. Chance, D.J. Jacob, T.P. Kurosu, R.J.D. Spurr, E. Bucsela, J.F. Gleason, P.I. Palmer, I. Bey, A.M. Fiore, Q. Li, R.M. Yantosca, and R.B.A. Koelemeijer, An improved retrieval of tropospheric nitrogen dioxide from GOME, *J. Geophys. Res*. 107, 4437, doi:10.1029/2001JD0010127 (2002).
18. R. Spurr, M. van Roozendael, J. Lambert, and C. Fayt, The GODFIT direct fitting algorithm: A new approach for total column retrieval, *Proc. 2004 ENVISAT & ERS Symposium*, ESA publication SP-572 (2004).
19. S.F. Singer and R.C. Wentworth, A method for the determination of the vertical ozone distribution from a satellite, *J. Geophys. Res*. 62, 299–308 (1957).
20. D.F. Heath, C.L. Mateer, and A.J. Krueger, The Nimbus-4 backscatter ultraviolet (BUV) atmospheric ozone experiment - two years' operation, *Pure Appl. Geophys*. 106–108, 1238–1253 (1973).
21. K.V. Chance, J.P. Burrows, D. Perner, and W. Schneider, Satellite measurements of atmospheric ozone profiles, including tropospheric ozone, from UV/visible measurements in the nadir geometry: A potential method to retrieve tropospheric ozone, *J. Quant. Spectrosc. Radiat. Transfer* 57, 467–476 (1997).
22. C. Caspar and K. Chance, GOME wavelength calibration using solar and atmospheric spectra, *Proc. Third ERS Symposium on Space at the Service of our Environment*,

edited by T.-D. Guyenne and D. Danesy, European Space Agency Special Publication SP-414 (1997).
23. J. Joiner, P.K. Bhartia, R.P. Cebula, E. Hilsenrath, R.D. McPeters, and H. Park, Rotational Raman scattering (Ring effect) in satellite backscatter ultraviolet measurements, *Appl. Opt*. 34, 4513–4525 (1995).
24. K. Chance and R.J.D. Spurr, Ring effect studies: Rayleigh scattering, including molecular parameters for rotational Raman scattering, and the Fraunhofer spectrum, *Appl. Opt*. 36, 5224–5230 (1997).
25. M. Vountas, V.V. Rozanov, and J.P. Burrows, Ring effect: Impact of rotational Raman scattering on radiative transfer in Earth's Atmosphere, *J. Quant. Spectrosc. Radiat. Transfer* 60, 943–961 (1998).
26. K. Chance, T.P. Kurosu, and C.E. Sioris, Undersampling correction for array detector-based satellite spectrometers, *Appl. Opt.* 44, 1296–1304 (2005).
27. L.A. Hall, and G.P. Anderson, High-resolution solar spectrum between 200 and 3100 Å, *J. Geophys. Res*. 96, 12,927–12,931 (1991).
28. D.R. Bates, Rayleigh scattering by air, *Planet. Space Sci*. 32, 785–790 (1984).
29. B.A. Bodhaine, N.B. Wood, E.G. Dutton, and J.R. Slusser, On Rayleigh optical depth calculations, *J. Atmos. Ocean. Tech*. 16, 1854–1861 (1999).
30. J.F. Grainger and J. Ring, Anomalous Fraunhofer line profiles, *Nature* 193, 762 (1962).
31. A.P. Vasilkov, J. Joiner, J. Gleason, and P.K. Bhartia, Ocean Raman scattering in satellite backscatter UV measurements, *Geophys. Res. Lett*. 29, 1837, doi:10.1029/2002GL014955 (2002).
32. L.S. Rothman, D. Jacquemart, A. Barbe, D. Chris Benner, M. Birk, L.R. Brown, M.R. Carleer, C. Chackerian, Jr., K. Chance, L.H. Coudert, V. Dana, V.M. Devi, J.-M. Flaud, R.R. Gamache, A. Goldman, J.-M. Hartmann, K.W. Jucks, A.G. Maki, J.-Y. Mandin, S.T. Massie, J. Orphal, A. Perrin, C.P. Rinsland, M.A.H. Smith, J. Tennyson, R.N. Tolchenov, R.A. Toth, J. Vander Auwera, P. Varanasi, and G. Wagner, The HITRAN 2004 molecular spectroscopic database, *J. Quant. Spectrosc. Radiat. Transfer* 96, 139–204 (2005).
33. J. Orphal and K. Chance, Ultraviolet and visible absorption cross sections for HITRAN, *J. Quant. Spectrosc. Radiat. Transfer* 82, 491–504 (2003).
34. S. Goldman, *Information Theory* (Prentice-Hall, New York, 1953).
35. S. Slijkhuis, A. von Bargen, W. Thomas, and K. Chance, Calculation of undersampling correction spectra for DOAS spectral fitting, *Proc. ESAMS'99 - European Symposium on Atmospheric Measurements from Space*, 563–569 (1999).
36. R.J.D. Spurr, T.P. Kurosu, and K. Chance, A linearized discrete ordinate radiative transfer model for atmospheric remote sensing retrieval, *J. Quant. Spectrosc. Radiat. Transfer* 68, 689–735 (2001).
37. R.J.D. Spurr, LIDORT V2PLUS: A comprehensive radiative transfer package for UV/VIS/NIR nadir remote sensing; A general quasi analytic solution, *Proc. SPIE, Remote Sensing of Clouds and the Atmosphere VIII* 5235 (2003).
38. R.F. Van Oss and R.J.D. Spurr, Fast and accurate 4-stream linearized discrete ordinate radiative transfer models for ozone profile retrieval, *J. Quant. Spectrosc. Radiat. Transfer* 75, 177–220 (2002).
39. V.V. Rozanov, D. Diebel, R.J.D. Spurr, and J.P. Burrows, GOMETRAN: A radiative transfer model for the satellite project GOME - the plane-parallel version, *J. Geophys. Res*. 102, 16,683–16,695 (1997).

40. V.V. Rozanov, M. Buchwitz, K.-U. Eichmann, R. de Beek, and J.P. Burrows, SCIATRAN - a new radiative transfer model for geophysical applications in the 240–2400 nm spectral region: The pseudo-spherical version, *Adv. Space Res*. 29, 1831–1835 (2002).
41. C.A. McLinden, J.C. McConnell, E. Griffioen, and C.T. McElroy, A vector radiative transfer model for the Odin/OSIRIS project, *Can. J. Phys*. 80, 375–393 (2002).
42. J.F. De Haan, P.B. Bosma, and J.W. Hovenier, The adding method for multiple scattering calculations of polarized light, *Astron. Astrophys*. 183, 371–391 (1987).
43. P. Stammes, Spectral radiance modelling in the UV-visible range, in: *IRS 2000: Current Problems in Atmospheric Radiation*, edited by W.L. Smith and Y.M. Timofeyev (A. Deepak, Hampton, VA, 2001), pp. 385–388.
44. I. Bey, D.J. Jacob, R.M. Yantosca, J.A. Logan, B.D. Field, A.M. Fiore, Q. Li, H.Y. Liu, L.J. Mickley, and M.G. Schultz, Global modeling of tropospheric chemistry with assimilated meteorology: Model description and evaluation, *J. Geophys. Res*. 106, 23,073–23,096 (2001).
45. G.P. Brasseur, D.A. Hauglustaine, S. Walters, P.J. Rasch, J.-F. Muller, C. Granier, and X.X. Tie, MOZART: A global chemical transport model for ozone and related chemical tracers, Part 1. Model description, *J. Geophys. Res. 103*, 28,265–28,289 (1998).
46. D.A. Hauglustaine, G.P. Brasseur, S. Walters, P.J. Rasch, J.-F. Muller, L.K. Emmons, and M.A. Carroll, MOZART: A global chemical transport model for ozone and related chemical tracers, Part 2. Model results and evaluation, *J. Geophys. Res*. 103, 28,291–28,335 (1998).
47. A.J. Fleig, R.D. McPeters, P.K. Bhartia, B.M. Schlesinger, R.P. Cebula, K.F. Klenk, S.L. Taylor, and D.F. Heath, Nimbus-7 Solar Backscatter Ultraviolet (SBUV) Ozone Products User's Guide, NASA Reference Publication, 1234, National Aeronautics and Space Administration, Washington, DC (1990).
48. R.D. McPeters, A.J. Krueger, P.K. Bhartia, and J.R. Herman, Earth Probe Total Ozone Mapping Spectrometer (TOMS) Data Products User's Guide, NASA Reference Publication 1998–206895, National Aeronautics and Space Administration, Washington, DC (1998).
49. R. Munro, R. Siddans, W.J. Reburn, and B. Kerridge, Direct measurement of tropospheric ozone from space, *Nature* 392, 168–191 (1998).
50. X. Liu, K. Chance, C.E. Sioris, R.J.D. Spurr, T.P. Kurosu, R.V. Martin, and M.J. Newchurch, Ozone profile and tropospheric ozone retrievals from Global Ozone Monitoring Experiment: Algorithm description and validation, *J. Geophys. Res*. 110, D20307, doi:10.1029/2005JD006240 (2005).
51. X. Liu, K. Chance, C.E. Sioris, T.P. Kurosu, R.J.D. Spurr, R.V. Martin, M. Fu, J.A. Logan, D.J. Jacob, P.I. Palmer, M.J. Newchurch, I. Megretskaia, and R. Chatfield, First directly-retrieved global distribution of tropospheric column ozone from GOME: Comparison with the GEOS-CHEM model, *J. Geophys. Res*., in press (2006).
52. W. Thomas, E. Hegels, S. Slijkhuis, R. Spurr, and K. Chance, Detection of biomass burning combustion products in Southeast Asia from backscatter data taken by the GOME spectrometer, *Geophys. Res. Lett*. 25, 1317–1320 (1998).
53. C.E. Sioris, T.P. Kurosu, R.V. Martin and K. Chance, Stratospheric and tropospheric NO_2 observed by SCIAMACHY: First results, *Adv. Space Res. Special issue: Trace Constituents in the Troposphere and Lower Stratosphere* 34/4, 780–785 (2004).
54. R.V. Martin, D.J. Jacob, K. Chance, T.P. Kurosu, P.I. Palmer, and M.J. Evans, Global inventory of nitrogen oxide emissions constrained by space-based observations of NO_2 columns, *J. Geophys. Res*. 108(D17), 4537, doi:10.1029/2003JD003453 (2003).

55. R.V. Martin, D.D. Parrish, T.B. Ryerson, D.K. Nicks Jr., K. Chance, T.P. Kurosu, A. Fried, B.P. Wert, D.J. Jacob, and E.D. Sturges, Evaluation of GOME satellite measurements of tropospheric NO_2 and HCHO using regional data from aircraft campaigns in the southeastern United States, *J. Geophys. Res*. 109, D24307, doi:10.1029/2004JD004869 (2004).
56. L. Jaeglé, L. Steinberger, R.V. Martin, and K. Chance, Global partitioning of NO_x sources using satellite observations: Relative roles of fossil fuel combustion, biomass burning and soil emissions, *Faraday Discuss*. 130, 407–423, doi:10.1039/b502128f (2005).
57. L. Jaeglé, R.V. Martin, K. Chance, L. Steinberger, Kurosu, T.P., D.J. Jacob, A.I. Modi, V. Yoboué, L. Sigha-Nkamdjou, and C. Galy-Lacaux, Satellite mapping of rain-induced nitric oxide emissions from soils, *J. Geophys. Res*. 109, D21310, doi:10.1029/2004JD004787 (2004).
58. Y. Choi, Y. Wang, T. Zeng, R.V. Martin, T.P. Kurosu, and K. Chance, Evidence of lightning NO_x and convective transport of pollutants in satellite observations over North America, *Geophys. Res. Lett*. 32, L02805, doi:10.1029/2004GL021436 (2005).
59. K. Kreher, P.V. Johnston, S.W. Wood, B. Nardi, and U. Platt, Ground-based measurements of tropospheric and stratospheric BrO at Arrival Heights, Antarctica, *Geophys. Res. Lett*. 24, 3021–3024, 1997.
60. T. Zeng, Y. Wang, K. Chance, E.V. Browell, B.A. Ridley, and E.L. Atlas, Widespread persistent near-surface O_3 depletion at northern high latitudes in spring, *Geophys. Res. Lett*. 30(24), 2298, doi:10.1029/2003GL018587 (2003).
61. V. Matveev, M. Peleg, D. Rosen, D.S. Tov-Alper, K. Hebestreit, J. Stutz, U. Platt, D. Blake, and M. Luria, Bromine oxide - ozone interaction over the Dead Sea, *J. Geophys. Res.* 106, 10,375–10,387 (2001).
62. J. Stutz, R. Ackermann, J.D. Fast, and L.A. Barrie, Atmospheric reactive chlorine and bromine at the Great Salt Lake, Utah, *Geophys. Res. Lett.* 29(10), doi:10.1029/2002GL014812 (2002).
63. N. Bobrowski, G. Hönninger, B. Galle, and U. Platt, Detection of bromine monoxide in a volcanic plume, *Nature* 423, 273–276 (2003).
64. K. Chance, P. Palmer, R.J.D. Spurr, R.V. Martin, T. Kurosu, and D.J. Jacob. Satellite observations of formaldehyde over North America from GOME, *Geophys. Res. Lett*. 27, 3461–3464 (2000).
65. P.I. Palmer, D.J. Jacob, A.M. Fiore, R.V. Martin, K. Chance, and T. Kurosu, Mapping isoprene emissions over North America using formaldehyde column observations from space, *J. Geophys. Res*. 108, 4180, doi:10.1029/2002JD002153 (2003).
66. D.S. Abbot, P.I. Palmer, R.V. Martin, K.V. Chance, D.J. Jacob, and A. Guenther, Seasonal and interannual variability of isoprene emissions as determined by formaldehyde column measurements from space, *Geophys. Res. Lett*. 30, 1886, doi:10.1029/2003GL017336 (2003).
67. C. Shim, Y. Wang, Y. Choi, P.I. Palmer, D.S. Abbot, and K. Chance, Constraining global isoprene emissions with GOME HCHO column measurements, *J. Geophys. Res*. 110, D24301, doi:10.1029/2004JD005629 (2005).
68. R. Volkamer, L.T. Molina, M.J. Molina, T. Shirley, and W.H. Brune, DOAS measurement of glyoxal as an indicator for fast VOC chemistry in urban air, *Geophys. Res. Lett*. 32, L08806, doi:10.1029/2005GL022616 (2005).
69. M.G. Dittman, E. Ramberg, M. Chrisp, J.V. Rodriguez, A.L. Sparks, N.H. Zaun, P. Hendershot, T. Dixon, R.H. Philbrick, and D. Wasinger, Nadir ultraviolet imaging spectrometer for the NPOESS Ozone Mapping and Profiler Suite (OMPS), *Proc. SPIE Earth Observing Systems VII* 4814, 111–119 (2002).

70. P.F. Levelt, G.H.J. van den Oord, M.R. Dobber, A. Malkki, H. Visser, J. de Vries, P. Stammes, J. Lundell, and H. Saari, The Ozone Monitoring Instrument, *IEEE Transactions on Geoscience and Remote Sensing*, in press (2006).
71. P. Magnan, Detection of visible photons in CCD and CMOS: A comparative view, *Nucl. Instrum. Meth. Phys. Res. A* 504, 199–212 (2003).

ESA SPECTROSCOPY STUDIES IN SUPPORT OF SPACEBORNE ATMOSPHERIC COMPOSITION SOUNDING

JÖRG LANGEN
ESA, Earth Observations Science and Applications Department, ESTEC, Keplerlaan 1, 2200 AG Noordwijk, The Netherlands

Abstract. This paper summarises the status of the European Space Agency's programme for observation of the composition of Earth's atmosphere: the three large spectrometers GOMOS (Global Ozone Monitoring by Occultation of Strars), MIPAS (Michelson Interferometer for Passive Atmospheric Sounding) and SCIAMACHY (Scanning Imaging Absorption Spectrometer for Atmospheric CHartographY) onboard Envisat (ENVIronment SATellite) since 2002, the opportunities in the Earth Explorer research programme and in the Earth Watch programme for operational missions in cooperation with European Union 'Global Monitoring for Environment and Security' (GMES) or Eumetsat. Two studies on molecular spectroscopy commissioned by ESA (European Space Agency) and targetted at the needs of potential ESA space instrumentation are reviewed. One of them addresses mainly the temperature-dependent measurement of collisional linewidth parameters in the mm/sub-mm wave range and the setup of a spectroscopic dataset dedicated to a possible future limb-sounding instrument; the other aims to establish the feasibility of a high accuracy determination of absorption cross sections of water vapour in the near infrared for a potential future H_2O lidar instrument.

Keywords: atmospheric composition, space instrumentation, spectroscopy.

1. Introduction

The European Space Agency's Earth Observation programme includes a considerable element on monitoring atmospheric composition and chemistry. This started with the Global Ozone Monitoring Experiment

A. Perrin et al. (eds.), Remote Sensing of the Atmosphere for Environmental Security, 27–39.

(GOME) onboard the ERS-2 satellite which was launched in 1995 and is still operational. GOME is directed at the monitoring of stratospheric ozone and related trace species. On Envisat (launched 2002) the atmospheric component was greatly increased in number of species, horizontal and vertical resolution and diurnal coverage. This allows much more detailed investigations and also first contributions to tropospheric and even mesospheric studies. So far, atmospheric chemistry has not been supported by a post-Envisat mission, but has now been prioritised in the ongoing call for ideas for new missions.

All spaceborne measurements of gaseous atmospheric constituents rely on spectrosopic features, either individual spectral lines or clusters, observed either in emission or in absorption. For the conversion of measured transmissions or radiances to trace gas concentrations, exact knowledge of the spectroscopy is necessary, either in the form of spectral line parameters or cross-sections in the atmospheric temperature / pressure regime. Spectroscopic errors have a large potential of dominating error budgets since they do not integrate down when temporal or spatial averages of data are taken. When different spectral features are used in the retrieval, their errors may be different and lead to complex error patterns, in particular when many parameters are fitted to the data. Often the selection of spectral features for the retrieval needs to be a function of the observed altitude, in order to avoid insensitivity or saturation. Then the retrieval error introduced by spectroscopy may depend on altitude and even on the concentration of the target species and spectrally interfering species. Thus, spectroscopic errors are not bound to be linear in the concentration, and therefore can present serious problems in bias correction when assimilating data.

2. Status of ESA's earth observation programme

2.1. ENVISAT

The Envisat satellite was launched in March 2002. It carries three instruments dedicated to atmospheric chemistry: GOMOS, MIPAS and SCIAMACHY. Their common primary scientific target is the ozone chemistry in the stratosphere and its evolution. In addition, each of them contributes to some other research areas.

GOMOS is a star occultation sensor, receiving the UV-visible and near-infrared spectra of stars setting behind the horizon as the satellite orbits around Earth. Vertical profiles of atmospheric constituents are derived from the altitude dependence of their absorption. The time delay between

broad-band signals measured by fast photometers in the red and blue is used to correct for scintillation originating from atmospheric turbulences, and to derive high resolution temperature profiles. The scintillation correction works well with vertical occultations; in oblique occultations, horizontal atmospheric inhomogeneities can lead to inconsistencies. GOMOS has been designed for high radiometric sensitivity to optimise global coverage. It works best at night but can also discriminate the star against background light at day. The main data product is ozone over the full stratosphere and mesosphere, but other species like NO_2, NO_3, aerosol extinction and H_2O as well as temperature are also obtained. GOMOS has had mechanical and electronic problems with its telescope, but is now back to operations.

The MIPAS instrument is a limb-sounding Fourier-Transform spectrometer in the infrared. It covers a large contiguous spectral range with high sensitivity which allows to operate in emission, achieving complete coverage at day and night from pole to pole. In the standard observation scenario, MIPAS covers the range from the upper troposphere to mid mesosphere. There are special observation modes, e.g. for UTLS (Upper Troposphere Lower Stratosphere) observations and upper atmosphere beyond 100km altitude. More than 20 chemical species, among them the complete NO_y family, CFCs and most other tracers, have been retrieved. MIPAS data have quickly gone into scientific exploitation, e.g. they have contributed to polar ozone chemistry and to the characterisation of the chemical impact of large solar proton events. Stratospheric ozone profiles have been assimilated into the operational chain at ECMWF (European Centre for Medium-Range Weather Forecats), nowadays trials with radiance assimilation sensitive to ozone, water vapour and temperature are running. Due to mechanical problems with the interferometer, MIPAS has been switched off for several months, and is now running at reduced spectral resolution (and enhanced spatial resolution) with a duty cycle of about 35%.

SCIAMACHY is an 8-band spectrometer (240-2400nm) observing backscattered radiation alternating in limb and nadir directions, with across-track scan, while on the dayside. It performs also solar and lunar occultations whenever possible. The instrument targets many species in the stratosphere and troposphere, and some in the mesosphere. For the nadir UV-VIS observations, it provides continuity to GOME which was launched in 1995 on the ERS-2 satellite and is still operational. Through its improved horizontal resolution (in comparison to GOME), SCIAMACHY provides detailed maps of tropospheric NO_2. SCIAMACHY is the first instrument to provide maps of CH_4 over land with boundary layer sensitivity. Many other data have been produced. The generation of efficient and accurate retrieval

algorithms is a challenge. The longest wavelength channels are affected by persistent ice condensation on the detector.

2.2. THE EARTH EXPLORER PROGRAMME

The Earth Explorer programme was created ten years ago with the vision to continue spaceborne research in the post-Envisat timeframe with innovative and scientifically more focussed missions, a transparent user-driven selection mechanism and a continuous funding scheme. Since that time, six missions have been selected and approved and are now in extended feasibility study or implementation phase, promising many innovative Earth observation data to come in the next years:

- **Cryosat,** an interferometric radar altimeter for precise determination of ice thickness in Antarctica and Greenland and Arctic sea ice. The launch in October 2005 failed. It is intended to re-build the satellite as soon as possible.
- **GOCE,** a set of gradiometers to measure the geoid with an accuracy of 1-2 cm. To be launched in 2006.
- **SMOS,** an L-band radiometer for soil moisture and ocean salinity measurements. To be launched in 2007.
- **ADM/Aeolus,** a UV Doppler wind lidar for tropospheric and lower stratospheric wind profiles. To be launched in 2008.
- **Swarm,** a constellation of three magnetometry satellites for measuring Earth's magnetic field and its evolution. To be launched in 2009.
- **EarthCARE (with Japan),** backscatter lidar, cloud profiling radar (Japanese contribution), multi-spectral imager, broad-band radiometer for quantification of aerosol-cloud-radiation interactions for improvement of climate and NWP models. To be launched in 2012. Financial commitments for the international cooperation are due 2008.

ESA released a call for ideas for the 7th Earth Explorer in 2005. Four priority areas have been identified for this call : the global water cycle, the global carbon cycle, atmospheric chemistry and its interaction with climate, and the human element. 24 valid proposals have been received. 9 of them address measurements of atmospheric composition, they are summarised in Table 1.

Table 1. Proposals for Earth Explorer 7 offering atmospheric composition measurements.

proposal name	main science issues	main payload
PREMIER	STE, gravity waves, convective transport radiative effects of gases and clouds in the UTLS	mm-wave limb-sounder IR limb-imaging spectrometer
GEOTROPE	European air pollution surface UV monit. / forecast	UV-vis spectrometer + FTIR on geostationary platform
ACCURATE	trends in climate and chemistry UTLS processes, GCMs, NWP	LEO-LEO radio and SWIR occultation constellation of ≥ 4 satellites
KLIMA	water vapour and radiation in the FIR sources and sinks of CO2	2 imaging nadir-viewing FTIRs
OLIVIA	stratospheric and mesospheric O3	star occultation spectrometer fast photometers
ILAC	lightning activity as a proxy for global warming deep convection, storm nowcasting	VHF lightning location interferometer optical lightning monitor OMI-type chemistry instrument
TRAQ	global and regional air quality climate impact of changing atm. composition	UV-VIS-NIR spectrometer static infrared (TIR+SWIR) FTS on inclined orbit
A-SCOPE	global carbon cycle, regional CO2 fluxes	laser absorption spectrometer / pulsed DIAL for CO2
ECOSAT	sources, transport and sinks of GHGs transport and cloud interaction of aerosol	broad-band near-IR limb and nadir viewing spectrometers

The proposals are currently being evaluated in 5 scientific and 3 technical / programmatic panels. ESA's Earth Science Advisory Committee will recommend a maximum of 6 of the 24 for a pre-feasibility study in 2006.

2.3. THE EARTH WATCH PROGRAMME / GMES

The intention of the Earth Watch programme which has been initiated in parallel to the Earth Explorer programme is to provide continuous reliable data streams to governmental, institutional, or commercial users for operational purposes. Several years ago, ESA joined forces with the EU in the "Global Monitoring for Environment and Security" initiative. The GMES programme has started in the last years with the establishment of prototype services using data of existing missions. The GMES space

component, i.e. its future satellite programme, is envisaged to include five missions, called “Sentinels”:

1. C-band SAR (interferometry)
2. Superspectral imager (Landsat, SPOT continuity)
3. Altimeter and multispectral sensor for ocean watch
4. Geostationary atmospheric composition for pollution monitoring
5. Atmospheric composition sounding in low Earth orbit

A study to define the requirements for sentinels 4 and 5 has just been completed. It identified the need to enhance the already planned operational system (EUMETSAT-Metop and NOAA-NPOESS) by a nadir-viewing component addressing air quality and climate protocol monitoring applications and a limb-sounding component contributing to climate monitoring and NWP applications and supporting the nadir component by providing vertical resolution. The nadir component could either be implemented by a system of a geostationary and a low Earth orbit platform in sun-synchronous orbit or by a constellation of three identical low Earth orbiting platforms in inclined (non-sun-synchronous) orbit. The trade-off between both options needs still to be performed.

Feasibility studies for sentinels 1-3 are currently ongoing; a pre-feasibility study for sentinels 4 and 5 will be initiated in 2006.

2.4. SUPPORT TO EUMETSAT

ESA also supports Eumetsat, procuring the space component of their meteorological missions such as Meteosat Second Generation and Metop/EPS. ESA is now involved in the preparation process for Meteosat Third Generation and the post-EPS programme. Eumetsat might eventually become user of GMES data, or parts of the GMES space component might be merged with parts of Eumetsat’s future programme.

3. Study on characterisation of mm-wave spectroscopic signatures

3.1. OBJECTIVES

A mm/sub-mm wave limb-sounder “MASTER” for the observation of stratosphere-troposphere exchange and radiative and chemical processes in the upper troposphere and lower stratosphere (UTLS) has been considered by ESA. Extended instrument feasibility studies, technology programmes and detailed scientific requirement and performance assessment studies have been carried out. An airborne demonstration

instrument “MARSCHALS” has been built and is currently being operated in campaigns on a stratospheric aircraft. MASTER has five wide spectral bands between 297 and 626 GHz. The high spectral resolution of this type of instrument leads to the need for accurate knowledge of the collisional line broadening parameters. For the correct retrieval of small emission features, such as the CO line at 345 GHz, strong interfering lines need to be modelled accurately, which implies accuracy requirements on their spectroscopy as well. Therefore ESA commissioned a study[1,2,3] with these objectives:

- systematic quantification of spectroscopic error sources for MASTER;
- reduction of spectroscopic uncertainties by
  - temperature-dependent measurement of pressure-broadening coefficients, including pressure shifts were appropriate; priorities determined by error analysis;
  - re-calculation of line intensity parameters where necessary;
  - a better characterisation of HNO_3 bands;
- generation of a spectroscopic database for MASTER.

3.2. QUANTIFICATION OF SPECTROSCOPIC ERRORS

As an input to the initial error analysis, a preliminary spectroscopic database was generated. This was based on HITRAN, JPL and SAO catalogues and further literature research and included lines of all species known to emit in the targetted spectral ranges. A conservative filter (threshold of 0.1K brightness temperature contribution within the MASTER bands at any observation geometry) reduced the size of the database by a factor of 4 to about 8000 lines.

The sensitivity of a representative multi-species global retrieval to the uncertainty of each spectrosopic parameter was tested in the initial error analysis. The main qualitative outcome was :

- ***Line positions*** are known with sufficient accuracy.
- An uncertainty in the ***line intensity*** gives similar effect on the retrieval of the species to which the line belongs.
- The ***air broadening parameters*** and their temperature exponents of a few strong lines dominate the spectroscopic error budget.
- ***Self broadening parameters*** have a small impact on the retrieval.
- ***pressure shifts*** have small impact on the retrieval (exception HNO_3).

- The retrieval of ***weak lines*** (e.g. BrO) is severely affected by intensity and air broadening errors of interfering strong lines.

The work programme for measurement of pressure broadening coefficients was optimised for maximum impact on retrieval accuracy, using the quantitative results of the spectroscopic error analysis (considering also other error sources such as noise). For several spectral lines, it was found that the measurement of the temperature exponent could be avoided by measuring the line broadening parameter in the middle of the atmospheric temperature range instead of room temperature, thereby reducing the sensitivity to the temperature dependence.

3.3. REDUCTION OF SPECTROSCOPIC UNCERTAINTIES

7 O_3 lines in the 300 GHz range and 9 HNO_3 lines were selected for lab measurements of pressure broadening parameters. Description of the measurement techniques and results can be found in Refs. (1,2,4). The accuracy of the pressure broadening coefficients is in the range of 1-2%, leading to a drastic reduction of the spectroscopic error budget. Pressure shifts were negligible.

HNO_3 presents a particular problem since it forms clusters of huge numbers of lines, and there is no chance to measure all of them. Therefore, an empirical fit of a limited number of broadening parameters to the rotational quantum number was performed (see Figure 1).

Line intensity calculations were performed with the following results.

- H_2O: dipole matrix elements were re-calculated; significant discrepancies with HITRAN were identified starting at second excited vibrational state.
- O_3: no significant changes were found.
- HNO_3: the partition function was re-calculated; good agreement with HITRAN was found (the JPL catalogue does not include vibrational part).
- N_2O: intensities were re-calculated. They are consistent with the values of the JPL catalogue – except that JPL misses the vibrational partition function. A 7% discrepancy with HITRAN was found; the origin of HITRAN N_2O intensities was unclear.
- BrO: a new partition function was computed since this species was not present in HITRAN.

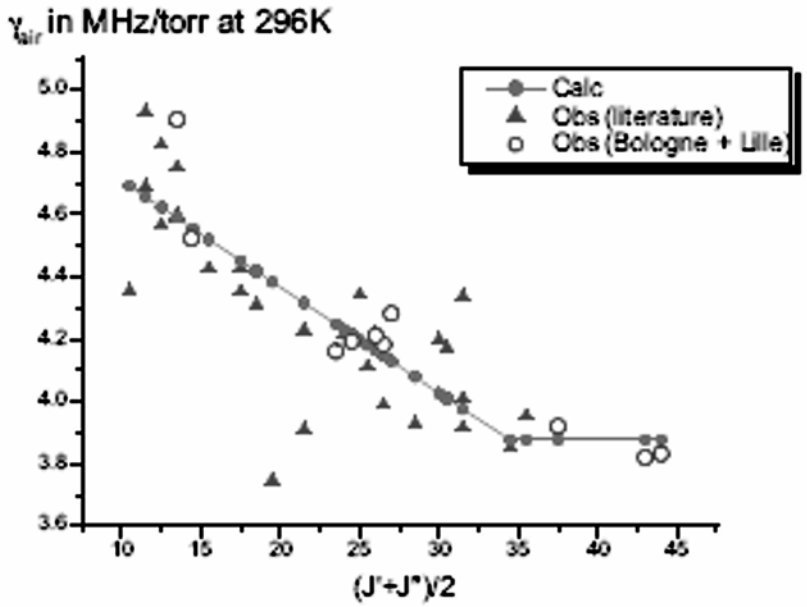

Figure 1. HNO_3 air broadening parameters at room temperature as a function of the rotational quantum number. open circle: data taken within this study; triangle: literature data; line: fit.

The error analysis was repeated with the new values and accuracy estimates of the measured and calculated quantities. Large error reductions were found.

The retrieval of species with only weak emission features (e.g. BrO and CO in the MASTER bands) often suffers from interferences of several much stronger foreign lines, e.g. ozone. The impact of spectroscopic errors of the interferences can be so severe that a spectroscopic characterisation will not be feasible with the accuracy that would be necessary for a correct modelling of that line. In the case of a single line of the interfering species, this does not present a problem since the retrieval will compensate the spectroscopic errors with a small "adjustment" of the concentration profile of the interfering species. However, when several lines of the interfering species need to be fitted and their spectroscopic errors are slightly different, the forward model will not be able to reproduce the measured spectrum, and large errors in the retrieval of the "weak" species may be generated. It was shown in this study that this problem can be overcome in the case of MASTER by fitting separate profiles for each of the strong ozone lines, thereby circumventing the spectrosopic inconsistencies.

3.4. SPECTROSCOPIC DATABASE

The initial spectroscopic database was updated with the data of the new measurements and intensity calculations and further literature research. It is now being used for the retrieval of data from the MARSCHALS airborne limb-sounder.

4. Study on H_2O spectroscopy in the near infrared

4.1. OBJECTIVES

A Lidar instrument for measurement of tropospheric water vapour profiles was proposed to ESA several years ago ("**WA**ter Vapour **L**idar **E**xperiment in **S**pace", WALES) and underwent a feasibility study. Among the many water vapour sensors in orbit, the role of this instrument would be to provide a standard of high accuracy and vertical resolution with a simple forward and retrieval procedure ("direct measurement"). The allocation for the spectroscopic error in the systematic error budget was 2%. The large dynamic range of the water vapour profile (mixing ratios of percents at the surface, several ppm at the tropopause) required a lidar with a cascade of 4 wavelengths with different absorption cross sections (centres of strong, medium and weak lines, and off-line). The selection of spectral lines needed to

- match the large dynamic range of H_2O abundance by a corresponding range of line strengths;
- minimise the sensitivity to temperature - this constrains the lower state energies of the transitions;
- minimise the spectral interference of other trace gases;
- take into account the uncertainty of the wavelength-dependence of aerosol extinction – this implies that all four wavelengths must be close to each other.

ESA issued a spectroscopy study[5] for this project with the primary objective to demonstrate the feasibility of measuring the absorption cross-sections of water vapour at the 4 lidar wavelengths with a 2% accuracy within the complete temperature, pressure and water vapour concentration regime to be expected within the troposphere. In addition, the determination of spectral line parameters would increase the credibility of the measurement results. The study was also to confirm the spectral line selection, in particular the absence of spectral lines in the "off-line" region.

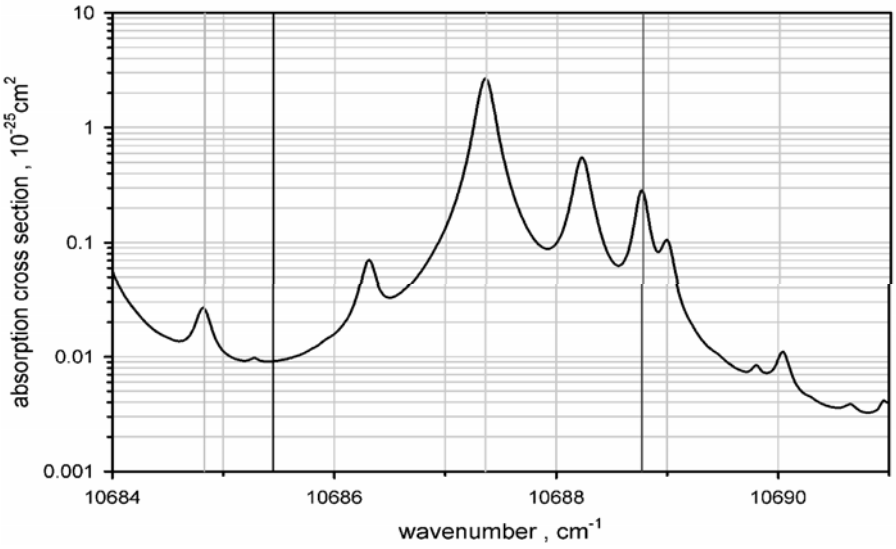

Figure 2. Water vapour absorption cross section spectrum in the 935nm region; WALES wavenumbers indicated by vertical lines.

4.2. MEASUREMENTS AND RESULTS

The measurements were performed using two complementary techniques. For the survey of a broad spectral range, a Fourier Transform spectrometer (FTS) was used. For high sensitivity and high spectral resolution measurements around the targeted wavelengths, Cavity Ring Down Spectrometry (CRDS) was applied. A limited overlap between the measurements with both techniques in the (T, p, H_2O) parameter space was used for an intercomparison which demonstrated qualitative agreement between the results. The measurements were performed in a N_2 environment, and line parameters were empirically corrected for air broadening. A more fundamental problem was the sharp decrease of the water vapour saturation pressure with temperature. This led to insufficient sensitivity even of the CRDS method at temperatures below 235K, and consequently to the need for determination of spectral line parameters which could be used to calculate cross-sections at lower temperatures. Other experimental issues included the calibration of the water vapour concentration in the cell, the temperature stability and homogeneity in the FTS cell, and laser mode hopping in the CRDS. Measurements were performed between 100 and 1000 hPa and between 236 and 301K. A

spectral line was found at the position foreseen for the "off-line" wavelength, resulting in a small shift of the latter. Accuracies of individual cross-section measurements varied between 1 and 10%. A complete set of line parameters (position, pressure shift, intensity, lower state energy, foreign broadening, self-broadening, temperature exponent of broadening) was fitted. The combination of all data in the fit leads to better accuracies. The quantification of the systematic errors is essential and at the same time a challenging task.

5. Conclusions and outlook

The status of ESA's Earth Observation programme, as seen from the perspective of atmospheric composition sounding, was reviewed. A large set of high quality data is available from Envisat and ERS-2 (and foreign satellites such as EOS-Aura and ACE) in this decade. In the near future, two missions focussing on observation of tropospheric greenhouse gas concentrations for the determination of surface fluxes are expected, NASA's OCO and JAXA's GOSAT. In the next decade, there are no firm plans for atmospheric chemistry missions beyond the contributions of meteorological systems (GOME-2 and IASI on Metop, and OMPS and CrIS on NPOESS). Main data gaps to be filled will be measurements of air quality parameters, climate gases and aerosol in the troposphere with good horizontal and temporal resolution, and upper troposphere / lower stratosphere measurements of chemical species, in particular radiatively active ones, with good vertical resolution. A pre-selection process for a future research missions is currently ongoing at ESA.

All three atmospheric chemistry instruments onboard Envisat (and many other space instruments) record contiguous medium to high resolution spectra over large ranges. Precise spectroscopic data are of prime importance for the correct interpretation of the data. ESA has been issuing several studies for spectroscopic measurements dedicated to specific space instruments. Two examples have been reported here. Other studies have been performed for, e.g., GOME and SCIAMACHY. A challenging task for the future could be a precision measurement of CO_2 and CH_4 lines in the short-wave infrared, should new instruments for this purpose be considered.

References

1. J. Demaison, S. A. Buehler, N. Koulev, T. Kuhn, C. Verdes, G. Cazzoli, L. Dore, C. Puzzarini, J.-M.Flaud, A. Perrin, B. Bakri, J.-M. Colmont, F. Rohart, and G.

Wlodarczak, Characterisation of mm-wave spectroscopic signatures, Final Report of ESTEC Study Contract No. 16377/02/NL/FF, March 2004

2. A. Perrin, C. Puzzarini, J.-M. Colmont, C. Verdes, G. Wlodarczak, G. Cazzoli, S. Buehler, J.-M. Flaud, and J. Demaison, Molecular line parameters for the "MASTER" (Millimeter wave Acquisitions for Stratosphere/Troposphere Exchange Research) database, *Journal of Atmospheric Chemistry,* 51, 161-205. (2005)
3. C.L.Verdes, S. A. Buehler, A. Perrin, J.-M. Flaud, J. Demaison, G. Wlodarczak, J.-M. Colmont, G. Cazzoli and C. Puzzarini A sensitivity study on spectroscopic parameter accuracies for a mm/submm limb sounder instrument, *J. Molec. Spectrosc.* 229, 266-275 (2005)
4. G. Wlodarczak, J.-M. Colmont, and F. Rohart, Quantitative rotational spectroscopy for atmospheric research; Microwave databases, need for future and oncoming satellite experiments (this book)
5. M.D. Andrés-Hernández et al., Characterisation of spectroscopic signatures in the 920-950nm spectral range for water vapour DIAL measurements, Final Report of ESTEC Study Contract No. 16502/02/NL/FF, August 2004

THE MIPAS EXPERIMENT ABOARD ENVISAT: REMOTE SENSING OF ATMOSPHERIC COMPOSITION

HERBERT FISCHER*
Institute for Meteorology and Climate Research (IMK-ASF), Forschungszentrum Karlsruhe and Universität Karlsruhe, P. O. Box 3640, 76021 Karlsruhe, Germany

Abstract. The European satellite ENVISAT has been successfully launched at 1 March 2002. Onboard ENVISAT the MIPAS (Michelson Interferometer for Passive Atmospheric Sounding) experiment has been carried to a sun-synchronous polar orbit. MIPAS is a mid-infrared high resolution (0.035 cm^{-1}) limb sounder. The measured spectra in the range between 4.1 and 14.6 μm are processed in order to derive global distributions of temperature and about 25 trace constituents. In addition, the detected broadband spectra allow to determine properties of Polar Stratospheric Clouds (PSCs) and aerosol amount. The status of the MIPAS experiment since its launch will be described. The strength of the MIPAS experiment is demonstrated by the simultaneous detection of a larger number of stratospheric trace species including $ClONO_2$ and ClO. In addition, it will be shown that essential properties of PSCs will be derived from corresponding spectra including the spatial distribution and temporal development of PSCs. MIPAS can also be used to study the tropospheric-stratospheric exchange (H2O distributions) and the mesospheric-stratospheric exchange (NO/NO2 distributions). Further investigations deal with the analysis of highly resolved spectra in order to determine the

*To whom correspondence should be addressed. Herbert Fischer, Institute for Meteorology and Climate Research (IMK-ASF), Forschungszentrum Karlsruhe and Universität Karlsruhe, P. O. Box 3640, 76021 Karlsruhe, Germany; e-mail: herbert.fischer@imk.fzk.de

A. Perrin et al. (eds.), Remote Sensing of the Atmosphere for Environmental Security, 41–56.

concentration profiles of isotopes (e.g. of water vapour). These results yield complementary information on dynamics and transport in the atmosphere. The article will be concluded with future expectations on MIPAS results

Keywords: infrared spectroscopy; trace constituents; atmospheric dynamics; atmospheric chemistry; stratosphere; ENVISAT; MIPAS

1. Introduction

At March 1, 2002 the European Space Agency (ESA) launched the ENVISAT satellite in a polar, sun-synchronous orbit. The large satellite with a mass of more than eight tons is orbiting in a height of about 800 km with a descending node of 10:00 h. From the ten experiments on board three are used to explore the composition of the atmosphere. One of them is the Michelson Interferometer for Passive Atmospheric Sounding (MIPAS).

The Institute for Meteorology and Climate Research (IMK) has developed in the past several MIPAS instruments which have been used in ground stations, aboard aircrafts and balloon gondolas (Fischer 1993). Finally, the IMK has proposed a corresponding satellite experiment to ESA who has included this MIPAS experiment in the core payload of ENVISAT.

In the meantime it has been demonstrated that the strength of MIPAS is the simultaneous detection of a larger number of stratospheric trace species. In addition, it has been shown that essential properties of thin ice clouds can be derived from MIPAS broadband spectra. These results yield complementary information on dynamics, transport, chemistry and microphysics in the atmosphere.

2. MIPAS/ENVISAT experiment

MIPAS is a high resolution Fourier Transform Spectrometer which measures the atmospheric limb emission simultaneously in four spectral bands in the middle infrared (Fischer et al., 2000). The whole spectral interval covers the range from 4.15 to 14.6 μm. The unapodized spectral resolution is 0.035 cm^{-1} which allows the detection of many single spectral emission lines. MIPAS is continuously performing measurements during day and night, providing each day a full coverage of the globe. During an orbit the instrument performs 75 limb scans and in addition calibration measurements when operating in the nominal mode. The instrument is very flexible, i.e. it can also be used for performing a considerable number of other observation modes with various scientific objectives.

By analysing a limb scan sequence vertical profiles of temperature and many trace gases can be derived. Furthermore, these data are appropriate to determine information about aerosols as well as particles of Polar Stratospheric and cirrus clouds.

Combining the profiles along an orbit, the distribution of the atmospheric parameters can be presented as a function of altitude and latitude.

The MIPAS instrument is a dual slide, dual port interferometer which is using all the incoming radiance for measurement and is in various instrumental parts redundant. Fig. 1 shows the optical design of MIPAS-ENVISAT including the azimuth and elevation scan unit, the telescope, the interferometer, and the focal plane subsystem with the detectors. Table 1 summarizes the main specifications of the MIPAS experiment.

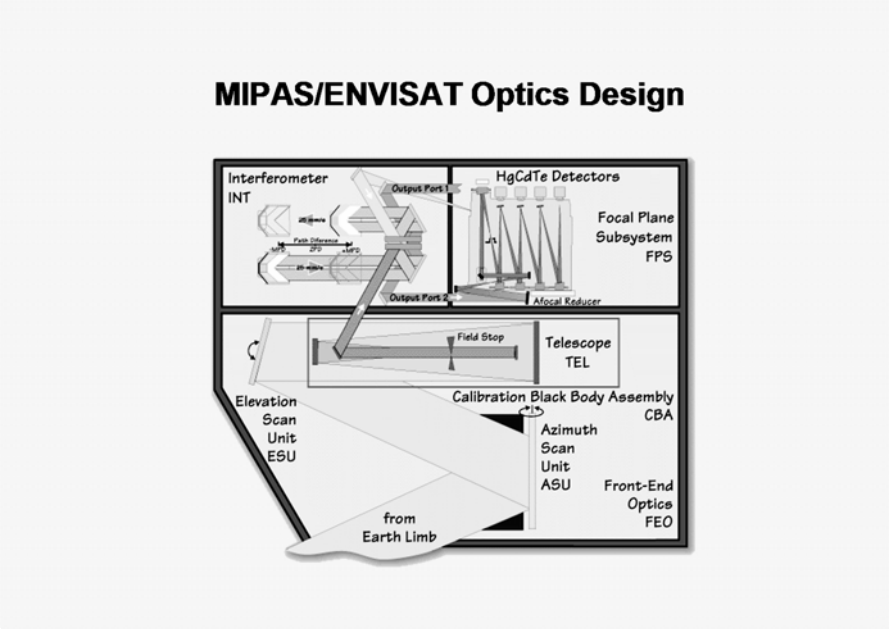

Figure 1. Optical design of the MIPAS/ENVISAT experiment.

The enormous amount of information in one MIPAS spectrum is shown in Fig. 2. This emission spectrum of the atmosphere associated to a tangent altitude of 26 km (definition see below in Fig. 3) impresses by the large number of spectral lines which stem from many atmospheric trace gases as indicated in the figure.

MIPAS-experiment aboard ENVISAT

ENVISAT launch: 1st March 2002
Michelson interferometer

Spectral range: 4.1 – 14.6 µm
Spectral resolution: 0.035 cm-1
Altitude range: Nominal mode: 6 – 68 km
several other observation modes

Global coverage: measurements from pole to pole
Measurement schedule: continuous

Measurement parameters:
- *p, T, H2O, O3, CH4, N2O, HNO3, NO2* → operational processing
- *NO, N2O5, HNO4, ClONO2, ClO, HOCl, CO, CFCs, NH3, C2H6, H2O2, HDO, O3* isotopomers and others (more than 25 parameters) } scientific processing

Table 1. Summary of MIPAS specifications.

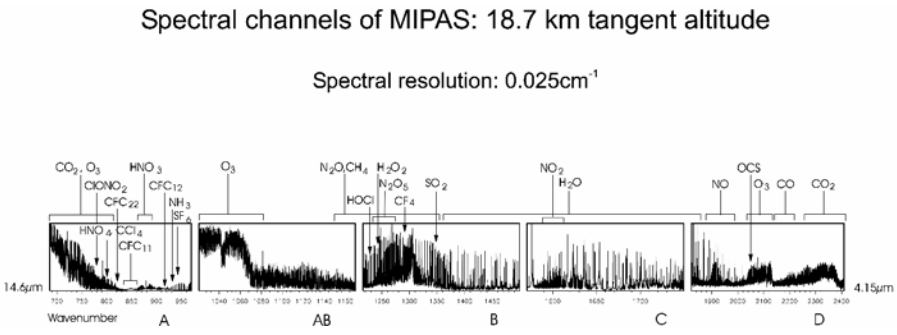

Figure 2. MIPAS spectrum for a tangent height of 26 km showing the enormous amount of information contained.

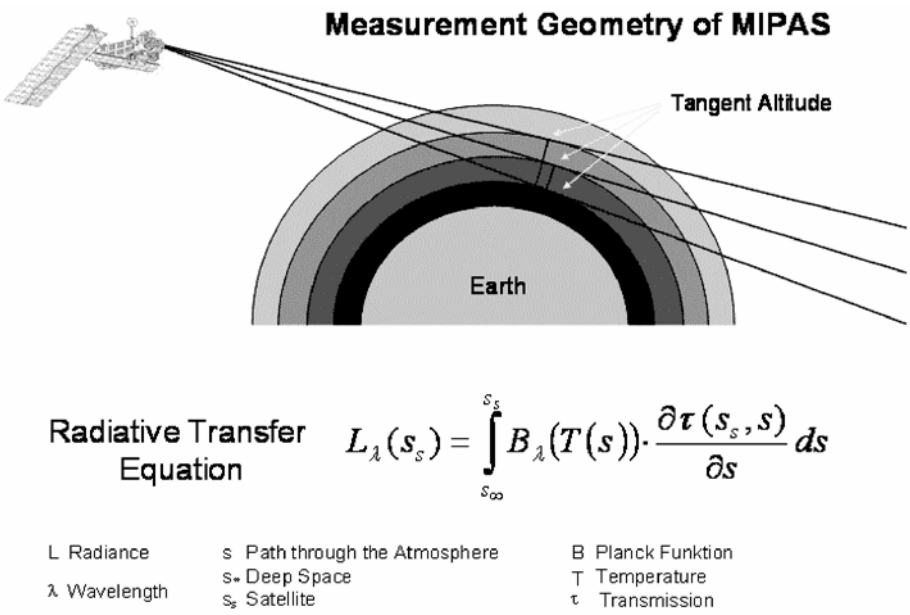

Figure 3. Limb sounding geometry and the Radiative Transfer Equation.

3. Data processing

The interferometer transforms the atmospheric radiance in an interferogram which has to be converted back to a spectrum by applying a Fourier transformation. In the following this spectrum has to be calibrated by using blackbody and deep space measurements. A further step in data processing is the inversion of spectral radiances in trace gas concentrations. A trace gas profile can be derived from a sequence of limb measurements.

The limb sounding geometry is shown in Fig. 3. The ray path is mainly defined by the tangent altitude which corresponds to the minimum distance between ray path and earth surface. The information about the vertical structure of the atmosphere is attained by scanning across the atmosphere.

Main characteristics of KOPRA

- Currently ~ 70 different trace species, many of them relevant in the UTLS only
- Non-LTE radiative transfer modelling
- Vertical variation of isotopomeric abundances
- Accurate modelling of spectroscopic features (CO_2, line mixing, self/air broadening, pressureshift, line shapes, continua, p/T-dependent cross-sections of heavy molecules, ...)
- Particle-caused absorption, emission and single scattering
- Pseudo-analytic derivatives
- Generic non-LTE state population model coupled into KOPRA
- Mie model for calculation of absorption and scattering coefficients and phase function coupled into KOPRA
- Raytracing for elliptical earth
- Consideration of horizontal inhomogeneities (P, T, vmr, ...) by 3-D fields
- Derivatives wrt
  - Chemical composition and microphysical properties of particles (size distribution,…)
  - Non-LTE process parameters (collision rates, production rates,…)

  are provided
- Modelling of instrument characteristics (FOV, ILS,…)
- User-defined numerical accuracy

Table 2. Main characteristics of the Radiative Transfer Code KOPRA.

The Radiative Transfer Equation (RTE) describes the connection between the measured radiances and the distribution of the atmospheric parameters. A corresponding computer code is called KOPRA (Stiller et al. 2000) which has been developed at the IMK. It is based on the up to date knowledge about the radiative processes in the atmosphere including the ray tracing for an elliptical earth, the consideration of horizontal inhomogeneities, and non-LTE (local thermodynamic equilibrium) effects (see Table 2).

In order to determine vertical profiles of atmospheric parameters from the radiance measurements the RTE has to be inverted. Methods for this retrieval are described by Rodgers (2000). We are using most often the optimal estimation method with a Tikhonov smoothing operator.

A sequence of limb emission measurements (between 68.4 km and 6.4 km tangent altitude) is shown in Fig. 4.

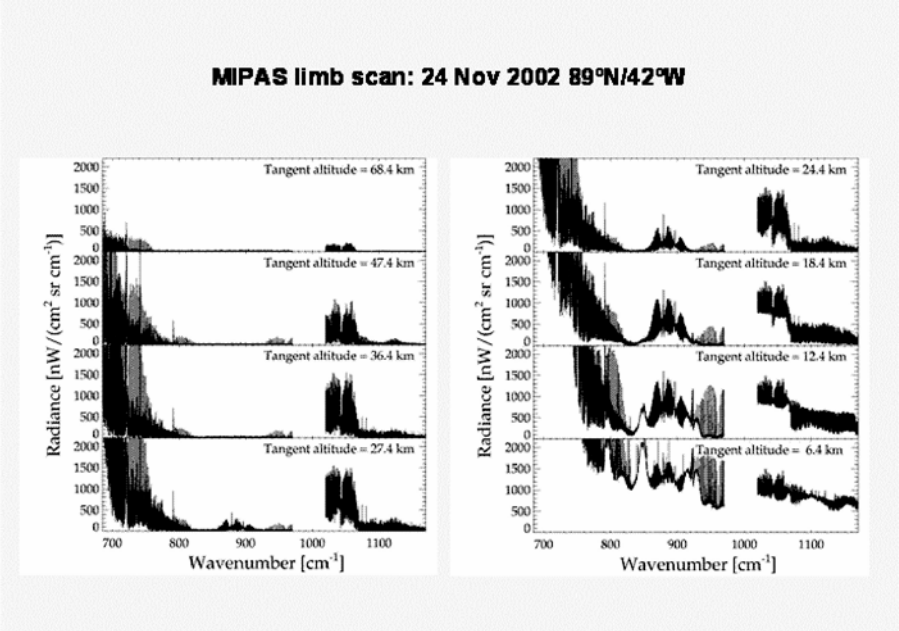

Figure 4. Sequence of limb emission spectra in the altitude region between 68.4 km and 6.4 km.

First of all, a gap of information can be recognized in the spectral range between 970 and 1020 cm^{-1}. At high altitudes the emitted radiance is relatively weak; only the CO_2-band below 760 cm^{-1} and the O_3-band around 1050 cm^{-1} are clearly visible. With decreasing tangent altitude the emitted radiance becomes stronger and additional absorption bands show up, e.g. the CO_2 laser band around 960 cm^{-1}, the HNO_3-bands around 875 cm^{-1}, and the CFC bands around 850 cm^{-1} and 920 cm^{-1}. The HNO_3 bands grow rapidly in the lower stratosphere due to the shape of the vertical profile of the HNO_3 mixing ratio. In the upper troposphere the spectrum exhibits some single strong lines in the range of the atmospheric window between 800 and 1000 cm^{-1}. They are caused by weak water vapour lines becoming visible in the upper troposphere due to the quickly increasing water vapour mixing ratio.

4. MIPAS results for the stratosphere and mesosphere

As mentioned above, from the sequences of measured limb radiance spectra vertical profiles of trace gases can be derived. Combining the vertical profiles along the satellite orbit allows to generate cross sections of atmospheric parameters. The good quality of the distributions of trace species concentrations from MIPAS observations has been demonstrated manifold (see e.g. validation workshop ESA 2004, http://envisat.esa.int). In the following examples of results will be shown which prove the enormous capability of the MIPAS experiment.

First of all, MIPAS can detect all the nitrogen-oxygen compounds (NOy) in the stratosphere simultaneously (except NO_3 which plays only during night a minor role). An example of cross sections of N_2O, HNO_3, $ClONO_2$, NO_2, NO and N_2O_5 is presented in Fig. 5.

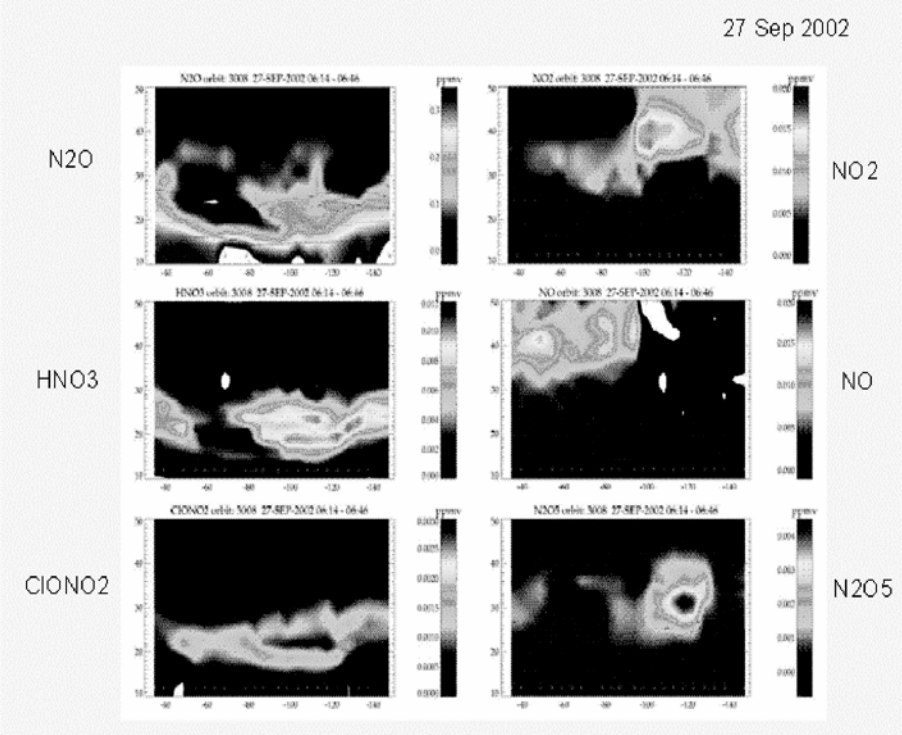

Figure 5. Simultaneous detection of NOy-compounds in the stratosphere (10 to 50 km) in the northern hemisphere (-40 and -140 correspond to 40°S, -90 to South Pole).

The day of observation is the 27 September 2002 when the Antarctic vortex splits into two parts as can be recognized very well in the N_2O plot. Obvious is also the concentration change of NO and NO_2 at the terminator. The distribution of the missing trace species HNO_4 has also been derived recently. Such data have been used for studying the NOy partitioning and denitrification during the Antarctic major warming event in September/October 2002.

Essential for the stratospheric ozone depletion is the concentration of ClO in the atmosphere; under high $ClONO_2$ concentrations this process is not effective. MIPAS is capable to measure ClO under disturbed chemical conditions as in the polar winter/spring. Fig. 6 shows the stratospheric cross sections of ClO and $ClONO_2$.

High amounts of ClO are only visible in the polar lower stratosphere at the day side. $ClONO_2$ shows the typical collar structure over Antarctic (see Höpfner et al. 2004a).

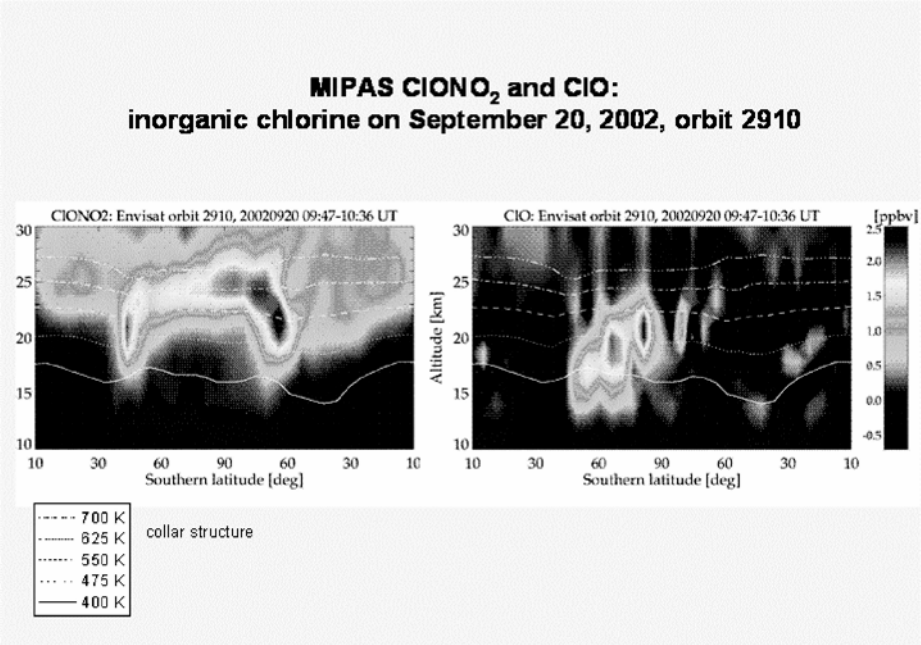

Figure 6. Stratospheric cross sections of ClO and ClONO2 for higher latitudes in the southern hemisphere at 20 September 2002.

Fig. 7 shows stratospheric cross sections of long-lived trace gases, potential vorticity (PV) and O_3 along the satellite orbit from 40°S across the South Pole to 40°S.

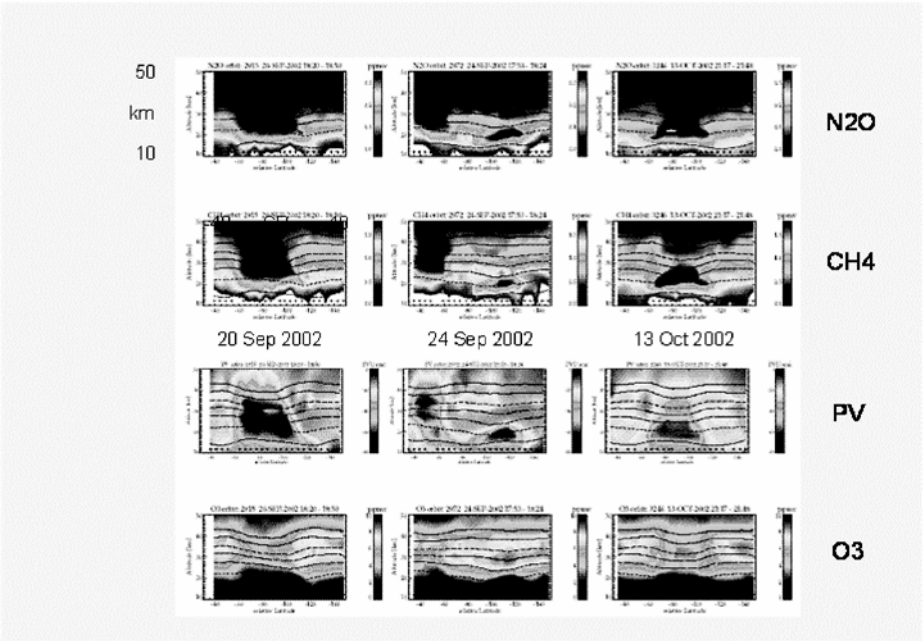

Figure 7. Stratospheric cross sections of trace gases and potential vorticity along the satellite orbit from 40°S across the South Pole to 40°S for three different dates.

The three columns are related to different dates: 20 September, 24 September, and 13 October 2002 (from left to right). The time period is also connected with the split of the Polar Vortex over Antarctic. At 20 September 2004 the Polar Vortex is seen very clearly by the low mixing ratios of N_2O and CH_4 in the lower stratosphere. The potential vorticity (PV) as derived from ECMWF-data confirms this statement. Simultaneously, low ozone values are obviously existing over Antarctic. The split up of the polar vortex is recognized at 24 September 2002 connected with high ozone concentrations at high southern latitudes.

At 13 October 2002 a re-establishment of the polar vortex has happened. On the other hand, this polar vortex is much less pronounced in the middle stratosphere as can be seen in the CH_4 cross section. This example shows clearly the comprehensive information content of the MIPAS data about the stratospheric dynamics (see also Glatthor et al. 2004).

MIPAS is a versatile instrument; from the measurements not only trace gas concentrations but also parameters of thin clouds can be derived. Höpfner et al. (2004b) have proven that high resolution broad-band IR spectra can be used to determine the mean size and the volume density of the cloud particles as well as their chemical composition.

The limb spectra of Polar Stratospheric Clouds (PSC) show very special signatures which are caused by a superimposition of cloud emitted radiance and scattered tropospheric radiance. The interpretation of the spectra as measured along different orbits across the Antarctic region has yielded spatial distributions of PSCs for different dates (see Fig. 8).

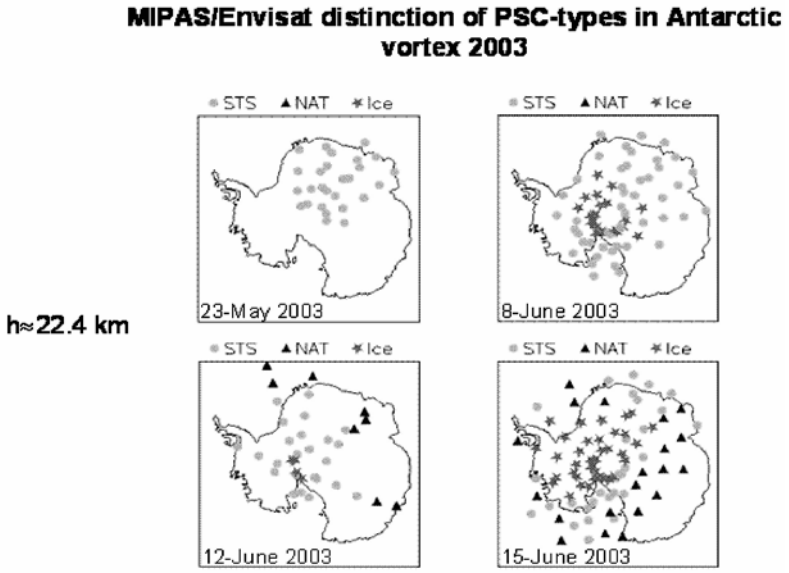

Figure 8. Spatial distribution of different types of PSCs over Antarctica at four dates.

These results show clearly that the development of the PSCs is connected with complex processes in the atmosphere depending on temperature, dynamics and chemical composition. Höpfner has already proven that thin cirrus clouds in the tropopause region exhibit the same typical spectral signatures as PSCs, i.e. also size distribution and volume density of these ice particles can be derived.

MIPAS measurements are very valuable for the investigation of the tropospheric-stratospheric exchange. For Fig. 9 the global water vapour distribution at an altitude of 18 km in summer is presented.

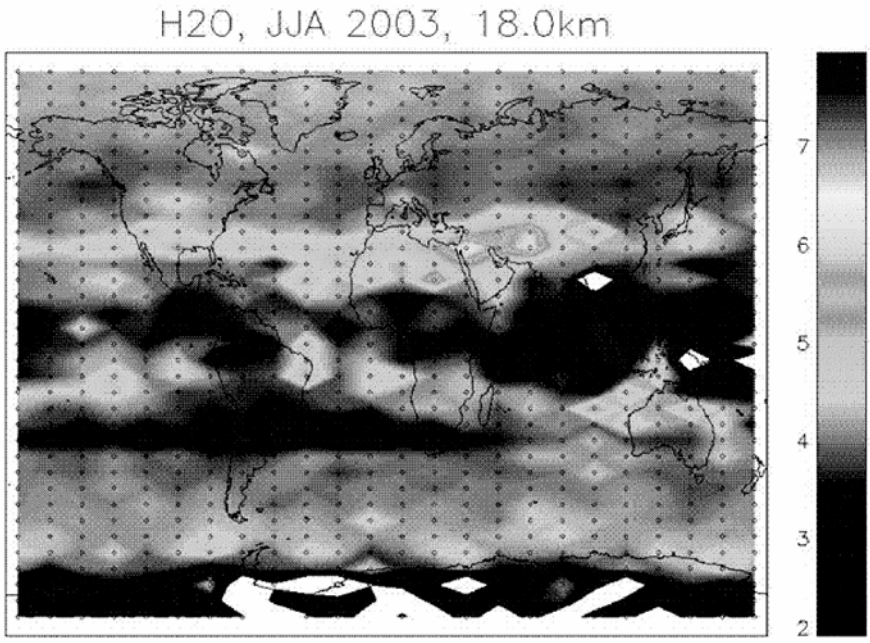

Figure 9. Global water vapor distribution at an altitude of 18 km; mixing ratios show relatively high values over Asia (Arab peninsula and Iran).

As expected the MIPAS H_2O distribution is not homogeneous. The relatively high values of H_2O mixing ratio over Asia (Arab peninsula and Iran) indicate stronger convective processes in the troposphere in this region. Additional information will be gained by distributions of isotope concentrations (e.g. HDO as more recently derived from MIPAS data).

Not very well known is the vertical transport of thermospheric air down into the mesosphere and upper stratosphere up to now. However, CO- and NOx- cross sections derived from MIPAS measurements show clearly the downwelling of air in the polar night regions (Funke et al. 2006).

Furthermore, the influence of solar proton events on the middle atmosphere can be observed in detail by MIPAS (Lopez-Puertas et al. 2006). The solar storm at the end of October 2003 has changed directly the ozone mixing ratio in the lower mesosphere over both polar regions (see Fig. 10).

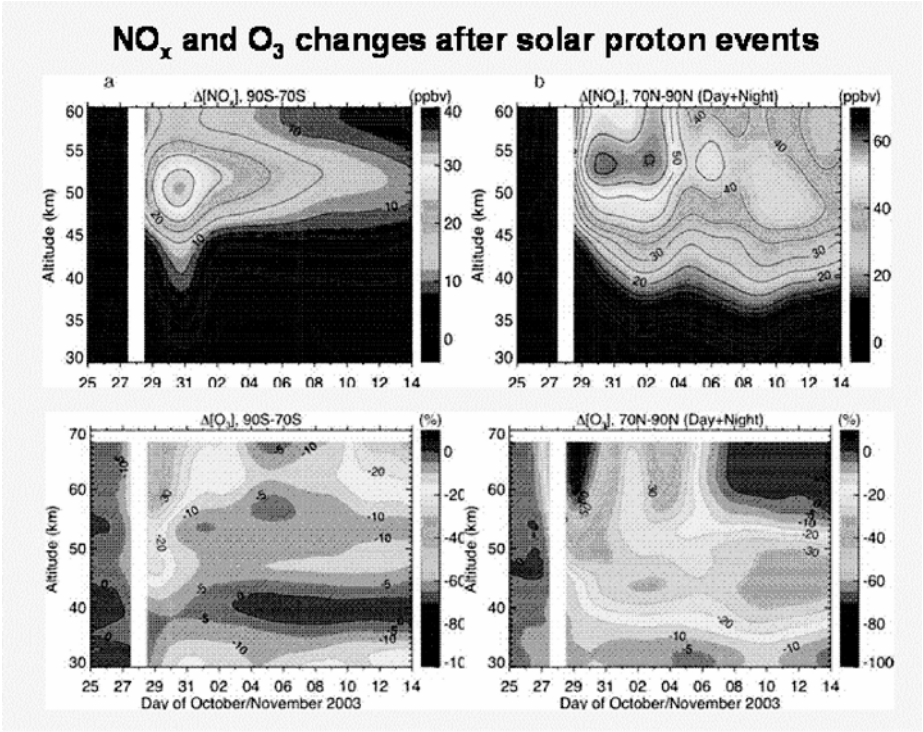

Figure 10. Mean NO_x- and O_3-profiles over the Antarctic and Arctic during the Solar Proton Event end of October 2003.

The change of NOx happens some days later; its effect on the ozone concentration is weak over the Antarctic but obvious over the Arctic. More details of this event are obtained by investigating the concentrations of other trace species like $ClONO_2$.

5. Conclusions and outlook

MIPAS provides high quality global measurements during day and night of temperature, more than 25 trace constituents and parameters of thin clouds. The validation of the results yields generally good agreement with the measurements of various other experiments. The partioning of nitrogen and chlorine compounds in the stratosphere is well observed. Distributions of various long-lived trace species indicate transport phenomena in stratosphere and mesosphere. Simultaneous measurements of trace gas concentrations and cloud parameter (PSC, thin cirrus) were performed. H_2O and HDO distributions illustrate tropospheric/stratospheric exchange. Solar storm events affect concentrations of NOx and O_3 in the stratosphere.

Future MIPAS measurements have to be carried out with lower spectral resolution (about 40%) and only 30% of time because the interferometer has a problem with the movement of the retroreflector slides. On the other hand, the lower spectral resolution does not reduce the information content of the measurements significantly. Measurements using the different observation modes will yield further insights in atmospheric processes.

Acknowledgement

The versatile contributions of members of the MIPAS Scientific Advisory Group, several ESA colleagues and many scientists of my institute are acknowledged.

References

Fischer, H., 1993, Remote sensing of atmospheric trace gase, Interdisciplinary Science Reviews **18**: 185 – 191.

Fischer, H., Blom, C., Oelhaf, H., Carli, B., Carlotti, M., Delbouille, L., Ehhalt, D., Flaud, J.-M., Isaksen, I., Lopez-Puertas, M., McElroy, C.T., and Zander, R., 2000, Envisat-MIPAS, the Michelson Interferometer for Passive Atmospheric Sounding; An instrument for atmospheric chemistry and climate research, ESA SP-1229, C. Readings and R.A. Harris, eds. (European Space Agency, Noordwijk, The Netherlands, 2000).

Funke, B., et al., 2006, Downward transport of upper atmospheric NOx into the polar stratosphere and lower mesosphere during the Antarctic 2003 and Arctic 2002/2003 winters, J. Geophys. Res., accepted.

Glatthor, N., et al., 2004, Mixing processes during the Antarctic vortex split in September/October 2002 as inferred from source gas and ozone distributions from MIPAS/ENVISAT, J. Atmos. Sci., Special issue on Antarctic Vortex 2002, accepted January 2004.

Höpfner, M., et al., 2004, First spaceborne observations of antarctic stratospheric ClONO2 recovery: austral spring 2002, J. Geophys. Res. **109**: D11308.

Höpfner, M., et al., 2005 ,MIPAS detects Antarctic stratospheric belt of NAT PSCs caused by mountain waves, Atm. Chem. Phys. (Discuss.), June 2005..

Lopez-Puertas, M., et al., 2006, Observation of NOx Enhancement and Ozone Depletion after the October-November 2003 Solar Proton Events, J. Geophys. Res., accepted.

Rodgers, C.D., 2000, Inverse Methods for Atmospheric Sounding: Theory and Practice, Vol. 2, edited by F.W. Taylor, World Scientific, River Edge, N.J.

Stiller, G.P., (Ed.), 2000, The Karlsruhe optimized and precise radiative transfer algorithm (KOPRA), Wiss. Ber. FZKA **6487**, Forschungszentrum Karlsruhe, Germany.

PERFORMANCES OF THE OPERATIONAL RETRIEVAL CODE FOR MIPAS ON ENVISAT AND POSSIBLE IMPROVEMENTS OF RETRIEVAL TECHNIQUES FOR ENVIRONMENT AND CLIMATE

BRUNO CARLI
(b.carli@ifac.cnr.it),
CLAUDIO BELOTTI AND
SAMUELE DEL BIANCO
IFAC-CNR - via Madonna del Piano, 10 - 50019
Sesto Fiorentino (FI) - Italy

Abstract. The MIPAS instrument, operating on board of the Envisat satellite, with its broad band and high resolution measurements has posed a major challenge to operational retrieval techniques. The code developed for the operational analysis of MIPAS measurements has proved that near-real-time operation is possible and that a three-dimensional picture of the atmospheric composition can be retrieved from satellite observations. The features and performances of MIPAS retrieval code are briefly recalled.

The breakthrough in retrieval techniques obtained with MIPAS can be the basis for further significant improvements. The correlation that exists among the observations and among the target parameters are more rigorously and more efficiently accounted for if the retrieval is made handling simultaneously correlated observations and correlated target parameters. This is the case of two-dimensional retrieval and multi-target retrieval. Another direction for further improvements is that of the effect of model errors. These can be better accounted either with the use of the variance covariance matrix of these errors or with the simultaneous retrieval of the main model errors. These retrieval approaches can be very demanding in terms of computing resources, but they change the ultimate accuracy possible with remote sensing techniques and must be taken into account in the planning of future instruments for environment and climate.

Keywords: retrieval techniques, limb sounding, atmospheric chemistry, Fourier transform spectroscopy

Abbreviations: MARSCHALS – Millimetre wave Airborne Receivers for Spectroscopic CHaracterisation of Atmospheric Limb Sounding; MIPAS – Michelson Interferometer for Passive Atmospheric Sounding; NLSF – Non-linear Least Square Fit; NLTE – Non-Local Thermal Equilibrium; NRT – Near Real Time; ORM – Optimised Retrieval Model; VCM – Variance-Covariance Matrix; VMR – Volume Mixing Ratio.

1. Introduction

MIPAS (Michelson Interferometer for Passive Atmospheric Sounding) is an instrument developed by ESA and mounted on board of the Envisat satellite for the observation of the atmospheric emission at the limb in the middle infrared spectral region. MIPAS, with its continuous, broad band and high resolution mea-

A. Perrin et al. (eds.), Remote Sensing of the Atmosphere for Environmental Security, 57–70.

surements, has a data flow which is significantly larger than previous typical atmospheric sounding instruments. This feature posed a major challenge to retrieval techniques. The operational analysis of MIPAS measurements requires a large number of operations that were difficult to perform with the computers of ten years ago, when the MIPAS code development started. At that time also the global fit approach was a relatively recent achievement (Carlotti, 1988) and most analyses were still performed using the onion peeling approach.

MIPAS results have now proven that near-real-time (NRT) operations are possible and that a three-dimensional (latitude, longitude and altitude) picture of the atmospheric composition can be retrieved from satellite observations. World maps of a set of atmospheric parameters and species (temperature, water vapour, ozone, nitric acid, methane and nitrous oxide) are daily measured and a computing chain that makes available the geophysical products within three hours from the measurement time was operated during the first two years of MIPAS measurements.

The breakthrough in retrieval techniques obtained with MIPAS can be the basis for further improvements. Improvements can be pursued in the direction of a reduction of the retrieval error and an improvement of the spatial resolution. In the inversion of indirect measurements the retrieved parameters are affected by some correlation among themselves and with the non-retrieved parameters that contribute to the forward model. The approach used for the handling of these correlations and dependencies is a critical choice which is often conditioned by the available computing resources. As better and better computers are becoming available several new retrieval approaches can be considered.

Four directions can be identified for possible future improvements of the MIPAS retrieval approach, namely :

- Two-dimensional retrieval, in which the set of limb sounding sequences that are measured in the same orbit plane are simultaneously analysed in order to better account for the horizontal variability of the atmosphere.
- Multi-target retrieval, in which all the species that are the objective of the observations and contribute to the same observed spectra are simultaneously retrieved in order to better account for their mutual spectroscopic interference.
- Wide-band retrieval, in which all spectral elements that contain information on the target species are fitted independently of the forward model errors, because these are considered in the cost function of the retrieval.
- Target and interference retrieval, in which not only the target parameters, but also some forward model parameters that significantly contribute to the observed spectra are simultaneously retrieved in order to reduce the forward model errors caused by these parameters.

These improvements can be implemented either individually or simultaneously.

The main features of the MIPAS instrument and of its operational retrieval approach are briefly recalled in Sect.s 2 and 3, respectively. The retrieval algorithm is recalled in Sect. 4 where also the mathematics implications of the MIPAS approach are identified. The possible future improvements with their features and mathematical implications are finally discussed in Sect. 5.

2. The MIPAS instrument

MIPAS (Fischer et al., 2000) is a high resolution Fourier transform spectrometer operating on board the Envisat satellite (Louet, 2001). It measures for the first time from space high resolution atmospheric limb emission spectra in the middle infrared. Four spectral bands are simultaneously observed in the spectral interval from 685 to 2410 cm^{-1} (corresponding to wavelengths from 14.6 to 4.15 μm) with an unapodised spectral resolution of 0.025 cm^{-1}, for a total of about 70,000 spectral channels for each spectrum. Each limb sequence is made of 16 spectra and during each orbit MIPAS performs 75 limb scans (plus measurements used for the instrument calibration). Measurements are made during both day and night and about 14 orbits are made in 24 hours. In this time a total of about one thousand limb sequences and one billion spectroscopic measurements are acquired.

The analysis of each limb sequence allows the determination of the vertical profile of several atmospheric constituents, as well as temperature and pressure profiles. Combining the 75 profiles of each orbit, the distribution of the geophysical parameters as a function of altitude and latitude can be determined and combining the measurements along the 14 orbits the latitudinal variability is observed. In this way three-dimensional global maps are daily obtained for a set of target parameters.

Figure 1 shows an example of the three-dimensional measurements obtained with MIPAS in the case of ozone. MIPAS has successfully met its objective of global and comprehensive measurements of the atmospheric chemistry with NRT operations.

The handling of such a large data flow in a complex data inversion problem requires a very efficient code that uses an optimised algorithm as well as a few tested physical approximations. To this purpose, an Optimised Retrieval Model (ORM) was developed (Ridolfi et al., 2000) with the very demanding requirements of providing accurate results in an automated way with computing time shorter than measurement time. The main features of the ORM retrieval approach are summarised in the following section.

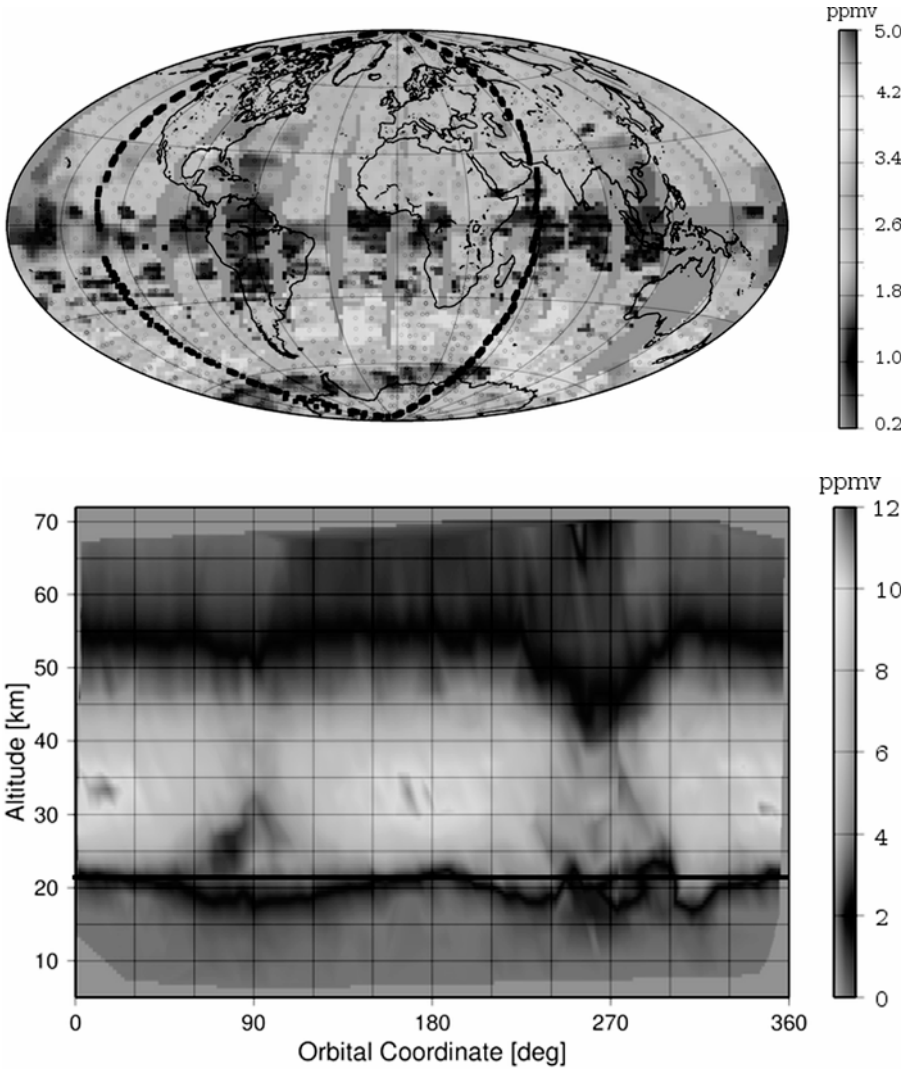

Figure 1. Horizontal and vertical sections of the global three-dimensional distribution of ozone measured by MIPAS on 30^{th} August 2003. The top-panel shows the VMR of ozone at 21 km altitude. In this map the black line indicates one orbit of the satellite for witch the vertical section is shown in the bottom-panel. Conversely the black horizontal line in this panel indicates the altitude at which the horizontal section is given. The orbital coordinate start from the equator at 0° encounter the North Pole at 90°, the equator again at 180° and the South Pole at 270°. A colour version of these maps can be found at `http://www.ifac.cnr.it/retrieval`.

3. The ORM retrieval approach

The code is designed to retrieve, starting from calibrated and geo-located spectra provided by the Level 1B processor (Lachance, 1999), atmospheric vertical profiles of temperature, tangent pressure (i.e the value of pressure corresponding to the tangent altitude of the limb measurement) and the Volume Mixing Ratio (VMR) of 6 target species (O_3, H_2O, CH_4, HNO_3, N_2O and NO_2). The retrieval approach is based upon three main choices, that are discussed in the following sub-sections. More detailed information on the ORM code can be found in (Ridolfi et al., 2000).

3.1. SEQUENTIAL RETRIEVAL OF THE SPECIES

The large number of unknowns are retrieved following an hierarchy of operations: first temperature and tangent pressures are retrieved simultaneously (p, T retrieval), then the target species VMR profiles are individually retrieved following the order of their reciprocal spectral interference, i.e.: H_2O first, followed by O_3, HNO_3, CH_4, N_2O and NO_2. Simultaneous p, T retrieval exploits the hydrostatic equilibrium assumption, that provides a relationship between temperature, pressure and geometrical altitude, the latter being determined by the engineering measurement of the pointing direction. Besides the target parameters, each retrieval determines also the parameters of atmospheric continuum (that includes all the emission effects that are not accounted for in line-by-line calculations) and instrument zero-level offset.

3.2. USE OF "MICROWINDOWS"

The retrieval is performed in a set of narrow (less than 3 cm^{-1} width) spectral intervals, called "microwindows" (Dudhia et al., 2002), that are selected as those that contain the best information on the target parameters and are less affected by systematic errors, such as for instance uncertain spectroscopic data, interference of non-target species, Non-Local Thermal Equilibrium (NLTE) and line mixing effects. Furthermore, for VMR retrievals, transitions with weak temperature dependence are preferred in order to minimise mapping of temperature uncertainties on to the VMR vertical profiles.

3.3. GLOBAL FIT ANALYSIS OF THE LIMB SCANNING SEQUENCE

A global fit approach (Carlotti, 1988) is adopted for the retrieval of each vertical profile. This means that all the spectral data related to a complete limb scan sequence are fitted simultaneously. The global fit provides a full exploitation of the information and a rigorous determination of the correlation between atmospheric parameters at the different altitudes.

4. The retrieval algorithm

The Forward Model which relates the measured spectroscopic values y to the target parameters x that are the objective of the measurement can be summarised by the following expression :

$$y = F(x, b) \tag{1}$$

where the parameters b are variables that are not the objective of the retrieval. Each of the involved quantities (y, x and b) has a size that depends on the complexity of the considered problem and may have more than one dimension (for instance, the spectral and the tangent altitude dependence in the case of the MIPAS measurements) even if in the concerned equations is considered as a one dimensional vector.

The retrieval involves the determination of the values x_R of the target parameters which minimise the cost function. In the non-linear least square fit (NLSF) approach the cost function is equal to :

$$\left(y - F\left(x_R, \hat{b}\right)\right)^T S_T^{-1} \left(y - F\left(x_R, \hat{b}\right)\right) \tag{2}$$

where S_T is the Variance-Covariance Matrix (VCM) of the residuals $\left(y - F\left(x_R, \hat{b}\right)\right)$ of the fit and $\hat{b}$ are our estimates of the non-target parameters. Two error sources affect the residuals: the error ϵ due to the instrumental noise that affects the measurements y and the uncertainties ϵ_b of $\hat{b}$. Therefore:

$$S_T = S_y + S_{FM} \tag{3}$$

where S_y is the VCM of the measurement errors, equal to:

$$S_y = [\epsilon\epsilon^T] \tag{4}$$

and S_{FM} is the VCM of the errors made in the estimates of the non-target parameters of the forward model, equal to :

$$S_{FM} = \sum_b [(K_b\epsilon_b)(K_b\epsilon_b)^T]. \tag{5}$$

The convention [ ] indicates the expectation value and

$$K_b = \left(\frac{\partial F}{\partial b}\right)_{\hat{b}} \tag{6}$$

is the Jacobian of the non-target parameters. The quantities $K_b\epsilon_b$ are often referred to as the error spectra of the forward model parameters.

The solution can be obtained with an iterative method and is equal to :

$$(x_R)_i = (x_R)_{i-1} + \left(K^T S_T^{-1} K\right)^{-1} \left(K^T S_T^{-1}\right) \left(y - F\left((x_R)_{i-1}, \hat{b}\right)\right) \tag{7}$$

where

$$K = \left(\frac{\partial F}{\partial x}\right)_{(x_R)_{i-1}} \tag{8}$$

is the Jacobian of the target parameters. The VCM of the solution this equal to:

$$S_x = \left(K^T S_T^{-1} K\right)^{-1}. \tag{9}$$

In the Optimal Estimation approach (Sivia, 1998) the cost function is equal to:

$$\left(y - F\left(x_R, \hat{b}\right)\right)^T S_T^{-1} \left(y - F\left(x_R, \hat{b}\right)\right) + (x_R - x_a)^T S_a^{-1} (x_R - x_a) \tag{10}$$

while the solution is equal to:

$$\begin{aligned}(x_R)_i \;=\; & (x_R)_{i-1} + \left(K^T S_T^{-1} K + S_a^{-1}\right)^{-1} \\ & \left(K^T S_T^{-1} \left(y - F\left((x_R)_{i-1}, \hat{b}\right)\right) + \; S_a^{-1} \left(x_a - (x_R)_{i-1}\right)\right)\end{aligned} \tag{11}$$

where x_a is the *a-priori* information and S_a its *a-priori* VCM. The VCM of the solution is equal to:

$$S_x = \left(K^T S_T^{-1} K + S_a^{-1}\right)^{-1}. \tag{12}$$

The above equations fully characterise the inversion problem, but significant variations may be introduced by the different retrieval approaches.

In the case of MIPAS the retrieval is well conditioned and the NLSF solution is adopted.

As we have seen in Sect. 3 the full set of measurements of a limb sequence is simultaneously analysed, but, because of computer memory constraints, the target species are sequentially retrieved. This implies that at each retrieval one target species x_R is retrieved while the others are considered as forward model parameters that have an estimate $\hat{x}$. Therefore, in the case of MIPAS the cost function is equal to:

$$\left(y - F\left(x_R, \hat{x}, \hat{b}\right)\right)^T S_T^{-1} \left(y - F\left(x_R, \hat{x}, \hat{b}\right)\right). \tag{13}$$

Furthermore, a "microwindow selection" is made is order to minimise the forward model errors. In this case the approximation can be made of neglecting them in the retrieval equation, assuming:

$$S_T = S_y. \tag{14}$$

In this way S_T can be represented by a block-diagonal matrix with a useful saving in memory occupation and number of operations. The cost function of Eq.13 becomes:

$$\left(y - F\left(x_R, \hat{x}, \hat{b}\right)\right)^T S_y^{-1} \left(y - F\left(x_R, \hat{x}, \hat{b}\right)\right). \tag{15}$$

The solution is given by equation:

$$\begin{aligned}(x_R)_i &= (x_R)_{i-1} + \left(K^T S_y^{-1} K\right)^{-1} \left(K^T S_y^{-1}\right)\left(y - F\left((x_R)_{i-1}, \hat{x}, \hat{b}\right)\right) \\ &= (x_R)_{i-1} + G\left(y - F\left((x_R)_{i-1}, \hat{x}, \hat{b}\right)\right) \end{aligned} \tag{16}$$

with

$$G = \left(K^T S_y^{-1} K\right)^{-1} K^T S_y^{-1} \tag{17}$$

and the retrieval error is equal to:

$$S_x = \left(K^T S_y^{-1} K\right)^{-1}. \tag{18}$$

However, the error budget of the retrieval is not represented by the retrieval error, because the latter does not include the forward model errors. The total error is equal to:

$$\begin{aligned}(S_x)_{TOT} &= \left(K^T S_y^{-1} K\right)^{-1} + \sum_b G[(K_b \epsilon_b)(K_b \epsilon_b)^T] G^T + \\ &+ \sum_{\hat{x}} G[(K_{\hat{x}} \epsilon_{\hat{x}})(K_{\hat{x}} \epsilon_{\hat{x}})^T] G^T \end{aligned} \tag{19}$$

where

$$K_{\hat{x}} = \frac{\partial F}{\partial \hat{x}} \tag{20}$$

and $\epsilon_{\hat{x}}$ are respectively the Jacobian and the the uncertainties of $\hat{x}$.

Figure 2 shows an example of the MIPAS error budget in the case of ozone. The diagonal elements of the VCMs of the different error sources are plotted as a function of altitude. A balance exists between the retrieval error and the total error induced by forward model uncertainties. This is the result of the microwindow selection process which extends the retrieval to further spectral elements as long as the forward model errors, which increase with added elements, are smaller than the retrieval errors, which decrease with added elements.

5. Future improvements

The successful results obtained with MIPAS are a major breakthrough in atmospheric composition measurements because for the first time the measurements have global coverage, good vertical resolution and involve a comprehensive set of species. Comparable performances have been obtained by the MLS/UARS instrument (Waters, 1998), but for a smaller set of species and by the ILAS instrument (Nakajima et al., 2002), but with fewer daily measurements. Furthermore, the innovative coverage of MIPAS has been obtained with NRT operations. Nevertheless, the limits of retrieval techniques have not yet been reached. Indeed, of the

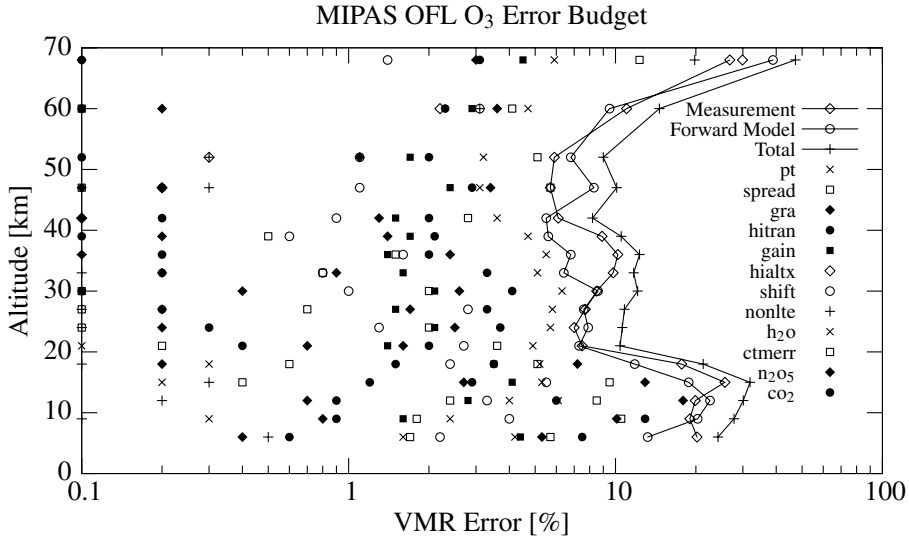

Figure 2. Error Budget of the ozone profile retrieved with the MIPAS operational analysis. The individual error sources are shown with different symbols according to the enclosed legend. Continuous lines summarise the contributions of the measurement error and of the forward model errors. The combination of the two provides the total error budget. (Data source `http://www-atm.physics.ox.ac.uk/group/mipas/err`)

one million spectral measurements that are obtained by MIPAS in each limb scan sequence less than 1% are used for the operational retrieval and the total error of the retrieved products is larger than what potentially feasible (see for instance Figure 2).

Four possible directions can be identified for the evolution of the retrieval approach. They are individually discussed in the following sub-sections, but approaches that simultaneously exploit more than one of these directions are also possible.

5.1. TWO-DIMENSIONAL RETRIEVAL

When the limb sequence is measured in the orbit plane of the satellite, as it is the case of MIPAS, the lines of sight of each limb sequence cross those of previous and subsequent sequences. This implies that the horizontal variability, observed by the contiguous limb sequences, is also observed within each limb sequence. Indeed the horizontal variability of the atmosphere is an error of the forward model when horizontal homogeneity is assumed. This dependence on the horizontal variability can be transformed from an error into a resource when the set

of limb sounding sequences measured in the same orbit plane are simultaneously analysed and the two-dimensional field of the target species is retrieved.

The two-dimensional retrieval approach does not change the formalism of the retrieval equations, but removes the forward model error due to horizontal homogeneity assumption and adds to the quantities involved in the Eq. 1 of the forward model the dependence on the orbit dimension. Accordingly, a larger computer memory is needed. A concern for memory requirements does not exists so much for the quantities that are proportional to size of the problem, such as the measurements and the unknowns, but rather for the matrices, such as S_y and K, in which both dimensions increase proportionally to the size of the problem. However, for these matrices a block-diagonal representation can often be adopted with a significant memory saving.

The two-dimensional retrieval was first proposed in (Carlotti et al., 2001) and now a few retrieval codes are developing this capability. Advantages of the two-dimensional retrieval are:

- the horizontal resolution of the retrieval can be independent of the horizontal sampling and better than the extent of the horizontal path;
- the measurements are better exploited because fitted with a more rigorous forward model and, for equal horizontal resolution the retrieval errors are smaller than in the case of single sequence retrieval.

5.2. MULTI-TARGET RETRIEVAL

The approach of sequential retrieval of species adopted in the case of MIPAS implies a significant saving of memory, because the extra dimension of species, when added to the unknowns and to the measurements, also directly applies to matrices (e.g., K and S_x) and no savings are usually possible with block-diagonal representations. This is due to the significant correlations that exist between the different species in the observed atmospheric spectra. The strategy of MIPAS has been that of avoiding with the microwindow selection the spectral channels affected by largest correlation between target species and to perform a sequential retrieval.

The same correlations that have motivate the MIPAS choice also point towards the importance of a simultaneous retrieval of the target species that makes possible the use of more spectral channels and correctly accounts for the correlations themselves. The number of target species that are simultaneously retrieved usually is not very large and the multi-target approach is quite feasible with modern computers. As for the two-dimension approach, also the objective of multi-target retrieval is to transform an error, which in this case is the interference of non-retrieved target species, into a resource.

The multi-target retrieval approach does not change the formalism of the retrieval equations, but removes the forward model error due to non-retrieved target species and adds to the quantities involved in Eq. 1 the dependence on the target dimension.

A code that simultaneously implements two-dimensional and multi-target retrieval has recently been developed (Carlotti et al., 2005) and is available as an open-source code.

The computing time of a multi-target retrieval is comparable with that of the sequential single target retrieval of the same species with the same microwindows. Of course the computing time of multi-target retrieval is longer when the opportunity is exploited of using more microwindows.

5.3. WIDE-BAND RETRIEVAL

Two-dimensional and multi-target retrieval eliminate some of the forward model errors, but several further errors are present in the error budget of Figure 2 and limit the number of the spectral channels that are selected with the microwindow approach. An alternative to the microwindow approach is the wide-band retrieval in which all relevant spectral channels are analysed irrespectively of their forward model errors. In this case the S_T (see Eq. 3) of the residual errors is no longer be approximated by S_y and the forward model errors are included in its calculation.

The drawback of this operation is that while S_y can often be represented by a block-diagonal matrix with useful savings in memory occupation and number of operations, the same does not happen in the case of S_{FM} which is usually a full matrix.

When the rigorous expression for S_T is used in the retrieval equation, the retrieval error of Eq. 9 is equal to the total error budget and this is an optimised budget because all error sources are taken into account in the retrieval equation and the available information is accordingly weighted for minimum error.

The wide-band approach has been applied in the code recently developed in an ESA study for the Level 2 analysis of the measurements of the MARSCHALS instrument (Bazzini et al., 2005).

MARSCHALS is a limb sounding heterodyne spectroradiometer that operates in the millimetre wave region. The relatively small number of spectral channels of this instrument makes feasible and effective the use of the wide-band approach.

Figure 3 shows the ozone error budget obtained for simulated retrievals of this instrument in the case in which the forward model errors are *a-posteriori* accounted for (Eq. 19) and in the case in which the forward model errors are taken into account in the retrieval (Eq. 9). A significant error reduction is observed in the latter case.

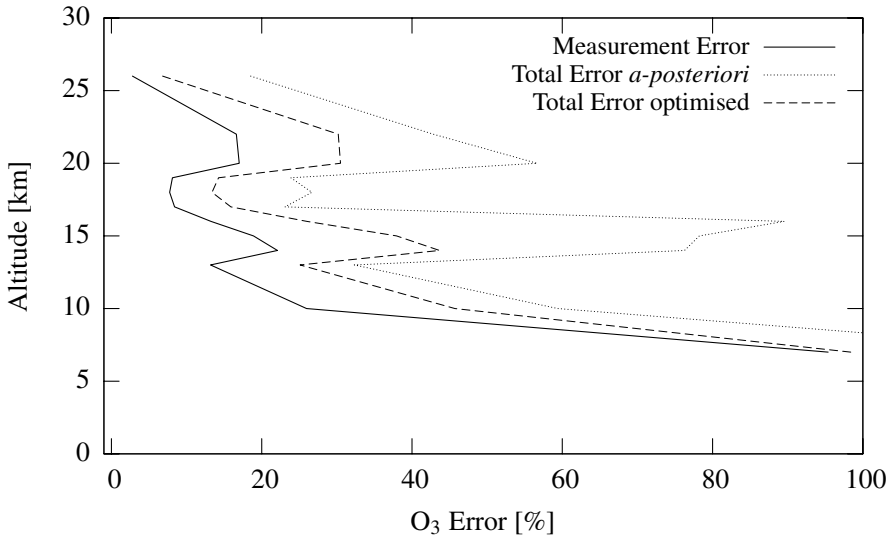

Figure 3. Ozone error budget for MARSCHALS simulated retrievals. Continuous line represents measurement errors, dotted line is the total error when forward model errors are included *a-posteriori* (Eq. 19), dashed line is the total error when the forward model errors are included in the retrieval (Eq. 9).

5.4. TARGET AND INTERFERENCE RETRIEVAL

A further reduction of the error budget of the retrieved products is obtained by reducing the forward model errors due to uncertainties in the non-target parameter. When a strong retrieval error is caused by a non-target parameters it means that the measurements are significantly affected by that parameter and may contain enough information for its retrieval. If optimal estimation is used, also parameters can be fitted that are poorly determined by the retrieval.

Indeed, optimal estimation is often described as the technique with which *a-priori* information is merged with the retrieved values of the target parameters, however, an important capability of optimal estimation is also that of improving the *a-priori* estimate of the non-target parameters with the measurement information. The boundaries between the known and unknown parameters is not always so well defined and both target and interfering non-target parameters can be improved with the retrieval.

If too many parameters are added to the retrieval vector, the target and interference retrieval can be rather demanding in terms of computing resources, but through an optimised determination of the forward model parameter allows a significant reduction of the associated errors and an improvement in the accuracy of the retrieved target parameters.

6. Final remarks

With the advent of new sounding instruments based on Fourier transform spectroscopy the number of measurements that are available for the inversion process has significantly increased. MIPAS is one of the first instruments with this characteristics and a few more have recently followed and will follow in the near future, e.g. ACE (Bernath et al., 2005), TES (Beer et al., 2001), IASI (Cayla and Javelle, 1995)). With MIPAS measurements a major advancement has occurred in operational retrieval techniques, however, not all the capabilities of the measurements have yet been exploited. Also considering the improvements of computer technology that will be possible in the next few years, more ambitious retrieval approaches for improved retrieval performances should be considered in the planning of future instruments for environment and climate. A few examples of the new directions that can be considered for these improvements have been discussed.

References

Bazzini, G., E. Castelli, S. D. Bianco, B. Dinelli, M. Gai, L. Magnani, L. Santurri, and B. Carli: 2005, 'The Scientific Analysis of Limb Sounding Observations of the Upper Troposphere'. MARSCHALS level 2B theoretical retrieval study, European Space Agency. ESA Contract 16530/NL/MM.

Beer, R., T. Glavich, and D. Rider: 2001, 'Tropospheric emission spectrometer for the Earth Observing System's Aura satellite'. *Applied Optics* **40**(15), 2356–2367.

Bernath, P. F., C. T. McElroy, M. C. Abrams, C. D. Boone, M. Butler, C. Camy-Peyret, M. Carleer, C. Clerbaux, P.-F. Coheur, R. Colin, P. DeCola, M. DeMazière, and J. R. Drummond: 2005, 'Atmospheric Chemistry Experiment (ACE): Mission Overview'. *Geophysical Research Letters* **32**.

Carlotti, M.: 1988, 'Global-fit approach to the analysis of limb-scanning atmospheric measurements'. *Applied Optics* **27**, 3250–3254.

Carlotti, M., G. Brizzi, E. Papandrea, M. Prevedelli, M. Ridolfi, B. M. Dinelli, and L. Magnani: 2005, 'GMTR: Two-Dimensional Multi-Target Retrieval Model for MIPAS/ENVISAT Observations'. *to appear in Applied Optics*.

Carlotti, M., B. M. Dinelli, P. Raspollini, and M. Ridolfi: 2001, 'Geo-fit approach to the analysis of limb-scanning satellite measurements'. *Applied Optics* **40**(12), 1872 – 1885.

Cayla, F. and P. Javelle: 1995, 'IASI instrument overview'. In: *The International Society for Optical Engineering*, Vol. 2583 of *The International Society for Optical Engineering*. pp. 271–281.

Dudhia, A., V. Jay, and C. Rodgers: 2002, 'Microwindow selection for high-spectral-resolution sounders'. *Applied Optics* **41**(18), 3665–3673.

Fischer, H., C. Blom, H. Oelhaf, B. Carli, M. Carlotti, L. Delbouille, D. Ehhalt, J. Flaud, I. Isaksen, M. Lopez-Puertas, C. McElroy, , and R. Zander: 2000, 'ENVISAT-MIPAS: an instrument for atmospheric chemistry and climate research'. In: *SP*, Vol. 1229 of *SP*. ESTEC, Noordwijk, The Netherlands.

Lachance, R. L.: 1999, 'MIPAS level 1B algorithm technical baseline document: an overview'. In: E. S. Agency (ed.): *European Symposium on Atmospheric Measurements from Space*, Vol. 1. ESTEC, Noordwijk, The Netherlands, pp. 51–63.

Louet, J.: 2001, 'The Envisat mission and system'. *European Space Agency Bulletin* **106**.

Nakajima, H., M. Suzuki, A. Matsuzaki, T. Ishigaki, K. Waragai, Y. Mogi, N. Kimura, N. Araki, T. Yokota, H. Kanzawa, T. Sugita, and Y. Sasano: 2002, 'Characteristics and performance of the Improved Limb Atmospheric Spectrometer (ILAS) in orbit'. *J. Geophys. Res.* **107**(D24), 8213.

Ridolfi, M., B. Carli, M. Carlotti, T. V. Clarmann, B. Dinelli, A. Dudhia, J. Flaud, M. Höpfner, P. Morris, P. Raspollini, G. Stiller, and R. Wells: 2000, 'Optimized forward model and retrieval scheme for MIPAS near-real-time data processing'. *Applied Optics* **39**(8), 1323–1340.

Sivia, D. S.: 1998, *Data Analysis: A Bayesian Tutorial*. Oxford, UK: Clarendon.

Waters, J.: 1998, 'Atmospheric measurements by the MLS experiments: Results from UARS and plans for the future'. *Adv. Space Res* **21**(10), 1363–1372.

NEW MEASUREMENTS OF TRACE SPECIES IN THE UPPER TROPOSPHERE FROM INFRA-RED SPECTRA OF THE ATMOSPHERE

J.J. REMEDIOS[1], D. P. MOORE, P. MEACHAM,
G. ALLEN[2], A.M. WATERFALL[3], AND H. SEMBHI
Earth Observation Science, Dept. of Physics and Astronomy, University of Leicester, LE1 7RH, United Kingdom.

Abstract. The challenge of understanding our environment requires global measurements of increasing numbers of trace species and requires some priority to be given to new observations of classes of species which may play fundamental roles in climate and chemistry interactions. Such compounds include "new" ozone depleting substances (ODS), greenhouse gases (GHGs) and indirect controlling influences such as key chemical oxidants. For many of these gases, relevant spectral signatures had, until recently, either not been well characterised globally or never been observed in the atmosphere. The launch of high-resolution spaceborne spectrometers, such as the Michelson Interferometer for Passive Atmospheric Sounding (MIPAS) on ENVISAT, is providing an unprecedented opportunity to examine spectra of the atmosphere and to determine new observable trace species. In this paper, MIPAS infra-red spectra of the upper troposphere are examined, methods for detecting weak spectral signatures in atmospheric spectra are discussed and key trace gas signatures demonstrated for HCFC-22 and ethane as examples of the potential for three-dimensional daily data of trace gases.

[1] To whom correspondence should be addressed. Dr. John Remedios, Earth Observation Science, Space Research Centre, University of Leicester, Leicester, LE1 7RH. United Kingdom. Email: j.j.remedios@leicester.ac.uk
[2] Currently at SEAES, University of Manchester, U.K.
[3] Currently at CCLRC, Chilton, Oxfordshire, U.K.

A. Perrin et al. (eds.), Remote Sensing of the Atmosphere for Environmental Security, 71–85.

Keywords: Remote sensing, atmospheric spectroscopy, MIPAS, HCFC-22, ethane

1. Introduction

Remote sensing is an essential technique for observing atmospheric composition, whether from satellite, aircraft, balloon borne or ground-based systems. These systems fundamentally require an understanding of molecular and particulate (liquid/solid) spectroscopy and the nature of radiative transfer through the Earth's atmosphere. Indeed it is the knowledge of this spectroscopy which determines our ability to observe and quantify the concentrations of many trace gases and particles. This intrinsic aspect of remote sensing is illustrated very well by new remote sensing observations of the upper troposphere, a key region in the atmosphere which is of significant importance for climate studies, weather forecasting and transport of pollutants.

The upper troposphere displays a number of very important aspects of environmental impacts, in particular the effect of anthropogenic emissions on regions which are at a distance from surface sources and the counter processes in which the composition of these more distant regions can dramatically influence the surface environment. Although the upper troposphere (UT) is located between 8 km and 12-18 km (depending on latitude), there are crucial impacts from a climate perspective. The most direct is that due to the radiative forcing effects of anthropogenic and natural greenhouse gases in the UT with impacts on surface temperature and potentially circulation. There are also important influences such as the long-range advection of pollutants with its direct influence on the UT and effects on lower tropospheric chemistry/composition through subsidence, and control of the injection of source gases into the stratosphere. The composition of the UT is of significance, therefore, for climate through both physical and chemical processes (climate-chemistry interactions), and it is essential for modelling of past and future climate scenarios that we test our understanding, on global and regional scales, of key markers of UT composition.

In pursuing observations of the UT, it is well recognised that observations of this vital region lead us to accelerating requirements for increasing spatial resolution (vertical and horizontal) and greater spatial (and temporal) coverage. Ideally, vertical profiles should extend down to 8 km or lower with vertical resolutions of 1-3 km and horizontal resolutions of better than 100 km. These imperatives will drive new satellite mission concepts for the future which will address these issues at regional and global scales.

It is arguably less well articulated, but no less important, that current research science and policy directives alike also call for *global*

measurements of increasing numbers of *trace species*. Hence some significant priority must be given to observations of new classes of species which may play fundamental roles in climate and chemistry interactions. In the case of pollutants in the UT, we can distinguish "new" ozone depleting substances (ODS), greenhouse gases (GHGs) and indirect controlling influences such as key chemical oxidants (such as volatile organic compounds or VOCs) and clouds. For many of these gases, relevant spectral signatures had, until recently, either not been well characterised globally or had not been observed previously in remote sensing observations of the atmosphere.

The launch of high-resolution spaceborne spectrometers are providing a new dimension to the observations of trace species since they observe remote regions of the globe hitherto unobserved by spectrometers on aircraft and balloons. Furthermore, the acquisition of large numbers of spectra also allows for averaging of spectra to improve signal-to-noise for detection of spectral signatures or consistency tests to demonstrate systematic behaviour. In this paper, we discuss the very new observations of the UT from the Michelson Interferometer for Passive Atmospheric Sounding (MIPAS) on ENVISAT which are providing an unprecedented opportunity to examine spectra of the atmosphere of the UT and to determine new observable trace species.

2. The MIPAS instrument

The MIPAS instrument (Fischer and Oelhaf, 1996; Fischer et al., 2000) is is a Fourier transform spectrometer (FTS) providing limb sounding spectra of atmospheric infra-red emission between 685 cm^{-1} (14.60 μm) and 2410 cm^{-1} (4.15 μm) at a spectral resolution of 0.025 cm^{-1} (unapodized). The data are recorded in five spectral channels but near-continuous coverage is available in the spectral domain albeit with narrow gaps between channels. Vertical profiles are scanned from 6 km to 68 km with a vertical spacing of 3 km in the UT and lower stratosphere commensurate with the vertical resolution of the instrument. Each profile requires approximately 75 s corresponding to an along-track distance of 500 km between vertical scans. Calibration of the spectra to produce geo-located, radiometrically corrected spectra (level 1b) incorporates data from views of an on-board blackbody near 240 K and views of "space" at greater than 200 km altitude above the Earth's surface. The quality of the level 1b spectra are excellent with offsets in the calibrated spectra believed to be less than 2 nW/cm2 sr cm^{-1} (Spang et al, 2005). Typical noise values for a single spectrum vary between 40 nW/cm^2 sr cm^{-1} at 800 cm^{-1} to less than half that value at 1200 cm^{-1}.

2.1. CLOUD EFFECTS IN MIPAS SPECTRAL DATA

Cloud particles absorb, emit, and potentially scatter radiation over a broad range of wavelengths in the infra-red. Limb sounding observations provide a very particular and highly interesting view of "high altitude" clouds (typically 6 km to 30 km). More particularly, for this purpose of this paper, cloud effects must be considered since they fundamentally alter the spectrum thus influencing our ability to observe trace gas signatures. In the upper troposphere, the chief influences arise from high altitude cirrus clouds, particularly in the tropics and in the poles.

Figures 1 and 2 show spectra (MIPAS band A) of tropical cirrus clouds at a tangent altitude of 13.5 km (Figure 1) and 16.5 km (Figure 2) from orbit 504 on April 5th 2002 (4 mins. apart). The influence of clouds is obvious as a distinct offset to the spectra of around 2 $\mu W / cm^2$ sr cm^{-1} (in brightness temperature such offsets can correspond to enhancement of up to 30 K from the local temperature). However, although both clouds show similar offsets, the gas contributions to the spectra are clearly different. Figure 1 shows emission lines from gases such as the very broad CFC-11 signature between 835 cm^{-1} and 855 cm^{-1}. Figure 2 shows gas absorption lines with emission lines from high altitudes. The absorption lines can originate either from a cold atmosphere above the cloud top or from upwelling tropospheric radiation scattered into the limb path (Spang et al., 2004; Hopfner et al., 2002). The presence of many weak water vapour lines indicates the latter explanation for many cases, a hypothesis confirmed by simplified radiative transfer calculations (Greenhough et al., 2005).

In order to discriminate "clear sky" spectra from cloudy spectra, we use the methods we have established using cloud detection indices (Spang et al., 2004), in which the methods of Spang et al., 2002, are extended from cloud thresholds in MIPAS band A to further frequencies in MIPAS bands B and D. Essentially, the method works by taking the ratio of two microwindows in a so-called microwindow pair and comparing the value to a pre-defined threshold; a pair of microwindows is used to reduce the temperature sensitivity of the test. The chief test applied in this paper is to examine whether a ratio of ratio of radiances in microwindow 1 (788.2 - 799.25 cm^{-1}) and microwindow 2 (832.3-834.4 cm^{-1}) is less than 1.8. This test is found to be sufficient to remove most cloud effects. However, it is also clear that cloud or aerosol particles can contribute a weak offset signal to upper tropospheric spectra and must always be taken into account when examining broadband spectral features of molecules.

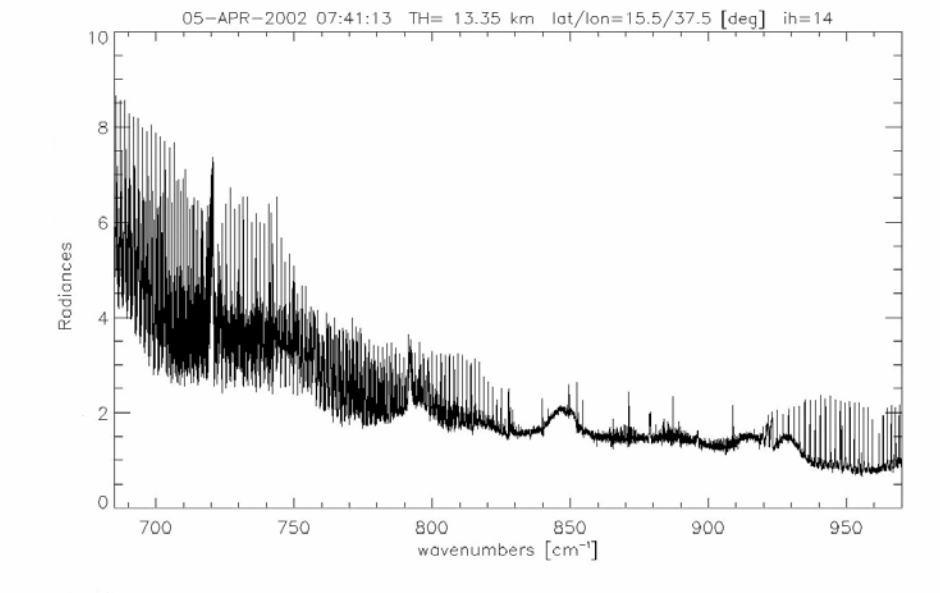

Figure 1. Spectrum of tropical cirrus clouds observed by the MIPAS on ENVISAT displaying gas lines in emission. Radiances are in nW / cm^2 sr cm^{-1}. Orbit 504 on April 5th 2002.

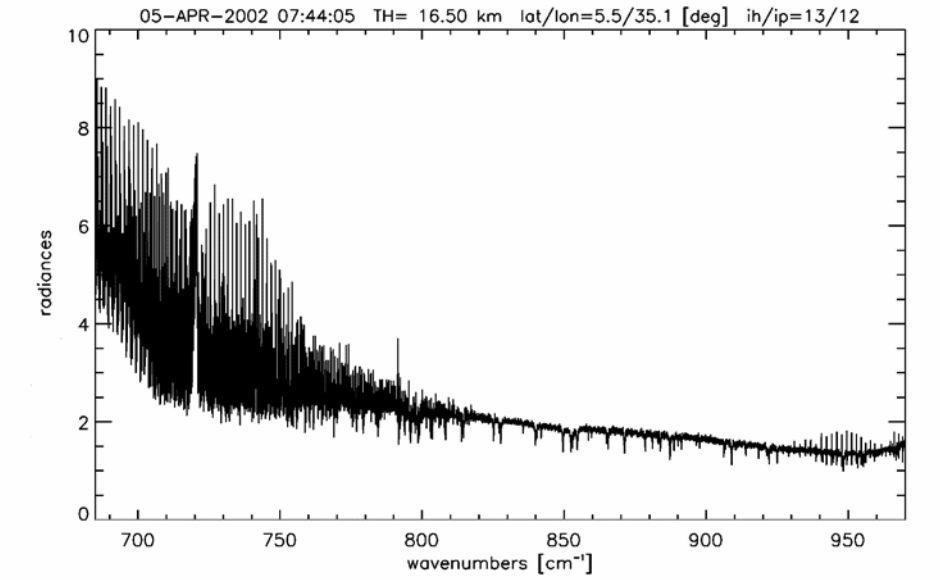

Figure 2. Spectrum of tropical cirrus clouds observed by the MIPAS on ENVISAT displaying gas lines in absorption presumably due to greater optical thickness than those of Figure 1 and larger particle sizes. Radiances are in nW / cm^2 sr cm^{-1}. Orbit 504 on April 5th 2002.

3. Spectral detection

In the spectra shown in Figures 1 and 2, more than thirty trace species contribute to the observed spectra. Key features of many of the gases are already well-known from previous experiments, particularly for the strong lines, but nonetheless it is the case that spectra of the UT contain signatures that have never been distinguished before. This raises the question of how well we can distinguish the spectral signatures of compounds from MIPAS spectra given "cloud-free" spectra, the unique spectral signature of the target species, and knowledge of the overlapping ("strong") known features. There are at least five possible methods applicable to infra-red spaceborne spectrometers depending on the structure of the target features, the structure to the target spectral signatures, the degree of overlap with other gas features and the noise on the spectra:

1. Direct band or line identification
   Line identification e.g. rotational line spacing, PQR branches
   Multiple band identification
2. Direct matching of spectral signatures
   Matching with calculated spectral signature
   Matching with Jacobian calculations (sensitivity of signal to 1% change of mixing ratio at tangent height)
3. Differential matching of spectral signatures
4. Residual matching of spectral signatures
5. Statistical/analytical methods: correlation analyses, gradient and area methods.

The first two methods constitute the simplest and most direct methods whereby the signature of a gas in the atmosphere is identifiable by visual inspection based on characteristic spectral features. Within one infra-red band, this might include the rotational spacing of lines within the vibration-rotation band, the variation of intensity within the bands and the shape of the band including not only its PQR branch structure but the width and intensity of the individual branches. Where there are overlapping lines due to other atmosphere gases then it may be necessary to perform line-by-line radiative calculations using a state of the art radiative transfer model such as the Oxford Reference Forward Model (RFM); the RFM is based on GENLN2 (Edwards et al., 1992) and was specifically designed for MIPAS characteristics (further details can be found at http://www-atm.physics.ox.ac.uk/RFM/). In this case, visual matching may be

performed by examining the measured and calculated spectral signature and comparing the two. Since, in the case of limb sounding for the UT, the observed spectral signature may be due to the presence of the target gas at higher altitudes along the line-of-sight, it is more rigorous to use a Jacobian calculation rather than the calculated spectrum. The Jacobian is defined as the change in the model spectrum (R_F) for a 1% change in gas concentration at a specified tangent altitude of interest. This quantity shows more clearly whether we would expect to see signals from the altitude of interest in the spectrum measured by the satellite at the top of the atmosphere.

We have seen how in the calculation we can deduce the likely perturbation of the satellite measured spectrum due to the target trace gas at the altitude of interest. One also has to be careful how one considers the measured spectrum for a given tangent height since the signal observed is an integration of the spectral lines over all the altitudes between the tangent point and the top of the atmosphere. One method (method 3) of differentiating the UT better is to difference spectra observed for UT tangent heights ("target" spectra) with spectra observed at higher altitudes just above the UT at the same location ("reference" spectra). The difference spectrum then represents the likely effect of the trace gases at the UT tangent altitudes provided that the trace gases at the higher tangent altitude do not vary in concentration in the time taken to record the spectra at the reference height and the upper tropospheric height. Fortunately, this is mostly true for UT differencing where the higher altitude "reference" spectra chosen are usually in the lower stratosphere. The difference spectrum can then be compared with simulated spectra using methods 1 and 2 or more sophisticated techniques.

For spectral signatures that are very weak, it may be that it is very difficult to observe the target spectral signature because of the presence of many overlapping and interfering lines and also because of the relative weakness of the signal. In this case, the best method is to remove the presence of the overlapping lines as accurately as possible using a line-by-line calculation for the altitude of interest. In effect one matches residual spectra (method 4). To do this, one can define a measured residual spectrum, ΔY which is the difference between the measured spectrum and a calculation of the spectrum without the target gas. One can then examine the residual spectrum directly using methods 1 or 2. Alternatively, the residual spectrum may be compared to a calculated residual spectrum, ΔF, which is the difference between a spectrum calculated with the target gas and one calculated without the target gas. For a perfect measurement with no associated error and for a numerically perfect simulation with accurate

reference data and prior knowledge of all other influencing gas concentrations, then $\Delta Y = \Delta F$.

Finally, all of the above methods are applicable through visual inspection but can be quantified through correlation analyses or analytical techniques where the residual structure from the tests and signal-to-noise permit. Such calculations usually work better for more isolated or better defined spectral features (methods 1 to 3) but are very useful in allowing fast analysis of thousands of spectra to identify those which might show the strongest spectral features of interest. Applications to HCFC-22 and ethane are discussed below.

4. Detection of HCFC-22 and ethane in MIPAS spectra of the UT

The detection of spectral signatures is illustrated very well by the similar examples of HCFC-22 and ethane in the UT from MIPAS-type data. Both features have been detected in spaceborne limb sounding observations prior to MIPAS but in solar occultation data rather than thermal emission observations where the signal-to-noise in the former is much greater than in the latter. However, the space-time coverage of the solar occultation technique is limited compared to the thermal emission technique as is well known.

4.1. HCFC-22

For HCFC-22, the chief features of the spectrum can be illustrated rather well by a radiative transfer calculation of the difference between spectra simulated with and without the inclusion of HCFC-22. Figure 3 shows results for the tropics at 12 km tangent altitude. The Oxford RFM has been employed along with trace gas mixing ratios from the MIPAS standard atmosphere V3.1 (Remedios, 1999) and spectroscopic data from the HITRAN 2000 database (Rothman et al., 2000). The Q branches are the most prominent features on the diagram and that near 829 cm^{-1} can be shown to be the most suitable for atmospheric detection. For the detection, method 2(b) has been employed, i.e., a correlation between the measured spectrum and a Jacobian sensitivity calculation for HCFC-22 at the 12 km tangent altitude. The Jacobian approach is suitable because it automatically accounts for decreased sensitivity to the target spectral feature due to saturation of the line or to overlapping lines.

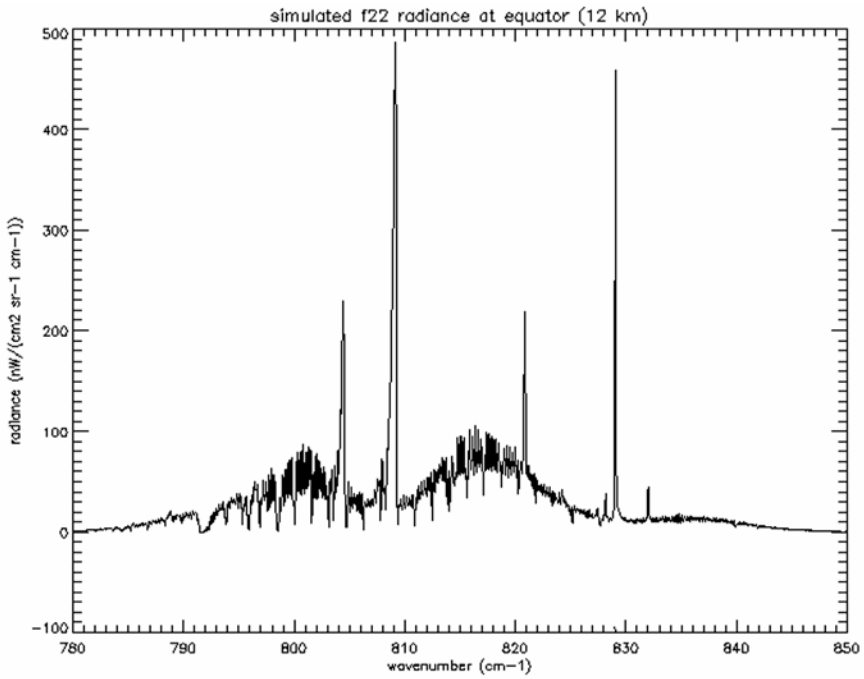

Figure 3. A difference plot of simulated line-by-line atmospheric limb emission spectrum for the 12.3 μm band of HCFC-22 (spectrum with all gases minus spectrum including all gases apart from HCFC-22). This plot corresponds to 12 km in the tropics and the calculation incorporates HITRAN 2000 line and cross-sectional data and the standard atmosphere climatology used is that of Remedios (1999).

Correlations were calculated for the MIPAS measurements in the wavenumber range between 828.95 to 829.15 cm^{-1} spectral region at a number of altitudes. Jacobian sensitivity functions were computed using the Oxford RFM using HITRAN 2000 (Rothman et al. 2000) spectroscopic parameters and reference atmosphere gas profiles (MIPAS V3.1 standard atmospheres; Remedios, 1999). The correlations were derived using a Pearson Product Moment Correlation and results are shown in Figure 4 for an approximate tangent altitude of 12 km. It is immediately apparent that the majority of the data are close to 1.0 with all deviations of less than 0.95 being ascribable to cloud contamination of the MIPAS sweeps (CI<1.8). Hence the test has been able to identify the HCFC-22 signature at this altitude and at all altitudes in the one orbit analysed (orbit 2081 of MIPAS data; July 24th 2002).

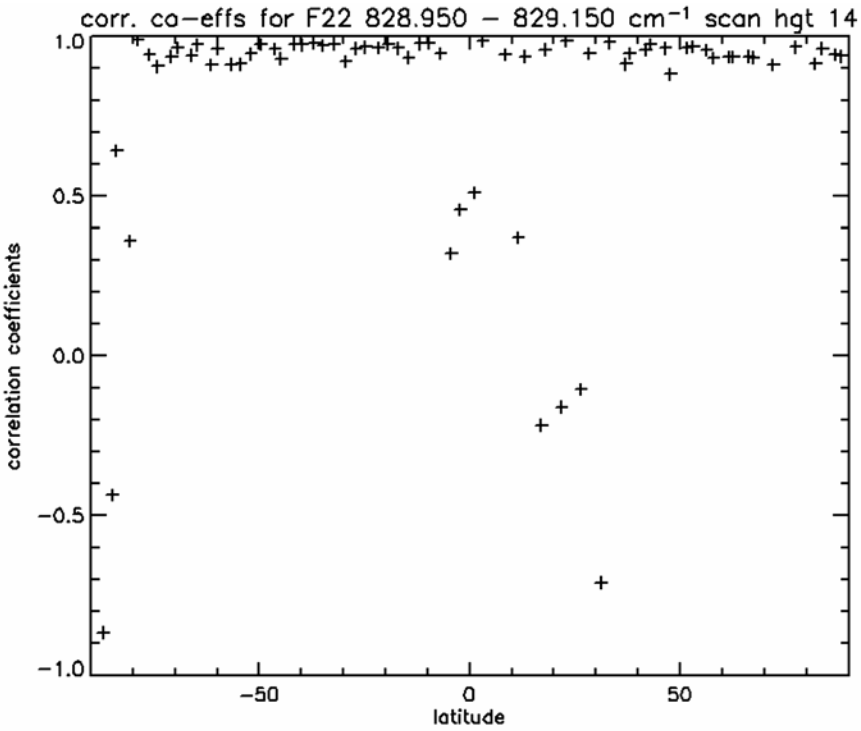

Figure 4. Correlation coefficients in the wavenumber range 828.95 to 829.15 cm^{-1} between MIPAS level 1b data, orbit 2081, at index height 14 (approximately 12 km) and the 12 km HCFC-22 Jacobian simulated using the RFM. Orbit 2081 was recorded on July 24th, 2002.

4.2. ETHANE

Given the role of organic compounds in the chemistry of the troposphere, it is clear we should target, if at all possible, some of the primary molecules of this type. However, although limited aircraft campaigns have been able to provide focused process studies in targeted regions, satellite estimates for organic species have not previously been derivable prior to MIPAS (formaldehyde has been derived from GOME but is weighted towards the near-surface). As a first step, we examine the detectability of ethane for which case the analysis can proceed in a similar manner to that for HCFC-22 since ethane also has spectral features with distinct peaks.

In this paper, we show some early results from an analysis of MIPAS level 1b data for April 2003 where MIPAS spectra at 9 km have been examined in an ethane-sensitive spectral region (822.2 to 822.45 cm^{-1}). The spectral data have been cloud flagged as described in section 2.1, potential baseline signals removed by subtraction of the minimum signal, and with higher altitude contributions subtracted to leave only signals which originate from, gaseous species at the tangent height concerned. The

resulting spectra were correlated with Jacobians (1% sensitivity calculation for ethane at the tangent height), the gradient of the correlation determined and an independent, integrated area method was also employed. Figure 5 shows the derived correlation coefficients versus the fitted gradients from each MIPAS spectrum at 9 km; fitted gradients were translated to concentrations via simulations with the RFM model. Positive correlations correspond to positive value concentrations derived from the gradient method as would be expected; negative correlations are most likely associated with residual spectral features of ozone. This detection of ethane is supported by Figure 6 which shows the correlation values compared to independently derived concentration estimates from the area integration method (area values were also converted to ethane concentrations through simulations). Although there is some scatter in the relationship, as would be expected from the weakness of the ethane signal, it is clear that a positive relationship exists. Therefore, the plots indicate that these methods may represent fast, "data mining" techniques for analysing large amounts of spectral data to indicate regions of relative enhancement of a given trace gas. Considerable further work is required to show that concentration values can themselves be believed and to ascribe reasonable errors, so for the moment the value of these approaches lie more in detection.

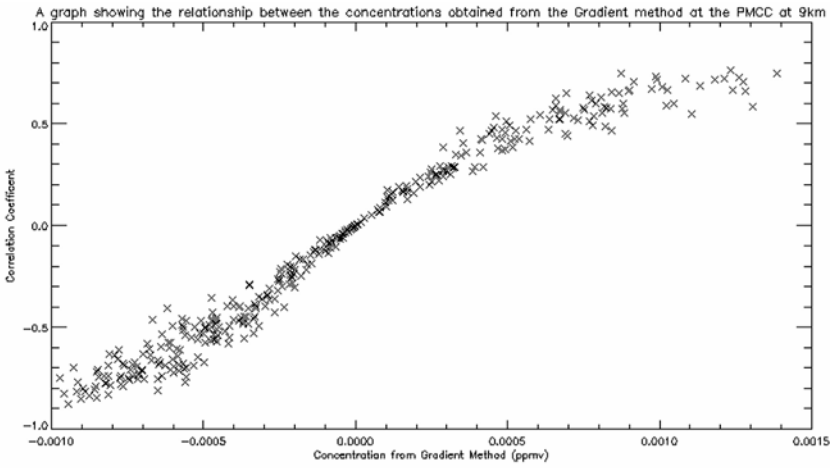

Figure 5. Correlation coefficients derived from MIPAS ethane spectra (822.2 to 822.45 cm^{-1}) versus concentrations derived from a gradient method applied to the same data. The analysis was performed for a tangent height of 9 km and all available data for April 2003 were used. See text for further details.

These methods give a reasonable confidence that MIPAS spectral data can be investigated in detail to reveal the signatures of weak trace species such as organic compounds, provided that the spectroscopy is well known. Since even for ethane, there are considerable uncertainties, a laboratory programme has been instituted at the University of Leicester to examine the spectral signatures of compound such as acetone and PAN. In recent studies, the spectroscopy of acetone (Waterfall, 2002) and peroxyacetyl nitrate or PAN (Allen et al., 2005a,b) have been investigated and cross-sectional data obtained under conditions appropriate to the upper troposphere; temperatures down to 220 K for acetone and 250 K for PAN. Typically, the accuracy of these laboratory cross-sections is of the order of 10%. The laboratory data have therefore been applied to atmospheric spectra obtained by MIPAS type instruments, producing substantial evidence that the spectral signatures of acetone and PAN can be observed (Waterfall, 2002, and Allen, 2005, respectively). These provide encouragement for future studies of these compounds and for exploitation of MIPAS spectra of the atmosphere.

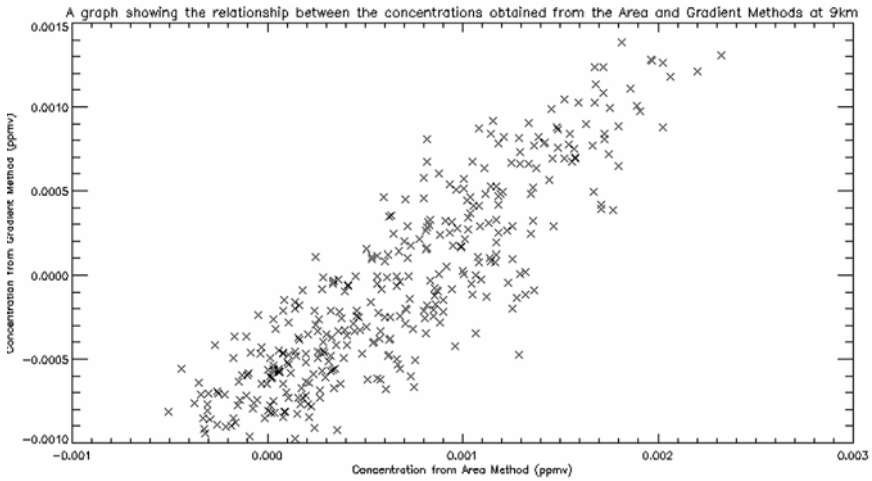

Figure 6. Concentrations derived from a gradient method applied to MIPAS ethane spectra (822.2 to 822.45 cm^{-1}) versus concentrations derived from an independent area integration method applied to the same data. The analysis was performed for a tangent height of 9 km and all available data for April 2003 were used. See text for further details.

5. Conclusions

In this paper, the use of spectral techniques to distinguish weak signatures of trace gases has been discussed. It has been shown that infra-red instruments in space, such as the MIPAS instrument on ENVISAT, are capable of delivering high quality information which can liberate new measurements of species that are key drivers of long-term change in the atmosphere. In particular, this study has considered a greenhouse gas and ozone-depleting substance, HCFC-22, and an organic compound, ethane, which is a tracer species and marker of hydroxyl radical activity. A key aspect of these compounds is that they provide important indications of our ability to monitor the atmosphere. A long-term goal of these studies is to realise the potential to measure global concentrations of organic compounds for the first time.

The results of studies such as these also provide an excellent indication for the need for accurate and detailed spectroscopic knowledge. Much further work is therefore required from laboratory and atmospheric spectroscopists, but the reward for these studies remains rather high and rather important for meeting the challenges of atmospheric climate change and pollution studies over the next decades. Similarly, it should be the aim of new observing strategies of the space agencies to ensure that spectrally resolving instruments are a key element. It is only with such instruments that the satellite community can truly respond to the evolving challenges in atmospheric composition with their enormous societal impacts.

Acknowledgements

The authors wish to thank the European Space Agency (ESA) for provision of operational level 1b and level 2 MIPAS data through the MIPAS Quality Working Group and CUTLSOM projects. The authors also wish to acknowledge support from the U.K. Natural Environment Research Council through its New Investigator, COSMAS, Molecular Spectroscopy Facility, and research student programmes. The support of Roland Leigh and the organizers of the NATO workshop in preparing this manuscript is gratefully acknowledged. Reinhold Spang kindly provided Figures 1 and 2.

References

Allen, G., J. J. Remedios, D. A. Newnham, K. M. Smith, P. S. Monks, 'Improved mid-infrared cross-sections for peroxyacetyl nitrate (PAN) vapour', *Atmospheric Chemistry and Physics*, **5**, 47-56, 2005a. (SRef-ID: 1680-7324/acp/2005-5-47)

Allen, G., J. J. Remedios, D. A. Newnham, K. M. Smith, P. S. Monks, 'Low temperature mid-infrared cross-sections for peroxyacetyl nitrate (PAN) vapour', *Atmospheric Chemistry and Physics*, **5**, 3153-3158, 2005b. (SRef-ID: 1680-7324/acp/2005-5-3153)

Allen, G.: The Infrared Remote Sensing of Peroxyacetyl Nitrate in the Upper Troposphere, Ph.D. thesis, *University of Leicester*, 2005.

Edwards, D.P., genln2: a general line-by-line atmospheric transmittance and radiance model: version 3.0 description and users guide, *Rep. NCAR /TN-367 +STR*, National Center for Atmospheric Research, Boulder, Colorado, 1992.

Fischer, H., and H. Oelhaf, Remote sensing of vertical profiles of atmospheric trace constituents with MIPAS limb-emission spectrometers, *Appl. Opt.*, 35, 2787-2796, 1996.

Fischer, H., Blom, C., Oelhaf, H., Carli, B., Carlotti, M., Delbouille, L., Ehhalt, D., Flaud, J.-M., Isaksen, I., Lopez-Puertas, M., McElroy, C.T., and Zander, R.: Envisat-MIPAS – An instrument for atmospheric chemistry and climate research, editors: C. Readings and R.A. Harris, *ESA Publication SP-1229*, European Space Agency, 2000.

Greenhough, J., J.J. Remedios, H. Sembhi and L.J. Kramer, 'Towards cloud detection and cloud frequency distributions from MIPAS infra-red observations', *Adv. in Space Res.,* **36**, 800-806, 2005.

Höpfner, M. et al. Evidence of scattering of tropospheric radiation by PSCs in mid-IR emission spectra: MIPAS-B observations and KOPRA simulations, Geophys. Res. Lett. **29**, 10.1029/2001GL014443, 2002.

Remedios, J. J.: Extreme atmospheric constituent profiles for MIPAS, *Proceedings of the European*

Remedios, J. J.: Extreme atmospheric constituent profiles for MIPAS, *Proceedings of the European Symposium on atmospheric measurements from space,* Vol. 2, ESTEC, Nordwijk, Netherlands, 20-22nd Jan, 779-783, 1999.

Rothman, L. S., Barbe, A., Benner, D.C., Brown, L. R., Camy-Peyret, C., Carleer, M. R., K. Chance, K, Clerbaux, C., Dana, V., Devi, V. M., Fayth, A. Flaud, J.M., Gamache, R. R., Goldman, A., Jacquemart, D., Jucks, K. W., Lafferty, W. J., Mandin, J.-Y., Massie, S. T., Nemtchinov, V., Newnham, D. A., Perrin, A., Rinsland, C. P., Schroeder, J., Smith, K. M., Smith, M. A. H., Tang, K., Toth, R. A., Vander Auwera, J., Varanasi, P., and Yoshino, K.: The HITRAN molecular spectroscopic database: edition of 2000 including updates through 2001. *J. Quant. Spect.*, 82(1-4): 5-44, 2003.

Spang R., Remedios, J.J., and Barkley M.P., Colour indices for the detection and differentiation of cloud types in infra-red limb emission spectra, Adv. Space Res., 33, 7, 1041-1047, 2004.

Spang, R., Eidmann, G., Riese, M., Preusse, P., Offermann, D., Pfister, L., and Wang, P.H.: CRISTA observations of cirrus clouds around the tropopause, J. Geophys. Res., 107(D23), 8174, doi:10/1029/2002JD000698, 2002.

Waterfall, A. M.: Measurement of organic compounds in the upper troposphere using remote sensing, DPhil thesis, *Oxford University*, 2003.

REMOTE SENSING OF THE NON-LTE ATMOSPHERE

M. López-Puertas and B. Funke (puertas@iaa.es, bernd@iaa.es)
Instituto de Astrofísica de Andalucía (CSIC), Apdo. 3004, 18008 Granada, Spain

Abstract. The fundamentals on non-local thermodynamic equilibrium (non-LTE) in the atmosphere are briefly described as well as for which atmospheric emissions, in which regions and for which instruments (viewing geometry, spectral coverage and resolution), non-LTE processes are more important. The retrieval of atmospheric species from non-LTE infrared emissions and the different options for performing non-LTE retrievals are discussed. The IMK/IAA non-LTE retrieval scheme for inverting atmospheric species from the MIPAS spectra and its application to the retrievals of the CO and NO abundances and non-LTE parameters related to the CO_2 levels emitting near 4.3 μm are described. Finally, a non-LTE parameterization of the CO_2 4.3 μm daytime outgoing radiation in the nadir view is described and its potential application to low altitude atmospheric temperature sounding from nadir infrared instruments is discussed.

Keywords: Non-LTE, remote sensing, MIPAS, AIRS, CO, NO, retrieval, troposphere, stratosphere

1. Introduction

With the advent of high resolution and high sensitivity instruments mounted on satellite platforms, remote sensing of the middle and upper atmosphere from infrared limb measurements is nowadays commonly used. Also, high spectral resolution IR instruments are used now for sounding the lower atmosphere in the nadir. Both techniques are used to derive the temperature structure and the atmospheric composition and are generally based on the assumption that the atmospheric compounds emit according to the Planck function at the local kinetic temperature, the so-called "local thermodynamic equilibrium" or LTE, approach. It is known, however, that many of the IR emitting states of the atmospheric constituents have excitation temperatures which greatly differ from the local kinetic temperature at some conditions and in some atmospheric regions. The availability of such measurements, the high accuracy in the retrieved parameters demanded by models and our understanding of the atmosphere, the available knowledge of required non-LTE processes, and the availability of computers for performing high time consuming retrievals have led to the recent development of retrieval algorithms incorporating non-LTE.

A. Perrin et al. (eds.), Remote Sensing of the Atmosphere for Environmental Security, 87–121.

In Section 2 we describe the basics physics of non-LTE processes and give an overview of how they can affect the retrieval in the different spectra regions. In Sec. 3 we give the prescriptions needed for extending an LTE retrieval to non-LTE conditions and discuss the different ways in which non-LTE can be treated. The non-LTE retrieval scheme developed by IMK/IAA for the inversion of MIPAS spectra and its application to the retrieval of CO and NO abundances as well as to the retrieval of non-LTE parameters are discussed in Sec. 4. Finally, in Sec. 5, a parameterization of the *nadir* radiance of CO_2 in the 4.3 μm region is described and its potential application to the sounding of the temperature in the lower atmosphere from nadir infrared instruments is explored.

2. Non-local thermodynamic equilibrium

We give in this section a brief introduction to the concept of non-LTE and review the physical-chemical processes taking place in the atmosphere that give rise to molecular non-LTE populations. Before describing the concept of non-LTE let us remind the concepts of thermodynamic equilibrium and local thermodynamic equilibrium.

2.1. THERMODYNAMIC EQUILIBRIUM AND LOCAL THERMODYNAMIC EQUILIBRIUM

Let us consider a gas parcel composed of molecules with excited electronic, vibrational and rotational energy levels, and interacting with radiation. If the gas parcel is completely enclosed and isolated, it will attain thermodynamic equilibrium and a single, constant temperature T can be defined. Under these conditions, the distribution of the molecular velocities is given by Maxwell's distribution at temperature T and the excited states are populated accordingly to the Boltzmann's law at the same temperature. The radiative properties of the system are described by Kirchhoff's law, and, hence, the absorption coefficient k_ν and the source function J_ν depends only on T, and the radiative field is characterized by the Planck's function, B_ν(T).

The atmosphere is not a closed system and so true thermodynamic equilibrium never applies, –for example, there is a temperature gradient, while in thermodynamic equilibrium temperature should be the same everywhere– and atmospheric emission is not Planckian at all frequencies. However, in most regions, particularly in the lower ones, exchanges between different translational modes adjust so much more quickly than the internal energy modes, that exchanges of translational energy to and from other energy forms are not sufficient to force each atmospheric parcel from its translational equilibrium.

Thus, although not strictly true, a Maxwellian distribution of molecular velocities for a local kinetic temperature can be assumed with a high degree of accuracy

at each atmospheric height from the surface up to the exosphere, i.e., we can assume a local kinetic temperature T_k which defines the translational equilibrium at each atmospheric altitude z.

If collisions between the atmospheric molecules are fast enough, the population of a given internally excited state (electronic, vibrational or rotational) at a given atmospheric altitude is then given by the Boltzmann's law at this local kinetic temperature. Then, the radiating properties of transitions associated with the excited internal energy modes depends only on T_k, and the source function is described by Planck's function at the local T_k. This is the condition we call 'local thermodynamic equilibrium' or LTE. Thus:

- In LTE we first assume that a translational temperature can be defined and then that the excited internal states, which interact with and emit radiation, are coupled with it by collisions.
- LTE can apply to individual forms of internal energy, and not necessary for all internal modes at the same time. Thus, LTE may prevail for rotational but not for vibrational levels, or for one vibrational mode but not another.
- In LTE the source function is given by Planck's function, $J_\nu = B_\nu(T_k)$, but the intensity of radiation L_ν might differ from B_ν.

In order to find out, in a general way, under which conditions the population of an excited state, or the radiation it emits, is in LTE, we need to solve the statistical equilibrium equation which takes into account all of the microscopic processes that affect its population. A simple case is described below.

2.2. NON-LTE PROCESSES

Let us consider a two-level transition of a given molecule in the atmospheric parcel. Interaction of the excited energy with translational energy occurs through thermal collisional processes, i.e.,

$$\mathrm{n(1) + M} \overset{\mathrm{K}}{\rightleftharpoons} \mathrm{n(0) + M + \Delta E} \tag{1}$$

where M is any 'air' molecule, and $\Delta E = h\nu_0$ is the energy difference of the upper and lower levels. The rate of loss of molecules per volume in the upper state is given by $K\,[M]\,n_1$, or by $l_t\,n_1$ where l_t is the *specific loss* of n_1, $l_t = K\,[M]$ (in units of mol $\mathrm{cm^3 s^{-1}}$), K is the *rate coefficient* of process (1) in the forward direction, and [M] the number density of collision partners. Analogously, the rate of production of n_1 is given by $p_t\,n_0$, where $p_t = K'\,[M]$, and K' is the proportional constant of process (1) in the reverse direction given by

$$\frac{K'}{K} = \frac{g_1}{g_0}\exp\left(-\frac{h\nu_0}{kT}\right). \tag{2}$$

The particles exchange energy with the radiation field by emission at a rate A_{10}, and by absorption at rate B_{01}, being these the Einstein coefficients for spontaneous emission and absorption, respectively (stimulated emission was neglected). Particles can be excited and de-excited by other processes, the so-called non-thermal processes (see below) at rates p_{nt} and l_{nt}. The statistical equilibrium equation under steady conditions for the population of the upper level, n_1, referred to that of the lower level, n_0, is given by detailed balance:

$$\frac{n_1}{n_0} = \frac{B_{01}\bar{L}_{\Delta\nu} + K'[M] + p_{nt}}{A_{10} + K[M] + l_{nt}}. \tag{3}$$

It is followed then that the number density of the excited level, n_1, will be determined by a competition among the different processes. If it is dominated by thermal collisional processes, then, from Eqs. (3) and (2),

$$\frac{n_1}{n_0} = \frac{g_1}{g_0} \exp\left(-\frac{h\nu_0}{kT}\right) \tag{4}$$

and n_1 will be in LTE. In the case that the population of the excited level is driven by radiative processes, in general, n_1 would be in non-LTE since the radiation field is of non-local nature with an absolute intensity, directional distribution and frequency spectrum that usually have no similarity with the Planck's function at the local kinetic temperature. The non-thermal processes act in a similar way than the radiative ones and when they dominate, a non-LTE population of the excited level is expected. Let us now illustrate different non-LTE situations that take place in the atmosphere.

2.3. THE 'CLASSICAL' NON-LTE CASE.

Let consider first the traditionally non-LTE case in which the most important processes involved are thermal collisions and radiative de-excitation, but the absorption of radiation is not significant.

A rough estimation of the altitude at which a transition depart from LTE is given by that at which the collisional de–excitation rate, $K\,[M]$, is of the same order as the spontaneous emission rate, A, $K\,[M] \sim A$. As thermal collisional excitation is proportional to pressure, non-LTE situations are then expected to occur more frequently in the rarified upper atmosphere. Note that under these conditions, the number density of the upper state (n_1) in the non-LTE region is smaller than that corresponding to LTE.

Another important factor when estimating the height at which an energy level start departing from LTE is its energy. Levels with smaller energy are more efficiently thermalized, and are then expected to be in LTE up to higher altitudes. For example, CO_2 4.3 μm starts departing from LTE at ~40 km (Fig. 6); while

the $O(^3P)$ states emitting at 63 μm and the rotational levels of the atmospheric molecules are in LTE up the high altitudes in the thermosphere.

The levels whose principal transition is optically thick in the region where the collisional relaxation and the radiative lifetime are similar do not depart from LTE at altitudes where $K[M] \sim A$, but higher. For these cases, a very good estimation of the altitude of LTE departure is given by that where $K[M] \sim A\tau^\star$, being $\tau^\star$ the probability of photons to escape to space. This situation is rather common in the atmospheres of Mars and Venus.

Another case involving non-LTE only with thermal collision and radiative processes, is when there exist a strong radiative field (either atmospheric –from the Earth's surface, troposphere or stratosphere– or external –solar radiation–). In this case, the absorption of radiation makes the population n_1 to be larger than for LTE, particularly in the mesosphere. In this case, the height of LTE-departure depends on the intensity of the radiative field but, in general, it is lower than when absorption of radiation is negligible.

2.4. NON-THERMAL PROCESSES

There are other conditions when the dominant process controlling the population of the upper state is neither thermal collisions not the radiative processes but non-thermal processes. Typical examples of such processes are:

1. Vibrational-vibrational energy transfer (V–V), where vibrational energy is exchanged in collisions among vibrational levels, being at least one of them in non-LTE.
2. Electronic to vibrational energy transfer, as in: $N_2 + O(^1D) \rightarrow N_2(1) + O(^3P)$.
3. Chemical recombination, e.g., when the molecule emerging from the chemical reaction is vibrationally excited. The most typical examples are the excitation of the O_3 infrared bands: $O + O_2 + M \rightarrow O_3^*(v_1, v_2, v_3) + M$, and the chemical reactions giving rise to most of the infrared airglow.
4. Photochemical reactions, as the daytime O_2 infrared systems at 1.27 μm and 1.58 μm, principally produced by O_3 photolysis in the Hartley bands; and dissociative recombination.

2.5. EFFECTS OF NON-LTE ON RADIANCE MEASUREMENTS

Non-LTE in the atmosphere is important in two major fields: in the retrieval of atmospheric parameters (temperature, composition and non-LE parameters) from radiance measurements and, in the energy budget (radiative heating and cooling, chemical heating). In this paper we will focus on the former. In this section we

discuss the altitude regions where deviations from LTE are expected, and the potential impact of non-LTE upon emission/absorption measurements.

In the long-wave spectral range ($\gtrsim$20 μm), non-LTE are not important in general. The collisional rates for the thermalization of the rotational energy, K_{R-T}, is normally several orders of magnitude larger than that corresponding to vibrational levels, K_{V-T}. Hence, the height of LTE departure, given by approximately that where $K\,[M] \sim A$ (see above), occurs at much higher altitudes than where the vibrational levels do. That is particularly true for the rotational levels in the *ground* vibrational state, because the Einstein coefficient for pure rotational transitions (e.g., among the same vibrational state) are much smaller than for ro-vibrational lines. Hence, rotational levels in the ground vibrational state are expected to be in LTE up to the high thermosphere.

There have been given evidence, however, of non-LTE in rotational levels of vibrationally *excited* states, e.g., in CO_2(001), CO(1) and NO(1) at z$\geq$120 km; in OH Meinel bands in $J \geq 7$, $3 \leq v \leq 7$; and in the high$-J$ (24-29) states in OH(v=0-2) (400-1000 cm^{-1}) in the upper mesosphere (see, e.g., López-Puertas and Taylor (2001) for a review).

For the shortwave spectral region ($\lesssim$4 μm), most of the emissions are produced by the absorption of solar radiation in the uv/vis, in the near-IR or by photochemical reactions. They constitute the atmospheric airglow which is normally produced in the higher altitudes of the atmosphere. The pressure is so low there that they are not thermalized and hence, they are generally in non-LTE.

Most of molecular vibration-rotation emission of atmospheric species fall into in the mid-IR region (4–20 μm), and this is where the concept of non-LTE is usually applied. In general, the majority of the vibrational levels of atmospheric molecules are in LTE in the troposphere and stratosphere. Some levels depart from LTE in the stratosphere, e.g., the CO(1) and NO(1). The departure from LTE is most important in the mesosphere, where, because of the temperature decrease, radiation from below and from the sun (apart from the processes described in section 2.4) lead the vibrational levels to have populations larger than the low LTE ones dictated by the cold temperature.

In general, non-LTE has to be considered for all vibrational bands in the mid-infrared. It depends, however, on the species and the measurement technique. For example, non-LTE effects are of little importance for very minor species (only detectable in troposphere/lower stratosphere), although, the potential overlap with strong non-LTE emissions have to be considered. Also, in general, non-LTE effects are more important for limb view than for nadir emission; and they are of small significance for absorption measurements since these are sensitive to the ground and lower-energy states which are in general weakly affected by non-LTE.

3. Retrievals from Non-LTE mid-IR emissions

The radiance measured by a limb sounding instrument is given by (e.g., López-Puertas and Taylor, 2001))

$$L(x_{\rm obs}) = \int_{\Delta\nu}\int_{x_{\rm s}}^{x_{\rm obs}} J_\nu(x)\,\frac{d\mathcal{T}_\nu(x)}{dx}\,dx\,F(\nu)\,d\nu, \tag{5}$$

where $F(\nu)$ is the instrumental response function, $J_\nu(x)$ the source function, and $\mathcal{T}_\nu(x)$ the transmission function defined by

$$\mathcal{T}_\nu(x, x_{\rm obs}) = \exp\left(-\int_x^{x_{\rm obs}} k_\nu(x')\,n_a(x')\,dx'\right), \tag{6}$$

where k_ν is the molecular absorption coefficient, and n_a is the number density of absorbing molecules.

In contrast to LTE, the Planck function, $B_\nu(x)$, has been replaced by the source function, $J_\nu(x)$, related by

$$J_\nu = B_\nu\, r_2\,\frac{\bar{k}_\nu}{k_\nu}, \tag{7}$$

and the absorption coefficient in non-LTE, k_ν, is related to its LTE value, $\bar{k}_\nu$, by

$$\frac{k_\nu(x)}{\bar{k}_\nu(x)} = r_1\left[\frac{1-\Gamma r_2/r_1}{1-\Gamma}\right] \tag{8}$$

where r_2 and r_1 are the population ratios with respect to LTE of the upper and lower states of the transition, respectively, and the Boltzmann factor, Γ, is given by $\Gamma = \exp(-E/kT)$, being E the energy difference between the upper and lower levels. Thus, for performing radiance calculations under non-LTE we need to know, in addition to the LTE parameters, the population ratios of the upper and lower states of the transition in question, being the former the most important. These ratios are computed by non-LTE models where all information about the physic-chemical parameters controlling the non-LTE populations of the levels is fed in. Examples of such non-LTE models for the most important atmospheric infrared emitters are described, for example, by López-Puertas and Taylor (2001).

Although this has been described for the case of a limb emission instrument, its extension to a nadir instrument is straightforward by simply adding the surface radiation contribution. The extension to an absorption instrument is also simple since only the absorption term (Eq. 8) has to be taken into account.

A typical scheme for retrieving atmospheric parameters from measurements of infrared radiances is shown in Fig. 1. The major change with respect to the inversion process under LTE condition is the addition of the "non-LTE model" module which provide to the algorithm the necessary information about the non-LTE populations, r_ν. To be able to perform such retrieval in non-LTE we also

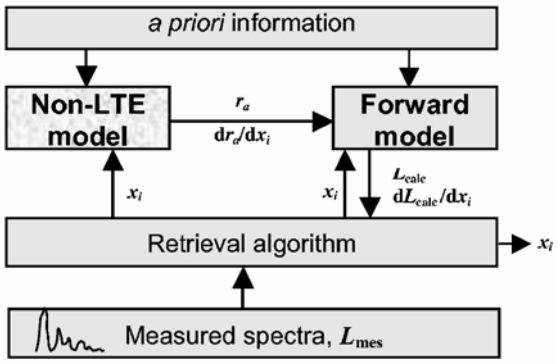

Figure 1. Retrieval scheme under non-LTE conditions.

need to make the appropriate changes in the forward (radiance) calculation as described above (Eqs. 7 and 8). We need that not only for the computation of the forward radiances but also to calculate the Jacobians with respect to the desired quantities to be retrieved. Having done that we are in a position to perform non-LTE retrievals.

3.1. NON-LTE RETRIEVAL SCHEMES

As shown above, a retrieval under non-LTE conditions requires as input our knowledge of the non-LTE populations of the emitting levels in question, that is, a non-LTE model coupled with the forward model calculation. This normally represents a problem since we want the retrievals to perform very rapidly, but the calculation of the non-LTE populations normally entails a high computational cost. This is caused by: i) the need for computing radiative transfer contributions; ii) by the fact that many vibrational levels are necessary to be computed at a time (even if we are interested in only one level) because of their collisional or radiative coupling; and iii) in some cases, because the non-LTE populations are abundance-dependent and hence, the non-LTE populations have to be computed in each iteration of the inversion process.

Then, several options have been advanced for including the non-LTE into the inversion of atmospheric quantities, which are detailed below in order of increasing difficulty.

3.1.1. *Avoid non-LTE*

This is the most simple case. It can be applicable when the deviation from non-LTE is known to be small and then non-LTE is accepted as an additional systematic error source to the error budget. Examples of this are H_2O and CH_4 in the upper stratosphere. Also, if we have a high spectral resolution instrument,

non-LTE can be significantly avoid by selecting the appropriately narrow spectral regions. In this way non-LTE is minimized or eliminated as it could not be in a wideband instrument. One typical example is the O_3 in the 10 μm region where significant contribution from the CO_2 well-spaced 10 μm laser bands takes place. This option has been followed recently in the operational inversion of MIPAS data (Ridolfi et al., 2000; Raspollini et al. 2005), where non-LTE was considered as a systematic error, previously calculated, and used later in the selection of narrow spectral windows (micro-windows) for species retrieval by minimizing the overall error budget.

3.1.2. *Tabulation of non-LTE populations*

For the species that are strongly affected by non-LTE and its inclusion is computationally very expensive, the alternative is to tabulate beforehand the non-LTE populations. First, the quantities on which non-LTE depends have to be identified (e.g., solar zenith angle, abundance, lower atmospheric conditions) and then the appropriate tabulation has to be performed. One major difficulty in this case is to provide the accurate non-LTE population when it is close to LTE, since it depends strongly on the measured kinetic temperature and this is very variable. Thus, its tabulation is difficult because it is complicated to include in the tabulation all possible actual cases. Under these conditions it is quite normal that the error in the non-LTE correction is as large as the correction itself. As an example of this option we can cite the retrieval of CO from the ISAMS/UARS instrument (López-Valverde et al., 1996).

In this option, the quantity tabulated was the non-LTE populations, in any of its different variants, e.g., vibrational temperatures or population ratio with respect to LTE, and normally applied to the case of a limb-viewing instrument. Recently, a similar approach has been followed for the case of the AIRS instrument but tabulating the measured nadir radiance (e.g., Eq. 5), instead of the population profiles (Eq. 7) (DeSouza-Machado et al., 2005). In this case the non-LTE contribution to the outgoing radiance at the top of the atmosphere was parameterized as function of the solar zenith angle, viewing observing angle and the altitude where the bands start deviating from LTE from precomputed accurate line-by-line non-LTE forward calculations.

3.1.3. *On-line calculation of non-LTE populations*

This is the easier and more accurate option which is used when computer resources is not an issue. The non-LTE model is integrated in the retrieval scheme (Fig. 1) and called as many times as necessary during the inversion process. This scheme is becoming nowadays more frequently used since we have better computational resources. For example, that is being used in the retrieval of temperature and CO_2 and O_3 abundances from the SABER/TIMED wide-band IR radiances

(Mertens et al., 2002; 2004); and in the inversion of MIPAS high resolution spectra into the abundances of NO, NO_2, and CO (Funke et al., 2004; 2005a,b).

3.1.4. *Retrieval of non-LTE parameters*

One can also use the retrieval scheme of Fig. 1 not only for retrieving temperature and species abundances but also to retrieve the parameters in the non-LTE model affecting the non-LTE populations; or even all these quantities simultaneously. For this, it is obviously required that there should be enough information in the measurements, i.e., as in high resolution measurements covering an extensive spectral range.

A particular interesting case is when the measurements consist of high resolution spectra covering both ro-vibrational optically thin and optically thick lines, and thus providing information about the populations of the upper (excited) and lower (ground) states of the transition and, hence, about the non-LTE parameters and species abundances, simultaneously.

Other cases of interest are those where simultaneous emission in two (or more) different bands are measured, one in LTE, and hence providing information on the species abundance, and others in non-LTE, from whose emission the non-LTE parameters controlling their populations can be derived.

To our knowledge, this scheme has only been applied very recently for inverting non-LTE parameters from the MIPAS/Envisat spectra (López-Puertas et al., 2005). An example of this kind is discussed in Sec. 4.3 for the case of CO_2.

4. Retrievals from MIPAS non-LTE infrared emissions

In this section we describe some examples of retrieval under non-LTE conditions. In particular we discuss the retrieval of NO and CO abundances and of some non-LTE parameters affecting the CO_2 levels emitting near 4.3 μm from the high resolution spectra measured by MIPAS carried out by the IMK and IAA groups.

MIPAS is a high resolution limb sounder on board the ENVISAT satellite, successfully launched on 1 March 2002 into its sun-synchronous polar orbit of 98.55° inclination at about 800 km altitude (Fischer and Oelhaf, 1996; ESA, 2000). It has several advantages which makes it a very good instrument for studying the atmospheric non-LTE emissions: (i) its wide spectral coverage (4.15–14.6 μm or 680–2275 cm^{-1}), allowing for measuring emissions from a given compound in different spectral regions; (ii) high spectral resolution (0.035 cm^{-1}), enabling to discriminate emissions from different species and between different bands of the same species; and (iii) its high sensitivity allowing to measure the emission in the upper atmosphere where non-LTE emissions are most important. In addition, MIPAS has a global pole-to-pole spatial coverage and a day and night temporal coverage. MIPAS scans the limb operationally from 6 km up to 68 km and up to

170 km in the upper atmosphere modes of observation. MIPAS orbits the Earth at 14.3 times a day, taking about 72 profiles per orbit.

The forward model used for calculating the limb radiance (see Fig. 1) is the Karlsruhe Optimised and Precise Radiative transfer Algorithm (KOPRA) (Stiller et al., 2002). KOPRA is a layer-by-layer line-by-line radiative transfer code for calculation of atmospheric transmission and radiance spectra along with the partial derivatives of the spectra with respect to atmospheric state parameters. Calculation of absorption coefficients are performed on an optimized internal non-equidistant wave number grid. Refraction of the ray-path, including the case of non-spherical Earth shape and line- mixing are included. In addition, vibrational, rotational as well as spin non-LTE are supported. It also allows to compute Jacobians for non-LTE conditions and an interface to the Generic RAdiative traNsfer AnD non-LTE population Algoritm (GRANADA) model has been programmed. The code has been tested against other well established codes (von Clarmann et al., 2002).

The inversion algorithm itself consists in a global fit least squares algorithm with a Levenberg-Marquardt damping and an user-defined regularization. More details on this can be found in von Clarmann et al. (2003).

The non-LTE model used is GRANADA (Funke et al., 2002). This is a generic non-LTE radiative transfer model for the calculations of non-LTE populations of the major atmospheric infrared emitters. It uses a generalized scheme, that is, the same for all molecules, being able to compute non-LTE vibrational populations for CO_2, O_3, H_2O, CH_4, N_2O, NO_2, NO, CO, and OH. For NO and OH it also computes rotational and spin-orbit non-LTE populations. The user can define which states and transitions to be included, which altitude range, iteration strategies, which collisional processes to be taken into account and other parameters. The radiative transfer processes can be treated using line-by-line and line independent algorithms. The inversion of the multilevel steady state equations can be solved either with the Lambda iteration or Curtis matrix formalisms. In the next section we discuss the specific examples of CO, NO and CO_2.

4.1. RETRIEVAL OF CO FROM THE 4.7-μm NON-LTE EMISSION

Figure 2 shows a vibrational temperature (T_v) profile for the CO(1) level during daytime conditions. The expected deviation from the LTE population, dictated by the kinetic temperature (T_k) is very large in the mesosphere and it is also sometimes significant even in the stratosphere. By applying the retrieval algorithm described above we have performed LTE and non-LTE retrievals for the scan measured by MIPAS on 26 Sep 2002 (Fig. 3). The effects are evident above around 35 km being larger than 200% in the mesosphere.

By applying the above-described non-LTE retrieval technique (Funke et al., 2004), we derive the CO abundance from MIPAS spectra in a semi-operational

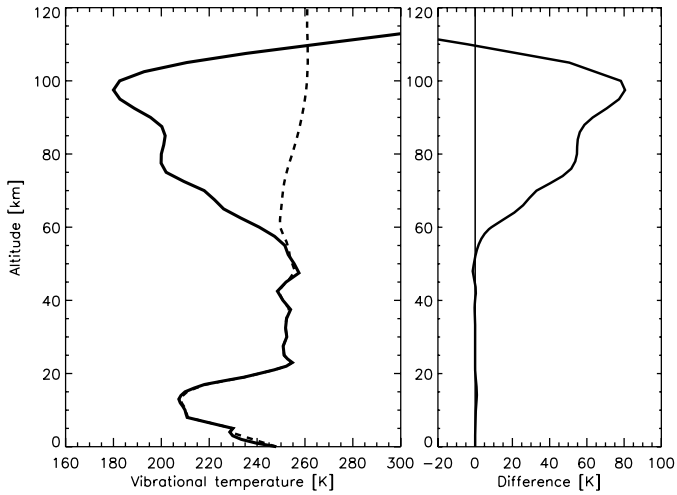

Figure 2. Vibrational temperature (dashed) of the CO(v=1) level for the kinetic temperature (solid) profile measured by MIPAS on 26 Sep 2002 at 82.4°S, 52.6°E, for a solar zenith angle of 83.5°. Right panel shows the T_v–T_k difference.

manner with a very good quality. Actually, the effects of non-LTE help in this case for obtaining a more precise abundance since the signal from daytime (non-LTE) conditions is much larger than it would be in LTE (see Fig. 2). The comparison of the CO derived from MIPAS against other instruments free from non-LTE effects,

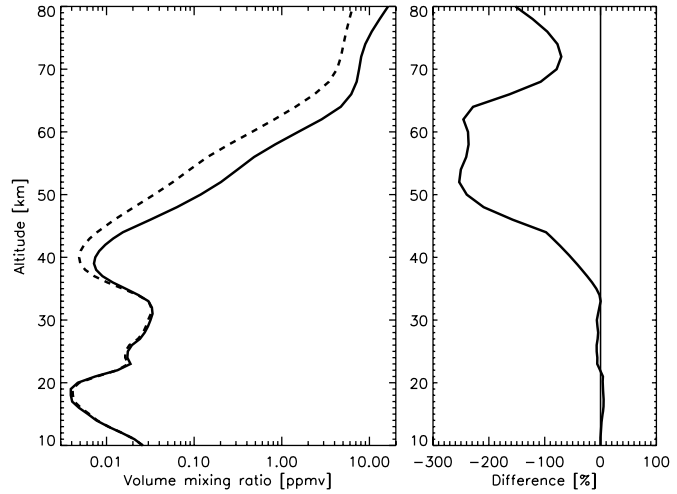

Figure 3. Retrieved CO abundance under LTE (solid) and non-LTE (dashed) for the case in Fig. 2. Right panel shows the (non-LTE–LTE)/non-LTE difference in %.

e.g. SMR in Odin and ACE-FTS, shows a very good agreement, thus validating the CO non-LTE retrieval scheme used for MIPAS data (Funke et al., 2005b).

4.2. RETRIEVAL OF NO FROM 5.3-μm EMISSION: EFFECTS OF NON-LTE

Figure 4 shows a typical daytime vibrational temperature profile for NO(v=1). The vibrational non-LTE effects for this state are very large and, for the retrieval of this species in the stratosphere we have to consider the non-LTE population all the way up to the middle thermosphere due to its large concentration there. It also worth noticing the non-thermal excitation of NO(1) in the daytime stratosphere produced by

$$NO_2 + O \rightarrow NO(v) + O_2 \quad (9)$$

$$NO_2 + h\nu \rightarrow NO(v) + O \quad (10)$$

which lead to enhancements in the vibrational temperature of NO(1) of 5–10 K (right panel of Fig. 4). This mechanism was proposed by Kaye and Kumer (1987) and has been recently confirmed by MIPAS measurements (Funke et al., 2005a).

In addition to vibrational non-LTE, the rotational and spin-orbit non-LTE of NO in the thermosphere (Funke and López-Puertas, 2000) are also important and induce significant differences in the retrieval of NO in the thermosphere and stratosphere (Funke et al., 2000).

Figure 5 illustrates the effects of the non-LTE photochemical excitation processes (9) and (10) in the stratosphere on the retrieved NO abundance in this region. NO and NO_2 are in photochemical equilibrium in this region. The figure shows the NO retrieved from MIPAS measurements versus that predicted from a photochemical model by including the simultaneous MIPAS measurements of pressure, temperature, NO_2, O_3 and ClO abundances and the photo-absorption coefficients for NO_2 and O_3 provided by the TUV model (version 4.2) (Funke et al., 2005a). We see that the NO concentrations would be increased in more than 5 ppbv (~20%) in the middle stratosphere if the non-LTE processes (9) and (10) are neglected. The retrieved NO has also been validated against "non-LTE free" instruments as HALOE and showed to be in good agreement (Funke et al., 2005a). This non-LTE retrieval of NO hence shows evidence that for deriving an accurate NO abundance in the stratosphere, the inclusion of non-LTE is essencial.

4.3. RETRIEVAL OF CO_2 4.3-μm NON-LTE PARAMETERS

Carbon dioxide has many vibrational transitions in the 4.3 μm spectral region, including its strongest atmospheric bands. These bands start departing from LTE around the stratopause, the departure being particularly important during daytime, when they are pumped by absorption of solar radiation mainly at 4.3 and 2.7 μm (see Fig. 6). It is very important to know accurately the non-LTE populations of the

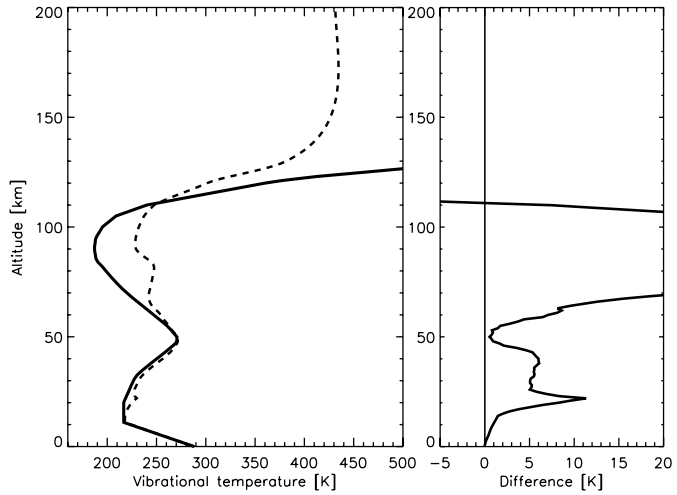

Figure 4. Vibrational temperature (dashed) of the NO(v=1) level for a mid-latitude kinetic temperature (T_k) (solid) and daytime conditions. Right panel shows the T_v–T_k difference.

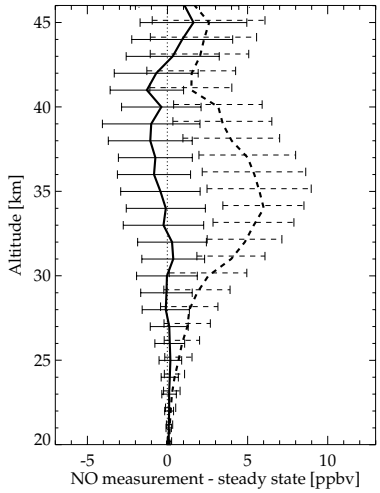

Figure 5. Differences between measured daytime NO and calculated daytime NO assuming photochemical equilibrium between NO and NO_2. Mean values and 1-σ variances (bars) of the differences are shown. The differences are shown for the retrieved NO in non-LTE (processes 9 and 10) (solid) and in LTE. Reproduced by permission of American Geophysical Union.

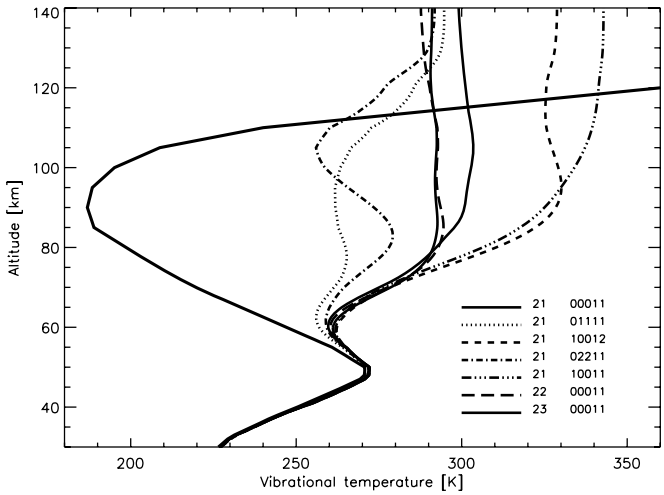

Figure 6. Vibrational temperatures of the CO_2 levels contributing to the MIPAS radiances in Fig. 7.

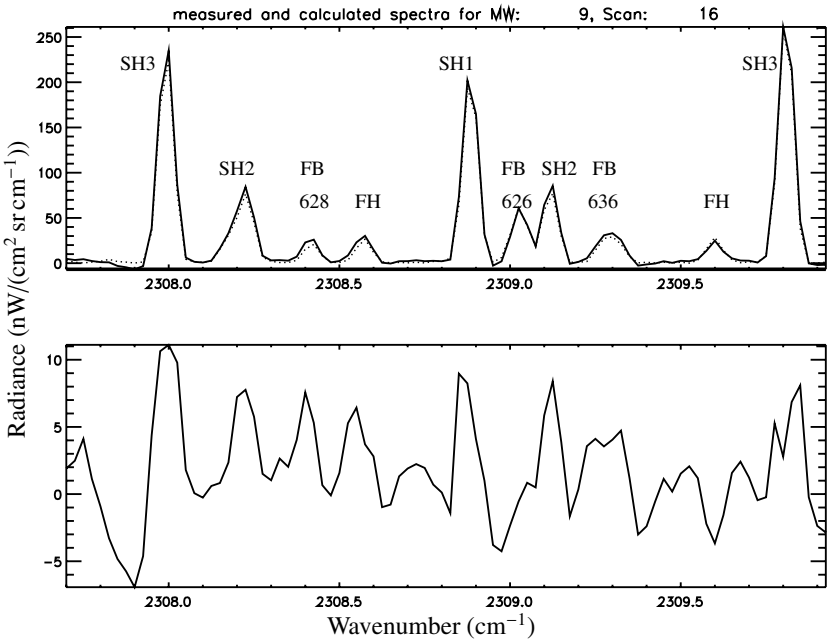

Figure 7. MIPAS daytime spectra in the 4.3-μm spectral region, dominated by CO_2 bands, at a tangent height of 82 km. Upper panel shows radiances: measured (solid), and simulated in the last iteration of the retrieval (dotted, hardly visible). The ten emission features in the spectra are due to lines in the shown 4.3-μm bands. See text for the meaning of the labels. The lower panel shows the residual (measured-simulated) radiances. Note the different scale. The noise of MIPAS in this channel is 4 nW/(cm^2 sr cm^{-1}).

upper states of these bands because they are normally used for retrieving the CO_2 abundance in the mesosphere and lower thermosphere (López-Puertas and Taylor, 1989; López-Puertas et al., 1998; Kaufmann et al., 2002; Mertens et al., 2002); and also because they affect the populations of CO_2 levels emitting in the 15-μm first and second hot bands, which are used for retrieving the kinetic temperature.

Several studies have been conducted for understanding these non-LTE populations in the past (see, e.g., López-Puertas and Taylor (2001) for a review). However, the lack of measurements with high spectral resolution has prevented from knowing accurately the individual contributions of these bands to the Earth limb emission. The high spectral resolution as well as the extensive spectral coverage of MIPAS offer an unprecedented opportunity to study them.

We have applied the retrieval scheme described above to retrieve non-LTE parameters, i.e., the collisional rates, among some of the energy levels emitting in this region. In particular, we have applied it to the spectra of the middle atmosphere taken by MIPAS on 2nd July 2002 at 47.5°N, 48.7°E and solar zenith angle of 32.8°, for retrieving the collisional rates between the upper states of the 4.3-μm second hot bands emitting in the 4.3 μm region, 10012, 02201, and 10001:

$$k_1 : CO_2(10012, 10011) + M \leftrightarrow CO_2(02201) + M \tag{11}$$

$$k_2 : CO_2(10002) + M \leftrightarrow CO_2(10001) + M. \tag{12}$$

The retrieved values of the collisional parameters k_1 and k_2 have values of 5.5×10^{-13} and 8×10^{-13} cm^3s^{-1}, which are very different from previous values commonly used in the literature of 1.5×10^{-13} and 3×10^{-11} cm^3s^{-1}, and thus differing by factors of 3.5 and 0.025. The retrieval has been performed by obtaining simultaneously the kinetic temperature and fitting also the CO_2 volume mixing ratio. (López-Puertas et al., 2004),

The goodness of the retrieval can be appreciated from the very small residuals achieved (see Fig. 7 for most of these bands. In this small spectral window, all of the ten lines, arising from seven different bands, are very well fitted. The top panel of Fig. 7 shows, from left to right, lines of the following bands: the second hot SH3: 10011→10001; the second hot SH2: 02211→02201; the fundamental band (FB) 00011→00001 of the 628 minor isotope; the first hot (FH) band 01111→01101 of the major isotope 626; the second hot SH1: 10012→10002; the fundamental band (FB) of the 626 major isotope; another SH2 line; the fundamental band of the 636 second major isotope; another FH 626 line; and another line of the the SH3 band. This clearly shows that the retrieval of non-LTE parameters described above works and the enormous usefulness of MIPAS spectra for improving our understanding of non-LTE processes in the atmosphere.

5. Retrieval of tropospheric and stratospheric temperature from CO_2 4.3-μm nadir emission

The non-LTE effects are most important for the limb emission measurements. However, there are some atmospheric bands which also show significant non-LTE effects when observed in nadir viewing. That is the case of the CO_2 4.3 μm bands studied in the previous section. Some of these bands are so optically thick that part of the radiance outgoing in the nadir is emitted in the stratosphere where most of these bands deviate from LTE (see Fig. 6).

Non-LTE has been so far mainly applied to *limb* emission infrared instruments. Very recently, however, its has also been applied to the hyper-spectral nadir infrared measurements of AIRS, on board the NASA Aqua satellite. With the goal of retrieving tropospheric and stratospheric temperature from the 4.3 μm daytime nadir radiance, DeSouza-Machado et al. (2006) have developed a fast forward non-LTE model of the outgoing nadir radiation by CO_2 in this spectral region. The parameterization is based on the GRANADA non-LTE model for CO_2 levels (Funke et al., 2002) using the radiative and collisional schemes of Lopez-Puertas and Taylor (2001). The model has been validated against AIRS measurements. Figure 8 shows the differences between top-of-the-atmosphere (TOA) radiances measured by AIRS and calculated by the model for night and daytime conditions for a wide spectral interval near 4.3 μm where many bands contribute. We can see the large differences found for daytime when assuming LTE, and how these are very similar to the nighttime radiance when non-LTE is incorporated. Figure 9 shows the differences as function of solar zenith angle (SZA) for two AIRS channels. More than a thousand of measurements are included in this figure. Figures 8 and 9 show the very good agreement between model and measurements found for all wavenumbers and SZA's, thus showing the validity of the model for using it for temperature sounding from nadir 4.3 μm daytime measurements. The next step in the future is to use the model for retrieving temperature in this spectral region and compare them to those retrieved in the usual 15 μm region.

6. Summary and conclusions

In this paper we have briefly described the fundamentals of non-LTE in the atmosphere. Then, a general discussion about which atmospheric emissions, in which regions, and for which instruments (viewing geometry and spectral coverage and resolution), non-LTE processes are more prominent. In general, non-LTE has to be taken into account when retrieving species from infrared limb sensors in the upper stratosphere and above, and for some species they are unavoidable even at lower altitudes. The retrieval of atmospheric species from non-LTE infrared emissions has also been discussed. The corrections needed for extending an LTE retrieval to

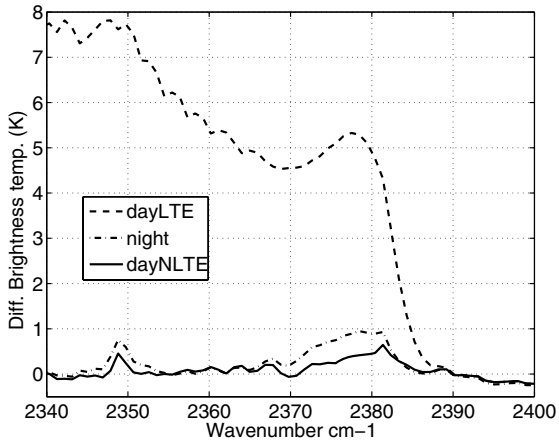

Figure 8. Differences between AIRS-measured and calculated outgoing top of the atmosphere (TOA) radiances (expressed in brightness temperature in K) for the CO_2 4.3 μm bands for night and daytime conditions.

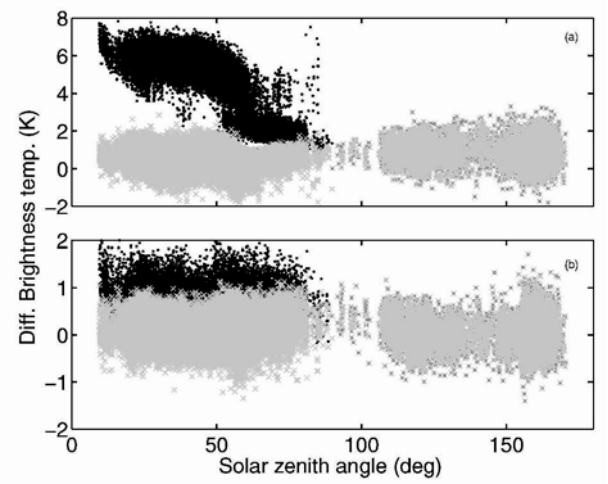

Figure 9. Differences between AIRS-measured and calculated TOA radiances against solar zenith angle for the 2380 cm^{-1} (top) and 2385 cm^{-1} (bottom) AIRS channels. Dark curves are the differences calculated in LTE and light ones those computed in non-LTE. Note the different scale.

non-LTE conditions have been prescribed and the different options for performing non-LTE retrievals have been discussed.

The IMK/IAA non-LTE retrieval scheme for inverting atmospheric species from the MIPAS spectra has been described, together with its application to the retrievals of the CO and NO abundances and non-LTE parameters related to the CO_2 levels emitting near 4.3 μm. The results have shown that the non-LTE retrieval is feasible nowadays and it is able to obtain highly accurate abundances of CO

and NO from their respective non-LTE emissions. Furthermore, such an inversion algorithm is also suitable for retrieving information on non-LTE parameters from the high resolution MIPAS spectra.

Finally, we have shown a non-LTE parameterization of the CO_2 4.3 μm daytime TOA outgoing radiation which will be potentially applicable to nadir infrared instruments sensing the lower atmosphere, such as the current AIRS instrument on board the Aqua satellite. This parametrization demonstrates that there is a real possibility of using the CO_2 4.3 μm region for temperature sounding both during day and night, either itself or in conjunction with the 15 μm region.

Acknowledgements

Part of this work has been supported by Spanish MEC under projects REN2001-3249/CLI and ESP2004–01556, and EC FEDER funds.

References

DeSouza-Machado, S.G., L.L. Strow, S.E. Hannon, H.E. Motteler, M. López-Puertas, B. Funke, and D. P. Edwards, 2005, Fast forward radiative transfer modeling of 4.3 μm non-local thermodynamic equilibrium effects for the Aqua/AIRS infrared temperature sounder, *Geophys. Res. Lett.*, submitted to.

European Space Agency, Envisat, MIPAS An instrument for atmospheric chemistry and climate research, 2000, ESA Pub. Div., Noordwijk, The Netherlands, SP-1229.

Fischer, H. and H. Oelhaf, 1996, Remote sensing of vertical profiles of atmospheric trace constituents with MIPAS limb-emission spectrometers, *Appl. Opt.*, **35**, 16, 2787–2796.

Funke, B., and M. López-Puertas, 2000, Nonlocal thermodynamic equilibrium vibrational, rotational, and spin state distribution of NO(v= 0,1,2) under quiescent atmospheric conditions, *J. Geophys. Res.*, *105*(D4), 4409–4426.

Funke, B., M. López-Puertas, G. Stiller, T. Clarmann, M. Höpfner and M. Kuntz, 2000, Non-LTE state distribution of nitric oxide and its impact on the retrieval of the stratospheric daytime NO profile from MIPAS limb sounding instruments , *Adv. Space Res.*, **26**, 947–950.

Funke, B., F. J. Martín-Torres, M. López-Puertas, M. Höpfner, F. Hase, M. Á. López-Valverde, and M. García-Comas, 2002, A generic non–LTE population model for MIPAS–ENVISAT data analysis, *Geophys. Res. Abs.*, **4**.

Funke, B. et al., 2004, CO in the middle atmosphere measured with MIPAS/ENVISAT, *Geophys. Res. Abstracts, 6*, 04358, SRef-ID: 1607-7962/gra/EGU04-A-04358.

Funke, B., M. López-Puertas, T. von Clarmann, G.P. Stiller, H. Fischer, N. Glatthor, U. Grabowski, M. Höpfner, S. Kellmann, M. Kiefer, A. Linden, G. Mengistu-Tsidu, M. Milz, T. Steck, and D.Y. Wang, 2005a, Retrieval of stratospheric NO_x from 5.3 and 6.2 μm non-LTE emissions measured by MIPAS on ENVISAT, *J. Geophys. Res.*, **110**, D09302, doi:10.1029/2004JD005225.

Funke, B. et al., 2005b, Carbon monoxide observations by MIPAS/Envisat during the major warming event in September/October 2002, *J. Geophys. Res.*, to be submitted.

Kaufmann, M., O. A. Gusev, K. U. Grossmann, R. G. Roble, M. E. Hagan, C. Hartsough, and A. A. Kutepov, 2002, The vertical and horizontal distribution of CO_2 densities in the upper mesosphere and lower thermosphere as measured by CRISTA, *J. Geophys. Res., 107*(D23), 8182, doi:10.1029/2001JD000704.

Kaye, J. A., and J. B. Kumer, 1987, Nonlocal thermodynamic equilibrium effects in stratospheric NO and implications for infrared remote sensing, *Appl. Opt.*, *26*(22), 4747–4754.

López-Puertas, M., and F. W. Taylor, 1989, Carbon dioxide 4.3-μm emission in the Earth's atmosphere. A comparison between NIMBUS 7 SAMS measurements and non-LTE radiative transfer calculations, *J. Geophys. Res., 94*, 13045–13068.

López-Puertas, M. G. Zaragoza, M.A. López-Valverde, and F.W. Taylor., 1998, Non-LTE atmospheric limb radiances at 4.6 μm as measured by UARS/ISAMS II. Analysis of the daytime radiances, *J. Geophys. Res.*, *103*, 8515–8530.

López-Puertas, M. and F. W. Taylor, 2001, *Non-LTE Radiative Transfer in the Atmosphere*, World Scientific Publishing Co., Singapore.

López-Puertas, M. et al., 2004, Mesospheric and lower thermospheric temperature and carbon dioxide volume mixing ratio as measured by MIPAS/Envisat, *Geophys. Res. Abs.*, **6**, 04672.

López-Puertas, M. B. Funke, S. Gil-López, M.Á. López-Valverde, T. Clarmann, H. Fischer, H. Oelhaf, G. Stiller, M. Kaufmann, M.E. Koukouli and J.-M. Flaud, 2005, Atmospheric non-local thermodynamic equilibrium emissions as observed by the Michelson interferometer for passive atmospheric sounding (MIPAS), *C. R. Physique*, **8**, 848-863, doi 10.1016/j.crhy.2005.07.012.

López-Valverde, M.A. et al., 1996, Validation of measurements of carbon monoxide from the improved stratospheric and mesospheric sounder, *J. Geophys. Res., 101*, 9929-9955.

Mertens, C. J., M. G. Mlynczak, M. López-Puertas, P. P. Wintersteiner, R. H. Picard, J. R. Winick, L. L. Gordley, and J. M. Russell III, 2002, Retrieval of kinetic temperature and carbon dioxide abundance from non-local thermodynamic equilibrium limb emission measurements made by the SABER experiment on the TIMED satellite, *Proc. SPIE, 4882*, 162-171.

Mertens, C.J., F.J. Schmidlin, R.A. Goldberg, E.E. Remsberg, W.D. Pesnell, J.M. Russell, M.G. Mlynczak, M. López-Puertas, P.P. Wintersteiner, R.H. Picard, J.R. Winick and L.L. Gordley, 2004, SABER observations of mesospheric temperatures and comparisons with fallling sphere measurements taken during the 2002 summer MaCWAVE campaign, *Geophys. Res. Lett.*, **31**, L03105, doi:10.1029/2003GL018605.

Raspollini, P., C. Belotti, A. Burgess, B. Carli, M. Carlotti, S. Ceccherini, B. M. Dinelli, A. Dudhia, J.-M. Flaud, B. Funke, M. Höpfner, M. López-Puertas, V. Payne, C. Piccolo, J.J. Remedios, M. Ridolfi, and R. Spang, 2005, 'MIPAS Level 2 Operational Analysis with ORM Code', *Atmos. Chem. Phys.*, submitted.

Ridolfi, M., B. Carli, M. Carlotti, T.v. Clarmann, B.M. Dinelli, A. Dudhia, J.-M. Flaud, M. Höpfner, P.E. Morris, P. Raspollini, G. Stiller, and R.J. Wells, 2000, Optimized forward model and retrieval scheme for MIPAS near-real-time data processing, *Appl. Opt.*, *39*(8), 1323–1340.

Stiller, G. P., T. von Clarmann, B. Funke, N. Glatthor, F. Hase, M. Höpfner, and A. Linden, 2002, Sensitivity of trace gas abundances retrievals from infrared limb emission spectra to simplifying approximations in radiative transfer modelling, *J.Q.S.R.T*, **72**(3), 249–280.

Taylor, F. W. and M. López-Puertas, 2003, Radiative Transfer: Non Local Thermodynamic Equilibrium, in *Encyclopedia of Atmospheric Sciences*, Edited by J.R. Holton, J. Pyle and J.A. Curry, 1874-1882, Academic Press, Amsterdam.

von Clarmann, T., A. Dudhia, D.P. Edwards, B. Funke, M. Höpfner, B.J. Kerridge, V. Kostsov, A. Linden, M. López-Puertas and Yu. Timofeyev, 2002, Intercomparison of radiative transfer codes under non-local thermodynamic equilibrium conditions, *J. Geophys. Res.*, **107**, (D22), 4631, doi:10.1029/2001JD001551.

von Clarmann, v.T., N. Glatthor, U. Grabowski, M. Höpfner, S. Kellmann, M. Kiefer, A. Linden, G. Mengistu Tsidu, M. Milz, T. Steck, G. P. Stiller, D. Y. Wang, H. Fischer, B. Funke, S. Gil-López and M. López-Puertas, 2003, Retrieval of temperature and tangent altitude pointing from limb emission spectra recorded from space by the Michelson Interferometer for Passive Atmospheric Sounding (MIPAS), *J. Geophys. Res.*, **108**, 4736, doi:10.1029/2003JD003602.

QUANTITATIVE SPECTROSCOPY AND ATMOSPHERIC MEASUREMENTS

J.-M. FLAUD*, A. PERRIN, B. PICQUET-VARRAULT, A. GRATIEN, J. ORPHAL, AND J.-F. DOUSSIN
Laboratoire Interuniversitaire des Systèmes Atmosphériques, Universities Paris 12&7 and CNRS, 61 av. du Général de Gaulle, 94010 Créteil Cédex,France

Abstract. Optical measurements of atmospheric minor constituents are performed using spectrometers working in the UV-visible, infrared and microwave spectral ranges. In particular recently the satellite ENVISAT has been launched with three spectrometers on board, SCIAMACHY and GOMOS working in the UV-visible spectral region and MIPAS working in the thermal infrared. The analysis and interpretation of the atmospheric spectra require good knowledge of the molecular parameters of the species of interest as well as of the interfering species. This is true not only in the spectral domain used to retrieve the species (Thermal infrared for MIPAS for example) but also in the other spectral domains used by other instruments: Meaningful comparisons of profiles retrieved by various instruments using different spectral domains require indeed that the spectral parameters are consistent in these spectral domains. To illustrate these points we will concentrate on three molecules namely nitric acid, formaldehyde and ozone. For HNO_3 we will show the difficulty to measure line intensities in the laboratory and we will describe how a comparison of MIPAS profiles with those obtained by another instrument operating in a different spectral range (Far infrared) may be used to validate the HNO_3 line parameters in the mid-infrared. For the measurement of atmospheric formaldehyde concentrations, mid-infrared and ultraviolet absorptions are both used by ground, air or satellite instruments. It is then of the utmost importance to have consistent spectral parameters in these various spectral

* *To whom correspondence should be addressed.: Jean-Marie Flaud, Labotoire Inter-Universitaire des Systèmes Atmosphériques (LISA), Universities Paris 12 and 7 & CNRS, 61 Avenue du Général de Gaulle, 94010 Créteil, France ; Email : flaud@univ-paris12.fr.

A. Perrin et al. (eds.), Remote Sensing of the Atmosphere for Environmental Security, 107–121.

domains. Consequently the aim of the study performed at LISA was to intercalibrate formaldehyde spectra in the infrared and ultraviolet regions. The experiments were performed by acquiring simultaneously UV and IR spectra at room temperature and atmospheric pressure using a common optical cell. The reactor contains two multiple reflection optical systems interfaced to a Fourier transform infrared spectrometer and to an UV-visible absorption spectrometer. The results are discussed and compared with previous ones. In the mid-infrared range, the 10 μm ozone band is very strong and is the most widely used to derive concentration profiles. In the UV region, various bands are currently used for spectroscopic remote-sensing of ozone. In this paper we present two sets of results:

- First a careful comparison of four sets of ozone line intensities measured independently in the 10 μm region has been achieved. From them new and more accurate transition moment constants for the ν_1 and ν_3 bands of $^{16}O_3$ were derived and used to generate new line positions and intensities. These new spectroscopic parameters allowed one to simulate atmospheric spectra better than the previous spectroscopic parameters showing that on a relative basis the new spectral parameters are of better quality.

- Second, we present intercomparisons of ozone absorption cross sections in the UV and mid-infrared regions, using the absorption of ozone at 254 nm and in the Huggins region. In the case of the Huggins region the comparison has been performed by acquiring simultaneously UV and infrared spectra at room temperature and atmospheric pressure using the same reactor as for H_2CO.

Keywords: Molecular spectroscopy, Infrared intensities, Ultra violet and visible absorption cross sections, Atmospheric sounding, Minor atmospheric constituents' retrievals

1. Introduction

Molecular spectroscopy, besides its own research themes, represents a powerful tool in a number of fields (Atmospheric physics, astrophysics, atmospheres of the planets, combustions, leakage and process control …) to probe the medium of interest. It allows one indeed to measure in a non-intrusive way numerous properties of the medium (Temperature, pressure, abundance of constituents…). As far as atmospheric physics is concerned the past years have seen a noticeable increase of studies aiming at (1) a

better understanding of the different phenomena driving the atmospheric system and (2) the prediction of its evolution in the future. In particular human activities, important since the beginning of the industrial period, are strongly changing the atmospheric composition. One can quote for example the enhanced green house effect due to the emission of gases such as carbon dioxide or methane, or the loss of ozone in the stratosphere clearly observed over the poles (ozone hole), or even pollution for which issues such as air quality, free tropospheric ozone levels, acidic deposition, natural versus anthropogenic emissions are still open.

These questions are studied both theoretically and experimentally. From the experimental point of view atmospheric measurements are performed using various platforms (ground networks, balloons, planes, satellites) and different techniques. Among them optical remote sensing methods are widely used (Fischer et al., 2005; Chance et al., 2005; Carli et al., 2005). In particular, measurements from space are the only ones able to provide a continental or global view of the atmosphere. This is why a number of satellite experiments using various optical techniques (radiometers, grating spectrometers, Fourier transform interferometers …) have been launched. Recently, high quality optical remote sensing instruments working either in the middle and thermal infrared such as MIPAS (Michelson Interferometer for Passive Atmospheric Sounding) or in the visible-ultraviolet such as SCIAMACHY (**SC**anning **I**maging **A**bsorption Spectro**M**eter for **A**tmospheric **CH**artograph**Y)**, have been launched on the ESA's Environmental Satellite (ENVISAT). In all cases the analysis of the measurements requires the best possible knowledge of the spectral parameters (line positions, intensities, widths, absorption cross sections ...) of the measured species and of their variations with temperatures and pressures. This is particularly true for the recent instruments which cover wide spectral ranges at rather high spectral resolutions with excellent signal to noise ratios. The spectral parameters are derived from experimental and/or theoretical spectroscopy and, since obviously the accuracy of the retrieved profiles depends highly on the quality of the spectroscopic parameters, given the improved capabilities (higher spectral resolution, better signal to noise ratio ...) of the new instruments, it is clear that new laboratory studies using the best experimental techniques and/or sophisticated theoretical models are required. This is true not only in the spectral domain used to retrieve the species (thermal infrared for MIPAS for example) but also in the other spectral domains used by other instruments: Meaningful comparisons of profiles retrieved by various instruments using different spectral domains require indeed that the spectral parameters are consistent in these spectral domains. To illustrate these

points we will concentrate on three molecules, namely nitric acid, formaldehyde, and ozone. The paper is organized as follows:

The case of the HNO_3 molecule for which it is only recently that accurate line positions and intensities have been derived will be described first. Then we will discuss the case of the formaldehyde molecule showing that some measurements are not consistent both in the infrared and visible spectral domains. Finally for the ozone molecule it will be shown that despite a number of studies there is still a problem of consistency between the mid-infrared and ultraviolet cross sections.

2. The nitric acid (HNO_3) molecule

In the troposphere, nitric acid is an almost permanent sink for nitrogen oxides through many processes including the reaction between OH and NO_2 (Atkinson, 2000) or the heterogeneous hydrolysis of N_2O_5 (Dentener and Crutzen, 1993). It is also involved in the stratospheric chemistry that leads to ozone destruction. As a consequence it is of the utmost importance to retrieve as precisely as possible its atmospheric concentrations in order to constraint efficiently the atmospheric models. HNO_3 is absorbing in various spectral domains in the mid-infrared and among them the 11.2 μm spectral region where absorb the ν_5 and the $2\nu_9$ cold bands as well as the $3\nu_9$-ν_9 and the $\nu_9 + \nu5 - \nu_9$ hot bands is widely used for atmospheric retrievals. However it is only recently that new high resolution infrared Fourier transform spectra were recorded (Chackerian et al., 2003; Flaud et al., 2003a; Toth et al., 2003) and that substantial progress (Perrin et al., 2004) has been made as far as theory is concerned allowing one to improve noticeably the spectral parameters of the various bands. In particular the modeling of the P- and R- branch of the cold bands has been greatly improved for the high values of the rotational quantum numbers (see Fig. 1). However it is worth stressing that one of the main problems lies in the determination of accurate "absolute" line intensities, a problem which is still controversial since several previous and ongoing efforts in various laboratories give results which do not agree.

The first experimental studies concerned measurements of the integrated band intensities at 11 μm using low resolution spectra (Goldman et al., 1971; Giver et al., 1984; Massie et al., 1985; Hjorth et al., 1987). They led to integrated strengths at 300 K varying from 483 to 630 cm^{-2} atm^{-1} (see Table 1) showing clearly the difficulty of such measurements.

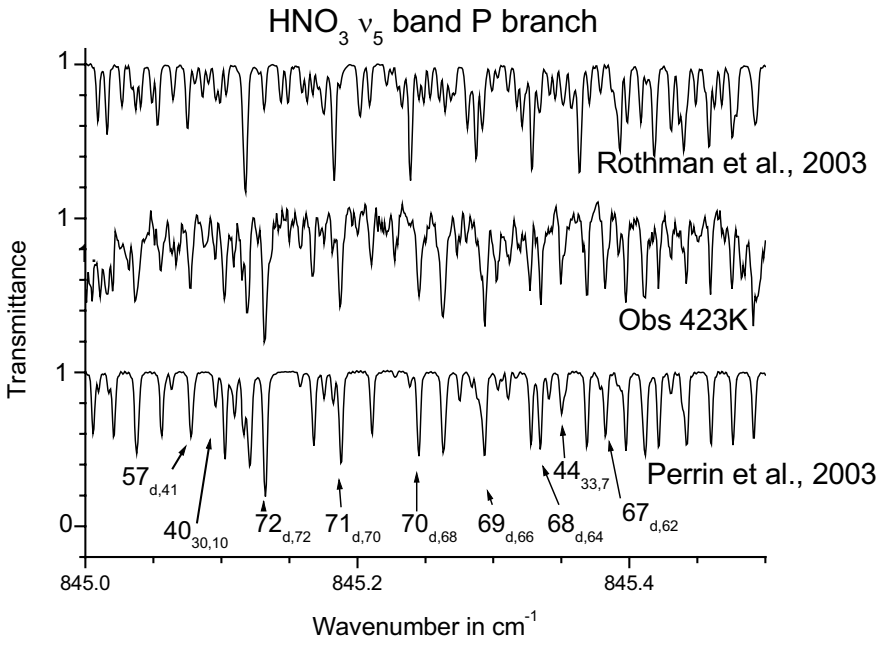

Figure 1. Part of the R branch of the $2\nu_9$ band at 925.6 cm^{-1} (Perrin et al., 2004). Upper trace: line by line calculation using the HITRAN2K line list (Rothman et al., 2003); medium trace: observed spectrum recorded at 423 K; lower trace: new line by line calculation (Perrin et al., 2004). It is obvious that the new calculation is in much better agreement with the observation. Some high $J_{K_a K_c}$ assignments in the upper state are given (d stands for degenerate transitions).

Table 1. Comparison of measured HNO_3 integrated band intensities in the 11.2 μm spectral region.

References	Integrated band intensity	
	cm^{-2} atm^{-1}	cm^{-1}/mol cm^{-2}
Goldman et al. (1971)	585	$2.48(37) \times 10^{-17}$
Giver et al. (1984)	637	$2.57(13) \times 10^{-17}$
Massie et al. (1978)	483	$1.95(30) \times 10^{-17}$
Hjorth et al. (1987)	541	$2.18(33) \times 10^{-17}$

Note: The band intensities are given in the two most commonly used units.

The situation was not better for individual line intensity measurements since the results obtained using a diode laser technique (Brockman et al., 1978) are on the average 20% lower than those using Fourier transform spectra (Perrin et al., 1993). Also there existed a discrepancy between the low and high resolution measurements. For example the band strength derived at 11 μm from Perrin et al (1993) is about 30% weaker than the value measured by Giver et al. (1984). All these discrepancies show the difficulty of the problem.

Very recently two new studies were devoted to the measurements of HNO_3 line intensities at 11 μm:

- An extensive set of HNO_3 individual line intensities were measured using Fourier transform spectra (Toth et al., 2003). The goal was one more time to measure accurate absolute intensities in the 11 μm region while adopting special experimental precautions to minimize and/or estimate correctly the HNO_3 decomposition. On the average these new line intensities lead to integrated band strength about 13% weaker than the value provided by Giver et al. (1984).
- Fourier transform absorbances were measured at PNNL (Chackerian et al., 2003) for different samples of nitrogen - nitric acid mixtures at a spectral resolution of 0.112 cm^{-1} and used to determine integrated cross sections in various spectral domains. For the 11 μm region, the integrated intensity is about 6% lower than the value reported by Giver et al. (1984) and about 7% higher than the intensities derived from the measurements of Toth et al. (2003).

Now, given all these various results one has to decide which sets of experimental intensity data should be used in the MIPAS database (Flaud et al., 2003b). Such a problem is not easy. In fact the choice was made performing an intercomparison of MIPAS atmospheric spectra (11.2 μm) and far infrared atmospheric spectra recorded by the IBEX (Infrared Balloon EXperiment) experiment. Indeed the HNO_3 line intensities in the far infrared can be calculated accurately since the permanent dipole moment is derived from Stark measurements which do not need to know the abundance of the species in the cell. This intercomparison (Mencaraglia et al, 2005) showed that the intensities from Toth et al. (2003) give the best agreement between the two sets of atmospheric measurements. As a consequence at 11.2 μm it is reasonable to retain Toth et al.'s intensities. Figure 2 shows the good agreement between the HNO_3 profiles retrieved using the new intensities at 11.2 μm and the far infrared spectral region.

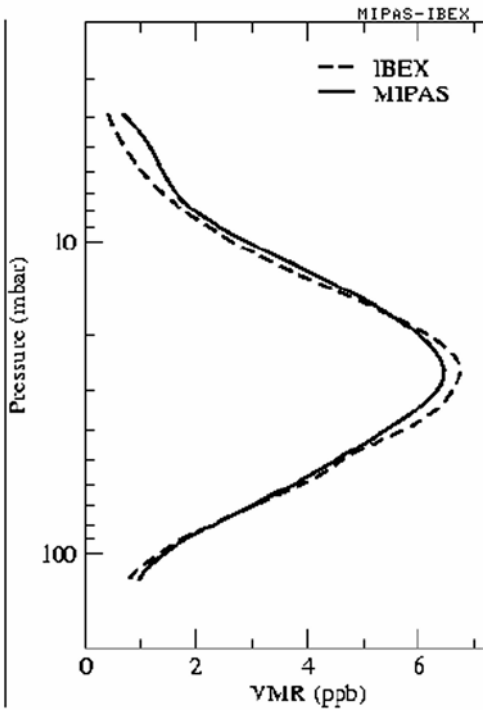

Figure 2. Comparison of MIPAS and IBEX HNO_3 profiles (Mencaraglia et al., 2005).

In conclusion of this section one can say that, even for a molecule such as HNO_3 which does not seem to pose *a priori* strong problems as far as the determination of its abundance in a cell is concerned, it is only after a number of studies and efforts that accurate line intensities have been determined. This is a crucial point for atmospheric retrievals since with the new intensities the atmospheric profiles are shifted by about 13%. Also it is worth noticing that in this case it has been extremely useful to compare spectra in two spectral regions (in one of them, the far infrared, it was not necessary to know the abundance of the species in the cell to get the line intensities) in order to assess the proper line intensities.

3. The formaldehyde (H_2CO) molecule

Formaldehyde which is a product of most of the atmospheric VOC (Volatil organic compounds) oxidation processes and which is involved in many photochemical processes, especially in the production of HO_x radicals in the troposphere (Carlier et al., 1986), is an atmospheric key species. To have a good understanding of the physical and chemical processes in which it is

involved, very accurate atmospheric concentration profiles are required. For this reason, many ground-based, air-borne, and balloon-borne or satellite measurements of formaldehyde are performed routinely using spectrometers working in the UV-visible and mid-infrared spectral ranges. Consequently, the knowledge of the formaldehyde absorption cross-sections and of their consistency is of the utmost importance. Hence a large number of experimental determinations of its UV and mid-infrared cross sections have been performed. However experimental studies which have ever verified the consistency between the cross-sections in the two spectral ranges are to our knowledge absent, preventing meaningful comparisons of formaldehyde concentration profiles obtained by spectrometric measurements in the mid-infrared and UV spectral regions. Therefore a study aiming at intercomparing infrared and UV absorption cross-sections for this molecule has been undertaken at LISA (Gratien et al., 2006).

3.1. EXPERIMENTAL DETAILS

In order to get rid of the overarching problem of measuring the abundance of the species in the cell experiments were performed by acquiring simultaneously UV and IR spectra at room temperature and atmospheric pressure using a common optical cell. This cell is made of a Pyrex reactor which contains two multiple reflection optical systems interfaced to a Fourier transform infrared (FTIR) spectrometer and to an UV-visible absorption spectrometer. Details concerning spectrometric devices are presented in Figure 3.

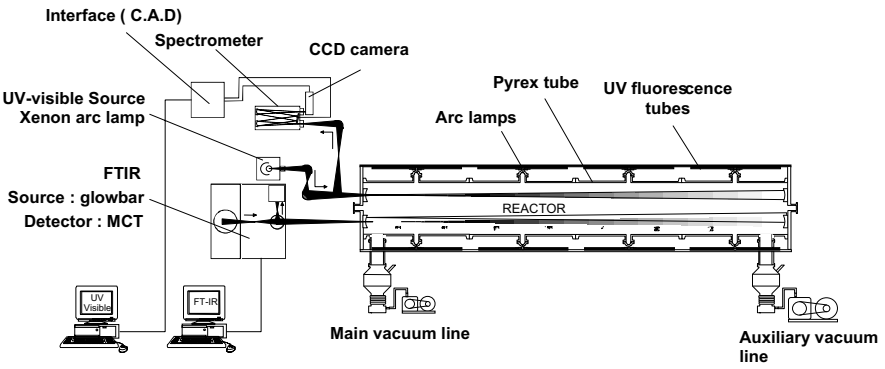

Figure 3. General setup of the reactor and spectrometers (Picquet-Varrault et al., 2005). Note that the infrared and UV path lengths can be set up independently allowing one to obtain the best recording conditions in both spectral domains.

Several spectra were recorded simultaneously in the mid IR and in the UV spectral regions. Figure 4 shows examples of such spectra acquired with UV and IR path lengths of 72 m and 12 m, respectively.

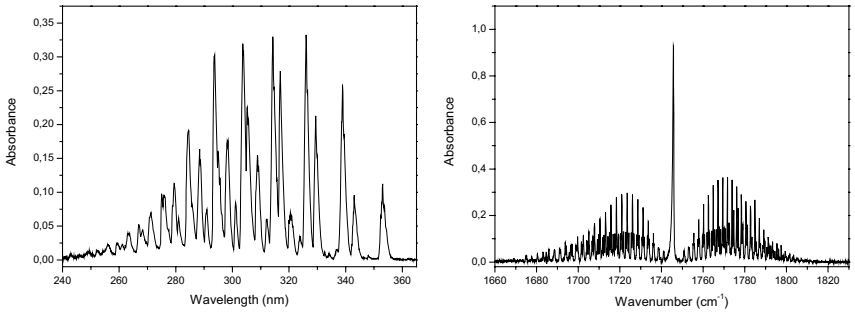

Figure 4. Example of UV and IR spectra of formaldehyde acquired simultaneously. Note the excellent signal to noise ratios obtained in both spectral domains.

3.2. RESULTS AND DISCUSSION

From these experiments, the IR quantities $(\int(A.d\sigma)/l)_{IR}$ where A is the absorbance and l is the optical path length were plotted versus the UV quantities $(\int(A.d\lambda/l)_{UV}$ leading to a straight line whose slope corresponds to the ratio of the integrated band intensities IBI_{IR}/IBI_{UV}. In the infrared and ultraviolet regions, the measured absorbances were integrated between 1660 and 1820 cm^{-1} and between 300 and 360 nm respectively. This ratio was then compared to the various ratios that can be obtained when using IR and UV integrated band intensities published in the literature (see Table 2).

Table 2. Comparison of measured H_2CO integrated band intensities in the IR (1660-1820 cm^{-1}) and in the UV (300- 360 nm) spectral regions.

FORMALDEHYDE

	LISA ratio	Hisatsune et al.	Nakanaga et al.	Sharpe et al.	Herndon et al.	Klotz et al.
		Meller et al.	Meller et al.	Meller et al.	Meller et al.	Meller et al.
IBI_{IR} / IBI_{UV} *	**11.04**	8.45	10.78	11.27	11.07	10.95
Deviation	**-**	**27%**	**2%**	**-2%**	**-0.3%**	**1%**

	LISA ratio	Hisatsune et al.	Nakanaga et al.	Sharpe et al.	Herndon et al.	Klotz et al.
		Rogers	Rogers	Rogers	Rogers	Rogers
IBI_{IR} / IBI_{UV} *	**11.04**	9.93	12.67	13.24	13.02	12.87
Deviation	**-**	**11%**	**-14%**	**-18%**	**-16%**	**-15%**

	LISA ratio	Hisatsune et al.	Nakanaga et al.	Sharpe et al.	Herndon et al.	Klotz et al.
		Cantrell et al.	Cantrell et al.	Cantrell et al.	Cantrell et al.	Cantrell et al.
IBI_{IR} / IBI_{UV} *	**11.04**	10.07	12.84	13.42	13.19	13.04
Deviation	**-**	**9%**	**-15%**	**-19%**	**-18%**	**-17%**

* : in $nm^{-1} \times cm^{-1}$

From the results presented in Table 2, one can observe that a good consistency (better than about 5%) exists between the UV data of Meller and Moortgat (2000) and four out of the five infrared data, i.e. Nakanaga et al. (1982); Sharpe et al. (2004); Herndon et al. (2005), and Klotz et al. (2004). The fifth one published by Hisatsune et al. (1955) is about 20% lower than the others leading to a disagreement of 27% with the UV absorption coefficients published by Meller and Moortgat (2000). On the other hand systematic differences of about 16% are observed between the LISA ratio and those obtained when using the UV data published by Rogers (1990) and Cantrell et al. (1990) and the four infrared data sets which are in good agreement. Hence, if one assumes that the infrared data which are in good agreement are correct, these results suggest that the cross-sections published by Rogers (1990) and Cantrell et al. (1990) could be overestimated by about 15%. This is a serious problem since the cross-sections measured by Cantrell et al. (1990) are included in the HITRAN database. As a consequence the formaldehyde concentrations retrieved from remote-sensing experiments using the HITRAN cross-sections would be underestimated by about 15%. Nevertheless, before making definite conclusions, we think that additional cross-sections determinations in both spectral ranges are needed.

4. The ozone (O_3) molecule

Ozone plays an important role as far as the chemistry and the radiative properties of the atmosphere are concerned. Consequently its atmospheric concentration has been and is the subject of a number of measurements. Among the various techniques used to measure atmospheric ozone, optical remote sensing techniques are widely used. They cover large parts of the electromagnetic range (MW, IR, UV) and this is why a number of studies have been devoted to the measurements of line intensities and/or absorption cross sections in these various spectral domains; for example for a list of references see (Flaud et al., 2003c; Orphal, 2003). As also for many other molecules the quantitative measurements were usually made only in a given spectral domain, and therefore there exist rather few intercomparisons of absorption cross sections. In the following we present a summary of the various recent measurements performed in the infrared followed by a discussion of problems arising from recent intercomparison experiments.

4.1. OZONE LINE INTENSITIES AT 10 MICRONS

In the infrared the 10 μm region is of particular interest since it corresponds to an atmospheric window and to the strongest infrared absorption of this

molecule. Accordingly a large number of atmospheric ozone measurements are performed in this spectral domain. This is why a number of laboratory line intensities measurements have been performed at 10 μm. When dealing with O_3 line intensity measurements, the main difficulty is to determine precisely the ozone concentration in the cell. To do so, two main methods are used: making direct pressure measurements or employing, as a reference standard, the UV absorption of O_3 at 254 nm. This determination of the amount of O_3 in the cell is critical to all measurements. The direct pressure measurements rely upon the purity and stability of the O_3 concentration while using the UV method may lead to some dissociation of ozone. A recent paper (Flaud et al., 2003c) has made an analysis and a synthesis of the various infrared measurements showing that three sets of independent measurements (De Backer Barilly and Barbe, 2001; Wagner et al., 2002; Claveau et al., 2001) are highly consistent (dispersion of ~0.8% and standard deviation of ~1.9%) whereas the fourth set of data (Smith et al, 2001) gives intensities which are 4.4% higher. The problem here is that, while the data of Smith et al. (2001) are in very good agreement with the HITRAN2K line intensities (Rothman et al., 2003) which were derived from the calculation of Flaud et al. (1990), there is a 4% discrepancy with the three other sets of infrared data and consequently with the new calculation of Flaud et al. (2003c).

4.2. INTERCOMPARISON OF OZONE LINE INTENSITIES IN THE 10 MICRONS INFRARED AND THE ULTRAVIOLET (300-350 AND 253.7 NM) SPECTRAL REGIONS

Two papers dealing with the intercomparison of ozone absorption at 10 μm and in the ultraviolet have been recently published. The first one (Dufour et al., 2004) has remeasured using a diode laser system a few ozone lines at 10 μm and, using the corresponding measured values, have determined the ozone absorption at 253.7 nm. The main findings of this paper are that (1) the newly measured infrared lines are in excellent agreement with the recent line intensity calculation (Flaud et al., 2003c) and (2) are highly consistent with the ozone UV absorption coefficient at 253.7 nm as measured by Hearn (1961). Such results suggest that the new calculation, based, as already said, on three independent infrared measurements, is valid and is consistent with the ozone absorption at 253.7nm. The second paper (Picquet-Varrault et al., 2005) has compared the ozone absorptions at 10 μm and in the Huggins bands between 300 and 350 nm. The results shows that there is a good agreement between the IR HITRAN2K data and the UV cross sections of various authors (Bass and Paur, 1985; Malicet et al., 1995;

Burrows et al., 1999, Bogumil et al., 2001) whereas there is a discrepancy of about 5% with the calculation of Flaud et al. (2003c).

4.3. DISCUSSION

If one tries to summarize the situation one can say:

- There exist three sets of infrared data in good agreement.
- These three sets are consistent with the ozone UV absorption cross sections at 253.7 nm.
- They are not consistent with a fourth set of infrared data and with the HITRAN2K line intensities.
- The fourth set of infrared data is in good agreement with the HITRAN2K line intensities and with ozone UV absorption cross sections in the Huggins bands (300-350 nm).

It is then clear that all these experiments do not provide consistent results and that more experimental work is needed. In fact this example shows that quantitative spectroscopy is difficult and that extreme care is needed when accuracies of the order of the percent are to be reached.

5. Conclusion

It was not the goal of this paper to give a complete overview of the infrared spectroscopy applied to atmospheric and or astrophysical measurements but rather to show on a few selected examples recent progress, both experimental and theoretical, achieved by modern molecular spectroscopy. For example it was shown on HNO_3 that new careful line intensity measurements combined with spectroscopic sophisticated theoretical models lead to a significant improvement in the quality of the line parameters. Also it was shown that it is necessary to use in the laboratory the best experimental techniques if one wants to get accurate measurements and even when doing so it appears that discrepancies of a few percents exist between different authors demonstrating that extreme care is required when dealing with high accuracy (~ one percent) quantitative spectroscopy.

References

Atkinson R., 2000, Atmospheric chemistry of VOCs and NO_x, Atmos. Environment **34**: 2063-2101.

Bass A. M., and Paur R. J., 1985, The ultraviolet cross-sections of ozone, I: The measurements; D. Reidel, Norwell, MA.

Bogumil K., Orphal J., Flaud J.-M., and Burrows J. P., 2001, Vibrational progressions in the visible and near-ultraviolet absorption spectrum of ozone, *Chem. Phys. Lett.* **349**: 241-248.

Brockman P., Bair C. H., and Allario F., 1978, High resolution spectral measurement of the HNO_3 11.3-micron band using tunable diode lasers, *Appl. Optics* **17**: 91-100.

Burrows J. P., Richter A., Dehn A., Deters B., Himmelmann S., Voigt S., and Orphal, J., 1999, Atmospheric remote-sensing reference data from GOME: 2. Temperature-dependent absorption cross sections of O_3 in the 231-794 nm range, *J. Quant. Spectrosc. Radiat. Transf.* **61:** 509-517.

Cantrell C. A., Davidson J. A., McDaniel A. H., Shetter R. E., and Calvert J. G., 1990, Temperature-dependent formaldehyde cross sections in the near-ultraviolet spectral region, *J. Phys. Chem.* **94:** 3902-3908.

Carlier P., Hannachi H., and Mouvier G., 1986, The chemistry of carbonyl compounds in the atmosphere – a review, *Atmos. Environ*. **20**: 2079-2099.

Chackerian C., Sharpe S. W., and Blake T. A., 2003, Anhydrous nitric acid absolute integrated absorption cross sections: 820 to 5300 cm^{-1}, *J. Quant. Spectrosc. Radiat. Transf.* **82**: 429-441.

Chance K. V., 2006, Spectroscopic measurements of stratospheric and tropospheric composition from satellite measurements in the ultraviolet and visible: Steps toward continuous pollution monitoring from space, *this issue.*

Claveau C., Camy-Peyret C., Valentin A. and Flaud J.-M., 2001, Absolute intensities of the ν_1 and ν_3 bands of $^{16}O_3$, *J. Mol. Spectrosc.* **206**: 115-125.

De Backer-Barilly M. R., and Barbe A., 2001, Absolute intensities of the 10 μm bands of $^{16}O_3$, *J. Mol. Spectrosc.* **205**: 43-531.

Dentener F., and Crutzen P. J., 1993, Reaction of N_2O_5 on tropospheric aerosols: impact on the global distribution of NO_x, O_3 and OH, *J. Geophys. Res*. *D* **98**: 7149-7163.

Dufour G., Valentin A., Henry A., Camy-Peyret C., and Hurtmans D., 2004, Concentration measurements of ozone in the 1200 to 300 ppbv range : an intercomparison between the BNM ultraviolet standard and infrared methods, *Spectrochim. Acta A* **60**: 3345-3352.

Fischer H., 2006, The MIPAS experiment aboard ENVISAT: Remote sensing of atmospheric composition, *this issue.*

Flaud J.-M., Camy-Peyret C., Rinsland C.P., Smith M. A. H., and Malathy Devi V., 1990, Atlas of ozone spectral parameters from microwave to medium infrared, Academic Press, Cambridge, Massachusetts.

Flaud J.-M., Perrin A., Orphal J., Kou Q., Flaud P.-M., Dutkiewicz Z., and Piccolo C., 2003a, New analysis of the $\nu_5+\nu_5-\nu_9$ hot band of HNO_3, *J. Quant. Spectrosc. Radiat. Transf.* **77**: 355-364.

Flaud J.-M., Piccolo C., Carli B., Perrin A., Coudert L. H., Teffo J.-L. and Brown L. R., 2003b, Molecular line parameters for the MIPAS (Michelson Interferometer for Passive Atmospheric Sounding) experiment, *J. Atm. Ocean Opt.* **16**: 172-182.

Flaud J. M., Wagner G., Birk M., Camy-Peyret C., Claveau C., De Backer-Barilly M. R., Barbe A., and Piccolo C., 2003c, Ozone absorption around 10 μm, *J. Geophys. Res. D* **108**: 4269, doi:10.1029/2002JD002755.

Giver L. P., Valero F. P. J., Goorvitch D., and Bonomo F. S., 1984, Nitric-acid band intensities and band-model parameters from 610 to 1760 cm^{-1}, *J. Opt. Soc. Am. B* **1**: 715-722.

Goldman A., Kyle T. G., and Bonomo F. S., 1971, Statistical band model parameters and integrated intensities for the 5.9-μ, 7.5-μ, and 11.3-μ bands of HNO_3 vapor, *Appl. Optics* **10**: 65-73.

Gratien A., Picquet-Varrault B., Orphal J., Doussin J.-F., and Flaud J-M., 2006, Laboratory intercomparison of the formaldehyde absorption coefficients in the infrared (1660-1820 cm^{-1}) and ultraviolet (300-360 nm) spectral regions, *J. Geophys. Res. D*, submitted.

Hearn A.G., 1961, The absorption of ozone in the ultraviolet and visible regions of the spectrum, *Proc. Phys. Soc. London* **78**: 932-940.

Herndon S. C., Nelson D. D, Li Y., and Zahniser M. S., 2005, Determination of line strengths for selected transitions in the ν_2 band relative to the ν_1 and ν_5 bands of H_2CO, *J. Quant. Spectrosc. Radiat. Transf.* **90**: 207-216.

Hisatsune I. C. and Eggers D. F., 1955, Infrared intensities and bond moments in formaldehyde, *J. Chem. Phys.* **23**: 487-492.

Hjorth J., Ottobrini G., Cappellani F., and Restelli G., 1987, A Fourier transform infrared study of the rate constant of the homogeneous gas-phase reaction N_2O_5+H_2O and determination of absolute infrared band intensities of N_2O_5 and HNO_3, *J. Phys. Chem.* **91**: 1565-1568.

Klotz B., Barnes I., and Imamura T., 2004, Product study of the gas-phase reactions of O_3, OH and NO_3 radicals with methyl vinyl ether, *Phys. Chem. Chem. Phys*. **6**: 1725-1734.

Massie S. T., Goldman A., Murcray D. G., and Gille, J. C., 1985, Approximate absorption cross sections of F12, F11, $ClONO_2$, N_2O_5, HNO_3, CCl_4, CF_4, F21, F113, F114, and HNO_4, *Appl. Opt.* **24**: 3426-3427.

Mencaraglia F., Bianchini G., Boscaleri A., Carli B., Ceccherini S., Perrin A., and Flaud J.-M., 2006, Comparison of rotational and vibrational spectroscopic data of HNO_3 for the validation of MIPAS satellite measurements, *J. Geophys. Res*. *D*, in press.

Malicet J., Daumont D., Chardonnier J., Parisse C., Chakir A., and Brion J., 1995, Ozone UV spectroscopy. II. Absorption cross-sections and temperature dependence, *J. Atmos. Chem.* **21**: 263-273.

Meller R. and Moortgat G. K., 2000, Temperature dependence of the absorption cross sections of formaldehyde between 223 and 323 K in the wavelength range 225-375 nm, *J. Geophys. Res*. *D* **105**: 7089-7101.

Nakanaga T., Kondo S. and Saëki S., 1982, Infrared band intensities of formaldehyde and formaldehyde-d2, *J. Chem. Phys*. **76**: 3860-3865.

Orphal J., 2003, A critical review of the absorption cross-sections of O_3 and NO_2 in the ultraviolet and visible, *J. Photochem. Photobiol. A* **157**: 185-209.

Perrin A., Flaud J.-M., Camy-Peyret C., Jaouen V., Farrenq R., Guelachvili G., Kou Q., Le-Roy F., Morillon-Chapey M., Orphal J., Badaoui M., Mandin J.-Y., and Dana V., 1993, *J. Mol. Spectrosc*. **160**: 524-532.

Perrin A., Orphal J., Flaud J.-M., Klee S., Mellau G., Mäder H., Walbrodt D. and Winnewisser M., 2004, New analysis of the ν_5 and $2\nu_9$ bands of HNO_3 by infrared and millimeter wave techniques: line positions and intensities, *J. Mol. Spectrosc.* **228**: 375-391.

Picquet-Varrault B., Orphal J., Doussin J.-F., Carlier P., and Flaud J.-M., 2005, Laboratory intercomparison of the ozone absorption coefficients in the mid-infrared (10 μm) and ultraviolet (300-350 nm) spectral regions, *J. Phys. Chem. A* **109**: 1008-1014.

Rogers J. D., 1990, Ultraviolet absorption cross sections and atmospheric photodissociation rate constants of formaldehyde, *J. Phys. Chem.* **94**: 4011-4015.

Rothman L. S., Barbe A., Chris Benner D., Brown L. R., Camy-Peyret C., Carleer M. R., Chance K., Clerbaux C., Dana V., Devy V. M, Fayt A., Flaud J.-M., Gamache R. R., Goldman A., Jacquemart D., Jucks K. W., Lafferty W. J., Mandin J.-Y., Massie S. T., Nemtchinov V., Newnham D. A., Perrin A., Rinsland C. P., Schroeder J., Smith K. M., Smith M. A. H., Tang K., Toth R. A., Vander Auwera J., Varanasi P., and Yoshino K., 2003, The HITRAN molecular spectroscopic

database: edition of 2000 including updates through 2001, *J. Quant. Spectrosc. Radiat. Transf.* **82**: 5-44.

Sharpe S. W., Johnson T. J., Sams R. L., Chu, P. M., Rhoderick G. C., and Johnson P. A., Gas-phase databases for quantitative infrared spectroscopy, *Appl. Spectrosc*. **58**:1452-1461, 2004.

Smith M. A. H., Malathy Devi V., Benner D. C., and Rinsland C. P., 2001, Absolute intensities of $^{16}O_3$ lines in the 9-11 μm region, *J. Geophys. Res. D* **106**: 9909-9921.

Toth R. A., Brown L. R., and Cohen E. A., 2003, Line strengths of nitric acid from 850 to 920 cm^{-1} , *J. Mol. Spectrosc*. **218**: 151-168.

Wagner G., Birk M., Schreier F., and Flaud J.-M., 2002, Spectroscopic database of ozone in the fundamental spectral region, *J. Geophys. Res. D* **107**: ACH10-1-10-18.

QUANTITATIVE LABORATORY SPECTROSCOPY OF ATMOSPHERIC TRACE GASES

JEAN VANDER AUWERA* (jauwera@ulb.ac.be)
Service de Chimie Quantique et Photophysique, Université Libre de Bruxelles, C.P. 160/09, 50 avenue F. D. Roosevelt, B-1050 Brussels, Belgium

Abstract. The analysis of spectra of the terrestrial atmosphere recorded using remote sensing techniques requires reference spectroscopic information, measured in the laboratory. This article describes laboratory measurements of reference absolute absorption intensities for atmospheric trace species using Fourier transform spectroscopy in the infrared spectral range. Emphasis is put on measurements of quantitative information for chemically unstable species.

Key words: Fourier transform spectroscopy, infrared, absolute intensities, minor atmospheric constituents, databases.

1. Introduction

Most of our knowledge and understanding about the physical and chemical properties of the terrestrial atmosphere and how they are affected by human activities comes from observations: they are the key information from which chemical and climate models are developed and to which predictions from these same models are compared. Among the techniques and methods used to carry out observations, Molecular Spectroscopy plays a key role as it is at the heart of optical remote sensing measurements. Indeed, retrieval of the concentrations of chemically and radiatively active molecular species from observed spectra of the atmosphere using available spectroscopic databases and atmospheric models has become fairly routine.

The quality of the reference information available, compiled in databases such as the ATMOS (Brown et al., 1996), GEISA (Jacquinet-Husson et al., 2005) and HITRAN (Rothman et al., 2005) databases, has obviously a strong impact on the accuracy of the retrieved atmospheric properties (Dudhia et al., 2002). In many cases, reference data are unfortunately inadequate, mostly because of problems encountered in the laboratory when trying to measure them. These deficiencies

* Senior research associate with the F.N.R.S. (Belgium)

A. Perrin et al. (eds.), Remote Sensing of the Atmosphere for Environmental Security, 123–137.

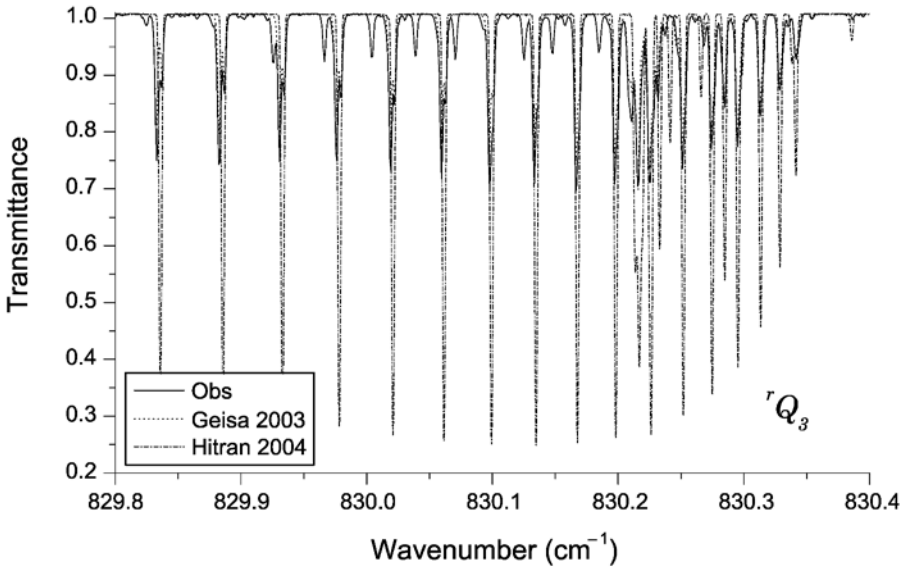

Figure 1. Comparison between the observed spectrum of the $^rQ_3$-branch of the ν_9 fundamental band of ethane recorded using Fourier transform spectroscopy and spectra calculated using line parameters available in GEISA (Jacquinet-Husson et al., 2005) and HITRAN (Rothman et al., 2005).

have a large variety of origins: difficulties of measurement, incorrect assessment of measurement errors (Sinnhuber et al., 1999), no measurements available, etc. As an example of problematic reference data, Fig. 1 compares the observed spectrum of the $^rQ_3$-branch of the ν_9 fundamental band of ethane recorded in our laboratory using Fourier transform spectroscopy and spectra calculated using line parameters available in GEISA (Jacquinet-Husson et al., 2005) and HITRAN (Rothman et al., 2005). If the data available in GEISA reproduce the observations reasonably well, those compiled in HITRAN do not.

The main objective of the work described in this contribution is to try to fill in those deficiencies for spectroscopic parameters related to the quantitative aspects: ***absolute intensities***. Our work relies mainly on means and methods developed in the *Service de Chimie Quantique et Photophysique* at the *Université Libre de Bruxelles*, allowing measurements of spectral intensities to be made using high resolution Fourier transform infrared spectroscopy. The various quantitative measurements performed up to now in Brussels and the related references are listed in Table I. Apart from HOCl, the species that we studied so far are chemically stable molecules. We determine their particle density in the cell from the measurement of the total pressure of a high-purity sample using appropriate gauges (see section 2). With HOCl, we started to measure quantitative information for chemically unstable species, for which such a method can not be used.

Table 1. Quantitative measurements performed by the author of this article (Except when indicated, the most abundant isotopologue is concerned).

Species	Range (cm^{-1})	References
Line intensities measurements		
C_2H_2	3199 – 3364	(Vander Auwera et al., 1993)
	1248 – 1415	(Vander Auwera, 2000a)
	6448 – 6685	(El Hachtouki and Vander Auwera, 2002)
	12582 – 12722	(Herregodts et al., 2003)
OCS	2500 – 3100	(Errera et al., 1995)
	827 – 2938	(Vander Auwera and Fayt, 2005)
$HO^{35}Cl$, $HO^{37}Cl$	1178 – 1320	(Vander Auwera et al., 2000)
N_2O	3800 – 5200	(Daumont et al., 2001)
$^{13}CO_2$	3096 – 3917	(Vander Auwera et al., 2005)
Absorption cross sections measurements		
N_2O_4	1180 – 1830	(Hurtmans et al., 1993)
HCFC-22 ($CH^{35}ClF_2$, $CH^{37}ClF_2$)	700 – 1500	(Ballard et al., 2000)
HFC-152a (HF_2CCH_3)	600 – 1700	(Vander Auwera, 2000b)
1,2-dichloroethane	600 – 1700	(Vander Auwera, 2000b)

After a description of our experimental means and procedures, we describe in some details ongoing measurements of absorption line intensities for the chemically unstable molecules HOBr (hypobromous acid) and HCOOH (formic acid).

2. Experimental details

A general view of the laboratory is presented in Fig. 2. It shows the Fourier transform spectrometer Bruker IFS120HR used for all the quantitative measurements listed in Table I (except for HOCl), a multiple reflections Pyrex gas cell and a gas handling system. The Fourier transform spectrometer is characterized by a maximum optical path difference (MOPD) programmable up to 450 cm (maximum resolution = 0.002 cm^{-1}). It was very recently upgraded to a Bruker IFS125HR, characterized by a MOPD programmable up to 714 cm, thus yielding a maximum resolution of 0.00126 cm^{-1}. The instrument has all the equipement required to operate from the far infrared (20 cm^{-1}) to the ultraviolet (45000 cm^{-1}), with a "hole" between about 300 and 600 cm^{-1}.

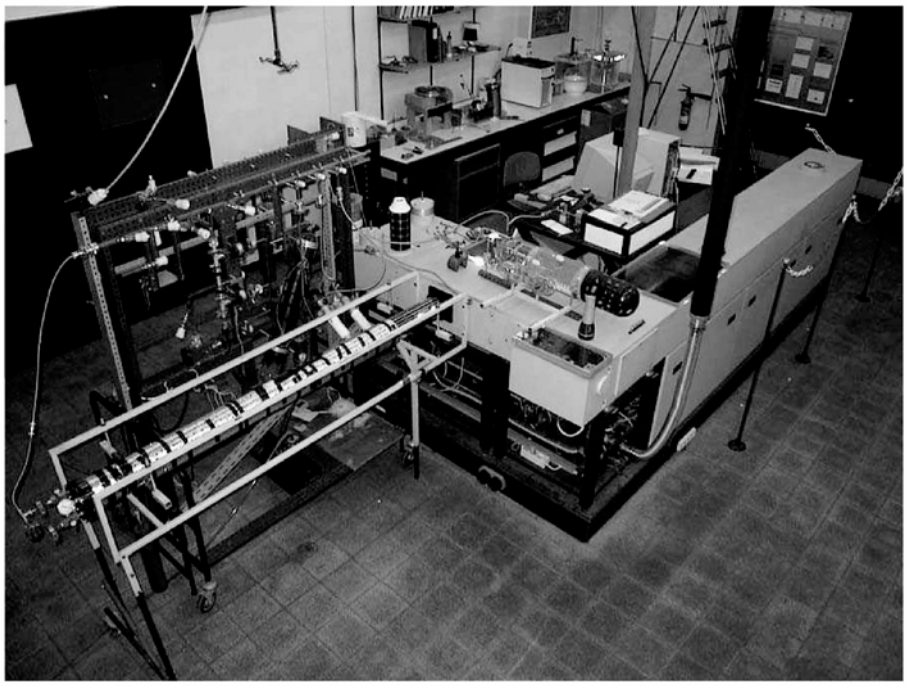

Figure 2. View of the laboratory showing the Fourier transform spectrometer Bruker IFS120HR used for all the quantitative measurements listed in Table I (except for HOCl), a multiple reflections Pyrex gas cell and a gas handling system.

We have two kind of gas cells available: two commercial multiple reflections non-thermostatic cells and we have built a number of single-pass thermostatic cells.

The two multiple reflections cells are of White-type. They consist in a Pyrex tube containing the mirrors separated by 15 and 172 cm respectively, thus providing base path length of 67 and 698 cm (including the distance between the field mirror and the windows). The largest path length that we have been able to achieve is 240 cm with the short cell and 55.1 m with the long one. The longest cell appears in Fig. 2. The temperature of the sample in these cells is as defined by an air-conditioning system regulating the temperature of the room, with an uncertainty of ±1 K. It is measured using a high-precision thermometer fixed on the outside wall of the cells.

We have built several single-pass cells, made of either anodized aluminium or stainless steel. Their length, *i.e.* the distance between the inner side of the windows, range from 1.2985(7) to 21.1(2) cm. It was measured using a calliper rule for cell lengths larger than about 2.5 cm and, for the shorter cells, *in situ* using

the interferometer to record the weak fringe signature in interferograms taken with the cell empty, resulting from these cells acting as (very poor) Fabry-Perot interferometers. The cells are designed to fit in the sample compartment of the spectrometer and built according to the same model. They consist in a 10-cm outside diameter cylinder closed by two KBr or CaF_2 windows (50 mm diameter and 5 mm thickness). They are double jacketed, allowing the heat-conveying liquid (water or methanol) to circulate in a closed loop involving an external thermostat (ThermoHaake model DC50-K20) or cryostat (NESLAB model ULT-80). The cell temperature can be stabilized at any temperature in the range from about 200 to 300 K and is measured using chromel-alumel thermocouples fixed on the outside cell wall. We estimate that the accuracy of measurement of the temperature is 0.35% at 300 K.

The sample pressure is measured using two model 690A MKS Baratron capacitance gauges of 10 and 100 Torr full-scale range. Their accuracy is estimated by the manufacturer to be better than 0.15% of reading from full scale down to 1% of full scale. To be on the safe side, we state our accuracy of measurement of the pressure as 3 times that figure, *i.e.* 0.5% of the measurement.

The gas handling system is made of pyrex and stainless steel tubing, with `Young` vacuum valves to seal it up. Vacuum is maintained to less than 10^{-4} mbar by an Edwards model EO 40/55 diffusion pump, backed by a two-stage rotary pump. Two glass vessels allow gases to be stored and eventually purified by vacuum distillation. Commercial lectures bottles can be connected to the system to allow transfer of the gases to be studied into the absorption cells.

3. Line intensities measurements

We measure the individual line intensities using an interactive computer program, written for the Microsoft Windows operating system. Briefly, this program determines absorption line parameters by adjustment of *one* synthetic spectrum to one observed spectrum, using a Levenberg-Marquardt least squares fitting procedure adapted from (Press et al., 1994) (function `MRQMIN` and dependencies). The synthetic spectrum is calculated as follows:

$$I(\tilde{\nu}) = \left[I_0(\tilde{\nu})\, exp \left\{ -P\ell \sum_k S_k\, g(\tilde{\nu} - \tilde{\nu}_k) \right\} \right] \otimes f_{ils}(\tilde{\nu}) \qquad (1)$$

In this expression, $I_0(\tilde{\nu})$ and $I(\tilde{\nu})$ are the irradiance before and after absorption by the gaseous sample respectively, $\tilde{\nu}$ is the wavenumber, P and ℓ are respectively the sample pressure and absorption path length, $\tilde{\nu}_k$ and S_k are the position and absolute intensity of the k^{th} line, and $f_{ils}(\tilde{\nu})$ is the instrument line shape function of the Fourier transform spectrometer used ($\otimes$ represents the convolution). The line profile $g(\tilde{\nu} - \tilde{\nu}_k)$ is either a Gauss, Lorentz or Voigt function. The wavenumber

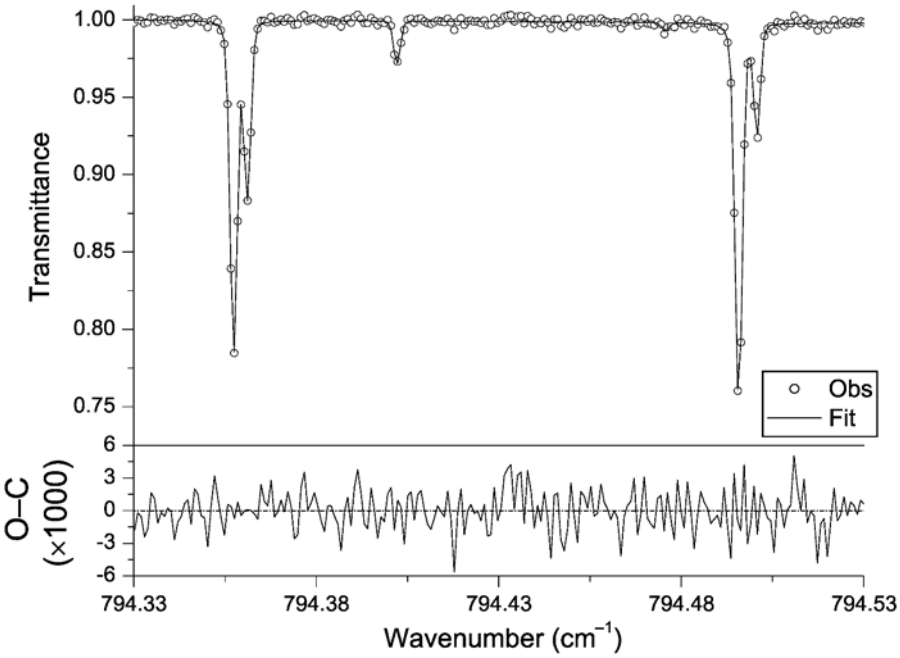

Figure 3. Least squares fit of the Fourier transform spectrum (242 K, 185.8 Pa, 19.7 cm) of both σ components of the ${}^{p}P_3(15)$ and ${}^{p}P_4(13)$ lines of the ν_9 band of $^{12}C_2H_6$ (Moazzen-Ahmadi et al., 2005). Upper panel: observed spectrum (open circles) and spectrum calculated at the end of the fit (solid curve); lower panel: corresponding residuals.

range on which $f_{ils}(\tilde{\nu})$ and $g(\tilde{\nu} - \tilde{\nu}_k)$ are generated are under user control. To avoid errors resulting from the minimal sampling of the spectrum, the synthetic spectrum is computed on an interpolated sampling comb. We usually use an interpolation factor between 4 and 16 as experimentation showed that these values are a good compromise between accuracy and speed of the calculation. In the least squares fitting procedure, adjustable parameters include

- *For each fitted line*: the position $\tilde{\nu}_k$, the absolute intensity S_k, the Gauss width (although it is usually fixed at the value calculated for the Doppler width), the pressure *self* and *buffer gas* broadening parameters.
- *For the instrument line shape* $f_{ils}(\tilde{\nu})$: the diameter of the entrance aperture of the interferometer and the residual phase error. Up to now, the latter parameter was always held fixed at zero.
- *For the background* $I_0(\tilde{\nu})$: the background is modeled by a second order polynomial expansion of the form $I_0(\tilde{\nu}) = a + b(\tilde{\nu} - \tilde{\nu}_c) + c(\tilde{\nu} - \tilde{\nu}_c)^2$, where $\tilde{\nu}_c$ is the wavenumber at the center of the spectral region, and a, b and c are adjustable parameters.

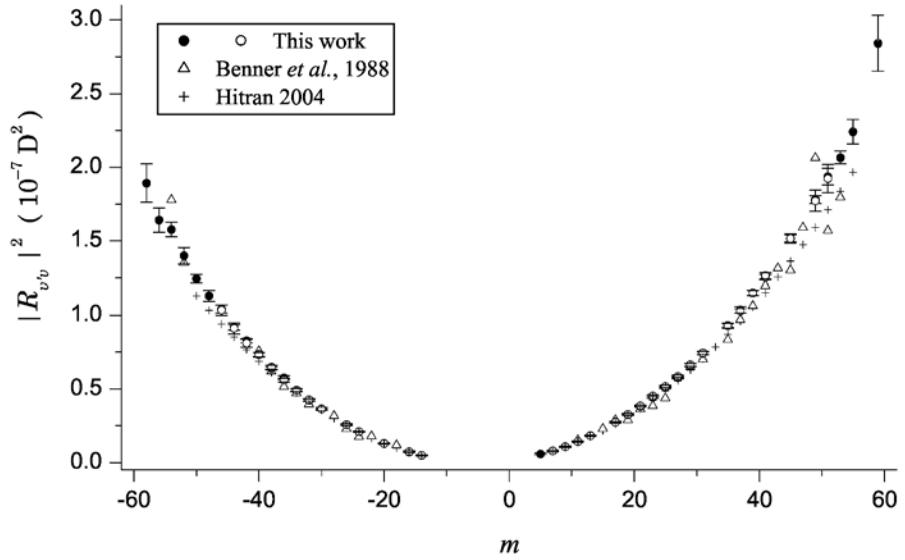

Figure 4. Comparison of the square of the vibrational transition dipole moment measured in Brussels (Vander Auwera et al., 2005) for the 21102 – 00001 band of $^{13}C^{16}O_2$ with those reported in (Benner et al., 1988) and in the latest version of the HITRAN database (Rothman et al., 2005) ($m = -J''$ and $J'' + 1$ for P- and R-branch lines respectively).

The user has full control on the value of all the parameters involved and on whether each of them is fitted or remains fixed at the value given. The initial values of the line parameters required by the fitting procedure are taken from a variety of sources, including the `HITRAN` database (Rothman et al., 2005). Any number of lines (limited by available memory) can be fitted simultaneously, although in practice, because of the limited spectral range considered at once (usually less than 1 cm^{-1}), each fit actually involves less than about 10 lines.

Figure 3 presents the results of the fit of the Fourier transform spectrum of the $^pP_3(15)$ and $^pP_4(13)$ lines of the ν_9 band of $^{12}C_2H_6$ (Moazzen-Ahmadi et al., 2005). The absolute intensities measured are characterized by a precision of about 0.5% or better in the best cases and we estimate that their accuracy is about 3%. Figure 4 compares the square of the vibrational transition dipole moment of the 21102 – 00001 band of $^{13}C^{16}O_2$ derived from line intensities measured in Brussels (Vander Auwera et al., 2005) with literature (Benner et al., 1988; Rothman et al., 2005).

4. Quantitative spectroscopy of chemically unstable species

Chemically unstable molecules usually exist only in equilibrium with other species and tend to degrade or react at the walls or windows of the cell leading to various products. The particle density of such species in the cell can then not be inferred from the measurement of the total sample pressure. Other methods must therefore be used to provide quantitative information.

In this section, we describe in some details ongoing measurements of infrared absorption line intensities for two chemically unstable molecules: HOBr (hypobromous acid) and HCOOH (formic acid). For the former, we proceed in exactly the same way as we did for HOCl (Vander Auwera et al., 2000), and we developed a new method for the latter.

4.1. THE ν_2 BAND OF HOBR

The aim of this work is to measure, for the first time, absolute line intensities in the ν_2 band of two isotopologues of hypobromous acid, namely $HO^{79}Br$ and $HO^{81}Br$, observed near 1162 cm^{-1} (see Figure 5). Indeed, because it lies in an atmospheric window, this band could be used to probe hypobromous acid in the atmosphere. This work is carried out in the frame of a collaboration with H. Bürger, G. Pawelke and J. Kleffmann at the *Bergische Universität Wuppertal* (Germany), and J.-M. Flaud at the *Université de Paris 7 et 12* (France).

Being a short-lived, very reactive molecule, HOBr exists only in the presence of its unavoidable decomposition products like Br_2 and H_2O. In order to overcome this problem, we measured at the same time four lines of the infrared ν_2 band and K clusters of the pure rotational spectrum observed in the far infrared (FIR). The concentration of HOBr is then determined from the measured intensities of *b*-type FIR lines, provided the ground state dipole moment μ_0 is exactly known. Accurate experimental values of the *a* and *b* components of μ_0 have very recently been determined using microwave Stark spectroscopy (Merke et al., 2005).

The spectra were recorded at the *Physikalische Chemie* (FB9) department of the *Bergische Universität Wuppertal*, using a cross-shaped glass cell. The longer arm of 262 cm length equipped with polyethylene windows served to measure the FIR pure rotational spectrum, using a Bruker IFS120HR Fourier transform spectrometer. The orthogonal shorter path had a length of 32.6 cm and was used to record near 1178 cm^{-1} simultaneously 4 lines in the infrared ν_2 band, employing a tunable diode laser (TDL) spectrometer. HOBr was prepared by passing in vacuo Br_2 over wet HgO.

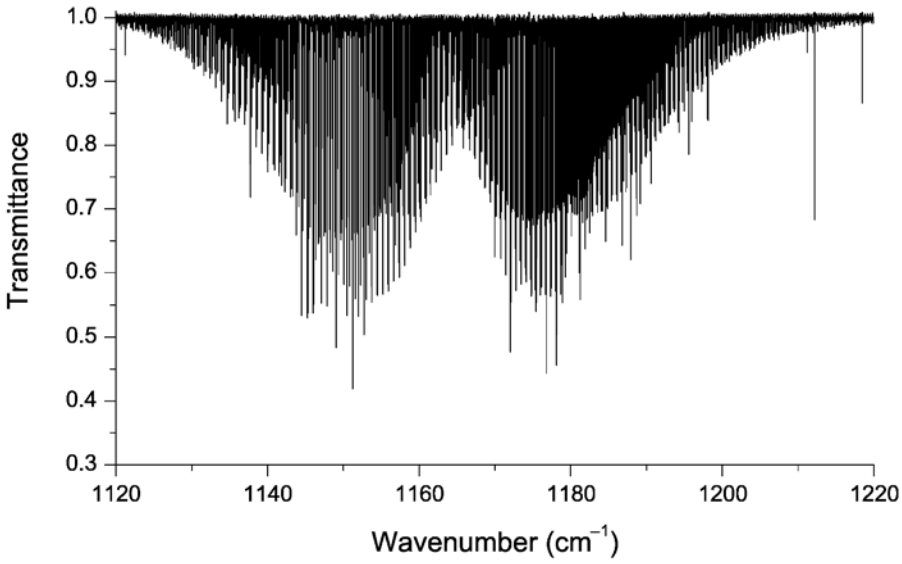

Figure 5. High-resolution absorption spectrum of the ν_2 band of $HO^{79}Br$ and $HO^{81}Br$ (298 K, 142 cm, 600 Pa of Br_2 + H_2O, resolution = 0.0038 cm^{-1}), recorded using a Bruker IFS120HR at the *Bergische Universität Wuppertal* (Germany).

After some conditioning of the cell, the decomposition of HOBr at or slightly below 298 K was such that the intensity of the four ν_2 band lines dropped by not more than 1% within ca. 10 min (see Fig. 6). Such an evolution could be measured because of the short acquisition time of spectra by the TDL spectrometer (about 1 min). The decay rate of HOBr was slow enough to collect as many scans as were needed to obtain source `OFF` and source `ON` far infrared spectra. A total of four experiments were conducted, each corresponding to a different total pressure of gas in the cell, ranging between 400 and 900 Pa. Each experiment resulted in one source `OFF` and one source `ON` Fourier transform far infrared spectra and about 40 infrared tunable diode laser spectra. In order to assess a possible Herman-Wallis dependence of the individual ν_2 line intensities, a high-resolution (0.0038 cm^{-1}) Fourier transform spectrum of the ν_2 band was also recorded. It is presented in Fig. 5.

The analysis of these experimental data is in progress. As shown in Fig. 6, the evolution with time of the amount of HOBr in the cell has been evaluated. Such a dependence is currently used to properly average the FIR spectra recorded and correct them for blackbody emission.

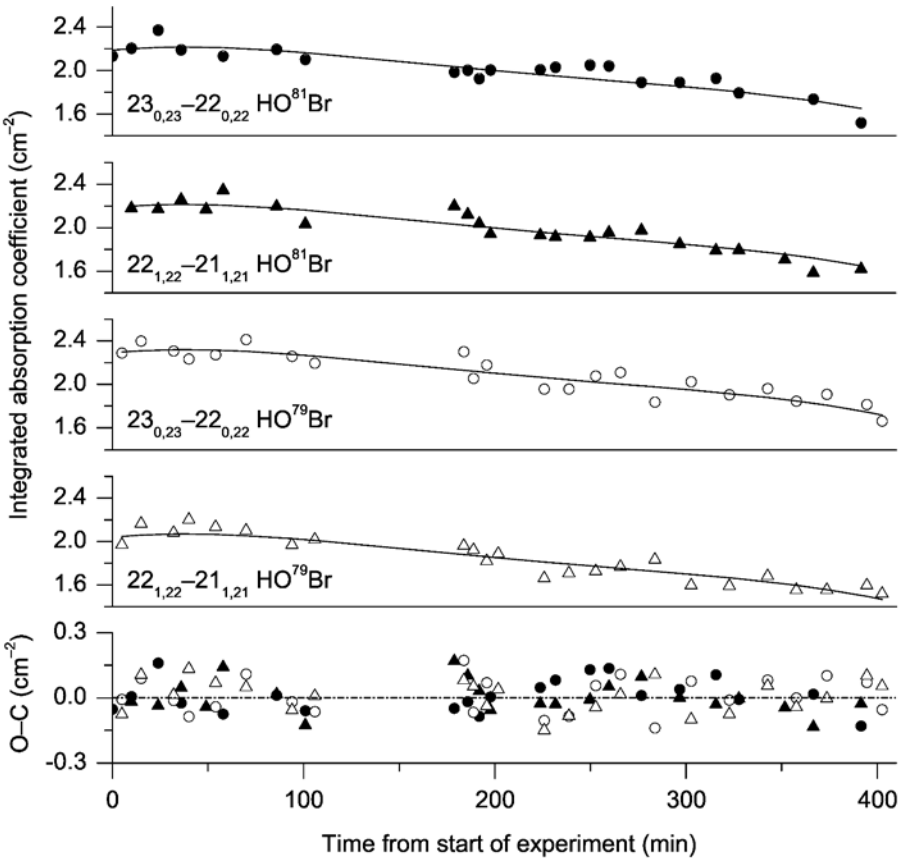

Figure 6. Evolution with time of the integrated absorption coefficient of the four vibration-rotation lines in the ν_2 band of two isotopologues of hypobromous acid, observed in one of the four experiments conducted using a tunable diode laser spectrometer.

4.2. ABSOLUTE LINE INTENSITIES IN THE ν_6 BAND OF HCOOH

The ν_6 band corresponds to the strongest infrared band of formic acid. It exhibits at 1105 cm^{-1} a sharp *Q*–branch structure, therefore located in an atmospheric window and commonly used for the detection of tropospheric formic acid by infrared technique (Perrin et al., 1999). Although formic acid presents two rotamers, *cis* and *trans*, this work deals only with the *trans* form, which is 800 times more abundant than the *cis* form at room temperature. With this work carried out in the frame of a collaboration with F. Keller and A. Perrin at the *Université de Paris 7 et 12* (France), we aim to provide absolute line intensities in the ν_6 band of *trans*-$H^{12}C^{16}O^{16}OH$.

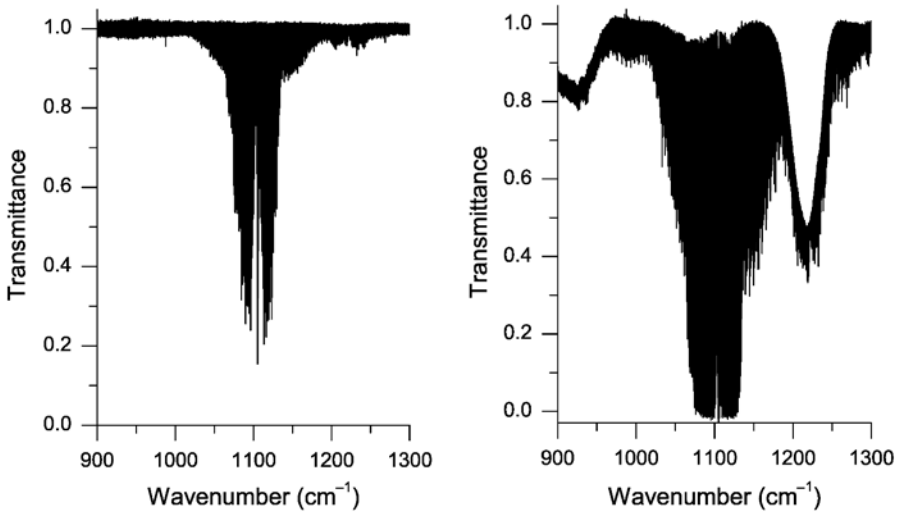

Figure 7. High-resolution Fourier transform spectrum of the ν_6 band of *trans*-formic acid (296 K, 19.7 cm), recorded at the lowest (11 Pa, left) and highest (310 Pa, right) pressures. The broad absorption features observed at higher pressure are due to the dimer $(HCOOH)_2$.

A total of 11 high-resolution (0.002 cm^{-1}) Fourier transform spectra of purified formic acid were recorded between 600 and 1900 cm^{-1} at pressures ranging from 11 to 310 Pa. Figure 7 presents the region around the ν_6 band recorded at the lowest and highest total pressures. The broad absorption features observed at high pressure and barely seen in the low-pressure spectrum are due to the dimer $(HCOOH)_2$ (Georges et al., 2004), identified as "FAD" here after. This latter species is indeed present because of the well-known equilibrium

$$(HCOOH)_2 \rightleftharpoons 2\ HCOOH \tag{2}$$

characterized by the constant $K_p = P_{\mathrm{FAM}}^2/P_{\mathrm{FAD}}$, where P_{FAM} is the partial pressure of the formic acid monomer HCOOH (or "FAM") and P_{FAD} is that of the dimer. As a result, it can be easily shown that the partial pressure of the monomer depends on the measured total sample pressure $P_{tot} = P_{\mathrm{FAM}} + P_{\mathrm{FAD}}$ in the following way:

$$P_{\mathrm{FAM}} = \frac{-K_p + \sqrt{K_p^2 + 4K_p P_{tot}}}{2} \tag{3}$$

The value of the equilibrium constant K_p has been measured several times (Chao and Zwolinski, 1978), but the uncertainty on these values seems to be rather large. To avoid relying on such values, we proceeded in the following way to obtain absolute line intensities for *trans*-HCOOH. We measured 439 integrated

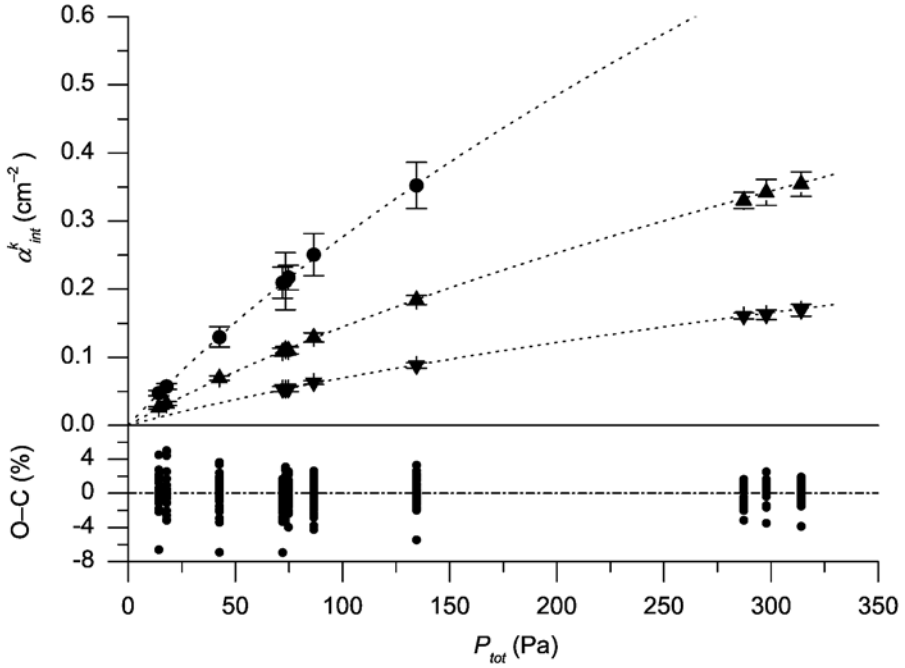

Figure 8. Integrated absorption coefficients of 3 lines of the ν_6 band of *trans*–HCOOH as a function of the total sample pressure (upper panel). The symbols represent the observed values for three lines and the error bars the precision of measurement (1σ). The dotted curves represent calculated values at the end of the least squares fit to Eq. 4. The residuals for all the lines at the end of the fit are plotted in the lower panel.

absorption coefficients of 73 lines of the ν_6 band of *trans*-HCOOH in the 11 absorption spectra recorded. As examples of the measurements, Fig. 8 shows values determined for a strong, medium and weak absorption line as a function of the total pressure. The 439 measured integrated absorption coefficients α^k_{int} were then fit simultaneously to the following equation:

$$\alpha^k_{int} = S_k \times P_{\mathrm{FAM}} = S_k \times \frac{-K_p + \sqrt{K_p^2 + 4K_p P_{tot}}}{2} \tag{4}$$

where S_k is the absolute intensity of the k^{th} line. Such a fit yielded the absolute intensity of the 73 lines of *trans*-HCOOH, together with the value of K_p.

From these measured absolute line intensities, a linelist was generated by A. Perrin. Figure 9 compares a part of the observed spectrum of the ν_6 band with spectra calculated using data taken from (Perrin et al., 1999) and (Rothman et al., 2003), and the new linelist.

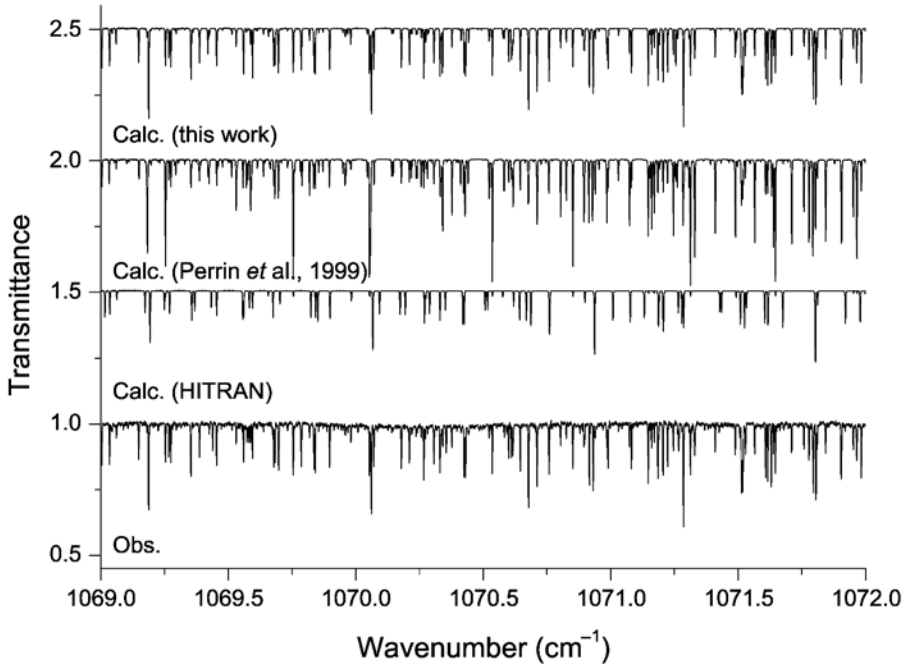

Figure 9. Comparison between a part of the absorption spectrum of the ν_6 band of *trans*-HCOOH and spectra calculated using line parameters obtained in the present work and from (Perrin et al., 1999) and the HITRAN database (Rothman et al., 2003).

5. Conclusion

This article described the means and methods we use to measure in the laboratory reference absolute absorption line intensities for atmospheric trace species using Fourier transform spectroscopy in the infrared spectral range. For chemically stable molecules such as N_2O, C_2H_2 and OCS, the concentration of which can be inferred from the measurement of the total pressure of gas in the cell, we estimate that our accuracy of measurement is around 3%. For chemically unstable molecules existing only in mixtures involving one or more partner(s), such method can not be used. To determine their concentration in the cell, we rely either on line intensities of pure rotation lines and knowledge of the permanent electric dipole moment of the molecules (HOCl and HOBr) or, for species involved in a binary equilibrium such as formic acid, on the dependence of the integrated absorption coefficients of the lines with the total pressure of the sample. In the case of HOCl, we estimated that the absolute line intensities obtained were accurate to 7 – 9%.

Acknowledgements

Financial support from the *Fonds National de la Recherche Scientifique* (FNRS, Belgium, contracts FRFC), the *Communauté française de Belgique* (*Action de Recherches Concertées*), the European Union (*Quantitative Spectroscopy for Atmospheric and Astrophysical Research*, QUASAAR, contract MRTN-CT-2004-512202) and NATO are acknowledged. Some of the work reported here was performed in the frame of the "LEA HiRes".

References

Ballard, J., Knight, R. J., Vander Auwera, J., Herman, M., Di Lonardo, G., Masciarelli, G., Nicolaisen, F. M., Beukes, J. A., Christensen, L. K., McPheat, R., Duxbury, G., Freckleton, R., and Shine, K. P. (2000), *J. Quant. Spectrosc. Radiat. Transfer* **66**, 109–128.

Benner, D. C., Devi, V. M., Rinsland, C. P., and Ferry-Leeper, P. S. (1988), *Appl. Opt.* **27**, 1588–1597.

Brown, L. R., Gunson, M. R., Toth, R. A., Irion, F. W., Rinsland, C. P., and Goldman, A. (1996), *Appl. Opt.* **35**, 2828–2848.

Chao, J. and Zwolinski, B. J. (1978), *J. Phys. Chem. Ref. Data* **7**, 363–377.

Daumont, L., Vander Auwera, J., Teffo, J.-L., Perevalov, V. I., and Tashkun, S. A. (2001), *J. Mol. Spectrosc.* **208**, 281–291.

Dudhia, A., Jay, V. L., and Rodgers, C. D. (2002), *Appl. Opt.* **41**, 3665–3673.

El Hachtouki, R. and Vander Auwera, J. (2002), *J. Mol. Spectrosc.* **216**, 355–362.

Errera, Q., Vander Auwera, J., Belafhal, A., and Fayt, A. (1995), *J. Mol. Spectrosc.* **173**, 347–369.

Georges, R., Freytes, M., Hurtmans, D., Kleiner, I., Vander Auwera, J., and Herman, M. (2004), *Chem. Phys.* **305**, 187–196.

Herregodts, F., Kerrinckx, E., Huet, T. R., and Vander Auwera, J. (2003), *Mol. Phys.* **101**, 3427–3438.

Hurtmans, D., Herman, M., and Vander Auwera, J. (1993), *J. Quant. Spectrosc. Radiat. Transfer* **50**, 595–602.

Jacquinet-Husson, N., Scott, N. A., Chédin, A., Garceran, K., Armante, R., Chursin, A. A., Barbe, A., Birk, M., Brown, L. R., Claveau, C., Clerbaux, C., Coheur, P.-F., Dana, V., Daumont, L., Debacker-Barilly, M.-R., Flaud, J.-M., Goldman, A. A., Hamdouni, A., Hess, M., Köpke, K., Mandin, J.-Y., Massie, S., Nemtchinov, V., Newham, D., Régalia-Jarlot, L., Rublev, A., Schreier, F., Schult, L., Smith, K. M., Tashkun, S. A., Teffo, J.-L., Toth, R. A., Tyuterev, V. G., Vander Auwera, J., Varanasi, P., and Wagner, G. (2005), *J. Quant. Spectrosc. Radiat. Transfer* **95**, 429–467.

Merke, I., Pawelke, G., and Giesen, T. (2005), private communication.

Moazzen-Ahmadi, N., Lepère, M., Blanquet, G., and Vander Auwera, J. (2005) Absolute line intensities in the ν_9 band of ethane: Measurements and theoretical treatment, In D. Bermejo, J. L. Doménech, and M. A. Moreno (eds.), *Proceedings of the 19th Colloquium on High Resolution Spectroscopy, Salamanca (Spain), 11-16 September 2005*, Sociedad Española de Óptica.

Perrin, A., Rinsland, C. P., and Goldman, A. (1999), *J. Geophys. Res.* **D104**, 18661–18666.

Press, W. H., Teukolsky, S. A., Vetterling, W. T., and Flannery, B. P. (1994) *Numerical Recipes in C*, Cambridge (USA), Cambridge University Press, second edition.

Rothman, L. S., Barbe, A., Benner, D. C., Brown, L. R., Camy-Peyret, C., Carleer, M., Chance, K. V., Clerbaux, C., Dana, V., Devi, V. M., Fayt, A., Flaud, J.-M., Gamache, R. R., Goldman,

A., Jacquemart, D., Jucks, K. W., Lafferty, W. J., Mandin, J.-Y., Massie, S. T., Nemtchinov, V., Newnham, D., Perrin, A., Rinsland, C. P., Schroeder, J., Smith, K. M., Smith, M. A. H., Tang, K., Toth, R., Vander Auwera, J., Varanasi, P., and Yoshino, K. (2003), *J. Quant. Spectrosc. Radiat. Transfer* **82**, 5–44.

Rothman, L. S., Jacquemart, D., Barbe, A., Benner, D. C., Birk, M., Brown, L. R., Carleer, M., Chackerian Jr., C., Chance, K. V., Dana, V., Devi, V. M., Flaud, J.-M., Gamache, R. R., Goldman, A., Hartmann, J.-M., Jucks, K. W., Maki, A. G., Mandin, J.-Y., Massie, S., Orphal, J., Perrin, A., Rinsland, C. P., Smith, M. A. H., Tennyson, J., Tolchenov, R. N., Toth, R., Vander Auwera, J., Varanasi, P., and Wagner, G. (2005), *J. Quant. Spectrosc. Radiat. Transfer* **96**, 139–204.

Sinnhuber, B.-M., Müller, R., Langer, J., Bovensmann, H., Eyring, V., Klein, U., Trentmann, J., Burrows, J. P., and Künzi, K. F. (1999), *J. Atmos. Chem.* **34**, 281–290.

Vander Auwera, J. (2000)a, *J. Mol. Spectrosc.* **201**, 143–150.

Vander Auwera, J. (2000)b, *J. Quant. Spectrosc. Radiat. Transfer* **66**, 143–151.

Vander Auwera, J., Claveau, C., Teffo, J.-L., Tashkun, S. A., and Perevalov, V. (2005), *J. Mol. Spectrosc.*, in press.

Vander Auwera, J. and Fayt, A. (2005), *J. Mol. Struct.*, in press.

Vander Auwera, J., Hurtmans, D., Carleer, M., and Herman, M. (1993), *J. Mol. Spectrosc.* **157**, 337–357.

Vander Auwera, J., Kleffmann, J., Flaud, J.-M., Pawelke, G., Bürger, H., Hurtmans, D., and Pétrisse, R. (2000), *J. Mol. Spectrosc.* **204**, 36–47.

GLOBAL MODELING OF HIGH-RESOLUTION SPECTRA OF LINEAR MOLECULES CO_2, N_2O AND C_2H_2

V.I. PEREVALOV*, S.A. TASHKUN, O.M. LYULIN
Laboratory of Theoretical Spectroscopy, Institute of Atmospheric Optics SB RAS, Akademicheskii 1, 634055 Tomsk, Russian Federation

J.-L. TEFFO
Laboratoire de Physique Moléculaire pour l'Atmosphère et l'Astrophysique, Place Jussieu 4, 75252 Paris Cedex 05, France

Abstract. The global modeling of high-resolution spectra of linear molecules which our group performs is aimed to generate high-resolution spectroscopic databanks for the atmospheric and high-temperature applications. The method of effective operators which is used for the modeling is briefly discussed. The main goal of our modeling is to attain the near experimental accuracy of the line position and line intensity calculations in a wide spectral range from microwave to visible. The recent results achieved in the modeling of high-resolution spectra of CO_2, N_2O, and C_2H_2 molecules are presented.

Keywords: high-resolution spectra; linear molecules; global modeling; databases; carbon dioxide; nitrous oxide; acetylene

*To whom correspondence should be addressed. V.I. Perevalov, Institute of Atmospheric Optics SB RAS, Akademicheskii 1, 634055 Tomsk, Russia; e-mail: vip@lts.iao.ru

A. Perrin et al. (eds.), Remote Sensing of the Atmosphere for Environmental Security, 139–159.

1. Introduction

The nowadays accuracy achieved in the global modeling of high-resolution spectra of linear molecules is acceptable for the majority of the applications. Owing to this fact we use the global modeling as a tool to generate spectroscopic databanks for linear molecules for the purposes of atmospheric and high-temperature applications.

There are two methods of global modeling of high-resolution spectra of a molecule: variational method and method of effective operators. The variational method is based on the potential energy surface which determines the energy spectrum of a molecule and on the dipole moment surface which determines the transition moments in absorption and in emission. These surfaces are modeled with the help of the analytical functions the parameters of which are fitted to the observed line positions and to the observed line intensities. Sometimes the *ab initio* calculations are also involved to determine the initial values of these parameters. Within the framework of the variational method the solution of the stationary Schrödinger's equation consists in diagonalizing the matrix of the vibration-rotation Hamiltonian in a given infinite basis of the Hilbert space. The method of effective operators is based on the perturbation theory which is formulated in such a way as to simplify the matrix of the transformed vibration-rotation Hamiltonian in the basis of zero-order approximation and thus to reduce considerably the volume of the calculations.

It is necessary to emphasize two advantages of the method of effective operators in the case of linear molecules. Firstly, the method of effective operators allows one to perform global modeling of high-resolution spectra of linear molecules with an accuracy approaching the uncertainties of the modern experiment. Secondly, from the computational point of view it does not need powerful computers. Because of these two advantages we have chosen the method of effective operators for global modeling of high-resolution spectra of linear molecules.

2. Method of effective operators

The vibration-rotation states of linear semi-rigid molecules are described by the vibration-rotation Hamiltonian of Wilson-Howard-Watson[1-3]. Within the framework of the method of effective operators, the vibration-rotation Hamiltonian H_{VR} is transformed with the help of the unitary transformations to the effective one

$$H^{eff} = \exp(iS) H_{VR} \exp(-iS), \tag{1}$$

the matrix of which in the basis of harmonic oscillators and rigid rotor eigenfunctions, as a rule, has block-diagonal form. As a consequence to find eigenvalues and eigenvectors of this matrix one can diagonalize each block separately thereby decreasing considerably the time of the calculations.

The effective Hamiltonian globally describing vibration-rotation states of triatomic linear molecules was discussed by many authors[4-12]. Amat and Nielsen[4], and Amat-Nielsen-Tarrago[5] have derived the effective Hamiltonian up to fourth order of perturbation theory in the case of the absence of the accidental resonances. Pliva[6] has developed this Hamiltonian introducing the resonance interaction terms for N_2O molecule. Then Chedin[7], Chedin and Teffo[8], Fayt et al[9] have suggested effective Hamiltonians for different linear triatomic molecules in which higher-order terms and resonance interaction terms of different kinds have been taken into account. Later Teffo et al[10,11] have considered the procedure of the reduction of the effective Hamiltonians for CO_2 and N_2O molecules.

As for the effective Hamiltonian for the tetratomic molecules globally describing vibration-rotation states, it has been suggested for the first time by Pliva[12] for the calculation of the high-resolution spectra of the C_2H_2 molecule. Then this Hamiltonian has been developed by Hietanen[13], Herman et al[14-16] and Perevalov et al[17,18]. In the above cited papers the higher-order terms have been taken into account and new resonance interaction terms of different kinds have been included. Perevalov et al[17,18] have also considered the reduction procedure of this Hamiltonian. It is necessary also to mention the paper of Yamada et al[19] in which the effective Hamiltonian for the simultaneous description of the vibration-rotation states having the same principal quantum numbers has been suggested.

The absorption line strength $S_{b\leftarrow a}(T)$ on the vibration-rotation transition $b \leftarrow a$ in unities cm^{-1}/molecule cm^{-2} at temperature T K is given by well known equation

$$S_{b\leftarrow a}(T) = \frac{8\pi^3}{3hc} C g_a \nu_{b\leftarrow a} \frac{\exp(-hcE_a / kT)}{Q(T)} \left[1 - \exp(-hc\nu_{b\leftarrow a} / kT)\right] W_{b\leftarrow a}. \quad (2)$$

Here c is the speed of the light, h is the Planck's constant, k is the Boltzmann's constants, C is the isotopic abundance, $Q(T)$ is the total internal partition function, E_a and g_a are the energy and degeneracy of the lower level, and $W_{b\leftarrow a}$ is the transition moment squared. Within the framework of the effective operator approach the transition moment squared can be calculated using the following equation

$$W_{b\leftarrow a} = 3\sum_{M\ M'} \left| \left\langle \psi^{eff}_{bM'} \left| \mu^{eff}_{Z} \right| \psi^{eff}_{aM} \right\rangle \right|^2 . \tag{3}$$

M and *M'* are the magnetic quantum numbers of the lower and upper states, $\left|\psi^{eff}_{aM}\right\rangle$ and $\left|\psi^{eff}_{bM'}\right\rangle$ are the eigenfunctions of the effective Hamiltonian (Eq. (1)), and μ^{eff}_{Z} is the effective dipole moment operator which is obtained from the dipole moment operator μ_Z with the help of the same unitary transformations as effective Hamiltonian from vibration-rotation Hamiltonian

$$\mu^{eff}_{Z} = \exp(iS)\,\mu_Z \exp(-iS) . \tag{4}$$

The method of the line intensity calculations within the framework of the effective operator approach in the case of linear molecules has been developed by Perevalov et al[20-24]. In the case of the polyad model of the effective Hamiltonian all effective dipole moment parameters can be divided into subsets each of which is responsible for the line intensities of a defined series of the transitions. In Fig. 1 we present schematically the matrix of effective Hamiltonian for the CO_2 molecule and the series of transitions.

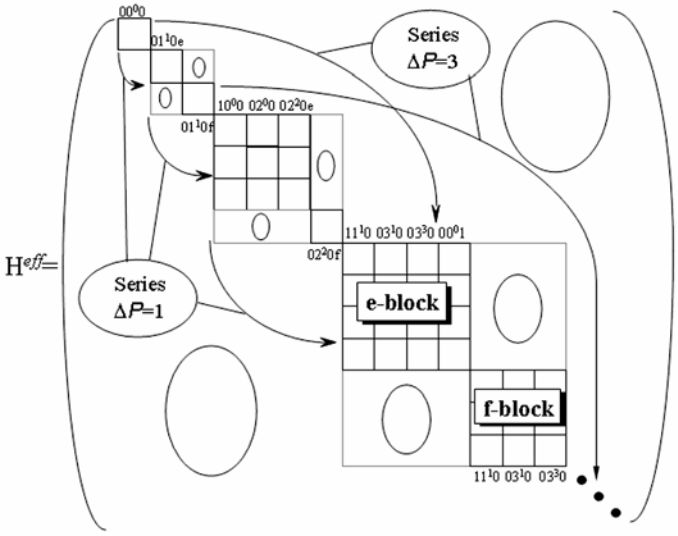

Figure 1. Effective Hamiltonian matrix and series of transitions for CO_2 molecules.

Unitary transformations (Eq. 1) are performed within the framework of the operator formulations of the perturbation theory. One of these formulations is the method of contact transformations[25,26]. In the result of these transformations an effective Hamiltonian and effective dipole moment operator are represented as the power series of the elementary vibration and rotation operators. Since the modeling of the high-resolution molecular spectra is a semi-empirical problem then it is not necessary to perform the perturbation calculations in the explicit form. It is enough to write down the symmetry allowed combinations of the powers of the elementary vibration and rotation operators and to introduce the empirical parameters for these combinations. Namely this approach is used in our case.

2.1. EFFECTIVE HAMILTONIAN

An effective Hamiltonian globally describing the vibration-rotation states of a triatomic linear molecule in the ground electronic state can be presented by its matrix elements in the basis of the eigenfunctions of harmonic oscillators $\left|V_1\ V_2\ \ell_2\ V_3\right\rangle$ and rigid rotor $\left|J\ M\ \ K=\ell_2\right\rangle$ operators. Here V_i (i=1, 2, 3) are the principal vibrational quantum numbers, ℓ_2 is the vibrational angular momentum quantum number, J and K are the quantum numbers of the total angular momentum and its projection on the molecular-fixed axis z. Below as an example we present the matrix elements of the effective Hamiltonian for the CO_2 molecule[10,27,28]. Only one matrix element for each type of operators is presented.

Diagonal matrix element

$$\left\langle V_1 V_2^{\ell_2} V_3 J\right| H^{eff} \left|V_1 V_2^{\ell_2} V_3 J\right\rangle = \sum_i \omega_i V_i + \sum_{ij} X_{ij} V_i V_j + X_{\ell\ell}\ell_2^2 + \sum_{ijl} Y_{ijl} V_i V_j V_l$$
$$+\sum_i Y_{i\ell\ell} V_i \ell_2^2 + \sum_{ijlk} Z_{ijlk} V_i V_j V_l V_k + \sum_{ij} Z_{ij\ell\ell} V_i V_j \ell_2^2 + Z_{\ell\ell\ell\ell}\ell_2^2$$
$$+(B_e - \sum_i \alpha_i V_i + \sum_{ij} \gamma_{ij} V_i V_j + \gamma_{\ell\ell}\ell_2^2 + \sum_{ijl} \varepsilon_{ijl} V_i V_j V_l + \sum_i \varepsilon_{i\ell\ell} V_i \ell_2^2)[J(J+1) - \ell_2^2]$$
$$-(D_e + \sum_i \beta_i V_i)[J(J+1) - \ell_2^2]^2 + H_e[J(J+1) - \ell_2^2]^3 \qquad (5)$$

ℓ-doubling matrix element

$$\left\langle V_1 V_2^{\ell_2} V_3 J \left| H^{eff} \right| V_1 V_2^{\ell_2 \pm 2} V_3 J \right\rangle = \{L_e + \sum_i L_i V_i + \sum_{ij} L_{ij} V_i V_j + L_J [J(J+1) - (\ell_2 \pm 1)^2]\}$$

$$\times \sqrt{(V_2 \mp \ell_2)(V_2 \pm \ell_2 + 2)[J(J+1) - \ell_2(\ell_2 \pm 1)][J(J+1) - (\ell_2 \pm 1)(\ell_2 \pm 2)]} \quad (6)$$

Matrix element of resonance Fermi interaction

$$\left\langle V_1 V_2^{\ell_2} V_3 J \left| H^{eff} \right| V_1 - 1 (V_2 + 2)^{\ell_2} V_3 J \right\rangle = \{F_e + \sum_i F_i V_i + \sum_{ij} F_{ij} V_i V_j + F_{\ell\ell} \ell_2^2 + F_J [J(J+1) - \ell_2^2]\}$$

$$\times \sqrt{V_1 (V_2 + \ell_2 + 2)(V_2 - \ell_2 + 2)}, \quad (7)$$

Matrix element of Fermi+ ℓ-type resonance interaction

$$\left\langle V_1 V_2^{\ell_2} V_3 J \left| H^{eff} \right| V_1 - 1 (V_2 + 2)^{\ell_2 \pm 2} \; V_3 J \right\rangle = \{F_e^L + \sum_i F_i^L V_i + F_J^L [J(J+1) - (\ell_2 \pm 1)^2]\}$$

$$\times \sqrt{V_1 (V_2 \pm \ell_2 + 2)(V_2 \pm \ell_2 + 4)[J(J+1) - \ell_2(\ell_2 \pm 1)][J(J+1) - (\ell_2 \pm 1)(\ell_2 \pm 2)]}. \quad (8)$$

Matrix elements of resonance Coriolis interaction

$$\left\langle V_1 V_2^{\ell_2} V_3 J \left| H^{eff} \right| V_1 - 1 (V_2 - 1)^{\ell_2 \pm 1} V_3 + 1 J \right\rangle = \{C_e + \sum_i C_i V_i + \sum_{ij} C_{ij} V_i V_j +$$

$$+ C_J [J(J+1) - \ell_2 (\ell_2 \pm 1)]^2 \} \sqrt{V_1 (V_2 \mp \ell_2)(V_3 + 1)[J(J+1) - \ell_2(\ell_2 \pm 1)]}, \quad (9)$$

The matrix elements (Eqs. (5)-(9)) are written up to the sixth order of the perturbation theory. A part of the terms is absent in these matrix elements because of the partial reduction performed according to the scheme suggested in our paper[10]. Another part is absent because they were found insignificant when fitting the parameters of the matrix elements to the observed line positions.

2.2. TRANSITION MOMENT SQUARED

The eigenfunctions of the effective Hamiltonian can be written in the Wang basis

$$\left| V_1 V_2 \left| \ell_2 \right| V_3 J M \varepsilon \right\rangle = \frac{1}{\sqrt{2}} \left(\left| V_1 V_2 \ell_2 V_3 \right\rangle \left| JMK = \ell_2 \right\rangle + \varepsilon \left| V_1 V_2 - \ell_2 V_3 \right\rangle \left| JM - K = -\ell_2 \right\rangle \right),$$

$$\left| V_1 V_2 0 V_3 J M \varepsilon = 1 \right\rangle = \left| V_1 V_2 0 V_3 \right\rangle \left| JM0 \right\rangle \quad (10)$$

in the following way

$$\psi^{eff}_{NJM\varepsilon} = \sum_{V_1V_2\ell_2V_3} {}^{J}C^{V_1V_2\ell_2V_3}_{N\varepsilon} \left|V_1V_2\right|\ell_2\left|V_3JM\varepsilon\right\rangle. \tag{11}$$

In Eq. (11) N is a vibrational state label and $\varepsilon = \pm 1$ is the parity of the state. After the substitution in Eq. (4) $\psi^{eff}_{NJM\varepsilon}$ by Eq. (11) and the evaluation of the matrix elements of the effective dipole moment operator one has the following equation for the transition moment squared in the case of linear triatomic molecules[20-22]

$$W_{N'J'\varepsilon'\leftarrow NJ\varepsilon} = (2J+1)\left(\sum_{V_1V_2\ell_2V_3} \sum_{\substack{\Delta V_1+\Delta V_2+\Delta V_3=\Delta P \\ \Delta\ell_2=0,\ \pm1,\ldots}} {}^{J}C^{V_1\ V_2\ \ell_2\ V_3}_{N\varepsilon}\ {}^{J'}C^{V_1+\Delta V_1\ V_2+\Delta V_2\ \ell_2+\Delta\ell_2\ V_3+\Delta V_3}_{N'\varepsilon'}\ M^{|\Delta\ell_2|}_{\Delta V} \right.$$

$$\times\sqrt{f^{\Delta\ell_2}_{\Delta V}(V,\ell_2)\left(1+\delta_{\ell_2,0}+\delta_{\ell'_2,0}-2\delta_{\ell_2,0}\delta_{\ell'_2,0}\right)}\ \left(1\ \Delta\ell_2\ J\ \ell_2\middle|J'\ \ell_2+\Delta\ell_2\right)$$

$$\left.\times\left(1+\sum_i \kappa^{\Delta V}_i V_i + F^{\Delta\ell_2}_{\Delta V}(\ell_2,J)\right)\right)^2. \tag{12}$$

Here $\left(1\ \Delta\ell_2\ J\ \ell_2\middle|J'\ \ell_2+\Delta\ell_2\right)$ is the Clebsh-Gordan coefficient, $f^{\Delta\ell_2}_{\Delta V}(V,\ell_2)$ are known vibrational functions which can be found in our publications[23,24]. P is the polyad number which will be introduced below for each molecule. The Herman-Wallis-type functions $F^{\Delta\ell_2}_{\Delta V}(\ell_2,J)$ in Eq. (12) can be written as[20-22]

$$F^{\Delta\ell_2}_{\Delta V}(J,\ell_2) = b^{\Delta V}_J m + d^{\Delta V}_J\left(J(J+1)+m-\ell_2^2\right) \tag{13}$$

for $\Delta\ell_2$=0 matrix elements,

$$F^{\Delta\ell_2}_{\Delta V}(J,\ell_2) = -\tfrac{1}{2}b^{\Delta V}_J(2\ell_2\Delta\ell_2+1) + d^{\Delta V}_{JQ}\left(J(J+1)-\ell_2^2-\Delta\ell_2(\ell_2+\tfrac{\Delta\ell_2}{2})\right) \tag{14}$$

for the Q branch of the transition involving $\Delta\ell_2$=±1 matrix elements, and

$$F^{\Delta\ell_2}_{\Delta V}(J,\ell_2) = -\tfrac{1}{4}(d^{\Delta V}_{JQ}-d^{\Delta V}_J) - \tfrac{1}{2}(b^{\Delta V}_J + d^{\Delta V}_{JQ})(2\ell_2\Delta\ell_2+1) - d^{\Delta V}_{JQ}\ell_2^2 + b^{\Delta V}_J m$$

$$+d^{\Delta V}_J m^2 + (d^{\Delta V}_{JQ}-d^{\Delta V}_J)\ m\ (\ell_2\Delta\ell_2+\tfrac{1}{2}) \tag{15}$$

for P and R branches of the same transitions. Here m = -J, 0 and J+1 for P, Q, and R branches, respectively. The $M^{|\Delta\ell_2|}_{\Delta V}$, $\kappa^{\Delta V}_i$ (i=1,2,3), $b^{\Delta V}_J$, $d^{\Delta V}_J$ and $d^{\Delta V}_{JQ}$ parameters of the effective dipole moment matrix elements describe simultaneously the line intensities of cold and hot bands belonging to the

same series of transitions characterized by a value ΔP. The values of these parameters can be found by fitting to the experimental line intensities. The small terms with $|\Delta\ell_2| > 1$ are omitted in Eq. (12). The expressions for the $\Delta\ell_2 = \pm 2$ terms can be found in our papers[10,22].

3. CO_2 molecule

We have published a series of papers[10,20-22,27-38] which are devoted to the global modeling of high-resolution spectra of the carbon dioxide molecule and its isotopic species. In all cases the polyad model of effective Hamiltonian was used. This model takes into account all resonance interactions arising due to the approximate relations between harmonic frequencies

$$\omega_1 \approx 2\omega_2, \omega_3 \approx 3\omega_2. \tag{16}$$

These relations lead to the polyad structure of the vibrational energy levels. Each polyad can be labeled with the polyad number P which is related to the vibrational quantum numbers with the help of the following equation

$$P = 2V_1 + V_2 + 3V_3. \tag{17}$$

The examples of the matrix elements of the effective Hamiltonian are given by Eqs. (5)-(9). The list of the resonance interaction matrix elements which were taken in to account is presented in Table 1.

The effective Hamiltonian parameters have been found by the least-squares fittings to the observed line positions collected from the literature. The GIP computer code[39] has been used for the fittings. Each isotopic species has been considered separately. The aim of the fitting procedure was to minimize the weighted dimensionless standard deviation defined according to the usual formula

$$\chi = \sqrt{\frac{\sum_i \left[\left(\nu_i^{obs} - \nu_i^{calc} \right) / \varepsilon_i \right]^2}{N - n}}, \tag{18}$$

where ν_i^{obs} and ν_i^{calc} are the observed and calculated line positions, ε_i is the experimental uncertainty of the ν_i^{obs}, N is the number of the fitted line positions, and n is the number of the adjusted parameters.

Table 1. The list of the resonance interaction matrix elements of the effective Hamiltonian for CO_2 molecule.

ΔV_1	ΔV_2	ΔV_3	$\Delta \ell_2$	Number of parameters
Anharmonic resonance interactions				
-1	2	0	0	12
-2	4	0	0	5
-3	0	2	0	5
-2	-2	2	0	5
-1	-4	2	0	1
0	-6	2	0	1
Anharmonic + ℓ-type resonance interactions				
-1	2	0	±2	5
-2	4	0	±2	1
-2	-2	2	±2	1
Resonance Coriolis interactions				
-1	-1	1	±1	12
-2	1	1	±1	5
0	-3	1	±1	5

Before the fittings, the majority of the observed line positions were subjected to minor recalibration, to make them consistent with the most accurately measured transitions. The calibration factors have been found with the help of the Ritz principle

$$(1+\delta^k)\nu^k_{j\leftarrow i} = E_j - E_i\,, \tag{19}$$

where $\nu^k_{j\leftarrow i}$ is the observed line position belonging to the kth spectrum, δ^k is the calibration offset for this spectrum, and E_i and E_j are the energies of the lower and upper states, respectively. The quantities δ^k have been set to zero for the microwave and laser heterodyne spectra and have been considered as unknowns for other spectra. The overdetermined system of linear equations has been solved in the least-squares sense to determine values of energies and calibration offsets.

In Table 2 the summary of the fittings of the line positions of five isotopic species of carbon dioxide molecules is presented[30,33-35,40].

Table 2. Results of fittings of CO_2 line positions.

Isotope	$^{12}C^{16}O_2$	$^{13}C^{16}O_2$	$^{16}O^{12}C^{18}O$	$^{16}O^{12}C^{17}O$	$^{16}O^{13}C^{18}O$
Number of lines	29000	14650	6600	1800	4190
Number of bands	364	181	72	30	38
RMS [a)], cm^{-1}	0.002	0.002	0.001	0.001	0.001
χ	1.69	2.00	2.15	1.63	2.13
Number of parameters	130	96	73	45	48

[a)] RMS is the root of mean squares of the residuals

As for line intensities we have performed their modeling for four isotopic species of carbon dioxide[20-22,28,29,31,32,36-38,41]. The effective dipole moment parameters have been found by the least-squares fittings to the observed line intensities collected from the literature. As in the case of the line positions the aim of the fitting procedure was to minimize the weighted dimensionless standard deviation defined according to the usual formula

$$\chi = \sqrt{\frac{\sum_{i=1}^{N}\left(\frac{S_i^{obs} - S_i^{calc}}{\delta_i}\right)^2}{(N-n)}}, \qquad (20)$$

where S_i^{obs} and S_i^{calc} are the observed and calculated values of the intensity for the *i*-th line, respectively, δ_i is absolute experimental uncertainty of the line intensity determination, *N* is the number of the fitted line intensities, and *n* is the number of the effective dipole moment parameters. In Table 3 we give the results of the line intensities fittings for four most abundant isotopic species of carbon dioxide[28,31,32,36-38,41].

To check the physical meaning of the fitted values of the effective dipole moment parameters we have derived expressions[20,21] for some of them in terms of the force field constants and dipole moment derivatives using contact transformation method[25,26]. We were interested especially by the fitted values of the $\kappa_i^{\Delta V}$ parameters because of their correlations with the principal parameters $M_{\Delta V}^{|\Delta \ell_2|}$ of the effective dipole moment matrix elements. Using the force field constants and dipole moment derivatives of Wattson and Rothman[42] we have performed numerical calculations of these parameters. The results are presented in Table 4 where the comparison with the latest fitted values[41] is given. As one can see from this table there is a good agreement between calculated and fitted values for the presented parameters, except, maybe, the b_J^{110} parameter.

Table 3. Results of fittings of CO_2 line intensities.

ΔP series	Number of lines	Number of bands	J_{max}	χ	RMS, %	Number of parameters
$^{12}C^{16}O_2$						
1	1280	18	85	1.2	3.2	9
3	1647	44	86	1.2	5.8	13
5	2348	44	80	2.7	9.5	15
7	828	15	60	2.1	6.8	15
9	486	6	66	0.6	2.6	7
11	280	10	48	0.8	5.0	9
13	80	3	40	0.7	9.4	2
$^{13}C^{16}O_2$						
1	285	6	58	0.5	2.9	6
3	333	14	68	1.0	11.3	9
5	470	13	63	0.8	4.5	12
7	504	7	62	0.7	3.5	8
9	524	9	55	0.7	3.5	7
11	172	4	53	0.6	3.2	4
13	57	2	38	0.7	10.4	2
$^{16}O^{12}C^{18}O$						
1	462	9	66	0.9	4.4	6
2	371	4	65	0.9	4.4	2
3	207	6	64	1.0	15.4	7
4	551	5	65	0.8	13.3	5
6	68	1	47	0.5	1.6	1
$^{16}O^{12}C^{17}O$						
1	335	6	56	1.0	4.8	5
2	104	2	43	0.9	4.2	3
3	152	5	68	1.0	10.2	6
4	143	3	42	0.7	14.3	3

Using the fitted values of the effective Hamiltonian and effective dipole moment parameters we have generated two versions of Carbon Dioxide Spectroscopic Databank (CDSD): version for the atmospheric applications (ftp://ftp.iao.ru/pub/CDSD-296) and version for the high temperature applications[43] (ftp://ftp.iao.ru/pub/CDSD-1000). The version for the atmospheric applications is presented in more details in another paper also in this book. To simplify the access to the data for the users we have elaborated the Internet accessible CDSD information system[44] (http://cdsd.iao.ru, http://cdsd.lpma.jussieu.fr). This system gives the

possibility to the users to select data in a defined spectral region, for a defined isotopic species or for a defined band, to plot intensity histogram versus wavenumbers, to model absorption coefficients, radiances, absorption and transmission functions at different thermodynamics conditions for different kinds of spectral instruments of different resolution.

Table 4. Calculated and fitted values of the effective dipole moment parameters for $^{12}C^{16}O_2$

Parameter	ΔV_1	ΔV_2	ΔV_3	Calculated*)	Fitted[41]	Units
κ_2	0	1	0	-0.64	-0.56(4)	10^{-2}
κ_1	0	0	1	-1.81	-1.71(8)	10^{-2}
κ_2	0	0	1	-0.27	-0.16(4)	10^{-2}
M	1	1	0	0.136	0.140(1)	10^{-2} Debye
M	1	-1	0	-0.90	-0.86(6)	10^{-2} Debye
M	-1	0	1	5.14	5.05(1)	10^{-2} Debye
b_J	0	1	0	0.94	0.97(2)	10^{-3}
b_J	0	0	1	-0.15	-0.19(1)	10^{-3}
b_J	1	1	0	5.34	2.92(5)	10^{-3}
b_J	1	-1	0	1.41	1.41(30)	10^{-3}

*) Force field constants and dipole moment derivatives of Wattson and Rothman[42]

4. N_2O molecule

For the first stage of the global modeling of high-resolution spectra of nitrous oxide molecule we have used the polyad model of effective Hamiltonian[11]. The vibrational energy clustering in this molecule arises due to the following approximate relations between harmonic frequences[6]

$$\omega_3 \approx 2\omega_1 \approx 4\omega_2. \tag{21}$$

Because of these relations the vibrational polyad of the number P consists of the vibrational states quantum numbers of which satisfy the following equation

$$P = 2V_1 + 4V_2 + V_3. \tag{22}$$

The effective Hamiltonian within the framework of this model takes into account two types of accidental resonance interactions: anharmonic resonance interactions and anharmonic $+\ell$-type resonance interactions. The

list of the matrix elements of the resonance interaction operators up to sixth order of perturbation theory is presented in Table 5.

Table 5. The list of the resonance interaction matrix elements of the polyad model of effective Hamiltonian for N_2O molecule.

ΔV_1	ΔV_2	ΔV_3	$\Delta \ell_2$	Number of parameters
Anharmonic resonance interactions				
-1	2	0	0	12
-2	0	1	0	12
-1	-2	1	0	12
0	-4	1	0	5
-2	4	0	0	5
-4	0	2	0	5
-3	-2	2	0	1
-2	-4	2	0	1
Anharmonic + ℓ-type resonance interactions				
-1	2	0	±2	5
-1	-2	1	±2	5
0	-4	1	±2	1
-2	4	0	±2	1

Using this model of effective Hamiltonian we have performed the global fitting of the collected from the literature line positions of the principal isotopic species of N_2O molecule[45]. The obtained set of effective Hamiltonian parameters reproduces in a good way the line positions of the majority of the bands. But for several bands lying in the high frequency region the residuals between observed and calculated values are very large reaching 1.2 cm^{-1}. We had analyzed this situation and have found that it is caused by interpolyad resonance anharmonic and Coriolis interactions[46-48]. It has been suggested a new nonpolyad model of effective Hamiltonian, which takes into account these interpolyad resonance interactions. The matrix of this new model of effective Hamiltonian is no more block-diagonal. Schematically the vibrational matrix (J=0) for 30 lowest polyads is presented in Fig. 2.

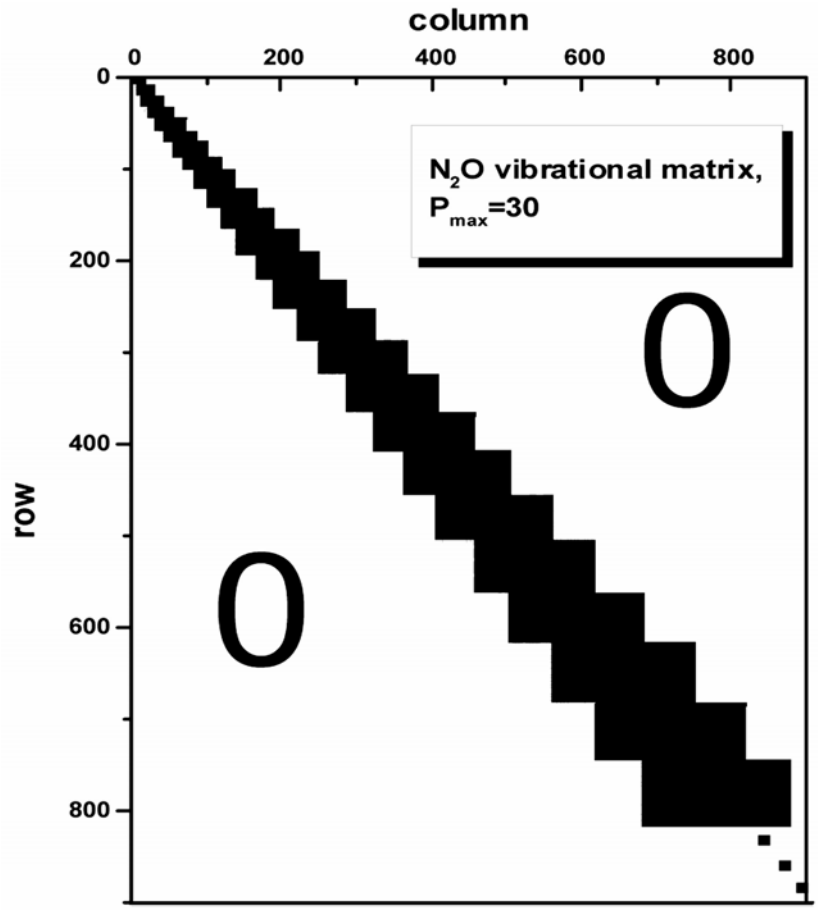

Figure 2. Graphical view of the matrix of the nonpolyad model of effective Hamiltonian for N_2O molecule.

The diagonalization of this matrix is a time consuming procedure. In our fittings we had to diagonalize on each iteration for each J and for each Wang symmetry the matrices whose sizes exceed 3000×3000. The preliminary result of fitting is presented in Table 6. In this table we also present the result of fitting of the parameters of the polyad model of the effective Hamiltonian to the cleaned set of input data. The bands which are perturbed by interpolyad resonance interactions have not been taken into account in the last case.

Both sets of parameters have been successfully used to assign and to analyze the high-resolution spectra of nitrous oxide molecule[46-49].

Table 6. Results of fittings of N_2O line positions.

Model	Number of parameters	Number of lines	Number of bands	J_{max}	χ	RMS, 10^{-3} cm^{-1}
Polyad	155	25000	250 [a)]	104	3.16	2.2
Nonpolyad	145	28500	339	104	6.53	12.0

[a)] The bands perturbed by interpolyad resonance interactions are excluded

The line intensities of N_2O can be described by the same Eqs. (2), (12)-(15) which are used in the case of CO_2 molecule. When eigenfunctions of the nonpolyad model of the effective Hamiltonian are used for the line intensity calculations one has to introduce summation over ΔP into Eq.(12). In Table 7 the results of the global fittings of the line intensities for the principal isotopic species of N_2O molecule are presented. For the ΔP = 2, 4 series of transitions the eigenfunctions of the polyad model of effective Hamiltonian have been used in the calculations[50,51]. And for the ΔP = 7, 8, 9, 10, 11, 12, 13 and 14 series of transitions the eigenfunctions of the nonpolyad model of effective Hamiltonian have been used[52,53]. Only band intensities have been modeled for $\Delta P = 1$, 3, 5, and 6 series of transitions[54]. The fitted values of the effective dipole moment parameters have been used for the refinement of the first and second derivatives of the dipole moment function of N_2O molecule[55].

Table 7. Results of fittings of N_2O line intensities.

ΔP series	Number of lines	Number of bands	χ	RMS, %	Number of parameters
2	1136	11	1.3	4.2	11
4	652	10	0.4		12
7-9	3788	69	1.0	2.9	47
10-14	5645	53	1.5	4.9	44

5. C_2H_2 molecule

A series of our papers[17,18,23,24,56-59] is devoted to the global modeling of high-resolution spectra of acetylene molecule. In the case of C_2H_2 molecule there exist the following approximate relations between harmonic frequences[60]

$$\omega_1 \approx \omega_3 \approx 5\omega_4 \approx 5\omega_5, \quad \omega_2 \approx 3\omega_4 \approx 3\omega_5. \tag{23}$$

This leads to the polyad structure of the vibrational energy levels. Each polyad P consists of the vibrational states the quantum numbers which satisfy the following equation

$$P = 5V_1 + 3V_2 + 5V_3 + V_4 + V_5. \quad (24)$$

The acetylene molecule has five normal vibrations. Three of them are nondegenerate stretching vibrations: $\omega_1(\Sigma_g^+), \omega_2(\Sigma_g^+), \omega_3(\Sigma_u^-)$, and two others are degenerate bending vibrations: $\omega_4(\Pi_g)$ and $\omega_5(\Pi_u)$. Hence the acetylene molecule has two vibrational angular momentum quantum numbers ℓ_4 and ℓ_5. Because of this the form of the effective Hamiltonian for acetylene molecule differs slightly from that for the triatomic molecules. The main difference is in appearance of the additional term which is diagonal relative to the principal vibrational quantum numbers and nondiagonal relative to the vibrational angular momentum quantum numbers[12]. This term is called a vibrational ℓ-doubling. The polyad model of effective Hamiltonian for acetylene molecule up to the six order of the perturbation theory is presented in our paper[18]. This effective Hamiltonian has been used[57] to fit the line positions of C_2H_2 lying in the region 50 - 10120 cm^{-1}. The derived set of 150 effective Hamiltonian parameters reproduces 9046 observed line positions of 142 bands with RMS = 0.005 cm^{-1}.

To perform the global modeling of C_2H_2 line intensities we had to modify the Eqs. (12)-(15). The necessity of the modification results from the difference of the Sayvetz condition $K = \ell_4 + \ell_5$ for the tetratomic linear molecules from that $K = \ell_2$ for triatomic linear molecules. This difference leads to the specific transitions in the case of tetratomic molecules $\Delta K = 0, \Delta\ell_4 \neq 0, \Delta\ell_5 \neq 0$ and to the appearance of the additional term in the Eq. (12). The respective equations and their detailed discussions are given in our papers[23,24]. Using these equations and the eigenfunctions of the effective Hamiltonian obtained in the result of the global fitting of the line positions we have performed the global fittings of the line intensities of the bands belonging to the five series of transitions[24,58,59]. The results are presented in Table 8.

Table 8. Results of C_2H_2 line intensities fittings.

Series	ΔP=1	ΔP=2	ΔP=3	ΔP=5	ΔP=10
Region (cm^{-1})	750	1330	2000	3270	6550
Number of bands	6	3	15	20	4
Number of lines	431	115	535	591	269
Number of parameters	4	3	18	6	4
RMS (%)	3.6	4.4	4.7	4.2	1.3
χ	0.8	1.0	1.0	0.6	0.7

Conlusion

In this paper we present briefly the work made by our group on the global modeling of high-resolution spectra of linear molecules. The goal was to generate databanks based on this modeling and to elaborate Internet accessible information systems based on these databanks. This work is practically completed for the carbon dioxide molecule. In the result of our activity the CDSD databank and information system have been elaborated which are now widely used in many applications. We are also close to the main goal of our activity to generate the spectroscopic databanks for nitrous oxide and acetylene molecules.

Acknowledgments

We would like to thank our colleagues J. Vander Auwera, L. Daumont, A. Campargue, E. I. Lobodenko, C. Claveau, A. Valentin, J.-Y. Mandin, V. Dana, D. Jacquemart, D. Bailly, T.R. Huet, E. Bertseva, S.-M. Hu, L. Wang, Y. Ding, A. Barbe, L. Regalia-Jarlot and M.-R. De Backer-Barilly who contributed to the results presented in this paper.

References

1. E. B. Wilson, J. B. Howard, The vibration-rotation energy levels of polyatomic molecules, *J. Chem. Phys.* 4 (4), 260-268 (1936).
2. J. K. G. Watson, Simplification of the molecular vibration-rotation Hamiltonian, *Mol. Phys.* 15(5), 479-490 (1968).
3. J. K. G. Watson, The vibration-rotation Hamiltonian of linear molecules, *Mol. Phys.* 19(4), 465-487 (1970).

4. G. Amat and H. H. Nielsen, Vibrational ℓ-type doubling and ℓ-type resonance in linear polyatomic molecules, *J. Mol. Spectrosc.* 2(2), 152-162 (1958).
5. G. Amat, H. H. Nielsen, and G. Tarrago, Rotation-vibration of polyatomic molecules (Dekker, New York, 1971).
6. J. Pliva, Molecular constants of nitrous oxide, $^{14}N_2{}^{16}O$, *J. Mol. Spectrosc.* 27(1-4), 461-488 (1968).
7. A. Chedin, The carbon dioxide molecule. Potential, spectroscopic, and molecular constants from its infrared spectrum, *J. Mol. Spectrosc.* 76(1-3), 430-491 (1979).
8. J.-L. Teffo and A. Chedin, Intranuclear potential and equilibrium structure of the nitrous oxide molecule from rovibrational data, *J. Mol. Spectrosc.* 135(2), 389-409 (1989).
9. A. Fayt, R. Vandenhaute, and J. G. Lahaye, Global rovibrational analysis of carbonyl sulfide, *J. Mol. Spectrosc.* 119(2), 233-266 (1986).
10. J.-L. Teffo, O. N. Sulakshina, and V. I. Perevalov, Effective Hamiltonian for rovibrational energies and line intensities of carbon dioxide, *J. Mol. Spectrosc.* 156(1), 48-64 (1992).
11. J.-L. Teffo, V. I. Perevalov, and O. M. Lyulin, Reduced effective Hamiltonian for a global treatment of rovibrational energy levels of nitrous oxide, *J. Mol. Spectrosc.* 168(2), 390-403 (1994).
12. J. Pliva, Molecular constants for the bending mode of acetylene $^{12}C_2H_2$, *J. Mol. Spectrosc.* 44(1), 165-182 (1972).
13. J. Hietanen, The ℓ-resonance effects in the hot bands $3\nu_5 \leftarrow 2\ \nu_5$, $(\nu_4+2\ \nu_5) \leftarrow (\nu_4+\ \nu_5)$ and $(2\nu_4+\ \nu_5) \leftarrow 2\ \nu_5$ of acetylene, *Mol. Phys.* 49(5), 1029-1038(1983).
14. T. R. Huet, M. Herman, and J. W. C. Johns, The bending levels in C_2D_2 ($\tilde{X}\,^1\Sigma_g^+$), *J. Chem. Phys.* 94(5), 3407-3414 (1991).
15. M. Abbouti Temsamani and M. Herman, The vibrational energy levels in acetylene $^{12}C_2H_2$: Towards a regular pattern at higher energies, *J. Chem. Phys.* 102(16), 6371-6384 (1995).
16. Y. Kabbadj, M. Herman, G. Di Lonardo, L. Fusina, and J. W. C. Johns, The bending energy levels of C_2H_2, *J. Mol. Spectrosc.* 150(2), 535-565 (1991).
17. V. I. Perevalov and O. N. Sulakshina, Reduced effective vibration-rotation Hamiltonian for bending vibrational levels of acetylene molecules, in: *Proceedings of Eleventh Symposium and School on High-Resolution Molecular Spectroscopy,* edited by A. I. Nadezhdinskii, Y. N. Ponomarev and L. N. Sinitsa, *Proc. SPIE* 2205, 182-187 (1994).
18. V. I. Perevalov, E. I. Lobodenko, and J.-L. Teffo, Reduced effective Hamiltonianin for global fitting of C_2H_2 rovibrational lines, in: *Proceedings of Twelfth Symposium and School on High-Resolution Molecular Spectroscopy,* edited by L. N. Sinitsa, Y. N. Ponomarev, and V. I. Perevalov, *Proc. SPIE* 3090, 143-149 (1997).
19. K. M. T. Yamada, F. W. Birss, and M. R. Aliev, Effective Hamiltonian for polyatomic linear molecules, *J. Mol. Spectrosc.* 112(2), 347-356 (1985).
20. V. I. Perevalov, E. I. Lobodenko, O. M. Lyulin, and J.-L. Teffo, Effective dipole moment and band intensities problem for carbon dioxide, *J. Mol. Spectrosc.* 171(2), 435-452 (1995).
21. J.-L. Teffo, O. M. Lyulin, V. I. Perevalov, and E. I. Lobodenko, Application of the effective operator approach to the calculation of $^{12}C^{16}O_2$ line intensities, *J. Mol. Spectrosc.* 187(1), 28-41 (1998).
22. S. A. Tashkun, V. I. Perevalov, J.-L. Teffo, and Vl. G. Tyuterev, Global fit of $^{12}C^{16}O_2$ vibrational-rotational line intensities using the effective operator approach, *J. Quant. Spectrosc. Radiat. Transfer.* 62(5), 571-598 (1999).

23. V. I. Perevalov, O. M. Lyulin, and J.-L. Teffo, Global treatment of line intensities of vibrational-rotational transitions of acetylene molecule. Approach and design formulas, *Atmospheric and Oceanic Optics.* 14(9), 730-738 (2001).
24. V. I. Perevalov, O. M. Lyulin, D. Jacquemart, C. Claveau, J.-L. Teffo, V. Dana, J.-Y. Mandin, and A. Valentin, Global fitting of line intensities of acetylene molecule in the infrared using the effective operator approach, *J. Mol. Spectrosc.* 218(2), 180-189 (2003).
25. M. R. Aliev and J. K. G. Watson, in: Molecular Spectroscopy: Modern Research, edited by K. Narahari Rao (Academic Press, Orlando, 1985), v.3, pp. 1-67.
26. Vl. G. Tyuterev and V. I. Perevalov, Generalized contact transformations for quasi-degenerate levels, *Chem. Phys. Lett.* 74(3), 494-502 (1980).
27. S. A. Tashkun, V. I. Perevalov, J.-L. Teffo, L. S. Rothman, and Vl. G. Tyuterev, Global fit of $^{12}C^{16}O_2$ vibrational-rotational line positions using the effective operator approach, *J. Quant. Spectrosc. Radiat. Transfer.* 60(5), 785-801 (1998).
28. S. A. Tashkun, V. I. Perevalov, J.-L. Teffo, M. Lecoutre, T. R. Huet, A. Campargue, D. Bailly, and M. P. Esplin, $^{13}C^{16}O_2$: Global treatment of vibration-rotation spectra and first observation of the $2\nu_1+ 5\nu_3$ and $\nu_1+ 2\nu_2+ 5\nu_3$ absorption bands, *J. Mol. Spectrosc.* 200(2), 162-176 (2000).
29. J.-L. Teffo, C. Claveau, Q. Kou, G. Guelachvili, A. Ubelmann, V. I. Perevalov, and S. A. Tashkun, Line intensities of $^{12}C^{16}O_2$ in the 1.2-1.4 μm spectral region, *J. Mol. Spectrosc.* 201(2), 249-255 (2000).
30. S. A. Tashkun, V. I. Perevalov, and J.-L. Teffo, Global fittings of the vibration-rotation line positions of the $^{16}O^{12}C^{17}O$ and $^{16}O^{12}C^{18}O$ isotopic species of carbon dioxide, *J. Mol. Spectrosc.* 210(1), 137-145 (2001).
31. J.-L. Teffo, L. Daumont, C. Claveau, A. Valentin, S. A. Tashkun, and V. I. Perevalov, Infrared spectra of $^{16}O^{12}C^{17}O$ and $^{16}O^{12}C^{18}O$ species of carbon dioxide: The region 500-1500 cm^{-1}, *J. Mol. Spectrosc.* 213(1), 145-152 (2002).
32. J.-L. Teffo, L. Daumont, C. Claveau, A. Valentin, S. A. Tashkun, and V. I. Perevalov, Infrared spectra of $^{16}O^{12}C^{17}O$ and $^{16}O^{12}C^{18}O$ species of carbon dioxide: II. The 1500-3000 cm^{-1} region, *J. Mol. Spectrosc.* 219(2), 271-281 (2003).
33. Y. Ding, V. I. Perevalov, S. A. Tashkun, J.-L. Teffo, A.-W. Liu, and S.-M. Hu, $^{16}O^{13}C^{18}O$: high-resolution absorption spectrum between 4000 and 9500 cm^{-1} and global fitting of vibration-rotational line positions, *J. Mol. Spectrosc.* 222(2), 276-283 (2003).
34. Y. Ding, P. Macko, D. Romanini, V.I. Perevalov, S.A. Tashkun, J.-L.Teffo, S.-M. Hu, and A. Campargue, High sensitivity *cw*-cavity ring down and Fourier transform absorption spectroscopies of $^{13}CO_2$, *J. Mol. Spectrosc.* 226(2), 146-160 (2004).
35. Z. Majcherova, P. Macko, D. Romanini, V.I. Perevalov, S.A. Tashkun, J.-L. Teffo, and A. Campargue, High-sensitivity CW-cavity ring down spectroscopy of $^{12}CO_2$ near 1.5 μm, *J. Mol. Spectrosc.* 230(1) 1–21 (2005).
36. L. Wang, V.I. Perevalov, S.A. Tashkun, A.-W. Liu, and S.-M. Hu, Absorption spectra of $^{12}C^{16}O_2$ and $^{13}C^{16}O_2$ near 1.05 μm, *J. Mol. Spectrosc.* 233(2), 297–300 (2005).
37. L. Wang, V.I. Perevalov, S.A.Tashkun, Y. Ding, and S.-M Hu, Absolute line intensities of $^{13}C^{16}O_2$ in the 4200 – 8500 cm^{-1} region, *J. Mol. Spectrosc*. 234(1), 84-92 (2005).
38. J. Vander Auwera, C. Claveau, J.-L. Teffo, S. A. Tashkun, and V. I. Perevalov, Absolute line intensities of $^{13}C^{16}O_2$ in the 3090 – 3920 cm^{-1} region, *J. Mol. Spectrosc.* in press.
39. S. A. Tashkun and Vl. G. Tyuterev, GIP a program for experimental data reduction in molecular spectroscopy, in: *Proceedings of Eleventh Symposium and School on High-*

Resolution Molecular Spectroscopy, edited by A. I. Nadezhdinskii, Y. N. Ponomarev and L. N. Sinitsa, *Proc. SPIE* 2205, 188-191 (1994).

40. V. I. Perevalov and S. A. Tashkun, New global fittings of $^{16}O^{12}C^{17}O$ and $^{16}O^{12}C^{18}O$ line positions, to be published.
41. V. I. Perevalov and S. A. Tashkun, Refined sets of effective dipole moment parameters for four isotopic species of carbon dioxide, to be published.
42. R. B. Wattson and L. S. Rothman, Direct numerical diagonalization: wave of the future, *J. Quant. Spectrosc. Radiat. Transfer.* 48(5/6), 763-780 (1992).
43. S. A. Tashkun, V. I. Perevalov, J.-L. Teffo, A. D. Bykov, and N. N. Lavrentieva, CDSD-1000, the high-temperature carbon doxide spectroscopic databank, *J. Quant. Spectrosc. Radiat. Transfer.* 82(1-4), 165-196 (2003).
44. S. A. Tashkun, V. I. Perevalov, J.-L. Teffo, A. D. Bykov, N. N. Lavrentieva and Y. L. Babikov, CDSD-1000, the high-temperature carbon doxide spectroscopic databank and information system, in: *Proceedings of Fourteenth Symposium on High-Resolution Molecular Spectroscopy,* edited by L. N. Sinitsa and S. N. Mikhailenko, *Proc. SPIE* 5311, 102-112 (2004).
45. V. I. Perevalov, S. A. Tashkun, and J.-L. Teffo, Global fittings of rovibrational line positions of nitrous oxide, in: *Program and Abstracts of Sixteenth Colloquium on High Resolution Molecular Spectroscopy* (Université de Bourgogne, Dijon, 1999), p.103.
46. A. Campargue, G. Weirauch, S. A Tashkun, V. I. Perevalov, and J.-L. Teffo, Overtone spectroscopy of N_2O between 10000 and 12500cm^{-1}: a test of the polyad approach, *J. Mol. Spectrosc.* 209(2), 198-206 (2001).
47. Y. Ding, V. I. Perevalov, S. A. Tashkun, J.-L. Teffo, S. Hu, E. Bertseva, and A. Campargue, Weak overtone transitions of N_2O around 1.05 μm by ICLAS-VECSEL, *J. Mol. Spectrosc.* 220(1), 80-86 (2003).
48. E. Bertseva, A. Campargue, V. I. Perevalov, and S. A. Tashkun, New observations of weak overtone transitions of N_2O by ICLAS-VECSEL near 1.07 μm, *J. Mol. Spectrosc.* 226(2), 196-200 (2004).
49. E. Bertseva, A. A. Kachanov, and A.Campargue, Intracavity laser absorption spectroscopy of N_2O with vertical external cavity surface emitting laser*, Chem. Phys. Lett.* 351(1), 18-26 (2002).
50. L. Daumont, C. Claveau, M.-R. De Backer-Barilly, A. Hamdouni, L. Regalia-Jarlot, J.-L. Teffo, S. A. Tashkun, and V. I. Perevalov, Line intensities of $^{14}N_2{}^{16}O$: the 10 micrometers region revisited, *J. Quant. Spectrosc. Radiat. Transfer*. 72(1), 37-55 (2002).
51. O. M. Lyulin, V. I. Perevalov, and J.-L. Teffo, Fitting of line intensities using the effective operator approach: the 4 μm region of $^{14}N_2{}^{16}O$, *J. Mol. Spectrosc*. 180(1), 72-74 (1996).
52. L. Daumont, J. Vander Auwera, J.-L. Teffo, V. I. Perevalov, and S. A. Tashkun, Line intensity measurements in $^{14}N_2{}^{16}O$ and their treatment using the effective dipole moment approach, *J. Mol. Spectros*. 208(2), 281-291 (2001).
53. L. Daumont, J. Vander Auwera, J.-L. Teffo, V. I. Perevalov, and S. A. Tashkun, N_2O line intensities in the region from 4200 to 6600 cm^{-1}, in: *Program and Abstracts of the Nineteenth Colloquium on High Resolution Molecular Spectroscopy* (CSIC, Salamanca, 2005), p.130.
54. O. M. Lyulin, V. I. Perevalov, and J.-L. Teffo, Effective dipole moment and band intensities of nitrous oxide, *J. Mol. Spectrosc*. 174(2), 566-580 (1995).
55. E. I. Lobodenko, V. I. Perevalov, O. M. Lyulin, and J.-L. Teffo, Dipole-moment derivatives of nitrous oxide, *J. Mol. Spectrosc*. 205(2), 239-247 (2001).

56. O. M. Lyulin, V. I. Perevalov, S. A. Tashkun, and J.-L. Teffo, Global fitting of the vibrational-rotational line positions of acetylene molecule, in: *Proceedings of Thirteenth Symposium and School on High-Resolution Molecular Spectroscopy,* edited by L. N. Sinitsa, Y. N. Ponomarev, V. I. Perevalov, *Proc. SPIE* 4063, 126-133 (2000).
57. O. M. Lyulin, V. I. Perevalov, and J.-L. Teffo, Global fitting of vibration-rotation line positions of acetylene molecule in the far and middle infrared regions, in: *Proceedings of Fourteenfth Symposium on High-Resolution Molecular Spectroscopy,* edited by L. N. Sinitsa and S. N. Mikhailenko, *Proc. SPIE* 5311, 134-143 (2004).
58. O. M. Lyulin and V. I. Perevalov, Line intensities of vibration-rotation transitions of acetylene molecule in the 1.5 μm region, *Atmospheric and Oceanic Optics.* 17(7), 485-488 (2004).
59. O. M. Lyulin, V. I. Perevalov, J.-Y. Mandin, V. Dana, D. Jacquemart, L. Regalia-Jarlot, and A. Barbe, Line intensities of acetylene in 3 μm region: New measurements of weak hot bands and global fitting, *J. Quant. Spectrosc. Radiat. Transfer*. 97(1), 81-98 (2006).
60. M. E. Kellman and Gengxing Chen, Approximate constants of motion and energy transfer pathways in highly excited acetylene, *J. Chem. Phys.* 95(11), 8671-8672 (1991).

CDSD-296, THE HIGH-PRECISION CARBON DIOXIDE SPECTROSCOPIC DATABANK: VERSION FOR ATMOSPHERIC APPLICATIONS

S.A. TASHKUN*, V.I. PEREVALOV
Laboratory of Theoretical Spectroscopy, Institute of Atmospheric Optics SB RAS, Akademicheskii Av. 1, 634055, Tomsk, Russia

J.-L. TEFFO
Laboratoire de Physique Moléculaire et Applications, CNRS, Université Pierre et Marie Curie, Boite 76, 4 Place Jussieu, 75252 Paris, Cedex 05, France

Abstract. We present CDSD-296 a version of the Carbon Dioxide Spectroscopic Databank aimed at processing signals from the satellite based sensors. The databank contains line parameters (positions, intensities as well as HITRAN air- and self-broadened halfwidths and coefficients of temperature dependence of air-broadened halfwidths) of the four most abundant isotopic species of CO_2. The reference temperature is T_{ref}=296 K, the intensity cutoff is I_{cut}=10^{-28} cm^{-1}/(molecule cm^{-2}) and the spectral range is 405-12784 cm^{-1}. The databank was generated within the framework of the method of effective operators and based on the global fittings of parameters of the models to observed data collected from the literature. Calculated line positions were systematically replaced where possible by the differences between experimental term values derived from recalibrated observed line positions with the help of the combination Ritz principle. The databank includes statistically justified confidence intervals for each line position and intensity.

Keywords: carbon dioxide; databank; radiative properties; HITRAN; atmospheric applications

* To whom correspondence should be addressed. Tashkun Sergei, Institute of Atmospheric Optics, Akademitcheskii av. 1, 634055 Tomsk Russia; e-mail: tashkun@mail.tomsknet.ru

A. Perrin et al. (eds.), Remote Sensing of the Atmosphere for Environmental Security, 161–169.

1. Introduction

Precise knowledge of the radiative properties of CO_2 is required for many scientific and industrial applications. Carbon dioxide is one of the major greenhouse gases and plays an important role in the chemical-physical processes in the terrestrial atmosphere and in planetology. Spectroscopic rovibrational line parameters (positions, intensities, halfwidths, etc.) of CO_2 are used by various radiative transfer codes to model properties of the terrestrial atmosphere as well as atmospheres of Venus and Mars. Information of CO_2 data are used by a number of already working or planned satellite-borned sensors (MIPAS[1], IASI[2], OCO[3]) to retrieve atmospheric temperature profile and to monitor the column amount of CO_2 across the globe. Spectroscopic line parameters of atmospheric gases are accumulated in a well known database HITRAN[4]. The carbon dioxide HITRAN data are in fact a mixture of measured and calculated line parameters. According to the adopted approach, when possible high-quality measurements are put into the database. In situations where direct measurements are unavailable, the calculated data either from the previous version of the CDSD atmospheric databank[5] or (if required data are absent from CDSD) from the DND calculations[6] were used. The accuracy of calculated line positions covers the 0.0001 – 0.01 cm^{-1} range. The accuracy of calculated line intensities depends on the experimental data used for fitting the parameters of theoretical dipole models and varies from 2% to 50%.

Modern requirements of the accuracy of this data are stricter. For example in order to provide a 0.5% measurement precision in retrieved values of total column CO_2 in the 1.6 μm region the line position uncertainties less than 0.5×10^{-4} cm^{-1} are required[7]. As for line intensities, they must be known with accuracy ~0.3% according to the OCO specifications[3]. It is clear that neither CDSD nor DND calculations fail to meet these requirements.

Another important point is availability of realistic confidence intervals for calculated line parameters. HITRAN-2004 provides IER integer codes for position and intensity uncertainties. Their values, however, often do not reflect the actual uncertainties. The inclusion of statistically justified confidence intervals for line parameters into a spectroscopic database is an important requirement posed by the IASI-METOP working group[2].

In this study we present a database of line positions and line intensities of CO_2 aimed at spectroscopic applications and called CDSD-296. The principal goal is to supply the scientific community with enlarge and more precise data on four most abundant isotopologues $^{12}C^{16}O_2$, $^{13}C^{16}O_2$, $^{12}C^{16}O^{18}O$, and $^{12}C^{16}O^{17}O$ of the carbon dioxide molecule.

2. Theoretical background

The creation of the CDSD-296 databank includes several principal stages. Firstly, the theory of effective operators is used to build phenomenological models of the effective Hamiltonian[8] and of the effective dipole moment operator[9]. Secondly, the parameters of these models are fitted to the observed data (position and intensities) collected from the literature. Finally, a dedicated version of the databank is generated from the fitted parameters by calculating all possible lines, which have intensities above the threshold I_{cut} at the reference temperature T_{ref}. Following this receipt the high-temperature version CDSD-1000 with T_{ref}=1000 K and $I_{cut}=10^{-27}$ cm^{-1}/(molecule cm^{-2}) was created[10]. In order to improve the quality and reliability of the data, the generation of CDSD-296 includes two additional stages.

2.1. TRANSITION FREQUENCIES

The first step is to use the Ritz combination principle to retrieve energy levels (term values) from a set of measured line positions. These positions were collected from a number of observed microwave, laser-heterodyne, saturation Fourier-transformed, intracavity laser absorption and cavity ring-down spectra. Data used were entered with an effective calibration factor for each spectrum. Calibration factors associated with laser heterodyne and microwave spectra are set to one. A least squares procedure then adjusted these effective calibration factors together with values of energy levels in order to provide a set of energy levels with the greatest consistency[10]. Perhaps the dominant effect of this procedure is to compensate in an average way, over each spectrum, for the differing pressure shifts. In cases where a level is involved in many observed transitions the program provides for averaging, which eliminates to a certain extent contributions of line shifts and gives more reliable estimates than a classical combination difference approach. This procedure may be seen as providing a set of energy levels as close as possible to the low-pressure energy levels of the molecule. In this study the formulation of the Ritz principle is

$$(1+\delta^s)\nu_{\alpha\to\beta}^{s,i} = E_\alpha^i - E_\beta^i, \qquad (1)$$

where s is the spectrum index, i is the isotopologue index, α is the upper state quantum number multi-index, β is the lower state quantum number multi-index, $\nu_{\alpha\to\beta}^{s,i}$ is the observed frequency of a transition of i-th isotopologue in s-th spectrum. E_α^i and E_β^i are energy levels of upper and lower states of i-th isotopologue. The values δ^s and E_α^i are considered as

unknowns. The resulting set of levels can be considered as the set of *experimental* energy levels of CO_2.

Let us denote $\mathbf{E}^{\mathbf{i}}_{\boldsymbol{\alpha}}$ energy levels calculated from fitted effective Hamiltonian parameters. For each calculated transition frequency $\nu^i_{\alpha\to\beta} = \mathbf{E}^{\mathbf{i}}_{\boldsymbol{\alpha}} - \mathbf{E}^{\mathbf{i}}_{\boldsymbol{\beta}}$ we check whether both $\mathbf{E}^{\mathbf{i}}_{\boldsymbol{\alpha}}$ and $\mathbf{E}^{\mathbf{i}}_{\boldsymbol{\beta}}$ are in the set of experimental energy levels. If so we replace $\nu^i_{\alpha\to\beta}$ by the difference $E^i_\alpha - E^i_\beta$. If not, we rest $\nu^i_{\alpha\to\beta}$ untouched. This approach enables us to fill the databank where possible with more accurate transition frequencies.

2.2. TRANSITION INTENSITIES

It is known that the method of linear least-squares, which is widely used for fitting parameters of spectroscopic models to observed data has zero breakdown point[11]. That is even a single outlier in a set of fitted data can totally offset the least squares estimator. In order to overcome this drawback robust methods of estimation were developed. For our purposes particularly useful is the LTS (Least Trimmed Squares) linear regression method[12], which has the highest possible breakdown point and enables to explicitly detect outliers in fitted data. We found that LTS is extremely useful to fit parameters of a dipole moment operator to a set of observed intensities. The rationale is that outliers are frequently encountered among measured intensities especially for weak bands. We used LTS to fit parameters of the lineralized effective dipole moment operator. Our numerical experiments demonstrated that the LTS fitted effective dipole moment parameters have better extrapolation properties than least-squares fitted parameters. That is why we used the LTS fitted parameters to calculate transition intensities of the CDSD-296 databank.

2.3. CONFIDENCE INTERVALS

It is well known that exact expressions for confidence intervals of a property which depends on fitted parameters exist only for linear regression models[13]. It is clear that Eq. (1) is linear and it is possible to calculate exact intervals for Ritz transitions. If the calculation of a transition is based on an effective Hamiltonian model then only an approximate interval can be given[13].

To obtain exact confidence intervals for line intensities we use linear dependence of the transition moment on dipole moment parameters.

Confidence intervals in the CDSD-296 databank correspond to the 95% confidence level.

3. Presentation of CDSD-296

A previous version of CDSD-296 and the high-temperature version CDSD-1000[10] are based on measurements of positions and intensities collected from the literature. The summary of these measurements is given in ref. 10. Since that time new measurements were published[14-27]. We also added data from Ref. 28 which has been overlooked. The most important ones are measurements of positions and intensities of $^{13}C^{16}O_2$ isotopologue. These new measurements were added to position and intensity datafiles. The datafiles were then used as input information to fit effective Hamiltonian and dipole moment parameters of four most abundant isotopologues. Finally the fitted parameters were used to calculate linelists for these isotopologues using the reference temperature T_{ref}=296 K and the intensity cutoff I_{cut}=10^{-28} cm^{-1}/(molecule cm^{-2}). The datafiles were also used to derive a set of experimental energy levels and calibration factors. Linewidths, lineshifts and coefficients of temperature dependence of linewidths were taken from the HITRAN databank[4]. A flowchart of CDSD-296 creation is given in Figure 1.

Two computer codes were used to create CDSD-296. The RITZ code solves Eq. (1) in least-squares sense. The GIP code[9-10] performs line by line fitting of effective operator parameters to a set of line positions and intensities.

Table 1. Summary of CDSD-296 and HITRAN databanks.

Databank	Nisotops	Icutoff [1]	Nlines	Range (cm^{-1})
HITRAN-2004	8	10-27	62913	442-12784
CDSD-296	4	10-28	124580 (49208) [2]	405-12784

[1] in units cm^{-1}/(molecule cm^{-2})

[2] number of Ritz transitions are in brackets

Figure 2 gives a graphical overview of the CDSD-296 databank.

4. Conclusion

A spectroscopic carbon dioxide databank CDSD-296 for atmospheric applications is presented. The databank is aimed at processing signals from space-borne sounders MIPAS, IASI, *etc*. A number of computational and statistical methods were used in order to improve the precision of spectroscopic data. We believe that CDSD-296 is the most precise high-resolution calculated CO_2 spectroscopic databank.

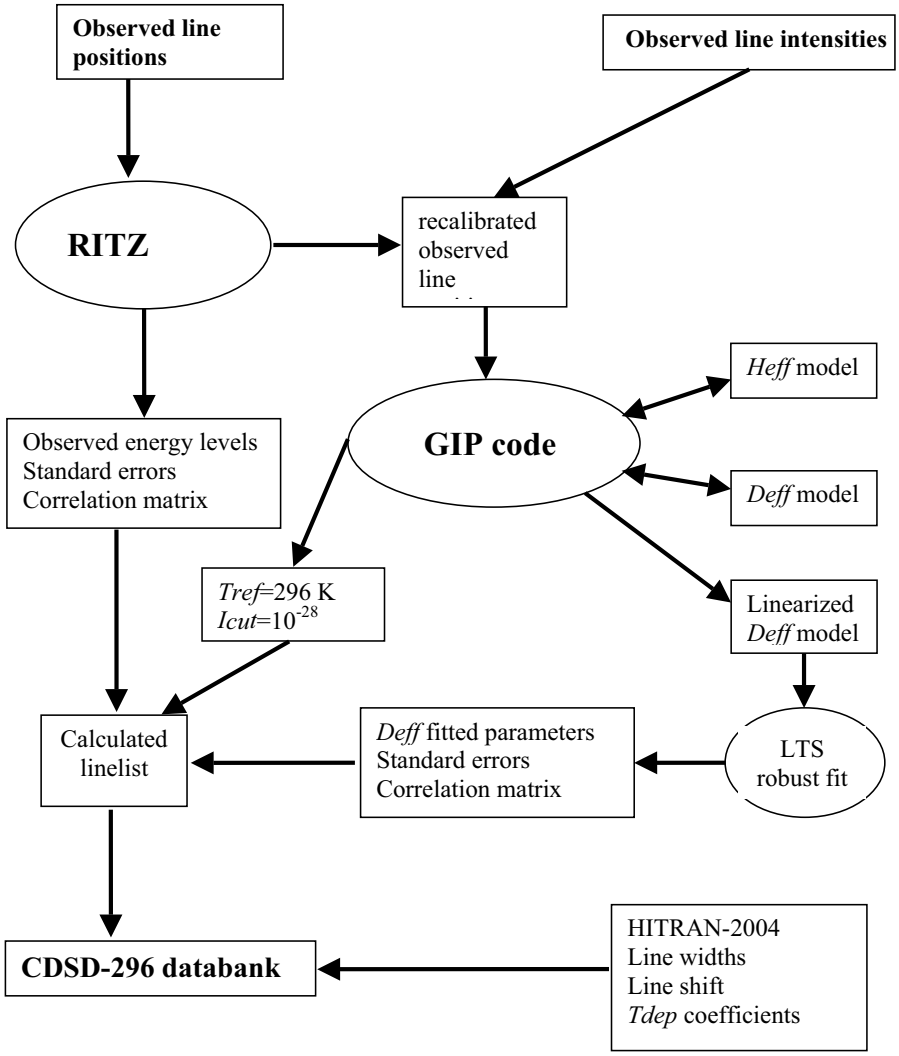

Figure 1. Flow diagram that outlines the way the CDSD-296 databank was created.

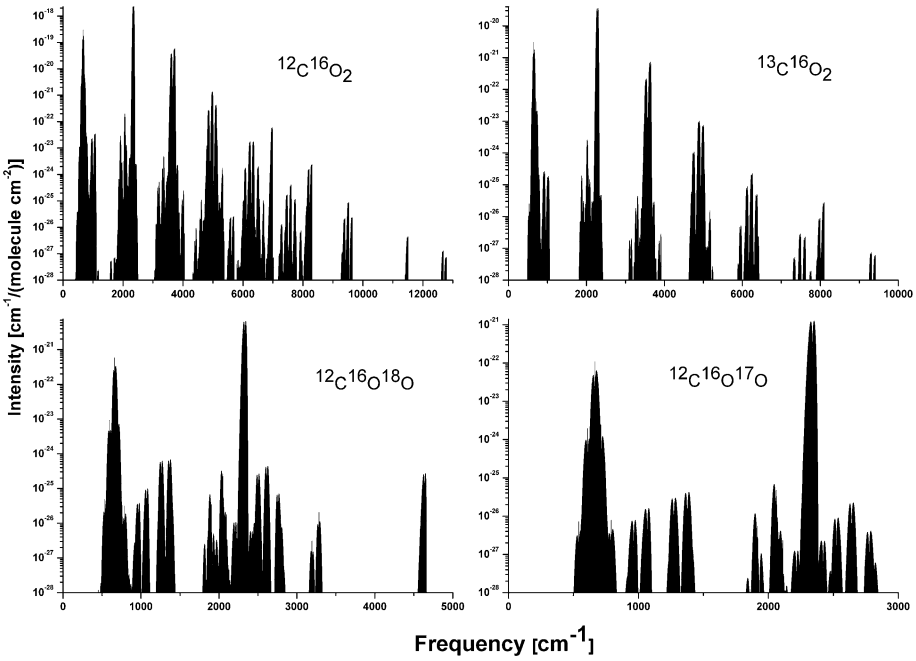

Figure 2. A graphical overview of the CDSD-296 databank.

Acknowledgements

The authors are grateful to the following co-workers for discussions and supplying them with files of experimental data: Dr's. L. S. Rothman, D. Bailly, J. Y. Mandin, M. P. Esplin, C. Claveau, A. Valentin, A. Campargue, V. Dana, R. B. Wattson, L. P. Giver, M. Fukabori, T. R. Huet, G. Guelachvili, Q. Kou, A. Barbe, M. R. De Backer-Barilly, L. Daumont, J. Henningsen, J. Vander Auwera, S. M. Hu, L. Wang, L. Regalia-Jarlot, and D. C. Benner

References

1. J. M. Flaud, C. Piccolo, B. Carli, A. Perrin, L. H. Coudert, J. L. Teffo, and L. R. Brown, Molecular line parameters for the MIPAS (Michelson Interferometer for Passive Atmospheric Sounding) experiment, *J. Atmos and Oceanic Optics* 16, 194-205 (2004).
2. http://www.esa.int/esaME/iasi.html

3. D. Crisp, R. M. Atlas, F. M. Breon, L. R. Brown, J. P. Burrows, P. Ciais, B. J. Connor, S. C. Doney, I. Y. Fung, D. J. Jacob, C. E. Miller, D. O'Brien, S. Pawson, J. T. Randerson, P. Rayner, R. J. Salawitch, S. P. Sander, B. Sen, G. L. Stephens, P. P. Tans, G. C. Toon, P. O. Wennberg, S. C. Wofsy, Y. L. Yung, Z. Kuang, B. Chudasama, G. Sprague, B. Weiss, R. Pollock, D. Kenyon, and S. Schroll, The Orbiting Carbon Observatory (OCO) mission, *Adv. in Space Research* 34, 700–709 (2004).
4. L. S. Rothman, D. Jacquemart, A. Barbe, D. Chris Benner, M. Birk, L. R. Brown, M. R. Carleer, C. Chackerian Jr., K. Chance, L. H. Coudert, V. Dana, V. M. Devi, J.-M. Flaud, R. R. Gamache, A. Goldman, J. M. Hartmann, K. W. Jucks, A. G. Maki, J.-Y. Mandin, S. T. Massie, J. Orphal, A. Perrin, C. P. Rinsland, M. A. H. Smith, J. Tennyson, R. N. Tolchenov, R. A. Toth, J. Vander Auwera, P. Varanasi, and G. Wagner, The HITRAN 2004 molecular spectroscopic database, *J. Quant. Spectrosc. Radiat. Transfer* 96, 139-204 (2005).
5. S. A. Tashkun, V. I. Perevalov, J.-L. Teffo, A. D. Bykov, and N. N. Lavrentieva, CDSD-296, the carbon dioxide spectroscopic databank: version for atmospheric applications. XIV Symposium on High Resolution Molecular Spectroscopy, Krasnoyarsk, Russia, July 6–11, 2003; See also ftp://ftp.iao.ru/pub/CDSD-296/.
6. R. B. Wattson and L. S. Rothman, Direct numerical diagonalization: wave of the future, *J. Quant. Spectrosc. Radiat. Transfer* 48, 763–780 (1992).
7. Z. H. Yang, G. C. Toon, J. S. Margolis, and P. O. Wennberg, Atmospheric CO_2 retrieved from ground-based near IR solar spectra, *Geophys. Res. Lett.* 29, 1339-1343 (2002).
8. S. A. Tashkun, V. I. Perevalov, J.-L. Teffo, L. S. Rothman, and Vl. G. Tyuterev, Global fitting of $^{12}C^{16}O_2$ vibrational–rotational line positions using the effective Hamiltonian approach, *J. Quant. Spectrosc. Radiat. Transfer* 60, 785–801 (1998).
9. S. A. Tashkun, V. I. Perevalov, J.-L. Teffo, and Vl. G. Tyuterev, Global fitting of $^{12}C^{16}O_2$ vibrational–rotational line intensities using the effective operator approach, *J. Quant. Spectrosc. Radiat. Transfer* 62, 571–598 (1999).
10. S. A. Tashkun, V. I. Perevalov, J.-L. Teffo, A. D. Bykov, and N. N. Lavrentieva, CDSD-1000, the high-temperature carbon dioxide spectroscopic databank, *J. Quant. Spectrosc. Radiat. Transfer* 82, 165–196 (2003).
11. P. J. Rousseeuw and A. M. Leroy, *Robust regression and outlier detection*, (Wiley-Interscience, New York, 1987)
12. P. J. Rousseeuw and K. Van Driessen, Computing LTS regression for large data sets; http// www.agoras.ua.ac.be
13. R. J. Le Roy, Uncertainty, sensitivity, convergence, and rounding in performing and reporting least-squares fits, *J. Mol. Spectrosc.* 191, 223-231 (1998).
14. C. E. Miller and L. R. Brown, Near infrared spectroscopy of carbon dioxide I. $^{16}O^{12}C^{16}O$ line positions, *J.Mol.Spectrosc.* 228, 329-354 (2004).
15. C. E. Miller, M. A. Montgomerya, R. M. Onoratoa, C. Johnstonea, T. P. McNicholasa, B. Kovarica, and L. R. Brown, Near infrared spectroscopy of carbon dioxide. II: $^{16}O^{13}C^{16}O$ and $^{16}O^{13}C^{18}O$ line positions, *J.Mol.Spectrosc.* 228, 355-374 (2004).
16. V. Malathy Devi, D. C. Bennea, M. A. H. Smith, L. R. Brown, and M. Dulick, Multispectrum analysis of pressure broadening and pressure shift coefficients in the $^{12}C^{16}O_2$ and $^{13}C^{16}O_2$ laser bands, *J. Quant. Spectrosc. Radiat. Transfer* 76, 411-434 (2003).
17. Z. Majcherova, P. Macko, D. Romanini, V. I. Perevalov, S. A. Tashkun, J. L. Teffo, and A. Campargue, High-sensitivity CW-cavity ringdown spectroscopy of $^{12}CO_2$ near 1.5 μm, *J.Mol.Spectrosc*. 230, 1-21, (2005).

18. V. Malathy Devi, D. C. Benner, M. A. H. Smith, and C. P. Rinsland, Nitrogen broadening and shift coefficients in the 4.2–4.5-μm bands of CO_2, *J. Quant. Spectrosc. Radiat. Transfer* 76, 289-307 (2003).
19. L. P. Giver, L. R. Brown, C. Chackerian Jr., R. S. Freedman, The rovibrational intensities of five absorption bands of $^{12}C^{16}O_2$ between 5218 and 5349 cm^{-1}, *J. Quant. Spectrosc. Radiat. Transfer* 78, 417-436 (2003).
20. Y. Ding, P. Macko, D. Romanini, V. I. Perevalov, S. A. Tashkun, J. L. Teffo, S.-M. Hu, and A. Campargue, High sensitivity cw-cavity ringdown and Fourier transform absorption spectroscopies of $^{13}CO_2$, *J.Mol.Spectrosc.* 226, 146-160 (2004).
21. J. Vander Auwera, R. El Hachtouki, and L. R. Brown, Absolute line wavenumbers in the near infrared: $^{12}C_2H_2$ and $^{12}C^{16}O_2$, *Mol.Phys.* 100, 3563-3576 (2002)
22. F. Andre, M. Y. Perrin, and J. Taine, FTIR measurements of $^{12}C^{16}O_2$ line positions and intensities at high temperature in the 3700–3750 cm^{-1} spectral region, *J.Mol.Spectrosc.* 228, 187-205 (2004).
23. A. Amy-Klein, H. Vigue, Ch. Chardonnet, Absolute frequency measurement of $^{12}C^{16}O_2$ laser lines witha femtosecond laser comb and new determination of the $^{12}C^{16}O_2$ molecular constants and frequency grid, *J.Mol.Spectrosc.* 228, 206-212 (2004).
24. Y. Ding, E. Bertseva, and A. Campargue, The $2v_1+3v_3$ Triad of $^{12}CO_2$, *J.Mol.Spectrosc.* 212, 219-222 (2002).
25. Y. Ding, A. Campargue, E. Bertseva, S. A. Tashkun, V. I. Perevalov, Highly sensitive absorption spectroscopy of carbon dioxide by ICLAS-VeCSEL between 8800 and 9530 cm^{-1}, *J.Mol.Spectrosc.* 231, 117-123 (2005).
26. L. Wang, V. I. Perevalov, S. A. Tashkun, Y. Ding, and S.-M. Hu, Absolute line intensities of $^{13}C^{16}O_2$ in the 4200–8500 cm^{-1} region, *J.Mol.Spectrosc.* 234, 84-92 (2005).
27. J. Vander Auwera, C. Claveau, J. L. Teffo, S. A. Tashkun, and V. I. Perevalov, Absolute line intensities of $^{13}C^{16}O_2$ in the 3090-3920 cm^{-1} region, *J.Mol.Spectrosc.* in press
28. Ch. Chardonnet, A. van Lerberghe, and Ch. J. Bordé, Absolute frequency determination of super-narrow CO_2 saturation peaks observed in an external absorption cell, *Opt.Comm.* 58, 333-337 (1986).

THEORETICAL QUANTITATIVE SPECTROSCOPY: COMPUTER SIMULATION OF MOLECULAR SPECTRA

SERGEI N. YURCHENKO (yurchenko@mpi-muelheim.mpg.de),
JINGJING ZHENG (jjzheng@mpi-muelheim.mpg.de),
WALTER THIEL (thiel@mpi-muelheim.mpg.de)
Max-Planck-Institut für Kohlenforschung, Kaiser-Wilhelm-Platz 1, D–45470 Mülheim an der Ruhr, Germany

MIGUEL CARVAJAL (miguel.carvajal@dfa.uhu.es)
Departamento de Fisica Aplicada, Facultad de Ciencias Experimentales, Avda. de las FF.AA. s/n, Universidad de Huelva, 21071, Huelva, Spain

HAI LIN (hai.lin@cudenver.edu)
Department of Chemistry, University of Colorado at Denver, PO Box 173364, Denver, Colorado 80217, U. S. A.

PER JENSEN (jensen@uni-wuppertal.de)
FB C – Theoretische Chemie, Bergische Universität, D–42097 Wuppertal, Germany

Abstract. We present the results of theoretically simulating, by variational methods, rotation-vibration spectra of NH_3 and PH_3. The simulations carried out for NH_3 are based solely on *ab initio* calculations, i.e., they are purely theoretical and involve no fitting to experiment. The PH_3 simulations are made from a potential energy function refined to reproduce experimental data and from an *ab initio* dipole moment function. We show that our simulations reproduce observed rotation-vibration intensities with an accuracy approaching that obtained in fittings to these intensities in terms of models involving an effective dipole moment operator. Our results suggest that theoretical simulations of spectra are now close to attaining a level of accuracy where they can successfully compete with quantitative-spectroscopy measurements of intensities and thus assist in the interpretation of remote-sensing spectra.

Keywords: spectrum simulations, line intensities, NH_3, PH_3

1. Introduction

In atmospheric studies, remote-sensing techniques are important tools for determining molecular concentrations in the upper layers of the atmosphere. These techniques employ the methodology of high-resolution molecular spectroscopy;

A. Perrin et al. (eds.), Remote Sensing of the Atmosphere for Environmental Security, 171–183.

in principle the molecular concentrations are obtained from experimental molecular spectra. To determine a molecular concentration, or a column density, from the measured intensity of a molecular transition in emission or absorption, it is necessary to know the 'molecule-intrinsic' factors that influence the intensity, in particular the line strength (see below). Obviously line strength values can be obtained from laboratory measurements of intensities for molecules with known concentrations. Such measurements, however, appear to be exceedingly difficult. For example, for the molecules ozone O_3 and formaldehyde H_2CO, there exist several recent measurements of the intensities of the same molecular transitions whose results seriously disagree (Flaud, 2005). It is sometimes said that in present-day science, computer simulation of phenomena occurring in nature constitutes an alternative not only to experiment, but also to traditional theoretical work involving (simple) mathematical models. Computer simulations of rotation-vibration spectra are a potential alternative to the very difficult experimental intensity measurements. Also, they can assist in the assignment of complicated spectra, in locating 'dark' states, and in providing spectral information about molecules under conditions where the experiment is difficult.

In exploratory calculations, we have sought to assess the accuracy to which the simulation of rotation-vibration spectra can be carried out. As example molecules, we have chosen NH_3 and PH_3 for which there is a large amount of experimental wavenumber and intensity data available for comparison with the simulations. For selected bands of $^{14}NH_3$ and $^{31}PH_3$, we have made detailed simulations of the rotational structure. The calculations are carried out by means of recently developed computational procedures for describing the nuclear motion and are based on a high-level *ab initio* potential energy surface, and high-level dipole moment surfaces, for the electronic ground states of NH_3 and PH_3 [see Lin *et al.* (2002) and Yurchenko *et al.* (2003; 2005a; 2005b; 2005c; 2005d; 2005f)].

The paper is structured as follows: In Section 2 we give a very brief outline of the theory involved in the direct computer simulation of spectra by variational methods that we present here. Section 3 describes some of the results we have obtained, and Section 4 offers conclusions.

2. Theory

2.1. THE LINE STRENGTH

The intensities of electric dipole absorption transitions are determined by the absorption coefficient $\epsilon(\tilde{\nu})$ entering into the Lambert-Beer law [see, for example, Bunker & Jensen (2004)]; $\epsilon(\tilde{\nu})$ depends on the absorption wavenumber $\tilde{\nu}$. If we assume the absorbing molecules to be in thermal equilibrium at an absolute

temperature T, the integral of $\epsilon(\tilde{\nu})$ over an absorption line is given as

$$I(f \leftarrow i) = \int_{\text{Line}} \epsilon(\tilde{\nu})\, d\tilde{\nu} = \frac{8\pi^3 N_A \tilde{\nu}_{if}}{(4\pi\epsilon_0)3hc} \frac{\mathrm{e}^{-E_{\text{rve}}^{(n'',j'')}/kT}}{Q} \left[1 - \exp(-hc\tilde{\nu}_{if}/kT)\right] S(f \leftarrow i). \quad (1)$$

This expression is valid for the transition from the state i with energy $E_{\text{rve}}^{(n'',j'')}$ to the state f with energy $E_{\text{rve}}^{(n',j')}$, where $hc\tilde{\nu}_{if} = E_{\text{rve}}^{(n',j')} - E_{\text{rve}}^{(n'',j'')}$, N_A is the Avogadro constant, h is Planck's constant, c is the speed of light in vacuum, k is the Boltzmann constant, ϵ_0 is the permittivity of free space, and, finally, Q is the partition function defined as $Q = \sum_j g_j \exp(-E_j/kT)$, where g_j is the total degeneracy of the state with energy E_j and the sum runs over all energy levels of the molecule. Experimental values of $I(f \leftarrow i)$ are obtained by numerical integration of experimentally determined $\epsilon(\tilde{\nu})$-values.

The 'molecule-intrinsic' factor $S(f \leftarrow i)$ in Eq. 1 is called the *line strength*. It is given as

$$S(f \leftarrow i) = \sum_{\Phi_{\text{rve}}^{(n',j')}, \Phi_{\text{rve}}^{(n'',j'')}} \sum_{A=X,Y,Z} \left| \left\langle \Phi_{\text{rve}}^{(n',j')} \left| \mu_A \right| \Phi_{\text{rve}}^{(n'',j'')} \right\rangle \right|^2 \quad (2)$$

where $\Phi_{\text{rve}}^{(n',j')}$ and $\Phi_{\text{rve}}^{(n'',j'')}$ are eigenfunctions of the molecular Hamiltonian corresponding to the eigenvalues $E_{\text{rve}}^{(n',j')}$ and $E_{\text{rve}}^{(n'',j'')}$, respectively. In the case of degeneracies, that is if there is more than one eigenfunction $\Phi_{\text{rve}}^{(n',j')}$ (or $\Phi_{\text{rve}}^{(n'',j'')}$) corresponding to the eigenvalue $E_{\text{rve}}^{(n',j')}$ (or $E_{\text{rve}}^{(n'',j'')}$), we obtain the line strength by adding the individual transition probabilities for all transitions between the degenerate states; this is indicated by the sum over $\Phi_{\text{rve}}^{(n',j')}$ and $\Phi_{\text{rve}}^{(n'',j'')}$ in Eq. 2. In this equation, μ_A is the component of the molecular dipole moment operator along the A axis ($A = X$, Y, or Z); the XYZ axis system having origin at the molecular center of mass and space fixed orientation. The operator μ_A is given by $\mu_A = \sum_q e_q A_q$ with e_q and A_q as the charge and A coordinate of the qth particle in the molecule, where q runs over all nuclei and electrons.

The intensities of electric dipole emission transitions are determined from the Einstein coefficients [see, for example, Penner (1959) or Woodgate (1970)]; these coefficients are proportional to the line strength in Eq. 2 as explained in Section 2.2 of Yurchenko *et al.* (2005b).

In the Born-Oppenheimer approximation [see, for example, Bunker & Jensen (2000)], the rovibronic wavefunction of a molecule is expressed as

$$\Phi_{\text{rve}}^{(n,j)} = \Phi_{\text{elec}}^{(n)} \Phi_{\text{rv}}^{(n,j)} \quad (3)$$

where $\Phi_{\text{elec}}^{(n)}$ is the electronic wavefunction, depending on electronic and nuclear coordinates, and $\Phi_{\text{rv}}^{(n,j)}$ is the nuclear wavefunction, depending on the nuclear

coordinates only. The index n labels the electronic states, and j labels the rovibrational states associated with a given electronic state. The wavefunction $\Phi_{\rm elec}^{(n)}$ is an eigenfunction of the electronic Hamiltonian, obtained with the nuclei fixed in space, and the corresponding eigenvalue is the Born-Oppenheimer potential energy function $V_{\rm BO}$ which depends on the nuclear coordinates.

Having determined $V_{\rm BO}$ as a function of the nuclear coordinates in *ab initio* calculations, we solve the rotation-vibration Schrödinger equation

$$\hat{H}_{\rm rv}\Phi_{\rm rv}^{(n,j)} = E_{\rm rv}^{(n,j)}\Phi_{\rm rv}^{(n,j)}, \tag{4}$$

with

$$\hat{H}_{\rm rv} = \hat{T}_{\rm rv} + V_{\rm BO}, \tag{5}$$

where $\hat{T}_{\rm rv}$ is the kinetic energy operator associated with rotation and vibration.

As a first step towards computing the matrix elements in the expression for the line strength (Eq. 2), we express the space-fixed dipole moment components in terms of the components (μ_x, μ_y, μ_z) along the *molecule-fixed axes xyz*. This axis system is chosen such that it follows the rotational motion of the molecule; for details of the general theory see, for example, Papoušek & Aliev (1982), Bunker & Jensen (1998), or Sarka & Demaison (2000), and for the application to XY_3 molecules, see Yurchenko *et al.* (2005a). We have

$$\mu_A = \sum_{\alpha=x,y,z} \lambda_{\alpha A}\,\mu_\alpha, \tag{6}$$

where the $\lambda_{\alpha A}$ are direction cosines [see, for example, Bunker & Jensen (1998)] effecting the transformation between the *xyz* and *XYZ* axis systems.

When we consider the intensities of transitions within a single electronic state $\Phi_{\rm elec}^{(n)}$, they depend on the electronically averaged dipole moment

$$\bar{\mu}_\alpha^{(n)} = \left\langle \Phi_{\rm elec}^{(n)} \,|\, \mu_\alpha \,|\, \Phi_{\rm elec}^{(n)} \right\rangle_{\rm el}, \quad \alpha = x, y, z; \tag{7}$$

where the subscript 'el' indicates that integration is over the electronic coordinates only. The quantity $\bar{\mu}_\alpha$ depends on the nuclear coordinates and, for given values of these coordinates, we can calculate the value of $\bar{\mu}_\alpha$ by *ab initio* methods.

2.2. VARIATIONAL CALCULATIONS

Experimental intensity studies normally analyze the observed intensities in terms of a model involving an *effective Hamiltonian* and an *effective dipole moment operator* [see Papoušek & Aliev (1982) or the review articles by Aliev & Watson (1985) and Sarka & Demaison (2000), respectively]; these operators are obtained from the nuclear Hamiltonian $\hat{H}_{\rm rv}$ and the dipole moment components μ_A (A = X, Y, Z), respectively, by means of perturbation theory and contain parameters

whose values can be determined in fittings to experimental data. In a variational calculation we – at least initially – calculate the energies and intensities from first principles. We solve the Schrödinger equation in Eq. 4 by diagonalizing numerically (i.e., without the use of perturbation theory) a matrix representation of $\hat{H}_{\rm rv}$ set up in a suitable basis set. The potential energy function $V_{\rm BO}$ is represented by a suitable parameterized function, the parameter values being determined by fitting to a set of $V_{\rm BO}$-values obtained *ab initio*. In the present work, we are concerned with variational calculations for XY_3 pyramidal molecules, for which we choose the basis functions so that the rotation-vibration wavefunctions $|\Phi_{\rm rv}^{(n,j)}\rangle$ can be expressed as given in Eq. (65) of Yurchenko *et al.* (2005a):

$$|\Phi_{\rm rv}^{(n,j)}\rangle = \sum_{VK\tau_{\rm rot}} C_{VK\tau_{\rm rot}}^{(n,j)} |V\rangle\, |J\, K\, m\, \tau_{\rm rot}\rangle,\ K \geq 0, \tag{8}$$

where $C_{VK\tau_{\rm rot}}^{(n,j)}$ is an expansion coefficient obtained as an eigenvector component in the diagonalization of the Hamiltonian matrix (Yurchenko *et al.*, 2005a), and the vibrational basis functions $|V\rangle$ are

$$|V\rangle = \ |n_1\rangle\, |n_2\rangle\, |n_3\rangle\, |n_{\rm b}, l_{\rm b}, \tau_{\rm bend}\rangle\, |n_{\rm i}, J, K, \tau_{\rm inv}\rangle; \tag{9}$$

V is used as a short-hand notation for all the quantum numbers and symmetry labels n_1, n_2, n_3, $n_{\rm b}$, $l_{\rm b}$, $\tau_{\rm bend}$, $n_{\rm i}$, and $\tau_{\rm inv}$ that label the vibrational basis functions. All the functions $|J\, K\, m\, \tau_{\rm rot}\rangle$, $|n_1\rangle$, $|n_2\rangle$, $|n_3\rangle$, $|n_{\rm b}, l_{\rm b}, \tau_{\rm bend}\rangle$, and $|n_{\rm i}, J, K, \tau_{\rm inv}\rangle$ occurring in Eqs. 8-9, and the quantum numbers labeling them, are defined in detail in Yurchenko *et al.* (2005a): $|J\, K\, m\, \tau_{\rm rot}\rangle$ is a symmetrized rotational wavefunction defined in Eqs. (66) and (67) of Yurchenko *et al.* (2005a), $|n_1\rangle$, $|n_2\rangle$, and $|n_3\rangle$ are one-dimensional Morse oscillator eigenfunctions describing the stretching motion of the XY_3 molecule, $|n_{\rm b}, l_{\rm b}, \tau_{\rm bend}\rangle$ is a symmetrized eigenfunction of the two-dimensional harmonic oscillator modelling the small-amplitude bending motion, and $|n_{\rm i}, J, K, \tau_{\rm inv}\rangle$ is a symmetrized inversion basis function obtained by numerical solution of a zero-order inversion Schrödinger equation. Concerning the quantum numbers, it suffices to say here that each of the three quantum numbers $\tau_{\rm rot}$, $\tau_{\rm bend}$, and $\tau_{\rm inv}$ assumes the values 0 or 1 in such a way that the parity (Bunker & Jensen, 1998) of $|J\, K\, m\, \tau_{\rm rot}\rangle$ is $(-1)^{\tau_{\rm rot}}$, the parity of $|n_{\rm b}, l_{\rm b}, \tau_{\rm bend}\rangle$ is $(-1)^{\tau_{\rm bend}}$, and the parity of $|n_{\rm i}, J, K, \tau_{\rm inv}\rangle$ is $(-1)^{\tau_{\rm inv}}$.

As a prerequisite to computing line strengths from the variationally-determined wavefunctions in Eq. 8, we compute *ab initio* values of the electronically averaged dipole moment (Eq. 7) and fit analytical, parameterized functions through the computed values. We then simply insert Eqs. 6, 7, and 8 in the expression for the line strength (Eq. 2). The resulting expression is simplified by use of the techniques described, for example, in Chapter 14 of Bunker & Jensen (1998) and the simplified form can be used for computing the line strengths numerically. The application of this strategy to XY_3 pyramidal molecules is described in detail

by Yurchenko *et al.* (2005b; 2005c). Analogous work for triatomic molecules is described by Jensen & Špirko (1986) and by Jensen (1988) [see also Tennyson (2000) and references therein]. Having made the initial, *ab initio* calculation of molecular energies and line strengths we can, of course, refine the parameters of the analytical representations of the potential energy and the dipole moment components by fitting to experimental data.

In the variational approach to calculating intensities, *resonances* (i.e., energetically close-lying vibrational states) cause no problems. All resonances are explicitly treated in the variational calculation and, in consequence, the resulting intensity stealing (Bunker & Jensen, 1998) is accounted for. This is in contrast to the conventional theoretical approach involving an effective Hamiltonian and an effective dipole moment operator, where the theoretical model must normally be modified to describe the resonances of a particular molecule so that different models are sometimes required for isotopically substituted molecules.

3. Applications

We present here some results of applying our spectrum-simulation computer program to the molecules $^{14}NH_3$, $^{15}NH_3$, and $^{31}PH_3$. The calculations for $^{14}NH_3$ and $^{15}NH_3$ are based on the *ab initio* potential energy surface CBS**-51816 described in detail by Yurchenko *et al.* (2005d) [see also Lin *et al.* (2002)]. Further, we employ the *ab initio* ATZfc dipole moment function described by Yurchenko *et al.* (2005b; 2005c). Thus it should be noted that the NH_3 calculations presented here are purely theoretical; they do not involve any fitting to experiment.

The simulations are made with a basis set [see Yurchenko *et al.* (2005b)] defined by

$$P = 2(n_1 + n_2 + n_3) + n_i + n_b \leq 8, \tag{10}$$

where the principal quantum numbers n_1, n_2, n_3, n_i, and n_b are defined in connection with Eq. 9; we consider transitions involving states with $J \leq 18$. In calculating the integrated absorption coefficients from Eq. 1, we set $T = 295$ K, the temperature appropriate for the experimental spectra (Cottaz *et al.*, 2000; Fabian *et al.*, 1995; Kleiner *et al.*, 1995; Kleiner *et al.*, 1999) with which we compare the simulations, and we use a value of the partition function obtained at this temperature from the $J \leq 18$ term values calculated variationally below 6000 cm^{-1} [see Yurchenko *et al.* (2005b)].

In Fig. 1 we show simulations of the ν_1, ν_2, ν_3, and ν_4 fundamental absorption bands of $^{14}NH_3$. In these stick diagrams, the heights of the sticks represent integrated absorption coefficients computed from Eq. 1 in units of $cm^{-2}\,atm^{-1}$. The ν_1 and ν_3 bands are artificially separated according to the assignment of the upper state. That is, in the 3000–3800 cm^{-1} wavenumber region we plot in

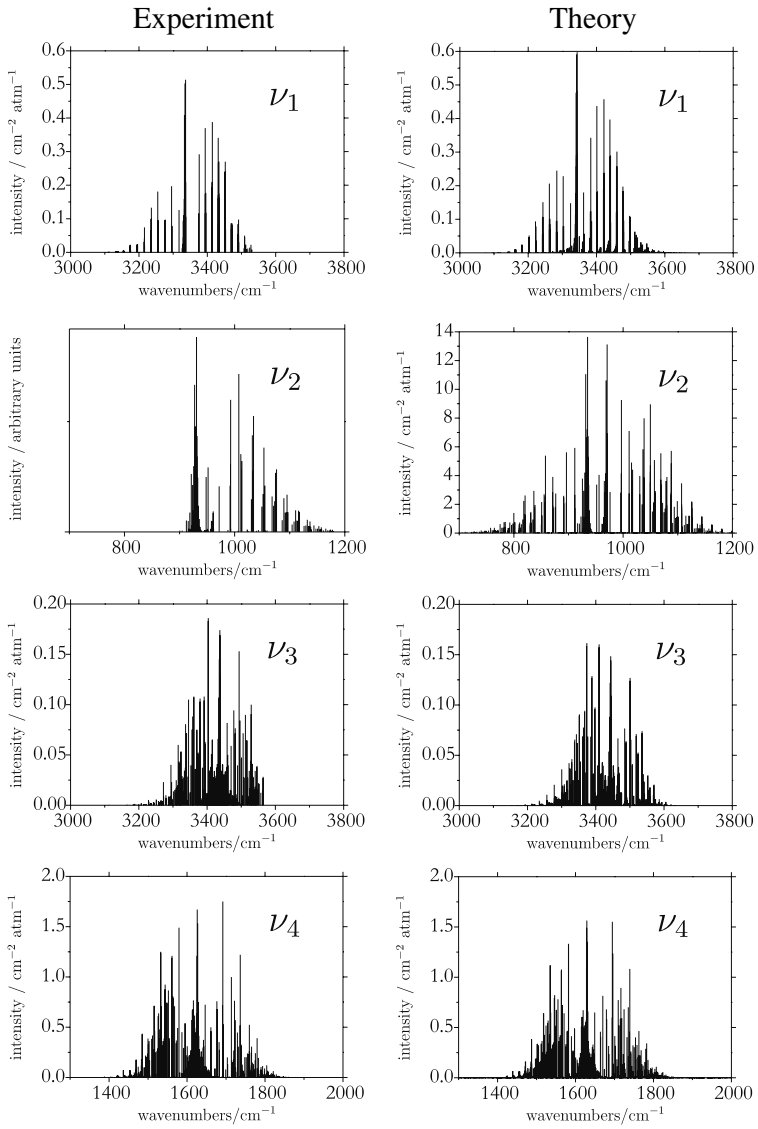

Figure 1. Comparison of simulated and observed absolute intensities for the ν_1 (Kleiner *et al.*, 1999), ν_2 (Fabian *et al.*, 1995), ν_3 (Kleiner *et al.*, 1999), and ν_4 (Cottaz *et al.*, 2000) bands of $^{14}NH_3$, where the references are to the experimental work providing the observed intensities. For the ν_2 band, the only available experimental intensity data are relative intensities for transitions in the wavenumber region 900–1180 cm^{-1} (Fabian *et al.*, 1995).

Table 1. Calculated integrated absorption coefficients $I_{\rm calc}$ (in $\rm cm^{-2}\,atm^{-1}$) for the strongest rotation-vibration transitions in the ν_1 bands of $^{14}NH_3$ and $^{15}NH_3$, together with the available observed transition wavenumbers $\tilde{\nu}_{\rm obs}$ (in $\rm cm^{-1}$) and intensities $I_{\rm obs}$ (in $\rm cm^{-2}\,atm^{-1}$) for $^{14}NH_3$ (Kleiner *et al.*, 1999). In the transition labels, J_i, K_i, and Γ_i (J_f, K_f, Γ_f) are the J-value, K-value, and $\boldsymbol{D}_{3h}$(M) rotation-vibration symmetry, respectively, of the initial (final) state. The relative deviation $\Delta(\%) = 100 \times |I_{\rm obs} - I_{\rm calc}|/I_{\rm obs}$.

						$^{14}NH_3$				$^{15}NH_3$
J_i	K_i	Γ_i	J_f	K_f	Γ_f	$\tilde{\nu}_{\rm obs}$	$I_{\rm obs}$	$I_{\rm calc}$	$\Delta(\%)$	$I_{\rm calc}$
3	3	A''	3	3	A'	3336.39046	0.514	0.598	16.3	0.598
3	3	A'	3	3	A''	3334.59825	0.503	0.591	17.5	0.592
6	6	A'	6	6	A''	3333.02520	0.408	0.482	18.1	0.489
6	6	A''	6	6	A'			0.477		0.484
3	0	A'	4	0	A''	3414.63633	0.388	0.457	17.8	0.430
2	0	A''	3	0	A'	3393.80352	0.370	0.437	18.1	0.415
4	0	A''	5	0	A'	3431.88520	0.341	0.397	16.4	0.369
1	0	A'	2	0	A''	3367.26976	0.292	0.343	17.5	0.330
4	4	E'	4	4	E''	3335.97602	0.278	0.287	3.2	0.300
4	3	A''	4	3	A'			0.294		0.302
4	3	A'	4	3	A''	3335.63576	0.277	0.291	5.1	0.299
4	4	E''	4	4	E'	3334.16807	0.272	0.283	4.0	0.296
5	0	A'	6	0	A''	3452.52248	0.270	0.302	11.9	0.280
4	3	A''	5	3	A'	3433.97824	0.270	0.290	7.4	0.277
4	3	A'	5	3	A''	3432.22513	0.267	0.287	7.5	0.274
5	5	E''	5	5	E'	3335.47572	0.258	0.261	1.2	0.276
5	5	E'	5	5	E''	3333.64481	0.245	0.258	5.3	0.272

separate displays the transitions to the ν_1 and ν_3 states, respectively. Each simulated band is compared to an 'experimentally derived' stick spectrum drawn with experimental values for transition wavenumbers and intensities taken from Kleiner *et al.* (1999) for ν_1 and ν_3, Fabian *et al.* (1995) for ν_2, and Cottaz *et al.* (2000) for ν_4. The experimentally derived spectra show only the transitions assigned in the respective experimental studies (Kleiner *et al.*, 1999; Fabian *et al.*, 1995; Cottaz *et al.*, 2000) and this explains why the experimental spectra generally contain less lines than the simulated ones. Note that the same absolute intensity scale is used for the two members of each theoretical/experimental spectrum pair except in the case of the ν_2 band, where the experimental results from Fabian *et al.* (1995) are given in arbitrary units as these authors report relative intensities only. In this case, we have drawn the 'Experimental' display such that the stick representing the strongest absorption transition has the same height as in the corresponding 'Theory' display. Furthermore, Fabian *et al.* (1995) recorded spectra in the wavenumber region 900–1180 $\rm cm^{-1}$ only; this explains the lack of lines below 900 $\rm cm^{-1}$ in the 'Experimental' ν_2 display of Fig. 1.

We calculate the vibrational transition moment of the ν_1 band as μ_{if}(Calc.) = 0.027 D, in very good agreement with the experimental value μ_{if}(Obs.) =

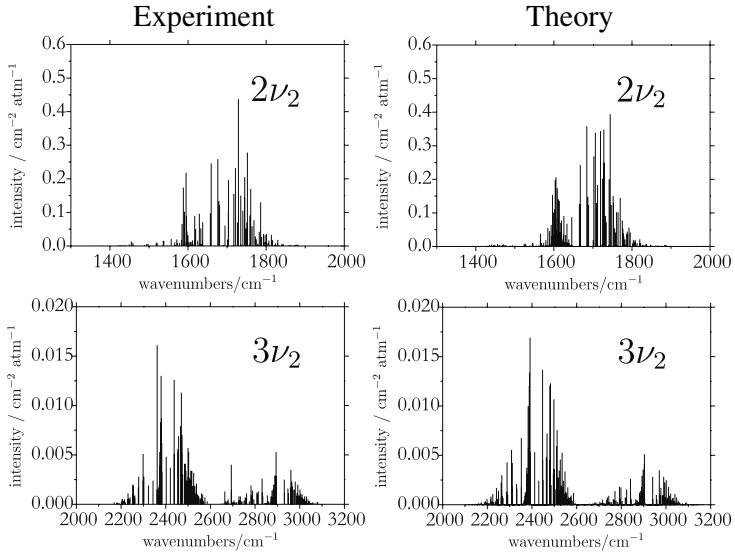

Figure 2. Comparison of simulated and observed absolute intensities for the $2\nu_2$ (Cottaz *et al.*, 2000) and $3\nu_2$ (Kleiner *et al.*, 1995) bands of $^{14}NH_3$, where the references are to the experimental work providing the observed intensities.

0.0262(1) D (Kleiner *et al.*, 1999), where we give in parentheses the quoted uncertainty in units of the last digit. For this band, we present in Table I the integrated absorption coefficients for the strongest, individual rotation-vibration transitions of $^{14}NH_3$ and $^{15}NH_3$. In the table, the states involved in the transitions are labeled by the 'standard' quantum numbers J and K together with Γ, the rovibrational symmetry in the molecular symmetry group $\boldsymbol{D}_{3h}$(M) (Bunker & Jensen, 1998) of NH_3. For $^{14}NH_3$, the calculated intensity values are compared with experimental values from Kleiner *et al.* (1999). Two strong calculated lines, ^{Q}Q transitions with (J_i, K_i) = (4,3) and (6,6), respectively, apparently have not been assigned since they cannot be found in Appendix 1 of Kleiner *et al.* (1999) but for completeness we include their calculated intensities in Table I. The calculated intensities in the table are systematically larger than the measured ones, in keeping with the fact that μ_{if}(Calc.) > μ_{if}(Obs.). For the 15 transitions in Table I, where a comparison between theory and experiment is possible, the percentage deviation $\Delta(\%)$ lies between 1.2% and 18.1% with an average of 11.2%.

In Fig. 2, we compare the simulations of the overtone band $2\nu_2$, and the second-overtone band $3\nu_2$, of $^{14}NH_3$ with experiment in a manner analogous to the comparisons in Fig. 1. For the $2\nu_2$ and $3\nu_2$ bands, the experimental intensities are determined by Cottaz *et al.* (2000) and Kleiner *et al.* (1995), respectively.

We compare in Fig. 3 simulations of the ν_2 and ν_4 fundamental absorption bands of $^{31}PH_3$ with experimental results (Brown *et al.*, 2002). The simulations

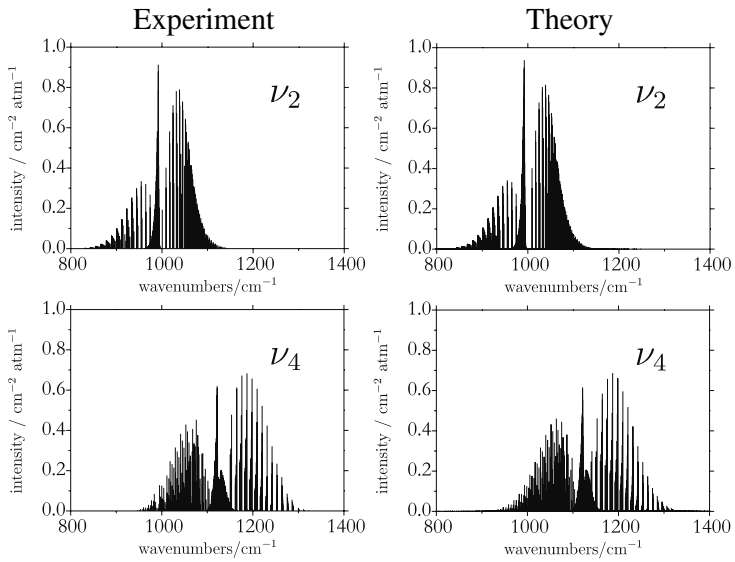

Figure 3. Comparison of simulated and observed absolute intensities for the ν_2 and ν_4 fundamental bands of PH_3. The observed intensities are from Brown *et al.* (2002).

are made with a 'spectroscopic' potential energy surface, obtained by adjusting the *ab initio* CCSD(T)/aug-cc-pVTZ potential energy surface from Wang *et al.* (2000) in a simultaneous fit to *ab initio* data and to the available, experimentally determined vibrational term values of PH_3. The PH_3 potential energy surface and the dipole moment surface employed in the present work will be described elsewhere (Yurchenko *et al.*, 2005e). The potential energy surface is a further refinement of that reported by Yurchenko *et al.* (2003) and used by Yurchenko *et al.* (2005f) to calculate the rotational energy structure for $J \leq 80$ in the vibrational ground state of PH_3. Yurchenko *et al.* (2005f) showed that the rotational levels form near-degenerate six-fold energy clusters analogous to the four-fold clusters formed in triatomic dihydrides H_2X (see, for example, Jensen (2000) and references therein). In the PH_3 calculations of the present work, we considered states with $J \leq 18$, and we used the basis set defined by Eq. 10.

4. Conclusion

One of the most important aims of our theoretical work is to assist the interpretation and understanding of high-resolution molecular spectroscopy experiments. We have already been able (Yurchenko *et al.*, 2005a) to provide assistance of this kind in that, with our calculated values for the rotational energies in the $4\nu_2^+$ vibrational state of $^{14}NH_3$, we could verify (and, for a few transitions, refute) the

tentative assignment to the $4\nu_2^+$ band made by Kleiner *et al.* (1999) for 55 weak transitions that they had observed in their experimental study of the ν_1, ν_3, and $2\nu_4$ bands of $^{14}NH_3$. Also, it is obvious that there is a high degree of similarity between the simulated and experimental spectra in Figs. 1-3 and, in view of this, we believe that with the computational method presented here, in conjunction with high-quality *ab initio* potential energy and dipole moment surfaces, we can simulate rotation-vibration spectra of XY_3 pyramidal molecules prior to observation with sufficient accuracy to facilitate the observation and interpretation of these spectra.

But are our theoretical absolute intensities sufficiently accurate that they can be of assistance in quantitative spectroscopy and in the interpretation of remote sensing experiments? At this point in time, we have not yet made extensive, line-by-line comparisons between the simulated and observed spectra. However, inspection of Figs. 1-3 and the figures in Yurchenko *et al.* (2005b; 2005c) suggests that the 10-20% deviations found for the transitions in Table I are not untypical, at least for the strong lines dominating the spectra. For comparison, Kleiner *et al.* (1999) have fitted their observed line intensities for the ν_1, ν_3, and $2\nu_4$ bands of $^{14}NH_3$ in terms of a model involving an effective dipole moment function. In these fittings, they obtain root-mean-square relative deviations of 5.0% for 165 lines in the ν_1 band, 11.9% for 325 lines in the ν_3 band, 13.9% for 123 lines in the $2\nu_4(\ell_4 = 0)$ band, and 14.6% for 328 lines in the $2\nu_4(\ell_4 = 2)$ band. Better agreement (1.5% for 399 lines in the ν_2 band and 2.1% for 580 lines in the ν_4 band) was achieved by Brown *et al.* (2002) in fittings of the ν_2/ν_4 'dyad' intensities for PH_3. The agreement with experiment obtained in our theoretical calculations is poorer than that obtained in fittings to experimental intensities, but not hopelessly so. Our results suggest that theoretical simulations of spectra are now approaching a level of accuracy where they can successfully compete with quantitative-spectroscopy measurements of intensities. They should thus be capable of resolving problems such as those mentioned by Flaud (2005), where different measurements of the intensities of the same transitions are in serious disagreement.

Acknowledgements

We acknowledge support from the European Commission through contract no. HPRN-CT-2000-00022 "Spectroscopy of Highly Excited Rovibrational States" (SPHERS) and contract no. MRTN-CT-2004-512202 "Quantitative Spectroscopy for Atmospheric and Astrophysical Research" (QUASAAR).

References

Aliev, M. R., and Watson, J. K. G. (1985) Higher-Order Effects in the Vibration-Rotation Spectra of Semirigid Molecules, In K. Narahari Rao (ed.), *Molecular Spectroscopy: Modern Research*, Vol. III, New York, Academic Press.

Brown, L. R., Sams, R. L., Kleiner, I., Cottaz, C., and Sagui, L. (2002) Line Intensities of the Phosphine Dyad at 10 μm, *J. Mol. Spectrosc.* **215**, 178-203.

Bunker, P. R., and Jensen, P. (1998) *Molecular Symmetry and Spectroscopy*, 2nd edition, Ottawa, NRC Research Press.

Bunker, P. R., and Jensen, P. (2000) The Born-Oppenheimer Approximation, In P. Jensen and P. R. Bunker (eds.), *Computational Molecular Spectroscopy*, Chichester, Wiley.

Bunker, P. R., and Jensen, P. (2004) *Fundamentals of Molecular Symmetry*, Bristol, IOP Publishing.

Cottaz, C., Tarrago, G., Kleiner, I., Brown, L. R., Margolis, J. S., Poynter, R. L., Pickett, H. M., Fouchet, T., Drossart, P., and Lellouch, E. (2000) Line Positions and Intensities in the $2\nu_2/\nu_4$ Vibrational System of $^{14}NH_3$ near 5-7 μm, *J. Mol. Spectrosc.* **203**, 285-309.

Fabian, M., Ito, F., and Yamada, K. M. T. (1995) N_2, O_2, and Air Broadening of NH_3 in ν_2 Band Measured by FTIR Spectroscopy, *J. Mol. Spectrosc.* **173**, 591-602.

Flaud, J.-M. (2005) Quantitative Spectroscopy and Atmospheric Measurements, Lecture at NATO-ARW No. 981624, "Remote Sensing of the Atmosphere for Environmental Security," Rabat, Morocco, 17-19 November 2005.

Jensen, P. (1988) Calculation of Rotation-Vibration Line Strengths for Triatomic Molecules Using a Variational Approach: Application to the Fundamental Bands of CH_2, *J. Mol. Spectrosc.* **132**, 429-457.

Jensen, P. (2000) An Introduction to the Theory of Local Mode Vibrations, *Mol. Phys.* **98**, 1253-1285.

Jensen, P., and Špirko, V. (1986) A New Morse-Oscillator Based Hamiltonian for H_3^+: Calculation of Line Strengths, *J. Mol. Spectrosc.* **118**, 208-231.

Kleiner, I., Brown, L. R., Tarrago, G., Kou, Q.-L., Picqué, N., Guelachvili, G., Dana, V., and Mandin, J.-Y. (1999) Positions and Intensities in the $2\nu_4/\nu_1/\nu_3$ Vibrational System of $^{14}NH_3$ near 3 μm, *J. Mol. Spectrosc.* **193**, 46-71.

Kleiner, I., Tarrago, G., and Brown, L. R. (1995) Positions and Intensities in the $3\nu_2/\nu_2 + \nu_4$ Vibrational System of $^{14}NH_3$ near 4 μm, *J. Mol. Spectrosc.* **173**, 120-145.

Lin, H., Thiel, W., Yurchenko, S. N., Carvajal, M., and Jensen, P. (2002) Vibrational Energies for NH_3 Based on High Level *ab initio* Potential Energy Surfaces, *J. Chem. Phys.* **117**, 11265-11276.

Papoušek, D., and Aliev, M. R. (1982) *Molecular Vibrational/Rotational Spectra*, Amsterdam, Elsevier.

Penner, S. S. (1959) *Quantitative Molecular Spectroscopy and Gas Emissivities*, Reading MA, Addison-Wesley.

Sarka, K., and Demaison, J. (2000) Perturbation Theory, Effective Hamiltonians and Force Constants, In P. Jensen and P. R. Bunker (eds.), *Computational Molecular Spectroscopy*, Chichester, Wiley.

Tennyson, J. (2000) Variational Calculations of Rotation-Vibration Spectra, In P. Jensen and P. R. Bunker (eds.), *Computational Molecular Spectroscopy*, Chichester, Wiley.

Wang, D., Shi, Q., and Zhu, Q.-S. (2000) An *ab initio* quartic force field for PH_3, *J. Chem. Phys.* **112**, 9624-9631.

Woodgate, G. K. (1970) *Elementary Atomic Structure*, Maidenhead, McGraw-Hill.

Yurchenko, S. N., Carvajal, M., Jensen, P., Herregodts, F., and Huet, T. R. (2003) Potential Parameters of PH_3 Obtained by Simultaneous Fitting of *ab initio* Data and Experimental Vibrational Band Origins, *Chem. Phys.* **290**, 59-67.

Yurchenko, S. N., Carvajal, M., Jensen, P., Lin, H., Zheng, J. J., and Thiel, W. (2005a) Rotation-Vibration Motion of Pyramidal XY_3 Molecules Described in the Eckart Frame: Theory and Application to NH_3, *Mol. Phys.* **103**, 359-378.

Yurchenko, S. N., Thiel, W., Carvajal, M., Lin, H., and Jensen, P. (2005b) Rotation-Vibration Motion of Pyramidal XY_3 Molecules Described in the Eckart Frame: The Calculation of Intensities with Application to NH_3, *Adv. Quant. Chem.* **48**, 209-238.

Yurchenko, S. N., Carvajal, M., Lin, H., Zheng, J. J., Thiel, W., and Jensen, P. (2005c) Dipole Moment and Rovibrational Intensities in the Electronic Ground State of NH_3: Bridging the Gap Between *ab initio* Theory and Spectroscopic Experiment, *J. Chem. Phys.* **122**, 104317/1-14.

Yurchenko, S. N., Zheng, J. J., Lin, H., Jensen, P., and Thiel, W. (2005d) Potential Energy Surface for the Electronic Ground State of NH_3 Up to 20000 cm^{-1} Above Equilibrium, *J. Chem. Phys.* **123**, 134308/1-14.

Yurchenko, S. N., Carvajal, M., Jensen, P., and Thiel, W. (2005e) *Ab initio* Dipole Moment and Theoretical Rovibrational Intensities in the Electronic Ground State of PH_3, *to be published.*

Yurchenko, S. N., Thiel, W., Patchkovskii, S., and Jensen, P. (2005f) Theoretical Evidence for the Formation of Rotational Energy Level Clusters in the Vibrational Ground State of PH_3, *Phys. Chem. Chem. Phys.* **7**, 573-582.

RECENT RESULTS ON INFRARED MOLECULAR LINE BROADENING AND SHIFT PARAMETERS

MARY ANN H. SMITH*
Science Directorate
NASA Langley Research Center
Hampton, VA 23681-2199 U.S.A.

*To whom correspondence should be addressed. Mary Ann H. Smith, NASA Langley Research Center, Mail Stop 401A, Hampton, VA 23681-2199 U.S.A.; e-mail: Mary.Ann.H.Smith@nasa.gov

Abstract. Infrared instruments designed to monitor atmospheric pollutants from space use observed radiances in specific spectral regions for retrievals of global distributions and atmospheric concentration profiles of the gases of interest, including CO, CH_4, O_3, HCN, NO_2 and H_2O. However, particularly for the troposphere, errors in the spectral line broadening and shift parameters and in the line shape models used in the "forward calculation" can contribute significantly to the total errors in retrievals of atmospheric gas concentration profiles. Line parameters in the HITRAN database for many of the gases mentioned above were significantly updated in the 2000 and 2004 editions. Nevertheless, uncertainties remain in some spectral regions, particularly in the understanding of line shapes, line mixing, and the temperature dependences of line broadening and shift parameters. The recent updates of broadening and shift parameters in the spectroscopic databases are reviewed, and new laboratory results are discussed.

Keywords: infrared spectroscopy, remote sensing, line parameters, databases

1. Introduction

Several instruments in NASA's Earth Observing System (EOS) focus on monitoring tropospheric pollutants and greenhouse gases (CO, CH_4, O_3, NO_2 and H_2O). These include MOPITT (Measurements Of Pollution In The

A. Perrin et al. (eds.), Remote Sensing of the Atmosphere for Environmental Security, 185–201.

Troposphere) on the Terra satellite, AIRS (Atmospheric Infrared Sounder) on the Aqua satellite, and TES (Tropospheric Emission Spectrometer) on the Aura satellite. High-resolution space-based infrared instruments such as ATMOS (Atmospheric Trace Molecule Spectroscopy) have measured other species such as HCN which is a marker of biomass burning (Notholt et al., 2003). The current EOS missions have benefited from remote-sensing expertise developed during earlier missions such as the highly successful Upper Atmosphere Research Satellite (UARS).

It has been shown (Smith and Gordley, 1983) that uncertainties in line broadening and shift parameters propagate into retrievals of stratospheric ozone concentrations. For remote sensing of the troposphere, where ambient pressures are typically in the 100 mb – 1000 mb range, errors in the spectral line broadening and shift parameters and in the line shape models used in the "forward calculation" can contribute significantly to the total errors in retrievals of concentration profiles for most species of interest. Since temperatures can vary from below 200 K at the tropopause to above 300 K near the Earth's surface, the temperature dependences of line broadening and shift parameters must also be reasonably accurate in the "forward calculation".

Line parameters in the HITRAN database for many of the gases mentioned above were significantly updated in the 2000 (Rothman et al., 2003) and 2004 (Rothman et al., 2005) editions. Nevertheless, uncertainties remain in some spectral regions, particularly in the understanding of the line broadening and shift parameters, line shapes, and line mixing. The temperature-dependences of line widths and shifts are not well-known in many cases. Departures from the standard Lorentz and Voigt line shapes at low temperatures have been observed for a few CO and CH_4 infrared transitions in laboratory diode laser studies, but they have not been assessed for larger spectral regions. Line mixing has been observed in laboratory spectra of some bands of CO_2, CO, and CH_4, and mixing has been recently observed in a few H_2O transitions. However, line mixing has not yet been examined for other molecular bands of atmospheric interest.

In this paper the recent updates of broadening and shift parameters in the spectroscopic databases will be reviewed, and new laboratory results for HCN, NO_2, H_2O, O_3 and CH_4 will be discussed.

2. A brief review of terminology

The following several paragraphs and equations describe the broadening and shift parameters and their temperature dependences using notation originated by the late K. Narahari Rao (Smith et al., 1985;Smith et al., 1992b). These definitions are implemented in the multispectrum nonlinear

least-squares fitting algorithm (Benner et al., 1995) used in most of the analyses presented here.

The Lorentz halfwidth and pressure-induced shift of an air-broadened spectral line, and their temperature dependences, are given by

$$b_L(p,T) = p\left[b_L^0(air)(p_0,T_0)(1-\chi)\left[\frac{T_0}{T}\right]^{n1} + b_L^0(self)(p_0,T_0)\chi\left[\frac{T_0}{T}\right]^{n2}\right] \tag{1}$$

$$\nu = \nu_0 + p\left[\delta^0(air)(1-\chi) + \delta^0(self)\chi\right] \tag{2}$$

$$\delta^0(T) = \delta^0(T_0) + \delta'\left[T - T_0\right]. \tag{3}$$

In the above equations, $b_L{}^0$ and δ^0 represent the pressure broadening and pressure-induced shift coefficients (cm^{-1} atm^{-1} at 296 K), respectively. b_L (p, T) is the Lorentz halfwidth (cm^{-1}) of the spectral line at pressure p and temperature T, and $b_L{}^0(Gas)(p_0, T_0)$ is the Lorentz halfwidth of the line at the reference pressure p_0 (1 atm) and temperature T_0 (296 K) and *Gas* is either *air* or *self* (the absorbing gas). χ is the ratio of the partial pressure of the absorbing gas to the total pressure of the gas mixture. The unitless temperature dependence exponents of the pressure-broadening coefficients are given by *n1* and *n2*, for air and, respectively. $\delta^0(T)$ and $\delta^0(T_0)$ represent the pressure-induced shift coefficients at T and T_0 (296 K), respectively. The temperature dependence of the pressure induced shift coefficient is δ'. This linear expression for the temperature dependence of the shift was adopted (Smith et al., 1992a) to allow for the possibility that the sign of the shift could change with temperature.

In the absence of direct measurements, air-broadening and shift parameters can be calculated from laboratory measurements of N_2- and O_2-broadening and shift parameters, for example:

$$b_L{}^0(air)(p_0,T_0) = 0.79 \times b_L{}^0(N_2)(p_0,T_0) + 0.21 \times b_L{}^0(O_2)(p_0,T_0). \tag{4}$$

However, a directly-measured air-broadening or shift parameter is preferable because it carries the uncertainty from only one set of measurements, while the parameter calculated from N_2- and O_2-broadening measurements incorporates the uncertainties of two sets of measurements.

Collisional line mixing causes modification of the Lorentz line shape when transitions are close enough to have overlapping profiles. In situations where it is not known which lines are mixing with each other, for

sufficiently low gas pressures and sufficient separation between spectral lines, the Rosenkranz formulation (Rosenkranz, 1975) may be used to calculate the spectrum. In this formulation the absorption is given by the addition of line contributions in which line mixing is taken into account through first order coefficients $Y_l^{Gas-X}(T)$, where *Gas* is the absorber and *X* is the broadener.

For higher pressures more typical of those near the Earth's surface, it is usually necessary to use the relaxation matrix in calculating the absorption spectrum. The practical details of this calculation have been reviewed elsewhere (Levy et al., 1992). The diagonal elements of the relaxation matrix *W* are related to the Lorentz widths b_{Lj} and pressure-induced shifts δ_j of the individual transitions as shown in Eq. (5).

$$Wjj = b_{Lj} + \boldsymbol{i}\,\delta_j \tag{5}$$

where $\boldsymbol{i}$ is the square root of −1. If the off-diagonal matrix elements of *W* are set to zero, the line shape factor reduces to the sum of N Lorentz profiles, where N is the number of lines that are assumed to be mixing. Nonzero values of off-diagonal elements are in the same units as the Lorentz halfwidth and the pressure-induced shift, and these off-diagonal elements create the line mixing profile. Like the Lorentz widths and pressure-induced shifts, the off-diagonal relaxation matrix elements are proportional to pressure and temperature.

Each pair of lines in a mixed set has two corresponding off-diagonal elements in the relaxation matrix, one above the diagonal and one below the diagonal. In thermodynamic equilibrium these elements are related by the detailed balance shown in Eq. (6).

$$W_{jk} = W_{kj}\frac{\rho_j}{\rho_k} \tag{6}$$

where ρ_j and ρ_k are energy densities calculated via Boltzmann terms involving the lower state energy of each transition. If only two lines are mixing, as has been observed in selected cases for H_2O (Brown et al., 2005), the relative values of W_{jk} and W_{kj} can be constrained by Eq. (6), allowing one to solve for a single parameter in the analysis of laboratory spectra. The situation is more complex if three or more lines are mixing, as is typical in Q branches of linear molecules. It should be noted that symmetry forbids line mixing between transitions with different statistical weights.

3. Updates of HITRAN 2004 broadening and shift parameters

Laboratory spectroscopic studies carried out at NASA Langley Research Center and at Jet Propulsion Laboratory in support of past (ATMOS, UARS) and current (AQUA and AURA) missions have contributed significantly to the updating of line broadening and shift parameters for the 2004 edition of the HITRAN database. These updates are documented in the HITRAN journal article (Rothman et al., 2005) as well as in a number of individual publications.

3.1. CARBON MONOXIDE (CO)

In response to the TES science team's stated requirements for line parameter accuracies, the quality of the HITRAN 2000 database (Rothman et al., 2003) for CO was evaluated in light of recent laboratory studies. Key problems with the HITRAN 2000 database were that a too-low constant value (n = 0.6) had been assumed for the temperature-dependence exponent of air broadening, and that all pressure-induced CO line shifts by air were zero.

A new CO database was written for the 5 μm region used by TES. The air broadening and shift parameters incorporated the results of several recent laboratory studies (Regalia-Jarlot et al., 2005; Sung and Varanasi, 2004; Zou and Varanasi, 2002), along with an improved fit to a large collection of self-broadening measurements. The TES linelist has been used as the basis for updating all CO broadening and shift parameters for the 2004 edition of HITRAN.

3.2. HYDROGEN CYANIDE (HCN)

The HCN air-broadened widths on the HITRAN database from 1986 through 2000 were scaled room-temperature N_2-broadening lab measurements (Smith et al., 1984) and included a typographical error in R branch values. In the absence of available measurements, a constant value (n = 0.5) had been assumed for the temperature-dependence exponent of air broadening. All pressure-induced line shifts by air and all HCN self-broadening coefficients had been set to zero by default.

In the new HCN database air broadened widths and their temperature dependences are based primarily on recent infrared measurements (Malathy Devi et al., 2004; Rinsland et al., 2003), and the air-induced shifts have been added for the bands measured. The average value of new air-broadening temperature-dependence exponents is closer to 0.8, significantly larger than the HITRAN 2000 value. Measured HCN self-broadening

coefficients from at least six recent laboratory studies were fit to obtain values that could be assigned to all HCN transitions on the 2004 database. These self-broadening coefficients are significantly different from zero, varying from around 0.15 cm^{-1} atm^{-1} at high J″ values to over 1.2 cm^{-1} atm^{-1} near J″ = 10.

3.3. METHANE (CH_4)

A major update of methane parameters in the 500 to 5500 cm^{-1} region (Brown et al., 2003) became available to HITRAN users in 2001 and has been carried forward into the 2004 edition. Measured self- and air-broadened widths and air-broadened pressure-induced frequency shifts were inserted on a line-by-line basis for both CH_4 and CH_3D, and empirical estimates were used to assign these parameters for unmeasured transitions. For this update, the temperature dependence exponents of the air-broadened widths were estimated by averaging measured values (Malathy Devi et al., 1994;Smith et al., 1992a) according to *m*, where *m* is the lower state *J* for *P* and *Q* branch transitions and the upper state *J* for *R* branch transitions.

3.4. NITROGEN DIOXIDE (NO_2)

The NO_2 air-broadening and shift parameters on the HITRAN database through 2000 had similar issues as for HCN and CO, in that a constant value (n = 0.5) had been assumed for the temperature-dependence exponent of air broadening and all air-induced line shifts had been set to zero. The air-broadening coefficients had been primarily based on about 100 N_2-broadening laboratory measurements with large uncertainties and very few measurements of the same transition by more than one laboratory. The new NO_2 database incorporates recent air broadening and shift measurements with temperature dependences for over 1000 ν_3 transitions (Benner et al., 2004) obtained using a multispectrum fitting technique to analyze 27 spectra simultaneously in selected regions. These measured temperature-dependence exponents average about 0.75, larger than the previous HITRAN default value (0.5), but smaller than the average value (about 1.0) from the few previous available studies (Malathy Devi et al., 1982;May and Webster, 1990).

3.5. OZONE (O_3)

The empirical O_3 air-broadened widths and temperature dependences developed for the MIPAS database, based on N_2- and O_2-broadening measurements (Wagner et al., 2002), were used in the HITRAN 2004

database to replace the "scaled calculations" from previous editions. While the air-broadened widths agree with our laboratory measurements (Malathy Devi et al., 1997; Smith et al., 1994a; Smith et al., 1994b; Smith et al., 1997) within 5%, the temperature-dependence exponents show larger disagreements. Mean air-induced line shift values from our laboratory studies were assigned to transitions in bands where shifts had been measured (ν_1, ν_2, ν_3, $\nu_1+\nu_3$, $3\nu_3$) but remained set to zero for other bands. Empirical polynomial expressions fit to experimental results for the ν_1, ν_2, $\nu_2+\nu_3$, $\nu_1+\nu_3$, and $2\nu_3$ bands (Malathy Devi et al., 1997; Smith et al., 1991; Smith et al., 1997) were used to assign self-broadened widths to all ozone transitions based on the rotational quantum numbers J″ and K_a″.

3.6. WATER VAPOR (H_2O)

While the air-broadening and shift parameters for H_2O transitions on the HITRAN database through 2000 had been continuously updated as new laboratory measurements became available, reliable estimates of the air-broadening temperature-dependence exponents were inhibited by the lack of measurements for many transitions. Our recent laboratory study (Toth et al., 2006) determined *n*-values for over 500 transitions in the 6-μm region from 31 air-broadened H_2O spectra recorded at 241 K to 388 K. Average $|m|$-dependent *n*-values were determined ($m = -J''$ for $\Delta J = -1$, $m = J''$ for $\Delta J = 0$, and $m = J''+1$ for $\Delta J = +1$), and these values (ranging from $n = 0.78$ at $|m| = 1$ to n ~ 0.4 for $|m| > 10$) have been applied to all assigned H_2O transitions in the HITRAN 2004 database.

4. New results

Several recently-completed and ongoing laboratory spectroscopic studies at NASA Langley Research Center and at Jet Propulsion Laboratory are providing new results that are likely to be incorporated in updates of the HITRAN database in the near future.

4.1. HYDROGEN CYANIDE (HCN)

The HCN air-broadened widths, temperature dependences, and shifts in the 2004 HITRAN database are based on our recent measurements in the ν_1 band system at 3-μm (Rinsland et al., 2003) and in the $2\nu_2$ band system at 7-μm (Malathy Devi et al., 2004). Both of these are parallel bands. We have now completed analysis of air- and self-broadening and shift parameters in the ν_2 fundamental band system at 14-μm (Bouanich et al., 2005; Malathy Devi et al., 2005), including the first experimental

determinations of the temperature dependences of HCN self-broadened widths. Because of severe line overlap occurring at high pressures, *Q* branches (of the $H^{12}C^{14}N$ ν_2 as well as the various isotopomers and hot bands) had to be excluded from the spectral fits, and the full set of broadening and shift parameters were determined only for transitions up to $|m| = 28$ in the *P* and *R* branches of the ν_2 band of $H^{12}C^{14}N$.

While the air- and self-broadening coefficients in the ν_2 band do not differ significantly from those measured in the ν_1 and $2\nu_2$, it is interesting to compare the temperature exponents and the pressure-induced line shifts (Figs. 1 and 2).

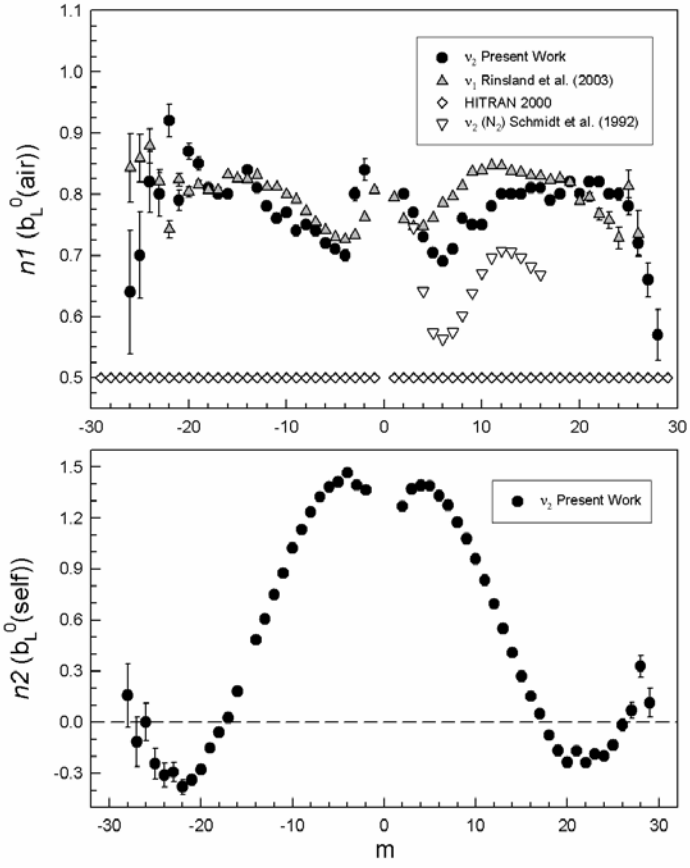

Figure 1. Temperature-dependence exponents of air-broadened (upper panel) and self-broadened (lower panel) HCN transitions (Malathy Devi et al., 2005).

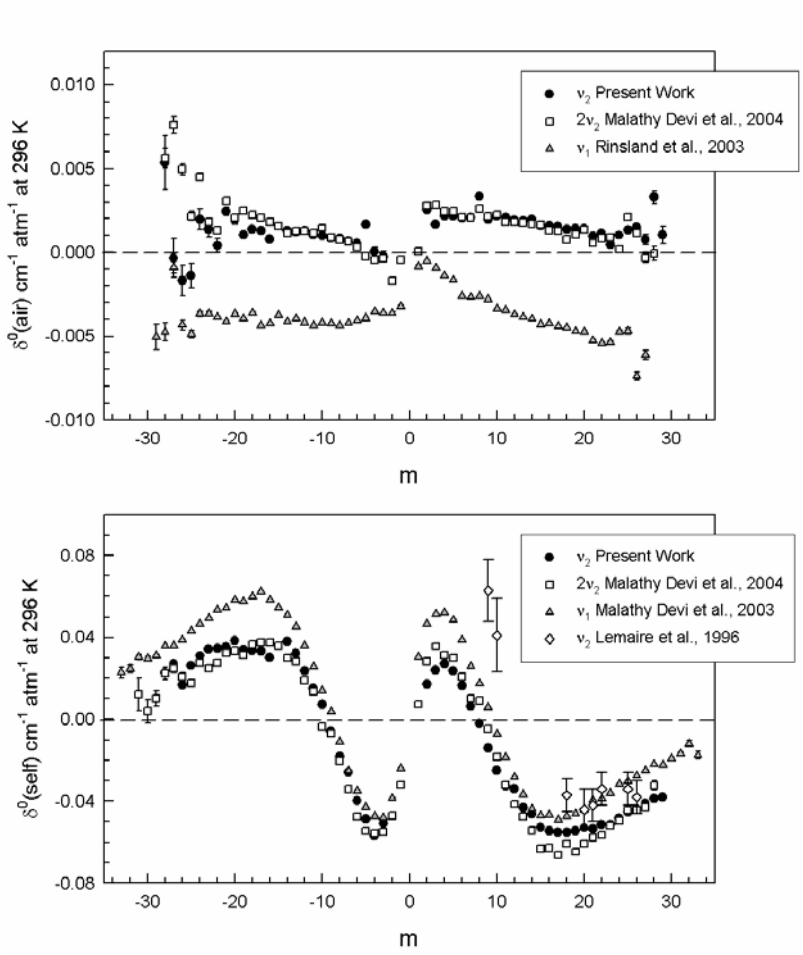

Figure 2. Comparison of measured air- (upper panel) and self-induced (lower panel) line shifts in three bands of HCN (Malathy Devi et al., 2005).

In both figures the differences in magnitudes and *m*-dependence between the self- and air-broadening values of *n* and δ^0 are quite obvious. In Fig. 1 we see that while the air-broadening *n* exponents for the ν_1 and ν_2 bands are similar, the R branch minimum value occurs for a higher m value in the ν_2 band, and that this minimum value occurs as the same *m* for both air-broadening (Malathy Devi et al., 2005) and N_2-broadening (Schmidt et al., 1992). In Fig. 2 we notice that for both air-and self-shifts, the measured values for the ν_2 and $2\nu_2$ bands are nearly identical. The self-shifts for all three bands, including some earlier ν_2 measurements (Lemaire et al., 1996), exhibit a similar *m*-dependence, while the air-shifts in the ν_1 band are quite different from those in the ν_2 and $2\nu_2$ bands.

4.2. OZONE (O_3) AIR-BROADENING AND SHIFTS

The strong 9.6-μm bands of O_3 are used by many infrared remote-sensing experiments for retrievals of terrestrial atmospheric ozone concentration profiles. Previous measurements of the temperature-dependence of air-broadening parameters for O_3 (Larsen et al., 2001; Malathy Devi et al., 1997; Smith et al., 1997) focused on the ν_1, ν_2 and rotational bands. Low-temperature studies in the ν_3 band (Spencer et al., 1992; Spencer et al., 1993; Wagner et al., 2002) measured N_2-broadened and O_2-broadened widths separately and did not report the corresponding pressure-induced line shifts. We are analyzing a set of 31 high-resolution self- and air-broadened O_3 spectra covering the ν_3 band at temperatures from 160 to 300 K. To date we have reported broadening and shift parameters and their temperature dependences for 41 selected transitions in the P branch of this band (Smith et al., 2005). These transitions lie in the spectral region between 1016 and 1025 cm^{-1}, and their lower state quantum number ranges are $J'' = 15 – 26$ and $K_a'' = 0 – 11$.

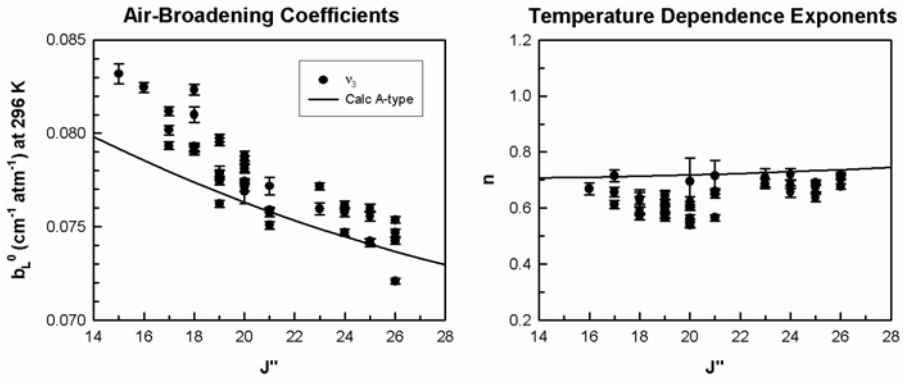

Figure 3. Measured air-broadening coefficients and their temperature dependences in the ν_3 band of O_3 (Smith et al., 2005) compared to values for A-type transitions (solid curve) calculated using the empirical polynomials of Wagner et al. (2002).

In Fig. 3, where the air-broadening coefficients and their temperature dependences are plotted as functions of J'' along with the calculated values (Wagner et al., 2002) that were adopted for HITRAN 2004, it appears that the majority of measured widths are above the calculated curve and nearly all of the measured *n* values are below the calculated curve. However, due to the limited number of transitions we have analyzed to date, this comparison is not definitive. Comparison of our ν_3 results with those for transitions with the same lower-state quantum numbers in the B-type rotational, ν_2 and ν_1 bands (Larsen et al., 2001; Malathy Devi et al., 1997; Smith et al., 1997) indicates that air-broadened widths in the rotational band and the three vibration-rotation fundamental bands are in agreement within

the absolute uncertainties of the measurements (typically 5% or better). Air-induced shifts measured in the three fundamental bands are, within their uncertainties, consistent with each other. Comparison of the present ν_3 widths and shifts with our previous results in the A-type $3\nu_3$ band (Smith et al., 1994a; Smith et al., 1994b) shows no discernable vibrational dependence of the widths, but the $3\nu_3$ shifts are significantly larger than those observed in the ν_3 band.

4.3. WATER VAPOR (H_2O) LINE MIXING

Line mixing has been observed and quantified for two pairs of transitions in the ν_2 fundamental band of H_2O (Brown et al., 2005). The characteristic residuals of line mixing were observed in least-squares fits of high-resolution FTS spectra of self-broadened H_2O at pressures up to 29 Torr

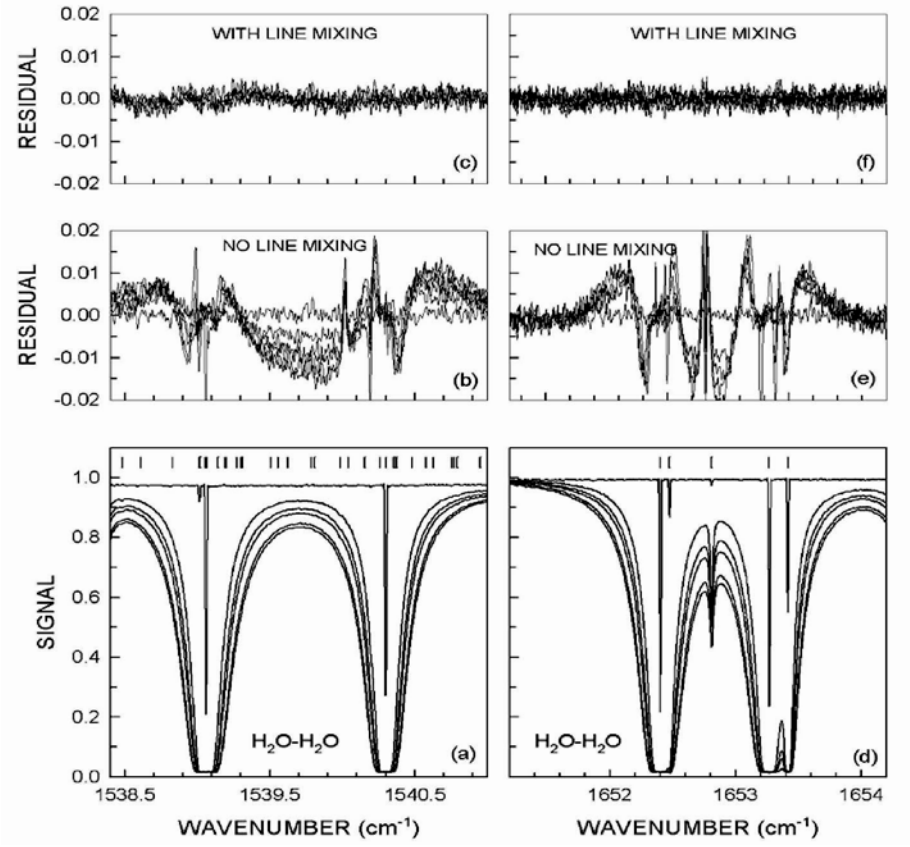

Figure 4. Observed spectra and residuals from multispectrum fits of six self-broadened H_2O spectra recorded at pressures between 0.01 and 29 Torr. Results are shown for the P branch pair of lines on the left, and the R branch pair on the right. Observed spectra are shown in panels (a) and (d) along with tic marks indicating line positions. The middle panels (b) and (e) show residuals from fitting the spectra *without* line mixing, and the top panels (c) and (f) show the residuals from fits *with* line mixing.

and mixtures of H_2O with H_2, He, CO_2, N_2, O_2 and air at pressures up to 999 Torr. The positions and rotational assignments of the four lines (in terms of the rotational quantum numbers J, K_a and K_c) are given as follows:

- *P branch lines*: (1 0 1)←(2 1 2) at 1539.061 cm^{-1} mixing with (2 1 2)←(3 0 3) at 1540.300 cm^{-1};
- *R branch lines*: (3 0 3)←(2 1 2) at 1652.400 cm^{-1} mixing with (2 1 2)←(1 0 1) at 1653.267 cm^{-1}.

For each broadening gas, groups of three to seven spectra were analyzed using multispectrum fitting (Benner et al., 1995) to determine halfwidths, pressure-induced shifts and off-diagonal relaxation matrix elements. An example of the fit residuals with and without line mixing is shown for self-broadened H_2O in Fig. 4. Since all of the spectra had been recorded with samples near room temperature, the temperature dependences of the broadening, shift, and line mixing parameters could not be determined. However, it was possible to compare the mixing parameters retrieved for the various broadening gases. For the two pairs of ν_2 transitions analyzed, the largest mixing effects were observed for self-broadening and H_2-broadening, and the smallest effects were found for He-broadening. While inclusion of line mixing in the fits did not significantly affect the retrieved line intensities and widths (except for self- and H_2-broadening), the retrieved values of the pressure-induced shifts were affected by mixing for all broadeners except He.

Although this study examined only two pairs of transitions in the ν_2 band of H_2O, it is expected that additional mixed pairs will be found through further analysis of high-resolution spectra of H_2O and HDO.

4.4. METHANE (CH_4) LINE MIXING

At the request of the TES science team, we undertook an investigation of line mixing in the ν_4 band of methane near 7.6 μm. Line mixing has not previously been investigated in this band. Our previous analysis of the temperature dependence of air- and N_2-broading in this CH_4 band (Smith et al., 1992a) had been completed before the multispectrum technique (Benner et al., 1995) was developed; thus the present study also became an opportunity to compare the results of single-spectrum and multispectrum analyses of the same data. While the work is currently in progress, a few preliminary results have been obtained.

Fitting of 10 self-broadened CH_4 spectra, recorded at room temperature and pressures up to 450 Torr, in the region of the ν_4 Q branch revealed the characteristic residual signature of line mixing when the fits were carried out using only the Voigt line shape. Including first-order Rosenkranz

mixing coefficients for 75 Q branch lines significantly reduced the residuals of the fit. A speed dependent Voigt line shape function was then added, but this resulted in no further improvement in the residuals.

Multispectrum fits of more than 20 air-broadened CH_4 spectra, recorded at temperatures between 210 K and 314 K and broadening gas pressures between 50 and 550 Torr (Smith et al., 1992a), have been carried out for selected R-branch manifolds in the ν_4 band. The air-broadened widths and temperature dependences, as well as shifts of unmixed lines, retrieved using the multispectrum fits are in excellent agreement with the earlier values determined from single-spectrum fits. However, the statistical errors of the multispectrum results are about an order of magnitude smaller. To date, line mixing has been analyzed and relaxation matrix elements retrieved for a pair of F species transitions in the R(3) manifold and another pair in the R(5) manifold. As was the case for H_2O, the inclusion of line mixing was seen to have a greater effect on the retrieved values of the line shifts than on the retrieved values of other parameters. For one transition the shift actually changed sign when line mixing was added to the fit. We expect that, as the analysis continues to the more complex manifolds at higher rotational quanta, many more CH_4 line mixing parameters will be determined from our data.

5. Concluding remarks

From comparison of broadening and shift parameters measured in different laboratories, or the same laboratory at different times, we have observed that there can be significant differences, depending on the measurement conditions, analysis technique, and other factors. Even for well-measured molecules (e.g., CO), air-broadened widths from different laboratories disagree by 3 to 5% or more. The disagreement can be much larger for molecules that tend to decompose or condense, such as O_3 or H_2O.

Pressure-induced line shifts cannot be ignored, particularly for higher overtone and combination bands of most atmospheric species. The simultaneous determination of line widths and shifts from the same spectra will also provide useful data for validation of theoretical calculations. Unfortunately, a number of modern experimental studies fail to measure both line shifts and widths

Knowledge of line mixing and line shape parameters is becoming important for accurate atmospheric species and temperature retrievals, not only in Q branches, but also in P and R branches. The present edition of the HITRAN database (Rothman et al., 2005) contains line mixing parameters only for about 300 Q branches of CO_2. In the future, the database will be required not only to expand its coverage of line mixing in CO_2, but also to

add line mixing parameters for other molecules, including H_2O and CH_4. Laboratory measurements will be required to determine these mixing parameters.

Acknowledgements

The results reported here would not have been possible without the tireless efforts of co-investigators V. Malathy Devi and D. Chris Benner of the College of William and Mary, as well as Linda R. Brown and Robert A. Toth of Jet Propulsion Laboratory. Other contributors to the data analysis include C. P. Rinsland of NASA Langley Research Center, A. Predoi-Cross of the University of Lethbridge, Alberta, Canada, C. Boulet and J.-P. Bouanich of the Laboratoire de Photophysique Moleculaire, Orsay, France, and high-school students A. M. Cox and T. J. Pittman who participated in the New Horizons Governor's School for Science and Technology mentorship program at NASA Langley. S. W. Sharpe, R. L. Sams and T. A. Blake of Pacific Northwest National Laboratory, Richland, Washington, not only recorded spectra at their facility, but also provided helpful guidance related to the analysis of the Bruker data. Mike Dulick, Detrick Branston, Claude Plymate and Jeremy Wagner of the National Solar Observatory provided invaluable assistance in recording spectra at Kitt Peak over many years. NSO is operated by the Association of Universities for Research in Astronomy, Inc. (AURA), under contract with the National Science Foundation. We thank NASA's Upper Atmosphere Research Program for their support of the McMath-Pierce FTS facility. We are especially grateful to Charles Solomon and Harry Walthall, now retired from the NASA Langley glass shop, for their assistance in the design, construction and testing of the 50 cm coolable cell and the ozone-generation system. We also thank the late Dr. Charles Chackerian of NASA Ames Research Center for the loan of a 10 cm coolable cell for ozone measurements in 1998.

References

Benner, D. C., Blake, T. A., Brown, L. R., Malathy Devi, V., Smith, M. A. H., and Toth, R. A., 2004, Air-broadening parameters in the ν_3 band of $^{14}N^{16}O_2$ using a multispectrum fitting technique, *J. Mol. Spectrosc.* **228:** 593-619.

Benner, D. C., Rinsland, C. P., Malathy Devi, V., Smith, M. A. H., and Atkins, D., 1995, A multispectrum nonlinear least squares fitting technique, *J. Quant. Spectrosc. Radiat. Transfer* **53:** 705-721.

Bouanich, J.-P., Boulet, C., Predoi-Cross, A., Sharpe, S. W., Sams, R. L., Smith, M. A. H., Rinsland, C. P., Benner, D. C., and Malathy Devi, V., 2005, A multispectrum analysis of

the ν_2 band of $H^{12}C^{14}N$: Part II. Theoretical calculations of self-broadening, self-induced shifts and their temperature dependences, *J. Mol. Spectrosc.* **231:** 85-95.

Brown, L. R., Benner, D. C., Champion, J. P., Malathy Devi, V., Fejard, L., Gamache, R. R., Gabard, T., Hilico, J. C., Lavorel, B., Loete, M., Mellau, G. Ch., Nikitin, A., Pine, A. S., Predoi-Cross, A., Rinsland, C. P., Robert, O., Sams, R. L., Smith, M. A. H., Tashkun, S. A., and Tyuterev, V. G., 2003, Methane line parameters in HITRAN, *J. Quant. Spectrosc. Radiat. Transfer* **82:** 219-238.

Brown, L. R., Benner, D. C., Malathy Devi, V., Smith, M. A. H., and Toth, R. A., 2005, Line mixing in self- and foreign-broadened water vapor at 6 μm, *J. Mol. Struct.* **742:** 111-122.

Larsen, R. W., Nicolaisen, F. M., and Sorensen, G. O., 2001, Determination of self-, air- and oxygen-broadening coefficients of pure rotational absorption lines of ozone and of their temperature dependence, *J. Mol. Spectrosc.* **210:** 259-270.

Lemaire, V., Babay, A., Lemoine, B., Rohart, F., and Bouanich, J.-P., 1996, Self- and foreign-gas-broadening and shifting of lines in the ν_2 band of HCN, *J. Mol. Spectrosc.* **177:** 40-45.

Levy, A., Lacome, N., and Chackerian, C., 1992, Collisional line mixing, in *Spectroscopy of the Earth's Atmosphere and Interstellar Medium,* Narahari Rao, K. and Weber, A., eds., Academic Press, Boston, MA, pp. 261-337.

Malathy Devi, V., Benner, D. C., Smith, M. A. H., and Rinsland, C. P., 1994, Temperature dependence of Lorentz air-broadening and pressure-shift coefficients of $^{12}CH_4$ lines in the 2.3-μm spectral region, *J. Quant. Spectrosc. Radiat. Transfer* **51:** 439-465.

Malathy Devi, V., Benner, D. C., Smith, M. A. H., and Rinsland, C. P., 1997, Air-broadening and shift coefficients of O_3 lines in the ν_2 band and their temperature dependence, *J. Mol. Spectrosc.* **182:** 221-238.

Malathy Devi, V., Benner, D. C., Smith, M. A. H., Rinsland, C. P., Predoi-Cross, A., Sharpe, S. W., Sams, R. L., Boulet, C., and Bouanich, J.-P., 2005, A multispectrum analysis of the ν_2 band of $H^{12}C^{14}N$: Part I. Intensities, broadening and shift coefficients, *J. Mol. Spectrosc.* **231:** 66-84.

Malathy Devi, V., Benner, D. C., Smith, M. A. H., Rinsland, C. P., Sharpe, S. W., and Sams, R. L., 2004, A multispectrum analysis of the $2\nu_2$ spectral region of $H^{12}C^{14}N$: Intensities, broadening and pressure-shift coefficients, *J. Quant. Spectrosc. Radiat. Transfer* **87:** 339-366.

Malathy Devi, V., Fridovich, B., Jones, G. D., Snyder, D. G. S., and Nuendorffer, A., 1982, Temperature dependence of the widths of N_2-broadened lines of the ν_3 band of $^{14}N^{16}O2$, *Appl. Opt.* **21:** 1537-1538.

May, R. D. and Webster, C. R., 1990, Laboratory measurements of NO_2 line parameters near 1600 cm^{-1} for the interpretation of stratospheric spectra, *Geophys. Res. Lett.* **17:** 2157-2160.

Notholt, J., Kuang, Z., Rinsland, C. P., Toon, G. C., Rex, M., Jones, N., Albrecht, T., Deckelmann, H., Kreig, J., Weinzierl, C., Bingemer, H., Weller, R., and Schrems, O., 2003, Enhanced upper tropical tropospheric COS: Impact on the stratospheric aerosol layer, *Science* **300:** 307-310.

Regalia-Jarlot, L., Thomas, X., Von Der Heyden, P., and Barbe, A., 2005, Pressure-broadened line widths and pressure-induced line shifts coefficients of the (1-0) and (2-0) bands of $^{12}C^{16}O$, *J. Quant. Spectrosc. Radiat. Transfer* **91:** 121-131.

Rinsland, C. P., Malathy Devi, V., Smith, M. A. H., Benner, D. C., Sharpe, S. W., and Sams, R. L., 2003, A multispectrum analysis of the ν_1 band of $H^{12}C^{14}N$: II. Air- and N_2-broadening, shifts and their temperature dependences, *J. Quant. Spectrosc. Radiat. Transfer* **82:** 343-362.

Rosenkranz, P. W., 1975, *IEEE Trans. Antennas Propag.* **AP-23:** 498-

Rothman, L. S., Barbe, A., Benner, D. C., Brown, L. R., Camy-Peyret, C., Carleer, M. R., Chance, K., Clerbaux, C., Dana, V., Malathy Devi, V., Fayt, A., Flaud, J.-M., Gamache, R. R., Goldman, A., Jacquemart, D., Jucks, K. W., Lafferty, W. J., Mandin, J.-Y., Massie, S. T., Nemtchinov, V., Newnham, D. A., Perrin, A., Rinsland, C. P., Schroeder, J., Smith, K. M., Smith, M. A. H., Tang, K., Toth, R. A., Vander Auwera, J., Varanasi, P., and Yoshino, K., 2003, The HITRAN molecular spectroscopic database: Edition of 2000 including updates through 2001, *J. Quant. Spectrosc. Radiat. Transfer* **82:** 5-44.

Rothman, L. S., Jacquemart, D., Barbe, A., Benner, D. C., Birk, M., Brown, L. R., Carleer, M. R., Chackerian, C., Chance, K., Coudert, L. H., Dana, V., Malathy Devi, V., Flaud, J.-M., Gamache, R. R., Goldman, A., Hartmann, J.-M., Jucks, K. W., Maki, A. G., Mandin, J.-Y., Massie, S. T., Orphal, J., Perrin, A., Rinsland, C. P., Smith, M. A. H., Tennyson, J., Tolchenov, R. N., Toth, R. A., Vander Auwera, J., Varanasi, P., and Wagner, G., 2005, The HITRAN 2004 molecular spectroscopic database, *J. Quant. Spectrosc. Radiat. Transfer* **96:** 139-204.

Schmidt, C., Lambot, D., Walrand, J., Blanquet, G., and Bouanich, J.-P., 1992, Diode-laser measurements of N_2-broadening coefficients in the ν_2 band of HCN, *J. Mol. Spectrosc.* **151:** 292-302.

Smith, M. A. H. and Gordley, L. L., 1983, Sensitivity of ozone retrievals in limb-viewing experiments to errors in line-width parameters, *J. Quant. Spectrosc. Radiat. Transfer* **29:** 413-418.

Smith, M. A. H., Harvey, G. A., Pellett, G. L., Goldman, A., and Richardson, D. J., 1984, Measurements of the HCN ν_3 band broadened by N_2, *J. Mol. Spectrosc.* **105:** 105-112.

Smith, M. A. H., Malathy Devi, V., Benner, D. C., and Rinsland, C. P., 1997, Temperature dependence of air-broadening and shift coefficients of O_3 lines in the ν_1 band, *J. Mol. Spectrosc.* **182:** 239-259.

Smith, M. A. H., Rinsland, C. P., Fridovich, B., and Narahari Rao, K., 1985, Intensities and collision broadening parameters from infrared spectra, in *Molecular spectroscopy: Modern research, Vol. III,* Narahari Rao, K., ed., Academic Press, New York, pp. 111-248.

Smith, M. A. H., Rinsland, C. P., and Malathy Devi, V., 1991, Measurements of self-broadening of infrared absorption lines of ozone, *J. Mol. Spectrosc.* **147:** 142-154.

Smith, M. A. H., Rinsland, C. P., Malathy Devi, V., and Benner, D. C., 1992a, Temperature dependence of broadening and shifts of methane lines in the ν_4 band, *Spectrochimica Acta* **48A:** 1257-1272.

Smith, M. A. H., Rinsland, C. P., Malathy Devi, V., Benner, D. C., and Cox, A. M., 2005, Temperature-dependence of air-broadened line widths and shifts in the ν_3 band of ozone, Presented at the 7th Atmospheric Spectroscopy Applications Meeting, Reims, France, September 6-8, 2005 (Paper AP20).

Smith, M. A. H., Rinsland, C. P., Malathy Devi, V., and Prochaska, E. S., 1994a, Erratum "Measurements of pressure broadening and shifts of O_3 lines in the 3-μm region" by M.A.H. Smith, C.P. Rinsland, V. Malathy Devi, and E.S. Prochaska, *J. Mol. Spectrosc.* **165:** 596-596.

Smith, M. A. H., Rinsland, C. P., Malathy Devi, V., and Prochaska, E. S., 1994b, Measurements of pressure broadening and shifts of O_3 lines in the 3-μm region, *J. Mol. Spectrosc.* **164:** 239-259.

Smith, M. A. H., Rinsland, C. P., Malathy Devi, V., Rothman, L. S., and Narahari Rao, K., 1992b, Intensities and collision broadening parameters from infrared spectra: An update, in *Spectroscopy of the Earth's Atmosphere and Interstellar Molecules,* Narahari

Rao, K. and Weber, A., eds., Academic Press, Inc., Cambridge, Massachusetts, pp. 153-260.

Spencer, M. N., Chackerian, C., Flannery, C., and Steinfeld, J. I., 1992, Temperature dependence of nitrogen broadening of ozone ν_3 rovibrational transitions, *Spectrochim. Acta* **48A:** 1273-1282.

Spencer, M. N., Chackerian, C., Flannery, C., and Steinfeld, J. I., 1993, Temperature dependence of oxygen-broadening of ozone ν_3 rovibrational transitions, *J. Quant. Spectrosc. Radiat. Transfer* **49:** 525-533.

Sung, K. and Varanasi, P., 2004, Intensities, collision-broadened half-widths, and collision-induced line shifts in the second overtone band of $^{12}C^{16}O$, *J. Quant. Spectrosc. Radiat. Transfer* **83:** 445-458.

Toth, R. A., Brown, L. R., Smith, M. A. H., Malathy Devi, V., Benner, D. C., and Dulick, M., 2006, Air-broadening of H_2O as a function of temperature: 696 - 2163 cm^{-1}, *J. Quant. Spectrosc. Radiat. Transfer,* in press.

Wagner, G., Birk, M., Schreier, F., and Flaud, J.-M., 2002, Spectroscopic database for ozone in the fundamental spectral regions, *J. Geophys. Res.* **107:** 4626-4643.

Zou, Q. and Varanasi, P., 2002, New laboratory data on the spectral line parameters in the 1-0 and 2-0 bands of $^{12}C^{16}O$ relevant to atmospheric remote sensing, *J. Quant. Spectrosc. Radiat. Transfer* **75:** 63-92.

HALF-WIDTHS AND LINE SHIFTS OF WATER VAPOR FOR ATMOSPHERIC APPLICATIONS: MEASUREMENT AND THEORY

ROBERT R. GAMACHE* AND BOBBY K. ANTONY
Department of Environmental, Earth, and Atmospheric Sciences
Intercampus Graduate School of Marine Sciences and Technology
University of Massachusetts Lowell, 265 Riverside Street, Lowell, MA 01854-5045, USA

Abstract. Pressure-broadened half-widths are the principal source of error in the retrieval of concentration profiles for the Earth's atmosphere. The importance of the pressure-induced line shift is now becoming understood. In this work the current state of knowledge of the line shape parameters for water vapor transitions is discussed with respect to the experimental record and the theory. The measurement databases that have been compiled and the intercomparisons of measurements are discussed. The theoretical determination of the line shape parameters via the Complex Robert-Bonamy (CRB) formalism is presented. The dependence of the line shape parameters on rotational state, vibrational state, imaginary terms, temperature, intermolecular potential, collision dynamics, and method of calculation are discussed. Finally a comparison of the CRB line shape parameters with the measurement database is made and compared with the intercomparisons of the measurements.

Keywords: Complex Robert Bonamy formalism, half-width, line shift, spectral lines, H_2O, temperature dependence of half-width, vibrational dependence of half-width

* To whom correspondence should be addressed. Robert R. Gamache, Department of Environmental, Earth, and Atmospheric Sciences, University of Massachusetts Lowell, 265 Riverside Street, Lowell, MA 08154, e-mail: Robert_Gamache@uml.edu

A. Perrin et al. (eds.), Remote Sensing of the Atmosphere for Environmental Security, 203–220.

1. Introduction

Water vapor is the strongest absorber of radiation and is therefore the most important gas controlling Earth's surface temperature. There are about 50 000 spectral transitions for H_2O ranging from microwave to the visible range of the spectrum. The interpretation of remote sensing measurements and study of the radiative property of atmosphere depends on the knowledge of spectral parameters for the gases present in the atmosphere. Of the parameters needed for inverting remotely sensed data, the air-broadened half-width is the least well known for atmospheric applications.[1] The effects of uncertainty in half-widths on the accuracy of retrieved parameters is well understood.[2-5] The spectroscopic and remote sensing communities[6-8] have determined that for accurate retrievals the half-width and its temperature dependence should be known with an uncertainty of **3%** for strong lines and **10%** for weak lines. The effect of the line shift on reducing data from remote sensing measurements is now known to be significant.[9-11]

In order for retrievals to be successful, spectral parameter data must be available for all transitions of absorbing molecules in the spectral channels of the measurement. Here the focus is on the collision broadened half-widths, γ, and pressure-induced line shifts, δ, of water vapor transitions. Many measurements have been performed to determine γ for H_2O in a bath of N_2, O_2, air, and H_2O; a lesser number of measurements have been made for the line shifts. A question of prime importance is what are the uncertainties of the measurements? Because it is not practical to make observations in the laboratory for all transitions for all the conditions encountered in the Earth's atmosphere, an additional question should be is there a theory capable of computing the needed half-widths that meets the needs of the remote sensing community? In Section 2 the state of the measurements of collision-broadened half-widths of H_2O is addressed. In section 3 the complex formulation of Robert-Bonamy is presented and the calculations of γ and δ discussed. The measurements and calculations are compared in section 4 and the current state of affairs is discussed in section 5.

2. Measurements of collision broadened half-widths of water vapor

In 1994 Gamache *et al*. undertook a critical survey[12] of measured half-widths of water vapor perturbed by H_2O, N_2, O_2, air, CO_2, and Ar. There were four goals identified in that work: (1) To use the available data to draw conclusions concerning the influence of vibration, relations between half-widths and their temperature dependence, ratios between broadening by different collision partners, etc. (2) To extract different broadening

values for selected transitions in which one may be very confident by comparing measurements from different authors. Such accurate etalon lines should be of great use to experimentalist as tests of their measurement procedures, for remote sensing, and comparisons with theoretical models. (3) To propose measurements that are crucially missing in order to complete the selected set in regard to the requirements of applications and testing of theoretical models. (4) To make a first test of theoretical results. Unfortunately, the disagreement among the data was much larger than the stated experimental uncertainty making it difficult to address the goals of the work. Goal 1 was addressed as well as could be done at the time with the available data; goal 2 yielded a very small number of transitions for which the confidence in the half-width was high; they were able to address goal 3 based on the measurements at the time, and goal 4 was not possible.

Over the past ten years there have been a number of newer measurements of pressure-broadened half-widths. The data sets have grown to 7 683, 598, 14 067, and 10 596 measurements of N_2-, O_2-, air-, and self-broadened half-widths. Gamache and Hartmann[13] have taken these newer data and added them to their databases and performed intercomparisons of the measurements with the aim of addressing the goals of their first study.

The vibrational dependence of the half-widths of water vapor was addressed in a number of studies,[14-18] in a survey paper[12] and in several workshops.[1,6,8] It was estimated that in general the effect of the vibrational states of the transition was smaller than experimental uncertainties and could change the half-width by ~3-5%. However, a recent theoretical work[19] on the vibrational dependence of the half-widths of water vapor lines found that the half-widths of certain transitions (doublet transitions where Kc=J or J-1) exhibit a strong vibrational dependence. The difference in the half-widths can be up to a factor of 6 for high J transitions for bands involving 4 quanta of stretch modes. Using the database of measured half-widths the authors were able to confirm their prediction with experimental data. Because of this fact, intercomparisons can only be made between measurements made by different groups for transitions with the same quantum numbers; v_1'v_2'v_3'J'Ka'Kc' ← v_1"v_2"v_3"J"Ka"Kc".

Grouping the data for a particular ro-vibrational transition gave groups of 2, 3, 4, …, 8 points depending on the number of measurements made. The procedure yields 499, 19, 3514, and 440 ro-vibrational transitions for which intercomparisons of half-widths could be made for N_2, O_2, air, and self broadening, respectively. Table 1 lists the number of intercomparisons of half-widths made as a function of the number of points in the group, the number of the intercomparisons for which the estimated uncertainty is less than or equal to 3, 5, and 10%, the number with estimated uncertainty greater than 10%, and the maximum estimated uncertainty. It should be

noted that most of the intercomparisons are for pairs of points, from 80% for air-broadening to 93% for self-broadening. Certainly at the same level of agreement more confidence is gained as the number of points compared increases. Unfortunately, the number of intercomparisons with n greater than 3 is small; 6, 10, 2, and 0.9 percent for nitrogen-, oxygen-, air-, self-broadening, respectively.

Table 1. Half-width intercomparisons: Number of data in 2, 3, 4…8 point intercomparisons, number of intercomparisons with estimated uncertainties (U) in the given ranges, and maximum estimated uncertainty for the H_2O-N_2, H_2O-O_2, H_2O-air, and H_2O-self systems.

data in intercomparison		2	3	4	5	6	7	8
H_2O-N_2	N†	420	48	30			1	
	U ≤ 3%	46						
	3% < U ≤ 5%	67	6	1				
	5% < U ≤ 10%	216	30	25				
	10% < U	91	12	4			1	
	Umax= 140.%							
H_2O-O_2	N†	16	1	1		1		
	U ≤ 3%							
	3% < U ≤ 5%	1						
	5% < U ≤ 10%	4	1	1		1		
	10% < U	11						
	Umax= 51.8%							
H_2O-air	N†	2818	615	63	11	4	2	1
	U ≤ 3%	65	48					
	3% < U ≤ 5%	297	83	8	1	1		
	5% < U ≤ 10%	967	382	37	5	1	1	
	10% < U	1489	102	18	5	2	1	1
	Umax= 137.%							
H_2O-self	N†	409	27	3	1			
	U ≤ 3%	2						
	3% < U ≤ 5%	3						
	5% < U ≤ 10%	156	8					
	10% < U	248	19	3	1			
	Umax= 186.%							

† number of intercomparisons

The intercomparisons for nitrogen broadening show no 3 point or larger data sets with estimated uncertainty less than or equal to 3%. Table 1 shows that most of the estimated uncertainties are in the range greater than 5% to less than or equal to 10% with a fair number greater than 10%. One ro-vibrational transition, the $3_{12} \leftarrow 2_{20}$ of the rotational band or 183 GHz line, was studied by 7 groups and here the estimated uncertainty is greater than 10%. These data are shown in Fig. 1. This plot is typical of the intercomparisons. Often the data are separated by more than the uncertainty assigned to it. This fact leads to questions about the uncertainties reported in the literature. For the line shifts there are only intercomparisons of pairs of points.

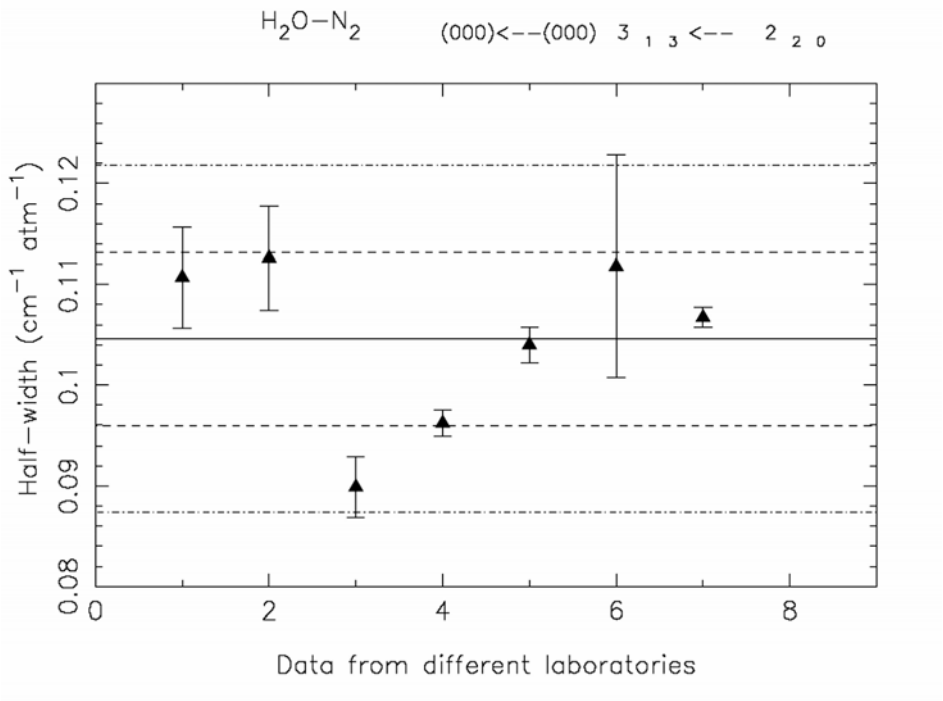

Figure 1. Measured half-widths (cm^{-1} atm^{-1}) for nitrogen-broadening of the 183 GHz line of water vapor with reported uncertainties. Solid line is the average half-width, dashed lines are 1 and 2 standard deviations.

For oxygen-broadening of water vapor there are only 19 intercomparisons: mostly pairs of data. The estimated uncertainties are mostly greater than 10%. There are no shift measurements for intercomparison.

The largest data set is for air-broadening of H_2O which allows 3514 intercomparisons to be made. Unfortunately, only 81 of the intercomparisons have more than 3 data points. Of these intercomparisons none meet the 3% uncertainty criterion of the spectroscopic community. Most of the error estimates are in the 5-10 % range or above 10%. There are two transitions for which 7 measurements have been made. The first is typical of many of the air-broadening plots with the error bars of the data points not overlapping. While for the second the error bars do overlap, the overall 2 sigma uncertainty is almost 3 times that needed for remote sensing. The intercomparisons for the line shifts only occur as pairs of measurements.

The self-broadening data set allows 440 intercomparisons of half-widths to be made. There are no intercomparisons of the line shifts. For intercomparisons with more than 3 data points the estimated uncertainty is greater than 10%.

3. Complex Robert Bonamy formalism

The model chosen is the semiclassical complex formalism of Robert and Bonamy [20,] (CRB) for several reasons.

1. The formalism is complex valued, yielding half-widths and line shifts from a single calculation.
2. The cumulant expansion incorporated in the RB formalism allows for the inclusion of higher order terms in the S matrix, eliminating an awkward cutoff procedure that characterized earlier theories.
3. The intermolecular dynamics are treated more realistically than in earlier theories, i.e. using curved rather than straight line trajectories. This has important consequences in the description of close intermolecular collisions (small impact parameters).
4. Connected to item (3) is the incorporation in the RB theory of a short range (Lennard-Jones 6-12[21]) atom-atom component to the intermolecular potential. This component has been shown to be essential for a proper description of pressure broadening, especially in systems where electrostatic interactions are weak.[22] (Here, the notion of strong and weak collisions adopts the definition of Oka.[23])

A detailed description of the theory may be found in Refs. 24-26 and references therein. Here only the salient features are discussed. In the CRB approach half-width and line shifts for a ro-vibrational transition $f \leftarrow i$ are given by the real and imaginary part of the expression,

$$\left(\gamma - i\delta\right)_{f\leftarrow i} = \frac{n_2}{2\pi c}\left\langle \mathrm{v} \times \left[1 - e^{-\left(S_2(f,i,J_2,v,b) + i\,S_1(f,i,J_2,v,b)\right)}\right]\right\rangle_{v,b,J_2} \qquad (1)$$

where, n_2 is the number density of perturbers and $\langle\rangle_{\mathrm{v,b,J2}}$ is the average over all trajectories, with impact parameter b and relative velocity v, and initial rotational state J_2 of the collision partner. The real $^1S_1$ and complex S_2 terms are the first and second order terms in the successive expansion for the scattering matrix. S_1 and S_2 depend on the ro-vibrational states (and the associated collision induced transitions between these levels), the intermolecular potential and the collision dynamics involved. The expressions for these terms are explicitly defined in Refs. 24-26.

Most of the molecular parameters needed in the calculations are well known and the best available values from the literature are used. Many studies have been carried out and the results allow the investigation of the dependencies of the line shape parameters.

3.1. EFFECTS OF THE EXPANSION OF THE ATOM–ATOM POTENTIAL

When expressed in spherical tensor form, the atom-atom potential can be understood as two simultaneous expansions. One is defined by the tensorial ranks ℓ_1 and ℓ_2, which determine the symmetry of the interaction.[27, 28] A second expansion is defined by the sum $\ell_1+\ell_2+2w$,[29, 30] which we call the order of the expansion. It hardly needs to be emphasized that any calculation of line width or shift should be converged with respect to both order and rank. All of our CRB calculations begin with testing the convergence of the atom-atom potential. The order of the expansion, ranging from 0 to high order, and the tensorial rank from ℓ=0 to 2 are investigated to ensure convergence. An order equal to zero corresponds using only the electrostatic parts of the anisotropic potential.

The studies have indicated that the order of the potential needed to ensure convergence is dependent on the interacting system. The results have shown that convergence is achieved with expansions of 8^{th} order for the H_2O-N_2, H_2O-O_2, H_2O-CO_2 systems, 12^{th} order for H_2O-Ar, and 0^{th} order for H_2O-H_2O.

3.2. EFFECTS OF THE TRAJECTORIES

It is well known that the calculation of the line shape parameters is dependent on the trajectory model chosen. The trajectory model is studied for the system under consideration before routine calculations are made. The codes employed have the options to consider solutions of Hamilton's equations or the Robert and Bonamy parabolic model[20] both based on the isotropic potential yielding curved trajectories. We find that the RB model, which is correct to second order in time, yields results in agreement with the more exact and time consuming Hamilton's equations method. To simplify the trajectory calculations the isotropic part of the atom-atom expansion is fit to an isotropic Lennard-Jones 6-12 potential and the resulting parameters are used in the trajectory calculations. For H_2O broadened by N_2, O_2, CO_2, or Ar the change from straight line to curved trajectories has a marked effect on the half-width. However, for self-broadening of H_2O the trajectory model used has negligible influence.

Based on these observations the calculations presented here were made employing the RB parabolic model.

3.3. THE EFFECTS OF THE COMPLEX TERMS

As stated above, the complex Robert-Bonamy formalism leads to the imaginary components of the expanded S matrix appearing in the formula for the half-width. The contribution of these components to the half-width has remained a relatively unexplored facet of the theory because some of the imaginary resonance function integrals were only derived in the mid-nineties.[24]

Our studies on water vapor[24-26,31-33] have demonstrated the importance of the inclusion of imaginary components of the S_2 terms in the calculation of half-widths. Differences in the half-width from calculations with and without the imaginary terms can be as large as 25%.[33] For the H_2O-N_2 system, the difference between the real and complex calculations of γ are generally small with exceptions up to 10-15% observed. For the H_2O-O_2 system, the imaginary terms are more pronounced, accounting for up to 25% difference in the calculated half-width. For all the systems studied the imaginary components affect the half-width by more than the uncertainty criterion set by the remote sensing community hence they must be retained in the calculations if reliable results are to be obtained.

3.4. TEMPERATURE DEPENDENCE OF THE HALF-WIDTH

In order to reduce atmospheric remote sensing measurements the temperature dependence of the spectral parameters must be known. Here the temperature dependence of the collision broadened half-width is discussed. The standard model for temperature dependence of the half-width is the power law expression

$$\gamma(T) = \gamma(T_0)\left[\frac{T_0}{T}\right]^n \tag{2}$$

where $\gamma(T_0)$ is the half-width at the reference temperature T_0, and n is called the temperature exponent. The model works quite well over small temperature ranges, i.e. ΔT=50-100 K. The model becomes less valid for large temperature ranges, thus one must be cautious in applying Eq. (2) in combustion studies for example. Recently, Wagner *et al.*[34] discovered that for certain types of transitions for N_2-, O_2-, and air-broadening of H_2O the power law formula is not valid. This occurs when the energy jumps for collisionally induced transitions for the active and bath molecule do not match yielding large energy gaps. These collisions are said to be “off resonance” and the result is the rotational contributions to the half-width become small and the process is dominated by the vibrational terms. At large J” values the resulting temperature exponents are negative and the

power law, while giving a reasonable fit, is not theoretically correct. At intermediate J" values (~8-10) the contributions to the half-width are a mix of rotational and vibrational terms and the power law does not fit to the data.

Chu *et al*.[4] have studied the effect of changing the temperature exponent on retrieved mixing ratios. They found that changing *n* from 0.5 to 0.7 results in roughly a 4 percent change in the mixing ratio at 10 km. Given these results it is clear that the use of the temperature exponent for the ro-vibrational transition in question will yield the best results. Gamache and Rothman[35] have also shown that temperature exponents averaged as a function of J" or fit by polynomials in the rotational quantum numbers do not give reliable predictions for all transitions.

The temperature exponents for 2029 transitions in the ν_2 band of the H_2O-N_2 system are plotted in Fig. 2 versus (J"+J')/2. What is clear from the figure is that fitting the data with a polynomial will not yield reliable results. Also the use of a constant value, which is the default on HITRAN[36], will not give good results either. As J increases the range of the temperature exponents increases. For example at (J"+J')/2 equal to 14.5, *n* varies form 0.5 to -0.75. As shown by Chu *et al*. a deviation of a default or polynomial value from the true value will lead to large error in the mixing ratio at 10 km.

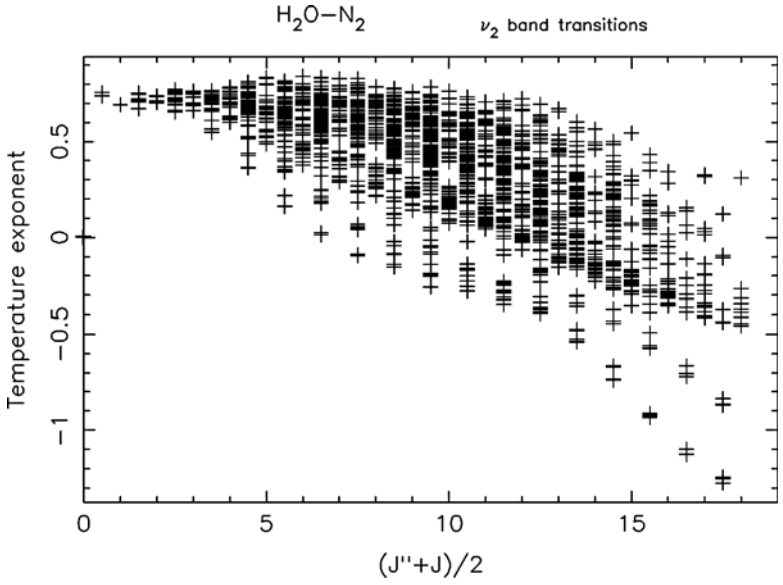

Figure 2. Temperature dependence of the half-width versus (J"+J')/2 for ν_2 transitions of H_2O perturbed by nitrogen.

3.5. VIBRATIONAL DEPENDENCE

There have been a number of studies into the dependence of the half-width on vibration. Mandin *et al.*[14, 15] took ratios of their measured half-widths to those of the HITRAN database[36] in the 8500-9300 and 9500-11500 cm^{-1} regions. From this they concluded that there was a small (±3%) vibrational dependence of the half-width. Grossman and Browell[16], reported a 5% difference between transitions in the $3\nu_1+\nu_3$ and $2\nu_1+2\nu_2+\nu_3$ bands with the $3\nu_1+\nu_3$ lines having the larger broadening values. This study compared average broadening values, not J dependent half-widths. In a 1996 study by Brown and Plymate[17] on H_2O broadened by hydrogen, the ratios of half-widths for the same set of rotational quantum numbers were formed for the rotation and ν_1 bands divided by the ν_2 band. For rotational/ν_2 transitions the rms ratio is 1.016 (±2.6%) and is 1.08 (±4%) for ν_1/ν_2 transitions. Brown and Plymate concluded that these differences are too large to be caused by experimental error and that there is a small vibrational dependence in the half-width.

Zou and Varanasi, in a 2003 study[18], investigated the vibrational dependence of self- and air-broadening of water vapor in the 950-2100 and 3000-4050 cm^{-1} regions. They considered ratios of the half-widths for the same rotational transition for the $2\nu_2$ and the ν_2 bands, the ν_1 and the ν_2 bands, and the $2\nu_2$ and the ν_1 bands for both self- and air-broadening. From the analysis of the self-broadening data they concluded that the half-widths in the $2\nu_2$ band are smaller than their counterparts in the ν_2 band by about 10%. The differences in the ratios for the ν_1 and the ν_2 bands, and the $2\nu_2$ and the ν_1 bands contained too much scatter to state conclusively if there was a definite vibrational dependence. Their analysis of the air-broadening data indicated that the half-widths in the ν_1 band are larger than the corresponding half-widths in the ν_2 band by about 5%. This is in rough agreement with the work of Brown and Plymate[17]. There were too few ratios for the $2\nu_2$ and the ν_2 bands and the $2\nu_2$ and the ν_1 bands to draw any solid conclusions.

The vibrational dependence of the half-widths of water vapor was addressed in a survey paper[12] and several workshops.[1, 6, 8] It was estimated that in general the effect of the vibrational states of the transition was smaller than experimental uncertainties and could change the half-width by ~3-5%. However, a recent theoretical study[19] on the vibrational dependence of the half-widths of water vapor lines found that the half-widths of certain transitions (doublet transitions where Kc=J or J-1) exhibit a strong vibrational dependence. The calculations show up to a factor of 8 at J=16 for a change of 6 stretch quanta. This fact was sought in the measurement database and is shown in Fig. 3 where the half-width, in mk/atm, is plotted on a log scale versus m (m=-J for P-type transitions and

m=J+1 for R-type transitions). The lines with error bars are the measurements, the circles are the CRB calculations for a change of 3 stretch quanta, and the triangles are calculations for the ν_2 band. Comparison of the measurements with the three quanta calculations shows good agreement. The comparison of the ν_2 band calculations to the $3\nu_1$ band calculations shows the difference in the half-widths to be a ***factor*** of 2 for the J=15 transitions. Similar results are found for transitions with a change of 4 stretch quanta.

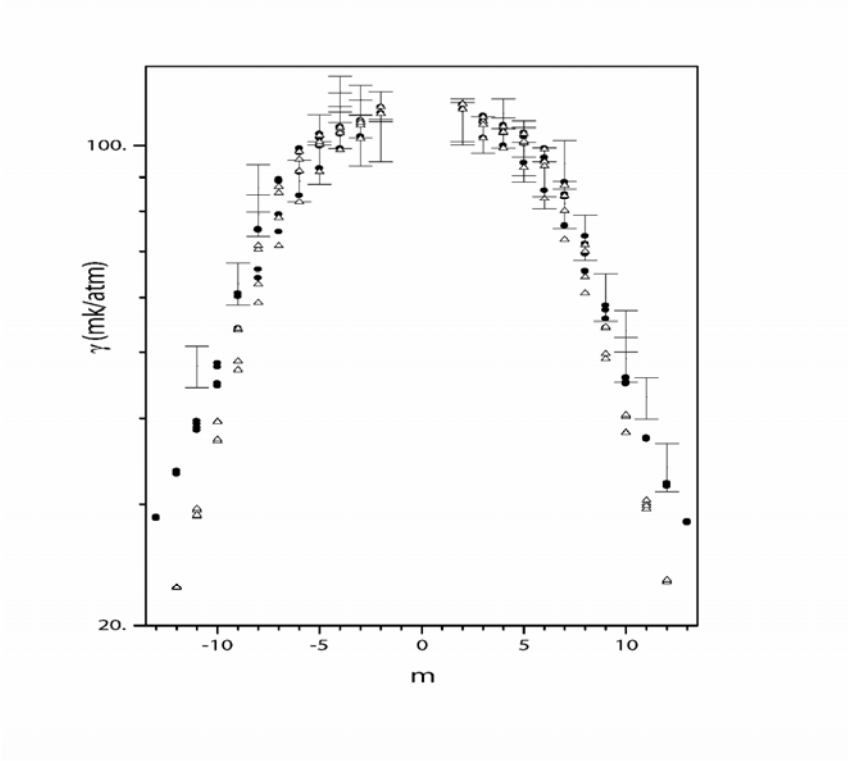

Figure 3. H_2O-N_2 half-widths for transitions with Kc=J in bands involving three quanta of stretching vibration. I are experimental values whereas ● and Δ are values calculated in the $3\nu_1$ band and in the ν_2 band, respectively. Units are in mk/atm, (1000 mk=1 cm^{-1}).

3.6. EFFECTS OF EXPLICIT VELOCITY AVERAGING

Most of the calculations presented here were made using the mean relative thermal velocity (mrtv) approximation to Eq. (1). In this approximation the integral over velocity is replaced by the mean relative thermal velocity for the temperature under consideration. Gamache and Rosenman[37] have shown that for water vapor transitions this approximation is within ~5% of the results obtained by doing the velocity integral at 296K. They found that the

agreement was due to a fortuitous cancellation of errors. In a study of the 500.4 GHz line ($34_{2\,32} \leftarrow 34_{1\,35}$ transition) of ozone with nitrogen as the bath molecule Gamache[38] compared results from a mrtv calculation and a velocity integral calculation with the measurements of Priem *et al.*[39] made at three temperatures. For all temperatures the velocity integrated results agree with measurement better than the mrtv results.

Recently Gamache[40] has compared velocity integrated (VI) calculations, mrtv calculations, and measurements for H_2O in a bath of nitrogen. In most cases the VI results agree with measurement much better than the mrtv results. Also, the very narrow lines that are observed, which have been a problem for the mrtv calculations, are better modeled by the VI-CRB calculations. Figure 4 shows two measured values for the pure rotation band $18_{2\,16} \leftarrow 17_{1\,17}$ transition and the corresponding VI and mrtv calculations. The VI result is a factor of ~1.6 smaller than the mrtv result and is in excellent agreement with experiment.

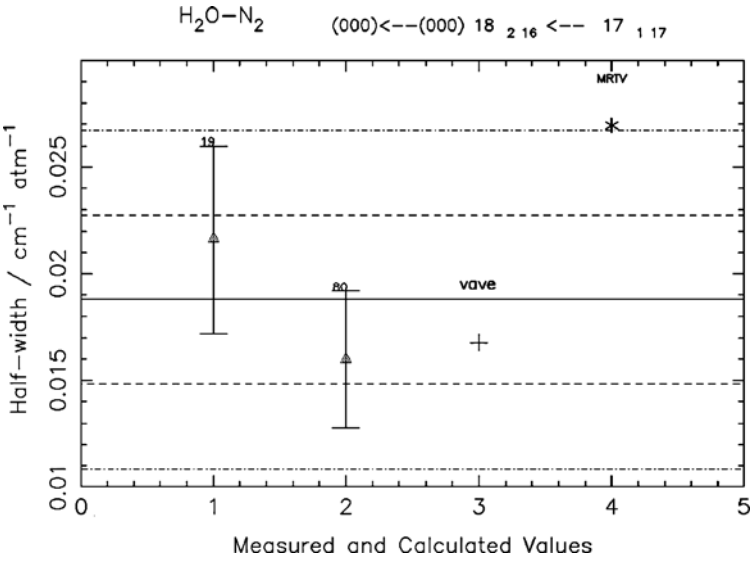

Figure 4. Measured N_2-broadened half-widths for the rotation band $18_{2\,16} \leftarrow 17_{1\,17}$ H_2O transition (triangle with error bars) and the corresponding VI (+ symbol) and mrtv (* symbol) calculations.

4. Comparison of measurement with measurement and calculations

The ultimate test of the theory is the comparison with measurement. The intercomparison of the experimental results[13] has brought into question the uncertainty of the measurements. Here the CRB calculations are compared with the measurements and related to the intercomparison of measurements.

A good number of comparisons of CRB calculated half-widths and a lesser number of comparisons of the pressure-induced line shift have been made. A subset of these comparisons are presented in Table 2.

Table 2. Comparison of measurements with CRB calculations for a number of systems.

	Band	Parameter	# lines	Ave % diff	SD	Ref.
H_2O-air	$3\nu_1+\nu_3$	γ	49	-2.00	3.54	16
		δ	78	0.43	6.37	
	$2\nu_1+2\nu_2+\nu_3$	γ	22	-3.71	-3.71	
		δ	29	-0.98	-0.98	
H_2O-N_2	203.4 GHz line	γ	1	-3.6		41
		n	1	22		
H_2O-N_2	325.2 GHz line	γ	1	-3.2		41
		n	1	58		
H_2O-O_2	203.4 GHz line	γ	1	-1.5		41
		n	1	2.3		
H_2O-O_2	325.2 GHz line	γ	1	-1.6		41
		n	1	-3.9		
H_2O-N_2	3.2 to 17.76 μm region	γ	1251	-1.97		42
H_2O-O_2	3.2 to 17.76 μm region	γ	377	-2.60		42
H_2O-air	3.2 to 17.76 μm region	γ	2139	-1.55		42
H_2O-CO_2	ν_1	γ	8	0.4		33
	$2\nu_2$		1	-0.8		
	ν_3		22	1.8		
H_2O-H_2	Rotation	γ	64	-1.9	4.2	17
	ν_1	γ	92	2.7	4.6	
	ν_2	γ	273	-2.8	5.4	
	ν_3	γ	137	3.9	4.2	
H_2O-Ar	$3\nu_1+\nu_3$	γ	80	-5.8	7.3	16
	$2\nu_1+2\nu_2+\nu_3$	γ	30	-10.8	-20.	
H_2O- H_2O	Many	γ	119	0.28		43
	Many		100	-4.65		44
	Many		132	0.70		45

We have also considered the agreement of the measured values with the average of the measurements and the agreement of the CRB calculations with the average measured value. Here the results for the H_2O-N_2 system are presented. These results are typical for other perturber gases. The intercomparison and comparison are made for cases where there are 2 or more measured data for a specific ro-vibrational transition. Table 3 presents the results for the comparison of measurement with measurement and measurement with calculations.

Table 3. Intercomparison of measurements and comparison of calculations with measurement for the H_2O-N_2 system.

	Exp-Exp	Exp-CRB
Standard deviation	7.35	8.42
Average absolute percent error	4.95	6.03
Number of points	672	322

As can be seen by the table the agreement among the measurements is roughly the same as the agreement of the calculations with the measurements. It should also be noted that the comparisons are biased toward the measurements. Tables 2 and 3 indicate that in general there is very good agreement between the CRB calculations and the measurements.

5. Discussion

Measurements of pressure-broadened half-widths have been made for a great number of transitions of water vapor in a bath of N_2, O_2, air, and H_2O and to a lesser extent for the line shifts. The results of the intercomparisons show that the current databases of measured parameters do not demonstrate good agreement with each other, certainly not of the quality needed to meet the needs of remote sensing. Trends in line shift parameters are now becoming evident, however more measurements are needed. The study of the temperature dependence of the half-width needs more measurements to identify trends, and the study of temperature dependence of the line shift is still in its infancy. There is much to be learned for both properties.

From the point of view of theory, measurements are needed for nitrogen-, oxygen-, and self-broadening. In particular, measurements for high J lines of bands such as the rotation and ν_2 band and the doublet transitions for high vibrational bands would be useful for adjusting the interaction potential. Temperature dependence of the half-width and line shift for these transitions would also be useful given the results of Refs. 19 and 34.

The following comments are made with respect to calculations of pressure-broadened half-widths and pressure-induced line shifts for ro-vibrational transitions of the systems discussed here. The effects of the imaginary components, the choice of potential, and the order of expansion of the potential vary from transition to transition and from system to system. To ensure reliable calculations, the potential in the CRB formalism must include the leading electrostatic terms, the atom-atom potential expanded to reach convergence, and the isotropic induction and dispersion potentials. The results of the studies discussed above demonstrate a profound dependence of the half-width on the imaginary terms in the calculation for all perturbing species. It has been observed that as the imaginary components and the atom-atom potential expanded to high order are included in the calculations, the results almost always move in the direction of measurement. Recent results also indicate that the line shifts calculated by the CRB method agree very well with experiment.

One advantage of the theory is that many aspects of the broadening and shifting mechanisms can be elucidated. The vibrational dependence of the H_2O-N_2 system is now well understood. Temperature dependence studies of the half-width have revealed some interesting results. In addition, the need to explicitly velocity average the optical cross-sections is becoming more clear. The authors are testing the CRB formulation on other radiator-perturbing systems and investigating the temperature dependence of the half-width and line shift.

Acknowledgements

The authors are pleased to acknowledge support of this research by the National Aeronautics and Space Agency grant no. NAG5-11064 and by the National Science Foundation through Grant No. ATM-0242537. Any opinions, findings, and conclusions or recommendations expressed in this material are those of the author(s) and do not necessarily reflect the views of the National Aeronautics and Space Agency or the National Science Foundation.

References

1. Workshop Proceedings, Atmospheric Spectroscopy Applications Workshop, ASA REIMS 96, Université de Reims Champagne Ardenne, Sept. 4-6, 1996. Edited by A. Barbe, 1996.
2. M. A. H. Smith and L. L. Gordley, Sensitivity of Ozone Retrievals in Limb-Viewing Experiments to errors in Line-width Parameters, J. Quant. Spectrosc. Radiat. Transfer 29, 413-418 (1983).

3. W. Traub and K. Chance, BIC-2 Campaign, private communication, 1985.
4. W.P. Chu, E.W. Chiou, J.C. Larsen, L.W. Thomason, D. Rind, J.J. Buglia, S. Oltmans, M.P. McCormick, and L.M. McMaster, Algorithms and Sensitivity Analysis for Stratospheric Aerosol and Gas Experiment II Water Vapor Retrieval, J. Geophys. Res. 98, 4857-4866 (1993).
5. James C. Liljegren, Sid-Ahmed Boukabara, Karen Cady-Pereira, Shepard A. Clough, The Effect of the Half-Width of the 22-GHz Water Vapor Line on Retrievals of Temperature and Water Vapor Profiles With a 12-Channel Microwave Radiometer, IEEE Trans. Geosci. Remote Sensing **43**, 1102-1108 (2005).
6. M. A. H. Smith, Editor, NASA Conference Publication 2396, NASA, Scientific and Technical Information Branch, 1985.
7. C. A. Reber, NASA Goddard Space Flight Center Publication 430-1003-001, (1985).
8. M. A. H. Smith, editor, Third Langley Spectroscopic Parameters Workshop, NASA Langley Research Center, Hampton, VA, 1992.
9. J. Bosenberg, Measurements of the pressure shift of water vapor absorption lines by simultaneous photoacoustic spectroscopy, Appl. Opt. **24**, 3531-3534 (1985).
10. H. C. Pumphrey and S. Buehler, Instrumental and Spectral Parameters :their effect on and measurement by microwave limb sounding of the atmosphere, J. Quant. Spectrosc. Radiat. Transfer, **64**, 421-437 (2000).
11. J. Margolis, Jet Propulsion Laboratory, private communication, 1997.
12. R.R. Gamache, J.-M. Hartmann, and L. Rosenmann, Collisional Broadening of Water-Vapor Lines : I. A Survey of Experimental Results, J. Quant. Spectrosc. Radiat. Transfer **52**, 481-499 (1994).
13. R. R. Gamache and J.-M. Hartmann, An intercomparison of measured pressure-broadening and pressure-shifting parameters of water vapor, Can. J. Chem. **82**, 1013-1027, 2004.
14. J.-Y. Mandin, J.P., Chevillard, C. Camy-Peyret, and J.-M. Flaud, N_2-Broadening Coefficients of $H_2{}^{16}O$ Lines between 9 500 and 11 500 cm^{-1}, J. Mol. Spectrosc. **138**, 272-281 (1989).
15. J.-Y. Mandin, J.P. Chevillard, J.-M. Flaud, and C. Camy-Peyret, N_2 Broadening Coefficients of $H_2{}^{16}O$ Lines between 8500 and 9300 cm^{-1}, J. Mol. Spectrosc. **132**, 352-360 (1988).
16. B.E. Grossmann and E.V. Browell, Water-Vapor Line Broadening and Shifting by Air, Nitrogen, Oxygen, and Argon in the 720-nm Wavelength Region, J. Mol. Spectrosc. **138**, 562-595 (1989).
17. L.R. Brown and C. Plymate, H_2-Broadened $H_2{}^{16}O$ in Four Infrared Bands Between 55 and 4045 cm^{-1}, J. Quant. Spectrosc. Radiat. Transfer, **56**, 263-282 (1996).
18. Q. Zou, and P. Varanasi, Laboratory measurement of the spectroscopic line parameters of water vapor in the 610–2100 and 3000–4050 cm−1regions at lower-tropospheric temperatures, J. Quant. Spectrosc. Radiat. Transfer **82**, 45-98 (2003).
19. Robert. R. Gamache and Jean-Michel Hartmann, "Collisional parameters of H_2O lines: effects of vibration," J. Quant. Spectrosc. Radiat. Transfer **83**, 119–147 (2004).
20 D. Robert and J. Bonamy, Short range force effects in semiclassical molecular line broadening calculations, Journal de Physique **40**, 923-943 (1979).
21. J. E. Jones, On the Determination of Molecular Fields-II. From the Equation of State of a Gas, Proc. Roy. Soc. **A106**, 463-477 (1924).
22. S. P. Neshyba, R. Lynch, R. Gamache, T. Gabard, and J.-P. Champion, Pressure Induced Widths and Shifts for the ν_3 band of Methane, J. Chem. Phys. **101**, 9412-9421 (1994).
23. T. Oka, *Advances in Atomic and Molecular Physics*, Ed. D. R. Bates, Academic Press, New York, 1973.

24. R. Lynch, *Ph.D. dissertation*, Physics Department, University of Massachusetts Lowell, June 1995.
25. R. R. Gamache, R. Lynch, and S. P. Neshyba, "New Developments in the Theory of Pressure-Broadening and Pressure-Shifting of Spectral Lines of H_2O: The Complex Robert-Bonamy Formalism," J. Quant. Spectrosc. Radiat. Transfer **59**, 319-335 1998.
26. R. Lynch, R. R. Gamache, and S. P. Neshyba, "N_2 and O_2 Induced Halfwidths and Line Shifts of Water Vapor Transitions in the (301)←(000) and (221)←(000) Bands," J. Quant. Spectrosc. Radiat. Transfer **59**, 595-613 (1998).
27. C. G. Gray and K. E. Gubbins, *Theory of Molecular Fluids*, Clarendon Press, Oxford 1984.
28. C. G. Gray, "On the theory of multipole interactions," Can J. Phys. **46**, 135-139 (1968).
29. R.A. Sack, "Two-Center Expansion for the Powers of the Distance Between Two Points, *J. Math. Phys.* 5 (1964) 260-268.
30. J. Downs, C. G. Gray, K. E. Gubbins, and S. Murad, "Spherical Harmonic Expansion of the Intermolecular Site-Site Potential, Molecular ," Mol. Phys. **37**, 129-140 (1979).
31 R. Lynch, R. R. Gamache, and S. P. Neshyba, "Pressure broadening of H_2O in the (301)←(000) Band: Effects of angular momentum and close intermolecular interactions," J. Quant. Spectrosc. Radiat. Transfer **59**, 615-626 (1998).
32 R. Lynch, R. R. Gamache, and S. P. Neshyba, "Fully Complex Implementation of the Robert-Bonamy Formalism: Halfwidths and Line Shifts of H_2O Broadened by N_2," J. Chem. Phys. **105**, 5711-5721 (1996).
33. R. R. Gamache, R. Lynch, J. J. Plateaux, and A. Barbe, "Halfwidths and Line Shifts of Water Vapor Broadened by CO_2:Measurements and Complex Robert-Bonamy Formalism Calculations," J. Quant. Spectros. Radiat. Transfer **57**, 485-496 (1997).
34. Georg Wagner, Manfred Birk, Robert. R. Gamache and Jean-Michel Hartmann, "Collisional parameters of H_2O lines: effects of temperature," J. Quant. Spectrosc. Radiat. Transfer **92**, 211-230 (2004).
35. R. R. Gamache and L. S. Rothman, "Temperature Dependence of N_2-Broadened Halfwidths of Water Vapor: The Pure Rotation and ν_2 Bands," J. Mol. Spectrosc. **128**, 360-369, 1988.
36. L.S. Rothman, D. Jacquemart, A. Barbe, D.C. Benner, M. Birk, L.R. Brown, M.R. Carleer, C. Chackerian, Jr K. Chance, V. Dana, V.M. Devi, J.-M. Flaud, R.R. Gamache, A. Goldman, J.-M. Hartmann, K.W. Jucks, A.G. Maki, J.-Y. Mandin, S.T. Massie, J. Orphal, A. Perrin, C.P. Rinsland, M.A.H. Smith, J. Tennyson, R.N. Tolchenov, R.A. Toth, J. Vander Auwera, P. Varanasi, G. Wagner, " The HITRAN 2004 Molecular Spectroscopic Database, J. Quant. Spectrosc. Radiat. Transfer **96**, 139-204, 2005.
37. R. R. Gamache and L. Rosenmann, "The Effects of Velocity Averaging in Broadening Coefficient Calculations," J. Mol. Spectrosc., **164**, 489-499, 1994.
38. Robert. R. Gamache, "Analytical evaluation of the Maxwell-Boltzmann velocity average in pressure-broadened half-width calculations," J. Mol. Spectrosc **208**, 79-86, 2001.
39. Dominique Priem, Jean-Marcel Colmont, François Rohart, Georges Wlodarczak, and R. R. Gamache, "Relaxation of the 500.4 GHz Line of Ozone Perturbed by N_2 and O_2**,"** J. Mol. Spectrosc., **204**, 204-215 (2000).
40. R. R. Gamache, University of Massachusetts Lowell, unpublished results, 2005.
41. Jean-Marcel Colmont, Dominique Priem, Georges Wlodarczak, and R. R. Gamache,"Linewidths Measurements and Calculations of two Rotational Transitions of Water Vapor perturbed by N_2, O_2, and Air," J. Mol. Spectrosc.**193**, 233-243 (1999).
42. Robert R. Gamache, "Line Shape parameters for water vapor in the 3.2 to 17.76 μm region for Atmospheric Applications," J. Mol. Spectrosc. **229**,9-18, 2005.

43. B.E. Grossmann and E.V. Browell, Spectroscopy of water vapor in the 720-nm wavelength region: Line strengths, self-induced pressure broadenings and shifts, and temperature dependence of linewidths and shifts, J. Mol. Spectrosc. **136**, 264-294 (1989).
44. R.A Toth, L.R. Brown, C. Plymate, Self-broadened widths and frequency shifts of water vapor lines between 590 and 2400 cm^{-1}, Journal of Quantitative Spectroscopy and Radiative Transfer **59,** 529-62 (1998).
45. S. Fally, P-F Coleur, M. Carleer, C. Clerbaux, R. Colin, A. Jenouvrier, M.-F.Merienne, C. Hermans, A. C. Vandaele, Water vapor line broadening and shifting by air in the 26000-13000 cm/sup -1/ region Journal of Quantitative Spectroscopy and Radiative Transfer **82,** *119-131* (2003).

QUANTITATIVE ROTATIONAL SPECTROSCOPY FOR ATMOSPHERIC RESEARCH

GEORGES WLODARCZAK*, JEAN-MARCEL COLMONT AND FRANCOIS ROHART
Laboratoire de Physique des Lasers, Atomes et Molécules, UMR CNRS 8523, Université des Sciences et Technologies de Lille, F-59655 Villeneuve d'Ascq, France

Abstract. The paper presents some recent advances in rotational spectroscopy linked to atmospheric studies. The preparation of the recent space missions such as Odin or EOS-MLS has induced strong spectroscopic efforts to provide accurate line shape parameters that minimize the errors in the retrieval procedures. A critical evaluation of these parameters is needed. The main points related to line positions, line intensities, line broadenings and line shifts are discussed.

Keywords: rotational spectroscopy; line broadenings; line shapes; databases; atmospheric species

1. Introduction

Microwave remote sensing techniques are playing an important role in probing the terrestrial atmosphere, complementary from the measurements performed in the other spectral ranges, with some specific advantages (Payan et al., 2005). The observations are made either from the ground or from space, and require an accurate knowledge of the spectroscopic parameters for a quantitative retrieval. A careful analysis of the accuracy of these spectroscopic parameters is also needed to estimate its impact on the total error budget.

*To whom correspondence should be addressed. Georges Wlodarczak, Laboratoire de Physique des Lasers, Atomes et Molécules, UMR CNRS 8523, Université des Sciences et Technologies de Lille, F-59655 Villeneuve d'Ascq, France; e-mail: gwlodarc@phlam.univ-lille1.fr

A. Perrin et al. (eds.), Remote Sensing of the Atmosphere for Environmental Security, 221–235.

The microwave radiometers operating from the ground are limited to millimeter wavelengths (frequencies below 300 GHz) and are devoted to the monitoring of stratospheric water vapor, ozone and chlorine monoxide. Very recently several missions have extended this spectral range to higher frequencies: the Submillimeter Limb Sounder (SLS) (Stachnik et al., 1999), the airborne ESA/MARSCHALS experiment (Oldfield et al., 2001) which will probe the upper troposphere and the lower stratosphere, the TeraHertz OH Measurement Atmospheric Sounder (THOMAS) aboard a DLR aircraft (Titz et al., 1995) and the balloon OH of JPL (Pickett, 2005) both equipped with a 2.5 THz limb sounder to monitor the OH radical. The development of satellite missions with millimeter or submillimeter limb sounders has also extended the accessible spectral range for observations and the spatial coverage of the measurements. The first two successful instruments were the Upper Atmospheric Research Satellite Microwave Limb Sounder (UARS-MLS) and the Millimeter-wave Atmospheric Sounder (MAS). More recently, the Odin satellite (a collaboration between Sweden, France, Finland and Canada) was launched in 2001, and its SubMillimeter Radiometer (SMR) is currently operating between 480 and 580 GHz (Mégie et al., 2002; Ricaud et al., 2005). Among Odin's objectives is a better understanding of the stratospheric ozone chemistry and the target molecules are O_3, ClO, N_2O, HNO_3, H_2O, NO, CO and isotopes of H_2O and O_3. One example of the SMR capabilities is given in Figure 1 (from Ricaud et al., 2005). The correlations between the concentrations of several target species at an altitude of 20 km are shown, and compared to a simulation realized with the REPROBUS chemical transport model. More details on the recent results can be obtained on the website http://smsc.cnes.fr/ODIN; see also the paper by Ricaud et al. in this volume.

The EOS/MLS instrument on board the Aura satellite launched by NASA in July 2004 covers the range 190-640 GHz and includes also a channel at 2.5 THz. More details on the instrument and on the first results of this mission can be found in Waters et al. (2005) or at the following website: http://mls.jpl.nasa.gov. The figure 2 (from Santee et al., 2005) represents the time evolution of the concentrations of some species implied in the ozone stratospheric chemistry. The channel at 640 GHz allows the detection of HCl, simultaneously with the determination of the ClO abundance for the first time.

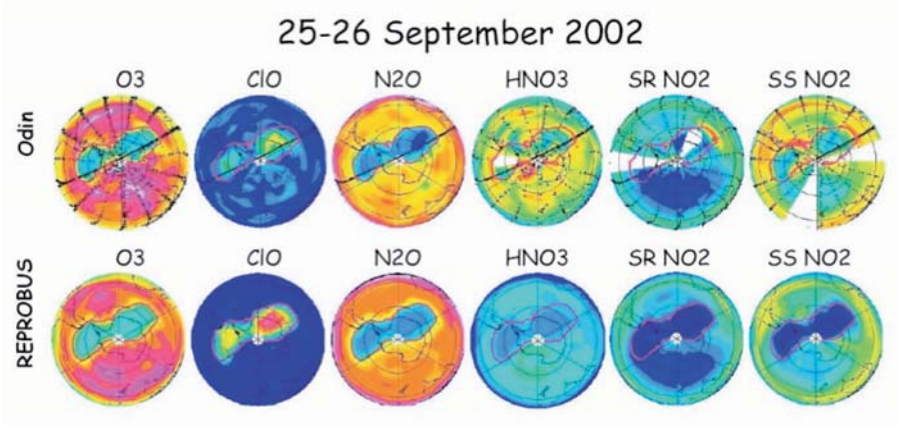

Figure 1. Odin-SMR O_3, ClO, N_2O, HNO_3 and NO_2 maps (up) during the splitting of the Antarctic polar vortex in September 2002, compared with a simulation computed with the REPROBUS model (down).

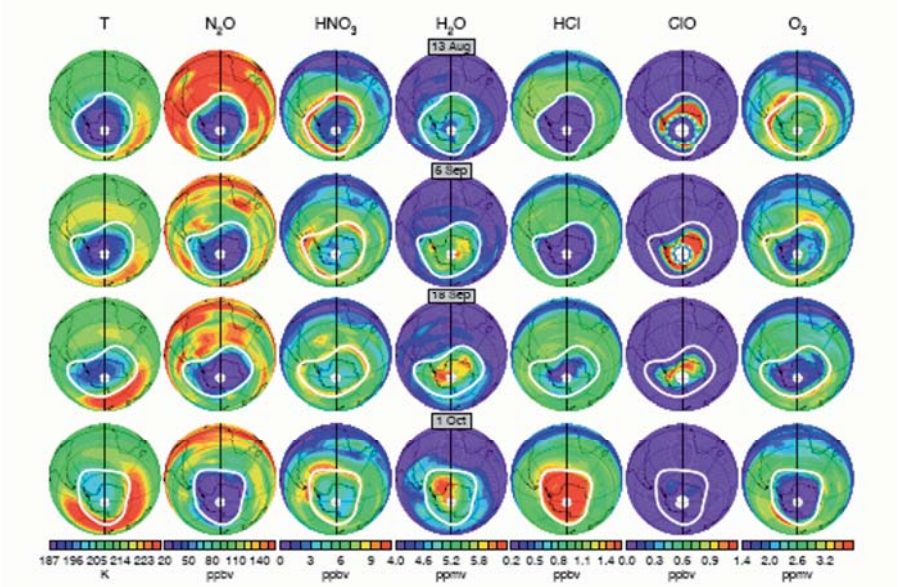

Figure 2. EOS-MLS T, N_2O, HNO_3, H_2O, HCl, ClO and O_3 maps for selected days during the 2004 Antarctic late winter.

New projects are scheduled for the near future: SMILES (Sub-Millimeter Limb Emission Sounder) to be placed aboard the International Space Station in 2008 will cover the 620-660 GHz frequency range. SMILES will have increased sensitivity due to the use of a helium cooled SIS receiver (Masuko et al., 2002). The use of a helium cooled SIS receiver in the range 604-662 GHz has been recently tested by the Airborne Submillimeter Radiometer (ASUR) experiment developed at the University of Bremen (Buehler et al., 2005). Another radiometer (Submillimeter Limb Sounder SLS-2) using a helium cooled SIS receiver in the range 600-690 GHz has also flown aboard a balloon experiment and shown a sensitivity increased by a factor of 20 when compared to an uncooled Schottky receiver. DLR has planned the successor of the THOMAS experiment, named the Terahertz Limb Sounder (TELIS), together with the dutch spatial agency (SRON) and the Rutherford Appleton Laboratory. This instrument is also based on SIS technology but in several channels hot electron bolometers will be used. The European Space Agency also has interest in the submillimeter domain (Langen, 2005), for which a review of the needed spectroscopic parameters has been recently published (Perrin et al., 2005). These parameters are the line positions (or frequencies), the intensities, the line-broadening coefficients with air (the self-broadening effect being usually negligible under atmospheric conditions), the pressure shifts and their temperature dependencies.

2. Line positions and intensities

2.1. LINE POSITIONS

For many of the target lines, the spectroscopy is well-known and the frequencies are listed in the JPL and HITRAN databases. Nevertheless the JPL catalog (Pickett et al., 1998) is recommended for the rotational transitions frequencies because it generally contains more information (fine or hyperfine structure) than the HITRAN database (Rothman et al., 2005). Concerning several atmospheric species like HNO_3, H_2CO, $(CH_3)_2CO$, O_3, CH_3Cl recent spectroscopic studies mixing infrared and microwave data have improved the available information. Some sub-Doppler measurements (on HCN or HCl for instance) have also allowed an increased accuracy on the quoted frequencies.

2.2. LINE INTENSITIES

Contrary to the infrared domain where intensity measurements are quite common, intensity measurements in the microwave region are not so easy and rather rare. Nevertheless, it is easier to calculate the line intensity, if the permanent dipole moment is known. This is the case for many atmospheric species, but for some isotopic forms like HDO or some ^{18}O derivatives, the data are not available. In these cases high level *ab initio* calculations are available to provide dipole moments accurate to 1%. The line intensities are given in the JPL and the HITRAN catalogs but they can differ by several %. One reason for differences in absolute intensities is the vibrational part of the partition function, which is not always taken into account in the calculations (i.e. in the JPL catalog). Another reason may be the origin (and the parameters used) of the calculations which is not always quoted in the databases. In a recent study (Perrin et al., 2005) some significant discrepancies have been observed on a simple molecule like N_2O: the new calculation indicates a deviation of 7% from the quoted value in HITRAN while it is compatible with the value quoted in JPL with a corrected partition function. It is recommended to carefully check these calculated intensities before their implementation in the databases.

3. Line broadenings

3.1. LABORATORY TECHNIQUES

In the millimeter-wave region, the Doppler width and the collisional width are of the same order of magnitude and then a Voigt profile is generally used to fit the experimental data. The experiments are usually performed at low pressures (up to 2-3 Torr) in most of the laboratories where conventional MMW absorption spectrometers are used: Lille and Bologna (Cazzoli et al., 2005), JPL (Drouin et al., 2005), OSU (Petkie et al., 1997), AIST (Yamada and Abe, 2003a), Ibaraki (Yamada et al., 2003). Measurements have been extended to the SMM region by using FIR molecular lasers (Farhoomand et al., 1985), THz photomixing at JPL (Matsuura et al., 2000) and NIST (Podobedov et al., 2004) or harmonic generation at JPL (Drouin et al., 2005). Acoustic detection of the absorption allows higher pressures (Nizhnii Novgorod) and the use of a resonator permits measurements at atmospheric pressure (Nizhnii Novgorod). Fourier transform infrared spectrometers can also be used in the far infrared (DLR, NIST) with a lower spectral resolution but allowing also high pressures. Time domain experiments have been made in Kiel and Lille.

3.2. INTERCOMPARISONS

Contrary to the IR domain, the measurements are usually made on isolated lines and inter-comparisons between different laboratories are not always possible. Nevertheless, when such comparisons are available, the differences observed for the same transition studied by different groups are usually larger than the quoted uncertainties. This indicates that systematic errors are larger than statistical errors. These systematic errors may be caused by the pressure measurement, the temperature determination and the homogeneity of the temperature within the sample, the power fluctuations of the source, the stability of the sample during the measurements, the line shape model,… An estimation of these systematic errors can be made by comparing the results obtained within the same group by using different techniques and/or by comparing the results obtained by two (or more) different groups. This was the conclusion of the International Workshop on Critical Evaluation of MM/SMM-Wave Spectroscopic Data for Atmospheric Observations, held in Ibaraki (Japan) in January 2004 (Drouin et al., 2004c).

Figure 3 (taken from Tretyakov et al., 2003) represents the evolution with time of the air-broadening parameter of one popular water vapor line. All measurements are laboratory data except values 9 and 10, which were retrieved from atmospheric satellite data.

More recently two different spectrometers, a video-type spectrometer and a frequency-modulated spectrometer, were used in Lille to measure the N_2-broadening parameter for two lines of ozone and one line of N_2O and the results agreed within 2% (Demaison et al., 2004). Similar results were obtained in Bologna on CO and OCS, measured either with an amplitude modulation or a frequency modulation technique (Puzzarini et al., 2002).

The air-broadening of the J=3-2 line of CO at 345 GHz has been investigated in Lille (video-type spectrometer, low pressure of N_2 or O_2, backward oscillator as a source), DLR (FTIR, high pressure of air) and Bologna (^{13}CO, frequency-modulated spectrometer, low pressure of N_2 or O_2, frequency-multiplied Gunn diode as a source). The values obtained in the three groups are respectively 2.728(17), 2.745(55) and 2.687(18) MHz/Torr, values which also agree within 2%. Similar conclusions were reported for ozone lines studied in Lille and Bologna respectively (Colmont et al., 2005). Larger deviations were pointed out for the $15_{6,10}$-$16_{5,11}$ line of ozone between JPL (Drouin et al., 2004b) and Ibaraki (Yamada and Amano, 2005): at 296K, the reported values for the air-broadening coefficient are respectively 2.988(19) and 2.835(11) MHz/Torr.

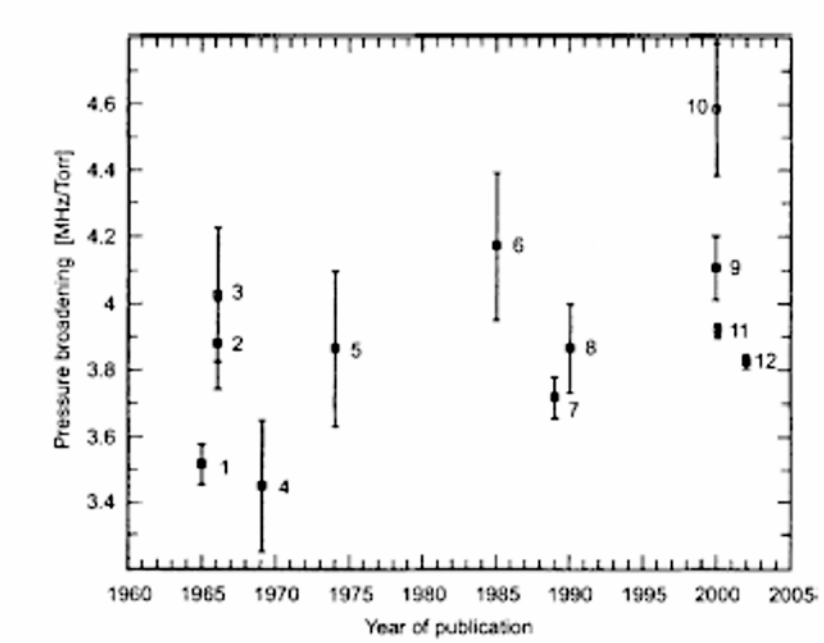

Figure 3. Measured values of the 183 GHz water line air-pressure broadening coefficient.

Nitric acid has also been the subject of inter-comparison campaigns. A first paper relating works at JPL and OSU showed an agreement within 5% for several rotational lines of nitric acid, compatible with the quoted uncertainties for the respective air-broadening parameters (Goyette et al., 1998). More recently an inter-comparison between Lille and Bologna showed an agreement within 2% (Cazzoli et al., 2005), and for one line a check was made also with the JPL/OSU value, showing an agreement within the error bars.

The temperature dependence of the air-broadening coefficient γ is usually expressed as a power law: $\gamma(T) = \gamma(T_0)\ (T_0/T)^n$, with T_0 usually equal to 296K and the exponent n is determined from measurements usually performed in the temperature range 200-300K. The agreement between the n values obtained by different groups for the same transition is generally within 10-15%, which is understandable because the accurate determination of this coefficient is not an easy task and because the temperature range which is explored is not wide enough. Other inter-comparisons were done on CO and ozone (Bauer et al., 1998) and BrO (Yamada et al., 2003).

Another check of results is the comparison with infrared data. The collisional broadening coefficient is usually not strongly dependent on the

vibrational state and therefore a comparison can be made with the corresponding coefficients in different ro-vibrational bands, for transitions with the same rotational quantum numbers. The rather large number of available data in the infrared allows quantitative comparisons. The procedure is easier for linear molecules for which only one rotational quantum number is needed (see for instance Rohart et al. (2003) for N_2O) than for asymmetric tops .

3.3. COMPARISON WITH THEORY

The comparison between experimental broadening coefficients and theoretical ones could also be considered as another way to check the experimental values. The theoretical calculations are usually done within the complex Robert-Bonamy formalism (with O_2 or N_2 as broadening gas), which provides simultaneously the line broadening and the line shift coefficients. This formalism is described in more details in the paper by R. R. Gamache in this volume. The results for water vapor are also discussed in this paper.

Concerning the molecules previously discussed, the case of ozone is interesting. Many rotational lines have been studied by various groups these last years and in most cases theoretical calculations have also been performed. The agreement is generally good, the deviation between theory and experiment being less than 5% in most cases (Priem et al., 2000, Drouin et al., 2004b).

For N_2O the agreement is less perfect, especially if we consider a combined set of microwave and infrared data. The general trend of the evolution of the broadening coefficient with the rotational quantum number is well reproduced but the discrepancies can reach 10% (Rohart et al., 2003, Nguyen et al., 2005). The calculations also reproduce the K-dependence of the broadening coefficient for symmetric tops like CH_3Cl or CH_3CN (Colmont et al., 2006)

The situation is not so good for some asymmetric tops like nitric acid, for which confident calculations are not yet available. In this case, due to the large number of rotational transitions present in the observational windows, an empirical modeling has been proposed (Perrin et al., 2005) based on two different linear interpolations for low and high rotational quantum number values respectively. This model provides more realistic value than the constant value quoted for all rotational transitions in the previous versions of HITRAN.

Due to the large uncertainties on the temperature exponent n, the comparison with calculated values is less conclusive.

3.4. LINESHIFTS

For rotational transitions the pressure shift is found generally small, and in many cases very difficult to determine with a good accuracy. For instance the

self-shift of the J=5-4 transition of CO at 576.3 GHz is 6(3) kHz/Torr in Markov et al. (2002) and 45.8(214) kHz/Torr in Yamada et al. (2003a). For ozone very small values have been measured in Bologna (Perrin et al., 2005), values compatible with those calculated by Gamache (Drouin et al., 2004b). Significantly larger values have been determined for ammonia, H_2O and recently at JPL for the J=1-0 line of HCl (Drouin, 2004a): the air-pressure shift δ is 146(3) kHz/Torr, a value confirmed by Morino and Yamada (2005). For water, the transition at 183 GHz was investigated at low-pressure (Golubiatnikov, 2005), δ = -93(8) kHz/Torr, and high-pressure (Tretyakov et al., 2003), δ = -92(25) kHz/Torr, in laboratory. These values are compatible with the value retrieved from atmospheric data (Pumphrey and Buehler, 2000), δ = -130(40) kHz/Torr. In this latter case the pressure shift was found to be necessary to reproduce the atmospheric spectra. For nitric acid, the shifts were also found negligible (Cazzoli et al., 2005).

3.5. LINE SHAPE ANALYSIS

Departures from Voigt profile have been observed in infrared spectra and more recently in rotational spectra for various molecules: O_3 (Priem et al., 2000, Colmont et al., 2005), N_2O (Rohart et al., 2003; Nguyen et al., 2005), CO (Priem et al., 2000a), NO (Colmont et al., 2001), CH_3Cl (Colmont et al., 2006), HCN, CH_3CN,… Figure 4 shows an example of such an effect on a rotational transition of N_2O, observed in Lille with a frequency-modulated spectrometer.

Two reasons are generally presented to explain this departure from a Voigt profile (D'Eu et al., 2002).

i) If we take into account the velocity/speed changing collisions, this leads to a narrowing of the profile (Dicke effect). This effect can be modeled with a Galatry profile (in case of soft collisions, when the mass of the absorbing molecule is larger than the mass of the collisional partner) or a Rautian profile (in case of hard collisions, when the mass of the absorbing molecule is smaller than the mass of the collisional partner). The description of the Galatry (or Rautian) profile needs a new parameter, the optical diffusion rate β.

ii) If we take into account the speed dependence of relaxation rates, this leads to the speed-dependent Voigt (SDV) profile. It has been shown in previous studies that a quadratic dependence for the relaxation rate, $\Gamma(v_a) = \Gamma_0 + \Gamma_2 [(v_a/v_{a0})^2-3/2]$ where v_a represents the absorber's speed, gives a good description of the observed narrowing effect. By contrast with many infrared experiments, the SDV profile has been used in most of the studies performed in the millimeter range, because the Galatry profile usually fails, at higher pressures, to fit the experimental signal (in fact the diffusion rate Γ does not

behave linearly with pressure). A more fundamental reason for the choice of the speed-dependent Voigt profile is the generality of this phenomenon.

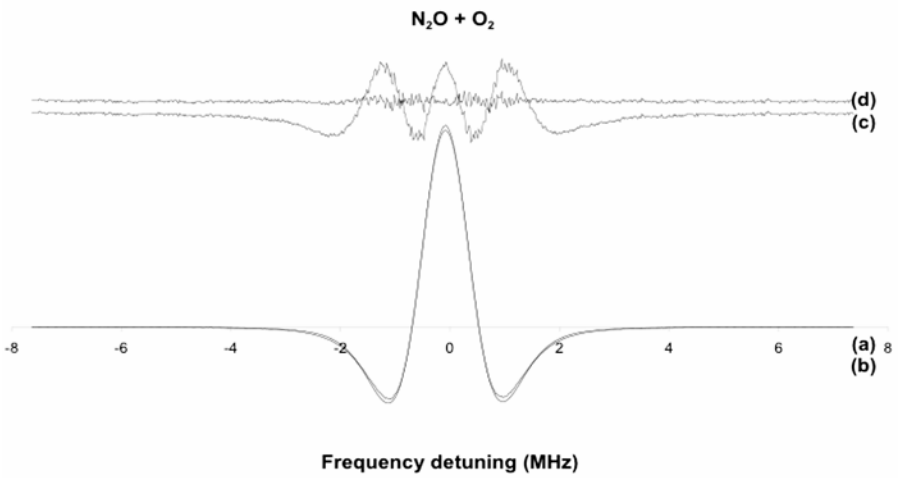

Figure 4. Relaxation of the J=24-23 line of N_2O in collision with O_2 at 296K (N_2O pressure: 8 mTorr, O_2 pressure: 170 mTorr). The experimental line shape (a) is fitted with a Voigt profile (b). Residuals are shown for Voigt (c), and SDV profiles (d), magnified by a factor 10.

With this alternative profile we observe also a deviation of the broadening coefficient, depending on the observed transition and of the molecule), which may reach 2% when compared to the coefficient retrieved from the Voigt profile. In atmospheric conditions this effect is supposed to be negligible, except may be in upper stratosphere. The use of these different profiles in the literature can make comparisons more difficult.

3.6. LINE MIXING

Line mixing is not very often observed in rotational spectra, compared to rovibrational spectra. It has been recently observed for the 60 GHz band of molecular oxygen by Tretyakov and co-workers (Tretyakov et al., 2005). From low-pressure experiments, accurate frequencies and line broadening parameters were determined. Then measurements at atmospheric pressure were undertaken, showing blended lines spread over 10 GHz, with a resulting profile different

from the sum of the individual profiles. From the analysis of these high-pressure data first order line mixing coefficients were determined, for pure oxygen and for air. The temperature dependence of the line mixing has not yet been investigated. The line parameters were updated in the MPM model.

4. Non-resonant processes

Recent FTS measurements of atmospheric transmission were performed at CSO (Mauna Kea, 4100 m) below 1 THz (Pardo et al., 2001) and beyond 1 THz (Pardo et al., 2005). The absorbing lines were modeled with a Van-Vleck-Weisskopf line shape and all H_2O lines up to 10 THz were taken into account, due to their far wings contribution. The residuals were analyzed by taking into account two continua. A dry continuum, due to collision-induced absorption of the N_2-N_2, N_2-O_2, O_2-N_2 and O_2-O_2 pairs, has been retrieved, in good agreement with recent theoretical calculations (Boissoles et al., 2003). A wet continuum, due to H_2O-N_2 and H_2O-O_2 opacity terms, has also been derived, showing a squared dependence on frequency, in rather good agreement with theory (Ma and Tipping, 2002). The laboratory data related to these processes include some recent measurements performed at NIST on H_2O-N_2 mixtures, between, 12 and 50 cm^{-1} (Podobedov et al., 2005).

5. Conclusion

The recent development of microwave limb sounders aboard satellites has induced a large quantity of laboratory studies devoted to the target molecules. In many cases a critical analysis of the error sources has been made and in some cases inter-comparisons have been performed, leading to a better estimate of the systematic errors. The implementation of all these new data within databases will allow a great improvement of the retrieval procedures as shown in Verdes et al. (2005).

Acknowledgments

The following institutions are acknowledged for financial support: CNRS (Programme National de Chimie Atmosphérique and LEA Hires), European Space Agency (contract n° 16377/02/NL/FF), the Galileo exchange program

between Lille and Bologna, and European Community via the Marie Curie Research and Training Network "QUASAAR". B. Drouin (JPL) is acknowledged for fruitful discussions.

References

Bauer A., Birk M., Wagner G., Colmont J.-M., Priem D., Wlodarczak G., Buehler S., von Engeln A., Kunzi K. and Perrin A., 1998, Study on a spectroscopic database for millimeter and submillimeter wavelengths, ESA-ESTEC contract n°11581/95/NL/CN, Final report

Boissoles J., Boulet C., Tipping R. H., Brown A. and Ma Q., 2003, Theoretical calculation of the translation-rotation collision-induced absorption in N_2-N_2, O_2-O_2, and N_2-O_2 pairs, *J. Quant. Spectrosc. Radiat. Transfer* **82**: 505-516

Buehler S. A., Verdes, C. L., Tsujimaru S., Kleinböhl A., Bremer H., Sinnhuber M. and Eriksson P., 2005, Expected performance of the superconducting submillimeter-wave limb emission sounder compared with aircraft data, *Radio Science* **40**: RS3016

Cazzoli G., Dore L., Puzzarini C., Bakri B., Colmont J.-M., Demaison J., Rohart F. and Wlodarczak G., 2005, Experimental determination of air-broadening parameters of pure rotational transitions of HNO_3 : inter-comparison of measurements by using different techniques, *J. Mol. Spectrosc.* **229**: 148-159

Colmont J.-M., D'Eu J.-F., Rohart F., Wlodarczak G. and Buldyreva J., 2001, N_2-and O_2-broadenings and lineshapes of the 551.53 GHz line of ^{14}NO, *J. Mol. Spectrosc*. **208**:197-208

Colmont J.-M., Bakri B., Rohart F., Wlodarczak G., Demaison J., Cazzoli G., Dore L. and. Puzzarini C., 2005, Inter-comparison between ozone broadening parameters retrieved from millimeter-wave measurements by using different techniques, *J. Mol. Spectrosc*. **231**:171-187

Colmont J.-M., Rohart F., Wlodarczak G. and Bouanich J.-P., 2006, K-dependence and temperature dependence of N_2- and O_2- broadening coefficients for the J=14-13 transition of methyl chloride $CH_3{}^{35}Cl$, *J. Mol. Struct*. **780-781**: 268-276

D'Eu J.-F., Lemoine B. and Rohart F., 2002, Infrared HCN lineshapes as a test of Galatry and speed-dependent Voigt profiles, *J. Mol. Spectrosc*. **212**:96-110

Demaison J., Buehler S., Koulev N., Kuhn T., Verdes C., Cazzoli G., Dore L., Puzzarini C., Flaud J.-M., Perrin A., Bakri B., Colmont J.-M., Rohart F. and Wlodarczak G., 2004, Characterization of millimeter wave spectroscopic signatures, *ESTEC Contract n°16377/02/NL/FF*

Drouin, B.J., 2004a, Temperature dependent pressure induced lineshape of the HCl J = 1-0 rotational transition in nitrogen and oxygen, *J. Quant. Spectrosc. Radiat. Transfer* **83**: 321-331

Drouin, B.J., Fisher J., Gamache R.R., 2004b, Temperature dependent pressure induced lineshape of O_3 rotational transitions in air, *J. Quant. Spectrosc. Radiat. Transfer* **83**: 63-81

Drouin B.J., Wlodarczak G. , Colmont J.-M., Rohart F., 2004c, Current status of quantitative rotational spectroscopy for atmospheric research, Proc. Int. Workshop on "Critical Evaluation of MM/SMM-Wave Spectroscopic Data for Atmospheric Observations", Ibaraki, Mito, Japan, January 2004.

Drouin B.J., Maiwald F.W. and Pearson J.C., 2005, Application of cascaded frequency multiplication to molecular spectroscopy, *Rev. Sci. Instrum*. **76**: 093113

Drouin B. J., 2006a, this volume

Farhoomand J., Blake G.A., Frerking M.A., and Pickett H.M., 1985, Generation of tunable laser sidebands in the far-infrared region, *J. Appl. Phys.* **57**: 1763-1766.

Goyette T.M., Cohen E.A.. and De Lucia F.C., 1998, An intercomparison of results in the millimeter wave region, *J. Quant. Spectrosc. Radiat. Transfer* **60**: 77-84

Golubiatnikov G. Yu., 2005, Shifting and broadening parameters of the water vapor 183-GHz line by H_2O, O_2, N_2, CO_2, H_2, He, Ne, Ar and Kr at room temperature, *J. Mol. Spectrosc.* **216**: 196-198

Langen J., 2006, this volume

Ma Q. and Tipping R. H., 2002, Water vapor millimeter wave foreign continuum: a Lanczos calculation in the coordinate representation, *J. Chem. Phys*. **117**: 10581-10596

Markov V. N., Golubniatnikov G. Y., Savin V. A., Sergeev D. A., Guarnieri A. and Mäder H., 2002, Line broadening and shifting studies of the J=5-4 transition of carbon monoxide perturbrd by CO, N_2 and O_2, *J. Mol. Spectrosc.* **212**: 1-5

Masuko H. et al., 2002, JEM/SMILES mission plan, version 2.1, technical report, Natl. Space. Dev. Agency of Jpn, Tokyo

Matsuura S., Chen P., Blake G.A., Pearson J.C., and Pickett H.M., 2000, A Tunable Cavity-locked Diode Laser Source for Terahertz Photomixing,, *IEEE Trans. Microwave Theory and Tech*. **48** : 380-387

Mégie G., Evans W.F., De La Noë J., Kyrölä E., McDade I.C., Ricaud P., Auvinen H., Haley C.S., Baron P., Oikarinen L., Sioris C., Pardo J.R., Savigny C.V., Hauchcorne A., Solheim B.H., Llewellyn E.J., McConnell J.C., Degenstein D.A., Strong K., Gattinger R.L., Richardson E.H., Lloyd N.D., Leppelmeier G.W., Murtagh D., Frisk U., Merino F., Ridal M., Jonsson A., Stegman J., Witt G., Eriksson P., Jiménez C., 2002, An overview of the Odin atmospheric mission, *Can. J. Phys*. **80**: 309-319 (the whole volume is dedicated to the Odin mission)

Morino I. and Yamada K.M.T., 2005, Absorption profiles of HCl for the J=1-0 rotational transition: foreign-gas effects measured for N_2, O_2 and Ar, *J. Mol. Spectrosc.* **233**: 77-85

Nguyen L. Buldyreva J., Colmont J.-M., Wlodarczak G. and Rohart F., 2005, Experimental and theoretical study of N_2O submillimeter spectral lineshapes, The 19th Colloquium on High Resolution Molecular Spectroscopy, Salamanca (11-16 sept. 2005), Poster P4

Oldfield M., Moyna B. P., Allouis E., Brunt R., Cortesi U., Ellison B.N., Eskell J., Forward T., Jones T., Lamarre D., Langen J., de Maagt P. J., Matheson D. N., Morgan I., Reburn J. and Siddans R., 2001, MARSCHALS: develoment of an airborne millimeter-wave limb sounder, *Proc. SPIE* **4540**: 221-228

Pardo J., Serabyn E. and Cernicharo J., 2001, Submillimeter atmospheric transmission measurements on Mauna Kea during extremely dry El Nino conditions: implications for broadband opacity contributions, *J. Quant. Spectrosc. Radiat. Transfer* **68**: 419-433

Pardo J., Serabyn E., Wiedner M. C. and Cernicharo J., 2005, Measured telluric continuum-like opacity beyond 1 THz, *J. Quant. Spectrosc. Radiat. Transfer* **96**: 537-545

Payan S., de La Noë J., Hauchecorne A. and Camy-Peyret C., 2005, A review of remote sensing techniques and related spectroscopy problems, *C. R. Physique* **6**: 825-835

Perrin, A., Puzzarini C., Colmont J.-M., Verdes C., Wlodarczak G., Cazzoli G., Buehler S., Flaud J.-M. and Demaison J., 2005, Molecular line parameters for the MASTER (Millimeter wave Acquisitions for Stratosphere/Troposphere Exchange Research) database, *J. Atmos. Chem.*, **50** : 161-205

Petkie D.T., Goyette T.M., Bettens R.A.P., Belov S.P., Albert S., Helminger P. and De Lucia F.C., 1997, *Rev. Sci. Instrum.* **68** : 1675-1683

Pickett H.M., Poynter R.L., Cohen E.A., Delitsky M.L., Pearson J.C., and Müller H.S.P., 1998, Submillimeter, Millimeter, and Microwave Spectral Line Catalog, *J. Quant. Spectrosc. Radiat. Transfer* **60**: 883-890

Pickett H.M., 2005, Microwave limb sounder THz module on Aura, *IEEE Trans. Geosci. Remote Sensing*, in press

Podobedov V.B., Plusquellic D.F. and Fraser G.T., 2004, THz laser study of self-pressure and temperature broadening and shifts of water vapor lines for pressures up to 1.4 kPa, *J. Quant. Spectrosc. Radiat. Transfer* **87**: 377-385

Podobedov V.B., Plusquellic D.F. and Fraser G.T., 2005, Investigation of the water vapor continuum in the THz region using a multipass cell, *J. Quant. Spectrosc. Radiat. Transfer* **91**: 287-295

Priem D., Colmont J.-M., Rohart F., Wlodarczak G. and Gamache R.R., 2000, Relaxation and lineshape of the 500.4 GHz line of ozone perturbed by N_2 and O_2, *J. Mol. Spectrosc*. **204**:204-215

Priem D., Rohart F., Colmont J.-M., Wlodarczak G. and Bouanich J.-P.., 2000a, Lineshape study of the J=3-2 rotational transition of CO perturbed by N_2 and O_2, *J. Mol. Struct.* **517-518**:435-454

Pumphrey H. C. and Buehler S., 2000, Instrumental and spectral parameters: their effect on and measurement by microwave limb sounding of the atmosphere, *J. Quant. Spectrosc. Radiat. Transfer* **64**: 421-437

Puzzarini C., Dore L. and Cazzoli G., 2002, A comparison of lineshape models in the analysis of modulated and natural rotational profiles: application to the pressure broadening of OCS and CO, *J. Mol. Spectrosc.* **216**: 428-436

Ricaud, P., Lefèvre F., Berthet G., Murtagh D., Llewellyn E.J., Mégie G., Kyrölä E., Leppelmeier G.W., Auvinen, H., Boonne C., Brohede S., Degenstein D.A., de La Noë J., Dupuy E., El Amraoui L., Eriksson P., Evans W.F.J., Frisk U., Gattinger R.L., Girod F., Haley C.S., Hassinen S., Hauchecorne A., Jimenez C., Kyrö E., Lautié N., Le Flochmoën E., Lloyd N.D., McConnell J.C., McDade I.C., Nordh L., Olberg M., Pazmino A., Petelina S.V., Sandqvist A., Seppälä A., Sioris C.E., Solheim B.H., Stegman J., Strong K., Taalas P., Urban J., von Savigny C., von Scheele F., and Witt G.**,** 2005, Polar vortex evolution during the 2002 Antarctic major warming as observed by the Odin satellite, *J. Geophys. Res.* **110**, D5*, D05302, 10.1029/2004JD005018*

Rohart F., Colmont J.-M., Wlodarczak G. and Bouanich J.P., 2003, N_2 and O_2 induced broadenings and shapes of millimeter lines of N_2O, *J. Mol. Spectrosc.* **222**: 159-171

Rothman L.S., Jacquemart D., Barbe A., Benner D.C., Birk M., Brown L.R., Carleer M.R., Chackerian Jr C., Chance K., Coudert L.H., Dana V., Devi V.M., Flaud J.-M., Gamache R.R., Goldman A., Hartmann J.-M., Jucks K.W., Maki A.G., Mandin J.-Y., Massie S.T., Orphal J., Perrin A., Rinsland C.P., Smith M.A.H., Tennyson J., Tolchenov R.N., Toth R.A., Vander Auwera J., Varanasi P. and Wagner G., 2005, The *HITRAN* 2004 molecular spectroscopic database, *J. Quant. Spectrosc. Radiat. Transfer* **96**: 139-204

Santee M.L., Manney G.L., Livesey N.J., Froidevaux L., MacKenzie I.A., Pumphrey H.C., Read W. G., Schwartz M.J., Waters J.W. and Harwood R. S., 2005, Polar processing and development of the 2004 Antarctic ozone hole: first results from Aura MLS, *Geophys. Res. Lett*. **32**, L12817, *10.129/2005GL022582*

Stachnik R.A., Salawitch R., Engel A. and Schmidt U., 1999, Measurements of chlorine partitioning in the winter Arctic stratosphere, *Geophys. Res. Lett.* **26**: 3093-3096

Titz R., Birk M., Hausamann D., Nitsche R., Schreier F., Urban J., Küllman H. and Röser H.P., 1995, Observation of stratospheric OH at 2.5 THz with an airborne heterodyne system, *Infrared Phys.* **36**: 883-891

Tretyakov M.Yu., Parshin V.V., Koshelev M.A., Myaskinova S.E.. and Krupnov A.F., 2003, Studies of 183 GHz water line: broadening and shifting by air, N_2 and O_2 and integral intensity measurements, *J. Mol. Spectrosc.* **218**: 239-245

Tretyakov M.Yu., Koshelev M.A., Dorovskikh V.V., Makarov D.S. and Rosenkrantz P.W., 2005, 60-GHz oxygen band: precise broadening and central frequencies of fine structure lines, absolute absorption profile at atmospheric pressure, and revision of mixing coefficients, *J. Mol. Spectrosc.* **231**: 1-14

Verdes, C.L., Buehler S.A., Perrin A., Flaud J.-M., Demaison J., Wlodarczak G., Colmont J.-M., Cazzoli G. and Puzzarini C., 2005, A Sensitivity Study on Spectroscopic Parameter Accuracies for a mm/sub-mm Limb Sounder Instrument, *J. Mol. Spectrosc.* **229** : 266-275

Waters J.W., Froidevaux L., Harwood R.S., Jarnot R.F., Pickett H.M., Read W.G., Siegel P.H., Cofield R.E., Filipiak M.J., Flower D.A., Holden J.R., Lau G.L., Livesey N.J., Manney G.L., Pumphrey H.C., Santee M.L., Wu D.L., Cuddy D.T., Lay R.R., Loo M.S., Perun V.S., Schwartz M.J., Stek P.C., Thurstans R.P., Boyles M.A., Chandra K.M., Chavez M.C., Chen G.-S., Chudasama B.V., Dodge R., Fuller R. A., Girard M.A., Jiang J.H., Jiang Y., Knosp B.W., LaBelle R.C., Lam J.C., Lee K.A., Miller D., Oswald J.E., Patel N.C., Pukala D.M., Quintero O., Scaff D.M., Van Snyder W., Tope M.C., Wagner P.A. and Walch M.J., 2005, The Earth Observing System Microwave Limb Sounder (EOS MLS) on the Aura satellite, *IEEE Trans. Geosci. Remote Sensing*, in press

Yamada, M.M., Kobayashi M., Habara H., Amano T., Drouin B.J., 2003, Submillimeter-wave measurements of the pressure broadening of BrO, *J. Quant. Spectrosc. Radiat. Transfer* **82**: 391-399

Yamada K.M.T. and Abe H., 2003a, The line broadening and shift effects on the CO J=5-4 transition at 576 GHz induced by collisions with rare gases, *J. Mol. Spectrosc.* **217**: 87-92

Yamada M.M. and Amano T., 2005, Pressure broadening measurement of submillimeter-wave lines of O_3, *J. Quant. Spectrosc. Radiat. Transfer* **95**: 221-230

PRESSURE-BROADENING OF THE 22.2 GHZ LINE OF WATER: BASIC RESULTS FOR REMOTE SENSING OF THE ATMOSPHERE

Gabriele Cazzoli* and Cristina Puzzarini
Dipartimento di Chimica "G. Ciamician", Università di Bologna, Via Selmi 2, I-40126 Bologna, Italy

Giovanni Buffa and Ottavio Tarrini
IPCF-CNR and Dipartimento di Fisica "E. Fermi", Università di Pisa, Largo Pontecorvo 3, I-56127 Pisa, Italy

Abstract. For atmospheric purposes, the self- and N_2-broadening parameters of the $J = 6_{1,6} \leftarrow 5_{2,3}$ (22.2 GHz) rotational transition of water has been investigated in the temperature range 296-338 K. This investigation should be considered of particular interest in monitoring the Earth's atmosphere because water is a fundamental component and it is well established that the accuracy of collisional broadening parameters has a crucial influence on reduction of remote sensing data. Therefore, a particular effort has been made in order to reduce instrumental as well as systematic errors. Experimental determinations have also been supported by theoretical calculations.

Keywords: pressure broadening, pressure shift, relaxation, rotational transition, water

1. Introduction

Over the last decades the physics and chemistry of the Earth's atmosphere have been the subject of many studies, for the composition of the atmosphere is indeed very important to understand chemical processes linked to depletion of stratospheric ozone and greenhouse effect. The vertical concentration profiles of atmospheric gases can be retrieved by remote sensing measurements, but they require the accurate knowledge of the parameters involved: line positions, transition intensities, pressure-broadened half-widths, pressure-induced frequency shifts and their temperature dependence. In particular, the collisional

* corresponding author

A. Perrin et al. (eds.), Remote Sensing of the Atmosphere for Environmental Security, 237–255.

broadening parameters have a crucial influence on reduction of remote sensing data.

Although water vapor is an important constituent of the terrestrial atmosphere, this molecule is well known to play a central role in the absorption of microwave as well as infrared radiation of the atmosphere; in fact, the absorption due to wings of the water lines is strong in most of the so-called "atmospheric windows" and gives rise to the problem of the continuum of water vapor. That is to say that models that do not account for absorption due to water cannot accurately reproduce the absorption observed in the atmospheric windows. Therefore, large effort has been devoted to this molecule both from a theoretical and experimental point of view (see for examples Refs. (Gamache et al., 1994; Bauer et al., 1995; Colmont et al., 1999; Bernath, 2002; Gamache and Fisher, 2003a; Gamache and Fisher, 2003b; Gamache, 2005) and references therein). Nevertheless, in the microwave region the data on pressure broadening, pressure shift and their temperature dependence of rotational water lines are still rather sparse and not always they have the proper accuracy. Furthermore, since water molecule represents a challenge for spectroscopists and an accuracy of about 3% is required in retrieval of gas composition profiles, improvements of available experimental data are often needed.

As far as the 22.2 GHz line of water is concerned, on one hand, the experimental data available in the literature are rather old and fairly in disagreement one another (Liebe and Dillon, 1969; Liebe et al., 1969; Kasuga et al., 1978). On the other hand, this transition has a relevant role in the retrievals of temperature and vertical gas profiles, as recently shown by Liljegren et al (Liljegren et al., 2005). It is worth noting that Liljegren et al showed that replacing for the air-broadened half-width of the 22 GHz line of water the value from Ref. (Liebe and Dillon, 1969) (previously used by Rosenkranz (Rosenkranz, 1998)) with the 5% smaller data from the HITRAN compilation (Rothman et al., 2003) largely eliminated the systematic differences in brightness temperatures. Additionally, since Liljegren et al also considered the results for the self-broadened half-width of this line from Ref. (Liebe et al., 1969) overestimated, instead they used an estimated value which was 4.8 times the air-broadened half-width, i.e., about 17.2 MHz/Torr.

The importance of an accurate knowledge as well as the need of improvements for the pressure broadening parameters for the 22.2 GHz line of water stimulated the present investigation.

2. Experimental details

A centimeter-wave spectrometer, working in the 8-40 GHz frequency range, has been employed; the block diagram is reported in Figure 1. The microwave source has been obtained by doubling the output of a computer controlled HP frequency synthesizer (Mod. HP 8276A: 12-18 GHz) whose external 10 MHz reference signal comes from a Rubidium standard. The measurements have been performed by using the source frequency modulation technique with the Lock-in amplifier tuned at twice the modulation frequency so that the second derivative of the natural line profile is recorded. The frequency modulation is performed by sine-wave modulating the signal of the synthesizer, and for each series of measurements the same modulation amplitude has been used for recording all the spectra.

The cell is a conventional P band wave guide 2 m long, and its temperature is measured through 3 thermocouples. The measurements

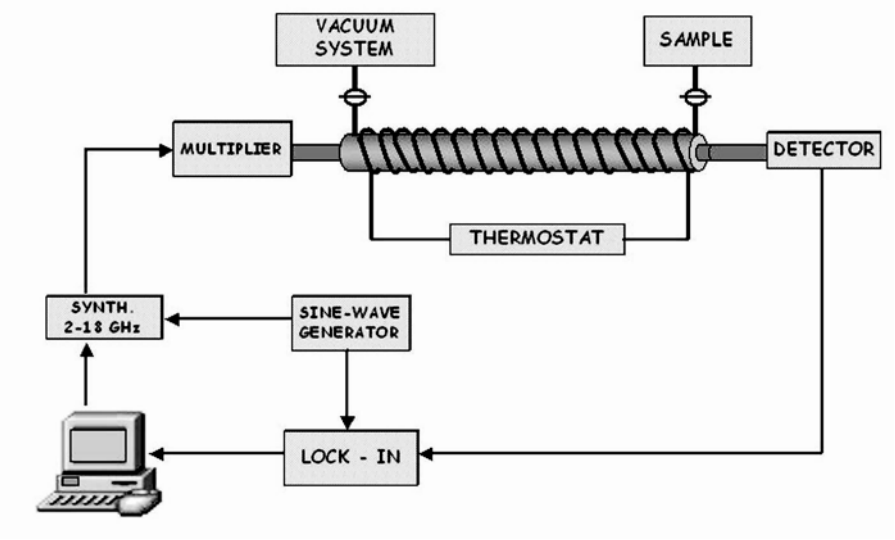

Figure 1. The block diagram of the 8-40 GHz spectrometer

have been performed at 296.7, 318.9 and 337.9 K, and the temperature has been kept fix by a thermostat (temperature accuracy: ±0.5 K). As depicted in Figure 1, the vacuum and sample input systems are directly connected to the cell. The sample pressure has been measured by a baratron gauge with a measurable pressure range of 10^{-4}-1 Torr, with 0.1 mTorr resolution; during the recording of a series of measurements the pressure of the gas has been found stable within 0.1-0.3 mTorr. The spectrometer is equipped with a HP Schottky diode detector, whose output signal is processed by means of a Lock-in amplifier. A computer-controlled data acquisition has been used: the driving of the spectrometer and the data processing are performed by means of a homemade software.

Water is a very challenging molecule from an experimental point of view because it is easily absorbed and desorbed by the walls of the cell. Consequently, it is difficult to keep the concentration of water constant during a series of measurements. This is not a real problem in the case of self-broadening; therefore, when water itself has been used as perturber, we proceeded in a standard way. More precisely, for all the temperatures considered, series of measurements (on the whole about 30-35 points) have been carried out and, for each series, we have chosen similar pressure ranges: pressure of ∼7-9 mTorr of H_2O have been employed as starting point, and then increasing quantities of water, in the range ∼20-150 mTorr, have been added. As far as N_2-broadening is concerned, at the beginning we proceeded as for the self-broadening case, but from the analysis of the measurements carried out at the three different temperature values we realized that the standard procedure was not suitable for either for the measurements at T = 297 and 319 K or for those at T = 338 since inconsistent pressure broadening parameters were obtained. After having performed different tests, the following procedure has been set up. It was found that during a regular series of measurements (i.e., 6-7 points at increasing pressure) the quantity of water inside the cell varies too much because of absorption or desorption phenomena. From the test measurements we have deduced that when water is introduced into the cell it is necessary to wait for about 10-20 minutes to reach a stable pressure of water into the cell and that this stable condition does not last for more than 10-15 minutes. Therefore, we adopted the strategy of short series of measurements, i.e., one record with only H_2O (P ∼8-12 mTorr) into the cell and 2 points at different values of partial pressure of nitrogen; consequently, it was necessary to increase the number of series of measurements (about 15-16) to have a total number of 30-

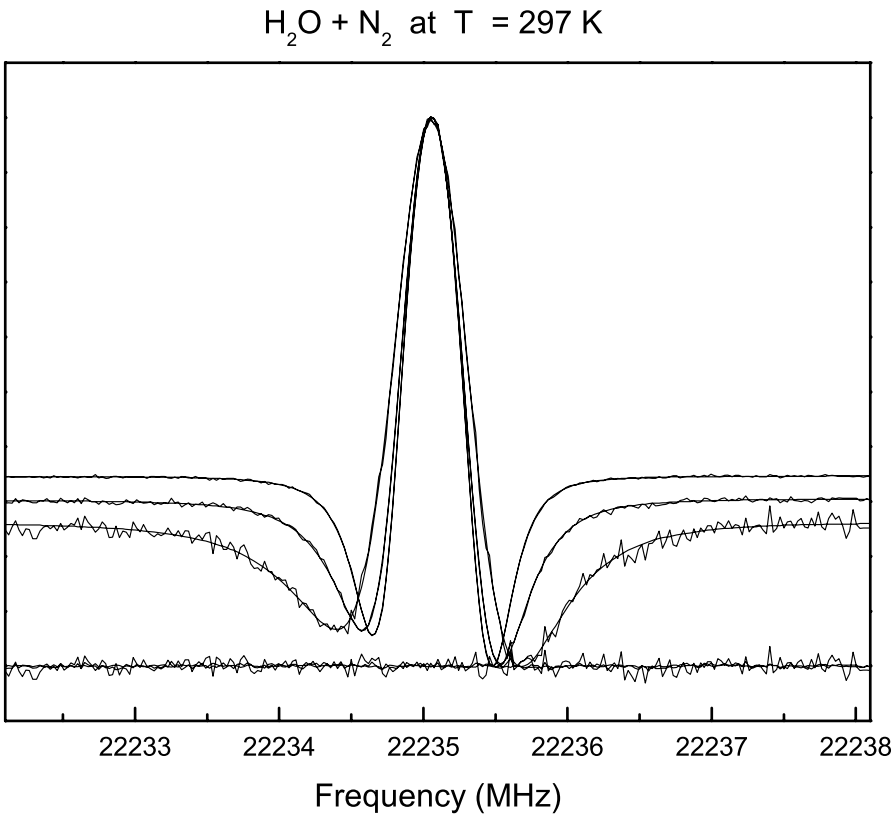

Figure 2. N_2-broadening: An example of a short series of measurements a T = 296.7 K. Residuals (observed - calculated differences) are also reported

35 points and cover a N_2 partial pressure range of 10-120 mTorr. An example of this short series of measurements carried out for studying N_2-broadening is given in Figure 2. We also took into consideration oxygen as perturber gas, but the test measurements for understanding the optimal and stable experimental conditions are still in progress. Finally, it should be mentioned that, since H_2O tends to be absorbed on the cell walls, it was found necessary to pump for a few days while heating the cell at a temperature a little bit higher than that into consideration; for example, the pumping procedure has been carried out at T$\sim$350 K for the subsequent measurements at T = 337.9 K.

Since the modulation technique has been used throughout, for each recorded spectrum, the collisional half-width has been determined by fitting the observed line profile to a model that explicitly accounts for frequency modulation as described in Refs. (Cazzoli and Dore, 1990; Puzzarini et al., 2002; Dore, 2003). The line profile analysis has been performed employing the Voigt model which is able to well reproduce the experimental line shapes. In fact, no relevant evidence of narrowing effects has been found (Dicke, 1953). Background subtraction has been performed in order to improve the line shape analysis, i.e., at the end of each series of measurements a spectrum at a pressure of about 600-700 mTorr of nitrogen has been recorded employing the same modulation amplitude and then subtracted by each spectrum of that series. A graphical example is provided by Figure 3.

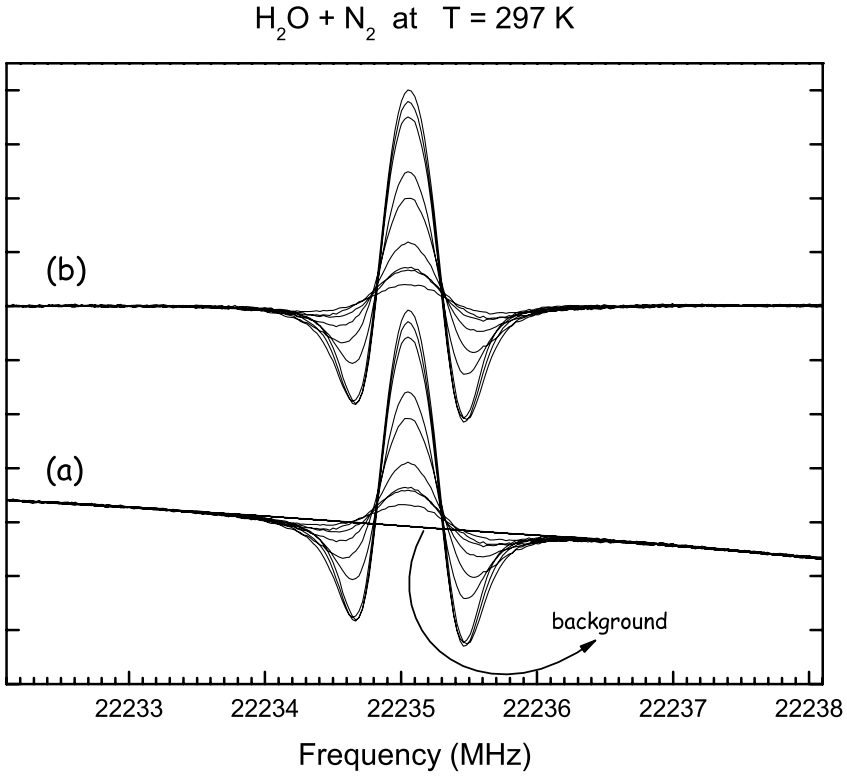

Figure 3. N_2-broadening at T = 296.7 K: An example of background subtraction. (a) Observed spectra. (b) Spectra after background subtraction

Since the same modulation amplitude has been employed along each series of measurements, the Pickett convolution method (Pickett, 1980) has also been applied for the line shape analysis and the corresponding determination of collisional half-width. This method is based on the comparison of two spectra: one at low pressure and one at higher pressure. More precisely, the method involves convoluting a low pressure reference spectrum with a Lorentzian shape function and comparing the convoluted spectrum with the higher pressure spectrum. The low pressure spectrum contains the information about modulation, Doppler and wall broadening, and, in general, all the pressure-independent effects, while the comparison with the higher pressure spectrum contains only information about pressure width and shift. Therefore, from this comparison the collisional half-width of the higher pressure spectrum is derived. Of course, this procedure has to be repeated for all the higher pressure spectra.

3. Theoretical details

At low pressures relaxation is due to binary collisions between absorber and perturber. The absorber is the molecule interacting with photon, in our case H_2O, while the perturber is the molecule inducing relaxation, in our case H_2O or N_2, or O_2. Collisional line width Γ and shift s are linear with the density n of perturbing gas. The phenomenon can be described within the impact approximation (Baranger, 1958a; Baranger, 1958b; Baranger, 1958c; Fano, 1963), which assumes that the duration τ of a collision is negligible with respect to the average time between two successive collisions and with respect to the inverse of the distance between line peak ν_ℓ and photon frequency:

$$|\nu - \nu_\ell| \ll \frac{1}{2\pi\tau} \, . \tag{1}$$

The pressure and frequency values of the case under consideration make impact approximation surely reliable; hence, the effect of a collision is described by scattering matrix S

$$S = \mathcal{O} \exp\left(-\frac{1}{\hbar} \int_{-\infty}^{+\infty} dt \; e^{iH_0 t/\hbar} V(t) e^{-iH_0 t/\hbar} \right) \, , \tag{2}$$

where $\mathcal{O}$ is time ordering operator, H_0 is the Hamiltonian of internal degrees of colliding molecules, and V is collisional interaction.

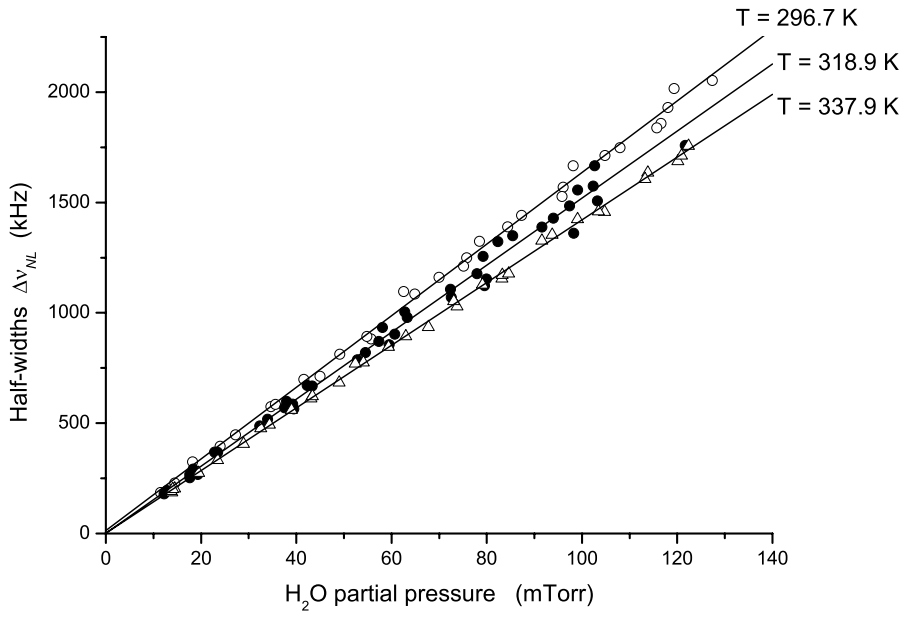

Figure 4. Self broadening: linear fits of the Lorentzian half-widths $\Delta\nu_{NL}$(T) against partial pressure of water at T = 296.7 K (○), T = 318.9 K (●), and T = 337.9 K (△). For depicting clarity purposes, error bars are not reported.

For a line $i \to f$, the relaxation efficiency of a collision is described by a complex function P which can be expressed in terms of the scattering matrix S:

$$P(r,k) = 1 - \sum_{r',k'} \langle i,r,k|S|i,r',k'\rangle \ \langle f,r',k'|S^{\dagger}|f,r,k\rangle \ , \qquad (3)$$

where r and r' are internal states of the perturber and k and k' are translational states.

Since a full quantum calculation of the scattering matrix can be done only for very simple collision partners, such as a linear molecule colliding with an atom, one is forced to resort to simplifying approximations. We will describe into details that used in our calculations.

We resorted to the semiclassical approximation which restricts quantum treatment to internal degrees of colliding molecules and uses classical mechanics for orbital dynamics. Within this theoretical framework,

the translational state k is characterized by impact parameter b and relative velocity v:

$$P = P(b, v, r). \tag{4}$$

The line width Γ and shift s are connected to the real and imaginary parts of P:

$$\Gamma + i\ s = n \sum_r \rho_r \int_0^\infty dv\ v\ f(v) \int_0^\infty db\ 2\pi b\, P(b, v, r)\ , \tag{5}$$

where ρ_r is the population of level r and $f(v)$ is the Maxwell velocity distribution.

Even in the frame of the semiclassical approximation, an exact calculation of the scattering matrix is not easily realized and further approximation are necessary. The problem is simple for the case of weak collisions, occurring at large impact parameters. In this case, the interaction $V(t)$ is small with respect to other energies involved in the problem and a low order (second order) perturbative expansion can be used in Eq. (2). This yields to an efficiency function $P^{\text{weak}}(b, v, r)$ which is asymptotically exact when $b \to \infty$.

Another case is solved on a plausibility ground: when the impact parameter is small, the collision is strong and the outgoing rotational state of the absorber is assumed to be completely uncorrelated to the ingoing one. As a consequence, one assumes that in Eq. (3) $\langle i, r, k|S|i, r', k'\rangle$ and $\langle f, r', k'|S^\dagger|f, r, k\rangle$ are very small and with a completely random phase. This yields

$$\operatorname{Re} P^{\text{strong}}(b, v, r) = 1, \tag{6a}$$

$$\operatorname{Im} P^{\text{strong}}(b, v, r) = 0\ . \tag{6b}$$

That is to say, strong collisions give full contribution to line broadening and no contribution to line shift.

While the cases of strong and weak collisions are easily solved, the same is not true for intermediate b values and different interpolation methods were used in the literature.

Some authors resort to a cutoff impact parameter $b_0(v, r)$ (Anderson, 1949; Tsao and Curnutte, 1962; Di Giacomo and Tarrini, 1969; Di Giacomo and Tarrini, 1970; Boulet et al., 1976; Frost, 1976). The perturbative efficiency function $P^{\text{weak}}(b, v, r)$ is extended to all b values larger then b_0, while the function $P^{\text{strong}}(b, v, r)$ of Eq. (6) is used when $b < b_0$. b_0 is defined by imposing an unitary bound to the perturbative

calculation performed for weak collisions. The bound can be imposed either to the real part of P, or to its absolute value, that is to say, one can define b_0 either by

$$\mathrm{Re}\, P^{\mathrm{weak}}(b_0, v, r) = 1 \,, \tag{7}$$

or by (Herman, 1963a; Herman, 1963b; Baldacchini et al., 1982)

$$|P^{\mathrm{weak}}(b_0, v, r)| = 1 \,. \tag{8}$$

Another interpolation is obtained by omitting the time order operator $\mathcal{O}$ in Eq. (2) (Murphy and Boggs, 1967; Murphy and Boggs, 1969; Robert and Bonamy, 1979). This allows to calculate all the perturbative terms in the exponential as powers of the lowest order term P^{weak} and yields an efficiency relaxation which, apart from minor differences, is related to P^{weak} by:

$$P(b, v, r) = 1 - e^{-P^{\mathrm{weak}}(b,v,r)} \,. \tag{9}$$

The efficiency function of Eq. (9) has the expected trend in both limits of large and small impact parameters. When b is large, P^{weak} is small and $P \simeq P^{\mathrm{weak}}$; when b is small, P^{weak} diverges and $P \simeq P^{\mathrm{strong}}$.

The choice of one or another interpolation procedure can change the calculated broadening parameter by about 10%. We resorted to the exponential smoothing interpolation of Eq. (9) that usually gives results smaller than the cutoff procedure and in better agreement with experiment. However, it is worthwhile noting that such an approximation cannot be considered as exact, even in the frame of a semiclassical treatment because the omission of time ordering $\mathcal{O}$ in Eq. (2) is justified only by the fact that it simplifies the calculation.

The methods used in the literature can differ also with respect to the description of translation dynamics. Straight lines trajectories at constant velocity may be assumed (Anderson, 1949), or parabolic trajectories osculating the true classical trajectory in the point of closest approach (Robert and Bonamy, 1979). We resorted to numeric integration of the classical translation dynamics induced by the spherical part of interaction potential.

The potential used in the calculation was composed by a long range electrostatic part and by a short range part given by the sum of atom-atom Lennard Jones potentials.

For the self perturbed case the electrostatic potential is the sum of dipole–dipole, dipole–quadrupole, quadrupole–dipole and quadrupole–

Table 1. Experimental[a] and calculated self-, N_2-, and O_2-broadening parameters for the 22.2 GHz line of water.

Temp. (K)	parameter	Self-broadening Exp: previous results	N_2-broadening Exp: previous results	O_2-broadening Exp: previous results
293(1)	Γ	13.9(7)[b]		
295(1)	Γ		4.14(50)[b]	
300(2)	Γ	17.99(18)[c]	4.10[d]	2.52[d]
〃	s	1.38(2)[c]		

Temp.	parameter	Self-broadening		N_2-broadening		O_2-broadening	
		Exp.	Theor.	Exp.	Theor.	Exp.	Theor.
296.7(5)	Γ	16.66(32)	17.95	3.797(32)	3.69	–	2.41
〃	s	0.84(10)	1.07				
318.9(5)	Γ	15.19(40)	17.05	3.533(44)	3.52	–	2.32
〃	s	0.63(8)	0.94				
337.9(5)	Γ	14.20(14)	16.35	3.434(64)	3.39	–	2.24
〃	s	0.60(13)	0.84				
	n	1.23(54)	0.76	0.83(34)	0.65	–	0.56

[a] Uncertainties in parentheses are 2 times the standard deviation (2σ).
[b] Ref. (Kasuga et al., 1978).
[c] Ref. (Liebe et al., 1969).
[d] Ref. (Liebe and Dillon, 1969).

qua-drupole interactions, while for the N_2 or O_2 perturbed case the electrostatic potential is simply dipole-quadrupole interaction.

The tensor expansion of the short range interaction was, as usual, truncated at the fourth order, while only the zero order term was used in the calculation of translation dynamics.

The results of calculations are reported in Table 1 and compared to measurements. As a consequence of the approximation involved in the theory their accuracy is estimated to be 10% for the broadening, while for the shift the error can amount up to a few percent of the broadening value.

4. Results and discussion

From an experimental point of view, the pressure-broadening coefficients Γ(T) at a given temperature T have been derived by a linear fit of the collisional half-widths $\Delta\nu_L$(T) against the partial pressure $P_{partial}$ of the perturber (H_2O or N_2):

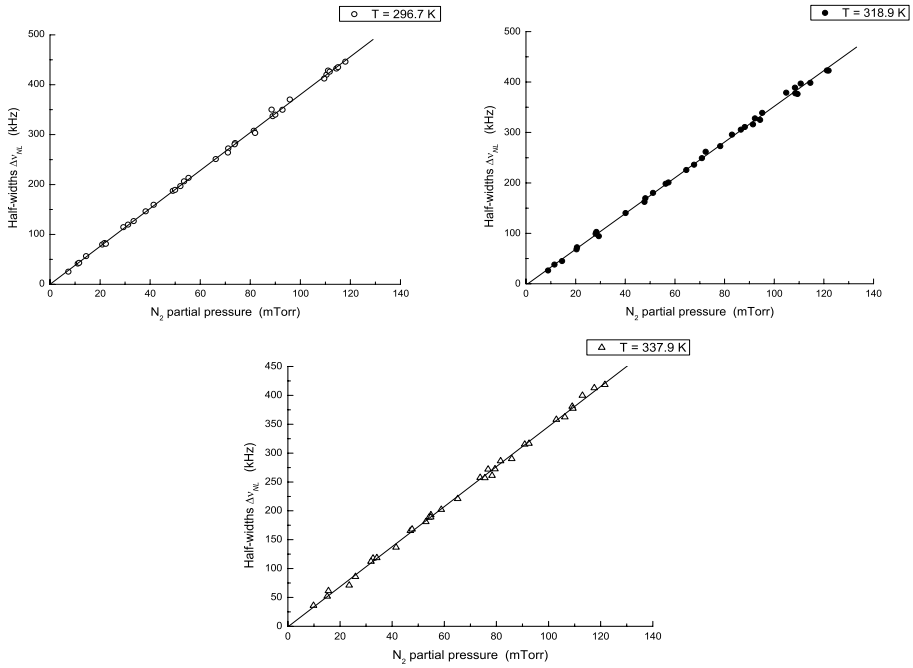

Figure 5. N_2-broadening: linear fits of the Lorentzian half-widths $\Delta\nu_{NL}(\mathrm{T})$ against partial pressure of nitrogen at T = 296.7 K (○), T = 318.9 K (●), and T = 337.9 K (△). For depicting clarity purposes, error bars are not reported.

$$\Delta\nu_L(T) = \Delta\nu_{P0} + \Gamma(T) \times P_{partial} \ . \tag{10}$$

As mentioned in the experimental details section, for each temperature some series of measurements have been carried out, and for each series of measurements, the pressure-broadening coefficient $\Gamma(\mathrm{T})$ has been derived by the above linear fit, in which the half-widths have been weighted according to the reciprocal of the squared uncertainties obtained from the profile analysis.

Since the series of measurements might be performed using different quantities of water, in order to put all the measurements together we have subtracted the value of the half width obtained by the fit for the first record, i.e., that with only water into the cell, to each $\Delta\nu_L(\mathrm{T})$. In this way, we have subtracted to the collisional half-widths the con-

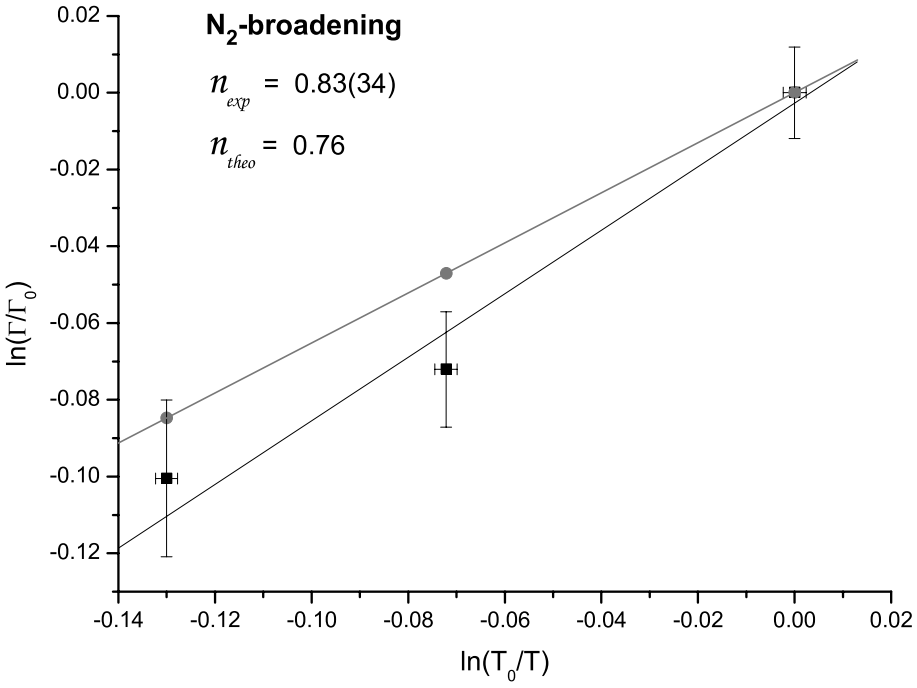

Figure 6. N_2-broadening: Determination of the temperature dependence parameter n. Experiment in black, theory in gray

tribution due to the absorber gas and to other type of broadening, e.g., wall broadening. Subsequently, a second fit involving all these updated half-widths $\Delta\nu'_L$(T) (all points for a given temperature and perturber gas) has been performed in order to obtain the final value of the pressure-broadening parameter Γ(T):

$$\Delta\nu'_L(T) = \Gamma(T) \times P_{partial} \ . \tag{11}$$

The least squares fits for the self- and N_2-broadening at the 3 temperatures are graphically displayed in Figures 4 and 5, respectively. The results are collected in Table I, where they are compared with the experimental data previously available in the literature and the theoretical values. As far as the self-broadening is concerned, an agreement between experiment and theory within about 10% on average is observed. With respect to the N_2-broadening, a better agreement

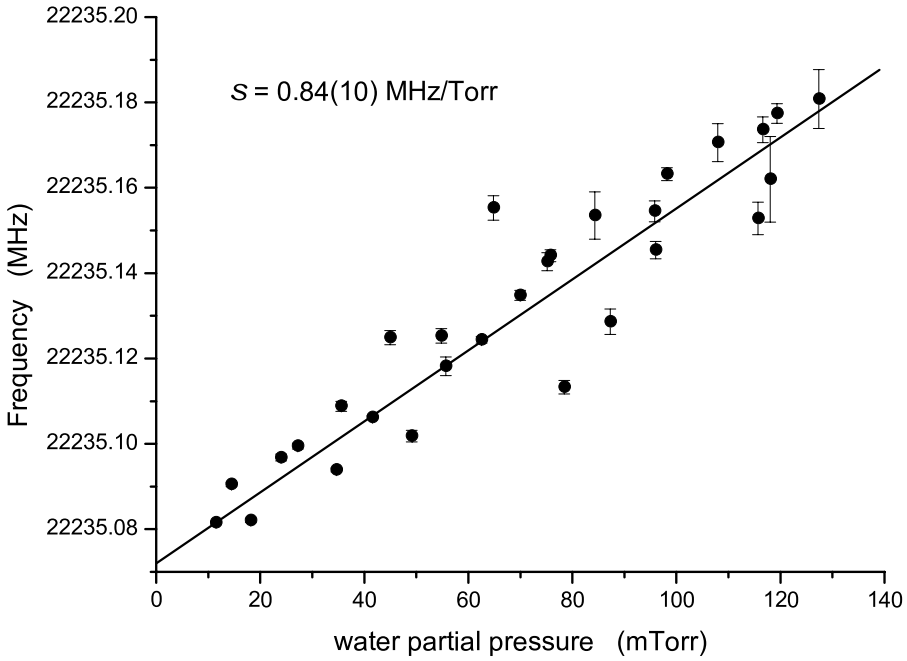

Figure 7. Self-broadening: Frequency shift against partial pressure of water at T = 296.7 K

has been found; in fact, the discrepancies are of the order of 1-3%. It is worth of mention that the uncertainties reported in Table I are 2 times the standard deviation, and therefore they should be considered underestimated because they do not account for systematic errors. Since water vapor is challenging molecule from an experimental point of view, a relative error of about 3-4% is a more reliable estimate of the experimental accuracy.

As previously mentioned, the Pickett convolution method has been additionally employed for deriving collisional half widths. We decided to also apply this method in order to confirm the results from the line shape analysis; in fact, the convolution method provides a way for determining Lorentzian widths independently from all the pressure-independent broadening, such as modulation, Doppler and wall broadening. The half widths obtained have then been fitted using Eq. (11). The results are not reported in Table I because for each temperature

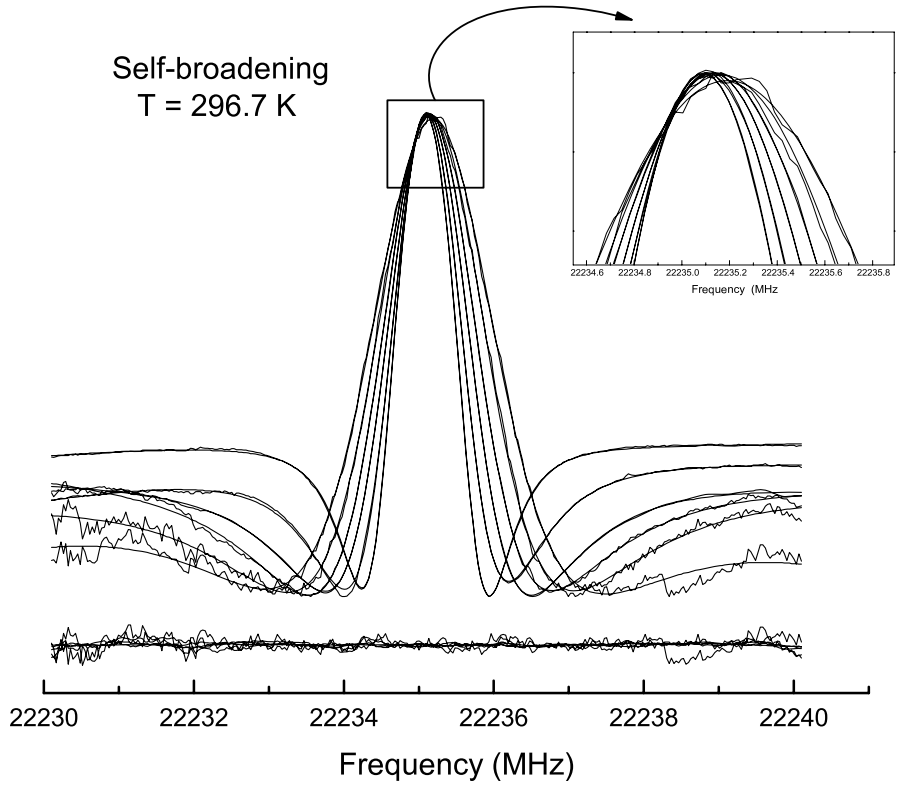

Figure 8. Self-broadening: An example of frequency shift along a series of measurements at T = 296.7 K. Residuals (observed - calculated differences) are also reported

and perturber considered only a few series of measurements (14-18 points) have been analyzed by employing the convolution method since it was essentially used for checking line shape results. Anyway, it should be noted that the results obtained are in very good agreement with those collected in Table I, hence confirming them.

From the measurements carried out at different temperatures, it is possible to determine the temperature dependence of the pressure broadening parameters. Following the semi-empirical law assumed for the pressure-broadening parameters $\Gamma(T)$ (Benedict and Kaplan, 1959):

$$\Gamma(T) = \Gamma_0(T_0) \left(\frac{T_0}{T} \right)^n \ , \tag{12}$$

the temperature exponent n has been derived for both self- and N_2-broaden-ing. In the above formula, Γ(T) is the pressure broadening coefficient determined at the temperature T and Γ_0(T_0) that at the temperature T_0. More precisely, a weighted least square fit in logarithmic scale has been performed:

$$ln \left(\frac{\Gamma(T)}{\Gamma_0(T_0)} \right) = n \ ln \left(\frac{T_0}{T} \right) \ , \tag{13}$$

where T_0 is the reference temperature, i.e., 296.7 K in this work, and n is the exponent of the power law to be determined. A graphical example is provided by Figure 6, where the comparison between experiment and theory for the N_2-broadening is given. From Eq. (13) it is clear that the temperature range considered has a fundamental role for an accurate determination of n. In fact, in Refs. (Gamache et al., 1998; Drouin et al., 2004) it has been demonstrated that the uncertainty Δn is greater than a quantity proportional to the relative error on Γ(T):

$$\Delta n \geq \sqrt{2} \frac{\Delta\Gamma(T)/\Gamma(T)}{ln(T_{max}/T_{min})} \ , \tag{14}$$

where $\Delta\Gamma$(T) is the error on Γ(T). The results are reported in Table I where they are compared to the theoretical data. In regard to self-broadening, one can notice that, on one hand, an experimental value that seems to be too large has been obtained, but, on the other hand, this data is affected by a very large error (2σ) which is due to both uncertainties on Γ(T) and on temperature itself. As concerns N_2-broadening, the experimental value is again larger than the theoretical one, even if in this case a better agreement is observed. In both cases 2 times the standard deviation seems to give a reliable estimate of the error; in fact, by applying Eq. (14) and considering for Γ a relative error of 3% one obtain that the uncertainty Δn should be greater than 0.33.

The pressure shift effect has also been considered. For each perturber and each temperature, the pressure shift parameter s(T) has been obtained by a linear fit of the transition frequency ν(T) against the partial pressure $P_{partial}$ of the perturber

$$\nu(T) = \nu_0 + s(T) \times P_{partial} \ , \tag{15}$$

in which the frequencies have been weighted according to the reciprocal of the squared uncertainties obtained from the profile analysis. A graphical example of the fit is provided by Figure 7, whereas in Figure 8 it is shown how noticeable the pressure shift is along a series of measurements.

The results obtained are collected in Table I. First of all, it should be noted that the pressure shift coefficient is large for self broadening, whereas is predicted to be very small in the case of N_2 and O_2 broadening. Actually, from both an experimental and theoretical point of view the pressure shift effect in the case of N_2-broadening has been found not determinable because smaller than the associated uncertainties. It is also interesting to notice that, as expected, the pressure shift coefficient increases by decreasing the temperature, as for the pressure broadening coefficients. As far as the comparison with theory is concerned, a substantial agreement is observed, i.e., experimental and calculated values agree within 4σ.

References

Anderson, P. W.: 1949, 'Pressure Broadening in the Microwave and Infra-Red Regions'. *Phys. Rev.* **76**, 647–661.

Baldacchini, G., S. Marchetti, V. Montelatici, G. Buffa, and O. Tarrini: 1982, 'Experimental and theoretical investigation of self-broadening and self-shifting of ammonia transition lines in the ν_2 band'. *J. Chem. Phys.* **76**, 5271–5277.

Baranger, M.: 1958a, 'General Impact Theory of Pressure Broadening'. *Phys. Rev.* **112**, 855–865.

Baranger, M.: 1958b, 'Problem of Overlapping Lines in the Theory of Pressure Broadening'. *Phys. Rev.* **111**, 494–504.

Baranger, M.: 1958c, 'Simplified Quantum-Mechanical Theory of Pressure Broadening'. *Phys. Rev.* **111**, 481–493.

Bauer, A., M. Godon, J. Carlier, and Q. Ma: 1995, 'Water vapor absorption in the atmospheric window at 239 GHz'. *J. Quant. Spectrosc. Radiat. Transfer* **53**, 411–423.

Benedict, W. S. and L. D. Kaplan: 1959, 'Calculation of line widths in H_2O-N_2 collisions'. *J. Chem. Phys.* **30**, 388–399.

Bernath, P. F.: 2002, 'The spectroscopy of water vapour: Experiment, theory and applications'. *Phys. Chem. Chem. Phys.* **4**, 1501–1509.

Boulet, C., D. Robert, and L. Galatry: 1976, 'Shifts of the vibrationrotation absorption lines of diatomic molecules perturbed by diatomic polar molecules. A theoretical analysis'. *J. Chem. Phys.* **65**, 5302–5314.

Cazzoli, G. and L. Dore: 1990, 'Lineshape measurements of rotational lines in the millimeter-wave region by second harmonic detection'. *J. Molec. Spectrosc.* **141**, 49–58.

Colmont, J.-M., D. Priem, G. Wlodarczak, and R. R. Gamache: 1999, 'Measurements and calculations of the halfwidth of two rotational transitions of water vapor perturbed by N_2, O_2, and air'. *J. Molec. Spectrosc.* **193**, 233–243.

Dicke, R. H.: 1953, 'The effects of collisions upon the Doppler width of spectral lines'. *Phys. Rev.* **89**, 472–473.

Di Giacomo, A. and O. Tarrini: 1969, 'A Graphycal Method for Determining the Width of Microwave Rotational Lines of Gases'. *Nuovo Cimento B* **62**, 1–12.

Di Giacomo, A. and O. Tarrini: 1970, 'Pressure Shift of Gases in the Microwave Region'. *Nuovo Cimento B* **68**, 165–174.

Dore, L.: 2003, 'Using Fast Fourier Transform to compute the line shape of frequency-modulated spectral profiles'. *J. Molec. Spectrosc.* **221**, 93–98.

Drouin, B. J., J. Fisher, and R. R. Gamache: 2004, 'Temperature dependent pressure induced lineshape of O_3 rotational transitions in air'. *J. Quant. Spectrosc. Radiat. Transfer* **83**, 63–81.

Fano, U.: 1963, 'Pressure Broadening as a Prototype of Relaxation'. *Phys. Rev.* **131**, 259–268.

Frost, B. S.: 1976, 'A theory of microwave lineshifts'. *J. Phys. B* **9**, 1001–1020.

Gamache, R. R.: 2005, 'Lineshape parameters for water vapor in the 3.2-17.76 μm region for atmospheric applications'. *J. Molec. Spectrosc.* **229**, 9–18.

Gamache, R. R., E. Arié, C. Boursier, and J.-M. Hartmann: 1998, 'Pressure-broadening and pressure-shifting of spectral lines of ozone'. *Spectrochim. Acta A* **54**, 35–63.

Gamache, R. R. and J. Fisher: 2003a, 'Half-widths of $H_2^{16}O$, $H_2^{18}O$, $H_2^{17}O$, $HD^{16}O$, $D_2^{16}O$: I. Comparison between isotopomers'. *J. Quant. Spectrosc. Radiat. Transfer* **78**, 289–304.

Gamache, R. R. and J. Fisher: 2003b, 'Half-widths of $H_2^{16}O$, $H_2^{18}O$, $H_2^{17}O$, $HD^{16}O$, $D_2^{16}O$: II. Comparison with measurement'. *J. Quant. Spectrosc. Radiat. Transfer* **78**, 305–318.

Gamache, R. R., J.-M. Hartmann, and L. Rosenmann: 1994, 'Collisional broadenming of water vapor lines–I. A survey of experimental results'. *J. Quant. Spectrosc. Radiat. Transfer* **52**, 481–499.

Herman, R. M.: 1963a, 'Impact Theory of the Noble-Gas-Broadened HCl Vibration-Rotation Lines'. *Phys. Rev.* **132**, 262–275.

Herman, R. M.: 1963b, 'Theory of pressure shifts of HCl lines caused by noble gases'. *J. Quant. Spectrosc. Radiat. Transfer* **3**, 449–460.

Kasuga, T., H. Kuze, and T. Shimizu: 1978, 'Determination of relaxation rate constants of the 22 GHz rotational transition of H_2O by coherent transient spectroscopy'. *J. Chem. Phys.* **69**, 5195–5198.

Liebe, H. J. and T. A. Dillon: 1969, 'Accurate foreign-gas-broadening parameters of the 22-GHz H_2O line from refraction spectroscopy'. *J. Chem. Phys.* **50**, 727–732.

Liebe, H. J., M. C. Thompson, and T. A. Dillon: 1969, 'Dispersion studies of the 22 GHz water vapor line shape. I. The Lorentzian behavior'. *J. Quant. Spectrosc. Radiat. Transfer* **9**, 31–47.

Liljegren, J. C., S. Boukabara, K. Cady-Pereira, and S. A. Clough: 2005, 'The effect of half-width of the 22-GHz water vapor line on retrievals of temperature and water vapor profiles with a 12-channel microwave radiometer'. *IEEE Transactions on Geoscience and Remote Sensing* **43**, 1102–1108.

Murphy, J. S. and J. E. Boggs: 1967, 'Collision Broadening of Rotational Absorption Lines. I. Theoretical Formulation'. *J. Chem. Phys.* **47**, 691–702.

Murphy, J. S. and J. E. Boggs: 1969, 'Collision Broadening of Rotational Absorption Lines. IV. Pressure Broadening of the Ammonia Inversion Spectrum'. *J. Chem. Phys.* **50**, 3320–3329.

Pickett, H. M.: 1980, 'Determination of collisional linewidths and shifts by a convolution method'. *Appl. Optics* **19**, 2745–2749.

Puzzarini, C., L. Dore, and G. Cazzoli: 2002, 'A Comparison of Lineshape Models in the Analysis of Modulated and Natural Rotational Line Profiles: Application to the Pressure Broadening of OCS and CO'. *J. Molec. Spectrosc.* **216**, 428–436.

Robert, D. and J. Bonamy: 1979, 'Short range force effects in semiclassical molecular line broadening calculations'. *J. Phys. (Paris)* **40**, 923–943.

Rosenkranz, P.: 1998, 'Water vapor continuum absorption: A comparison of measuremtns and models'. *Radio Sci.* **33**, 919–928.

Rothman, L. S., A. Barbe, D. C. Benner, L. R. Brown, C-Camy-Peyret, M. R. Carleer, K. Chance, C. Clerbaux, V. Dana, V. M. Devi, A. Fayt, J.-M. Flaud, R. R. Gamache, A. Goldman, D. Jacquemart, K. W. Jucks, W. J. Lafferty, J.-Y. Mandin, S. T. Massie, V. Nemtchinov, D. A. Newham, A. Perrin, C. P. Rinsland, J. Schroeder, K. M. Smith, M. A. H. Smith, K. Tang, R. A. Toth, J. V. Auwera, P. Varanasi, and K. Yoshino: 2003, 'The HITRAN molecular spectroscopic database: edition of 2000 including updates through 2001'. *J. Quant. Spectrosc. Radiat. Transfer* **82**, 5–44.

Tsao, C. J. and B. Curnutte: 1962, 'Line-widths of pressure-broadened spectral lines'. *J. Quant. Spectrosc. Radiat. Transfer* **2**, 41–91.

ROTATIONAL SPECTROSCOPY AT THE JET PROPULSION LABORATORY

BRIAN J. DROUIN*
California Institute of Technology, Jet Propulsion Laboratory, 4800 Oak Grove Dr., Pasadena, CA 91016, USA

Abstract. Environmental monitoring, atmospheric remote sensing and astrophysical studies promoted by NASA require a strong basis of spectroscopic information. The rotational spectroscopy capabilities at NASAs Jet Propulsion Laboratory (JPL) are currently maintained for the measurement of key mission priorities that enable modeling and retrieval of geophysical data from the atmosphere as well as validation of the space-borne instruments in the Earth Observing System, particularly the Microwave Limb Sounder. Rotational spectra are measured using a variety of spectroscopic techniques including pulsed-beam Fourier transform microwave spectroscopy (at CalTech); millimeter wavelength Stark spectroscopy; millimeter, submillimeter and THz FM spectroscopy; laser sideband spectroscopy and Fourier Transform far-infrared spectroscopy. Remote measurements of atmospheric rotational spectra are made using two limb-sounder instruments in the submillimeter and THz. Recent advances in the direct synthesis of THz radiation enables efficient laboratory science. Software for comprehensive and systematic study of different molecular systems is maintained at JPL, the software is freely available via http://spec.jpl.nasa.gov and is used by our group to create and sustain the JPL spectral line catalog also available online.

Keywords: remote sensing, rotational spectroscopy, catalog, lineshape, linewidth, frequency multiplication

*To whom correspondence should be addressed. Brian Drouin, M. S. 183-301, 4800 Oak Grove Dr. Pasadena, CA 91016, USA; e-mail: brian.j.drouin@jpl.nasa.gov

A. Perrin et al. (eds.), Remote Sensing of the Atmosphere for Environmental Security, 257–269.

1. Introduction

Environmental security is a fundamental driving force of earth science. Thorough understanding of physics, chemistry, geology, biology and mathematics are all required to secure the complex earth system. Spectroscopy has long served as a tool for probing the environment as well as performing controlled experiments. A focused combination of these methods at the Jet Propulsion Laboratory (JPL) has led to significant advances in remote and *in-situ* earth science. Each of the myriad of available spectroscopic techniques has unique capabilities for environmental remote sensing; this work will focus on efforts in rotational spectroscopy.

Rotational spectroscopy has several advantages for probing the earth system. These include: sensitivity to terrestrial emission which enables equivalent diurnal measurements; high sensitivity to radical species such as OH and ClO; line-of-sight measurement capability through cloud particles; and, due to the common origin (at zero frequency) of all rotational spectra, nearly all polar stratospheric species are observable in the available spectral windows. The Earth-Observing-System, Microwave Limb Sounder (EMLS, Waters *et al.* 1999) has been utilizing these aspects of rotational spectra to accomplish continuous global climate monitoring since its launch onboard the Aura satellite in July 2004. Supporting balloon-borne microwave radiometers also in use at JPL include the BOH (Pickett *et al.* 2005) and SLS (Stachnik *et al.* 1999) instruments.

At the outset, much of the required knowledge for remote sensing utilizing rotational spectra was either unknown, or scattered throughout the chemistry and physics literature. In the late 1970s Robert Poynter set out to fix this issue and created the Millimeter and Sub-millimeter Spectral Line Catalog (Pickett *et al.* 1998), which is now available online at http://spec.jpl.nasa.gov. A complimentary laboratory program, championed initially by Herbert Pickett and Edward Cohen and now continued by Brian Drouin, fills in the gaps of necessary quantitative spectroscopy as field instrumentation progresses. In addition to spectral characterization of many species, this group has also led many new laboratory spectroscopy developments (Matsuura et al. 2000, Farhoomand 1985, Drouin 2005a).

1.1. EMLS

Products of EMLS include daily global maps of geopotential height and ozone column, as well as global coverage of temperature, cloud ice density, and the following chemical species; O_3, H2O, OH, HO_2, CO, HCN, N_2O, HNO_3, HCl, HOCl, ClO, BrO, and SO_2 at a variety of altitudes. EMLS

sensitivity to chemical species is best in the stratosphere, where simultaneous measurements of chemically active and reservoir species provide tight constraints on global climate modeling. In the upper troposphere and lower stratosphere continuum blindness and increased cloud sensitivity hinder space-borne rotational spectroscopic remote sensing instruments. Much of the current research for EMLS is concentrated on analysis of this important region where pollution, weather and climate interact. Example spectra of ozone (O_3) and hydrogen chloride (HCl) from EMLS are given in Figure 1.

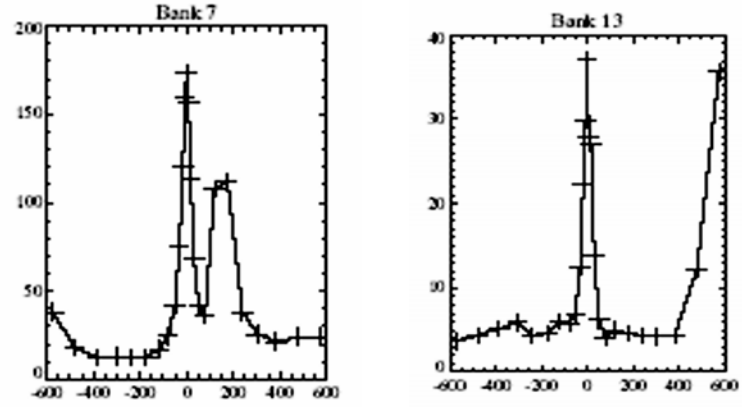

Figure 1. EMLS spectra of O_3 (Bank 7) and HCl (Bank 13) taken July 27th 2004. Radiance is given in Kelvin and the frequency scale is MHz from line-center.

1.2. LABORATORY STUDIES

Remote sensing of rotational transitions requires quantitative spectroscopic information including; 1) transition frequency, 2) lower state energy, 3) line intensity, and 4) air-broadened linewidth. The first two of these quantities are typically derived from high precision measurements of spectral features that are analyzed quantum-mechanically. Transition frequency is reliably determined when a high-resolution sweep through the resonance is completed using a referenced, phase-locked oscillator, or some other calibrated technique. Line intensities are best determined through measurements of the dipole moment using the Stark effect. Use of the measured dipole moment in a quantum-mechanical spectral prediction transfers the Stark measurement precision onto the entire rotational band (if centrifugal distortion of the dipole moment can be neglected). Finally, air-broadened linewidths present a continuing challenge to both laboratory and theoretical spectroscopists. State-of-the-art broadening measurements often remain as the limiting accuracy in a remote sensing measurement.

Improvements in remote sensing capabilities require more precise spectroscopy databases, which, in turn continues to drive laboratory spectroscopy to produce the necessary data. This manuscript will describe recent advances in frequency-multiplication as a source for quantitative spectroscopy as well as recent measurements in the laboratory.

1.3. THEORETICAL STUDIES AND CATALOGING

The compilation of predicted and measured rotational spectra in the JPL Spectral Line Catalog created a single reference for the three of the types of quantitative information mentioned in section 1.2 (transition frequency, lower state energy, line intensity). It also created a need for a procedure that could predict all of the different types of rotational spectra in a consistent manner. Generally, measured spectra are fit utilizing a model specific to a class of species, e.g. linear molecule, symmetric top, asymmetric top, open-shell linear molecule, open-shell symmetric top… Quantitative cataloging requires comprehensive inclusion of all of the possible combinations within one framework. For this purpose Herb Pickett produced SPFIT/SPCAT, a multi-purpose spectral fitting program. The complexities of molecular spectra manifest in a challenging user interface that allows nearly all spectra to be modeled within a cohesive framework. The fitting program SPFIT is utilized to analyze literature data or new lab measurements and the prediction program SPCAT is used to generate catalog format files. The program is continuously upgraded (Pickett 1997, Pickett 2004) to include more features important to compelling research problems.

2. Quantitative laboratory spectroscopy

The atmospheric laboratory spectroscopy program at JPL has been engaged in mission critical air-broadened linewidth measurements (Drouin 2004c, Drouin et al. 2004b, Yamada 2003, Drouin 2005e); as well as exploratory searches for new species (Drouin 2004d, Oh 2005, Miller and Cohen 2003); and extensions of existing models (Chen et al. 2005, Drouin et al. 2005c, Drouin and Maiwald 2005d, Fry et al. 2005, Groner et al. 2002, Pickett et al. 2005a).

The spectrometer and flow cell system is shown schematically in Figures 2 and 3. Figure 2 shows the static/flow cell system. For temperature control, methanol or isopropanol is passively cooled with liquid nitrogen and flowed continuously through an exterior jacket that is in direct contact with the white cell. A solenoid switch controls liquid nitrogen flowed through the alcohol reservoir. Inset polypropylene windows ensure that the

gas under study is completely enclosed in the temperature-controlled region.

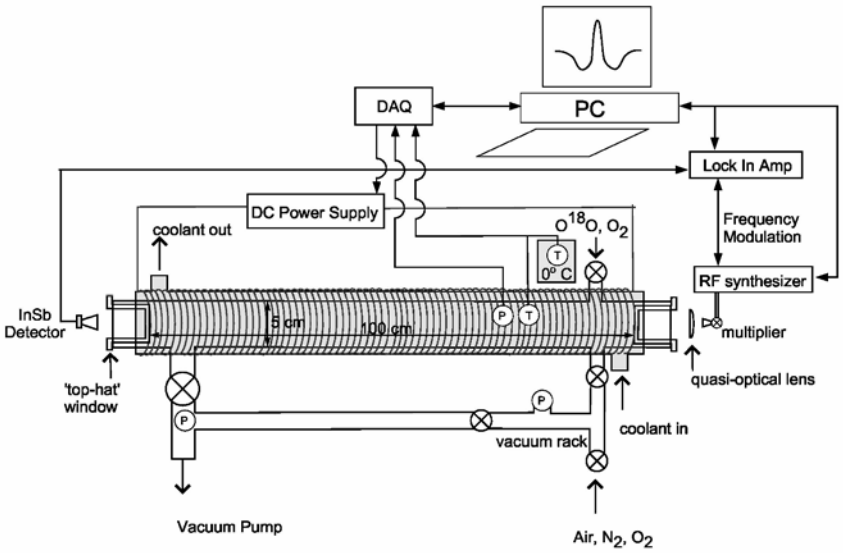

Figure 2. Spectrometer schematic.

Secondary windows are added when the cell is below 0°C to prevent condensation on the cold inset windows. Pressure is monitored using calibrated capacitance manometers directly in contact with the sample. A data-acquisition interface card (DAQ) in the control computer (PC) allows continuous recording of the pressure and temperature (thermocouple voltages) during spectral sweeping. The frequency source is a computer controlled sweep synthesizer multiplied up to the desired frequency. Either room temperature diode detectors or liquid helium cooled bolometers (InSb or Si) are utilized for phase-sensitive detection at the lock-in-amplifier.

Figure 3 illustrates the components used in a wide-band frequency multiplication source. The sweep synthesizer is continuously tunable in 1 Hz increments from 10 MHz – 26.5 GHz, it is utilized between 12 and 20 GHz for the frequency multiplication scheme. A tunable YIG filter is voltage tuned to track the sweep synthesizer to eliminate harmonics of the fundamental YIG oscillator in the sweep synthesizer. The mm-wave module is a sextupler, producing frequencies in the 72-120 GHz range, which can be immediately used for spectroscopy using free-space coupling to the gas-cell. For submillimeter wavelength generation the mm-wave module output is amplified using monolithic-membrane integrated circuit (Wang 2001) technology prior to injection into a cascaded set of harmonic

multipliers (Bruston 2000). Modulation applied at the sweep synthesizer is transferred directly to the higher frequency radiation.

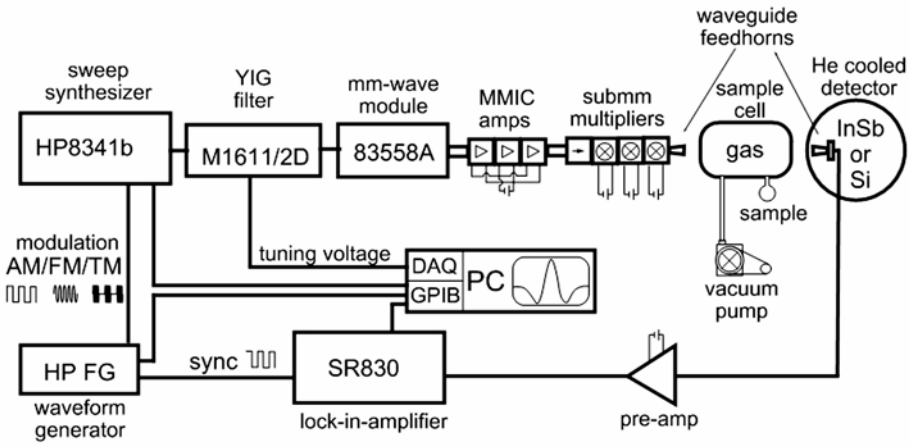

Figure 3. Cascaded frequency multiplier system.

Table 1. Harmonic multipliers in use at JPL. AMC & MUT are Millitech devices, VDI is Virginia Diodes, JPL devices were developed for Hershel/HIFI.

Device	Multi-plier	Range (THz)	Max Power (μW)	Typ. Power (μW)	Harmonic Content
AMC-15	4	0.05-0.07	4000	2000	< -30 dB
AMC-10	6	0.07-0.11	3000	1000	< -30 dB
Agilent 83558A	6	0.07-0.12	2000	1000	< -30 dB
MUT-05	3	0.14-0.22	400	50	< -30 dB
MUT-04	3	0.18-0.27	120	40	< -30 dB
VDI 1.9x5	5	0.40-0.60	40	10	-20 dB x6,x7
VDI 1.5x6	6	0.60-0.75	100	30	-20 dB x4
VDI 1.2x5	10	0.77-0.85	50	10	< -30 dB
JPL x2x2x2	8	0.70-0.83	800	50	-
JPL x2x2x3	12	0.84-0.95	400	50	-23 dB x8
JPL x2x2x3	12	1.05-1.28	100	30	-26 dB x16
JPL x2x3x3	18	1.55-1.65	12	4	-
JPL x2	2	1.65-1.75	< 0.1	<< 0.1	-10 dB x3
JPL x3	3	2.57-2.65	<0.01	<<0.01	10 dB x2

Table 1 shows the frequency range, maximum power, typical power and harmonic content of each source available for the system. In most cases sources can be interchanged with all other system components unchanged.

2.1. LINEWIDTH MEASUREMENTS

The most difficult to measure lineshape component that has direct impact on atmospheric composition retrievals is the pressure-broadened linewidth. Direct spectral analyses of absorption lineshapes requires attention to linewidth, lineshift, line-narrowing effects and instrumental effects. For practical purposes the convolution method (Pickett 1980) has allowed reliable determination of the Lorentzian (pressure broadened) linewidth and lineshift through comparisons of spectra without rigorous extraction of line-narrowing and instrumental parameters. The method requires a reproducible instrument function and minimization of systematic errors such as temperature drift. The convolution technique, combined with the stable sources of the frequency multiplication source spectrometer, allow a statistical parametric analysis (Drouin *et al.* 2004b) of the spectral results. In short, the temperature and pressure dependencies of the linewidth (or shift) are simultaneously extracted from all of the de-convoluted spectra. New system programming that enables automation of the pressure/flow settings allows highly stable and reproducible experimental conditions while simultaneously reducing user error and fatigue.

Recently published pressure broadening results include hydrogen chloride (Drouin 2004c) (broadening gases - N_2, O_2, air), ozone (Drouin *et al.* 2004b) (broadening gas - air) and bromine monoxide (Yamada *et al.* 2003) (broadening gases - N_2, O_2). More recently, broadening measurements of hypochlorous acid have been completed that indicate that the N_2-, Air- pressure-broadened linewidth of ${}^{r}Q_0$ branch transitions above J = 18 have reached the asymptotic limit (Drouin 2005e). A graph of the entire N_2 broadening data set (J = 17-22, T = 200-300 K, p = 0.1-1.5 Torr, Figure 4), normalized to room temperature is shown to indicate the relative precision ($2\sigma_{max}$ (Γ_T) = 1.4%) of the broadening and shift parameters ($2\sigma_{max}$ (δ_T) = 4.2%). The high precision of the broadening parameter over the full temperature range is immediately discernable by the tight correlation of the normalized data set (open circles in Figure 4). As yet unpublished broadening measurements of oxygen, isotopic oxygen $O^{18}O$, nitric acid, methyl cyanide, ozone, and sulfur dioxide have all been incorporated into EMLS retrievals.

The new ozone and sulfur dioxide linewidth measurements were made with the automated spectrometer. After detector and sample preparation, a flow of the sample gas and regulated air was allowed to pass through the spectrometer cell. The scanning program utilizes a table of frequencies and

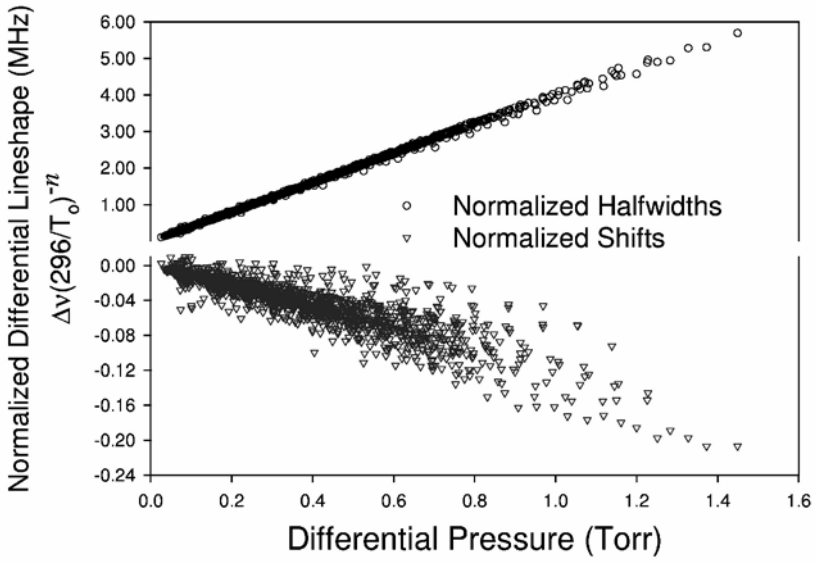

Figure 4. Broadening and shift measurements of HOCl $^rQ_0$-branch transitions near 630 GHz.

pressure settings to scan through spectral windows (15-25 MHz) encompassing the important transitions within the source bandwidth. After several unassisted hours of measurements at the full range of frequencies and pressures the user may intervene to change the system temperature and repeat the data collection procedure. In this manner data sets of 10-20 transitions measured at 7-12 pressures and 5-10 different temperatures can be recorded in a few days. Fifteen new temperature dependent air-broadening measurements of ozone in the 620-662 GHz range have been performed. Twenty-six new sulfur dioxide air-broadening measurements have also been made in the same frequency region.

2.2. CHEMISTRY EXPERIMENTS

There has been considerable interest in a minor product channel of the OH + NO_2 radical-radical association reaction. Knowledge of the overall rate constant for this reaction is critical to accurate modeling of atmospheric chemistry since catalytic HO_x and NO_x reaction cycles regulate ozone concentrations in the upper troposphere and stratosphere, as well as ozone formation and air quality in the lower troposphere. The major product, $HONO_2$, or nitric acid is characterized and currently monitored. The minor

product, HOONO, or peroxynitrous acid was first identified in the gas phase through photodissociation spectroscopy (Nizkorodov and Wennberg 2002). Our laboratory reported the first rotationally resolved spectra of the *cis-cis* conformer of this species (Drouin *et al.* 2004d) and has now completed analysis of the weak field Stark effect (see Figure 5) and the deuterated isotopologue (Drouin *et al.* 2005b).

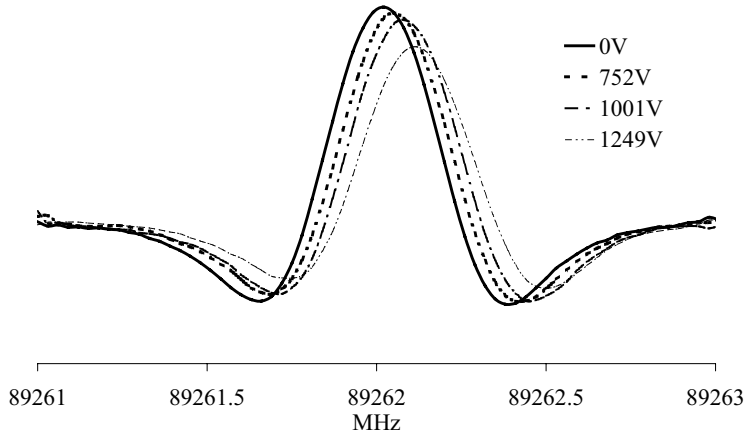

Figure 5. HOONO $18_{5,13}$ - $18_{4,14}$ Stark effect.

2.3. BROADBAND MEASUREMENTS

The wide-band frequency sources allow much more data collection than previously attainable using Klystron and Gunn Oscillator sources. Bandwidths of the frequency multiplier sources are comparable to BWOs, but the computer controlled phase lock of the sweep synthesizer releases the experimenter from the need to continuously monitor the experiment. Unlike the FASSST system (Petkie *et al.* 1997), the high-resolution wide-band sweeps are slow, using the step-and-stare data collection method. In comparison to FASSST, the advantages include no post-calibration of the frequency, no external etalon for frequency calibration and only one submillimeter wavelength beam to align and detect.

Table 2. Stark shift values for H2O, from ref X, Y and those predicted using SPCAT and the previous and current JPL catalog models. $\Delta\nu_{Stark} = ({}^0\Gamma + {}^2\Gamma M^2)\varepsilon^2$ units of Γ are $Hz(V/cm)^2$.

Levels		Literature	JPL05	%Diff JPL05	%Diff JPL99	1σ %(meas)
1_{11} (0←1)[x]	$^2\Gamma$	0.226644(45)	0.226678	0.02	-0.80	0.04
1_{10} (1←0) [x]	$^2\Gamma$	0.407086(81)	0.407111	0.01	-0.77	0.05
2_{11} (0←1) [x]	$^2\Gamma$	0.162902(32)	0.162935	0.02	-0.86	0.04
$3_{13} \leftarrow 2_{20}$ [y]	$^0\Gamma$	0.077514(11)	0.077389	-0.16	-0.63	0.14
$3_{13} \leftarrow 2_{20}$ [y]	$^2\Gamma$	-0.042180(17)	-0.042176	-0.01	-0.64	0.04
$6_{16} \leftarrow 5_{23}$ [y]	$^0\Gamma$	0.198564(110)	0.199024	0.23	-0.81	0.55
$6_{16} \leftarrow 5_{23}$ [y]	$^2\Gamma$	-0.009598(15)	-0.009607	0.10	-0.97	0.16

x. Dyke and Muenter 1973; y. Clough *et al.* 1973

Complex chemical systems, such as those used to identify HOONO and its various substituted isotopic forms require an intimate knowledge of the chemicals. During searches for isotopic HOONO we collected broadband spectra of isotopically substituted nitric acid. The strong ^aR-branch signatures were easily identified in the survey scans throughout the sub-millimeter. The isotopic nitric acid spectra have now been analyzed up through 800 GHz and reported in the JPL spectral line catalog and the Journal of Molecular Spectroscopy (Drouin *et al.* 2005c).

2.4. CATALOG UPDATES

The JPL catalog is continuously updated as new information becomes available in the literature, and as NASA mission needs require more detail. The perennial atmospheric species that are routinely improved are ozone and water. The most recent updates on these species include new extended frequency measurements of higher *J* and *K* quanta (H_2O - Chen *et al.* 2000, O_3 – DeNatale *et al.* 1997 and Colmont *et al.* 2005). Critical analyses of the dipole moment functions reproduce Stark measurements to experimental precision (H_2O – Clough *et al.* 1973, Dyke and Muenter 1973, O_3 – Mack and Muenter 1977). Absolute intensity measurements are reproduced near experimental precision (H_2O – 1.8% absolute, 14.1% relative, (Toth 1998), 0.7% absolute, 5.5% relative, (Brown and Plymate 1996); O_3 2σ relative (Birk *et al.* 1994)). In the case of water the previous entry in the JPL catalog (1999) appears to be inconsistent with Stark measurements. Table 2 displays the calculated Stark coefficient before and after the latest update. The previous discrepancy was, on the average, slightly less than 1%, the new analysis agrees with experimental Stark data to within the measurement precision of ~0.1%. Ozone intensities have significantly

changed only at higher J and K due to the centrifugal distortion corrections. The centrifugal distortion of the dipole moments for H_2O and O_3 are calculated to match a perturbative model of vibrational corrections to the ground state Hamiltonian (Pickett 1990).

Nitric acid has also been updated with new information (Petkie et al. 2003, Perrin et al. 2004) on vibrational states below 1000 cm^{-1}, and the partition function is given for the entire vibration-rotation manifold. The isotopically substituted forms of nitric acid (Drouin 2005c) are new entries in the catalog.

Other new entries (since 2001) include peroxynitrous acid (including a frequency and dipole update), hypochlorous acid (frequency extension, Drouin 2005e), perchloric acid (new species, Oh 2005), nitrous oxide (frequency update, Drouin and Maiwald 2005), propane, acetone, glycolaldehyde, dihydroxyacetone, and formyl chloride.

3. Conclusion

Detailed laboratory measurements of controlled chemical systems provides information necessary for critically sensing the Earth environment. The spectroscopic information made publicly available through the literature and through open databases is essential to earth science field mission planning and execution. Space and field instruments capable of measuring pollution, weather, and climate are currently in operation at JPL. Through concerted laboratory and field programs JPL provides science necessary for environmental security.

Acknowledgements

This research was performed in part at the Jet Propulsion Laboratory (JPL), California Institute of Technology, under contract with the National Aeronautics and Space Administration. The author thanks NATO for invitation to the Advance Research Workshop on Remote Sensing of the Atmosphere for Environmental Security.

References

Brown, L.R., Plymate, C., 1996, H_2-broadened $H_2{}^{16}O$ in four infrared bands between 55 and 4045 cm^{-1}, *J. Quant. Spec. Rad. Trans.* **56**: 263-282.

Birk, M., Wagner, G., Flaud, J-M., 1994, Experimental linestrengths of far-infrared pure rotational transitions of ozone, *J. Mol. Spec.* **163**: 245-261.

Bruston, J., Schlecht, E., Maestrini, A., Maiwald, F., Martin, S. C., Smith, R. P., Mehdi, I., Siegel, P. H., and Pearson, J., 2000, Development of 200 GHz to 2.7 THz multiplier chains for submillimeter-wave heterodyne receivers, *SPIE Int. Symp. on Astro. Tele. and Instr*.

Chen, P., Pearson, J. C., Pickett H. M., Matsuura, S., Blake, G. A. 2005, Measurements of $^{14}NH_3$ in the ν_2 = 1 state by a solid-state, photomixing, THz spectrometer and a simultaneous analysis of the microwave, terahertz, and infrared transitioins between the ground and ν_2 inversion-rotation levels, *J. Mol. Spectrosc.* submitted.

Clough, S. A., Beers, Y., Klein, G. P., Rothman, L. S. , 1973, Dipole-moment of water from stark measurements of H_2O, HDO, and D_2O, *J. Chem. Phys.* **59**: 2254-2259.

Colmont, J-M., Bakri, B., Demaison, J., Mader, H., Willaert F., Tyeuterev Vl. G., Barbe, A., 2005, Microwave Fourier transform, millimeterwave, and submillimeterwave spectra of ozone in its vibrational ground state, *J. Mol. Spec.* **233**: 203.

DeNatale, P., Lorini, L., Inguscio, M., Nolt, I. G., Park, J. H., DiLonardo, G., Fusina, L., Ade, P. A. R., Murray, A. G., Accurate frequency measurements for H_2O and $^{16}O_3$ in the 119 cm^{-1} OH atmospheric window, *Appl. Op.* **36**: 8526

Drouin, B. J., Wlodarczak, G., Colmont, J.-M., Rohart, F., 2004, Current status of quantitative rotational spectroscopy for atmospheric research, *Proc. Int. Workshop Crit. Eval. mm-/sub-mm- Spectrosc. Data Atmos. Obs*, Ibaraki, Mito, Japan.

Drouin, B. J., Fisher, J., Gamache, R. R., 2004, Temperature dependent pressure induced lineshape of O_3 rotational transitions in air, *J. Quant. Spec. Rad. Trans.*, **83(1)**: 63-81.

Drouin, B. J., 2004, Temperature dependent pressure induced lineshape of the HCl $J = 1 \leftarrow 0$ rotational transition in nitrogen and oxygen, *J. Quant. Spec. Rad. Trans.*, **83(3-4)**: 321-331.

Drouin, B. J., Fry, J. L., Miller, C. E., 2004, Rotational spectrum of *cis-cis* HOONO, *J. Chem. Phys.*, **120(12)**: 63-81.

Drouin, B. J., Maiwald, F. W., Pearson, J. C., 2005, Application of cascaded frequency multiplication to molecular spectroscopy, *Rev. Sci. Instr.* **76 (9)**: Art. No. 093113.

Drouin, B. J., Miller, C. E., Fry, J. L., Petkie, D. T., Helminger, P., Medvedev, I., 2005, Submillimeter measurements of isotopes of nitric acid," *J. Mol. Spec. accepted*

Drouin, B. J., Maiwald, F.W., 2005, Extended THz measurements of nitrous oxide, N_2O, *J. Mol. Spec. accepted*

Drouin, B. J., 2005, Submillimeter measurements of N_2 and air broadening of hypochlorous acid, *J. Quant. Spec. Radiat. Trans. submitted*

Dyke, T. R., Muenter, J. S., 1973, Electric dipole-moments of low *J* states of H_2O and D_2O, *J. Chem. Phys*, **59(6)**: 3125-3127.

Fry, J. L., Drouin B. J., Miller C. E., 2005, Rotational spectroscopy and dipole moment of *cis-cis* HOONO and DOONO, *J. Chem. Phys. in press*.

Groner, P., Albert, S., Herbst, E., De Lucia, F. C., Lovas, F. J., Drouin, B. J., Pearson, J. C., 2002, Acetone: laboratory assignments and predictions through 620 GHz for the vibrational-torsional ground state, *Astrophys. J. Sup.* **142 (1)**: 145-151.

Farhoomand, J., Blake, G. A., Frerking, M. A., Pickett, H. M., 1985, Generation of tunable laser sidebands in the far-infrared region, *J. Appl. Phys.* **57**: 1763-1766.

Mack, K. M., Muenter, J. S., 1977, Stark and Zeeman properties of ozone from molecular beam spectroscopy, *J. Chem. Phys.* **66(12)**: 5278-5283.

Matsuura, S., Chen, P., Blake, G. A., Pearson, J. C., Pickett, H. M., 2000, A tunable cavity-locked diode laser source for terahertz photomixing, *IEEE Trans. Microwave Theory and Tech.*, **48**: 380-387.

Miller, C. E., Cohen, E. A., 2003, Rotational spectroscopy of iodine dioxide, OIO, *J. Chem. Phys.* **118 (14)**: 6309-6317.

Nizkorodov, S. A., Wennberg P. O., 2002, First spectroscopic observation of gas-phase HOONO, *J. Phys. Chem. A* **106 (6)**: 855-859.

Oh J. J., Drouin, B. J., Cohen, E. A., 2005, The rotational spectrum of perchloric acid, $HClO_4$, *J. Mol. Spec.*, **234(1)**: 10-24.

Perrin, A., Orphal, J., Flaud, J-M., Klee, S., Mellau, G., Mader, H., Walbrodt, D., Winnewisser, M., 2004, New analysis of the ν_5 and $2\nu_9$ bands of HNO_3 by infrared and millimeter wave techniques: line positions and intensities *J. Mol. Spec.* **228**: 375-391.

Petkie, D. T., Goyette, T. M., Bettens, R. A. P., Belov, S. P., Albert, S., Helminger, P., De Lucia, F. C., 1997, A fast scan submillimeter spectroscopic technique, *Rev Sci Instrum* **68**: 1675-1683.

Petkie, D. T., Helminger, P., Butler, R. A. H., Albert, S., De Lucia, F. C., 2003, The millimeter and submillimeter spectra of the ground state and excited ν_9, ν_8, ν_7, and ν_6 vibrational states of HNO_3, *J. Mol. Spec.* **218**: 127-130.

Pickett H. M., 1980, Determination of collisional linewidths and shifts by a convolution method, *Appl. Opt.* **19 (16)**: 2745-2749.

Pickett, H. M., 1990, Centrifugal corrections to rotational intensities*, Lecture TF10, 45th Symposium on Molecular Spectroscopy*, Columbus, OH.

Pickett, H. M., 1997, Theoretical studies of internal rotation for an asymmetric top, *J. Chem. Phys.*, **107**: 6732-6735.

Pickett, H. M., Poynter, R. L., Cohen, E. A., Delitsky, M. L., Pearson, J. C., Muller, H. S. P., 1998, Submillimeter, millimeter, and microwave spectral line catalog, *J. Quant. Spec. Rad. Trans.*, **60**: 883-890.

Pickett, H. M., 2004, Spin eigenfunctions and operators for the D-n groups, *J. Mol. Spec.* **228(2)**: 659-663.

Pickett, H. M., Pearson, J. C., Miller, C. E., 2005, Use of Euler series to fit spectra with application to water, *J. Mol. Spec.* **233(2)**: 174-179.

Pickett, H. M., Drouin, B. J., Canty, T., Kovalenko, L. J., Salawitch, R. J., Livesey, N. J., Read, W. G., Waters, J. W., Jucks K. W., Traub, W. A., 2005, Validation of Aura MLS HO_x measurements with remote-sensing balloon instruments, *Geophys. Res. Lett., in press.*

Stachnik, R. A., Salawitch, R., Engel, A., Schmidt, U., 1999, Measurements of chlorine partitioning in the winter Arctic stratosphere, *Geo. Res. Lett.*, **26(20)**: 3093-3096.

Toth R. A., 1998, Water vapor measurements between 590 and 2582 cm^{-1}: line positions and strengths, *J. Mol. Spectrosc.* **190(2)**: 379-396.

Toon G. C., Blavier, J.-F., Sen B., Drouin, B. J., 2001, Atmospheric $COCl_2$ measured by solar occultation spectrometry, *Geophys. Res. Lett.*, **28 (14)**: 2835-2838.

Wang, H., Samoska, L., Gaier, T., Peralta, A., Liao, H. H., Leong, Y. C., Weinreb, S., Chen, R. C. C., Nishimoto, M., Lai, R., 2001, Power-amplifier modules covering 70-113 GHz using MMICs, *IEEE Trans. Micr. Theo. Tech.* **49**: 9-16.

Waters, J.W., Read, W. G., Froidevaux, L., Jarnot, R. F., Cofield, R. E., Flower, D. A., Lau, G. K., Pickett, H. M., Santee, M. L., Wu, D. L., Boyles, M. A., Burke, J. R., Lay, R. R., Loo, M. S., Livesey, N. J., Lungu, T. A., Manney, G. L., Nakamura, L. L., Perun, V. S., Ridenoure, B. P., Shippony, Z., Siegel, P. H., Thurstans, R. P., Harwood, R. S., Pumphrey, H. C., Filipiak, M. J., 1999, The UARS and EOS microwave limb sounder experiments, *J. Atmos. Sci.* **56**: 194 -218.

Yamada, M. M., Kobayashi, M., Habara, H., Amano, T., Drouin, B. J., 2003, Submillimeter-wave measurements of the pressure broadening of BrO, *J. Quant. Spec. Rad. Trans.*, **82(1-4)**: 391-399.

CORRELATION BETWEEN PRECIPITABLE WATER AND RAINFALL USING GLOBAL POSITIONING SYSTEM (GPS) TECHNIQUE

ABDELALI FADIL* AND DRISS BEN SARI
Mohammadia School of Engineering, Avenue Ibnsina B.P. 765 Rabat-Agdal, Rabat, Morocco

Abstract. We present the approach to remote sensing of water vapor based on the Global Positioning System (GPS). Signals propagating from GPS satellites to ground-based GPS receivers are delayed by atmospheric water vapor. Given surface meteorological measurements, this delay can be transformed into an estimate of the precipitable water overlying that receiver. We validate GPS precipitable water at rabt station with National Center for Environmental Prediction (NCEP) measurements. We show short-term correlation between GPS and rainfall during two different seasons, and we describe GPS tropospheric water vapor tomography, which could be utilized in operational weather forecasting and in fundamental research into atmospheric storm systems, the hydrologic cycle, atmospheric chemistry, and global climate change (severe events particularly).

Keywords: Global Positioning System (GPS); troposphere; precipitable water

1. Introduction

Water vapor plays a crucial role in atmospheric processes that act over a wide range of temporal and spatial scales, from global climate change to micrometeorology. Water vapor is the most variable of the major constituents of the atmosphere. Significant changes in the horizontal and

*To whom correspondence should be addressed. Abdelali Fadil, Civil Engineering Dept., LAPR, Mohammadia School of Engineering, Ibn Sina Avenue, Agdal, Rabat, Morocco, e-mail: fadil@chandler.mit.edu

A. Perrin et al. (eds.), Remote Sensing of the Atmosphere for Environmental Security, 271–284.

vertical distribution of water vapor can occur rapidly during active weather. Signals propagation from GPS satellites to ground-based GPS receivers are delayed by atmospheric water vapor. This delay is parameterized in terms of time-varying Zenith Wet Delay (ZWD), which is retrieved by stochastic filtering of the GPS data. Given surface temperature and pressure readings at the GPS receiver, the retrieved ZWD can be transformed with very little uncertainty into an estimate of the Integrated Water Vapor (IWV) overlying that receiver.

The Global Positioning System (GPS) has proven to be an accurate technique for the retrieval of integrated water vapor (IWV) above ground-based receivers (Bevis el al., 1992). The consistency of IWV retrieved from GPS with radiosondes and water vapor radiometers (WVR's) is about 1~2 kg/m^2 (i.e. 1~2 mm in precipitable water) (Tregoning et al., 1998; Elgered et al., 1998). This makes GPS-IWV an extremely interesting technique since water data are lacking over land (most contemporary space-borne instruments perform well over the ocean, but much less over land). Because of its increasing spatial density and its continuous recording, GPS offer the possibility of observing the horizontal distribution of IWV with unprecedented coverage and a temporal resolution of the order of 5 min with the above mentioned accuracy.

2. What is GPS?

The Global Positioning System (GPS) tracking network was established to provide high precision navigation and geodetic positioning. The system consists of satellites tracking at 20.200 km in 12 sidereal hours quasi-circular orbit around the earth and a ground-based network of support stations to update the ephemeredes and clocks. Four to eight satellites are visible anywhere in the world, at any time.

GPS satellites transmit atomic clock controlled L-band signals to receivers on the earth. Time delays of the signal travel paths from multiple satellites to a single receiver are used to establish the ground position of the receiver. The components of the satellite's message emitted every 30 sec are:

- Satellite's ephemeris factors.
- Fundamental frequency $f_0 = 10.23$ MHz.
- Carrier $L_1 = 154f_0$ and Carrier $L_2 = 120f_0$.
- 3 Pseudo Random Noise (PRN): C/A = $f_0/10$; P = f_0; W = $f_0/20$.
- Ionospheric coefficient Model.

Error sources affecting GPS measurements are classified into three classes:

- Instrumental errors: Antenna phase center, Signal scattering, Thermal noise, Interchannel biases and Clock drifts.
- Modeling errors: Satellite orbits, Ocean tides, Atmospheric pressure loading effects.
- Monument instability and multipath errors.
- Environmental errors: The atmosphere is divided into ionosphere (50 to 500 km altitude) dispersive medium for which the effect is largely eliminated by using dual frequency observations, and the neutral atmosphere (0 to 10 km altitude) especially the troposphere, non dispersive medium, for which the delay must be inferred from a profile of the medium refractivity of estimated from the GPS measurements themselves.

3. Modeling the neutral atmospheric delay

The ionosphere and the neutral atmosphere affect microwave transmission by slowing down the speed of the radio signals compared to that of the vacuum and curving the ray path. Both effects introduce propagation delays into the travel path length. The ionospheric delay is dispersive (frequency dependent) and can be determined by observing both of the frequencies transmitted by GPS satellites (L_1 and L_2) and exploiting the known dispersion relations for the ionosphere (Spilker, 1980; Brunner and Gu, 1991). The neutral atmospheric delay is effectively non-dispersive at GPS frequencies (below 15 GHz) and so cannot be corrected in this way. This delay can be decomposed into the "hydrostatic delay" associated with the induced dipole moment of the atmosphere and the "wet delay" associated with the permanent dipole moment of water vapor (Saastamoinen, 1972; Davis et al., 1985).

The (electrically) neutral atmosphere affects the propagation of electromagnetic signals by retarding and bending them. These effects can be determined if one knows the index of refraction n, or, more conveniently, the refractivity N, as defined as 10^6 (n -1). The refractivity of the atmosphere is a function of its temperature, pressure, and water vapor. Smith and Weintraub (1953) suggested the relationship:

$$N = 77.6\left(\frac{P}{T}\right) + 3.73\times10^5\left(\frac{P_v}{T^2}\right) \tag{1}$$

where P is the total atmospheric pressure in (millibars), T is the atmospheric temperature (in degrees Kelvin), and P_v is the partial pressure of water vapor (in millibars). A more accurate formula of refractivity is provided by Thayer (1974):

$$N = k_1\left(\frac{P_d}{T}\right) Z_d^{-1} + k_2\left(\frac{P_v}{T}\right) Z_v^{-1} + k_3\left(\frac{P_v}{T^2}\right) Z_v^{-1} \qquad (2)$$

where

$$k_1 = (77.604 \pm 0.014)\,\mathrm{K\ mbar}$$

$$k_2 = (64.790 \pm 0.080)\,\mathrm{mbar^{-1}}$$

$$k_3 = (3.776 \pm 0.004) \times 10^5\ \mathrm{K^2\ mbar^{-1}}$$

$$Z_d^{-1} = 1.00027$$

$$Z_v^{-1} = 1.00201$$

P_d is the partial pressure of dry air (in millibars), and Z_d^{-1} and Z_v^{-1} are the inverse compressibility factors for dry air and water vapor, respectively. The uncertainties in the constants of Equation (2) limit the accuracy with which the refractivity can be computed to about 0.02% (Davis et al., 1985).

The atmospheric delay is the integral of the refractivity along the ray path. It is useful to separate the zenith atmospheric delay as the sum of two terms (Davis et al., 1985): the hydrostatic delay and the wet delay.

Elgered et al., (1991) adopted a model in which the zenith hydrostatic delay (ZHD), in millimeters, is given by:

$$ZHD = (2.2779 \pm 0.0024)\frac{P_s}{f(\lambda, H)} \qquad (3)$$

where P_s is the total pressure (in millibars) at the Earth's surface, and

$$f(\lambda, H) = (1 - 0.00266\cos(2\lambda) - 0.00028H)$$

accounts for the variation in gravitational acceleration with latitude λ and the height H of the surface above the ellipsoid (in kilometers). This delay can be predicted to better than a millimeter with surface pressure accuracies of 0.4 mbar (Elgered et al., 1991).

The zenith wet delay (ZWD) is given by:

$$ZWD = 10^{-6}\left[k_2' \int\left(\frac{P_v}{T}\right) dz + k_3 \int\left(\frac{P_v}{T_2}\right) dz\right] \qquad (4)$$

where $k_2' = (17 \pm 10)\,\mathrm{K\ mbar^{-1}}$

and the integral is along the zenith path, and the delay is given in the units of z (Davis et al., 1985). It is usually adequate to approximate this expression by:

$$ZWD = (0.382 \pm 0.004)\ \mathrm{K}^2\ \mathrm{mbar}^{-1} \int \left(\frac{P_v}{T^2} \right) dz \tag{5}$$

The zenith wet delay can be accurately converted into precipitable water (PW) by using the expression (Bevis et al., 1994):

$$PW = (ZWD)\,\Pi(T_m, \rho_v) \tag{6}$$

where PW and ZWD are expressed in millimeters and $\Pi(\ T_m\ ,\ \rho_v\ )$ is given by :

$$\Pi = \frac{10^6}{\rho_v R_v \left[\left(\frac{k_3}{T_m} \right) + k_2' \right]} \tag{7}$$

where ρ_v is the density of liquid water, R_v (= 461.5 J kg^{-1} K^{-1}) is the specific gas constant for water vapor, and T_m is the mean temperature of the atmosphere, defined as:

$$T_m = \frac{\left(\int \left(\frac{P_v}{T} \right) dz \right)}{\left(\int \left(\frac{P_v}{T^2} \right) dz \right)} \tag{8}$$

The mean temperature depends on the vertical profile of P_v and atmospheric temperature. Fortunately, the mean temperature T_m has been empirically found to be well correlated with surface temperature T_s (Bevis et al., 1992). T_m can be estimated by:

$$T_m = 70.2 + 0.72\ T_s\ (\text{in degrees Kelvin}) \tag{9}$$

where T_s is the surface temperature, or computed from a numerical weather prediction model which predicts the three dimensional distribution of temperature.

4. GPS data analysis and results

We conducted a GPS experiment from June 2003 to June 2005 to study the correlation of GPS precipitable water and rainfall at the IGS station installed in Rabat (rabt) (Fig. 1).

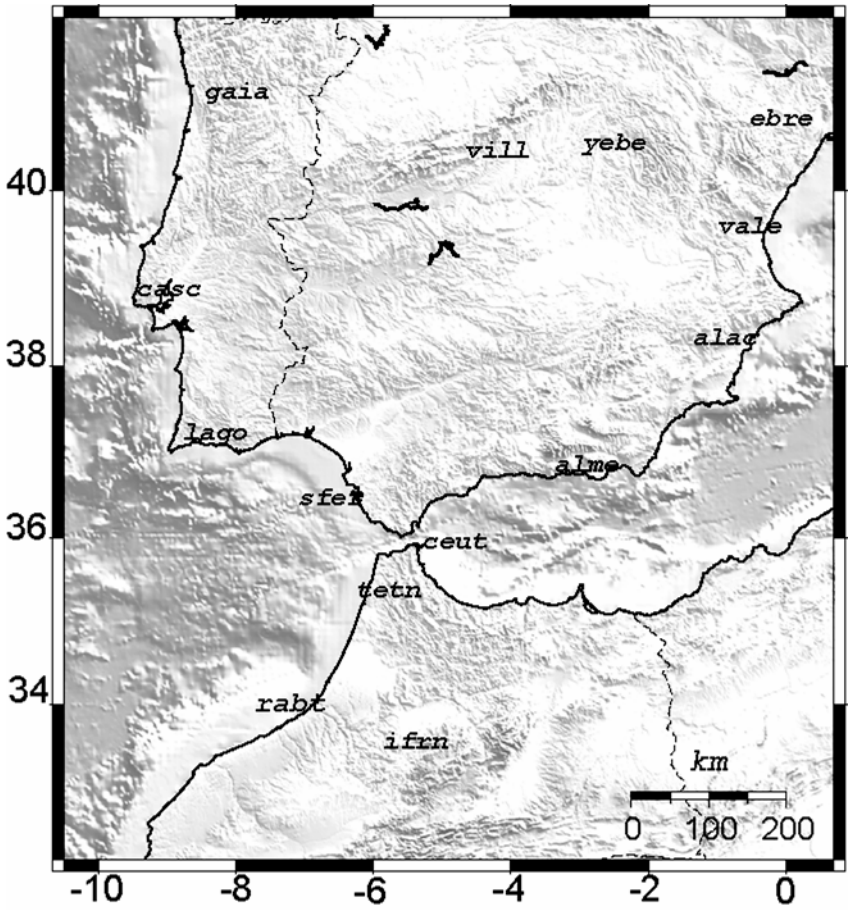

Figure 1. Geographical location of the GPS sites involved in the experiment.

The GPS observations consisted of data streams, simultaneously received from six to eight satellites, of undifferenced dual-frequency carrier-phase and pseudorange measurements obtained every 30 seconds. We analyze data using GAMIT software (King and Bock, 2004). We use GPS phase observations from each day to estimate station coordinates, the zenith delay of the atmosphere at each station, and orbital and earth orientation

parameters (EOP). We tightly constrain the positions of six IGS stations (alac, casc, ebre, rabt, sfer, vill) to the latest ITRF2000 values (Altamimi et al., 2002) and the satellite orbits to the final IGS ephemeredes.

The GAMIT software parameterizes the zenith atmospheric delay as a stochastic variation from the Saastamoinen model (Saastamoinen, 1972) with piecewise linear interpolation. The variation is constrained to be a Gauss-Markov process with a power density known as the zenith parameter constraint of 2 cm/√h.

In the absence of meteorological measurements, we have used National Center for Environmental Prediction (NCEP) global atmospheric fields to calculate 6-hourly pressure and temperature values at rabt station (Fig. 2) (Quinn and Herring, 1996).

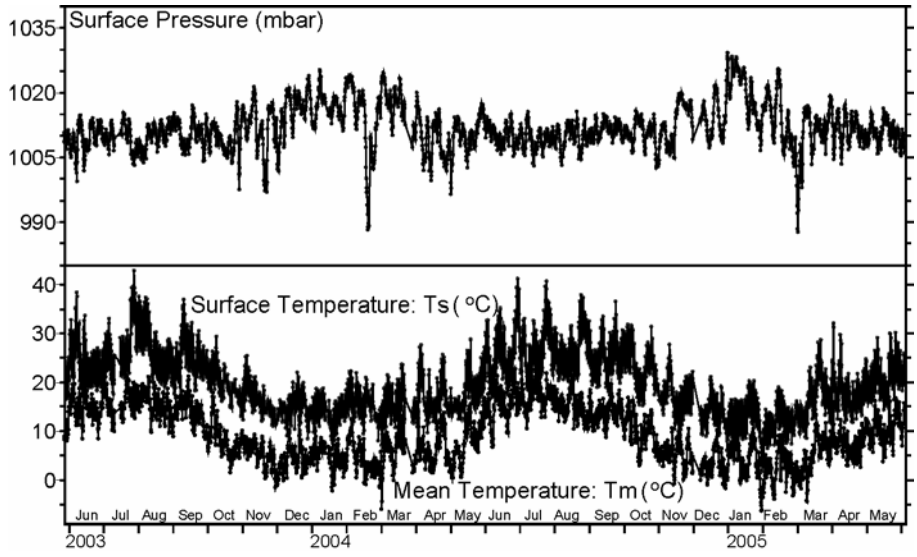

Figure 2. NCEP derived surface pressure estimates and NCEP derived surface and mean atmospheric temperature estimates (taken every 6 hours) at rabt station from June 2003 to June 2005.

The GPS zenith total delay obtained at rabt station is shown in Fig. (3). The NCEP zenith total delay, calculated theoretically according to Saastamoinen (1972), shows reasonable coherence with the GPS observations.

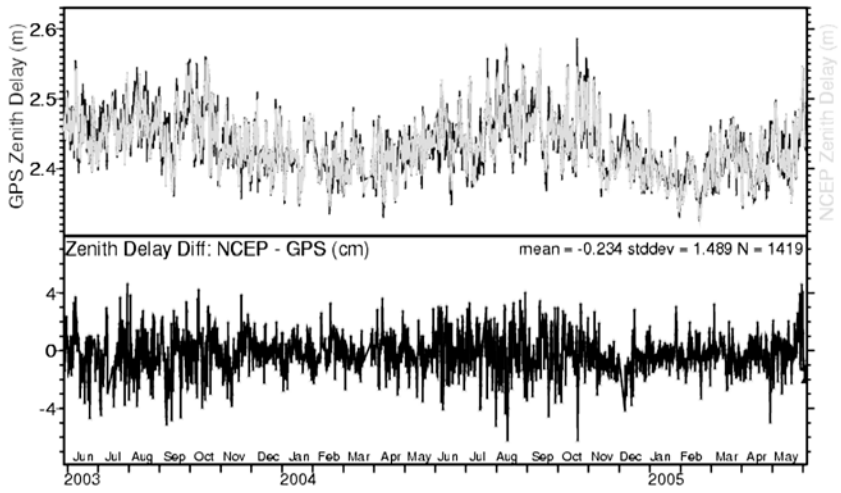

Figure 3. Estimates of zenith atmospheric delay from GPS (black) and NCEP (gray) measurements and their difference at rabt station over the whole experiment. N is number of observations.

To derive the precipitable water at rabt station from the estimates of zenith total delay we first calculated and subtracted the hydrostatic contribution. We used pressure at rabt station to compute the hydrostatic delays via Eq. (3). In general, the intercomparison between GPS precipitable water and other methods (e.g., NCEP, radiosondes, WVR's…) is useful to assess their differences and to validate future parameterizations of Numerical weather prediction (NWP) models (Fig. 4).

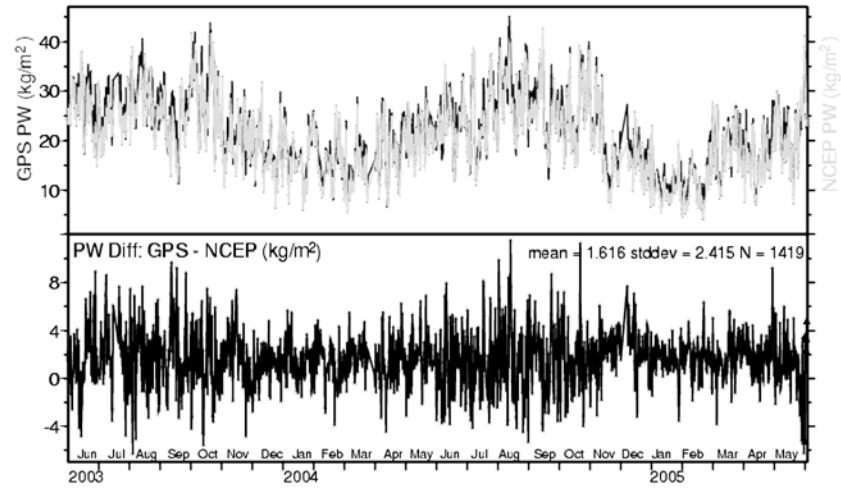

Figure 4. Estimates of precipitable water from GPS (black) and NCEP (gray) measurements and their difference at rabt station over the whole experiment. N is number of observations.

The monthly rainfall of two seasons S1 (from June 2003 to May 2004) and S2 (from June 2004 to May 2005) shows that S2 was dryer (rainfall) than S1 (Fig. 5) and the monthly mean precipitable water shows significant differences after December. At daily scale, any intense rainfall is preceded by a short period (e.g., A, B, C, and D in Fig. (6)) of increase in the

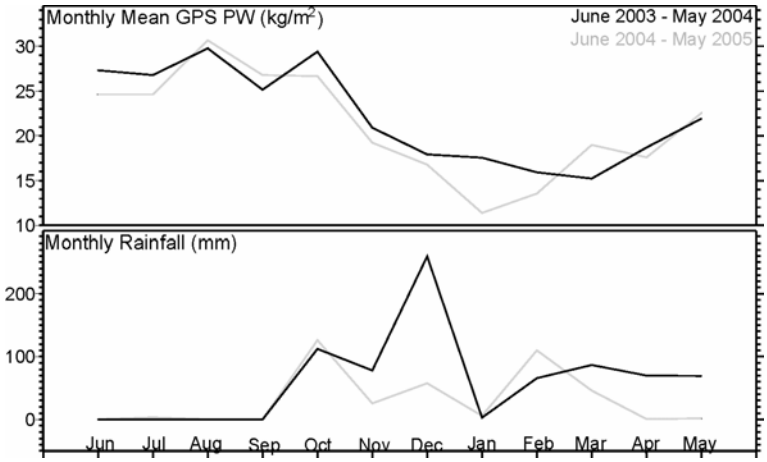

Figure 5. Monthly rainfall and monthly mean GPS precipitable water of the two seasons S1 and S2 at rabt station (see text).

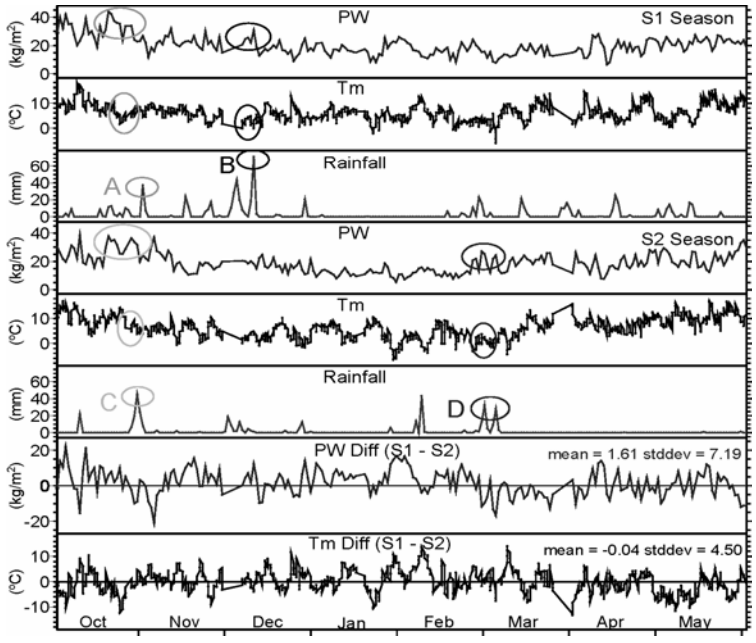

Figure 6. Daily precipitable water (PW), mean atmospheric temperature (Tm) and rainfall and daily differences of precipitable water and mean atmospheric temperature at rabt station during the two seasons S1 and S2 (see text).

precipitable water and a decrease in the atmospheric mean temperature. Therefore, the fact that S1 was wetter (precipitable water) than S2 was behind such different rainfall. To better study the short and long-term correlation between rainfall and precipitable water, the state of water vapor should be evaluated in its three-dimensional field.

5. Toward GPS tropospheric tomography

Recent studies show that it is possible to quantify the integrated water vapor in the line of sight of the GPS satellites (Ware et al., 1997; Alber et al., 2000; Braun et al., 2003). These observations can be used to study the three-dimensional heterogeneity of the troposphere using tomographic techniques, which have been intensively used in medicine to investigate human body or in seismology to describe the seismic velocity anomaly of the earth's interior.

Dense GPS network should be designed specifically to provide a good opportunity for the validation of the tomographic solution, for its interpretation, and for meteorological valorization.

The slant tropospheric delay (STD), with an elevation angle θ, can be computed from the hydrostatic and wet zenith delay via:

$$STD = (ZHD)M_h(\theta) + (ZWD)M_w(\theta) \tag{10}$$

where $M_h(\theta)$ is the hydrostatic mapping function and $M_w(\theta)$ is the wet mapping function (Niell, 1996). To introduce tropospheric heterogeneity in the GPS solution, the gradients in the North-South and East-West direction of the zenith tropospheric delay can be estimated (Fig. 7).

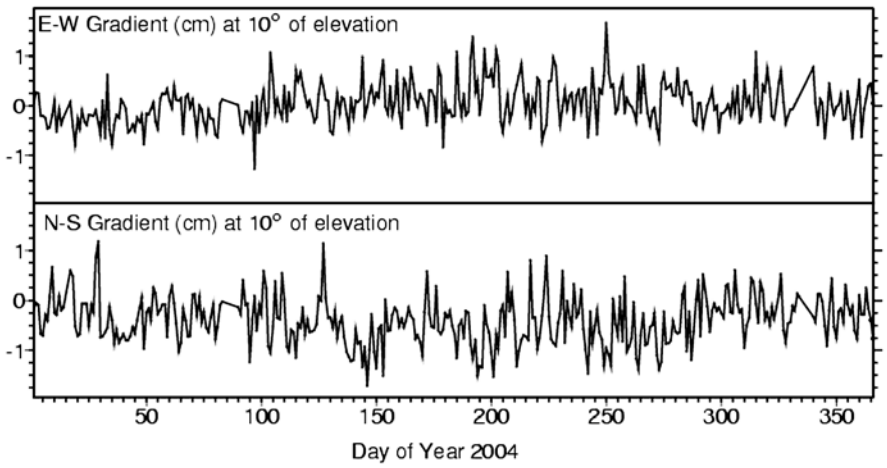

Figure 7. Horizontal tropospheric gradients (North-South and East-West) at 10° elevation observed at rabt station during the year 2004.

Following Chen and Herring (1997) the Slant Precipitable Water (SPW) can be expressed as:

$$\frac{SPW}{\Pi(T_m,\rho_v)} = m_w(\theta)(ZWD) + m_\Delta(\theta)[G_N\cos(\phi) + G_E\sin(\phi)] \quad (11)$$

where m_W is the molar mass of water vapor, θ is the elevation angle, Φ is the azimuth, G_N , G_E , and m_Δ being the N-S gradient , E-W gradient of zenith total delay, and the gradient mapping function, respectively.

The extraction of the GPS observable for tomographic inversion from the GAMIT analysis is in the following way: One-way SWD is evaluated from ZWD projected on satellite directions, and from wet gradients, obtained from total gradients observations from which a hydrostatic gradient is subtracted using surface pressure measurements. Then one-way post-fit residuals are added. These quantities are evaluated in the GAMIT analysis for every available station-satellite pair at every measurement epoch (Fig. 8) (Champollion et al., 2005).

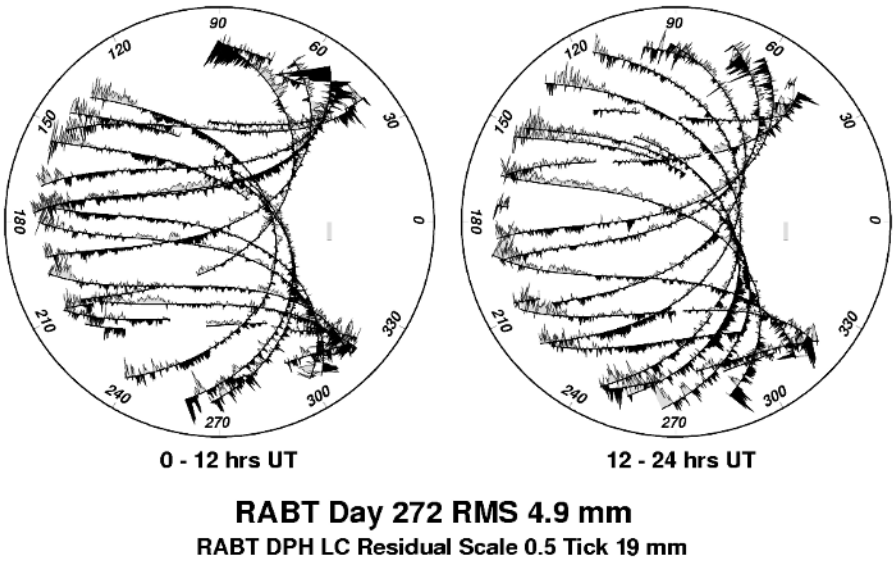

Figure 8. Post-fit one-way residuals for rabt station (day 272 of 2004). The phase observations are presented in the LC (ionosphere free) linear combination. The ticker smooth lines represent the orbital arcs of every satellite registered. The post-fit residuals are plotted on top of each arc, one value for every measurement epoch (every 30s), with positive values to one side, negative to the other side of the arc. The scale tick corresponds to 19mm. The mean residual is evaluated to 4.9 mm.

6. Conclusions and perspectives

The analysis of rabt GPS data has been presented in terms of the tropospheric parameters zenith delays and horizontal gradients. The inferred zenith delays have been validated with independent meteorological measurements (NCEP) confirming the good quality of the GPS data (Fig. 3). The zenith delay time series have been transformed into precipitable water observations. Precipitable water temporal variations can improve the understanding of large rainfall events. It allows an accurate and continuous description of the water vapor field variations before, during

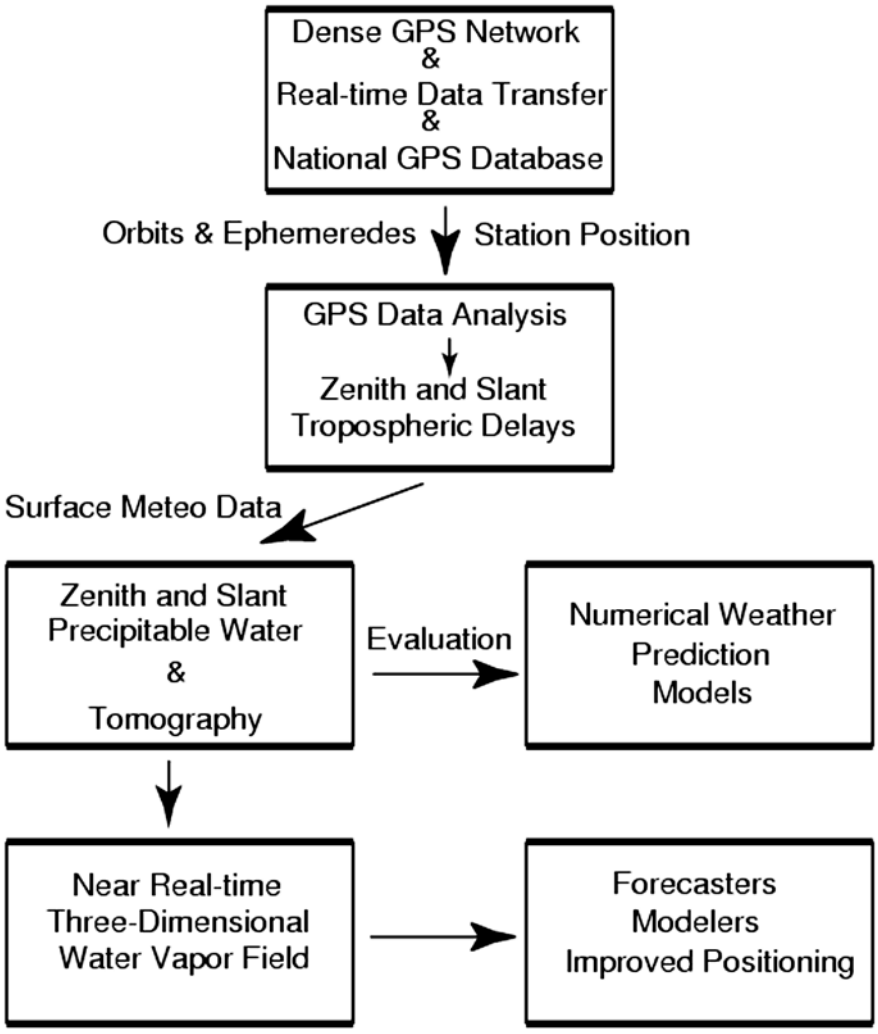

Figure 9. Demonstration GPS network hardware and software.

and after the heavy precipitation (Fig. 6). Building dense GPS network in Morocco will let to take advantage of GPS tomography (Fig. 9). The national database server will continuously download GPS precise predicted orbits and ephemeredes data from Scripps Orbit and Permanent Array Center (SOPAC), and GPS data from individual station. The GAMIT software will process this data in 5 min sliding window technique and will produces tropospheric delays. These values will be then processed with meteorological data from the stations to produce precipitable water estimates, which will be the input data to the tomography inversion then distributed to interested parties. This strategy can help understand the connection between the three-dimensional water vapor field and atmospheric processes (Fronts, precipitation…).

Acknowledgements

This research was supported in part by the Fulbright program. We are grateful to MACECE (Moroccan American Commission for Educational and Cultural Exchange) and AMIDEAST (AMERICA-MIDEAST EDUCATIONAL AND TRAINING SERVICES). The figures in this paper were produced using GMT (Generic Mapping Tools) software (Wessel and Smith, 1995).

References

Alber, C., Ware, R., Rocken, C., and Braun, J., 2000, Obtaining single path delays from GPS double differences. Geophys. Res. Lett. 27, 2661-2664.

Braun, J., Rocken, C., and Liljegren, J., 2003, Comparisons of line-of-sight water vapor observations using the global positioning system and a pointing microwave radiometer. J. Atmos. Ocean. Technol. 20 (5), 606-612.

Altamimi, Z., Sillard, P., and Boucher, C., 2002, ITRF2000: a new release of the international terrestrial reference frame for earth science applications. J. Geophys. Res. 107, pp. 2214–2232.

Bevis, M., Businger, S., Herring, T. A., Rocken, C., Anthes, R. A., and Ware, R. H., 1992, GPS meteorology: Remote sensing of atmospheric water vapor using the Global Positioning System. J. Geophys. Res., 97, 15787-15801.

Brunner, F. K., and Gu, M., 1991, An improved model for the dual frequency ionospheric correction of GPS observations. Manusc. Geod., 16, 205-214, 1991.

Champollion, C., Masson, F., Bouin, M. –N., Walpersdorf, A., Doerflinger, E., Bock, O., and Van Baelen, J., 2005, GPS water vapor tomography: Preliminary results from the ESCOMPTE field experiment. J. Atmos. Res. (74), 253-274.

Chen, G., and Herring, T. A., 1997, Effects of atmospheric azimuthal asymmetry on the analysis of space geodetic data. J. Geophys. Res., 102, 20489-20502.

Davis, J. L., Herring, T. A., Shapiro, I. I., Rogers, A. E., and Elgered, G., 1985, Geodesy by radio interferometry : Effects of atmospheric modeling errors on estimates of baseline lengths. Radio Sci., 20, 1593-1607.

Elgered, G., Davis, J. L., Herring, T. A., and Shapiro, I. I., 1991, Geodesy by radio interferometry: Water vapor radiometry for estimation of the wet delay. J. Geophys. Res., 96, 6541-6555.

Elgered, G., Johansson, J. M., and Ronnang, B. O., 1998, Measuring regional atmospheric water vapor using the Swedish permanent GPS network, Geophys. Res. Let., 24, 2663-2666.

Herring, T. A., Davis, J. L., and Shapiro, I. I., 1990, Geodesy by radio interferometry: The application of Kalman filtering to the analysis of very long baseline interferometry data. J. Geophys. Res., 95, 561-581.

King, R. W., and Bock, Y., 2004, Documentation for GAMIT analysis software, release 10.2, Mass. Inst. Of Technol., Cambridge.

Kuo, Y.-H., Guo, Y. –R., and Westwater, E. R., 1993, Assimilation of precipitable water into mesoscale numerical model. Mon. Wea. Rev., 121, 1215-1238.

Niell, A., 1996, Global mapping functions for the atmospheric delay at radio wavelengths. J. Geophys. Res., 101, 3227-3246.

Quinn, K. J., and Herring, T. A., 1996, GPS atmospheric water vapor measurements without the use of local barometers, Fall 1996 AGU Poster Presentation, G12A-06.

Saastamoinen, J., 1972, Atmospheric correction for the troposphere and stratosphere in radio ranging of satellites. The Use of Artificial Satellites for Geodesy, Geophys. Monogr. Ser. 15, Amer. Geophys. Union, 247-251.

Smith, E. K., and Weintraub, S., 1953, The constants in the equation for atmospheric refractive index at radio frequencies. Proc. IRE, 1035-1037.

Spilker, J. J., 1980, GPS signal structure and performance characteristics, in Global Positioning System, vol. 1, The Institute of Navigation, Washington, D.C., 1980.

Thayer, D. M., 1974, An improved equation for the radio refractive index of air. Radio Sci., 9, 803-807.

Tregoning, P., Boers, R., Obrien, D., and Hendy, M., 1998, Accuracy of absolute precipitable water vapor estimates from GPS observations, J. Geophys. Res., 103(D22), 28701-28710.

Ware, R., Alber, C., Rocken, C., and Solheim, F., 1997, Sensing integrated water vapor along GPS ray paths. Geophys. Res. Lett. 24, 417-420.

Wessel, P., and Smith, W. H. F., 1995, New version of generic mapping tools released, EOS, Trans. Am. Geophys. Union, 76, 329.

EXTREME VARIABILITY OF AEROSOL OPTICAL PROPERTIES: THE CAIRO AEROSOL CHARACTERIZATION EXPERIMENT CASE STUDY

STEPHANE C. ALFARO[1*] AND
MAGDY ABDEL WAHAB[2]

[1] *Laboratoire Interuniversitaire des Systèmes Atmosphériques, Universities Paris 12&7 and CNRS, 61 av. du Général de Gaulle, 94010 Créteil Cédex, France*
[2] *Astronomy and meteorological department, Cairo University, Giza, Egypt*

Abstract. Because they scatter and absorb solar and terrestrial radiation, aerosol plumes can easily be detected on satellite images. Thus, the time-dependent spatial extension of the aerosol clouds can be derived from space-borne observations. However, using remote observations for estimating particle concentrations, let alone for apportioning aerosol loads between all the potential sources of particulate matter, is less straightforward. Indeed, this apportionment would require perfect knowledge of the scattering and absorbing potential of particles of different origins as well as the spectral dependence of these potentials. Contrary to what can be done with most atmospheric gases, it is usually impossible to reproduce in the laboratory the complexity of natural atmospheric aerosols. As a consequence, measuring their wavelength-dependent optical properties can only be done during specially designed experiments performed in natural conditions. This is the case of the Cairo Aerosol CHaracterization Experiment (CACHE) that was performed in the Egyptian capital from the end of October 2004 to mid April 2005. During this period a wide variety of aerosol conditions have been sampled, but this work is focused on the spring intensive observation period during which several occurrences of

[*] To whom correspondence should be addressed. S. Alfaro, LISA, Université de Paris 12, 61 avenue du Général de Gaulle, 94010 Créteil, France. alfaro@lisa.univ-paris12.fr

A. Perrin et al. (eds.), Remote Sensing of the Atmosphere for Environmental Security, 285–299.

mineral dust transport to Cairo were observed. We detail the modifications of optical properties resulting from these inputs of mineral particles into the background 'urban aerosol' and show that scattering and absorption, as well as their spectral dependence are extremely sensitive to the proportions of the "urban pollution/mineral dust" mixtures that form over Cairo during the dust events. Unfortunately, this precludes the use of predefined aerosol models supposed to represent particularly simple aerosol types (e.g., urban pollution, mineral dust,…) for inverting satellite observations over areas where aerosol mixing is known to be the rule rather than the exception (e.g., over the eastern Mediterranean in spring, over or downwind of continental China during the dust season, over west Africa during the biomass burning period, …). In these cases, sophisticated parameterizations of the optical properties must be used for assessing the impact of aerosol mixtures on radiative transfer.

Keywords: Egypt, aerosol mixing, mineral dust, urban pollution aerosols, scattering, absorption, single scattering albedo

1. Introduction

In terms of mass, wind erosion in arid or semi-arid areas is the second largest source of atmospheric particles (aerosols). Because they scatter and absorb solar and terrestrial radiations, plumes of mineral dust particles can easily be observed from space either in the UV-visible or in the infrared. Thus, satellite observations make it possible to follow the general patterns of mineral dust transport from sources to deposition areas. This is a useful constraint for validating models aiming at reproducing the combination of processes (emission, transport, deposition) involved in the dust cycle, but this constraint would be even stronger if mass concentrations could be retrieved accurately from the satellite observations. Unfortunately, such retrieval is currently hindered by large uncertainties on the aerosol potential to scatter and absorb solar and terrestrial radiation. These uncertainties are themselves due to the extreme variability of aerosol characteristics that, according to the electromagnetic theory, condition their optical properties. Even in the simplest possible case, the one of 'pure' aerosols originating from a single source, the list of these characteristics includes size distribution, size-resolved composition, size-resolved shape, and affinity for water vapor. In the more complex case of aerosol mixing, the proportions of the mixture and the type of mixing (external when particules of different origins simply coexist or internal when they coagulate) also play a part.

Due to this complexity, Mie's theory that was originally designed for spherical and homogeneous particles does not apply to mineral dust and, in spite of some recent progress (Sokolik and Toon, 1999; Lafon, 2004) no other optical model allowing routine computation of the optical properties for this kind of aerosol has been validated yet. In consequence, the correlation between aerosol optical properties and their size and compositional characteristics must still be sought empirically. The objectives of the present work are 1) to summarize the principles of an experimental methodology imagined for doing so (Alfaro et al., 2004), and 2) to summarize and discuss the results obtained during two major dust events that were sampled in Cairo (Egypt) in the frame of the spring 2005 intensive observation period of the Cairo Aerosol CHaracterization Experiment (CACHE) (Alfaro et al., submitted to JGR)

2. Methodology and experimental set-up

2.1. THEORETICAL CONSIDERATIONS

The spatial distribution of scattering (σ_{scatt}) and absorbing (σ_{abs}) coefficients is necessary to compute the impact of an aerosol on radiative transfer. These coefficients are extensive quantities directly proportional to the aerosol mass concentration (usually, the mass concentration of particles with aerodynamic diameter less than 10 μm, alos referred to as PM10) whereas the mass scattering and mass absorption efficiencies (α_{scatt} and α_{abs}, respectively) obtained by dividing them by PM10 are intensive properties more useful for comparing different aerosols independently of their concentrations. Another intensive parameter commonly used in radiative transfer computations is the single scattering albedo (SSA or ϖ_0) defined as the fraction of extinction due to scattering alone:

$$\varpi_0 = \alpha_{scatt}/(\alpha_{scatt} + \alpha_{abs}) \quad (1)$$

Recently, values of this parameter have been retrieved by inverting remote sensing data collected over areas where dust was assumedly largely dominant (Tanré et al., 2001; Colarco et al., 2002; Dubovik et al., 2002). These results tend to show that mineral dust is less absorbing than was considered previously and that the single scattering albedo of mineral dust increases with wavelength in the solar spectrum. However, these studies suffer from two flaws: 1) They provide ϖ_0 values that are averaged vertically over the whole height of the aerosol column, and 2) they cannot allow assessment of the correlation linking optical properties and composition because the latter is not measured. The experimental protocol

proposed by Alfaro et al. (2004) is more adapted to this task. It consists in sampling the ambient aerosol for performing on it various simultaneous measurements including determination of 1) mass concentration, 2) scattering and absorbing properties, and 3) other aerosol characteristics (size distribution and composition) that have an influence on optical properties. This methodology that can be used indifferently in the laboratory or in natural outdoor conditions as was the case during CACHE is summarized below.

2.2. AEROSOL CHARACTERIZATION IN CAIRO

2.2.1. *Site location and aerosol sampling*

The terraced roof of the Physics department at Cairo University (lat: N 30° 01'33", long: E 31° 12' 25", Giza, Egypt) was used as a main experimental site for the intensive observation periods of CACHE. The elevation of the terrace was approximately 15 m above ground level and it was more than 200 m away from the closest street. Cairo University is located in the south western part of Greater Cairo, but in a bee-line the distance separating it from what is usually considered as the city center (Sadate Square) does not exceed three kilometers. Aerosol sampling was performed by using a rotating inlet to which were connected all the instruments or particles collection devices (up to 8 of them at the same time) used to characterize the aerosol directly in-situ or later in the laboratory. In the Cairo experimental conditions, the size cut-off of the sampling inlet was 10 μm.

2.2.2. *Measurements of mass concentration, size distribution, and composition*

A Tapered Element Oscillating Microbalance (TEOM, model 1400a, Rupprecht and Patashnick) operated at a controlled flow rate (F_T) of 3.0 L/min was used to provide a PM10 value every 6 minutes. In the meantime, an Optical Particle Counter (OPC) (Grimm, model G1.108) was used to sort particles in 15 size classes ranging from 0.3 to 20 μm. Measurements made every six seconds were averaged over periods of one minute.

For assessing the aerosol composition, a sampling line was used to collect PM10 particles on 0.4 μm pore diameter Nuclepore filters at a constant flow rate of 1 m^3/h. Sampling duration was typically 3 hours during the day and 15 seconds every minute for twelve hours (thus also amounting to 3h in all) during the night, but could be reduced to less than one hour during strong dust events. The purpose of particle collection was to perform X Ray Fluorescence analysis (XRF) and thus determine the aerosol concentration in some major elements (Si, Al, Ca, Fe, K, Mg, Na,

Cl, S…). In this study, Al is of particular interest because it is known to be a specific tracer of soil-derived particles and can thus be used as a proxy to quantify the importance of the mineral dust component in the overall aerosol.

In additions to the previous on-line filtration, an aethalometer (see below) was also used to provide an estimate of the mass concentration in Black Carbon (BC). This species that is released by fossil fuel combustion in industries or car-engines, by biomass and waste burning… will be considered as a tracer of locally-produced anthropogenic aerosols and its mass fraction (%BC) used to quantify the importance of the 'urban pollution' component in the 'pollution/dust' mixtures that are the object of this study.

2.2.3. *Aerosol optical properties at ground level*

An integrating nephelometer (TSI, model 3563) was used to measure the aerosol scattering coefficients (σ_{neph}) at 3 wavelengths (450, 550, and 700 nm). The instrument also monitored the relative humidity (rh) within the measurement chamber. The fact that measurements were performed at three wavelengths also allows quantification of the spectral dependence of scattering by the means of Angström's exponent. The nephelometer truncation error is corrected according to the method of Alfaro et al. (2004). The uncertainty on the aerosol mass scattering efficiency (α_{scatt}) is estimated to be less than 20% at all times.

A spectral aethalometer (Magee scientific, model AE-42) working at 7 wavelengths spanning the whole solar spectrum (370, 470, 520, 590, 660, 880, and 950 nm) was run at a controlled flow-rate (F_a = 5 L/min) for two different purposes: the first one was to provide the real time estimate of atmospheric concentration in black carbon that is necessary for the quantification of the proportions of the urban pollution/mineral dust mixtures (see above), and the second one was to determine the aerosol mass absorption efficiency (α_{abs}) at the 7 wavelengths of the instrument. For this, the attenuation measurements have been corrected for the effects due to the presence of the instrument filter and of non-absorbing particles that were mixed with the light-absorbing species (Petzold et al., 1997; Bond et al., 1999).

Finally, the aerosol single scattering albedo can be obtained directly by combining the mass scattering and absorption efficiencies according to equation (1).

3. Results

3.1. OCCURENCES OF MINERAL DUST/URBAN POLLUTION MIXING

Examination of Al concentration plotted versus time (Fig. 1) clearly reveals that 3 major dust events occurred during the spring intensive observation of CACHE. The first one was observed on March 31, at a time when for logistical reasons the TEOM microbalance and TSI nephelometer were not yet implemented on the experimental site. The second and third events took place on April 1 and April 8, respectively. The corresponding Al peaks (6.88 and 10.47 $\mu g/m^3$) coincide with PM10 maxima (835 and 862 $\mu g/m^3$) recorded by the TEOM microbalance (Fig.1). This temporal coincidence simply reflects the fact that the massive arrival of coarse, and hence heavy, dust particles at the sampling site has a direct effect on the atmospheric mass load.

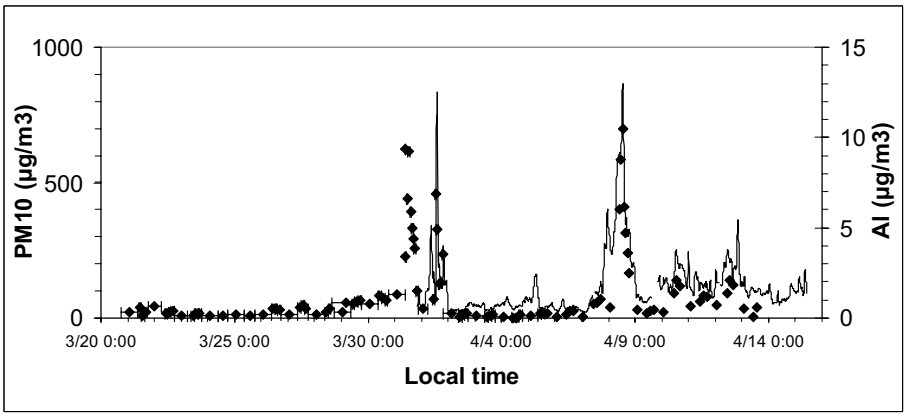

Figure 1. Temporal evolution of the PM10 mass concentration (solid line) measured in real time by the TEOM microbalance and of the Al mass concentration retrieved by XRF analysis of aerosol samples collected on nuclepore filters (losanges). Note that the PM10 measurements are only available after March 31, 2005.

The temporal structure of both dust events followed the same pattern: Al concentration increased sharply in the morning, reached a maximum in the early afternoon, and eventually faded away in the evening. The relative humidity (rh) measured at the sampling site during the dust events reveal that the air masses bringing dust to the city were particularly dry (rh<50%). In these conditions, the effect of humidity on the optical properties will be assumed to be negligible. The black carbon concentration measured by the aethalometer and averaged over the duration of each filter did not follow the Al concentration trend (results not shown). This decoupling of Al and BC behaviors suggests that the air masses transporting mineral dust from its

desert source to Cairo did not contain any significant carbonaceous component before they reached the city, and that the mixing of mineral dust particles with anthropogenic particles occurred for the first time over Greater Cairo. This supports *a posteriori* our choice of using BC as a specific tracer of the local 'pollution' component in the aerosol mixture. Our quantitative results for April 8 show that on this day the black carbon mass fraction varied by almost two orders of magnitude. Early in the morning, that is to say before the arrival of dust, %BC was maximal (around 10%). Afterwards, it decreased dramatically to reach its lowest value (only a fraction of %) at the peak of dust. After the passage of dust, %BC returned within a few hours only to larger values more representative of the city background aerosol. A quite similar time dependence of %BC is observed on April 1 except that %BC was even larger before the arrival of dust (around 25% between 7.00 and 9.00 AM).

The aerosol size distribution is also deeply affected by the passage of dust. The major feature accompanying dust arrival at the sampling site is the increase in concentration for the particles in the supermicron mode (Fig. 2a and 2b). This increase can be sudden as the one observed at 12.49 on April 1 or more progressive as the one occurring on April 8. Figures 2a and 2b also show that the temporal variability of particle concentrations in each size range is much larger on April 1 than on April 8. For example, it can be noted that such large peaks in submicron particle concentration as the one observed between 7.00 and 9.00AM on April 1 are not observed on April 8. The exact origin of these peaks cannot be ascertained before results of fast chemistry analysis become available, but it is highly probable that they can be attributed to anthropogenic sources of very fine particles whose influence on the sampling site is larger on April 1 than on April 8. This could also explain the previous observation that %BC peaked at much larger values on April 1 than on April 8 (25% as compared to 10%).

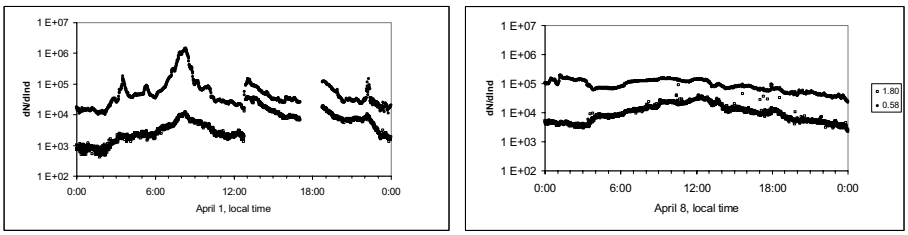

Figure 2. Particle number concentrations in the 0.50-0.65 (full circles) and 1.60-1.80 µm (open squares) size ranges for the a) April 1 and b) April 8 dust events. Full size distributions of the aerosol mixtures measured by the optical size analyzer in situations dominated by urban pollution (during the night of April 8) and at the peak of the dust event are also represented (c). In this latter case, values have been normalized to the total particle concentration in order to facilitate comparison.

3.2. IMPACT OF THE MIXING ON THE AEROSOL OPTICAL PROPERTIES

3.2.1. *Scattering*

The mass scattering efficiency derived directly from the nephelometer and microbalance measurements ($\alpha_{neph,\lambda}$) is quite sensitive to the incorporation of mineral dust into the background aerosol as denoted by the lowering of %BC on figure 3. On April 8, for instance, $\alpha_{neph,450}$ remained maximal and approximately constant (ca. 2.1 m^2/g) until the arrival of dust and the associated reduction in %BC made this parameter become less than 6%. Below this value, $\alpha_{neph,450}$ decreases with %BC and is reduced by approximately one order of magnitude at the peak of the dust events. This can be interpreted by recalling that the mass scattering efficiency of supermicron particles at solar wavelengths is smaller than the one of submicron particles. As a result, progressive incorporation of coarse dust particles into background pollution-dominated aerosols increases the overall aerosol mass concentration (PM10) much faster than it does $\sigma_{neph,450}$ and the ratio of the two quantities ($\alpha_{neph,450}$) is thus negatively correlated to the proportion of dust in the mixture.

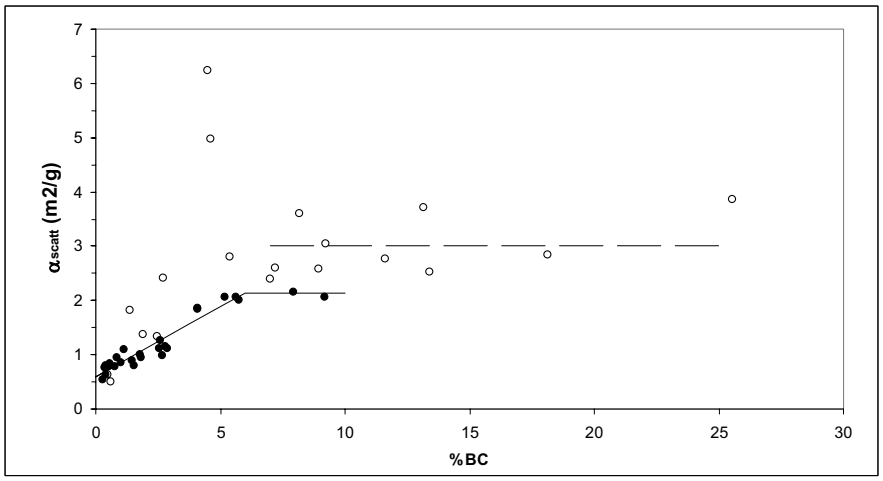

Figure 3. Influence of the proportions of the urban pollution/mineral dust mixture on the aerosol mass scattering efficiency at 450 nm. Results for April 1 (open circles) have been distinguished from those of April 8 (full circles). The scatter of data observed on April 1 is due to largest size distribution variability on this day (see text for details).

The limit towards which $\alpha_{neph,450}$ tends when %BC tends towards 0 is the value for pure dust, $\alpha_{neph,\ dust,450}$. This uncorrected mass scattering efficiency (0.60 m^2/g) is similar to the one measured in continental China

downwind of the Gobi desert (0.70 ± 0.16 m^2/g) during a major dust event (Alfaro et al., 2003). When corrected for the nephelometer truncation error, $\alpha_{neph,\ dust,450}$ finally becomes $\alpha_{scatt,dust,450} = 0.90\ (\pm 0.12)\ m^2/g$.

The results obtained on April 1 follow the same general pattern as on April 8 but with some noticeable differences. For instance, the large variability in size distribution observed on this day is responsible for a larger scatter in experimental results. In particular, the two points corresponding to the 8.00/9.00 AM period are completely atypical because of the exceptional richness of the aerosol in submicron particles that are very efficient at scattering solar light (see comments on the size-distribution above).

The Angström's exponent for scattering also varies rapidly with the proportions of the background aerosol/mineral dust mixture (Fig. 4). This is in good agreement with the electromagnetic theory predicting that scattering of solar light by supermicron particles is much less spectrally dependent than scattering by submicron particles.

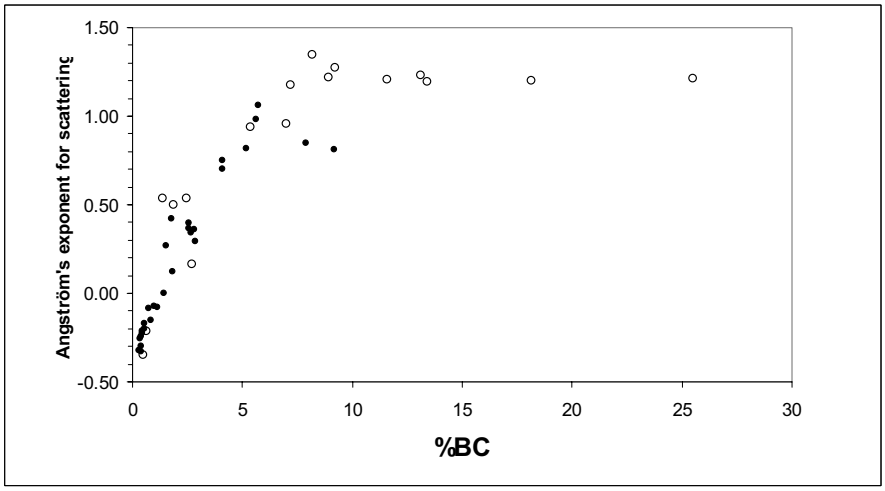

Figure 4. Influence of the proportions of the urban pollution/mineral dust mixture on the spectral dependence of scattering by urban pollution/mineral dust mixtures. Results for April 1 (open circles) have been distinguished from those of April 8 (full circles).

3.2.2. *Absorption*

The mass absorption efficiency ($\alpha_{abs,\lambda}$) of aerosol mixture is notably different in the near infrared (950 nm) and in the UV (370 nm) (Fig. 5). On April 1, as well as on April 8, absorption at the largest wavelength is almost perfectly proportional to the aerosol content in black carbon. Indeed, the best linear fit to the experimental data ($\alpha_{abs,950} = 0.163$ %BC, $n = 44$, $r^2 =$

0.995) is characterized by a very large value of r^2. This shows that absorption at 950 nm is only due to BC and does not dependent on the amount of mineral dust in the mixture which is consistent with the fact that iron-oxides do not absorb radiation in the near infrared. The only effect of dust particles in this wavelength range is a dilution effect similar to the one already observed for scattering. Progressive addition of coarse, non-absorbing particles to the background aerosols increases the mass concentration without having any effect on the absorption coefficient ($\sigma_{abs,950}$) and this results in a dramatic decrease in the ratio of the two quantities, i.e. in mass absorption efficiency. This decrease between initial pre-dust conditions and the dust peaks covers two orders of magnitude (Fig. 5).

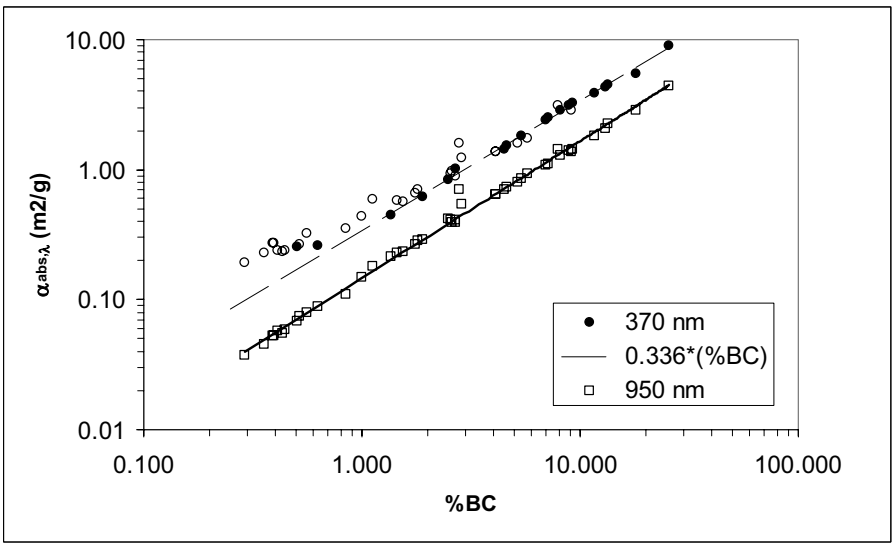

Figure 5. Evolution of the aerosol mass absorption efficiencies at 950 (open squares) and 370 (circles) nm with the proportions of the urban pollution/mineral dust mixtures. At 370 nm, results obtained during the April 1 dust event (full circles) have been distinguished from those of April 8 (see text for details).

At the shortest wavelength (370 nm), the dilution effect due to addition of mineral dust particles in the city aerosol is also observed at %BC values larger than approximately 4%. In these conditions, $\alpha_{abs,370}$ is again proportional to %BC ($\alpha_{abs,370}$ = 0.336 %BC), indicating that BC largely dominates absorption in the mixture. However, a positive departure from the previous linear trend is clearly observed when %BC becomes less than 2%. This means that absorption is then larger than the one one would

expect if BC were the sole light absorber in the aerosol mixture. In other words, dust particles, or rather the iron oxides they contain, are responsible for an absorption enhancement at particularly short solar wavelengths. Fig.5 shows that during the dust peaks this part played by mineral dust can become as large as the one played by BC. Indeed, the measured value of $\alpha_{abs,370}$ is approximately 0.2 m^2/g for %BC = 0.3%, whereas the one due to BC alone is only 0.1 m^2/g.

3.2.3. *Single scattering albedo*

Equation (1) shows that the aerosol single scattering albedo can be computed directly from the mass scattering and mass absorption efficiencies. Like these two quantities, ϖ_0 will thus depend at the same time on %BC and on λ. Sensitivity tests performed on the single scattering albedo computation show that the main source of uncertainty for this parameter is the correction of the nephelometer truncation error. Though the magnitude of this correction depends on the aerosol size distribution, we have used the same correction independently of the proportions of the pollution/dust mixtures. This implies uncertainties on the retrieval of ϖ_0 that are less than 3% for dust-dominated aerosols but can reach 15% for aerosol mixtures that are dominated by the anthropogenic component.

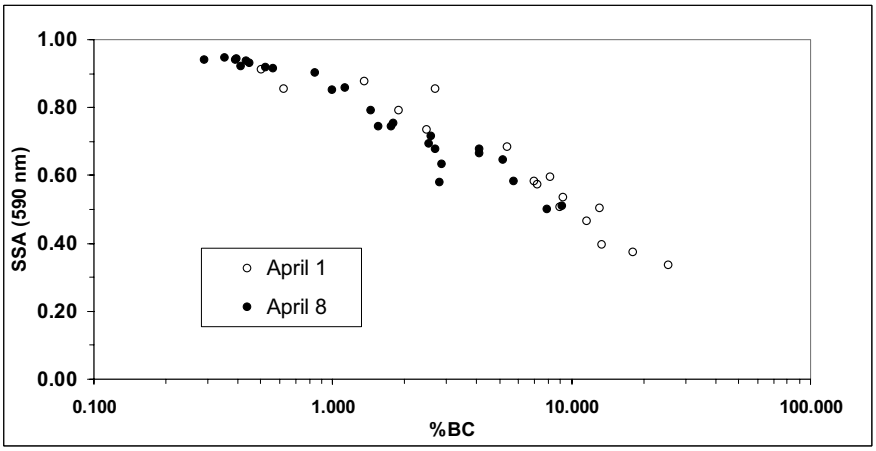

Figure 6. Sensitivity of the single scattering albedo (SSA) at 590 nm to the proportion of the urban pollution/mineral dust mixture. Uncertainties on values corresponding to situations dominated by urban pollution (largest %BC values) are ca. 15% whereas uncertainties corresponding to situations with a strong mineral dust component (lowest values of %BC) are ca. 3%.

At a fixed wavelength (e.g., 590 nm), ϖ_0 increases with the proportion of dust in the mixture (Fig. 6). Values for 'background' conditions are very low (ca. 0.40 ± 15%) and typical of aerosols whose BC component is particularly important. With the arrival of dust whose absorbing power is low at 590 nm, ϖ_0 increases and tends progressively towards a value (0.94 ± 3%) that is usually considered as typical of pure dust in this range of wavelengths (Tanré et al., 2001; Colarco et al., 2002; Dubovik et al., 2002; Alfaro et al, 2004).

It is also possible to determine the spectral dependence of ϖ_0 at fixed times, or equivalently at fixed %BC. Four such times have been selected on April 8: one in the night, before the arrival of dust, two during the dust event, and one in the afternoon when dust was already receding. The corresponding **%BC values are 8, 0.4, 0.3, and 1.8%, respectively. It can be seen on Figure 7** that for the night case, ϖ_0 is very low and practically independent of λ over the whole solar spectrum. Just six hours later, incoming dust has provoked a dramatic increase in ϖ_0, but this increase being less important at wavelengths shorter than 660 nm were iron oxides are efficient light absorbers, the ϖ_0 value of the mineral dust dominated mixtures is now characterized by a marked spectral dependence. Again after a few hours, that is to say during the receding phase of the dust storm, the single scattering albedo and its spectral dependence rapidly return to their pre-dust values.

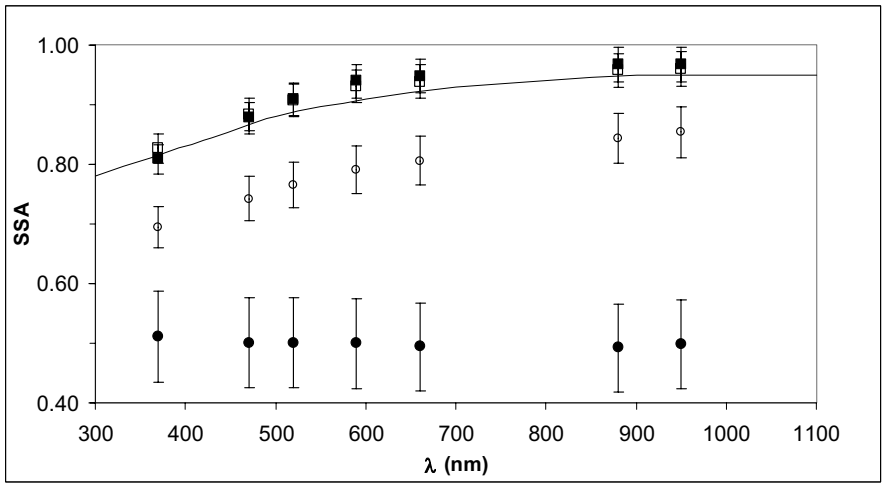

Figure 7. Spectral dependence of the scattering albedo in the four April 8 conditions reported on fig. 3: One nocturnal situation dominated by urban-pollution (%BC = 10%; full circles), two situations dominated by dust (%BC = 0.4 and 0.3%, full and empty squares, respectively), and an intermediate situation (%BC= 1.8%; open circles). For the sake of comparison, single scattering albedo obtained by inverting airborne radiative measurements performed over the Korean Strait during a strong dust event [Bergstrom et al.; 2004] are also reported.

4. Conclusion

During the second intensive observation period of the Cairo Aerosol CHaracterization Experiment two intense dust events have been sampled on the campus of Cairo University. Both events lasted several hours during which mineral dust particles coming from the desert mixed with the dense locally-produced urban pollution plume. The arrival of mineral dust at the sampling site induced very rapid and dramatic changes in aerosol optical properties. As compared to pre-dust urban pollution conditions, the mass scattering efficiency was approximately reduced by a factor 4, and the mass absorption efficiency by two orders of magnitude during the dust peaks. In the meantime, the spectral dependence of the aerosol properties was also dramatically modified. Indeed, Angström's exponent for scattering dropped from large (>1) values typical of submicron anthropogenic aerosols to slightly negative values typical of coarser mineral dust particles. The evolution of the spectral dependence of absorption was more complex. In urban pollution situations absorption varied with wavelength according to a negative power law. Due to iron oxides that absorb selectively at short solar wavelengths, absorption is specifically enhanced at these wavelengths and, as a matter of consequence, absorption can no longer be represented by a simple power law in presence of mineral dust. Our experimental results also confirm previous estimates [Alfaro et al., 2004] indicating that during strong dust events absorption by dust at short solar wavelengths can be of the same order of magnitude as the one by BC.

Finally, by combining the results obtained for scattering and absorption we have shown that the single scattering albedo and its dependence to wavelength are also mostly sensitive to the relative composition of the aerosol mixture. During the two dusty days, ϖ_0 evolved within just a few hours from a very low, spectrally independent value typical of strongly absorbing urban background aerosols to globally larger but wavelength-dependent values typical of mixtures dominated by mineral dust.

In summary, our results emphasize the great sensitivity of all optical properties, including spectral dependence, to the proportion of the aerosol mixture. For instance, inclusion of a small anthropogenic component into a dust plume or of a mineral dust component into a pollution plume will dramatically modify the aerosol single scattering albedo. It is of the utmost importance to take this into account when trying to interpret remote sensing observations or to quantify the effect of aerosol plumes on radiative transfer.

Acknowledgments

This work has been funded in part by the French Ministry of Foreign Affairs in the frame of the Imhotep program (contract 446538E) and the Institut National des Sciences de l'Univers (INSU). We are also grateful to the ADEME and PNCA (project: 'Espèces à courte durée de vie: interactions avec le climat') for their financial support. Last, but not least, we want to thank Cairo University at Giza for providing the experimental site.

References

Alfaro, S.C., L.Gomes, J.L. Rajot, S. Lafon, A. Gaudichet, B. Chatenet, M. Maille, G. Cautenet, F. Lasserre, and X.Y. Zhang, 2003, Chemical and optical characterization of aerosols measured in Spring 2002 at Chinese Ace-Asia Supersite (Zhenbeitai) China, *J. Geophys. Res,* Vol. 108, No. D23, 8641, doi10.1029/2002JD003214.

Alfaro, S.C., S. Lafon, J.L. Rajot, P. Formenti, A. Gaudichet, and M. Maille, 2004, Influence of Iron oxides on light absorption by pure desert dust : An experimental study, *J. Geophys. Res.,* Vol. 109, D08208, doi10.1029/2003JD004374.

Alfaro[1] S.C, E. Terrenoire[1], O. Favez[2], K.F. Mahmoud[3], M. Abdel Wahab[4], A. Gaudichet[1], J. Sciare[2], B. Chatenet[1], and M. Maillé[1], Optical properties of mineral dust and urban pollution mixtures in Cairo, Egypt, submitted to *J. Geophys. Res,*

Bergstrom, R. W., P. Pilewskie, J. Pommier, M. Rabbette, P. B. Russell, B. Schmid, J. Redemann, A. Higurashi, T. Nakajima, and P. K. Quinn, 2004, Spectral absorption of solar radiation by aerosols during ACE-Asia, *J. Geophys. Res.*, *109*, D19S15, doi:10.1029/2003JD004467.

Bond, T.C., T.L. Anderson, and D. Campbell, 1999, Calibration and intercomparison of filter-based measurements of visible light absorption by aerosols, *Aerosol Sci. Technol*., 38, 1823-1832.

Colarco, P.R., O. Toon, O. Torres, and P. Rasch, 2002, Determining the UV imaginary index of refraction of Saharan dust particles from Total Ozone Mapping Spectrometer data using a three-dimensional model of dust transport, *J. Geophys. Res,* Vol. 107, No. D16, doi :10.1029/2001JD00903.

Dubovik, O., B. Holben, T. F. Eck, A. Smirnov, Y. J. Kaufman, M. D. King, D. Tanre, and I. Slutsker**,** 2002, Variability of absorption and optical properties of key aerosol types observed in worldwide locations, *J. Atmos. Sci.*, *59*, 590–608.

Lafon, S., 2004, Les oxydes de fer dans l'aérosol désertique en relation avec ses propriétés optiques: caractérisation physico-chimique de poussières minerals générées en soufflerie, Ph.D Thesis, Université de Paris 12 Val de Marne, Créteil, France.

Petzold, A., C. Kopp, and R. Niessner, 1997, The dependence of the specific attenuation cross-section on black carbon mass fraction and particle size, *Atmos. Environ*., 31, 5, 661-672.

Sokolik, I.N., and O.B. Toon, 1999, Incorporation of mineralogical composition into models of the radiative properties of mineral aerosol from UV to IR wavelengths, *J. Geophys. Res,* Vol. 104, No. D8, 9423-9444.

Tanré D., Y.J. Kaufman, B.N. Holben, B. Chatenet, A. Karnieli, F. Lavenu, L. Blarel, O. Dubovik, L.A. Remer, and A. Smirnov, 2001, Climatology of dust aerosol size distribution and optical properties derived from remotely sensed data in the solar spectrum, *J. Geophys. Res,* Vol. 106, No. D16, 18,205-18,217.

URBAN AIR POLLUTION AND ITS PHOTOCHEMISTRY STUDIED BY LASER SPECTROSCOPIC METHODS

ZDENĚK ZELINGER*, PAVEL KUBÁT
J. Heyrovský Institute of Physical Chemistry, Academy of Sciences of the Czech Republic, Dolejškova 3, 182 23 Prague 8, Czech Republic

MICHAL STŘIŽÍK
VŠB – Technical University of Ostrava, Faculty of Safety Engineering, Lumírova 13, 700 30 Ostrava-Výškovice, Czech Republic
&
Institute of Thermomechanics, Academy of Sciences of the Czech Republic, Dolejškova 5, 182 00 Prague 8, Czech Republic

KLÁRA BEZPALCOVÁ, ZBYNĚK JAŇOUR
Institute of Thermomechanics, Academy of Sciences of the Czech Republic, Dolejškova 5, 182 00 Prague 8, Czech Republic

PAVEL DANIHELKA
VŠB – Technical University of Ostrava, Faculty of Safety Engineering, Lumírova 13, 700 30 Ostrava-Výškovice, Czech Republic

SYLVA DRÁBKOVÁ, MILADA KOZUBKOVÁ
VŠB – Technical University of Ostrava, Faculty of Mechanical Engineering, 17. listopadu 15, 708 33 Ostrava-Poruba, Czech Republic

PAVEL BERGER, ALEXANDR ČERNÝ, PAVEL ENGST
LIDAR, s.r.o., Washingtonova 17, 110 00 Prague 1, Czech Republic

*To whom correspondence should be addressed.

A. Perrin et al. (eds.), Remote Sensing of the Atmosphere for Environmental Security, 301–316.

Abstract. This work compares approaches both of mathematical and physical modelling of pollutant dispersion in simulated atmospheric boundary layer (ABL) with results of remote sensing of atmospheric pollutants. Measurements were performed over a highway outside a city and in an urban street canyon with extensive traffic under different meteorological conditions (autumn versus summer period). Time-resolved spatial distributions of pollutants (NO_2 and O_3) were measured by the combined DIAL (differential absorption light detection and ranging)/SODAR (sound detection and ranging) method and using spot analyzers appropriately located on the leeward and windward sides near the urban street canyon bottom. Qualitative agreement was found between the results obtained by remote sensing in the real atmosphere and those obtained by physical modelling in the simulated atmosphere of a wind tunnel for the autumn period. On the other hand, the analysis of the monitoring results and outputs of the physical modelling shows disagreement for the summer period. Besides neglecting the thermal effect during the sunny period, chemical reactions or photochemical processes taking place in the street canyon can affect the dispersion and distribution of pollutants very significantly. To improve the description of the system investigated, the Computational Fluid Dynamics (CFD) environment was tested for a basic implementation of photochemical reactions into the commonly used mathematical models of turbulence and dispersion processes as well.

Keywords: Air pollution, differential absorption LIDAR, physical modelling, photoacoustic detection, street canyon, atmospheric boundary layer, wind tunnel.

1. Introduction

Air pollution can be studied by direct monitoring methods[1] and by mathematical or physical modelling[2]. For complicated micro-scale cases the methods of physical simulation of processes on the scaled down models in wind tunnels are the most convenient and provide the most complete picture of the pollutant distribution. Study of the dispersion of pollutants in the atmosphere forms a basis for implementation of effective methods how to prevent environmental damage. The troposphere frequently exhibits dangerous pollutant concentrations, especially in the area of urban agglomerates. Atmospheric pollution has a number of detrimental consequences in the form of acid rain, photochemical smog and global climatic changes. The understanding of the complex processes occurring in

the atmosphere permits the creation of models that not only assist in suppressing and eliminating the instantaneous detrimental phenomena, but also provide predictions of how these detrimental consequences can be avoided over longer periods of time.

We applied two experimental spectroscopic techniques for investigation of air pollution. The DIAL (differential absorption light detection and ranging) technique[3] can provide 2D and 3D profiles of pollutant concentrations at high temporal resolution and over large distances. Its use has become more common over the last two decades. DIAL measurements are typically applied in order to acquire the vertical profiles of ozone and NO_2 concentrations.[4-8] The CO_2 laser photoacoustic spectrometry[9, 10] was used as an analytical tool for monitoring the methanol concentration in the simulated atmosphere. Methanol was chosen as a tracer substance simulating the pollutants. Models of a highway in open countryside and a street canyon together with the line permeation source of methanol vapour were used in measurements of cross-section profiles.

Qualitative estimates of the processes occurring within the modelled atmospheric boundary layer (ABL) in a wind tunnel can be made using various methods permitting the visualization of flow and dispersion of pollutant substances. The quantitative estimate of a flow field is often made using the Laser-Doppler anemometric method[11]. It is also important to estimate concentration levels in space and time in a quantitative way. This kind of concentration measurement is carried out by fast flame-ionization detectors, characterized by high sensitivity[12]. The high sensitivity of the analytical methods employed in simulation in a wind tunnel is important from the standpoint of the extent of spatial coverage of the monitored area. In addition to sensitivity, for obtaining quantitative concentration profiles an analytical method with a broad dynamic range must be available. This range should be on a linear scale. In this work we used the absorption spectroscopic method of laser photoacoustic detection as an analytical tool for monitoring in a wind tunnel.

Absorption spectroscopic methods[13] are based on the absorption of radiation passing through a sampling cell. In case of the use of infrared radiation sources, it is possible to monitor absorption in the vibration and rotation-vibration modes of selected molecules. Almost all molecular pollutants can be monitored in the infrared region. The application of this method in the atmosphere is complicated by difficulties caused by the absorption by atmospheric water and CO_2 covering an extensive spectral region and coinciding with potentially useful radiation sources. However, there are "atmospheric windows" where the absorption of these molecules is negligible. One of these windows is the spectral region around 10 μm, which was used in our measurements[14].

In this paper, we present qualitative comparison of results of DIAL measurement campaigns performed in the Czech Republic and model studies in the simulated ABL with neutral thermal stratification in the wind tunnel. We have chosen a highway out of the city and an urban agglomerate street canyon with extensive traffic as the objects of our studies. Under miscellaneous meteorological conditions, we performed a set of NO_2 spatial measurements in (and above) street canyons in Prague and Klatovy (Czech Republic) and above a highway out of the city of Pilsen (Czech Republic).

Some of the investigated cases were also particularly studied by mathematical modelling with the application of finite-volume method. For the mathematical models used, the physical conditions (i.e. the definition of emission source and meteorological conditions) were kept to be corresponding with the ones during experiments performed in simulated or real ABL.

The comparison of the LIDAR monitoring results and the results obtained by mathematical and physical modelling proves relatively good qualitative agreement. However, differences remain, and we have tried to interpret some disagreements by reactions taking place in the real ABL but neglected in the case of the model experiments.

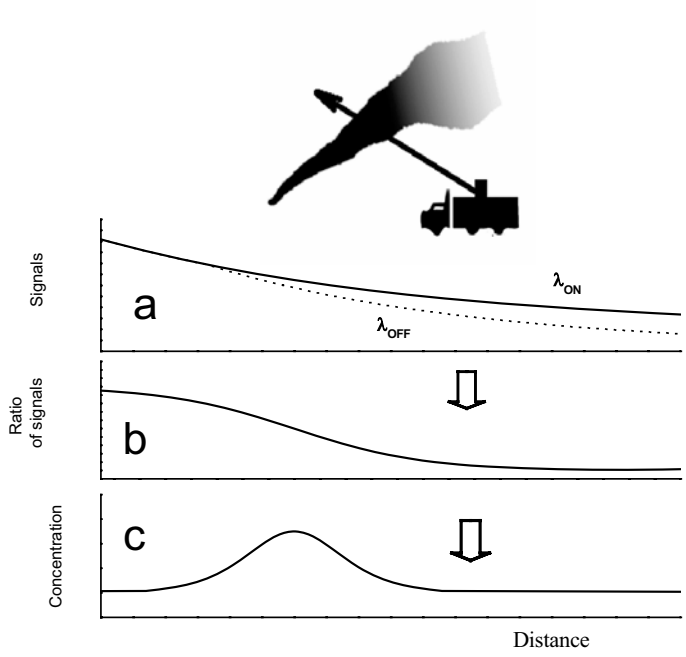

Figure 1. Principle of DIAL measurements: a) detection of the backscattered radiation at two wavelengths λ_{on} (resonance wavelength) and λ_{off} (reference wavelength), b) ratio of both signals, and c) calculated concentration profile using Eq. (1).

2. Experimental

DIAL is a laser remote sensing technique[15] that belongs to the group of LIDAR techniques[16] (Fig. 1). The DIAL system is composed of a transmitting and a receiving section. The laser transmitter emits laser pulses of two wavelengths λ_{on} and λ_{off} corresponding to large and small absorption by the pollutant of interest. In passing through the atmosphere, the emitted laser light of both wavelengths is elastically backscattered due to molecular (Rayleigh) and particulate (Mie) scattering. The backscattered light is detected by the receiving section: it is collected by a telescope, spectrally resolved by a monochromator, amplified by a photomultiplier, and recorded by a fast transient recorder. A time resolution of the backscattered signal enables assigning the power of the backscattered signal to a distance r from the DIAL system. The pollutant concentration profile $n(r)$ on the laser beam can be computed using the equation

$$n(r) = \frac{1}{2\Delta\sigma}\left(\frac{\partial}{\partial r}\ln\frac{P(r,\lambda_{off})}{P(r,\lambda_{on})}\right) \tag{1}$$

where $\Delta\sigma$ is the differential absorption cross-section of the measured pollutant and $P(r, \lambda_{on})$ and $P(r, \lambda_{off})$ are powers of the backscattered signals from the distance r at the wavelengths λ_{on} and λ_{off}. The maximum spatial resolution of the concentration profile is determined by the laser pulse duration.

Within performed measurement campaigns presented here, we employed the LIDAR 510M system[17] manufactured by Elight Laser Systems GmbH. The LIDAR 510M uses a tuneable pulse Titan-Sapphire laser pumped by xenon flash lamps with the repetition rate of 20 Hz. The tuning range is 700–900 nm. The pulse duration with a Q-switch is less than 40 ns. A specially designed 'double oscillator' permits alternating between two wavelengths λ_{on} and λ_{off}, with a bandwidth of less than 0.3 nm each. Non-linear crystals are employed in order to generate the second and the third harmonic frequency. The laser pulse energy, after the third harmonic generation, is more than 0.5 mJ. In the case of NO_2 concentration measurements, λ_{on} is 398.3 nm and λ_{off} is 397.0 nm. With O_3 concentration measurements, λ_{on} is 282.4 nm and λ_{off} is 286.3 nm (Figure 2). A rotating periscope enables measurement in any direction and the creation of horizontal or vertical maps of pollutant concentration.

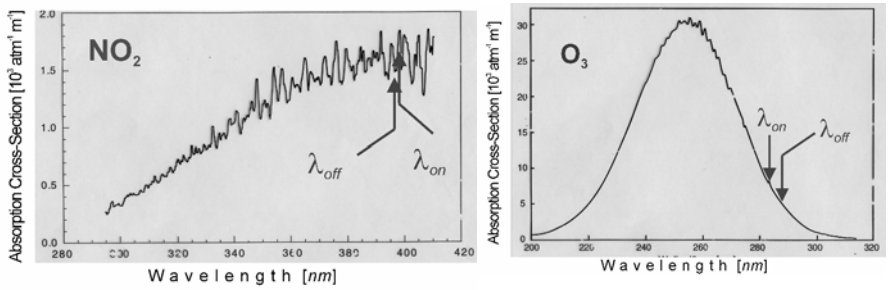

Figure 2. Wavelengths for NO_2 and O_3; a specially designed 'double oscillator' permits alternating between two wavelengths λ_{on} and λ_{off}, with a bandwidth of less than 0.3 nm each.

The DIAL system is integrated in a van and equipped with a trailer diesel-powered generator, which makes it fully mobile. Moreover, the van is also equipped with a Doppler SODAR PA2 system (sound detection and ranging), manufactured by Remtech (USA). This device enables the continuous measurement of wind speed and direction at heights ranging from 15 to 1000 m. Its measurement is accomplished by emitting a strong acoustic pulse in different directions and detecting the Doppler frequency shift of the received backscattered echo.

In these studies, beside classical flame ionization detectors the spectroscopic method of laser photoacoustic detection as an analytical tool for monitoring in a wind tunnel was used (Figure 3). Absorption spectroscopic methods are based on measuring the intensity difference between the entering and the leaving radiation. During the process of monitoring small concentrations of absorbing molecules, small differences are detected between the entering and leaving intensities of the radiation used. In this case and if an intensive radiation source (CO_2 laser) is used the photoacoustic detection is far more sensitive than the classical transmission method.

The CO_2 laser has a number of advantages that can be utilized for analytical applications: simplicity, high power and minimum interference with the absorption lines of atmospheric H_2O and CO_2. The combination of a CO_2 laser and photoacoustic detection provides high sensitivity and a linear dynamic range in the broad range of up to 6 orders of magnitude. This work utilizes the broad dynamic range together with the high sensitivity of the photoacoustic method. In our laboratory, we have carried out a number of spectroscopic and analytical studies using laser photoacoustic detection[18-23].

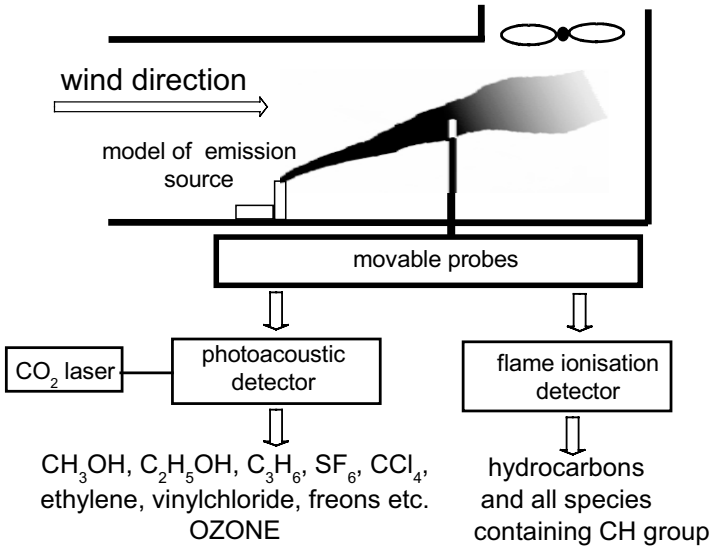

Figure 3. Experimental set-up for concentration measurements of methanol (simple model of air pollution) in an aerodynamic tunnel using photoacoustic spectrometry and flame ionization detector.

Details of the experimental system used in this investigation were described in a previous work[18-23]. In a wind tunnel with the cross section of 1.5 x 1.5 m is created a model of a highway in an open countryside or a symmetric idealized street canyon with the aspect ratio (ratio of street width and height) equalling 1, oriented perpendicularly to the wind direction. A 30 kW ventilator with a speed regulator can be used to simulate the boundary layer of the atmosphere[24] with an external velocity in the interval from 1 $m \cdot s^{-1}$ to 12 $m \cdot s^{-1}$. A line pollution source is located in the centre of the model street canyon, and is based on the principle of a permeation tube. This source could be filled under pressure in a reproducible way. It was weighed over a prolonged period of time to determine its concentration flux.

A spatially adjustable sampling probe was introduced into the wind tunnel (a moveable polyethylene tube connected through the photoacoustic cell with a pump), and was used for continuous sampling at defined places along the studied street canyon. To the first approximation, we limited the study to the monitoring of transverse central cross-section of the modelled street canyon to obtain a concept of the transverse concentration profile.

Samples were taken by the probe at a rate in the range of 3-4 $cm^3 \cdot s^{-1}$ – these are volumes that are negligible from the standpoint of the dynamics of the given wind tunnel. The photoacoustic cell used was a thermally stabilized (30 ± 1 °C) brass tube with a length of 38 cm and a diameter of 8 mm fitted with an electret microphone and IR windows. The infrared radiation of the discretely tuneable CO_2 laser (Edinburgh Instruments WL-8-GT) passed through the photoacoustic cell on a pyroelectric detector. The absorption of radiation caused by the presence of methanol in the atmosphere samples led to pressure changes in the cell, which were detected by a microphone and then electronically processed. Prior to the entrance into the cell, a concentration permeation standard could be inserted (for calibration of photoacoustic signals) in the entire sampling system, which was also weighed over a prolonged period of time and for which the exact flux value was known.

3. Results and discussion

During the DIAL monitoring campaign, a set of spatial measurements of NO_2 and O_3 concentration levels was performed in and above an urban agglomerate street canyon with extensive traffic. A distribution of NO_2 was investigated across a highway located at an open suburban area, as well. Physical modelling experiments were carried out on models placed in the wind tunnel described above. Measurements in real atmosphere and laboratory experiments were aimed at gaining some information about pollutants dispersion caused by line (vehicle) emission sources. Qualitative comparisons of the results of simulation approaches and real measurements were performed in all mentioned cases. Magnitudes of measured concentration cannot be directly compared (quantitative evaluation has to take into account model scale and source strength).

When wind direction is oriented perpendicularly to the axis of the highway, the line emission source in the open countryside produces a plume on the leeward side of the source (Figure 4). We clearly found such a plume in the case of the simulation experiment (Figure 4a). However, the plume detected by remote-sensing in the real atmosphere was accompanied by another one, containing NO_2 at lower concentration levels (Figure 4b). After the detailed evaluation of geographical conditions of the measurement site it was found that the perturbation was caused by the cross-roads situated near-by the area measured. Skipping this perturbation, the results of simulation and remote-sensing experiment are in a good agreement.

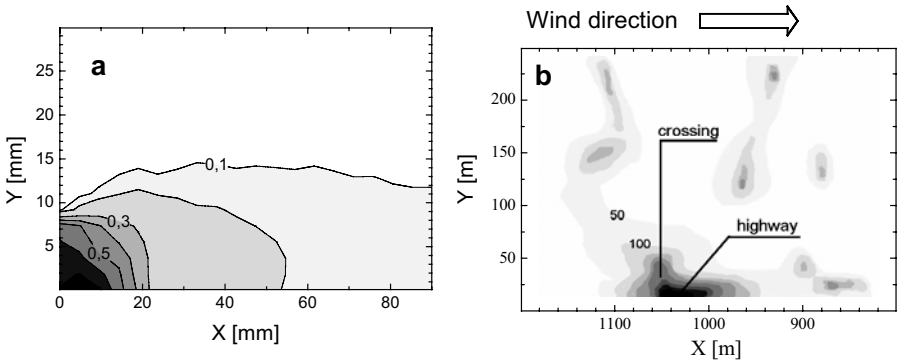

Figure 4 a). Spatial distribution of CH_3OH [$\mu g \cdot m^{-3}$] for the model of a highway in the open countryside; reference wind speed 1.5 m·s-1. b) Vertical distribution of NO_2 [$\mu g \cdot m^{-3}$] in the scan taken perpendicularly to the axis of a street in an open suburban area; wind speed 2.0 $m \cdot s^{-1}$, ground temperature approx. 18°C.

A study of pollutant dispersion caused by cars slowly moving in the urban agglomerate street canyon proved clearly high pollutant accumulation on the leeward side (Figure 5). It is caused by the formation of eddies inside the street canyon. The pollutant plume with concentration levels increasing from the windward to the leeward side was observed under the condition of perpendicular wind direction above the street canyon walls. The volume on the windward side is of much lower pollution load that means the windward side is ventilated with high efficiency. In this case, the comparison also confirmed qualitative accordance between model and DIAL measurements (Figure 5).

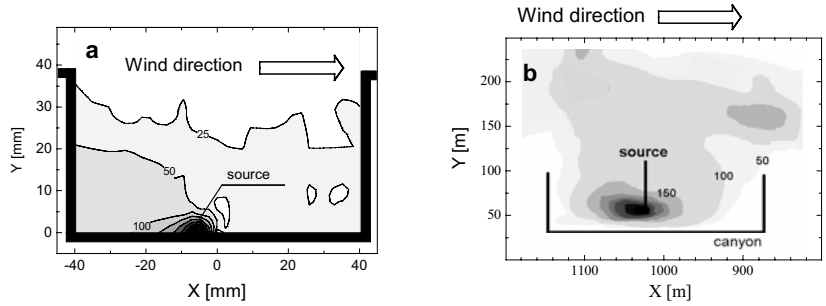

Figure 5 a). Spatial distribution of CH_3OH [$\mu g \cdot m^{-3}$] for the model of a street canyon; reference wind speed 1.5 $m \cdot s^{-1}$. b) Vertical distribution of NO_2 [$\mu g \cdot m^{-3}$] in the scan taken perpendicularly to the axis of a street in a street canyon; wind speed 2.0 $m \cdot s^{-1}$, ground temperature approx. 19°C.

During rush hours, an urban agglomerate street canyon with extensive traffic of vehicles slowly moving in a line represents a relatively well-defined line pollution source. As an example of such a street canyon, Legerova Street in Prague was chosen, and both mathematical simulation and physical modelling were performed. Monitoring in the real ABL by DIAL has been added to these simulation studies. Individual 2D vertical scans through the atmosphere were performed in such manner that they followed the diagonal of the street canyon ground plan. Time development of NO_2 concentration levels (Figure 6) was then constructed by the mathematical projection of individual 2D scans into 1D vertical profile[17].

The DIAL/SODAR system was located approximately 650 m from the traffic entry into the street canyon. This distance is ideal as regards a geometric compression of the measuring system, influencing correct evaluation of measured data as one of major factors. The monitored street canyon area was 700 m long. Monitoring was carried out during working days in summer and autumn periods. During the monitoring carried out in November (Figure 6a), the weather was cloudy, with ground temperatures around 4°C in the morning. The cloudiness was growing up during the day, up to overcast afternoon, with the ground temperature around 7°C and rain. By contrast, shine weather was in July days (Figure 6b), with temperatures between 20°C in the morning and 30°C at noon time. During the November measuring day, the west wind was blowing above the street canyon walls at speed between 2 $m \cdot s^{-1}$ and 6 $m \cdot s^{-1}$, and the speed reached up to 9 $m \cdot s^{-1}$ at the height of 200 m from the canyon bottom. In the lowest part of the canyon, along its walls, however, only weak southern blowing was monitored, in direction of the street axis (1 $m \cdot s^{-1}$ up to 2 $m \cdot s^{-1}$). In the days of July, the wind was of the east or south-east direction above the walls. Its speed was around 4 $m \cdot s^{-1}$. The down-to-earth flow inside the street canyon was identical with that from November.

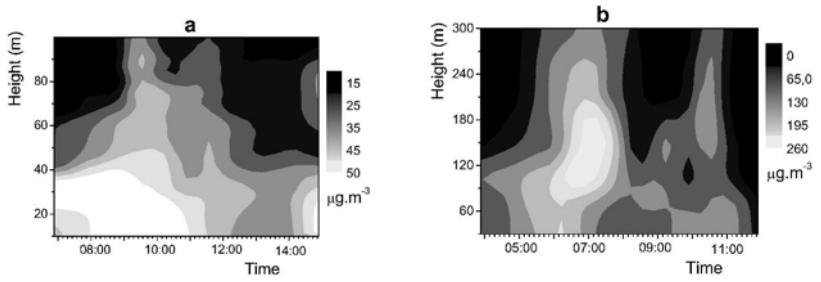

Figure 6. Time development of vertical NO_2 distribution in the atmosphere above Legerova Street, a) November 29, b) July 10.

DIAL measurements of NO_2 vertical profiles were accompanied by acquisition of NO, NO_2 and O_3 concentration levels monitored by conventional spot analyzer[25] near the bottom of the street canyon simultaneously. The results of DIAL measurements suggest that with an increasing distance from the canyon bottom, NO_2 concentration does not fall (Figure 6) so dramatically as a physical model in such cases would predict (Figure 5a). Most models apply only physical approach in order to solve the problem of pollutants propagation and disregard possible chemical reactions that necessarily occur in real systems. The differences between measured and simulated results (the simulations were performed under the same wind direction above the canyon) can be caused precisely by this neglect. The predicted effect of pollutant accumulation on the leeward side of the street canyon bottom was confirmed by measurements in a real system (Figure 7 a, b) for November period (which corresponds better with neutrally stratified ABL modelled in the wind tunnel).

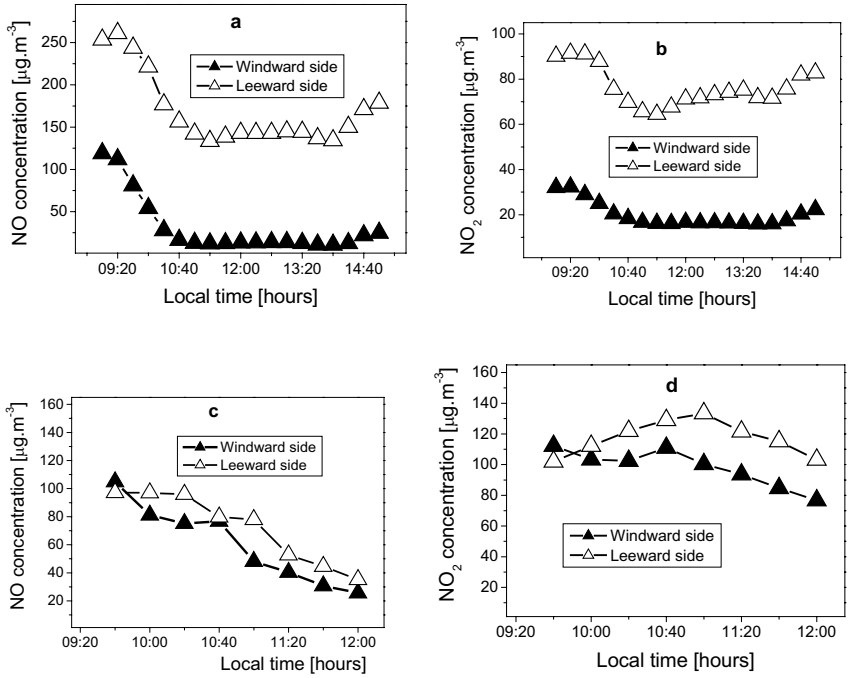

Figure 7. Distribution of nitrogen monoxide (a) and nitrogen dioxide (b) on the windward and leeward side at the bottom of a real urban agglomerate street canyon (Prague, Legerova Street, November 29), resp.distribution of nitrogen monoxide (c) and nitrogen dioxide (d) on the windward and leeward side at the bottom of a real urban agglomerate street canyon (Prague, Legerova Street, July 10).

Comparison of autumn campaign results with low sun radiation and summer measurements confirms this conclusion. However, for July period we have obtained results that do not agree with physical modelling (Figure 7 c, d). The flow field inside the street canyon can be also influenced by the intensity of solar irradiation and a change of flow field involves final pollutant distribution. Difference between windward and leeward side is not so clear for summer case. Disagreement with physical modelling is clearly visible from time development of NO_2 concentration levels (Figure 6b) constructed by the mathematical projection of individual 2D scans into 1D vertical profile. Decreasing tendency of NO_2 concentration with distance from bottom of street canyon is fully perturbed probably by photochemical reactions influence. Therefore DIAL measurements can motivate new modelling with basic simulations of chemical processes (chemistry of NO/NO_2/ozone) in order to approximate more precisely the reality.

To improve the description of the system investigated, the Computational Fluid Dynamics (CFD) environment was tested for a basic implementation of photochemical reactions into the commonly used mathematical models of turbulence and dispersion processes.

When investigating the dispersion of atmospheric pollutants emitted into the ABL by ground emission sources placed especially in urban or industrial areas, a dynamic turbulent model, based on the solution of three-dimensional, time-dependent conservation equations, is usually preferred over the one representing an application of the statistical theory of turbulent diffusion – the commonly used Gaussian plume model. Among others, the micro- and small scale dynamical modelling employs so called Reynolds Average Method based on time averaged quantities of turbulent flow and on Reynolds averaging the Navier Stokes equations. These models have also been developed and are integrated in the customary FLUENT[26] Computational Fluid Dynamics environment.

For the geometry of the street canyon physical model discussed above, at keeping the following boundary conditions, i.e.

(a) a well-premixed mixture consisting of 21% O_2 and 79% N_2 with the constant velocity of 0.15 $m \cdot s^{-1}$ at the inlet of the area investigated;

(b) a line source of pollutants defined as a mixture of 0.5% NO_2 and 99.5% N_2 with the outlet velocity of 10^{-7} $m \cdot s^{-1}$;

the problem of the dispersion of pollutant generated by the line source located in the axis of the street canyon was solved using the stationary k-ε dynamic model of turbulent flow. The objective was not only an investigation of passive contamination, but also the verification of a possibility of implementing the solar energy into the simulation of chemical reactions using the CFD FLUENT. In context of photochemical reactions considered in the studied street canyon system, a case of ozone generation as the consequence of NO_2 photochemical decay caused by absorption of radiation ($\lambda < 420$ nm) was solved as the first task. FLUENT predicts the

local mass fraction of each species through the solution of a convection-diffusion equation in which the source term enables to account for the net rate of production of species by chemical reaction. The reaction rates can be computed in FLUENT by one of three models:

- Laminar finite-rate model, in which the effects of turbulent fluctuations are ignored, and reaction rates are determined by Arrhenius expressions;
- Eddy-dissipation model, based on the assumption that reaction rates are controlled by the turbulence, so Arrhenius chemical kinetic calculations can be avoided;
- Eddy-dissipation-concept (EDC) model which enables to incorporate detailed Arrhenius chemical kinetics in turbulent flames.

In addition, FLUENT provides the finite-rate/eddy-dissipation model, where both the Arrhenius and eddy-dissipation reaction rates are calculated. The net reaction rate is taken as the minimum of these two rates.

Using the combined finite-rate/eddy-dissipation model, the influence of various values of pre-exponential factor A_k on concentration of NO and O_3 was tested. The initial value of $A_k = 4.52 \cdot 10^{16}$ was calculated based on literature data,[27] lower values were used to test the influence of A_k on the choice of the model. The finite-rate model was used for chosen values A_k of 4.52 and 452, the eddy-dissipation model influenced by turbulent quantities and neglecting the pre-exponential factor A_k was applied for values greater then 452. The fitted contours of distribution of generated O_3 are shown in the Figure 8.

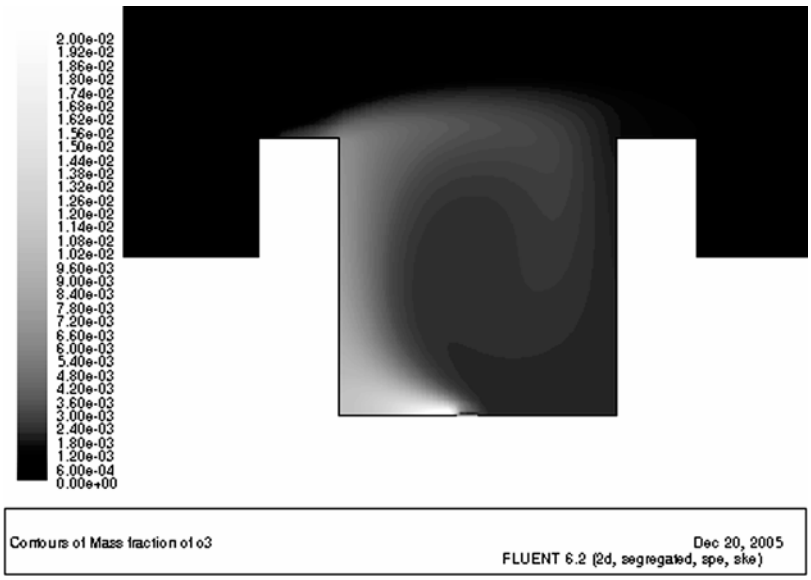

Figure 8. Contours of ozone distribution for A_k equal to 4.52.

The first results of simulations considering the ozone formation caused by photolysis of NO_2 in the dynamic street canyon environment clearly demonstrated that the solar energy (and consequently photochemical reactions) can be solved in the frame of dynamical dispersion modelling using the CFD FLUENT. The calculation must be organized step by step, which means the flow field neglecting chemical reactions has to be solved at first, consequently the calculation for chemical reaction has to be prepared and an appropriate model taking into account the chemical rate has to be chosen. Finally, the last calculation step is represented by the flow field solution including chemical reaction. With aspect to the different character of chemical reactions in the atmosphere (CFD FLUENT modules of chemical reactions have been primarily prepared for combustion modelling), it is essential to make a better specification of input constants using results of corresponding laboratory experiments. Even though the result obtained like that is not yet in accordance with observation in the real street canyon during the summer period, the ability of dynamic mathematical models to describe very complex phenomena like (photo)chemical reactions has been demonstrated well. We considered only NO_2 photolysis and consequent ozone formation as an example of possible chemical reactions which should be taken into account within mathematical modelling of micro-scale atmospheric processes, although atmospheric chemistry involves a complicated chain of interrelated chemical reactions. Therefore, the next testing will be focused on the use of EDC model, the investigation of other turbulent models more suitable for the description of atmospheric processes, and a possibility of solving the chemical reactions directed by radicals.

It is obvious that a real street canyon represents a system where physical and chemical processes of substantial dynamics take place. To solve a problem of such complexity, both approaches – mathematical or physical modelling together with measurements in the real atmosphere - have to be applied simultaneously and remain unavoidable.

Acknowledgments

This work was supported by the Ministry of Education, Youth and Sports of the Czech Republic (project no. OC723.001 in the frame of the COST 723 action and project no. 1P05ME766).

References

1. *Encyclopedia of Environmental Analysis and Remediation,* edited by R.A. Meyers (John Wiley, New York, 1998).
2. R. Berkowitz in *Urban Air Polluttion-Europian Aspects*, esited by J. Fenger, O. Hertel, F. Palmgren (Kluwer, London, 1998) p. 223
3. S. Svanberg, Differential absorption lidar (DIAL). *Air Monitoring by Spectroscopic Techniques*, edited by M.W. Sigrist (John Wiley, New York, 1994) pp. 85–161.
4. H.D. Kambezidis, D. Weidauer, D. Melas, M. Ulbricht, Air quality in the Athens basin during sea breeze and non-sea breeze days using laser-remote-sensing technique. *Atmospheric Environment,* 32(12), 2173–2182 (1998).
5. J. Zwozdziak, A. Zwozdziak I. Sowka, K. Ernst, T. Stacewicz, A. Szymanski, S. Chudzynski, A. Czyzewski,, W.Skubiszak, K. Stelmaszczyk, Some results on the ozone vertical distribution in atmospheric boundary layer from LIDAR and surface measurements over the Kamienczyk Valley, Poland. *Atmospheric Research,* 58, 55–70, (2001).
6. T. Fukuchi, T. Fujii, N. Cao, K. Nemoto, N. Takeuchi, Tropospheric O_3 measurement by simultaneous differential absorption lidar and null profiling and comparison with sonde measurement. O*ptical Engineering* 40(9), 1944–1949 (2001).
7. A. Thomasson, S. Geffroy, E. Frejafon, D. Weidauer, R. Fabian, Y. Godet, M. Nominé, T. Menard, P. Rairoux, D. Moeller, J.P. Wolf, Lidar mapping of ozone-episode dynamics in Paris and intercomparison with spot analyzers. *Applied Physics*, B74, 453–459 (2002).
8. M. Beniston, J.P. Wolf, M. Beniston-Rebetez, H.J. Kölsch, P. Rairoux, L. Wöste, Use of lidar measurements and numerical models in air pollution research. *Journal of Geophysical Research* 95(D7), 9879–9894 (1990).
9. Z. Zelinger, S. Civiš, Z. Jaňour, Laser photoacoustic spectrometry and its application for simulation of air pollution in a wind tunel. *Analyst*. 124, 1205–1208 (1999).
10. Z. Zelinger, M. Střižík, P. Kubát, Z. Jaňour, P. Berger, A. Černý, P. Engst, Laser remote sensing and photoacoustic spectrometry applied in air pollution investigation. *Opt. Lasers Eng.* 42 (4), 403–412 (2004).
11. R. J. Adrian, Particle-Imaging techniques for fluid mechanics. *Annu. Rev. Fluid Mech.*, 23, pp. 261, 1991.
12. M. Pavageau, *Concentration Fluctuations in Urban Street Canyons* (Meteorologisches Institut der Hamburg Universität, Hamburg, 1996).
13. M.W. Sigrist, Air Monitoring, Optical Spectroscopic Methods, in *Encyclopedia of Environmental Analysis and Remediation*, edited by R. A. Meyers (John Wiley, New York 1998) p. 84.
14. M.W. Sigrist, Air Monitoring by Laser Photoacoustic Spectroscopy, in *Air Monitoring by Spestroscopic Techniques*, edited by M. W. Sigrist (John Wiley, New York 1994).
15. R.M. Measures, *Laser Remote Sensing, Fundamentals and Applications* (Krieger Publishing, Florida, 1992).
16. U. Panne, Laser remote sensing. *Trends in Analytical Chemistry*, 17(8, 9), 491–500 (1998).
17. D. Weidauer, *Analyse und Bewertung von Smog-Situationen mittels LIDAR*, Dissertation (Freie Universität, Berlin, 1998).
18. Z. Zelinger, M. Střižík, P. Kubát, S. Civiš, Quantitative analysis of trace mixtures of toluene and xylenes by CO2 laser photoacoustic spektrometry. *Anal. Chim. Acta* 422, 179–185(2000).

19. S. Civiš, Z. Zelinger, M. Střižík, Z. Jaňour, Simulation of air pollution in a wind tunnel, in. *NATO Sci Ser II.: Mathematics, Physics and Chemistry*, Vol. 20. (Kluwer, Dordrecht, 2001) pp 275–299.
20. Z. Zelinger, Z. Papoušková, M. Jakoubková, P. Engst, Determination of trace quantities of freon by laser optoacoustic detection and by classical infrared-spectroscopy. *Coll. Czech. Chem. Commun*. 53(4), 749–755(1988).
21. V. Steiner, P. Engst, Z. Zelinger, M. Horák, Laser optoacoustic detection of trace concentration levels of ethylene, vinylchloride, and styrene in the troposphere *Coll. Czech. Chem. Commun*. 54 (10), 2667–2673, (1989).
22. Z. Zelinger, I. Jančik, P. Engst, Measurement of the NH_3, CCl_2F_2, $CHCIF_2$, $CFCl_3$, AND CCIF3 absorption-coefficients at isotopic $^{13}C^{16}O_2$ laser wavelength by photoacoustic spectroscopy. *Applied Optics* 31, 6974–6975(1992).
23. S. Civiš, M. Střižík, Z. Jaňour, J. Holpuch, Z. Zelinger, Wind tunnel simulation of air pollution dispersion in a street Canon. *J. AOAC International*, 85 (1), 243–248 (2002).
24. Z. Jaňour, A new atmospheric boundary layer wind tunnel at the Institute of Thermomechanics (EUROMECH Col. 338, Bologna, 1995).
25. HORIBA Europe GmbH. Tulnn. *The User Guide* (1992).
26. FLUENT Inc. Lebanon. *Fluent Users Guide, Tutorial Guide* (2002).
27. D. H. Ehhalt, Photo oxidation of trace gases in the troposphere. *Phys. Chem. Chem. Phys.*, 1 (24), 5401 – 5408 (1999).

THE ATMOSPHERIC CHEMISTRY ETHER GROUP: EXPERTISE AND DATABASE

PHILIPPE RICAUD* AND ROBERT DELMAS
Laboratoire d'Aérologie, UMR 5560, 14 Avenue Edouard Belin, 31400, Toulouse, France

FRANCOISE GIROD AND THIERRY PHULPIN
Centre National d'Etudes Spatiales, 18 Avenue Edouard Belin, 31401 Toulouse cedex 4, France

CATHY BOONNE
Institut Pierre-Simon Laplace, Université Paris VI, 4, place Jussieu, 75252 Paris, France

Abstract. The Ether system has been developed in France in order to support scientific studies based on atmospheric chemistry. Ether is the focal point for French and foreign scientists for studying processes from the local to the global scales via the mesoscale, from the troposphere to the stratosphere, within a wide temporal range (from the minute to the decade). A huge variety of products is stored from ground-based, balloon-, air-, and space-borne measurements, to modelled and assimilated constituent fields, together with spectroscopic and kinetic rates data sets. In addition, the development of added-value services such as interactive graphic tools, extraction software, scientific ground-segments as for the Odin/SMR experiment and ancillary data production like potential vorticity fields, helps the efficient use of these heterogeneous products. Finally, information relative to the ongoing activities within the scientific community is presented on the Web site (http://ether.ipsl.jussieu.fr/).

Keywords: Atmospheric chemistry; Database; Modelling; Assimilation; Data expertise; Added-value services

*To whom correspondence should be addressed: Philippe Ricaud, Laboratoire d'Aérologie, UMR 5560, 14 Avenue Edouard Belin, 31400, Toulouse, France; E-mail: philippe.ricaud@aero.obs-mip.fr

A. Perrin et al. (eds.), Remote Sensing of the Atmosphere for Environmental Security, 317–327.

1. Introduction

The aim of the Ether French atmospheric chemistry group is to be the focal point for French and foreign scientists in the studying of atmospheric chemistry processes from the local to the global scales via the mesoscale, and from the troposphere to the stratosphere, within a wide temporal range, from the minute to the decade. The Ether group: 1) assists the scientific community to locate, access and interpret atmospheric chemistry data, 2) provides data processing software and tools, 3) provides information on the data collection, and 4) promote the creation of different expertise networks on varying atmospheric chemistry topics. Ether is organized upon a Centre of Production and Services, i.e. a database containing a wide variety of data (ground-based, balloon-borne, airborne, satellite-borne measurements, together with modelled and assimilated data fields) and added-value services such as interactive graphic tools, and upon some Expertise Networks, mainly devoted to the development of scientific ground-segment applied to the analysis of satellite data (e.g. the Odin satellite and the "Infrared Atmospheric Sounding Interferometer" (IASI) instrument aboard the MetOp satellite).

The Centre of Production and Services is presented in section 2, while its organization and expertises are explained in section 3. Finally, the Ether future projects are listed in section 4.

2. The centre of production and services

2.1. THE CENTRE OF PRODUCTION

The Ether database (http://ether.ipsl.jussieu.fr, see Figure 1) is first of all a Centre of Production and Services i.e. it stores a huge quantity of products, basically ground-based, balloon-borne, aircraft and satellite measurements (see Table 1), modeled and assimilated data in the stratosphere (S), and troposphere (T).

Some data sets are provided through specific campaigns (e.g. the "Etude et Simulation de la QUalité de l'air en Ile de France" (ESQUIF) programme in 2000 and the "African Monsoon Multidisciplinary Analysis" (AMMA) programme in Western Africa in 2006, the VORCORE Antarctic campaign in 2005), or belong to long-term international programmes (e.g. the "Network for the Detection of Stratospheric Change" (NDSC), the "Measurement of OZone and water vapour by AIrbus in-service aircraft" (MOZAIC) commercial aircraft programme). Furthermore, the Ether Centre can produce various data coming from models e.g. the Reprobus stratospheric chemical-transport model, the "Modélisation Isentrope du

transport Méso-échelle de l'Ozone Stratosphérique par Advection" (MIMOSA) stratospheric advection model, or from space-borne instruments, e.g. the "Sub-Millimeter Radiometer" (SMR) aboard the Odin satellite.

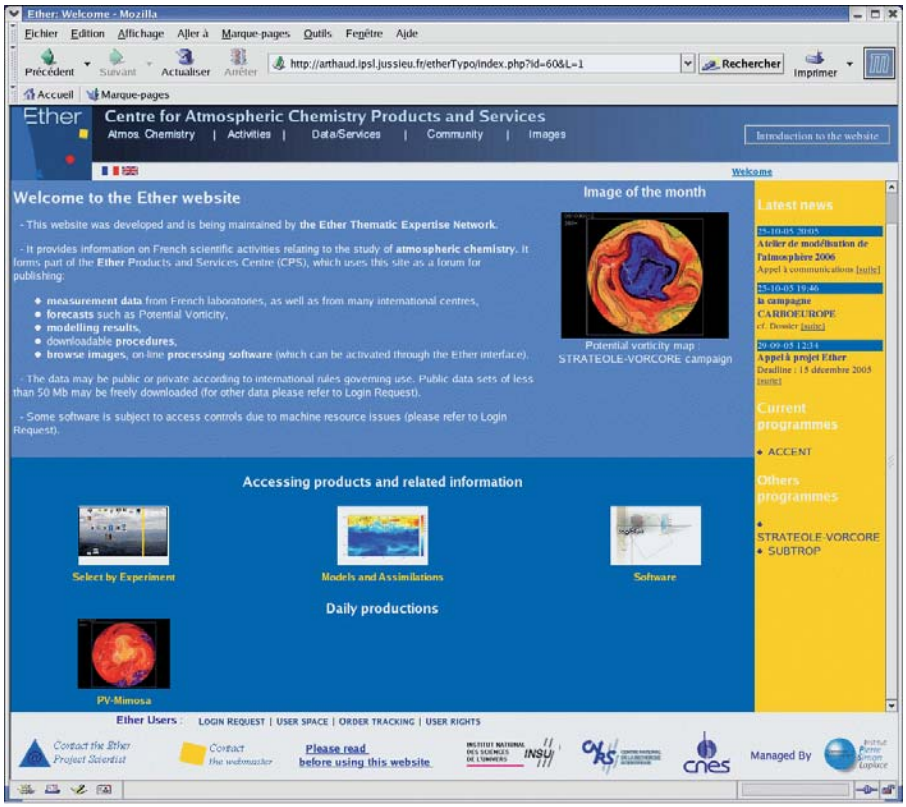

Figure 1. Front page of the Ether Web site.

These data are routinely produced but can also be created during specific campaigns like the VORCORE Antarctic campaigns in 2005. Indeed, daily analysis and forecasts production of potential vorticity and temperature fields are calculated by the MIMOSA model (Hauchecorne et al., 2002) for the Northern and the Southern hemispheres, and also in the tropics (see Figure 2). A daily production of 50 atmospheric constituent fields (O_3, ClO, NO_2, N_2O, BrO, etc.) is produced by using the Reprobus model (Lefèvre et al., 1994).

The level 2 products (basically O_3, ClO and N_2O vertical profiles) from the Odin/SMR instrument are continuously processed within Ether (see Figure 3) using the "Microwave Odin LIne Estimation and Retrieval" (MOLIERE) radiative transfer and retrieval code (Ricaud et al., 2005). Very recently, the output from assimilation experiments using the "MOdèle de Chimie Atmosphérique de Grande Echelle" (MOCAGE) chemical-transport model in terms of O_3 and N_2O have also been stored and archived in Ether.

Table 1. Data stored in the Ether database (stratosphere : S and troposphere : T).

Name of the experiment	Type of data (measurement, model, assimilation, …)	Atmospheric Layer
UARS	Space-borne measurement	S
Odin	Space-borne measurement	S
POAM II, III	Space-borne measurement	S
ILAS I	Space-borne measurement	T
IMG	Space-borne measurement	T
MOPITT	Space-borne measurement	T
GOMOS	Space-borne measurement	T
MOZAIC aircrafts	Measurement, programme	T, S
HIBISCUS balloons	Measurement, campaign	T, S
SCOUT-O3	Measurement, campaign	T, S
IASI Balloon	Measurement, campaign	T
REPROBUS	Chemical-transport model	S
MOCAGE	Chemical-transport model	T, S
MOCAGE-PALM	Assimilation	T, S
MSDOL	Assimilation	S
CHIMERE	Model	T
MIMOSA	Advection model	S
French NDSC stations	Ground-based measurements	S
French NDSC balloons	Measurements	S
ESQUIF	Campaign	T
PAES	Campaign	T
POVA	Campaign	T
AMMA	Measurement, model, campaign	T, S
Balloons	Measurement, campaign	S

In addition to the actual data stored in the Centre of Production and Services, Ether also redirects to existing databases specialized in different aspects of the atmospheric chemistry fields, namely chemical databases, spectroscopic databases, and international databases containing various network and/or satellite data (BADC, DAAC, NILU, WMO, etc.). References of data archived on other databases can be found in Ether.

For some particular topics, Ether can store and archive information that are not present in various well known international databases, e.g. chemical reaction kinetics, spectroscopic parameters**,** solar spectrum.

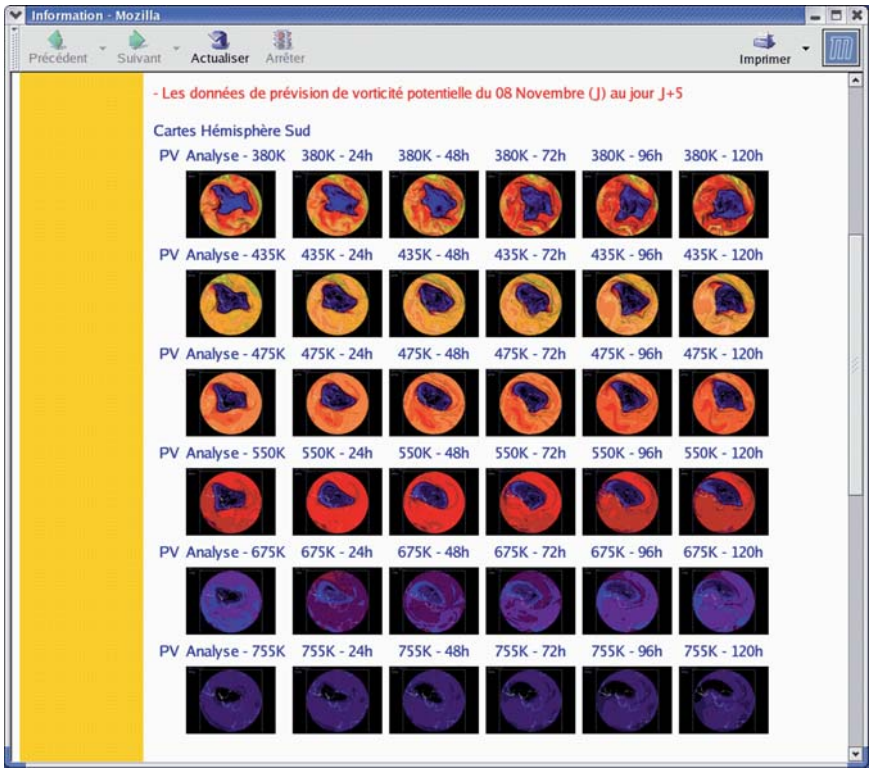

Figure 2. Forecasts (24-120h) of potential vorticity fields calculated by the advection model MIMOSA during the VORCORE programme at different isentropic levels: 380-755 K.

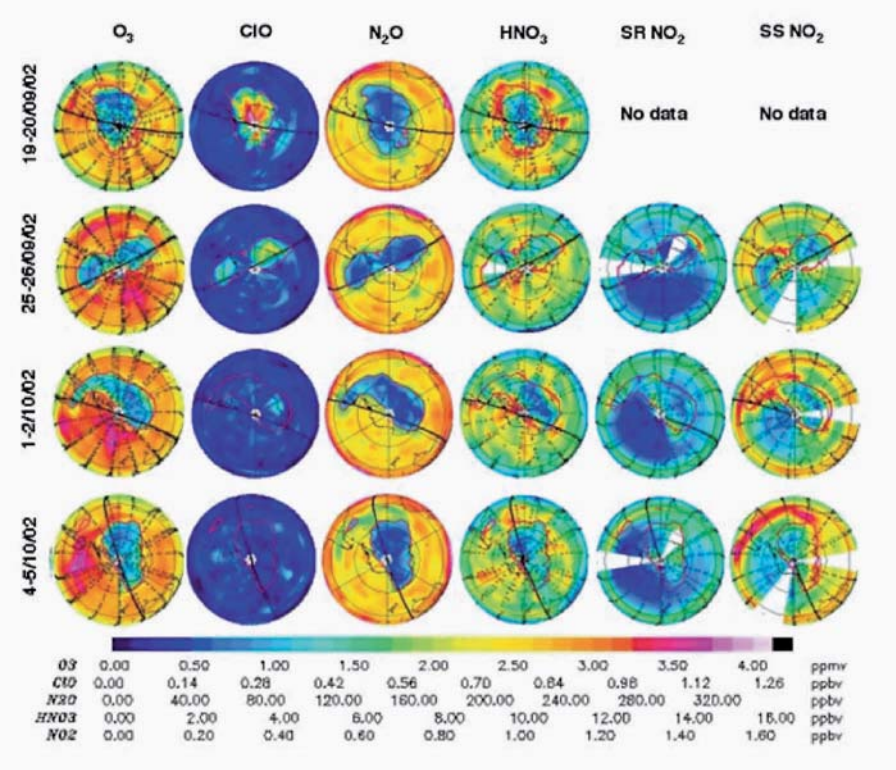

Figure 3. Odin/SMR measurements obtained within the Ether database during the split of the Antarctic vortex in 2002.

2.2. THE CENTRE OF SERVICES

Ether also provides a large variety of services in order to optimally use the stored data. Indeed, scientists can run specific software based upon scientific algorithms:

- Arletty software, developed by the Service d'Aéronomie (Hauchecorne, 1999) and the ACRi-ST company, through an interactive interface, can simulate temperature and pressure for any point around the Earth, from the surface to 100 km,
- Data visualization software for 206 datasets corresponding to 20 different experiments (see Figure 4),
- Line of sight simulation adapted for the "Global Ozone Monitoring by Occultation of Stars" (GOMOS) instrument geometry.

Scientists can run conversion routines in terms of units, temporal and geographical references. Ether products potential vorticity (PV) fields using the MIMOSA advection model developed at Service d'Aéronomie. For instance, for the VORCORE campaign, Ether provided near Real-Time Forecasts of PV fields.

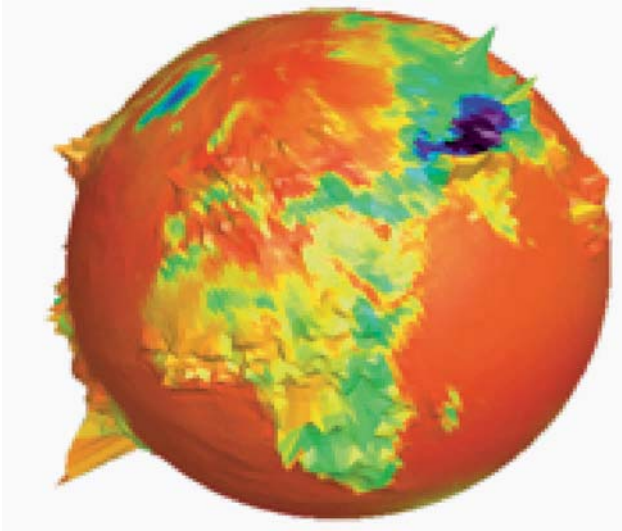

Figure 4. Example of graphic tools representing a three-dimensional field of CO onto a pressure surface from the chemical transport model MOCAGE.

Ether also uses data and/or software developed by the well-referenced Expertise Networks upon some specific topics. We can mention the Odin satellite project (development of the scientific ground-segment MOLIERE at Laboratoire d'Aérologie in Toulouse for producing level 2 data), the MIMOSA advection model (developed at Service d'Aéonomie for calculating potential vorticity fields around the Earth) and recently, the Reprobus chemical-transport model (developed at Service d'Aéronomie for the studying of 50 stratospheric chemical compounds).

3. The Ether rules and organization

3.1. THE RULES

Data is archived and referred in Ether according to the requests of scientists. A standard process is used to reference the data. Access rules are controlled by the Ether administrator.

Scientists owing data according to the Ether objectives have the opportunity of providing level 1 (calibrated data), level 2 (geophysical quantities), 3 (averaged data or data interpolated on a fixed horizontal and temporal grid) and 4 (added-value data like assimilated data) products to the Ether database. Scientists should provide information about the data and specify their access rules. They can deliver different versions of data. The Ether Users' Committee decides whether these data are integrated in Ether and whether new software needs to be developed. This software must be of interest for all scientists using the Ether database.

The Ether administrator is responsible for the technical quality of the scientific software and the scientist providing the software is responsible for their scientific quality.

Data suppliers can deliver data in any format. The Ether normalization tools have been defined in order to help data management (e.g. file formats, units, names, etc.). Users can order any files contained in Ether either in its original format or in Ether standards.

All scientists can offer their own data and software to be included in the Ether database.

3.2. THE ORGANIZATION

The Ether Atmospheric Chemistry Group (see Figure 5) is funded by the "Centre National d'Etudes Spatiales" (CNES) and the "Institut National des Sciences de l'Univers" (INSU), branch of the "Centre National de la Recherche Scientifique" (CNRS). It is managed by a Steering Committee. The Centre de Production and Services is managed by a technical staff, while the scientific content and projects are managed by a Scientist together with a Users Committee. The group then interacts with data and software providers (European laboratories, French Agencies, international databases) together with users (French and international scientists, international users, end-users).

The Ether strategy for the development of services and for the production of data is as follow. The requests and algorithms are specified by scientists. The development is managed by the technical centre. Scientific validation is performed by some scientists who have the expertise in a particular topic. Production is performed by the technical centre or by another centre with the agreement of the technical centre.

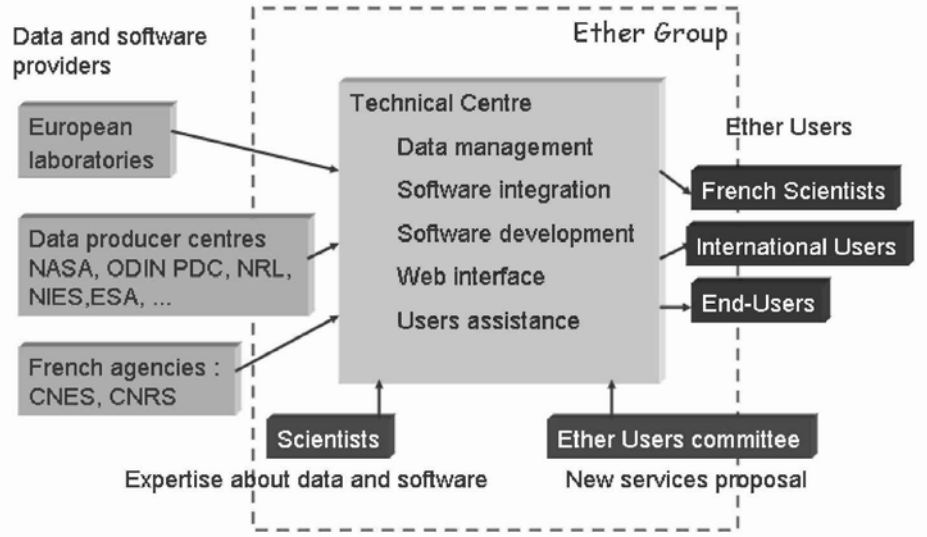

Figure 5. Organization of the Ether atmospheric chemistry group.

4. The future projects

Very recently, the Ether atmospheric chemistry group has been involved in new scientific fields, related to campaigns (e.g. AMMA), long-term programmes (e.g. MOZAIC, IASI) or and tools (e.g. Assimilation within the "Assimilation de Données pour les Modèles de Chimie Atmosphérique" (ADOMOCA) programme and ancillary data within the "Atmospheric Composition Change: a European NeTwork" (ACCENT) programme).

4.1. AMMA

Within the international AMMA programme, Ether is going to produce forecasts of the evolution of plumes coming from biomass burnings during the two periods January-February 2006 and June-August 2006. These forecasts will be based upon the coupling of near real-time satellite images of fire pixels (e.g. from MODIS) and the trajectory model FLEXPART. This will participate to the planning of aircrafts and balloon launches in Africa.

4.2. ANCILLARY DATABASE WITHIN ACCENT

The main goal of this project is to provide to the international scientific community (within e.g. the ACCENT programme) with a series of digital maps and time series of different data for global change studies (e.g.

pollution, biomass burning, fire studies and vegetation maps). The ancillary database will be integrated in the Ether system.

4.3. MOZAIC

Ether will help defining specifications and realization of a new MOZAIC database. Interoperability between MOZAIC and the Ether systems will be implemented and tested.

4.4. ASSIMILATION

Within the French atmospheric chemistry programme named ADOMOCA dedicated to the assimilation of satellite data with different chemical transport models (MOCAGE and LMDz-INCA) using the PALM coupler developed at CERFACS (Toulouse), the Ether system will integrate and archive all the assimilated data in the database.

4.5. IASI

The future IASI instrument onboard the MetOp platform will be launched in summer 2006. In parallel to the official data delivered by Eumetsat (columns of O_3 and CO), Ether will also help producing level 2 files of O_3 and CO vertical profiles, and will help characterizing the quality of the IASI measurements (Clerbaux et al., 2003).

5. Conclusions

The Ether atmospheric chemistry group is willing to:

- become a European system open to a wide scientific community,
- develop interfaces with international systems (e.g. the GeoMON proposed European programme),
- be the reference centre for scientific IASI data that will not be produced in the Eumetsat official centre,
- distribute assimilated data produced within the ADOMOCA French programme, and
- contribute to the planet security projects through data validation and data intercomparison with the aim of increase the reliability of knowledge and through the monitoring of pollution via the use of Chimere model data and satellite data coupled with assimilation techniques.

Finally, the mutual contribution of scientists through the Ether atmospheric chemistry group helps:

- defining common tools in order to answer to calls from International Announcement of Opportunity,
- designing methods or developing software to mix information from different origins, either from different space-borne instruments, or from airborne and ground-based instruments,
- analyzing the accuracy of the measurements, and quantifying their added-values with respect to the objectives of the atmosphere sounding.

References

Clerbaux, C., J. Hadji-Lazaro, S. Turquety, G. Mégie and P.F. Coheur, 2003. Trace gas measurements from infrared satellite for chemistry and climate applications, *Atmos.Chem. Phys. Discuss, 3, 2027-2058.*

Hauchecorne, Alain, 1999, Ether, service ARLETTY, description du modèle d'atmosphère. *Document interne, réf : ETH-NT-231-TECH-562-SA*

Hauchecorne, A., S. Godin, M. Marchand., B. Heese and C. Souprayen, 2002. Quantification of the transport of chemical constituents from the polar vortex to midlatitudes in the lower stratosphere using the high-resolution advection model MIMOSA and effective diffusivity, *J. Geophys. Res., 107(D20), 8289, doi: 10.1029/2001JD000491.*

Lefèvre, F., G.P. Brasseur, I. Folkins, A.K. Smith and P. Simon, 1994. Chemistry of the 1991-1992 stratospheric winter: Three-Dimensional model simulation, *JGR, 99, 8183-8195*.

Ricaud, P., F. Lefèvre, G. Berthet, D. Murtagh, E. J. Llewellyn, G. Mégie, E. Kyrölä, G. W. Leppelmeier, H. Auvinen, C. Boonne, S. Brohede, D. A. Degenstein, J. de La Noë, E. Dupuy, L. El Amraoui, P. Eriksson, W. F. J. Evans, U. Frisk, R. L. Gattinger, F. Girod, C. S. Haley, S. Hassinen, A. Hauchecorne, C. Jimenez, E. Kyrö, N. Lautié, E. Le Flochmoën, N. D. Lloyd, J. C. McConnell, I. C. McDade, L. Nordh, M Olberg, A. Pazmino, S. V. Petelina, A. Sandqvist, A. Seppälä, C. E. Sioris, B. H. Solheim, J. Stegman, K. Strong, P. Taalas, J. Urban, C. von Savigny, F. von Scheele, and G.Witt**,** 2005. Polar vortex evolution during the 2002 Antarctic major warming as observed by the Odin satellite, *J. Geophys. Res., Vol. 110, No. D5, D05302, 10.1029/2004JD005018*.

AN INTEGRATED APPROACH TO STUDY THE CHEMISTRY-CLIMATE INTERACTIONS IN THE ATMOSPHERE

PAUL C. SIMON*, MARTINE DE MAZIÈRE, MICHEL VAN ROOZENDAEL AND JEAN-CHRISTOPHER LAMBERT
Institut d'Aéronomie spatiale de Belgique

Abstract. The interaction between atmospheric chemistry and climate is an emerging topic for which the net impact on the Earth's system is still poorly quantified and understood.

It is well demonstrated that the changes in atmospheric chemistry strongly affect the climate. They are mainly due to anthropogenic activities with the emission of the greenhouse gases, pollutants, aerosols and ozone depleting substances. In addition, climate studies must take into account the various couplings between the radiative, dynamic and chemical processes occurring in both the troposphere and the stratosphere. Natural processes should also be studied and quantified in that context.

The understanding of climate-chemistry couplings requires a huge effort and a new approach to integrate the ground-based and the satellite observations. This new concept has been developed in the frame of international agencies and associations like the EC report GMES-GATO (A European Strategy for Global Atmospheric Observations), the Integrated Global Observing Strategy (IGOS) and the Integrated Global Atmospheric Chemistry Observations (IGACO) initiative serving the GEOSS aims for atmospheric composition.

The requirement for an integrated global observation system for climate-chemistry interactions will be described and the need for long-term atmospheric monitoring justified.

* To whom correspondence should be addressed. Paul C. Simon, Institut d'Aéronomie Spatiale de Belgique, avenue Circulaire 3, B-1180 Brussels, Belgium; e-mail: paul.simon@aeronomie.be

A. Perrin et al. (eds.), Remote Sensing of the Atmosphere for Environmental Security, 329–343.

The existing atmospheric observation systems based on remote sensing techniques will be reviewed, mainly the ground-based networks such as the WMO Global Atmospheric Watch (GAW) and the Network for the Detection of Stratospheric Change (NDSC). Data validation of some recent satellite sensors such as GOME, by means of infrared and UV-visible absorption spectroscopy will be briefly presented.

Keywords: atmospheric composition, climate, observing strategy, ground-based network, satellite validation.

1. Introduction

One the major scientific challenges for the XXIst century is the understanding of the natural and anthropogenic climate changes. The anthropogenic emissions of halogen compounds responsible for the depletion of the stratospheric ozone layer observed since the late seventies, the increase of primary pollutants, precursors of tropospheric ozone pollution, rising concentrations of greenhouses gases such as carbon dioxide and methane since the beginning of the industrial era with the related changes in the radiative balance of the Earth's atmosphere, reflect the increasing impact of human activity on the terrestrial atmosphere on a global scale.

The climate system and the atmospheric composition are strongly coupled and a key issue for climate studies is the understanding of the interaction between atmospheric chemistry and climate. As illustrated in Fig. 1, they are linked through a complex set of processes on a global scale involving the coupling between chemistry, radiation and dynamics which depends on the emissions of greenhouse gases, ozone precursors like nitrogen oxides (NO_x), volatile organic compounds (VOCs), methane (CH_4) and non-methane hydrocarbons (NMHC) and the emissions of ozone depleting substances (chlorine and bromine compounds).

In addition, transport of chemical between the stratosphere and the troposphere, in both directions must be taken into account.

The net impact of these interactions is currently poorly quantified and understood. Many scientific projects, including dedicated satellite missions are currently running or proposed for addressing those issues.

Long-term monitoring and observation is a prerequisite to better understand and quantify the atmospheric processes and for providing the scientific basis to understand how and why changes are occurring. Local monitoring activities collect information and give a detailed knowledge of

the behaviour and state of the atmosphere in a local and regional geographical scale. However, it is not sufficient to address climate-related issues on a planetary scale.

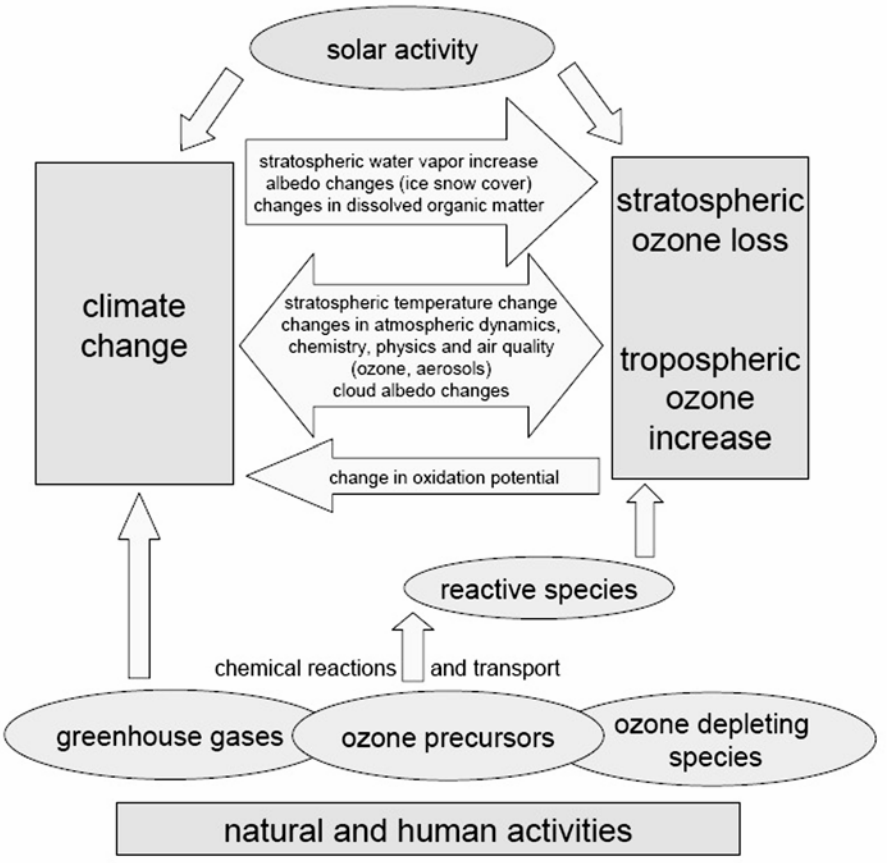

Figure 1. Atmospheric composition and climate interactions.

To insure long-term continuity and global scale, there is a mandatory need for combined and coordinated measurements with complementary sensors on different platforms (ground-based, balloon and aircraft, and space-borne) to provide integrated datasets, complemented with models and assimilation tools to make predictions reliable. The observations must be processed into information accessible to wide range of users including the scientific community, the environmental organisation, the policy-makers, and to verify the effectiveness of regulations and treaties. This data processing from Earth's observations to the information society relies, at each step, on updated and new scientific knowledge to close the gaps

towards the ultimate goal: product and information delivery required by the citizens (Fig. 2).

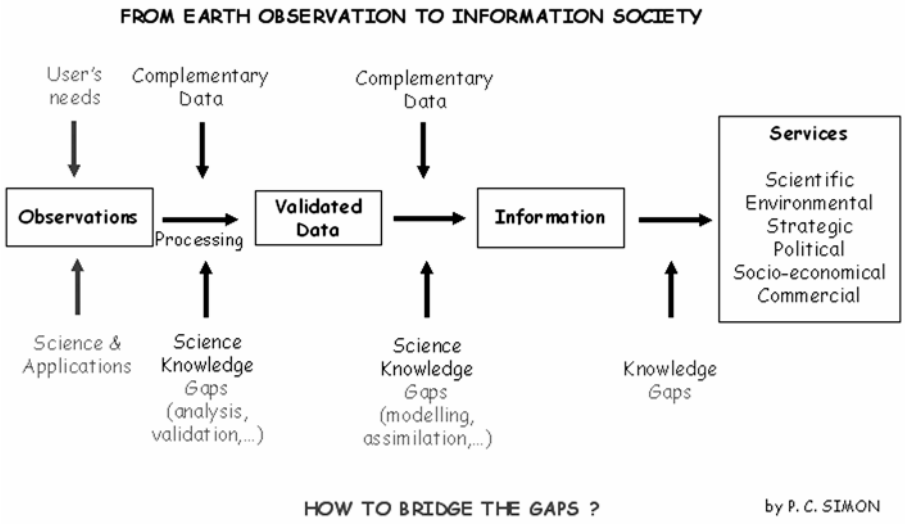

Figure 2. From Earth observation to information society: how to bridge the gaps?

2. Towards an integrated global observing system

The need of coordinated measurements to better study large-scale atmospheric phenomena was already recognized in the beginning of the 1950's with the preparation of the International Geophysical Year (IGY) which took place in 1957-1958. The IGY can be cited as the beginning of a large international effort towards networking, as for the first time scientists from around the world became involved *together* in a series of coordinated observations, exploring various geophysical phenomena covering the two hemispheres from the ground to the upper atmosphere. The global atmosphere was literally opened to detailed exploration taking advantage of the synoptic vision necessary to its study. In the same period of time, U.S.S.R. launched the first satellite on the 4th October 1957, initiating the space era.

Over the past decades, network operations evolved from a monitoring based on one single instrumental technique, e.g. the worldwide Dobson network for measuring ozone column abundances, to more complex instrumentations deployed in many ground-stations with a large variety of new experimental techniques.

The discovery of the ozone hole in 1985 thanks to a Dobson instrument installed at Halley Bay by the British Antarctic Survey revealed the

importance of ground-based networks. Indeed, the TOMS instrument onboard the satellite nimbus 7 launched at the end of 1978, did not make that discovery because the retrieval algorithms rejected the data apparently to low, by a priori decision of the scientific team. These circumstances put this emphasis on the importance of the calibration and the validation of satellite sensors by means of ground-based and in situ measurements. That initiated, for example, the concept of the Network for the detection of Stratospheric Change (NDSC, recently renamed NDACC) and, more recently the definition of the Integrated Global Observing Strategy (IGOS).

Considerable effort has been dedicated to instrument intercomparison campaigns and to satellite validation activities in order to improve the consistency among the various measurements. Satellites have enabled measurements to expand from the atmosphere above an isolated ground station to daily global coverage and have become essential in establishing a quasi-real time monitoring. More and more sophisticated instruments and techniques for ground-, space-based and/or for in situ use have been developed and together with the advances in numerical computation facilities, have broadened the potential to study, monitor and model atmospheric variables on a global scale. Today the networks not only support research related to the Earth's system and its expected evolution, but also allow scientific assessments on global change, e.g. the UNEP/WMO Ozone Assessment of Ozone Depletion and the IPCC report on Climate Change, and subsequent summaries and guidance for international policymaking.

Networks have thus been created to enhance the observing capability of the Earth's atmosphere. For example the National Oceanic and Atmospheric Administration (NOAA) and the Environmental Protection Agency (EPA) networks of observing stations, and similar facilities implemented by other agencies, provide data on the concentrations of greenhouse gases and ozone-depleting substances under the aegis of the international Global Atmosphere Watch (GAW) programme, a component of the World Meteorological Organization (WMO). Stratospheric ozone and key ozone-related compounds and parameters are measured through remote sensing by the international Network for the Detection of Stratospheric Change (NDSC). A European Commission effort providing substantial support to the NDSC network has been concentrated since the beginning of the 1990’s on several projects through long-term observations and related scientific activities at a large number of stations in Europe. Finally, activities including sounding measurements from several strategic locations are often combined either as part of regular programmes or in response of coordinated campaigns, e.g. the Arctic campaigns coordinated by the European Commission[1].

It is worthwhile to mention the general concept in which global measurement networks are integrated. Within the last decade, with the rapid evolution of technologies for environmental observations and the political recognition of the importance of global environmental problems, global observing systems integrating in situ and remotely sensed data, were planned and implemented, e.g., the Global Climate Observing System (GCOS), the Global Ocean Observing System (GOOS), and the Global Terrestrial Observing System (GTOS), each focusing on one of the major component of the biosphere. Such systems are concentrated towards the Integrated Global Observing Strategy (IGOS) that brings together the major satellite and ground-based systems for global environmental observations of the Earth's system in a framework that delivers maximum benefit and effectiveness in their final use. IGOS "is a partnership of international organisations that are concerned with global environmental change issues. It links research, long-term monitoring and operational programmes, bringing together the producers of global observations and the users that require them, to identify products needed, gaps in observations and mechanisms to respond to needs in the science and policy communities. Its principal objectives are to integrate satellite, airborne and in-situ observation systems". IGOS, established in 1998, has adopted a process of themes in which observations are made for selected fields of common interest among a group of partners. One of them concerns atmospheric chemistry: the "Integrated Global Atmospheric Chemistry Observations" (IGACO). The final report was approved in 2004.

GMES, a key challenge for Europe, was defined in 1999 as a European joint initiative between the European Commission and the European Space Agency (ESA). GMES aims at designing and establishing by 2008 a European capacity for the provision and use of operational services for Global Monitoring of Environment and Security.

The situation of the production of information presents the following shortcomings:

- Information is often not adequate, since it is not available in time or not reliable. However, there is in the mean time an increased amount of observation data and enhanced ability to process them with progress performed in sensors technique and information technologies;
- The production of synthetic and consolidated information is still very difficult. The variety of data, stemming from extremely wide sources, with various time-periods and geographic levels explains these difficulties;

- The lack of a continuous monitoring leads to gaps and incompatibilities in data series or even interruption in series. A particular data collection often ends with the research programme which supported it.

The key challenge for Europe is then clearly defined: identifying the means to secure sustainable, coherent and efficient information for environment and security policies.

On July 31, 2003, the International Earth observation Summit held in Washington, D. C., emphasized the vital importance of Earth Observation activities in the following Declaration:

"In order to monitor continuously the state of the Earth, to increase understanding of dynamic Earth processes, to enhance prediction of the Earth system, and to further implement our environmental treaty obligations, we recognize the need to support:

- Improved coordination of strategies and systems for observations of the Earth and identification measures to minimize data gaps, with a view to moving towards a comprehensive, coordinated, and sustained Earth observation system of systems;
- A coordinated effort to involve and assist developing countries in improving and sustaining their contributions to observing systems, as well as their access to and effective utilization of observations, data and products, and the related technologies by addressing capacity-building needs related to Earth observations".

The Global Earth Observation System of Systems (GEOSS) was borne.

3. The Global Atmospheric Watch (GAW) network

GAW is a component of the WMO aiming at making long-term, quality controlled observations of the chemical composition of the atmosphere. Its objective is to provide a basis for early detection of atmospheric change, the prediction of future atmospheric states, and the development of environmental policies[2]. It is thus considered as the atmospheric chemistry component of the Global Climate Observing System (GCOS).

More than 80 member countries are currently participating in GAW measurement programme. As of March 2005, there were some 300 GAW stations, of which 23 were global stations and the remaining were regional ones (Fig. 3).

Many contributing stations cooperate as well with GAW. The global stations measure many of the key variables, acting as standards for other stations in their region. Most regional stations carry out a narrower set of parameters[3].

Within the global measuring programme, high priority is given to measurements of the vertical distribution of ozone, total column ozone, greenhouse gases, precipitation chemistry, aerosol components, and UV. Ground-based observations are the backbone of the GAW network, but the need of aircraft, satellite and other remote sensing operations is also recognized in order to establish a quasi-real time monitoring capability and to offer sustainable support to the ground-based facilities[4].

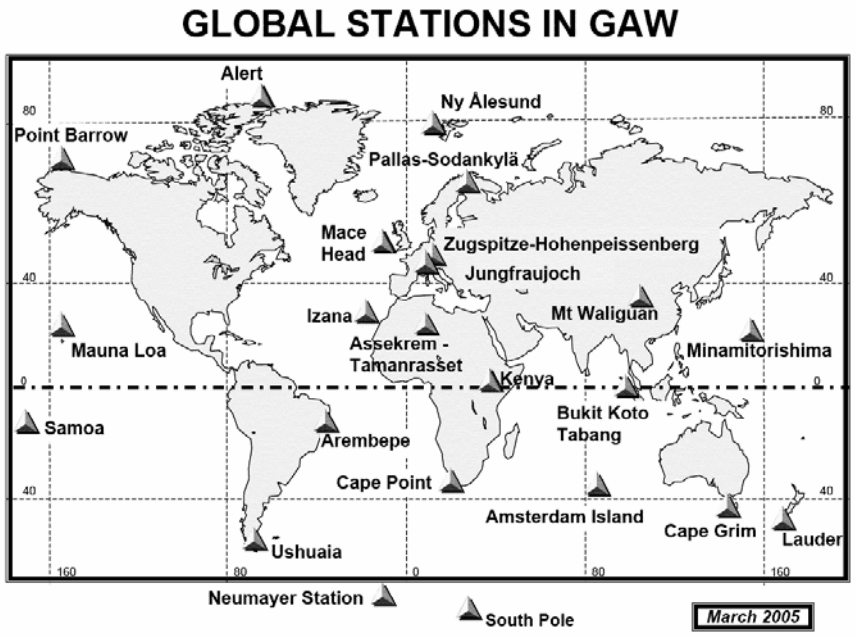

Figure 3. Global station network of the Global Atmospheric Watch (courtesy WMO-GAW).

To ensure the required high quality of GAW data, quality assurance and quality control procedures have been developed, including instrument calibration and intercomparison. Currently, four Quality Assurance/Science Activity Centres (QA/SACs) are implemented. While the QA/SACs perform a network-wide quality review, the stations have primary responsibility for the quality of the data generated at their sites Ten World Calibration Centres, assisted by Regional Calibration Centres, maintain calibration standards, provide instrument calibrations and training to the stations. To collect, process, analyse and distribute data obtained from the GAW stations, six World Data Centres are in operation, mostly focused on data archiving and data exchange: ozone and UV radiation (Toronto, Canada), greenhouse gases (Tokyo, Japan), precipitation chemistry

(Albany, USA), surface ozone (Kjeller, Norway), solar radiation (St Petersburg, Russia) and aerosols (Ispra, Italy). The GAW data are available from the Centres upon request to all organizations, scientific institutions and individual scientists[2].

GAW is not only a system for monitoring but also for assessment of the chemical composition and related physical characteristics of the global atmosphere. Scientific results made available from observations at the GAW stations stimulated the adoption of a number of international conventions and declarations aimed at protecting the atmosphere and the environment as a whole. Over the years, WMO has initiated and coordinated a number of scientific assessments on specific atmospheric parameters. The most recent is the 2002 Scientific Assessment of ozone depletion for the Parties of the Montreal Protocol. This assessment is a focused update of the state of understanding regarding the ozone depletion issue, based on the scientific literature and building upon the broad-scoped 1998 report[5].

Another essential task of GAW is to encourage and support modelling activities for assessing long-range atmospheric transport and deposition of pollutants as well as air pollution in urban and other areas affected by natural or man-made air pollution. Those activities are mainly implemented in cooperation with various regional programmes. To guide GAW towards its objectives, a strategic plan has been implemented, including detailed set of guidelines for establishing working plans and programmes and for developing GAW facilities[4]. The Commission for Atmospheric Sciences (CAS) that leads the programme has designated the EC Panel of Experts/CAS Working Group on Environmental Pollution and Atmospheric Chemistry (the Panel) as the overall steering body for the GAW. The Panel has established six Scientific Advisory Groups (SAGs), namely for ozone, radiation, aerosols, precipitation chemistry, greenhouse gases and reactive gases. Each of them is responsible for establishing and overseeing the observation network, and the data quality procedures and scientific work for its assigned parameters. Operational support for GAW and coordination with other WMO programmes is provided by the Environment Division of the Atmospheric secretariat also monitors the operation of the GAW. Many activities depend on Research and Environment Programme Department (the Secretariat).

4. The Network for the Detection of Stratospheric Change (NDSC)

The NDSC is another major component of the international atmospheric research effort initiated at the end of the 1980's. Started in 1991, it has been

a contributing part of the GAW programme since 1993 and is considered by WMO to be a very important complementary component.

The network (Fig. 4) is based on a set of high-quality, remote-sensing research stations designed to make worldwide observations through which changes in the physical and chemical state of the stratosphere can be determined and understood. Currently, the network operates at five primary stations, enhanced by more than 40 other worldwide sites (see the NDSC web site), where complementary measurements of one or more of the parameters of interest are performed. Over 20 countries are currently involved with NDSC research activities[7].

Figure 4. Site locations of the Network for the Detection of Stratospheric Change (NDSC).

High precision, state-of-the-art measurements are performed by several instruments including lidars, UV-visible spectrometers, Fourier Transform Infrared (FTIR) spectrometers, microwave radiometers and balloon sondes. The network is further supported by other existing ground-based monitoring networks and by satellite measurements. The NDSC measurement priorities are based on the assumption of continuing the ground-based monitoring of ozone, chemical species and dynamical tracers related to ozone chemistry, and providing an independent validation for satellite sensors. The “Institut d'Aéronomie Spatiale de Belgique” (IASB-BIRA) contributes to the NDSC measurements with systematic observations of atmospheric constituents, by

means of absorption spectroscopy, at three NDSC sites in Europe: Harestua (Norway), the "Observatoire de Haute Provence" (OHP) and the International Scientific Station of the Jungfraujoch (ISSJ). Bromine monoxide measurements[8] performed at Harestua are given in Fig. 5, and the NO_2 time series obtained at the ISSJ with an UV-visible instrument (SAOZ) with comparison with GOME and HALOE satellite observations[9] are displayed in Fig. 6.

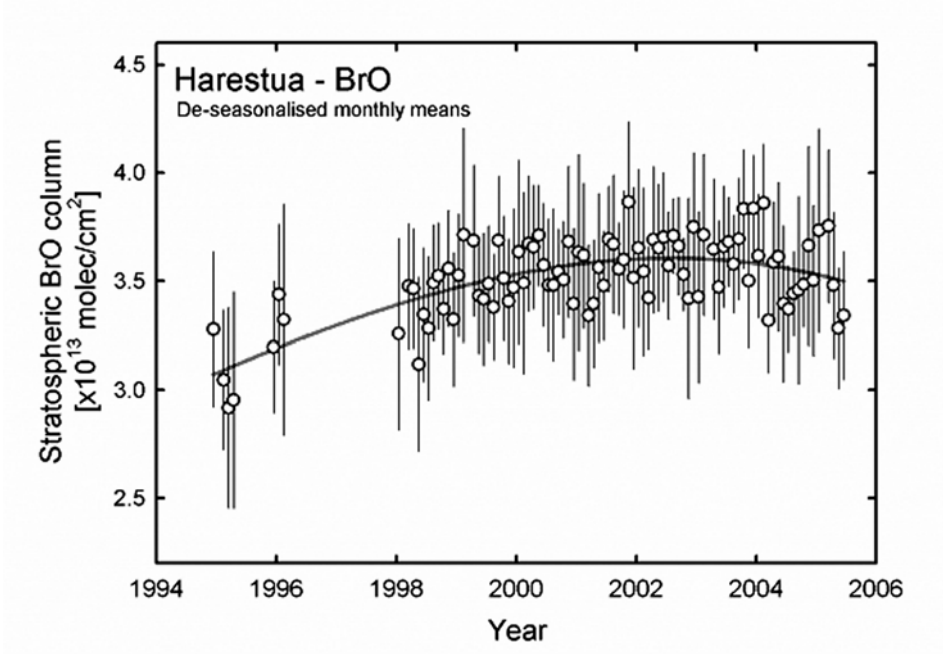

Figure 5. Stratospheric bromine monoxide column densities measured above Harestua (60.2° N, 10.8°E).

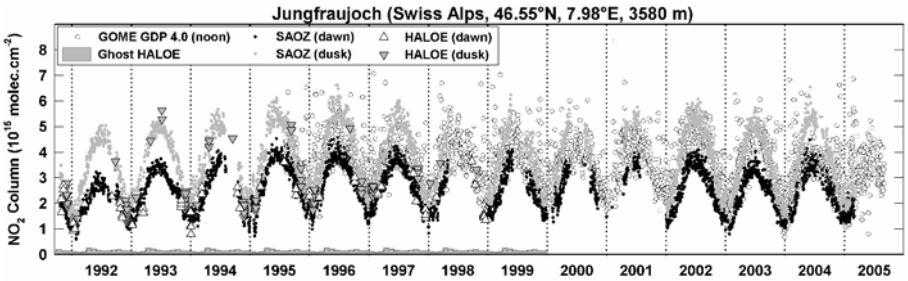

Figure 6. Time series of ozone and NO_2 total column measurements above ISSJ (46.5°N, 8°E), derived from regular UV-visible observations (SAOZ) carried out since 1992. Ozone ground-based data are compared with satellite measurements from GOME and HALOE.

Within the measuring programme of the NDSC, quality control procedures have been implemented, including an ongoing programme of instrument intercomparison and validation. Analysis and modelling of NDSC observations are also key components of the network. Moreover, results from the Network have made important contributions to various international reports, and, more recently, to the WMO Scientific Assessment of ozone depletion[5].

5. Other networks

Ozone sonde networks are also supporting the collection of ozone data through balloon-borne measurements launched at strategic locations all around the globe, for validation, processing, and/or modelling activities. In the northern hemisphere, over 650 sondes where launched from a network of 36 stations, in 20 countries, at mid and high latitudes, during THESEO-SOLVE 2000 and VINTERSOL-SOLVE II 2003-2004 campaigns coordinated by the European Commission and NASA, with the task to shed light on the processes that lead to stratospheric ozone loss in the Arctic and at middle latitudes[10].

6. Examples of recent satellites product validation

The atmospheric chemistry related satellite missions have been compiled by the NDSC Satellite Working Group (see web site in section 8).

Since the TOMS launch onboard Nimbus7 in 1978, new generation of sensors have been developed in the UV, visible and near infrared ranges. They are used in orbit for ozone and related species observations, e.g. GOME onboard the ERS-2 satellite, since 1995, atmospheric chemistry sensors onboard Envisat, since 2002, and OMI onboard AURA, since 2004. The NDSC directly contributes to their validation[11, 12, 13, 14, 15, 16] leading to improvement in the ground data processing as illustrated for the ozone product from GOME (fig. 8). NO_2 validation with respect to latitude is given in fig. 9.

7. Conclusions

The actual needs for observing the Earth's system are expanding and require more complex experiments covering a wide range of instruments and observed species on a global spatial and temporal scale. The value of an integrated global observing system is worldwide recognised: it is the only way to produce systematic, coherent data, with a well-known precision, accuracy and clearly documented quality, capable of addressing climate-

related issues in a global scale. The sources of such data are mainly to be found in the continuity of the combination of ground-based observations,

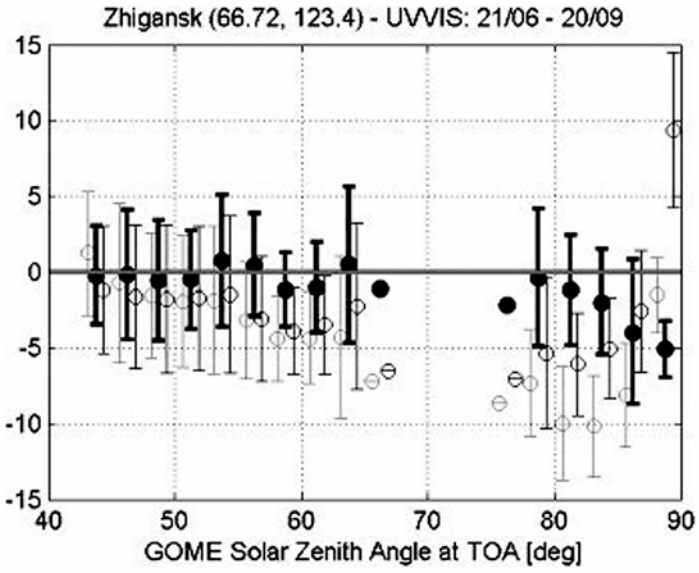

Figure 8. Relative differences in percent between GOME and UV-visible spectrometer total ozone measurements, for the recent GOME Data Processors (black dots: GDP version. 4.0).

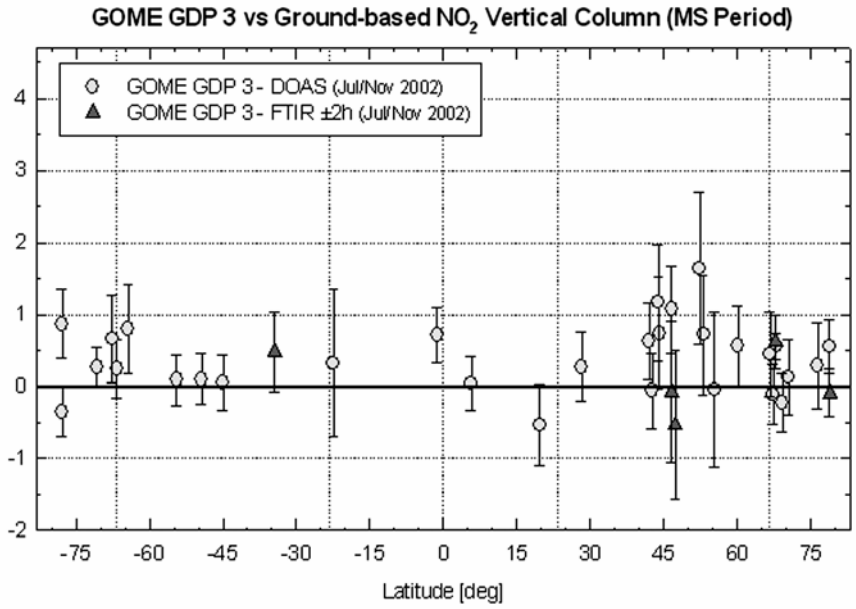

Figure 9. Validation of NO2 GOME measurement in July-Nov. 2002 time frame with NDSC UV-visible and Fourier Transform spectrometers, with respect to latitude. The vertical axis represents the absolute difference (10^{15} molecules/cm^2). Highest differences are observed at mid-latitude, in the Northern hemisphere (tropospheric pollution).

satellite and air-borne data (aircraft, balloon). They all play complementary roles in the establishment of a long-term monitoring capability of global coverage for process and global changes studies, and remain essential to constraint models and predict the future of our planet with reduced uncertainties.

8. List of related web sites

Background information about the international programmes, networks and satellite missions mentioned in this paper can be found at the following URL addresses:

- CEOS: http://www.ceos.org/
- ENVISAT: http://envisat.esa.int/
- EPA: http://www.epa.gov/
- GCOS: http://www.wmo.ch/web/gcos/whatisgcos.htm
- GMES: http://www.gmes.info/
- GOME: http://earth.esa.int/ers/gome/
- IGOS/IGACO: http://www.eohandbook.com/igosp/Atmosphere.htm
- MSC: http://exp-studies.tor.ec.gc.ca/e/ozone/ozone.htm
- NDSC: http://www.ndsc.ws
- NDACC (formerly NDSC): http://www.ndsc.ws/
- NDACC (formerly NDSC) Satellite Working Group: http://www.oma.be/NDSC_SatWG/Home.html
- SOLVE II: http://geo.arc.nasa.gov/sgg/SOLVE2-website/index.html
- THESEO 2000: http://www.nilu.no/projects/theseo2000/
- VINTERSOL: http://www.ozone-sec.ch.cam.ac.uk/VINTERSOL/
- WMO/GAW: http://www.wmo.ch/

References

1. A European Strategy for Global Atmospheric Monitoring, European Commission, EUR 21154, 2004.
2. The Fifth WMO Long-term Plan 2000-2009 (Global Atmospheric Watch report series).
3. Strategy for implementation of the Global Atmosphere Watch Programme (2001-2007). A contribution to the implementation of the WMO long-term plan (Global Atmospheric Watch report series No 142).
4. Global Atmosphere Watch Measurements Guide (Global Atmospheric Watch report series No 143).

5. Scientific Assessment of Ozone Depletion, UNEP/WMO 2002 report.
6. Sixth Session of the EC Panel of Experts/CAS Working Group on Environmental Pollution and Atmospheric Chemistry, Zurich, Switzerland, 8-11 March 1999 (Global Atmospheric Watch report series No 135).
7. Lambert, J.-C., M. Van Roozendael, M. De Mazière, P.C. Simon, J.-P. Pommereau, F. Goutail, A. Sarkissian, and J.F. Gleason, Investigation of pole-to-pole performances of spaceborne atmospheric chemistry sensors with the NDSC, *J. Atmos. Sci.* 56, Global Measurement Systems for Atmospheric Composition Special Issue, 176-193 (1999).
8. Van Roozendael, M., personal communication, 2005.
9. Lambert, J.-C, personal communication, 2006
10. A European Strategy for Global Atmospheric Monitoring, European Commission, EUR 21154, 2004.
11. NDSC Brochure; Network for the Detection of Stratospheric Change: a long-term international scientific investigation of the ozone layer and its links to global climate (2001).
12. Lambert, J.-C., M. Van Roozendael, P.C. Simon, J.-P. Pommereau, F. Goutail, J.F. Gleason, S.B. Andersen, D.W. Arlander, N.A. Bui Van, H. Claude, J. de La Noë, M. De Mazière, V. Dorokhov, P. Eriksen, A. Green, K. Karlsen Tørnkvist, B.A. Kåstad Høiskar, E. Kyrö, J. Leveau, M.-F. Merienne, G. Milinevsky, H.K. Roscoe, A. Sarkissian, J.D. Shanklin, J. Staehelin, C. Wahlstr¢m Tellefsen, and G. Vaughan, Combined characterisation of GOME and TOMS total ozone measurements from space using ground-based observations from the NDSC, Advances in Space Research, Vol. 26, 1931-1940, 2000.
13. Lambert, J.-C., J. Granville, M. Van Roozendael, J.-F. Müller, F. Goutail, J.-P. Pommereau, A. Sarkissian, P. V. Johnston, and J. M. Russell III, Global Behaviour of Atmospheric NO2 as Derived from the Integrated Use of Satellite, Ground-based Network and Balloon Observations, in Atmospheric Ozone - 19th Quad. Ozone Symp., Sapporo, Japan, 2000, Ed. by NASDA, 201-202, 2000.
14. Van Roozendael, M., T. Wagner, A. Richter, I. Pundt, D. W. Arlander, J. P. Burrows, M. Chipperfield, C. Fayt, P. V. Johnston, J.-C. Lambert, K. Kreher, K. Pfeilsticker, U. Platt, J.-P. Pommereau, B.-M. Sinnhuber, K. K. Tørnkvist, and F. Wittrock, Intercomparison of BrO Measurements From ERS-2 GOME, Ground-based and Balloon Platforms, Advances in Space Research, Vol. 29, 1661-1666, 2002.
15. Hendrick, F., B. Barret, M. Van Roozendael, H. Boesch, A. Butz, M. De Mazière, F. Goutail, C. Hermans, J.-C. Lambert, K. Pfeilsticker, and J.-P. Pommereau, Retrieval of nitrogen dioxide stratospheric profiles from ground-based zenith-sky UV-visible observations: Validation of the technique through correlative comparisons, reviewed in Atmospheric Chemistry and Physics Discussions, Vol. 4, pp. 2867-2904, 2004; published in Atmospheric Chemistry and Physics, Vol. 4, pp. 2091-2106, 2004
16. Piters, A. J. M., K. Bramstedt, J.-C. Lambert, and B. Kirchhoff, Overview of SCIAMACHY validation: 2002-2004, Invited paper opening the "Geophysical validation of SCIAMACHY: 2002-2004" Special Issue of Atmospheric Chemistry and Physics, MS-NR ACPD-2005-0125, 2005.

List of Contributors

Numbers in parentheses indicate the pages on which the author's contributions begin.

Abdel Wahab M.	*Astronomy and meteorological department, Cairo University, Giza, Egypt.*	(285)
Alfaro S.	*LISA, UMR-CNRS 7583, Universities Paris 12&7 and CNRS, 61, avenue du Général de Gaulle, 94010, Créteil, France.*	(285)
Allen G.	*Earth Observation Science, Dept. of Physics and Astronomy, University of Leicester, LE1 7RH, United Kingdom.*	(71)
Antony B.K.	*Department of Environmental, Earth, and Atmospheric Sciences, Intercampus Graduate School of Marine Sciences and Technology, University of Massachusetts Lowell, 265 Riverside Street, Lowell, MA 01854-5045, USA.*	(203)
Belotti C.	*IFAC-CNR - via Madonna del Piano, 10 - 50019 Sesto Fiorentino (FI) – Italy.*	(57
Ben Sari D.	*Mohammadia School of Engineering, Avenue Ibnsina B.P. 765 Rabat-Agdal, Rabat Morocco.*	(271)
Berger P.	*LIDAR, s.r.o., Washingtonova 17, 110 00 Prague 1, Czech Republic.*	(301)
Bezpalcová K.	*Institute of Thermomechanics, Academy of Sciences of the Czech Republic, Dolejškova 5, 182 00 Prague 8, Czech Republic.*	(301)
Boonne C.	*Institut Pierre-Simon Laplace, Université Paris VI, 4, place Jussieu, 75252 Paris, France.*	(317)
Buffa G.	*IPCF-CNR and Dipartimento di Fisica "E. Fermi", Universit`a di Pisa, Largo Pontecorvo 3, I-56127 Pisa, Italy.*	(237)
Carli B.	*IFAC-CNR - via Madonna del Piano, 10 - 50019 Sesto Fiorentino (FI) – Italy.*	(57)
Carvajal M.	*Departamento de Fisica Aplicada, Facultad de Ciencias Experimentales, Avda. de las FF.AA. s/n, Universidad de Huelva, 21071, Huelva, Spain*	(171)
Cazzoli G.	*Dipartimento di Chimica "G. Ciamician", Università di Bologna, Via Selmi 2, I-40126 Bologna, Italy.*	(237)
Černý A.	*LIDAR, s.r.o., Washingtonova 17, 110 00 Prague 1, Czech Republic.*	(301)
Chance K.	*Harvard-Smithsonian Center for Astrophysics, Atomic and Molecular Physics Division, 60 Garden Street, Cambridge, MA, 02138, USA*	(1)

Colmont J.-M.	*Laboratoire de Physique des Lasers, Atomes et Molécules, UMR CNRS 8523, Université des Sciences et Technologies de Lille, F-59655 Villeneuve d'Ascq, France.*	(221)
Danihelka P.	*VŠB – Technical University of Ostrava, Faculty of Safety Engineering, Lumírova 13, 700 30 Ostrava-Výškovice, Czech Republic.*	(301)
Del Bianco S.	*IFAC-CNR - via Madonna del Piano, 10 - 50019 Sesto Fiorentino (FI) – Italy.*	(57)
Delmas R.	*Laboratoire d'Aérologie, UMR 5560, 14 Avenue Edouard Belin, 31400, Toulouse, France.*	(317)
De Mazière M.	*Institut d'Aéronomie Spatiale de Belgique, avenue Circulaire 3, B-1180 Brussels, Belgium.*	(329)
Doussin J.-F.	*Laboratoire Interuniversitaire des Systèmes Atmosphériques, Universities Paris 12&7 and CNRS, 61 av. du Général de Gaulle, 94010 Créteil Cédex, France .*	(107)
Drábková S.	*VŠB – Technical University of Ostrava, Faculty of Mechanical Engineering, 17. listopadu 15, 708 33 Ostrava-Poruba, Czech Republic.*	(301)
Drouin B.J.	*California Institute of Technology, Jet Propulsion Laboratory, 4800 Oak Grove Dr., Pasadena, CA 91016, USA.*	(257)
Engst P.	*LIDAR, s.r.o., Washingtonova 17, 110 00 Prague 1, Czech Republic.*	(301)
Fadil A.	*Mohammadia School of Engineering, Avenue Ibnsina B.P. 765 Rabat-Agdal, Rabat Morocco.*	(271)
Fischer H.	*Institute for Meteorology and Climate Research (IMK-ASF), Forschungszentrum Karlsruhe and Universität Karlsruhe, P. O. Box 3640, 76021 Karlsruhe, Germany.*	(41)
Flaud J.-M.	*Laboratoire Interuniversitaire des Systèmes Atmosphériques, Universities Paris 12&7 and CNRS, 61 av. du Général de Gaulle, 94010 Créteil Cédex,France.*	(107)
Funke B.	*Instituto de Astrof˝ısica de Andaluc´ıa (CSIC), Apdo. 3004, 18008 Granada, Spain.*	(87)
Gamache R.	*Department of Environmental, Earth, and Atmospheric Sciences Intercampus Graduate School of Marine Sciences and Technology University of Massachusetts Lowell, 265 Riverside Street, Lowell, MA 01854-5045, USA.*	(203)
Girod F.	*Centre National d'Etudes Spatiales, 18 Avenue Edouard Belin, 31401 Toulouse cedex 4, France.*	(317)
Gratien A.	*Laboratoire Interuniversitaire des Systèmes Atmosphériques, Universities Paris 12&7 and CNRS, 61 av. du Général de Gaulle, 94010 Créteil Cédex, France.*	(107)

Jaňour Z.	*Institute of Thermomechanics, Academy of Sciences of the Czech Republic, Dolejškova 5, 182 00 Prague 8, Czech Republic.*	(301)
Jensen P.	*FB C – Theoretische Chemie, Bergische Universität, D–42097 Wuppertal, Germany.*	(171)
Kozubková M.	*VŠB – Technical University of Ostrava, Faculty of Mechanical Engineering, 17. listopadu 15, 708 33 Ostrava-Poruba, Czech Republic.*	(301)
Kubát P.	*J. Heyrovský Institute of Physical Chemistry, Academy of Sciences of the Czech Republic, Dolejškova 3, 182 23 Prague 8, Czech Republic.*	(301)
Lambert J.-Ch.	*Institut d'Aéronomie Spatiale de Belgique, avenue Circulaire 3, B-1180 Brussels, Belgium.*	(329)
Langen J.	*ESA, Earth Observations Science and Applications Department, ESTEC, Keplerlaan 1, 2200 AG Noordwijk, The Netherlands*	(27)
Lin H.	*Department of Chemistry, University of Colorado at Denver, PO Box 173364, Denver, Colorado 80217, U. S. A.*	(171)
Lòpez-Puertas M.	*Instituto de Astrofisica de Andalucıa (CSIC), Apdo. 3004, 18008 Granada, Spain.*	(87)
Lyulin O.M.	*Laboratory of Theoretical Spectroscopy, Institute of Atmospheric Optics SB RAS, Akademicheskii 1, 634055 Tomsk, Russian Federation*	(139)
Meacham P.	*Earth Observation Science, Dept. of Physics and Astronomy, University of Leicester, LE1 7RH, United Kingdom.*	(71)
Moore D.P.	*Earth Observation Science, Dept. of Physics and Astronomy, University of Leicester, LE1 7RH, United Kingdom.*	(71)
Orphal J.	*Laboratoire Interuniversitaire des Systèmes Atmosphériques, Universities Paris 12&7 and CNRS, 61 av. du Général de Gaulle, 94010 Créteil Cédex, France.*	(107)
Perevalov V.I.	*Laboratory of Theoretical Spectroscopy, Institute of Atmospheric Optics SB RAS, Akademicheskii 1, 634055 Tomsk, Russian Federation*	(139, 161)
Perrin A.	*Laboratoire Interuniversitaire des Systèmes Atmosphériques, Universities Paris 12&7 and CNRS, 61 av. du Général de Gaulle, 94010 Créteil Cédex,France.*	(107)
Phulpin Th.	*Centre National d'Etudes Spatiales, 18 Avenue Edouard Belin, 31401 Toulouse cedex 4, France.*	(317)
Picquet-Varrault B.	*Laboratoire Interuniversitaire des Systèmes Atmosphériques, Universities Paris 12&7 and CNRS, 61 av. du Général de Gaulle, 94010 Créteil Cédex,France.*	(107)

Puzzarini C.	*Dipartimento di Chimica "G. Ciamician", Universit`a di Bologna, Via Selmi 2, I-40126 Bologna, Italy.*	(237)
Remedios J.J.	*Earth Observation Science, Dept. of Physics and Astronomy, University of Leicester, LE1 7RH, United Kingdom.*	(71)
Ricaud Ph.	*Laboratoire d'Aérologie, UMR 5560, 14 Avenue Edouard Belin, 31400, Toulouse, France.*	(317)
Rohart F.	*Laboratoire de Physique des Lasers, Atomes et Molécules, UMR CNRS 8523, Université des Sciences et Technologies de Lille, F-59655 Villeneuve d'Ascq, France.*	(221)
Sembhi H.	*Earth Observation Science, Dept. of Physics and Astronomy, University of Leicester, LE1 7RH, United Kingdom.*	(71)
Simon P.C.	*Institut d'Aéronomie Spatiale de Belgique, avenue Circulaire 3, B-1180 Brussels, Belgium.*	(329)
Smith M.-A. H.	*Science Directorate, NASA Langley Research Center Hampton, VA 23681-2199 U.S.A.*	(185)
Střižík M.	*VŠB – Technical University of Ostrava, Faculty of Safety Engineering, Lumírova 13, 700 30 Ostrava-Výškovice, Czech Republic* *&* *Institute of Thermomechanics, Academy of Sciences of the Czech Republic, Dolejškova 5, 182 00 Prague 8, Czech Republic.*	(301)
Tarrini O.	*IPCF-CNR and Dipartimento di Fisica "E. Fermi", Universita di Pisa, Largo, Pontecorvo 3, I-56127 Pisa, Italy.*	(237)
Tashkun S.A.	*Laboratory of Theoretical Spectroscopy, Institute of Atmospheric Optics SB RAS, Akademicheskii 1, 634055 Tomsk, Russian Federation*	(139, 161)
Teffo J.-L.	*Laboratoire de Physique Moléculaire pour l'Atmosphère et l'Astrophysique, 4 Place Jussieu, 75252 Paris Cedex 05, France.*	(139, 161)
Thiel W.	*Max-Planck-Institut für Kohlenforschung, Kaiser-Wilhelm-Platz 1,* *D–45470 Mülheim an der Ruhr, Germany.*	(171)
Vander Auwera J.	*Service de Chimie Quantique et Photophysique, Université Libre de Bruxelles, C.P. 160/09, 50 avenue F. D. Roosevelt, B-1050 Brussels, Belgium.*	(123)
Van Roozendael M.	*Institut d'Aéronomie Spatiale de Belgique, avenue Circulaire 3, B-1180 Brussels, Belgium.*	(329)
Waterfall A.M.	*Earth Observation Science, Dept. of Physics and Astronomy, University of Leicester, LE1 7RH, United Kingdom.*	(71)

Wlodarczak G.	*Laboratoire de Physique des Lasers, Atomes et Molécules, UMR CNRS 8523, Université des Sciences et Technologies de Lille, F-59655 Villeneuve d'Ascq, France.*	(221)
Yurchenko S.N.	*Max-Planck-Institut für Kohlenforschung, Kaiser-Wilhelm-Platz 1, D–45470 Mülheim an der Ruhr, Germany.*	(171)
Zelinger Z.	*J. Heyrovský Institute of Physical Chemistry, Academy of Sciences of the Czech Republic, Dolejškova 3, 182 23 Prague 8, Czech Republic.*	(301)
Zheng J.	*Max-Planck-Institut für Kohlenforschung, Kaiser-Wilhelm-Platz 1, D–45470 Mülheim an der Ruhr, Germany.*	(171)

Index of Subjects

Subjects which appear several times in one article are indicated by a bold page number.